
ELECTRONIC PROPERTIES
OF NOVEL MATERIALS—
SCIENCE AND TECHNOLOGY OF
MOLECULAR NANOSTRUCTURES

DISTRIBUTION STATEMENT A
Approved for Public Release
Distribution Unlimited

20000816 026



Forest of Carbon Nanotubes standing up from a solid substrate
(see the contribution of Z. F. Ren et al. in Section IV, pp. 263-267).

ELECTRONIC PROPERTIES OF NOVEL MATERIALS— SCIENCE AND TECHNOLOGY OF MOLECULAR NANOSTRUCTURES

XIII International Winterschool

Kirchberg, Tirol, Austria February- March 1999

EDITORS

Hans Kuzmany
Universität Wien, Austria

Jörg Fink
*Institut für Festkörper- und Werkstoff-Forschung
Dresden, Germany*

Michael Mehring
Universität Stuttgart, Germany

Siegmar Roth
*Max-Planck-Institut für Festkörperforschung
Stuttgart, Germany*

AIP

American Institute of Physics

**AIP CONFERENCE
PROCEEDINGS 486**

Melville, New York

Editors:

Hans Kuzmany
Institut für Materialphysik
Universität Wien
Strudlhofgasse 4
A-1090 Wien, AUSTRIA
E-mail: kuzman@pap.univie.ac.at

Jörg Fink
Institut für Festkörper-und Werkstoff-Forschung
Postfach 270016
D-01171 Dresden, GERMANY
E-mail: j.fink@ifw-dresden.de

Michael Mehring
2. Physikalisches Institut
Universität Stuttgart
Pfaffenwaldring 57
D-70550 Stuttgart, GERMANY
E-mail: sk22@physik.uni-stuttgart.de

Siegmar Roth
Max-Planck-Institut für Festkörperforschung
Heisenbergstr. 1
D-70569 Stuttgart, GERMANY
E-mail: roth@klizix.mpi-stuttgart.mpg.de

Authorization to photocopy items for internal or personal use, beyond the free copying permitted under the 1978 U.S. Copyright Law (see statement below), is granted by the American Institute of Physics for users registered with the Copyright Clearance Center (CCC) Transactional Reporting Service, provided that the base fee of \$15.00 per copy is paid directly to CCC, 222 Rosewood Drive, Danvers, MA 01923. For those organizations that have been granted a photocopy license by CCC, a separate system of payment has been arranged. The fee code for users of the Transactional Reporting Service is: 1-56396-900-9/99/\$15.00.

© 1999 American Institute of Physics

Individual readers of this volume and nonprofit libraries, acting for them, are permitted to make fair use of the material in it, such as copying an article for use in teaching or research. Permission is granted to quote from this volume in scientific work with the customary acknowledgment of the source. To reprint a figure, table, or other excerpt requires the consent of one of the original authors and notification to AIP. Republication or systematic or multiple reproduction of any material in this volume is permitted only under license from AIP. Address inquiries to Office of Rights and Permissions, Suite 1N01, 2 Huntington Quadrangle, Melville, N.Y. 11747-4502; phone: 516-576-2268; fax: 516-576-2499; e-mail: rights@aip.org.

L.C. Catalog Card No. 99-65786
ISBN 1-56396-900-9
ISSN 0094-243X
DOE CONF- 990221

Printed in the United States of America

CONTENTS

Preface	xiii
Table of Previous Kirchberg Winterschools.....	xiv
Organizer, Patronage, Supporters, and Sponsors	xv

I. FULLERENE MATERIALS

The Jahn-Teller Distortion of C_{60}^- as Determined by ESR.....	3
W. Bietsch, J. Bao, A. Schilder, and M. Schwoerer	
Origin of Intrinsic Luminescence from C_{60} Single Crystals.....	7
I. Akimoto and K.-i. Kan'no	
Polymeric Fullerenes: From C_{60} to C_{70}.....	12
A. Soldatov, P. Nagel, V. Pasler, S. Lebedkin, C. Meingast, G. Roth, and B. Sundqvist	
In situ ATR-FTIR Spectroelectrochemical Comparison of Pristine and Polymerized C_{60} Films.....	16
H. Neugebauer, C. Kvarnström, H. Sitter, C. Jögl, H. Kuzmany, and N. S. Sariciftci	
Structure of Phototransformed C_{60} Revisited	20
T. Pusztai, G. Oszlányi, G. Faigel, K. Kamarás, L. Gránásy, and S. Pekker	
Atomic Force Microscopy Analysis of Nucleation and Diffusion of C_{60} on Hot Substrates.....	24
M. Haluška and H. Kuzmany	
NMR Study of C_{60}-C_7H_8 by Cross Polarization and Polarization Inversion of Rare-Spin Magnetization	28
A.-S. Grell, I. Messari, P. Pirotte, P. Tekely, R. Céolin, H. Szwarc, and F. Masin	
Is the Ground State of A_1C_{60} ($A=Rb, Cs$) Antiferromagnetic?	32
J. Rahmer, S. Knorr, A. Grupp, M. Mehring, J. Hone, and A. Zettl	
Comparative Study of Ferromagnetic and Non-Ferromagnetic Modifications of TDAE-C_{60}.....	37
D. Arčon, R. Blinc, P. Cevc, A. Omerzu, and D. Mihailović	
Spin-Singlets in Metallic Cubic Quenched CsC_{60}	42
V. Brouet, H. Alloul, F. Quéré, G. Baumgartner, and L. Forró	
Distinct Polymer Chain Orientations in KC_{60} and RbC_{60}	47
P. Launois, R. Moret, S. C. Erwin, J. Hone, and A. Zettl	
Low Symmetry Structures in the Li-Rb-C_{60} Phase Field.....	52
A. Lappas, E. Aslanis, K. Prassides, A. N. Fitch, and M. Hanfland	
Conduction Electron Spin Resonance in the Superconducting State of K_3C_{60}.....	56
N. M. Nemes, J. E. Fischer, G. Baumgartner, L. Forró, and A. Jánossy	

Orientational Ordering of Alkali Ammonia Clusters in Ammoniated Alkali Fullerenes (NH₃)K₃C₆₀ and (ND₃)K₃C₆₀	60
K. Ishii, T. Watanuki, A. Fujiwara, H. Suematsu, Y. Iwasa, H. Shimoda, T. Takenobu, and T. Mitani	
Electronic Properties of the Na₂AC₆₀ Family (A=K, Rb, Cs).....	64
N. Čegar, F. Simon, G. Baumgartner, A. Sienkiewicz, L. Forró, B. Ruzicka, L. Degiorgi, and L. Mihály	
Structure and Physical Properties of Cs₃C₆₀ under Ambient and High Pressures	69
Y. Kubozono, S. Fujiki, Y. Takabayashi, Y. Yoshida, S. Kashino, K. Ishii, A. Fujiwara, and H. Suematsu	
Structural Studies of Superconducting Li₃CsC₆₀.....	73
S. Margadonna and K. Prassides	
Structure of Ca₄(NH₃)C₆₀	78
G. Oszlányi, S. Pekker, G. Faigel, and L. Forró	

II. ENDOHEDRAL FULLERENES

Atoms in Molecular Cages	85
B. Pietzak, M. Waiblinger, K. Lips, and A. Weidinger	
IR and Raman Analysis of Diatomic Encapsulates in Fullerene Cages	90
M. Hulman, M. Krause, M. Inakuma, J. Dennis, H. Shinohara, and H. Kuzmany	
Endohedral Fullerenes with Lower Carbon Cage Sizes	95
L. Dunsch, P. Kuran, P. Georgi, and A. Gromow	
Atoms in Fullerene Traps as Probes for Local Fields.	101
C. Knapp, N. Weiden, H. Käß, and K.-P. Dinse	
Cerium Metallofullerenes	106
P. Georgi, P. Kuran, and L. Dunsch	
The Electronic Properties of Charged N@C₆₀.....	111
L. Udvardi	
Structural and Magnetic Studies of the Endohedral Metallofullerene Ce@C₈₂	115
C. J. Nuttall, Y. Watanabe, Y. Inada, K. Nagai, T. Muro, D. H. Chi, T. Takenobu, Y. Iwasa, and K. Kikuchi	
Dynamic Motion of Ce@C₈₀—Comparison Study with Ce@C₈₂	120
W. Sato, K. Suecki, K. Kikuchi, S. Suzuki, Y. Achiba, H. Nakahara, Y. Ohkubo, K. Asai, and F. Ambe	
Structural Phase Transitions of Endohedral Metallofullerene La@C₈₂ Studied by Single Crystal X-ray Diffraction	124
T. Watanuki, A. Fujiwara, K. Ishii, Y. Matsuoka, H. Suematsu, K. Ohwada, H. Nakao, Y. Fujii, T. Kodama, K. Kikuchi, and Y. Achiba	
Endohedral Rare Earth Fullerenes—Electronic and Dynamic Properties.	128
K. Vietze, G. Seifert, M. Richter, L. Dunsch, and M. Krause	

The Electronic Structure of Mono- and Dimetallofullerenes by Photoemission Spectroscopy	132
T. Pichler, M. S. Golden, P. Kuran, L. Dunsch, M. Knupfer, J. Fink, M. R. C. Hunt, P. Rudolf, M. Inakuma, and H. Shinohara	
A Raman Study of Empty C₈₄ Isomers D₂ and D_{2d} and Three Isomers of Sc₂@C₈₄	136
M. Krause, M. Hulman, H. Kuzmany, T. J. S. Dennis, M. Inakuma, and H. Shinohara	
A Vibrational Spectroscopic Structure Analysis of Eu@C₇₄	140
M. Krause, P. Kuran, and L. Dunsch	
Light-Induced Release of Nitrogen from Fullerene Cages	144
B. Goedde, N. Weiden, and K.-P. Dinse	
Atomic Hydrogen in the Si₈O₁₂ Cage	148
M. Waiblinger, B. Pietzak, K. Lips, T. J. S. Dennis, A. Weidinger, M. Päch, and R. Stösser	

III. NEW NANOSTRUCTURED MATERIALS

Oligomer-Fullerene Dyads and Triads as Model Compounds for Bulk-Heterojunction PV Cells	155
R. A. J. Janssen, E. Peeters, B. M. W. Langeveld-Voss, P. A. van Hal, J. Knol, and J. C. Hummelen	
Photo-Induced Charge-Transfer Processes in Fullerene-Containing Dyad and Triad Molecules	161
S. Knorr, A. Grupp, M. Mehring, G. Grube, and F. Effenberger	
C₅₉N on Silicon Surfaces: Monomers, Dimers, and Multilayers	165
M. J. Butcher, F. H. Jones, P. H. Beton, P. Moriarty, K. Prassides, and N. Tagmatarchis	
Homonuclear Bonds in BN Clusters?	170
P. W. Fowler, K. M. Rogers, T. Heine, and G. Seifert	
Synthesis and Characterisation of Organometallic Compounds of Fullerene Derivatives.....	175
N. Tagmatarchis and K. Prassides	
Non-IPR Fullerenes: C₃₆ and C₇₂.....	179
Z. Slanina, X. Zhao, F. Uhlík, and E. Ōsawa	
Effect of Alkali Doping on the Structural Stability of Solid C₃₆.....	183
A. Zettl, C. Piskoti, J. C. Grossman, M. L. Cohen, and S. G. Louie	
Isolation and Characterisation of [84]Fullerene Isomers	187
T. J. S. Dennis, H. Shinohara, S. Margadonna, K. Prassides, M. Hulman, and H. Kuzmany	
New Three-Component Systems Based on C₆₀.....	191
R. N. Lyubovskaya, D. V. Konarev, E. I. Yudanov, Y. M. Shul'ga, N. V. Drichko, and Y. V. Zubavichus	
Cluster-Assembled Amorphous Carbon Nano-Foam Synthesized by High-Pulse-Rate Laser Ablation.....	196
A. V. Rode, E. G. Gamaly, R. G. Elliman, A. S. Kheifets, and B. Luther-Davies	

Self-Formation of Nanostructures from Hydrated Aggregates and Nanocrystals of $(C_{60})_n$ Molecules on the Liquid Crystal Layer.....	200
E. Buzaneva, A. Gorchinskyi, A. Benilov, Y. Kirghisov, F. V. Pogorelov, Y. Astashkin, V. Bukalo, Y. Prilutski, G. S. Durov, P. Scharff, and G. Andrievsky	
Chains of Carbon Nanoparticles from the Interaction of Fullerenes with Thin Metal Films.....	205
H. Kanzow, A. Ding, H. Sauer, T. Belz, and R. Schlögl	
Electrochemical Preparation of Carbon Chains and Nanoparticles.....	209
L. Kavan	
Preparation of Carbyne-Like Films by Dehydrochlorination of Poly(Vinylidene Chloride)	213
T. Danno, K. Murakami, and R. Ishikawa	
X-Ray Emission Spectroscopy Study of C_2F Intercalated with Benzene	217
A. V. Antich, A. V. Okotrub, L. G. Bulusheva, and V. M. Paasonen	
Vanadium Pentoxide Nanowires.....	221
J. Muster, V. Krstic, M. Burghard, and S. Roth	
Production and Investigation of Vanadium Pentoxide (V_2O_5) Nanostructures Grown in IR Laser-Field.....	226
R. Vajtai, J. Janicskó-Csáthy, L. Thiên-Nga, L.-M. Bonard, and L. Forró	
Perfect Nanospheres from Polymerized Lipofullerenes	231
O. Vostrowsky, X. Camps, A. Hirsch, M. Hetzer, H. Clausen-Schaumann, S. Bayerl, and T. Bayerl	

IV. PREPARATION AND CHARACTERIZATION OF CARBON NANOTUBES

A Continuous Wave CO_2 Laser Reactor for Nanotubes Synthesis.....	237
J.-L. Cochon, J. Gavillet, M. Lamy de la Chapelle, A. Loiseau, M. Ory, and D. Pigache	
Synthesis, Purification, and Characterisation of Multi- and Single-Wall Nanotubes Produced by Catalytic Decomposition of Hydrocarbons.....	241
J.-F. Colomer, P. Piedigrosso, I. Willems, Z. Konya, A. Fonseca, and J. B. Nagy	
Production of Bundles of Single Walled Nanotubes by a Simple Laser Ablation Technique.....	245
W. K. Maser, E. Muñoz, A. M. Benito, M. T. Martínez, G. F. de la Fuente, E. Anglaret, and J.-L. Sauvajol	
Metal Mixtures Catalysed Carbon Nanotube Synthesis	249
Z. Kónya, N. Nagaraju, A. Tamási, K. M. Mukhopadhyay, A. Fonseca, and J. B. Nagy	
Solar Synthesis of Single Wall Carbon Nanotubes	254
L. Alvarez, T. Guillard, E. Anglaret, J. L. Sauvajol, P. Bernier, G. Flamant, G. Olalde, D. Laplaze, M. T. Martinez, A. Benito, and W. K. Maser	

Carbon Arc Plasma Doped with Fe and Co/Ni: Spectroscopy and Formation of Carbon Nanostructures	258
A. Huczko, H. Lange, P. Byszewski, A. Koshio, and H. Shinohara	
Large Arrays of Well-Aligned Carbon Nanotubes	263
Z. F. Ren, Z. P. Huang, J. W. Xu, D. Z. Wang, and J. H. Wang	
Sulfur: The Key for Filling Carbon Nanotubes with Metals	268
A. Loiseau, N. Demoncy, O. Stéphan, C. Colliex, and H. Pascard	
Alkali-Metal Intercalation in Carbon Nanotubes	273
F. Béguin, L. Duclaux, K. Méténier, E. Frackowiak, J. P. Salvetat, J. Conard, S. Bonnamy, and P. Lauginie	
About the Composition of Single Wall Carbon Nanotube Bundles: An Analysis from Optical, Raman, and IR Experiments	278
J. Kürti, M. Milnera, M. Hulman, O. Zhou, and H. Kuzmany	
Polymers of Single Wall Nanotubes: Geometry, Diffraction Pattern, and Electronic Spectrum Modelling	284
L. A. Chernozatonskii, E. G. Gal'pern, N. R. Serebryanaya, and I. V. Stankevich	
The Characterization of SWNT Containing Soot by Optical Spectroscopy	288
O. Jost, R. Friedlein, A. A. Gorbunov, T. Pichler, M. Reibold, H.-D. Bauer, M. Knupfer, M. S. Golden, L. Dunsch, J. Fink, and W. Pompe	
Evolution of Carbon Single-Walled Nanotubes Diameter as a Function of the Synthesis Parameters: A Raman Study	292
M. Lamy de la Chapelle, J. M. Benoit, S. Lefrant, C. Journet, and P. Bernier	

V. PROPERTIES OF CARBON NANOTUBES

Neutron Scattering Studies of Carbon Nanotubes	299
E. Anglaret, S. Rols, and J. L. Sauvajol	
Statistical Analysis of the Electronic Structure of Single Wall Carbon Nanotubes in Buckypaper	304
S. Eisebitt, I. Wirth, G. Kann, and W. Eberhardt	
Characterization of Single Wall Carbon Nanotubes by Scanning Tunneling and Scanning Force Microscopy	308
W. Clauss, M. Freitag, D. J. Bergeron, and A. T. Johnson	
STM Investigation of Single-Wall Carbon Nanotubes at Room Temperature	313
A. Hassanien, M. Tokumoto, Y. Kumazawa, H. Kataura, Y. Maniwa, S. Suzuki, and Y. Achiba	
Scanning Tunneling Microscopy of Carbon Nanotubes: Simulation and Interpretation	319
V. Meunier and P. Lambin	

The Use of Computer Simulation to Investigate Tip Shape and Point Contact Effects During Scanning Tunneling Microscopy of Supported Nanostructures	323
G. I. Márk, L. P. Biró, J. Gyulai, P. A. Thiry, and P. Lambin	
Optical Absorption and Resonance Raman Scattering of Carbon Nanotubes	328
H. Kataura, Y. Kumazawa, N. Kojima, Y. Maniwa, I. Umez, S. Masubuchi, S. Kazama, X. Zhao, Y. Ando, Y. Ohtsuka, S. Suzuki, and Y. Achiba	
<i>In situ</i> Raman Investigations of Single-Wall Carbon Nanotubes Pressurized in Diamond Anvil Cell	333
E. D. Obraztsova, H. T. Lotz, J. A. Schouten, M. E. Kooi, A. V. Osadchy, V. L. Kuznetsov, and V. I. Zaikovskii	
Surface Enhanced Raman Spectroscopy of Single Wall Carbon Nanotubes	338
G. S. Duesberg, J. Muster, M. Burghard, H. J. Byrne, and S. Roth	
Disorder Effects on Density of States and Electronic Conductance in Carbon Nanotubes	342
K. Harigaya	
Electronic Structure Studies of Carbon Nanostructures Using Electron Energy-Loss Spectroscopy in Transmission	346
T. Pichler, R. Friedlein, M. Knupfer, M. S. Golden, J. Fink, K. Mukhopadhyay, T. Sugai, H. Shinohara, and T. Cabioch	
The Effects of Dimensionality on the π-Plasmon-Dispersion in Multi-Wall Carbon Nanotubes	351
R. Friedlein, T. Pichler, M. Knupfer, M. S. Golden, K. Mukhopadhyay, T. Sugai, H. Shinohara, and J. Fink	
Molecular Mechanics Study of Carbon Nanotubes	355
I. László	
Knock-on Damage in Single Wall Carbon Nanotubes by Electron Irradiation	360
B. W. Smith and D. E. Luzzi	
Sliding, Stretching, and Tapering: Recent Structural Results for Carbon Nanotubes	364
V. H. Crespi, P. Zhang, and P. E. Lammert	

VI. ELECTRONICS OF MOLECULAR NANOSTRUCTURES

Temperature Dependence of the Resistivity of Individual Multi-Walled Pure/Boron Doped Carbon Nanotubes at Elevated Temperatures	371
B. Wei, R. Spolenak, P. Kohler-Redlich, M. Rühle, and E. Arzt	
Temperature Dependent Resistivity of Large Ropes of Single-Walled Carbon Nanotubes	375
J. Lefebvre, M. Radosavljevic, J. Hone, and A. T. Johnson	

Manipulation of the Transport Properties of Single-Walled Nanotubes by Alkali Intercalation and Local Charge Transfer	379
J. Hone, R. Antonov, A. T. Johnson, M. Bockrath, P. L. McEuen, and A. Zettl	
Femtosecond Time-Resolved Photoemission as a Probe of Electronic Transport in Single Wall Carbon Nanotubes.	384
T. Hertel and G. Moos	
One-Dimensional Transport in Bundles of Single-Walled Carbon Nanotubes	388
D. H. Cobden, J. Nygård, M. Bockrath, and P. L. McEuen	
Electrical Transport in Carbon Nanotube Rings: Coherence and Localization	393
P. Avouris, H. R. Shea, and R. Martel	
Quantentransport in Multi-Wall Carbon Nanotubes	399
C. Schönenberger, A. Bachtold, C. Strunk, T. Nussbaumer, J.-P. Salvetat, and L. Forró	
Electron Interference Effect in Multi-Wall Carbon Nanotubes.	403
A. Fujiwara, K. Tomiyama, H. Suematsu, M. Yumura, and K. Uchida	
Charge Transport in Carbon Nanotube Transistors.	407
K. Liu, M. Burghard, S. Roth, and P. Bernier	
Luttinger Liquid Behavior in Single-Wall Nanotubes.	411
A. Komnik and R. Egger	
Electric Resistivity and Magnetoresistance of Some Superhard and Ultrahard Fullerites in the Range 300-2K	416
V. D. Blank, S. G. Buga, G. A. Dubitsky, X.-M. Zhu, E. Nyeanchi, and B. Sundqvist	
Electron Transport Through a Gold-Bisthiolterthiophene-Gold Junction.	421
C. Kergueris, J.-P. Bourgoin, S. Palacin, D. Esteve, C. Urbina, M. Magoga, and C. Joachim	

VII. APPLICATIONS

Capacitance Properties of Carbon Nanotubes	429
E. Frackowiak, K. Méténier, R. Pellenq, S. Bonnamy, and F. Béguin	
Electron Field Emission from Carbon.	433
J. Robertson	
Field Emission from Carbon Nanotubes and Its Application to Electron Sources	439
Y. Saito and S. Uemura	
Thin Film Cold Cathode from Nanostructured Carbon.	444
A. N. Obraztsov, I. Y. Pavlovsky, A. P. Volkov, V. L. Kuznetsov, and A. L. Chuvilin	
Field Emission Properties of Carbon Nanowires from <i>ab initio</i> Calculations	448
M. Bianchetti, P. Buonsante, F. Ginelli, A. Lorenzoni, H. E. Roman, and R. A. Broglia	

Electrocatalytic Properties of the C₆₀, C₇₀, C₇₆, C₇₈, and C₈₄	
Fullerene Anions.....	452
F. D'Souza, J.-P. Choi, and W. Kutner	
Carbon Nanotubes and Gas Adsorption.....	456
I. Stepanek, L. C. de Menorval, R. Edwards, and P. Bernier	
Electrochemical Storage of Hydrogen in Carbon Single Wall Nanotubes.....	462
C. Nützenadel, A. Züttel, and L. Schlapbach	
Characterization of Multi-Walled Carbon Nanotubes-PMMA Composites.....	466
C. Stéphan, T. P. Nguyen, S. Curran, B. Lahr, and S. Lefrant	
Functionalisation of Carbon Nanotubes for Composites	470
S. Delpeux, K. Méténier, R. Benoit, F. Vivet, L. Boufendi, S. Bonnamy, and F. Béguin	
Chemical Functionalization of Carbon Nanotubes	474
S. Pekker, J.-P. Salvétat, E. Jakab, J.-M. Bonnard, and L. Forró	
Electronic Structures and Applications of Carbon Nanotubes	478
P. Kim, T. W. Odom, J. Huang, and C. M. Lieber	
Combinatorial Chemistry Approach to Development of Molecular	
Plastic Solar Cells.....	483
D. Godovsky, O. Inganäs, C. J. Brabec, N. S. Sariciftci, J. C. Hummelen, R. A. J. Janssen, M. Prato, M. Maggini, J. Segura, and N. Martin	
Charge Transfer and Relaxation Dynamics of Excited Electronic	
States in Organic Photoreceptor Materials With and Without C₆₀	487
C. Schlebusch, J. Morenzin, B. Kessler, and W. Eberhardt	
Optical Limiting Materials Based on Fullerene Derivatives	492
M. Prato, M. Maggini, G. Scorrano, G. Brusatin, M. Guglielmi, M. Meneghetti, R. Signorini, R. Bozio, and D. M. Guldi	
SPM Investigation of Superhard Carbon Prepared from C₆₀ Fullerene	497
A. Hassanien, M. E. Kozlov, and M. Tokumoto	
Raman Spectrum and Stability of (C₅₉N)₂	501
C. Jogl, H. Kuzmany, M. Krause, W. Plank, O. Dubay, N. Tagmatarchis, and K. Prassides	
Author Index.....	507

PREFACE

The present book contains the proceedings of the 13th International Winterschool on Electronic Properties of Novel Materials in Kirchberg, Tirol, Austria. It was held from 27th February to 6th March, 1999 in Hotel Sonnalp. The series of these schools started in 1985. Originally the school was held every second year and was devoted to conducting polymers. After the discovery of high temperature superconductors, the periodicity changed to annual format and the topic alternated between conjugated polymers and superconductors. Since fullerenes are both conjugated compounds and in some cases superconductors, it was tempting to choose fullerenes as topic for the Kirchberg schools. The evident extension of this topic is carbon nanotubes and so the title changed from Fullerenes via Fullerene Derivatives and Fullerene Nanostructures to Molecular Nanostructures. This gradual change enables us to keep a fairly large interdisciplinary scientific community together and to stimulate numerous international cooperations. A compilation of the previous Kirchberg Winterschools will be presented in the table at the end of this preface.

The term Molecular Nanostructures implies the "bottom-up" (synthetic) approach, as opposed to the "top-down" (lithography and etching) techniques in semiconductor technology. As for the physics, we are in a field where solid state physics and molecular physics overlap. This is nicely seen on the example of carbon nanotubes. Their diameter is in the order of a few nanometers, and thus perpendicular to their axis, nanotubes are molecular (different diameters lead to different electronic structures), while along their axis they are extended solids.

Most contributions to the winterschool were on carbon nanotubes and on fullerenes. In the proceedings we have two sections on nanotubes and two on fullerenes. One chapter deals with new nanostructured materials, and the sections on Electronics of Molecular Nanostructures and on Applications stress the technological aspects of this dynamic field of research.

The meeting could not have taken place without the support of the Bundesministerium für Wissenschaft und Forschung in Wien, the Forschungszentrum Technik und Umwelt in Karlsruhe, the US Army Research Development and Standardization Group in London, and the Verein zur Förderung der Winterschulen in Kirchberg, as well as from numerous industrial sponsors. Without their contribution, all the enthusiasm and dedication could be wasted and so we express our gratitude to the sponsors and supporters.

Finally, we are indebted, as ever, to the managers of the Hotel Sonnalp, Herrn Gradnitzer and Frau Jurgeit, and to their staff for their continuous support and for their patience with the many special arrangements required during the meeting.

H. Kuzmany, J. Fink, M. Mehring, S. Roth

Table of Previous Kirchberg Winterschools

Year	Titel	Published by
1985	Electronic Properties of Polymers and Related Compounds	Springer Series in Solid-State Sciences 63
1987	Electronic Properties of Conjugated Polymers	Springer Series in Solid-State Sciences 76
1989	Electronic Properties of Conjugated Polymers III - Basic Models and Applications	Springer Series in Solid-State Sciences 91
1990	Electronic Properties of High-T_c Superconductors and Related Compounds	Springer Series in Solid-State Sciences 99
1991	Electronic Properties of Polymers - Orientation and Dimensionality of Conjugated Systems	Springer Series in Solid-State Sciences 107
1992	Electronic Properties of High-T_c Superconductors	Springer Series in Solid-State Sciences 113
1993	Electronic Properties of Fullerenes	Springer Series in Solid-State Sciences 117
1994	Progress in Fullerene Research	World Scientific Publ. 1994
1995	Physics and Chemistry of Fullerenes and Derivatives	World Scientific Publ. 1995
1996	Fullerenes and Fullerene Nanostructures	World Scientific Publ. 1996
1997	Molecular Nanostructures	World Scientific Publ. 1998
1998	Electronic Properties of Novel Materials – Progress in Molecular Nanostructures	AIP Conference Proceedings 442 (1998)

ORGANIZER
Institut für Materialphysik
Universität Wien

PATRONAGE
Dr. Caspar Einem
Bundesminister für Wissenschaft und Verkehr

Magnifizenz
Univ. Prof. Dr. Wolfgang Greissenegger
Rektor der Universität Wien

Herbert Noichel
Bürgermeister of Kirchberg

SUPPORTERS
Bundesministerium für Wissenschaft und Forschung, AT
Forschungszentrum Karlsruhe, Technik und Umwelt, DE
US-Army Research, Development and Standardization Group, UK
Verein zur Förderung der Internationalen Winterschulen in Kirchberg, AT

SPONSORS
Aventi Research & Technologies, Industrial Park, Building G830,
D-65926 Frankfurt am Main 80, Germany
AVL LIST GmbH, Hans List Platz 1, A-8020 Graz, Austria
BRUKER Analytische Meßtechnik GmbH, Wikingersstraße 13,
D-76189 Karlsruhe, Germany
CREDITANSTALT BANKVEREIN, Nußdorferstraße 2, A-1090 Wien, Austria
NOVOCONTROL GmbH, Obererbacher Str. 9, D-56414 Hundsangen, Germany
OMIKRON Vacuumphysik GmbH, Idsteiner Str. 78, D-65232 Taunusstein, Germany
PIRELLI CAVI e SISTEMI S.p.A. Viale Sacra 222, I-20126 Milano, Italy
VAKUUM- und SYSTEMTECHNIK GmbH (ALCATEL), Hohenauergasse 10,
A-1190 Wien, Austria

The financial assistance from the sponsors and from the supporters is gratefully
acknowledged.

I. FULLERENE MATERIALS

The Jahn-Teller Distortion of C_{60}^- as Determined by ESR

W. Bietsch, J. Bao, A. Schilder, M. Schwoerer

*Experimentalphysik II and Bayreuther Institut für Makromolekülforschung (BIMF)
Universität Bayreuth, 95440 Bayreuth*

Abstract. $[P(C_6H_5)_4]_2C_{60}I$ is an ideal model system to study C_{60} mono radical anion in a charged surrounding since the C_{60} radical anions are well separated on a regular crystal lattice by the aid of large organic counter ions. They do not contribute to the ESR signal as they are all closed shell molecules. At low temperatures two Lorentzian ESR lines are observed which can be ascribed to two different orientations of the C_{60} molecules as detected by x-ray analysis of the crystal structure. The g-tensor of the two lines corresponds to the Jahn-Teller distortion of C_{60}^- . Tetragonal crystal symmetry, molecular symmetry together with the crystal field support the D_{2h} distortion of C_{60}^- which is in agreement with the observed non axial g-tensor.

INTRODUCTION

Since the availability of macroscopic amounts of fullerenes many attempts have been made to intercalate fullerenes with metal ions or with organic molecules. Interesting properties like superconductivity or ferromagnetism have been observed for C_{60} -based fullerenes. Among the fullerenes buckminsterfullerene C_{60} possesses the highest symmetry. As consequence of the high symmetry the C_{60} molecule has highly degenerated electronic and vibronic states which makes C_{60} Jahn-Teller active upon charging. On the other hand fullerenes are molecular solids with charged fullerenes in which many molecular properties essentially survive due to weakly bounded molecules. Since the fullerenes become charged in building up the fullerenes the Jahn-Teller distortion of C_{60} is an important molecular property and is found to be the driving mechanism for superconductivity [1], and a cooperative Jahn-Teller effect of C_{60}^- has been suggested for the magnetic ordering in TDAE- C_{60} [2]. Historically ESR provided the first experimental evidence of the Jahn-Teller effect in Cu^{2+} -salts [3]. Our ESR studies on TDAE- C_{60} [4] lead us to the question whether the Jahn-Teller distortion of C_{60}^- can be detected in ESR spectra.

MEASUREMENTS AND RESULTS

For this investigation we used single crystals of C_{60} -tetraphenylphosphoniumiodide ($[P(C_6H_5)_4]_2C_{60}I$) which are an excellent model system to study well separated C_{60}^-

CP486, *Electronic Properties of Novel Materials— Science and Technology of Molecular Nanostructures*,

edited by H. Kuzmany, J. Fink, M. Mehring, and S. Roth

© 1999 American Institute of Physics 1-56396-900-9/99/\$15.00

radical anions in a crystalline environment [5]. They were grown by electro-crystallization techniques according to a recipe of Pénicaud et al [6]. The temperature dependence of microwave conductivity measurements (figure 1) on powder samples of micro crystals reveal that the electron spins are localized on the C_{60}^- which are well separated due to the relatively large organic cations $P^+(C_6H_5)_4$ [5].

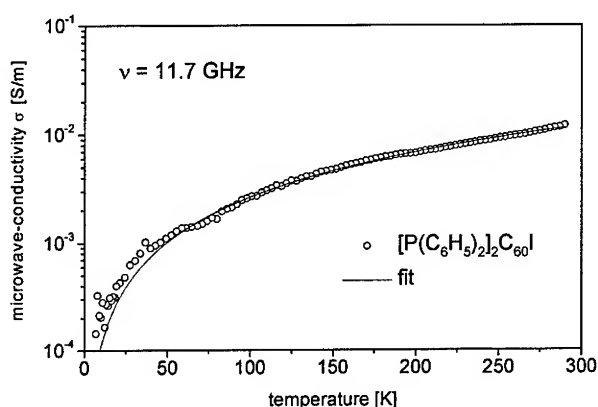


FIGURE 1. Temperature dependence of the microwave conductivity of $[P(C_6H_5)_4]_2C_{60}I$ at 11.7 GHz [4].

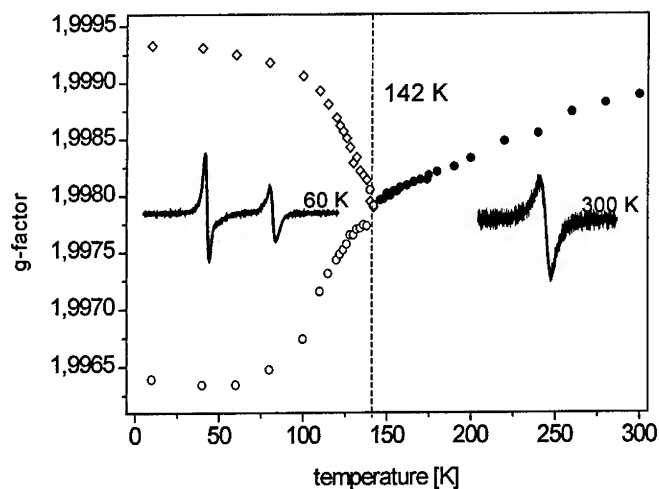


FIGURE 2. Temperature dependence of the g-factor of $[P(C_6H_5)_4]_2C_{60}I$ at 94 GHz (W-band).

At room temperature one single Lorentzian ESR line was observed (figure 2). Below 140 K this line starts to split into two Lorentzian lines. While lowering the temperature the splitting increases to a value of $\Delta g = g_1 - g_2 \approx 3 \cdot 10^{-3}$ at 4 K. The temperature below

of which the splitting of the two ESR lines occurs is found to be independent of the frequency (10 GHz, 34 GHz and 94 GHz, i.e. X-, Q, W-band). In agreement with the x-ray data the two observed ESR lines can be ascribed to two different sites of C_{60}^- within the tetragonal unit cell.

The g-value is isotropic above 140 K. Below 140 K the g-tensor of the two ESR lines becomes anisotropic: $g_x = 1,9961_2$, $g_y = 1,9964_5$, $g_z = 1,9995_6$ for $T = 50$ K (figure 3). The deviation from an axial type g-tensor is only slightly but still observable within experimental errors.

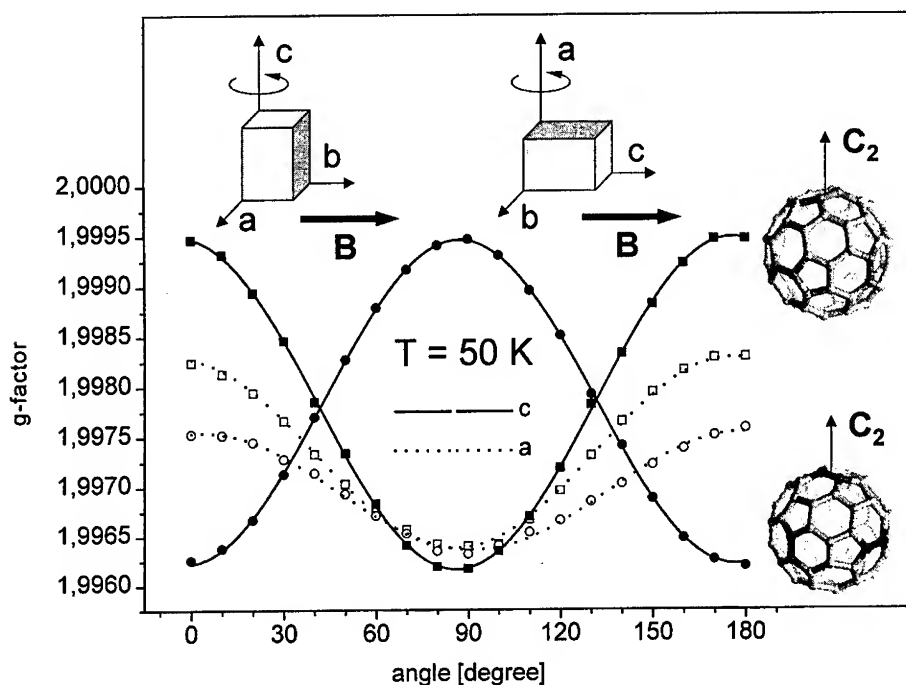


FIGURE 3. Angular dependence of the g-factor of $[P(C_6H_5)_4]_2C_{60}I$ at 50 K for rotation around the a- and the c-axis of the single crystal (top). The g-factor of the two lines rotated around c-axis are shifted by 90 degree which is in agreement with the two different sites (schematically shown by the depicted C_{60} orientations right) found by x-ray structure analysis.

DISCUSSION AND CONCLUSIONS

In the low temperature regime, i.e. below 140 K, the two observed Lorentzian ESR lines stem from localized electron spins on C_{60}^- . All counter ions ($P^+(C_6H_5)_4$ and I^-) are closed shell molecules and thus have no radical spins which contribute to the ESR signal. They form a charged environment, i.e. a crystal field for the C_{60} mono radical

ions shown schematically in figure 4. The C_2 axis of the C_{60}^- anion is parallel to the c axis of the crystal. Symmetry considerations for the Jahn-Teller distorted C_{60}^- and the crystal field of tetragonal symmetry lead to the conclusion that only the D_{2h} distortion fit together. This is in agreement with our ligand field calculations which stabilizes the D_{2h} distortion symmetry [7] and the experimentally observed non axial g-tensor. At low temperatures the dynamics of the charge distortion is hindered i.e. jumps between different possible D_{2h} orientations are not favored due to the charged surrounding (static Jahn-Teller effect). Increasing the temperature the distortion randomly jumps between symmetry equivalent D_{2h} states (or D_{5d} and D_{3d}) by phonon assisted tunneling. This corresponds to a pseudo rotation of the Jahn-Teller distortion [8] which results in averaging the g-tensor to an isotropic value (dynamic Jahn-Teller effect). This study has shown that two effects have to be distinguished: a charged environment prevents C_{60}^- anions from a free rotation due to a coordination with the counter ions. However, the electronic distortion still can jump independently until an intrinsic counter ion interaction prevails. This is seen in the frequency independent splitting temperature for the two lines with an anisotropic g-tensor which corresponds to the Jahn-Teller distortion of C_{60}^- .

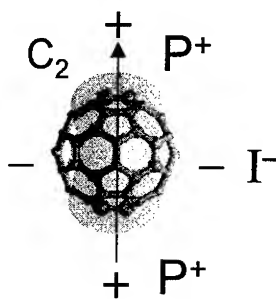


FIGURE 4. Schematic sketch of the charge environment of C_{60}^- . The arrow corresponds to the c-axis of the tetragonal unit cell which is the direction of the most favorable D_{2h} Jahn-Teller distortion of C_{60}^- (shaded area).

ACKNOWLEDGEMENTS

We are indebted to J. Gmeiner and I. Bauer for the help with the sample preparation, H.J. Kümmerer and G. Denninger (Universität Stuttgart) for the W-band measurements. Financial support by Sonderforschungsberich 279 and Fonds der Chemischen Industrie is acknowledged. J. Bao acknowledges financial support by Volkswagen-Stiftung.

REFERENCES

- [1] O. Gunnarson, *Review of Modern Physics* **69**, 575-606 (1997)
- [2] T. Kawamoto, *Solid State Comm.* **101**, 231-235 (1997)
- [3] B. Bleaney, K.D. Bowers, *Proc. Phys. Soc. (London)* **A65**, 667-668 (1952)
- [4] A. Schilder, W. Bietsch, M. Schwoerer, *New Journal of Physics* **1**, 5.1-5.11 (1999)
- [5] B. Gotschy, G. Völkel, *Appl. Magn. Reson.* **11**, 229-238 (1996) and references therein.
- [6] A. Pénicaud, A. Pérez-Benitez, R. Gleason, V.E. Munoz, R. Escudero, *J. Am. Chem. Soc.* **115**, 10392-10393 (1993)
- [7] C.C. Chancey, C.M. O'Brien, *The Jahn-Teller Effect in C_{60} and other Icosahedral Complexes*, Princeton: Princeton University Press, 1997
- [8] M. Bennati, A. Grupp, M. Mehring, *J. Chem. Phys.* **102**, 9457-9464 (1995)

Origin of Intrinsic Luminescence from C_{60} Single Crystals

Ikuko Akimoto and Ken-ichi Kan'no

Department of Physics, Kyoto University, Kyoto 606-8224, Japan

Abstract. Optical properties of pristine C_{60} single crystals have been studied in the temperature range from 4 K to 300 K by applying several spectroscopic techniques such as absorption, photoluminescence under one-photon and two-photon excitation, and site-selective luminescence line narrowing spectroscopy. Localized absorption characterized by the prominent vibrational structures is found around 1.69 eV below the fundamental absorption edge (1.81 eV), which apparently exhibits mirror-images of the well-known spectrum of photoluminescence called type A. Upon selective excitation into the band, luminescence line narrowing is observed: The spectra consist of sharp vibrational lines attributed to the progressions of eight Hg and two Ag modes and libron sidebands. These results indicate that the type A luminescence originates from the inhomogeneously broadened localized state which may be stabilized by the symmetry lowering and local rotational disorder spread over more than one molecule.

INTRODUCTION

Luminescence spectra from C_{60} single crystals have been known to depend on samples and sites of a crystal. Anomalous surface states affected by oxygen molecules and/or by photo-polymerization have been considered to be one of causes. [1] Three patterns of luminescence spectrum are generally observed under usual one-photon excitation at low temperatures [2]: a spectrum which exhibits an onset at 734 nm (1.69 eV, hereafter called *type A*), the one which exhibits an onset at 684 nm (1.81 eV, called *type B*) and that of a superposition of them (called *type A+B*). The spectrum of type A+B is observed in many cases, though relative intensities of types A and B bands change from sample to sample. [3, 4]

The type B luminescence is attributed to the Herzberg-Teller transitions coupled with vibrational modes of ungerade symmetry. [5] On the other hand, true character of type A luminescence is still controversial, though the spectrum itself has been well known. The present study will give a definite answer to the origin of photoluminescence from C_{60} single crystals.

EXPERIMENT

Single crystals of C_{60} were grown in a vacuum by the sublimation method starting from a 99.98% pure powder material (Term Co.). The crystals of $4 \times 3 \times 1 \text{ mm}^3$ in size were carefully treated in He gas atmosphere not to be affected by oxygen contamination, and were equipped in a liquid He cryostat (Oxford Ins., OptiBath) which is capable of gradually cooling down to 4 K. Details of optical measurements were described in previous reports. [3, 4]

RESULTS AND DISCUSSION

Two-photon excitation exhibits one and the same luminescence spectrum in the several specimens where strong sample dependence is recognized in the case of one-photon excitation. The bulk spectrum thus obtained at 5K is a superposition of types A and B. In raising temperature, peaks of the type B rapidly diminish to disappear. The spectrum, therefore, evolves into the type A at higher temperatures above 10 K. The details and a relevant kinetics will be presented

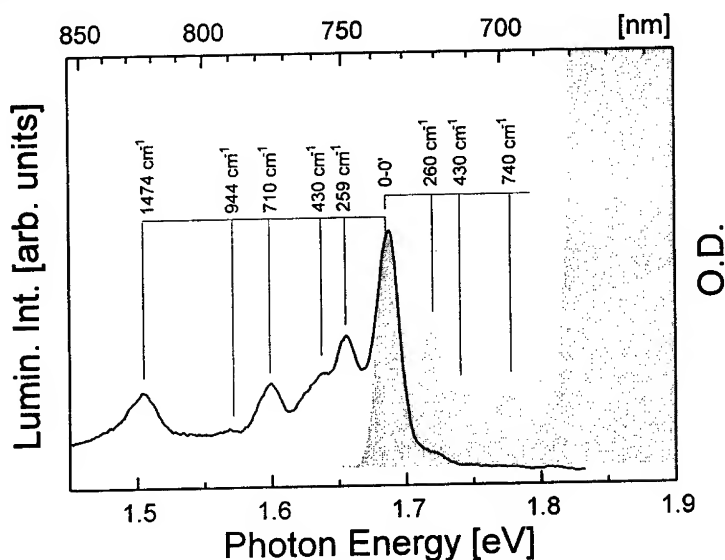


FIGURE 1 a typical type A luminescence spectrum at 12K (solid line) and an absorption spectrum at 5K (shadow part) in C_{60} single crystal

elsewhere. [6]

Precise measurements of optical transmittance in the band tail region allowed

us to confirm the existence of trapped states just below the fundamental absorption edge. Figure 1 shows the absorption spectrum (shadow), along with a typical spectrum of type A luminescence (solid line). A prominent peak at 1.69 eV and following three sub-peaks are clearly resolved as just mirror-image of the type A luminescence. The band width, 15 meV (120 cm^{-1} , FWHM), of the absorption and luminescence peaks come from inhomogeneous broadening, as mentioned below.

Luminescence line narrowing was found under site-selective laser excitation into the tail absorption. A typical example is shown in Fig.2 (a), of which spectrum consists of well-resolved vibronic lines accompanying with phonon side-bands. That is, the type A luminescence is to be evolved by gathering such a resonant luminescence from inhomogeneously broadened several sites. [4] The sharp lines are located at almost the same positions of vibrational modes of a molecule, two Ag and eight Hg modes and their combinations, as denoted by vertical bars in Fig.2 (b). Furthermore, one can recognize that every vibronic lines are accompanied by the phonon side bands of energy from 0 to 170 cm^{-1} , which are similar to *libron* band observed by neutron diffraction of powder sample. [7] As shown in Fig.2(c) the site-selective luminescence spectrum is successfully simulated, indicating vibronic transitions coupled with Raman-active gerade modes (Ag and Hg) of a single C_{60} molecule and crystal librational modes. This situation is totally different from that of the type B luminescence which is attributed to Frenkel exciton; i.e., the parity-forbidden HOMO-LUMO transitions vibronically allowed by coupling with ungerade symmetry modes.

As clearly seen in Fig.1, the main peak of the absorption and that of the emission coincides with each other without any Stokes-shift energy. The (0'-0) transition is located at 1.69 eV, being lower by 0.12 eV than the onset of the fundamental absorption due to HOMO-LUMO transitions (1.81 eV). This result unambiguously exclude the possibility of so far proposed several models such as self-trapped exciton, exciplex states, etc. The situation should usually be attributed to extrinsic luminescent centers such as impurities, defects, surface anomalies. Nevertheless, the luminescence of type A, as well as that of type B, must originate rather from the intrinsic nature of C_{60} single crystal itself, as mentioned below. Contrast to the type B luminescence, the type A will be closely related with some kind of lattice disorder including more than one molecule. According to spin-echo measurement [8] and fluorescence-microwave double resonance [2], the electronic state responsible for the type A luminescence is de-localized over a pair of molecules or more chain. In addition, recent theoretical study based on the cluster-model calculation [9] strongly suggests that adiabatic potential energy surfaces of the electronic ground and excited states exhibit multi-stability with respect to the lattice distortion coupled with rotational displacement of nearby C_{60} molecules.

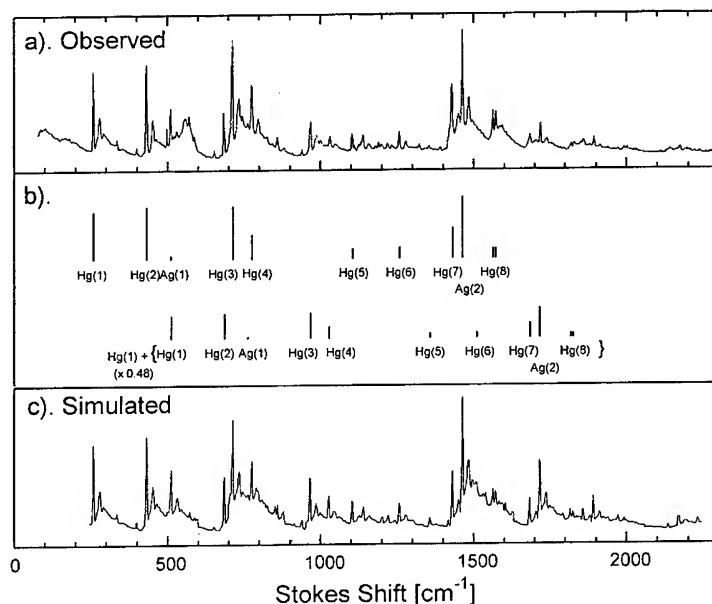


FIGURE 2 (a) a resonant site-selective luminescence at 5K excited at 1.69 eV, (b) the positions of coupled modes; in top column, single modes of two Ag and eight Hg modes are denoted, in bottom column, combined modes with Hg(1) are denoted. (c) simulated spectrum.

Thus, we conclude that de-localization of the electronic wavefunction over a pair or a few molecules is essential for the type A luminescence: The electronic transition from an odd-parity state of inter-molecular orbitals formed among the molecules comes to be parity-allowed, as reflecting in its vibrational characteristics of gerade symmetry. Then, molecular vibrations coupled with the electronic state are expected to still be tightly connected with localized vibrations within a molecule.

Inhomogeneous broadening with FWHM, 15 meV is most likely to arise from fluctuation of the intermolecular orientational correlation in a pair of molecules [4]. As reasonably imagined from spectral analysis on temperature dependence of the site-selective spectrum, rotational motion of molecules has been almost frozen at low temperature around 5K. Then the Coulombic interaction between adjacent molecules comes to play an important role for stabilizing local energy of mutual orientational configurations, because the density distribution of π -electrons is not homogeneous on the molecular surfaces. Such an intermolecular correlation will make local pair configurations at particular sites more stable.

REFERENCES

- [1] M.S.Dresselhaus, G.Dresselhaus and P.C.Eklund, Science of Fullerenes and Carbon Nanotubes (Academic Press, USA, 1996) .
- [2] D. J. van den Heuvel, I.Y.Chan, E.J.J.Groenen, M.Matsushita, J.Schmidt and G. Meijer; Chem. Phys. Lett. **233**, 284 (1995) .
- [3] I. Akimoto, J. Azuma, M. Ashida and K. Kan'no; J. Lumin. **76&77**, 206 (1998).
- [4] I. Akimoto, M. Ashida and K. Kan'no; Chem. Phys. Lett. **292**, 561 (1998).
- [5] D.J. van den Heuvel, G.J.B. van den Berg, E.J.J.Groenen, J.Schmidt, I. Holleman and G. Meijer; J. Phys. Chem. **99**, 11644 (1995).
- [6] I. Akimoto and K. Kan'no; in preparation.
- [7] L. Pintschovius, B. Renker, F. Gompf, R. Heid, S.L. Chaplot, M. Haluska and H. Kuzmany; Phys.Rev. Lett. **69**, 2662 (1992)
- [8] E.J.J.Groenen, O.G.Poluektov, M.Matsushita, J.Schmidt, J.H. van der Waals and G. Meijer; Chem. Phys. Lett. **197**, 314 (1992)
- [9] M. Suzuki; in private communication

Polymeric fullerenes: from C₆₀ to C₇₀

A. Soldatov^{1,2}, P. Nagel¹, V. Pasler¹, S. Lebedkin¹, C. Meingast¹, G. Roth³
and B. Sundqvist²

¹*Forschungszentrum Karlsruhe – Technik und Umwelt, Institut für Nukleare Festkörperphysik,
PO Box 3640, D-76021 Karlsruhe, Germany*

²*Department of Experimental Physics, Umeå University, S-901 87 Umeå, Sweden*

³*Rheinisch-Westfälische Technische Hochschule Aachen, Institut für Kristallographie,
D-52056 Aachen, Germany*

For the first time polymerization of both powder and single crystals of C₇₀ fullerene was established after their subjection to high pressure (1.1-2.0 GPa) at elevated temperature (500-580 K). High-resolution capacitance dilatometry, FTIR/Raman spectroscopy and thermal conductivity were employed to characterise the polymeric phase of C₇₀. The results demonstrate drastic changes in the physical properties of C₇₀ on polymerization. We report on a reverse transformation to the monomeric state on heating the polymer to 500 K at ambient pressure. The activation energy of depolymerization was determined to be 1.8(1) eV. We discuss our results in terms of existing structural models for polymerization of C₇₀ and compare the physical properties of C₇₀ and C₆₀ polymers.

INTRODUCTION

Since polymerization of C₆₀ was achieved along different pathways extending from irradiation and high-pressure treatment to doping the pristine material with alkali metals [1], analogous processes were expected to occur in the next simplest fullerene C₇₀. Indeed, LD mass spectra of C₇₀ thin films irradiated with UV light indicate the presence of clusters of C₇₀ molecules although FTIR spectra show no changes compared to those of pristine material [2]. The confusing situation was not resolved even after observation of new features in IR [3,4] and UV/visible [3] absorption spectra of C₇₀ after treatment at 5 GPa, 300 °C and 7.5 GPa, 250 °C, which were attributed to the formation of C₇₀ dimers. In [4] Raman spectroscopy was claimed insensitive to this process although this technique proved to be the most powerful tool in detecting polymeric structures in C₆₀. All this shows that the existence of a polymeric state in C₇₀ is still unclear and that this problem needs to be addressed.

Here we present the results of our studies of the structure and physical properties of polymeric which was produced by treating the material under moderate pressures (1.1-2 GPa) at elevated temperature.

EXPERIMENTAL

We used in our experiments sublimed C₇₀ powder of 99.9 % nominal purity (Foma USA, Houston, TX) and single crystal samples grown using the technique described

in detail elsewhere [5]. The pressure treatment was carried out in a piston and cylinder device. In the experiments on the single crystals we used the silicon oil as pressure transmitting medium. The powder material was subjected to 1.1-1.8 GPa and 220-300 °C for 12-16 hours, while the single crystals were annealed for 11 hours at 2 GPa and 300 °C. The thermal conductivity (λ) of polycrystalline material was measured at high pressure using the hot-wire technique. The structure of the samples after high p,T treatment was examined by X-ray (STOE Image Plate Diffraction System). FT-Raman (excitation at 1064 nm) and Infrared measurements were carried out at room T on a Bruker Equinox 55S spectrometer with resolution 2 cm^{-1} and 1 cm^{-1} respectively. Two high-resolution capacitance dilatometers with temperature ranges of 4-300 K and 150-500 K respectively, were employed in thermal expansion (α) experiments. Data were taken at constant heating/cooling rates in the range 0.2 – 20 mK/s.

RESULTS AND DISCUSSION

Structure/vibrational properties After the high p, T treatment the C_{70} powder becomes essentially insoluble in 1,2-dichlorobenzene, which is an indication of a polymeric transformation.

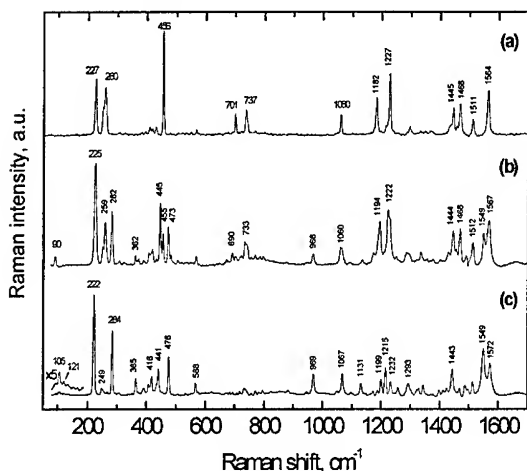


Fig. 1. Raman spectra of C_{70} before (a) and after treatment at: 1.1 GPa, 220 °C (polycrystal) (b), 2.0 GPa, 300 °C (single crystal), (c))

lowering and perturbation of the C_{70} molecule due to polymerization. The increase of reaction pressure from 1.1 to 2.0 GPa leads to a further evolution of the Raman spectrum (see Fig. 1 (c)): some modes (260, 455, 690 cm^{-1}) disappear, additional modes shift and/or split. The appearance of low-energy (intermolecular) modes at 90 cm^{-1} and at 105, 121 cm^{-1} in the Raman spectra of C_{70} annealed at 1.1 GPa, 220 °C and 2 GPa, 300 °C respectively is strong evidence for the formation of covalent bonds between molecules. The observed intermolecular vibrations scale well by frequency with the analogous vibrations in dimers [7] and chains polymers [8] of C_{60} which might be an indication of a possible presence of different types of polymeric

structures in our samples. FTIR spectra of the samples after polymerization differ significantly from the spectrum of the pristine C_{70} although they still contain the characteristic lines of the latter. It follows from our IR data that approximately 20% of the material treated at 1.1 GPa, 220 °C remains in the monomeric form. However, the fraction of unreacted C_{70} decreases in the samples annealed at higher pressure and temperature. The IR spectra of our samples are similar to the IR spectra observed in [3,4] for C_{70} treated at substantially higher pressures while its Raman spectra exhibit no changes in comparison to that of a monomer. X-ray analysis of the single crystals of C_{70} before polymerization reveals a hexagonal structure with lattice parameters $a = 10.13(1)$ Å and $c = 18.62(2)$ Å. A preliminary analysis of the diffraction pattern of the single crystal polymerized at 2.0 GPa, 300 °C shows that it can still be indexed as hexagonal with $a = 10.006(3)$ Å, $c = 18.08(7)$ Å. The contraction of the lattice along the c axis is more than twice that along the a axis which suggests a possible direction of polymerization. The overall lattice contraction due to polymerization is $\Delta V/V = 5.4\%$.

Thermal conductivity/dilatometry

In Fig. 2 we present the temperature dependence of λ of polycrystalline C_{70} at 0.87 GPa after polymerization at 1.1 GPa and 220 °C. We performed temperature cycling of the specimen in the temperature

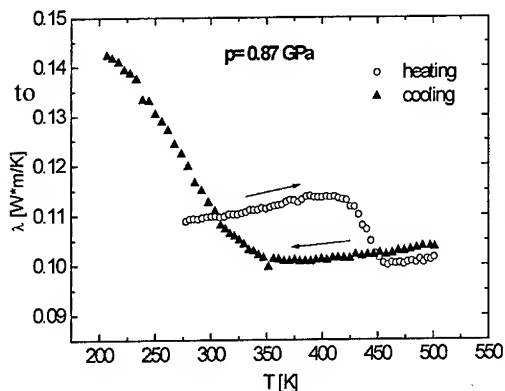


Fig. 2. Thermal conductivity of polycrystalline C_{70} after high p,T treatment

range 200-500 K. After an almost linear increase on heating, the thermal conductivity of polymerized C_{70} starts decrease abruptly at 420 K, which we associate with depolymerization. The gradual increase of λ with T is similar to that observed for the C_{60} polymer [9] and indicates a high degree of structural disorder, while the T dependence on cooling reproduces the typical behaviour of monomeric C_{70} [10].

The coefficient of linear thermal expansion $\alpha(T)$ was measured along three orthogonal directions, one of which was normal to the flat surface ("plane") of arbitrary chosen sample.

The $\alpha(T)$ of polycrystalline C_{70} polymerized at 1.8 GPa and 300 °C is shown in Fig. 3 together with the data for the monomeric phase [11]. As in the case of C_{60} , the $\alpha(T)$ of polymeric C_{70} exhibits no anomalies due to orientational phase transitions. Its magnitude is much smaller than that of monomer and close to that of a chain polymer of C_{60} [12]. α is highly anisotropic in both polycrystalline and single crystal polymeric C_{70} (inset Fig. 3). From the data on α of the single crystal it follows that polymerization takes place along the " c " axis in the crystal since the thermal expansion has its lowest value in this direction. We studied the kinetics of depolymerization of C_{70} in the dilatometer by heating the polycrystalline samples to 500 K at different rates and obtained the value 1.8(1) eV for the activation energy of this process. The volume gain on

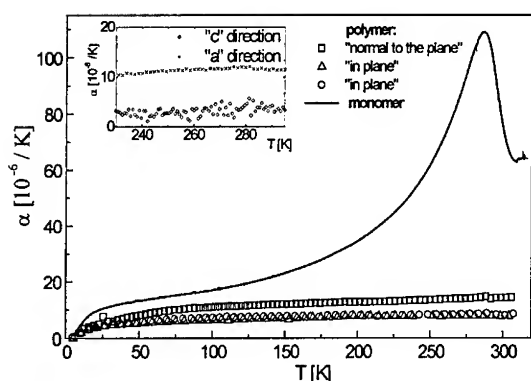


Fig. 3. Thermal expansion of polycrystalline and single crystal (inset) C_{70} in polymeric state (solid line—the results from [11] for the monomeric phase).

the 90 cm^{-1} mode with C_{70} dimers, while 105 and 121 cm^{-1} are attributed to longer polymeric chains extended along the c axis of the hexagonal structure. The activation energy of depolymerization is $1.8(1)\text{ eV}$, a value which is close to the energy barrier of this process for C_{60} dimers [12]. The thermal conductivity $\lambda(T)$ of C_{70} polymers indicates a high degree of structural disorder in analogy to that in C_{60} polymers.

depolymerization is about 4.4%, which is in good correspondence with the value 5.4% obtained from our X-ray experiments.

CONCLUSIONS

Polymerization of C_{70} was established by treatment at moderate pressure and elevated temperature. The volume decrease due to polymerization is about 5%. The formation of chemical bonds between C_{70} molecules results in the appearance of “intermolecular” Raman active modes at 90 , 105 and 121 cm^{-1} . We tentatively associate

ACKNOWLEDGMENTS

We thank Miro Haluska and Hans Kuzmany for providing single crystals of C_{70} for our experiments. AS acknowledges the fellowship from Forschungszentrum Karlsruhe.

REFERENCES

- [1] B. Sundqvist: *Adv. Phys.*, **48**, 1, 1 (1999).
- [2] A.M. Rao, et al.: *Chem. Phys. Lett.* **224**, 106 (1994).
- [3] Y. Iwasa, et al.: *Appl. Phys. A* **64**, 251 (1997).
- [4] M. Premila, et al.: *Solid State Comm.* **104**, 4, 237 (1997).
- [5] M. Haluska, et al.: *Appl. Phys. A* **56**, 161 (1993).
- [6] P.H.M. van Loosdrecht, et al.: *Phys. Rev. B* **47**, 7610 (1993).
- [7] S. Lebedkin, et al.: *Chem. Phys. Lett.* **285**, 210 (1998).
- [8] P.-A. Persson, et al.: *Chem. Phys. Lett.* **258**, 540 (1996).
- [9] A. Soldatov and O. Andersson: *Appl. Phys. A* **64**, 227 (1997).
- [10] A. Soldatov and B. Sundqvist: *J. Phys. Chem Solids* **57**, 1371 (1996).
- [11] C. Meingast, et al.: *Appl. Phys. A* **56**, 227 (1993).
- [12] P. Nagel, et al., in *Molecular Nanostructures*, ed. H. Kuzmany, J. Fink, M. Mehring and S. Roth, World Scientific, Singapore (1998) p. 365.

In situ ATR-FTIR spectroelectrochemical comparison of pristine and polymerized C₆₀ films

H. Neugebauer*, C. Kvarnström*[†], H. Sitter[‡], Ch. Jogl^{||}, H.
Kuzmany^{||} and N. S. Sariciftci*

*Physical Chemistry, Johannes Kepler University Linz, Altenbergerstraße 69, A-4040 Linz,
Austria

[†]Åbo Akademi University, Biskopsgatan 8, FIN-20500 Åbo, Finland

[‡]Institute of Semiconductor and Solid State Physics, Johannes Kepler University Linz,
Altenbergerstraße 69, A-4040 Linz, Austria

^{||}Institute of Material Physics, University of Vienna, Strudlhofgasse 4, A-1090 Vienna, Austria

Abstract. In situ spectroelectrochemical studies on the reduction processes of solid fullerene films in different organic electrolyte solutions using cyclic voltammetry and attenuated total reflection (ATR) FTIR spectroscopy are presented. IR bands from the electrochemically induced reduction states of pristine and polymerized C₆₀ films are compared with spectra of the stable polymeric RbC₆₀ phase.

INTRODUCTION

In contrast to the electrochemistry of C₆₀ in solution, where up to six consecutive reversible one-electron reductions are obtained [1], the electrochemical behavior of solid fullerene films is more complicated [2]. The cyclic voltammetric response depends on the structure and the morphology as well as the composition of the electrolyte solution [3,4]. Especially the nature of the cation in the electrolyte was found to highly influence the reaction mechanisms and the reaction products [2].

In the present paper, in situ spectroelectrochemical measurements on the electrochemical reduction of C₆₀ films in different electrolyte solutions using a combination of cyclic voltammetry and attenuated total reflection (ATR) FTIR spectroscopy are presented. Since the formation of dimeric [5] and polymeric phases during electrochemical reduction have been proposed, the spectra are compared with spectra of polymeric forms of C₆₀ (photopolymerized C₆₀ and the stable polymeric RbC₆₀ phase, for an overview of the polymeric forms of C₆₀ see e.g. [6]).

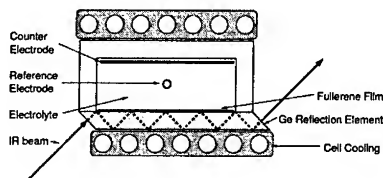


FIGURE 1. Spectroelectrochemical cell for *in situ* ATR-FTIR spectroscopy with Ag/AgCl reference electrode and Pt counter electrode.

EXPERIMENTAL

C_{60} films were prepared by solution casting or by hot wall beam epitaxy (HWBE) [7] on the surface of Pt covered Ge reflection elements used for ATR-FTIR spectroelectrochemistry (Fig. 1, for details of the method see [8]). Photopolymerization of C_{60} was done by illumination of the film with UV light under vacuum. The polymeric form of RbC_{60} was prepared by exposure to Rb vapor at 450 K and slowly cooling to room temperature. Electrolyte solutions were 0.1 M $TBAClO_4$ (TBA = tetrabutylammonium), $TBABF_4$, $LiClO_4$, KPF_6 , $NaBF_4$ and 0.01 M (due to the low solubility) $RbBPh_4$ (Ph = phenyl) in acetonitrile. During slow reductive potential scans FTIR spectra were recorded consecutively with a Bruker IFS66S spectrometer (MCT detector, resolution 4 cm^{-1}). For each spectrum 32 interferograms were coadded, which covers a range of about 90 mV in the cyclic voltammogram.

RESULTS AND DISCUSSION

Figure 2 shows difference spectra during the reduction processes of fullerene films in different electrolytes. Besides Rb^+ , all experiments were done with HWBE films. With Rb^+ , no electrochemical response was obtained with HWBE films, probably due to the low electrolyte concentration (low solubility of $RbBPh_4$). The spectra with Rb^+ were measured with a solution casted film. The resulting spectra were analyzed in respect to the frequency of the $F_{1u}(\omega_4)$ mode of C_{60} (characteristic for the amount of charge on C_{60} [6,9]) during reduction with different cations as follows: for TBA^+ (Fig. 2a): band at 1375 cm^{-1} , formation of C_{60}^{2-} in one step [3]; for Li^+ (Fig. 2b): a band at 1393 cm^{-1} evolves and shifts to 1382 cm^{-1} , two step reduction $C_{60} \rightarrow C_{60}^- \rightarrow C_{60}^{2-}$ [3]; for Na^+ (Fig. 2c): band at 1394 cm^{-1} , formation of C_{60}^- ; for K^+ (Fig. 2d): more complicated structure, a band at 1375 cm^{-1} is attributed to C_{60}^{2-} , but the shoulder at lower wavenumbers indicates also the formation of higher reduction states; for Rb^+ (Fig. 2e): the broad pattern around 1365 cm^{-1} indicates mainly the formation of C_{60}^{3-} in dropcasted C_{60} films, in contrast to photopolymerized C_{60} , Rb^+ (Fig. 2f): band at 1396 cm^{-1} attributed to the formation of C_{60}^- .

For comparison, the ATR spectra of polymeric forms are shown in Fig. 3. As

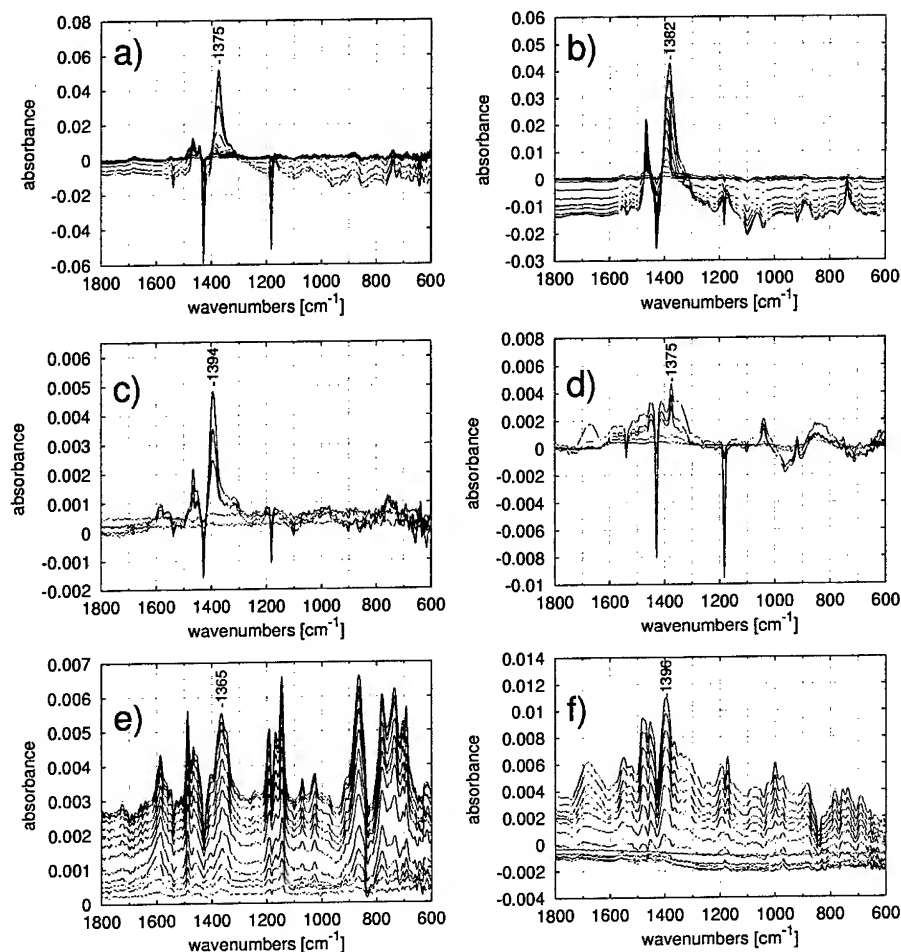


FIGURE 2. Difference spectra during reduction of C_{60} films in different electrolytes, reference spectrum: neutral form. a) HWBE C_{60} film in 0.1 M $TBAClO_4$, b) HWBE C_{60} film in 0.1 M $LiClO_4$, c) HWBE C_{60} film in 0.1 M $NaBF_4$, d) HWBE C_{60} film in 0.1 M KPF_6 , e) drop casted C_{60} film in 0.01 M $RbBPh_4$, f) photopolymerized HWBE C_{60} film in 0.01 M $RbBPh_4$.

can be seen, the reduction of C_{60} and of photopolymerized C_{60} in Rb^+ containing electrolyte does not result in the polymeric RbC_{60} structure obtained by vapor doping (Fig. 3a).

A spectral feature around 1460 cm^{-1} was found for photopolymerized C_{60} [6] (Fig. 3b) as well as for C_{60} dimers [10]. Bands in this spectral region are also observed during electrochemical reduction of C_{60} films in all electrolyte solutions used (Fig. 2).

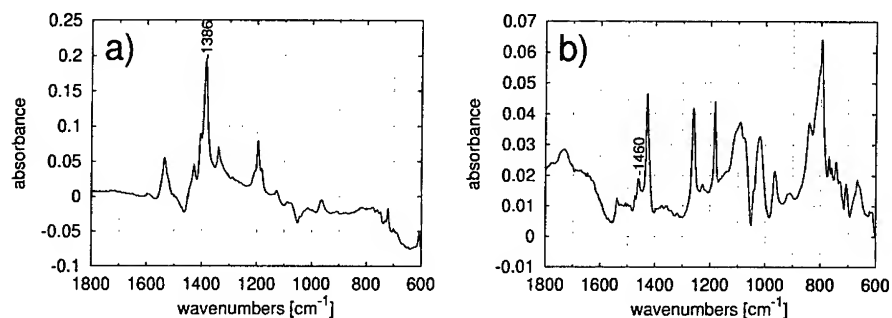


FIGURE 3. ATR spectra of polymeric forms. a) RbC₆₀. b) Photopolymerized C₆₀.

ACKNOWLEDGMENT

The work is supported by the "Fonds zur Förderung der wissenschaftlichen Forschung" of Austria (Project No. P11457-CHE). C.Kvarnström thanks the Research Institute of the Foundation of Åbo Akademi University for scholarship.

REFERENCES

1. Xie, Q., Perez-Cordero, E., and Echegoyen, L., *J. Amer. Chem. Soc.* **114**, 3978 (1992).
2. Chlistunoff, J., Cliffler, D., and Bard, A. J., in *Handbook of Organic Conductive Molecules and Polymers, Vol 1*, edited by Nalwa, H. S., Chichester: John Wiley & Sons Ltd., 1997, ch. 7, pp. 333-412.
3. Neugebauer, H., Kvarnström, C., and Sariciftci, N. S., in *Electronic Properties of Novel Materials - Progress in Molecular Nanostructures*, AIP Conference Proceedings 442, edited by Kuzmany, H., Fink, J., Mehring, M., and Roth, S., Woodbury: American Institute of Physics, 1998, pp. 249-252.
4. Kvarnström, C., Neugebauer, H., Matt, G., Sitter, H., and Sariciftci, N. S., *Synthetic Metals*, in press (Proceedings of the International Conference on Science and Technology of Synthetic Metals, July 1998, Montpellier, France).
5. Heinze, J., and Smie, A., in *Recent advances in the chemistry and physics of fullerenes and related materials*, Proceedings Volume 94-24, edited by Kadish, K. M., and Ruoff, R. S., The Electrochemical Society Inc., 1994, pp. 1117.
6. Dresselhaus, M. S., Dresselhaus, G., and Eklund, P. C., *Science of Fullerenes and Carbon Nanotubes*, San Diego: Academic Press, 1996.
7. Sitter, H., Nguyen Manh, T., and Stifter, D., *J. of Crystal Growth* **174**, 828 (1997).
8. Neugebauer, H., and Zhao Ping, *Microchim. Acta [Suppl.]* **14**, 125 (1997).
9. Pichler, T., Winkler, R., and Kuzmany, H., *Phys. Rev. B* **49**, 15879 (1994).
10. Komatsu, K., Wang, G.-W., Murata, Y., Tanaka, T., and Fujiwara, K., *J. Org. Chem.* **63**, 9358 (1998).

Structure of phototransformed C₆₀ revisited

T. Pusztai, G. Oszlányi, G. Faigel, K. Kamarás, L. Gránásy,
S. Pekker

Research Institute for Solid State Physics and Optics, H-1525 Budapest, POB. 49, Hungary

Abstract. We have produced phototransformed C₆₀ in powder form and in bulk quantities. The material has a face centered cubic lattice which is contracted by 0.25 Å relative to pristine C₆₀. A mixture of closed trimer and tetramer clusters are proposed as the structural building blocks of the phototransformed C₆₀.

I INTRODUCTION

Phototransformation of C₆₀ was the first case when direct intermolecular linkage of fullerene molecules via [2+2] cycloaddition was proposed [1]. While this result opened the field of fullerene and fulleride polymerization, the x-ray diffraction evidence for the photopolymer structure is still missing. This is mainly due to the inherent disorder in its bonding pattern and that up to now the photopolymer was produced only as thin films.

We have devised a simple technique to obtain the phototransformed material in bulk quantities. The availability of several milligrams of the material allowed us to collect good quality X-ray powder diffraction (XRD) data, infrared (IR) transmission spectra and perform differential scanning calorimeter (DSC) measurements.

II EXPERIMENTAL

Bulk quantities of C₆₀ photopolymer were produced by irradiating the C₆₀ powder by UV-visible light. To provide the inert atmosphere required for photopolymerization, a small cell was constructed which can be loaded in a glove box. At each loading, 5–10 mg of fine C₆₀ powder was spread between the two facing quartz windows of the cell. The C₆₀ powder was irradiated with a 1.5 kW Xe arc lamp providing a power density of 0.2–0.4 W/cm². Forced air cooling was applied to keep the temperature of the cell at ~50 °C, which is well below the depolymerization temperature. X-ray powder diffraction data were collected with an Image Foil Guinier Camera at a wavelength of 1.54051 Å. Infrared spectra were taken by a

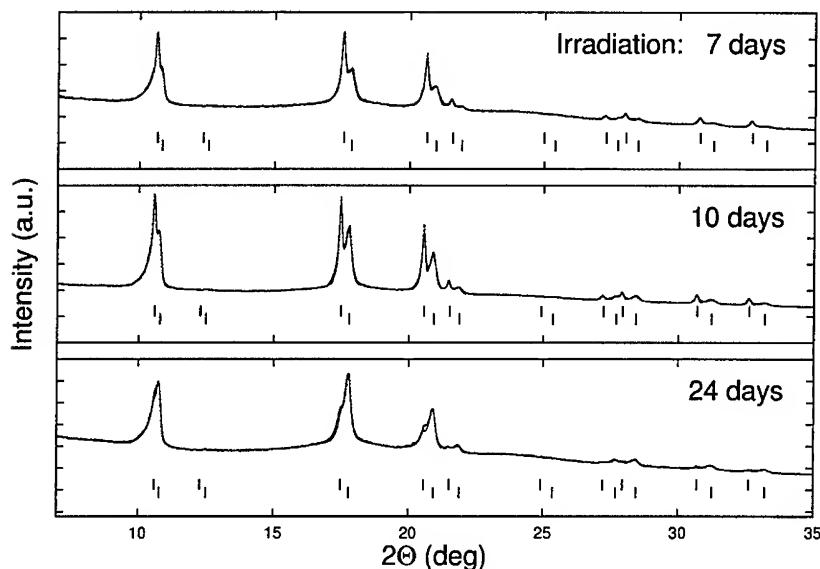


FIGURE 1. XRD patterns of C_{60} powder irradiated for different times. Dots and solid lines correspond to the experimental points and fitted curves. The top and bottom rows of tick marks below the spectra show the peak positions of the C_{60} and photopolymer phases, respectively.

TABLE 1.

irradiation time	photopolymer	
	relative quantity	lattice parameter
7 days	51%	13.94 Å
10 days	58%	13.92 Å
24 days	83%	13.92 Å

Bruker IFS-28 Fourier transform interferometer equipped with a microscope. DSC measurements were performed on a Perkin-Elmer DSC-2 calorimeter.

III RESULTS

XRD data of C_{60} photopolymer obtained after different irradiation times are shown in Figure 1. All three diffraction patterns can be fitted as a mixture of two phases: pristine and phototransformed C_{60} . The unit cell of the phototransformed material is still face centered cubic and the lattice parameter is contracted by 0.25 Å relative to C_{60} . Higher irradiation dose simply increases the amount of the photopolymer but leaves the lattice parameter unchanged, as shown in Table 1.

IR measurements could also follow the growth of the photopolymer phase. The change is apparent in Figure 2 as the diminishing of the C_{60} peak at 1428 cm^{-1} and the emerging of the photopolymer peak at 1422 cm^{-1} . However, this is only a

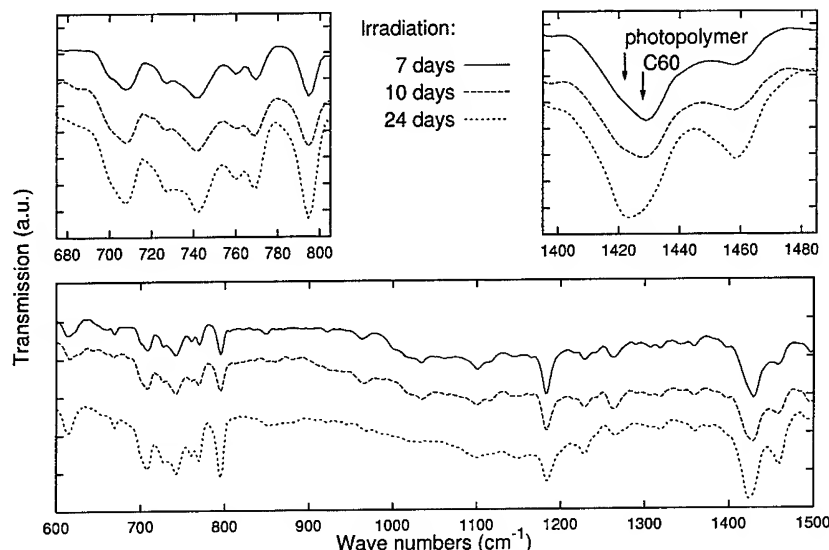


FIGURE 2. IR transmission spectra of phototransformed C_{60} produced by different irradiation times. The top two panels show enlarged views of selected regions.

quantitative change. The spectral features characteristic to the photopolymer are the same in all samples, showing that on this timescale the bonding configuration does not change with increased irradiation. The IR spectrum of the photopolymer is also very similar to literature data obtained for thin films.

Thermal properties of the irradiated samples were determined by DSC measurements at a heating rate of 20 K/min. The onset and peak temperatures of depolymerization are ~ 420 K and ~ 520 K, respectively. The enthalpy of transformation was found to be 22 J/g. This value is close to the formation enthalpy of the high pressure orthorhombic polymer phase of C_{60} determined by Iwasa *et al.* [5], in which the number of [2+2] cycloadduct bonds formed by a C_{60} molecule is two.

IV CONCLUSION

The limitations imposed by the fcc lattice and C_{60} molecular geometry already exclude the existence of long range ordered bonded structures, e.g. long chains or extended sheets. Further, the magnitude of the lattice contraction requires the molecules to shift off from the lattice sites so that both bonding and non-bonding distances take physically meaningful values. Therefore, the structure can only be built up from randomly oriented small closed clusters as already proposed by Refs. [2-4]. Considering the formation enthalpy of the phototransformed material and the enthalpy vs. bond number curve determined for C_{60} dimers and polymers [5], we conclude that the average number of [2+2] bonds per C_{60} is two. The

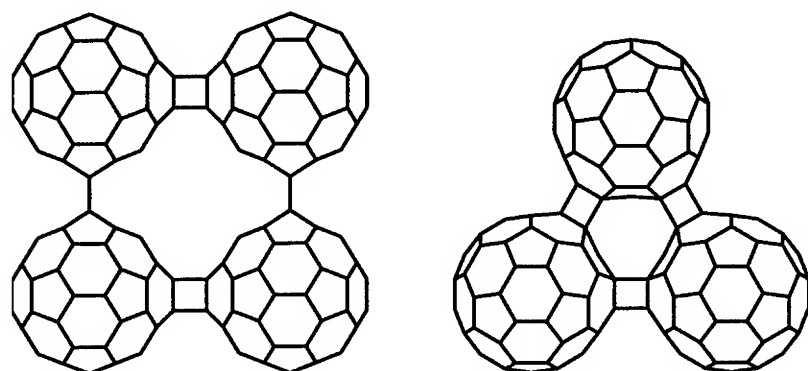


FIGURE 3. Closed trimer and tetramer clusters formed by C_{60} molecules.

value of the lattice parameter is also consistent with the formation of bonds towards 2 of the possible 12 nearest neighbors. The most likely structures are the closed trimers and tetramers, shown in Figure 3.

V ACKNOWLEDGEMENTS

This work was supported by OTKA grants No. T029931, T022404 and T019139 and by No. OTKA-NWO N26680.

REFERENCES

1. M. Rao, Ping Zhou, Kai-An Wang, G. T. Hager, J. M. Holden, Ying Wang, W.-T. Lee, Xiang-Xin Bi, P. C. Eklund, D. S. Cornett, M. A. Duncan, I. J. Amster, *Science* **259**, 955-957 (1993).
2. D. Porezag, M. R. Pederson, Th. Frauenheim, Th. Kohler *Phys. Rev. B* **52**, 14963-14970 (1995).
3. B. Burger, J. Winter, H. Kuzmany *Z. Phys. B* **101**, 227-233 (1996).
4. D. Porezag, G. Jungnickel, Th. Frauenheim, G. Seifert, A. Ayuela, M. R. Pederson, *Appl. Phys. A* **64**, 321-326 (1997).
5. Y. Iwasa, K. Tanoue, T. Mitani, T. Yagi *Phys. Rev. B* **58**, 16374-16377 (1998).

ATOMIC FORCE MICROSCOPY ANALYSIS OF NUCLEATION AND DIFFUSION OF C₆₀ ON HOT SUBSTRATES

M. Haluška, H. Kuzmany

Institut für Materialphysik, Universität Wien, A-1090 Vienna, Austria

C₆₀ deposits were prepared in an UHV-chamber on mica (001), Si (100) and polycrystalline Au substrates at certain temperatures ranging from 315 to 490 K. The concentration of C₆₀ crystallites was measured by atomic force microscopy. Different conditions for the deposition led to different types of growth mechanisms. On Si and Au substrates the polynuclear growth mechanism was observed below some critical temperature. Above this temperature the growth of isolated islands was detected. For mica substrates the growth of isolated islands was not observed. The activation energy for the surface desorption was determined.

1. INTRODUCTION

The preparation of solids from the vapour phase proceeds in two stages. The first stage includes the formation of thermodynamically stable clusters called critical nuclei. The second stage consists of the growth of critical nuclei. The creation of nuclei needs the presence of supersaturation to overcome barrier for cluster formation. This barrier is smaller in the case of the condensation on a substrate in comparison to the condensation in the mother phase. In the first case the substrate is covered to some extent by adsorbed molecules from the vapour. If the covering molecules are mobile they can condense to form clusters. The latter gain stability because of bonds between their building units and the substrate. For different substrates different sizes of critical nuclei can be expected.

The situation on the substrate surface may be described by the following processes. Molecules from the vapour arrive on the substrate surface with impingement flow

$$J_+ = \frac{p}{\sqrt{2\pi m k_B T_{cell}}}. \quad (1)$$

The adsorbed molecules diffuse on the surface with an average displacement

$$\lambda = \sqrt{2} a_0 \exp\left(\frac{E_{des} - E_{sd}}{2k_B T_{subs}}\right). \quad (2)$$

p , T_{cell} , T_{subs} , m , a_0 , E_{des} and E_{sd} are the saturated vapour pressures corresponding to the temperature of the source, the source temperature, the substrate temperature, the molecular weight, the lattice constant, and the desorption and surface diffusion energies, respectively. Adsorbed molecules can either create clusters or

CP486, *Electronic Properties of Novel Materials—Science and Technology of Molecular Nanostructures*,

edited by H. Kuzmany, J. Fink, M. Mehring, and S. Roth

© 1999 American Institute of Physics 1-56396-900-9/99/\$15.00

they can be captured at some special positions like steps or they can desorb. On the defect free surface the concentration of critical nuclei is [1]

$$\rho \sim \exp \left(\frac{2(2E_{des} - E_{sd})}{3k_B T_{subs}} \right). \quad (3)$$

ρ and λ are connected by $\rho \times \lambda^2 = 1$ [2].

2. EXPERIMENTAL

C₆₀ deposits were prepared in an evacuated chamber ($\sim 10^{-9}$ mbar) by a molecular beam epitaxy method. The super gold grade C₆₀ (Hoechst) material was first purified by a sublimation-condensation method in dynamical vacuum [3]. A quartz cell was filled with 300 mg of this purified material at ambient condition. The first few films prepared after inserting the source material into the UHV-chamber were not analysed because of possible inclusion of oxygen compounds. The vapour beam flux was controlled by the temperature of the source cell. A shutter was situated between the cell and the substrate to open or close the vapour beam.

Three types of substrates were used, namely Si (100), mica (001) and polycrystalline gold films condensed on Si (100) surface. Mica substrates were cleaved immediately before mounting on the substrate holder. Before preparation of films all substrates were heated to 495 K for 12 hours directly in UHV-chamber. The temperature of substrates could be controlled by the substrate heater in the temperature range between 300–500 K.

Two basic types of experiments were performed. In one C₆₀ deposits were grown at different substrate temperatures and simultaneously T_{cell} was kept constant at 598 K. In the other experiments the cell temperatures were different for different deposits and T_{subs} was kept constant at 440 K.

As prepared C₆₀ deposits were investigated by atomic force microscopy. The contact mode of TopoMetrix TMX 2000 Explorer was used with about 20 nm resolution.

3. RESULTS

Measured concentrations of crystallites prepared at $T_{cell}=598$ K and different substrate temperatures on different types of substrates are shown in Fig.1(left). The deposition time was 12 hours. The concentration of nuclei decreases with increasing T_{subs} for all types of substrates used. On Si and Au the polynuclear growth mechanism was observed below $T_{subs} \sim 380$ K and ~ 430 K, respectively. Above this temperature the growth of isolated islands was detected. For mica (001) substrates the growth of isolated islands was not detected. Films with connected crystallites were grown in the whole temperature range.

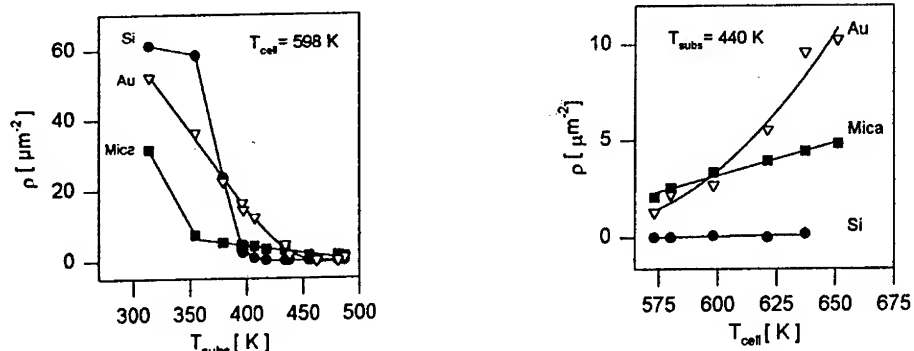


Figure 1: Dependence of concentration of nuclei, ρ , on substrate temperature, T_{subs} for $T_{\text{cell}}=598$ K (left). Dependence of concentration of nuclei, ρ , on cell temperature, T_{cell} for $T_{\text{subs}}=440$ K (right). Bullets: Si (100), squares: mica (001), and triangles: Au substrates, respectively.

The concentration of crystallites on different types of substrates prepared at $T_{\text{subs}}=440$ K and different cell temperatures is shown in Fig.1(right). It increases with increasing T_{cell} . The same amount of material was evaporated in each experiment. The maximum ρ observed for the Si substrate is $0.2 \mu\text{m}^{-2}$ in this case.

The desorption energy can be obtained from the slopes of Arrhenius plots for

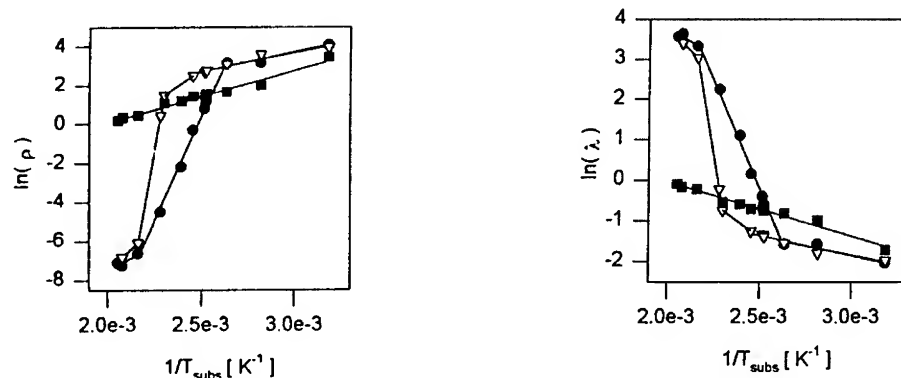


Figure 2: Dependence of $\ln(\rho)$ (left, ρ in μm^{-2}) and of $\ln(\lambda)$ (right, λ in μm) on $1/T_{\text{subs}}$. $T_{\text{cell}}=598$ K for all experiments. Bullets: Si (100), squares: mica (001), and triangles: Au substrates, respectively.

ρ and λ as results from equations 2 and 3, respectively. Such plots are shown in Fig.2 for all types of substrates used.

Activation energies obtained from Fig.2 are given in the following table.

Substrate	T_{subs} [K]	E_{des} [eV]
Mica	300-500	0.57
Si	<380	0.33
Si	380-460	5.08
Si	>460	1.12
Au	< 430	0.32
Au	435-460	11.6
Au	> 460	1.88

For Si and Au substrates and temperatures below 380 K and 430 K, respectively, $E_{des}/3$ is similar to the nearest neighbour interaction energy between two C_{60} molecules, which is 0.13 eV [4]. It means that E_{des} is the energy to remove one adsorbed molecule from the top of the (111) face of C_{60} solid in contact with three nearest neighbours. The energies obtained for higher T_{subs} describe behaviour of C_{60} on foreign substrates (Si, Au). For mica substrates E_{des} is constant in the whole temperature range and is larger than in the case of Si and Au for low temperature. This may originate from a different growth mechanism of the deposit.

4. CONCLUSION

The measurements indicate:

- the existence of a critical temperature for Si and Au substrates above which C_{60} deposits grow in the form of isolated three dimensional crystallites;
- that an increase of the substrate temperature (at constant source temperature) leads to a decrease of the concentration of the critical nuclei and thus to an increase in the size of crystallites;
- that an increase of the source temperature (at constant cell temperature) leads to an increase of the concentration of the critical nuclei and thus to a decrease in the size of crystallites.

Acknowledgement

The authors are grateful to F. Biscarini for useful discussion, to the Fonds zur Förderung der Wissenschaftlichen Forschung, Austria, project 10922-PHY and to the European Community, TMR project ERBFMRX-CT97-0155 for financial support and to Hoechst AG for support with C_{60} powder.

REFERENCES

1. K. Reichelt, Vacuum **38** 1988, 1083
2. L. Ickert, H. G. Schneider, Wachstum einkristalliner Schichten, VEB Deutscher Verlag, Leipzig, 1983
3. M. Haluška, H. Kuzmany, M. Vybornov, P. Rogl, P. Fejdi, Appl. Phys. A **56** 1993, 161
4. M. A. Verheijen, W. J. P. van Enckevort, J. Crystal Growth **172** 1997, 136

NMR study of $C_{60}.C_7H_8$ by cross polarization and polarization inversion of rare-spin magnetization

A.-S. Grell, I. Messari, P. Pirotte, P. Tekely *, R. Céolin †, H. Szwarc ‡, and F. Masin

Université Libre de Bruxelles, CP 232, Bvd. du Triomphe, 1050 Bruxelles, Belgium

** Groupe de Méthodologie RMN, Université de Nancy I, France*

† Laboratoire de Chimie Physique, Université R. Descartes, Paris, France

‡ Laboratoire de Chimie Physique des Matériaux Amorphes, UMR 8611, CNRS, Université de Paris Sud, France

Abstract. Solid state NMR spectroscopy has been used to study the molecular dynamics of the toluene-solvated C_{60} compound, $C_{60}.C_7H_8$. From the $^1H \rightarrow ^{13}C$ cross-polarization experiments (CP), we have obtained the cross polarization time, $T_{IS} = 12.6$ ms for C_{60} and 1H spin-lattice relaxation time in the rotating frame, $T_{1\rho} = 170$ ms. By using the cross polarization inversion method (ICP), we have deduced that all toluene molecules rotate (as seen by NMR) around the axis perpendicular to the cycle and are **strongly oriented** at an angle of 65° between the rotation axis of the toluene molecules and the direction of the principal magnetic field.

INTRODUCTION

Since the successful production (1) of C_{60} on the macroscopic scale, the study of this molecular crystal has become a very important field of research in solid state physics. One of these studies is related to the solvated- C_{60} . These solvated compounds are clearly different from C_{60} molecules containing solvent impurities due to the extraction technique of C_{60} molecules. These compounds are made of C_{60} and solvent molecules, often hydrocarbons, in a well determined stoichiometric ratio and are often neutral van der Waals complex. The structure and the physical properties of the solvated-crystal powder (2-4) obtained by slow evaporation depends on the nature of the solvent. The structure of the $C_{60}.C_7H_8$ is shown below (see figure 1(a)) and is in good agreement with our ^{13}C solid NMR results on this compound which are, as far as we know, the first NMR results on this compound.

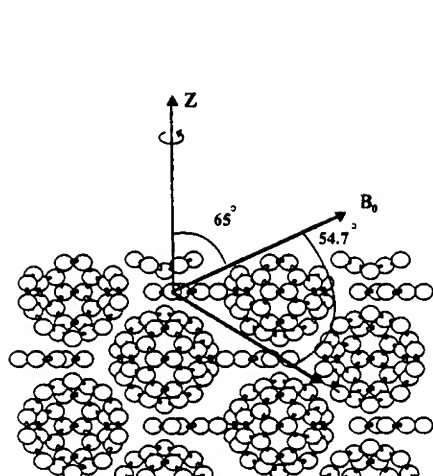


Figure 1(a) : Structure of $C_{60}.4C_6H_6$ with the representation of rotation axis, Z ; the principal magnetic field, B_0 ; and the rotor axis.

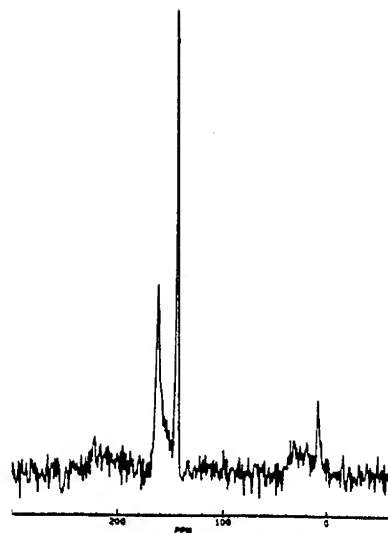


Figure 1(b) : ^{13}C CP NMR line shape of $C_{60}.C_7H_8$.

EXPERIMENTAL

Orthorhombic crystals of the C_{60} /toluene 1:1 solvate were obtained by slowly evaporating solutions of C_{60} in toluene during a few weeks at room temperature in the dark. The ^{13}C NMR measurements were performed on a Bruker MSL 300 spectrometer with a superconducting magnet of 7.05 Tesla (working frequency for ^{13}C : 75.47 MHz). All chemical shifts are given with respect to the ^{13}C resonance frequency in TMS. We used a 4 mm CP-MAS probe (Cross-Polarization with Magic Angle Spinning) for all of our measurements. Standard CP (5) and ICP (6) pulse sequences have been exploited.

RESULTS AND DISCUSSION

The room temperature ^{13}C solid CP NMR spectrum of $C_{60}.C_7H_8$ is shown in figure 1(b). On this figure we can see three main NMR lines. First of all, we will discuss the NMR line of C_{60} molecules. The NMR line of C_{60} molecules is a single narrow line (FWHM $\simeq 4$ ppm) and its isotropic chemical shift is the same as the crystalline C_{60} powder (7), at 143.68 ppm. This indicates that all carbon atoms composing the C_{60} molecules in this compound are magnetically equivalent and perform fast isotropic rotations. We may also conclude that there is no Knight shift and thus this toluene-solvated C_{60} compound is essentially a neutral van der Waals complex.

On figure 2(a), we have represented the time evolution of C_{60} ^{13}C magnetization as a function of contact time. From this curve we have obtained a cross-polarization time of 12.6 ms and a proton spin-lattice relaxation time in the rotating frame, $T_{1\rho}$, of 170 ms. These values are very similar to those obtained for the $C_{60}.4C_6H_6$ (8) and are extracted

from the following fit equation:

$$M_S(t) = M_{S0} \frac{\gamma_I}{\gamma_S} \frac{1}{1 - \lambda} (1 - e^{-(1-\lambda)t/T_{IS}}) \quad (1)$$

where

$$\lambda = T_{IS}/T_{1\rho} \quad (2)$$

γ_I and γ_S are respectively the 1H and ^{13}C magnetogyric ratio.

The toluene molecules are represented by two NMR signals at 163 ppm (aromatic carbons) and 8 ppm (CH_3 groups). The polarization inversion evolution of aromatic carbons is shown on figure 2(b). Considering an uniaxial rotation of the toluene molecules, we fitted our ICP curves with the following equation:

$$M_z(t) = -1 + e^{-R_{df}t} + e^{-\frac{1}{2}(R_{dp}-2R_{df})t} \cos\left(\frac{1}{2}bt\right) \quad (3)$$

whith

$$b = \frac{\gamma_I \gamma_S \hbar}{2r_{IS}^3} (3\cos^2\gamma - 1) \quad (4)$$

where R_{df} is the spin diffusion rate with a dipolar spin rate R_{dp} , r_{IS} is the I-S internuclei distance and γ is the angle between the rotation axis of the molecule and the direction of the static magnetic field.

The values obtained by this fit are presented in table 1.

Table 1: Parameters values obtained from the fit of our ICP curve for $C_{60}.C_7H_8$ (line at 163 ppm).

$T_{df} = 1/R_{df}$	$T_{dp} = 1/R_{dp}$	b	γ
0.88 ms	104.7 μs	5.922 kHz	65°

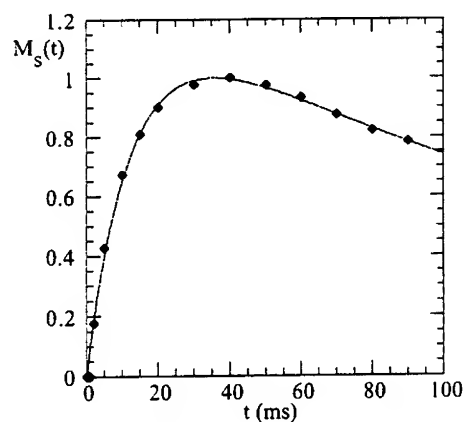


Figure 2(a) : CP curve of C_{60} molecules in $C_{60}.C_7H_8$

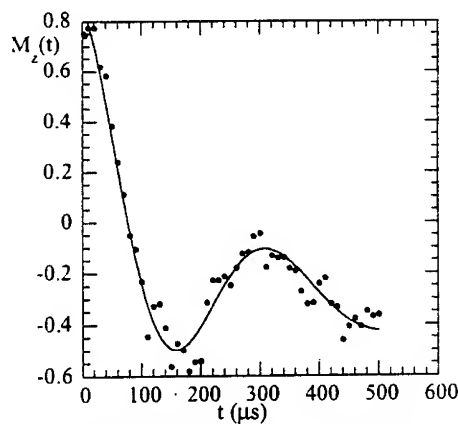


Figure 2(b) : ICP curve of the toluene molecules in $C_{60}.C_7H_8$.

CONCLUSIONS

Our NMR experiments show that the toluene molecules seen are in fast rotation on a NMR time scale. Their rotation axis is tilted towards the direction of the principal magnetic field (B_0) with an angle of 65° . Due to the fact, that the MAS rotor axis forms an angle of 54.7° (magic angle) with the static magnetic field B_0 , we obtain an angle of $65^\circ \pm 54.7^\circ = 119.7^\circ$ or 10.3° (see figure 1(a)) between the direction of the rotation axis of toluene molecules and the MAS rotor axis.

We obtained similar results on an other compound which is $C_{60}.4C_6H_6$ (8) and we showed that we can orient the sample by spinning at 250 Hz (low frequency) during 5 minutes. On the contrary a fast spinning at 2500 Hz can completely desorganize the sample. This is a stable and reversible mechanism, those experiments were reproduced after more than one year has elapsed and in two different laboratories (Brussels and Nancy). This looks like a reversible change between a nematic phase and an isotropic phase.

ACKNOWLEDGMENTS

This work was supported by the BNB (Banque Nationale de Belgique), A.-S. Grell acknowledges financial support from FRIA (Belgium), and I. Messari acknowledges the "Fondation of MEURS-FRANCOIS".

REFERENCES

1. Kratschmer, W., Lamb, L. D., Fostiropoulos, K., and Huffman, D.R., *Nature* **347**, 354-358 (1990).
2. Masin, F., Gall, D., and Gusman, G., *Solid State Commun.* **91**, 849 (1994).
3. Masin, F., Grell, A.-S., Messari, I., and Gusman, G., *Solid State Commun.* **106** (1), 59 (1998).
4. Tekely, P., Palmas, P., Mutzenhardt, P., Masin, F., Grell, A.-S., Messari, I., and Gelbcke, M., *Solid State Commun.* **106** (6), 391 (1998).
5. Mehring, M., *High Resolution NMR Spectroscopy in Solids*, Berlin Heidelberg New York, Springer-Verlag, 1976, ch. 4.
6. Palmas, P., Tekely, P., and Canet, D., *J. of Magn. Resonance, Series A* **104**, 26-36 (1993).
7. Tycko, R., Dabbagh, G., Fleming, R. M., Haddon, R. C., Makhija, A. V., and Zahurak, S. M., *Phys. Rev. Lett.* **67**, 1886 (1991).
8. Masin, F., Tekely, P., Messari, I., Grell, A.-S., to be published

Is the Ground State of A_1C_{60} ($A=Rb,Cs$) Antiferromagnetic?

J. Rahmer*, S. Knorr*, A. Grupp*, M. Mehring*,
J. Hone[†], and A. Zettl[†]

*2. Physikalisches Institut, Universität Stuttgart,
Pfaffenwaldring 57, 70550 Stuttgart, Germany

[†]Department of Physics, University of California at Berkeley,
and Materials Sciences Division, Lawrence Berkeley Laboratory,
Berkeley, California 94720

Abstract. EPR measurements in the metallic and the low-temperature orthorhombic phases of Rb_1C_{60} and Cs_1C_{60} powder samples have been performed at 9, 34, and 94 GHz. Detailed analysis reveals that all line features emerging in the low-temperature phase can be assigned to paramagnetic defects. We conclude that, in contrast to previous interpretations of the data, no signs of antiferromagnetic resonance (AFMR) have been observed. Furthermore we report on 94 GHz measurements of Rb_1C_{60} single crystals which show a clear angular dependence in the metallic regime.

INTRODUCTION

It is well established that upon cooling the polymer phase of the alkali fullerenes Rb_1C_{60} and Cs_1C_{60} undergoes a metal-to-insulator transition in the temperature range of 50 to 25 K. Despite considerable effort that has been put into the investigation of the insulating ground state, its nature is yet not fully understood. Chauvet *et al.* were the first to propose a magnetic ground state in analogy to the spin-density-wave (SDW) ground state of the Bechgaard salt $(TMTSF)_2PF_6$ [1]. Myon spin rotation (μ SR) experiments [2,3] confirmed the notion of a magnetic ground state by proving the existence of internal static magnetic fields. On the other hand μ SR oscillations which are characteristic of SDW materials like $(TMTSF)_2PF_6$ have not been observed in Rb_1C_{60} . This result led to the assumption of a high degree of magnetic disorder in the ground state. Despite this disorder Alloul *et al.* interpreted their observations of the temperature-dependent linewidths and relaxation times of ^{13}C , ^{87}Rb , and ^{133}Cs in Rb_1C_{60} and Cs_1C_{60} as indicative of an antiferromagnetic spin-flop phase [4]. This interpretation has received further support by the direct observation of antiferromagnetic resonance (AFMR) using high field EPR at 75, 150, and 225 GHz by Jánossy *et al.* [5].

Nonetheless the proposition of a magnetic ground state remains under debate. Investigations of EPR intensity, lineshape, and relaxation behavior on Rb_1C_{60} powder at 9 GHz by Atsarkin *et al.* favor a nonmagnetic ground state that could be the result of a spin-Peierls transition or the development of a charge-density-wave (CDW) [6]. A discussion of several ground state scenarios can be found in [7].

Here we present a detailed analysis of the EPR signal of Rb_1C_{60} and Cs_1C_{60} powder samples in Q (34 GHz) and W band (94 GHz) as well as measurements on Rb_1C_{60} single crystals in W band.

Before proceeding to experimental details, the following section outlines the signal behavior expected of magnetically ordered systems in EPR.

THEORY

Similarly to an antiferromagnet, a spin-density-wave ground state shows a very distinctive EPR behavior. The characteristic electron-spin-resonance features of the former are known as antiferromagnetic resonance [8]. For applied static fields H_0 larger than the spin-flop field H_F , which is a characteristic measure of the strength of the antiferromagnetic coupling, the anisotropy of the AFMR signal scales inversely with H_0 . For powder samples this means an inverse scaling of the AFMR linewidth with H_0 . If, on the other hand, the linewidth of a powder originates in g anisotropy, it scales linearly with the applied static field. Thus, these two cases can be discriminated by measuring the signal at different H_0 fields, i.e., different microwave frequencies.

An important feature of magnetically ordered systems is the strong exchange coupling of neighboring spins. This implies fast spin relaxation and thus saturation of AFMR line components is not expected at common microwave powers.

EXPERIMENTAL

EPR measurements at 34 and 94 GHz have been performed using standard Bruker spectrometers equipped with cylindrical cavities. All spectrometers allow the adjustment of signal and reference phase so that mixing of absorptive and dispersive signal components can be minimized. Measured spectra are the derivatives of absorption signals due to the application of lock-in technique for noise suppression.

Powder samples were prepared by K.-F. Thier following the standard route. Rb_1C_{60} single crystals were kindly provided by J. Hone of the Zettl group in Berkeley.

MEASUREMENTS

While in the conducting polymer phase Rb_1C_{60} and Cs_1C_{60} powder samples show only the conduction-electron-spin-resonance (CESR) peak, the signal turns into a

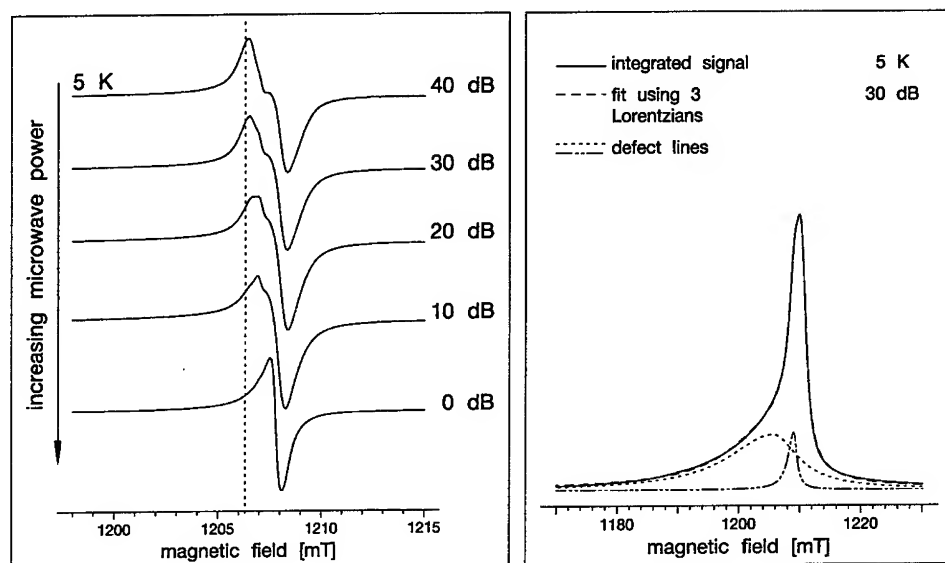


FIGURE 1. Low temperature spectra of Rb_1C_{60} at 34 GHz applying increasing microwave power, as measured (left). The spectra are labelled with the corresponding microwave attenuation values in decibel. Increasing the irradiated microwave power leads to the saturation of the line component indicated by the dashed line. The right figure shows the integrated spectrum at 30 dB fitted with three Lorentzians. Only the two line components that emerge at low temperatures are shown separately. The third component is a residual CESR signal. Note the different scaling of the field axes.

broad powder spectrum at low temperatures [5,7]. In order to determine whether this signal is composed of overlapping line components, the relaxation behavior was studied in saturation and by pulsed EPR experiments.

The left hand side of Fig. 1 displays cw EPR spectra of Rb_1C_{60} obtained at 5 K in Q band. The irradiated power differs by a factor of 10 between neighboring spectra. The signal component at the position of the dashed vertical line can be saturated by increasing the applied microwave power while the adjacent component at higher field values shows no signs of saturation. The broad wing to lower field values that is visible in the integrated spectrum in the right part of Fig. 1 also shows a decrease of intensity at an attenuation of 0 dB which corresponds to an irradiated power of roughly 135 mW. Hence, three different line components can be discriminated by their differing saturation behavior.

For this reason a fit using three Lorentzians to match the three line components in the integrated EPR signal has been applied (Fig. 1, right). It yields g factors of $g=2.0072$ for the broad component, $g=2.0024$ for the intermediate component, and $g=2.0010$ for the strongest component. A similar fit done on the cw spectrum at 94 GHz leads to the same g factors. By its position the strong component

can be identified as a residual signal of the CESR above the metal-to-insulator transition. The g factor of the intermediate line lies close to the g factor of free electrons. Therefore, this signal is attributed to electrons localized at intrinsic defect structures such as chain ends or broken C_{60} balls. For the third component a strongly coupled spin cluster is assumed to account for the broadness of the signal.

From Cs_1C_{60} powder samples similar spectra have been obtained, except that in this material the g factor of the broad component is 2.0037, and the residual CESR signal is much weaker than in Rb_1C_{60} .

Two-pulse experiments, which in general are sensitive to rather long-lived spin species only, show two line components at $g=2.0025$ and $g=1.9993$ for both Rb_1C_{60} and Cs_1C_{60} . The first component, also visible in the cw spectra, is the one previously assigned to localized radicals; the second is too weak to be seen in the cw spectrum. It is attributed to C_{60}^- ions since its g factor is close to that of C_{60}^- ions in solution [9].

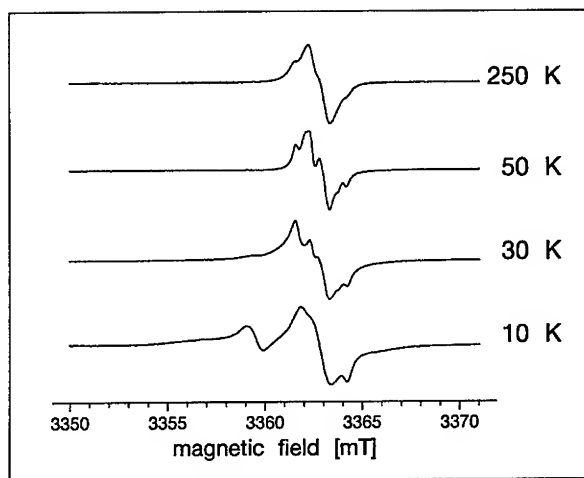


FIGURE 2. Rb_1C_{60} single crystal EPR signal for different temperatures at 94 GHz. At 50 K and above the signal exhibits an angular dependence that is not observed below the metal-to-insulator transition.

Beside the powder samples, Rb_1C_{60} single crystals have been investigated. At above approximately 400 K, these samples are true single crystals with a cubic lattice structure. Upon cooling to the orthorhombic polymer phase, domains with differently oriented polymer chains develop. There are six possible orientations of the orthorhombic cell within the crystal. Figure 2 shows a cw EPR signal of this crystal sample at different temperatures in W band. At 50 K a structured line is visible that can be fitted by six Lorentzians. The structure arises from the six CESR signals of the different domains that appear at different field values because of g anisotropy. Upon rotation of the crystal an angular dependence of the line pattern is observed. At higher temperatures an increased scattering rate of the

conduction electrons leads to a broadening of the CESR line components and thus to smoothening of the line pattern that can be observed in the 250 K spectrum in Fig. 2. At low temperatures the metal-to-insulator transition changes the signal significantly. The sixfold pattern disappears and broader components arise. This low-temperature signal is isotropic.

DISCUSSION

For the cw spectra in Q band as well as in W band all line features can be assigned to paramagnetic spins. None of the signal components shows characteristics of AFMR. In the Rb_1C_{60} crystal, an angular dependence of the signal was observed in the metallic phase. At low temperatures this angular dependence vanishes. This is in contrast to the expectations for a single crystal AFMR signal, that should have a strong angular dependence.

These observations might be explained by assuming that the AFMR is too broad and thus too weak to be detected in powders. In the crystal sample, interactions between different domains could also broaden a possible signal beyond detectability. Another explanation might be that there is no antiferromagnetic or spin-density-wave ordering in these alkali fullerides. This would imply that the metal-to-insulator transition leads to a spin-Peierls or charge-density-wave ground state.

REFERENCES

1. O. Chauvet, G. Oszlány, L. Forró, P. W. Stephens, M. Tegze, G. Faigel, and A. Jánossy, *Phys. Rev. Lett.* **72**, 2721 (1994).
2. W. A. MacFarlane, R. F. Kiefl, S. Dunsiger, J. E. Sonier, and J. E. Fischer, *Phys. Rev. B* **52**, R6995 (1995).
3. Y. J. Uemura, K. Kojima, G. M. Luke, W. D. Wu, G. Oszlány, O. Chauvet, and L. Forró, *Phys. Rev. B* **52**, R6991 (1995).
4. V. Brouet, H. Alloul, Y. Yoshinari, and L. Forró, *Phys. Rev. Lett.* **76**, 3638 (1996).
5. A. Jánossy, N. Nemes, T. Fehér, G. Oszlány, G. Baumgartner, and L. Forró, *Phys. Rev. Lett.* **79**, 2718 (1997).
6. V. A. Atsarkin, V. V. Demidov, and G. A. Vasneva, *Phys. Rev. B* **56**, 9448 (1997).
7. M. Bennati, R. G. Griffin, S. Knorr, A. Grupp, and M. Mehring, *Phys. Rev. B* **58**, 23 (1998).
8. S. Foner, in *Magnetism*, edited by G. T. Rado and H. Suhl, Academic Press, New York, 1963.
9. D. Dubois, T. Jones, and K. M. Kadish, *J. Am. Chem. Soc.* **114**, 6446 (1992).

Comparative Study of Ferromagnetic and Non-Ferromagnetic modifications of TDAE-C₆₀

D. Arčon, R. Blinc, P. Cevc, A. Omerzu, and D. Mihailovič

J. Stefan Institute, Jamova 39, 1000 Ljubljana, SLOVENIA

Abstract. The magnetic properties of two different modifications of TDAE-C₆₀ have been studied with the ESR and ¹H NMR. Well-annealed single crystals display a transition to a ferromagnetically ordered state as confirmed by the observation of the ferromagnetic resonance. On the other hand the magnetic ground state of the non-ferromagnetic modification is consistent with the singlet ground state. The gap between the singlet and low lying triplet excited state opens below 11 K and reaches about 15 K at 5 K. A possible structural differences and their impact on the observed magnetic properties of the two modifications are discussed.

INTRODUCTION

Magnetic ordering in fulleride derivatives has been so far observed only in three different systems: polymeric phase of AC₆₀ (A=Rb,Cs) [1], NH₃K₃C₆₀ [2] and TDAE-C₆₀ [3]. While in first two cases the magnetization vanishes at low temperatures due to the antiferromagnetic interactions, the magnetization of TDAE-C₆₀ strongly increases below T_C=16 K signaling a transition to a ferromagnetically ordered state. This is in particular surprising since TDAE-C₆₀ is built up of only light elements of the first row (H,C,N). Some of the main properties of TDAE-C₆₀ have been described already in the original report by Wudl et al. [3]: (i) sharp increase of the spontaneous magnetization below the transition temperature T_C, (ii) absence of the hysteresis between cooling and warming and (iii) very small spontaneous magnetization being only 0.11 μ_B/C₆₀. Based on a rather large room temperature conductivity it has been suggested [3] that TDAE-C₆₀ is the first organic itinerant ferromagnet. However later conductivity experiments [4,5] showed that TDAE-C₆₀ is a semiconductor thus ruling out the proposed model of itinerant ferromagnetism. All the models, which later on appeared in the literature [6], mainly tried to explain the surprisingly small spontaneous magnetization. They were ranging from superparamagnetism, weak ferromagnetism and inhomogeneous ferromagnetism.

In this contribution we report on the search for the (anti)ferromagnetic resonance modes which allowed us to discriminate between the proposed models. In addition to that we show that the magnetic properties of TDAE-C₆₀ are very sensitive to the conditions during the preparation and the heat treatment. Namely the samples grown at room temperature show a transition to S=0 state rather than to a ferromagnetic state. They can be transformed to a ferromagnetic modification with

extended annealing at or above the room temperature. The difference in the magnetic properties of the two modifications is discussed in view of the tinny structural differences.

RESULTS

First we describe the magnetic resonance results on the well annealed modification of TDAE-C₆₀ which shows a transition to the ferromagnetic ground state below 16 K. It is well known that in the magnetically ordered state one can not excite individual precessions of the paramagnetic spins (ESR). But what one can excite is a coherent precession of all the spins, i.e. the (sub)lattice magnetization around the effective magnetic field. This is called (anti)ferromagnetic resonance. As a general rule the number of resonance modes is equal to the number of the sublattice magnetizations. So in a simple ferromagnetic material we would expect to observe only one resonance mode while in antiferromagnets two resonance modes are predicted. We have tried to find these resonance modes in the microwave and radio frequency region between 30 MHz and 245 GHz in order to discriminate among the proposed models.

In microwave region we have observed below T_C only one very intense resonance line shifted away from the Larmor frequency by about 40 G-60 G [7]. The sign and the magnitude of the shift depend on the orientation of the crystal with respect to the external magnetic field. The resonance frequency varies almost linearly with resonance field in the microwave region and this does not allow a clear assigning of the observed line to ferromagnetic resonance. On the other hand in the radio-frequency region the relation between the resonance field and resonance frequency become strongly non-linear showing a typical dip when $allH_0$ (Fig. 1a) [8]. The dip disappears above T_C (Fig. 1c) as expected for the paramagnetic sample. The results can be explained in terms of uniaxial Heisenberg ferromagnetism with the anisotropy field being only 29 G [8].

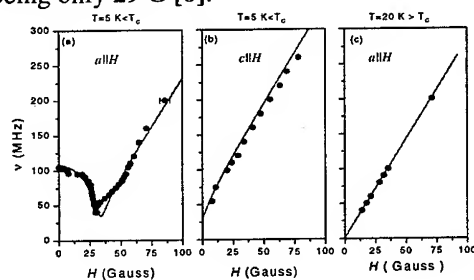


Fig. 1: Dependence of the resonance frequency versus resonance field in a well annealed TDAE-C₆₀ single crystal below (a,b) and above (c) transition temperature. The solid line represent the fit to the theoretical curve predicted for an uniaxial Heisenberg ferromagnet with the anisotropy field of 29 Gauss.

A completely different magnetic resonance response was found in the fresh TDAE-C₆₀ single crystals grown at temperatures at or below 0°C. SQUID measurements showed a complete absence of any signal even when sweeping the external magnetic field between 0 and 100 G [9]. This means that the ground state in these types of crystals has a total magnetization equal to zero. Such a case can be

realized either by antiferromagnetic long range ordering or by a transition to the $S=0$ ground state. We have again tried to apply ESR as well as ^1H NMR technique to study the magnetic properties of the non-ferromagnetic modification of the TDAE- C_{60} crystals and to compare the results with the ones obtained on a ferromagnetic modification.

Surprisingly the ESR results in the paramagnetic phase in the two different modifications studied are strikingly similar. The only major difference is in the temperature dependence of the ESR linewidth (Fig. 2). While in ferromagnetic modification the exchange narrowing narrows the line over the large temperature interval between 220 K and 75 K in the non-ferromagnetic modification the exchange narrowing starts at lower temperature around 180 K and the onset is much more abrupt. This difference might be due to the difference in the orientational ordering of the C_{60}^- ions.

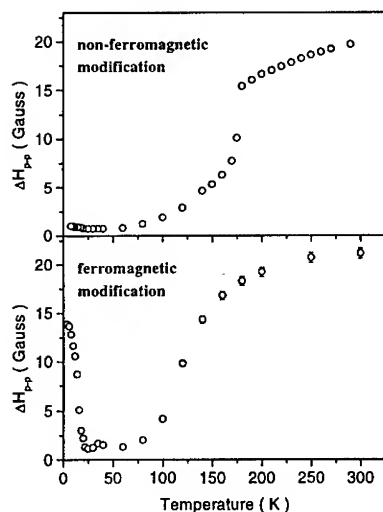


Fig. 2: Temperature dependence of the ESR peak-to-peak line-width measured in the non-ferromagnetic and ferromagnetic modifications. Note the difference in the narrowing of the line below 200 K.

However the main difference in the ESR response of the two modifications came at low temperatures. The ESR signal of the non-ferromagnetic crystals is composed at low temperatures only of a narrow ESR line at a Larmor frequency with $g=2.0001$ contrary to the previously described case of the ferromagnetic modification. The intensity of the ESR signal at high temperatures approximately follows a Curie law. Below 11 K the intensity of the signal suddenly starts to decrease consistent with the developing of the non-magnetic ground state. It should be noted that we have searched for the additional resonance lines in a broad field range between 0 and 12 kG at 9.6 GHz, 1.2 GHz and in the radio-frequency region. No additional resonance modes have been found. These rules out any long-range magnetic ordering like antiferromagnetic or spin-density wave type of ordering as we have failed to find the antiferromagnetic resonance.

We have therefore tried to fit the ESR susceptibility data with a singlet ground state model. Although the fit with the temperature independent gap between the singlet ground and low lying triplet excited state reproduces all the main features of the temperature variation of the ESR susceptibility (Fig. 3a), it can not fit the sharpness of the peak around 11 K. The fit can be significantly improved assuming that the gap between the singlet ground state and the excited triplet state is temperature dependent (Fig. 3a). The gap opens below 11 K and reaches the value of about 15 K at lowest

temperatures [10]. In the ferromagnetic modification on the other hand the ESR susceptibility increases by several orders of magnitude (insert to Fig. 3a) due to the transition to a ferromagnetically ordered state.

The ESR results are thus compatible with the singlet ground state and rule out any long range magnetically ordered state. How is this reflected in the ^1H NMR spectrum and spin-lattice relaxation time? ^1H NMR spectrum shows a difference between the ferromagnetic and non-ferromagnetic samples already at room temperature. In the ferromagnetic single crystals we have found two ^1H NMR lines, one exhibiting a Curie-type paramagnetic shift while the other showing almost temperature independent shift. In the non-ferromagnetic single crystals only non-shifted line have been found whose second moment first increases with decreasing temperature and then even slightly decreases below 11 K. The temperature dependence of the ^1H NMR line thus tells us that the spin density on the TDAE methyl-proton sites is in the non-ferromagnetic type of crystals significantly reduced with respect to the one found in ferromagnetic crystals. Therefore the only interaction between the unpaired electrons and the methyl protons is the dipolar interaction. If this is true the methyl proton spin-lattice relaxation rate should adopt an activated type of behavior below 11 K. Such a behavior has been indeed observed (Fig. 3b) and the temperature dependence of the ^1H spin lattice relaxation rate can be again simulated with singlet ground state model and the same parameters extracted from the ESR data.

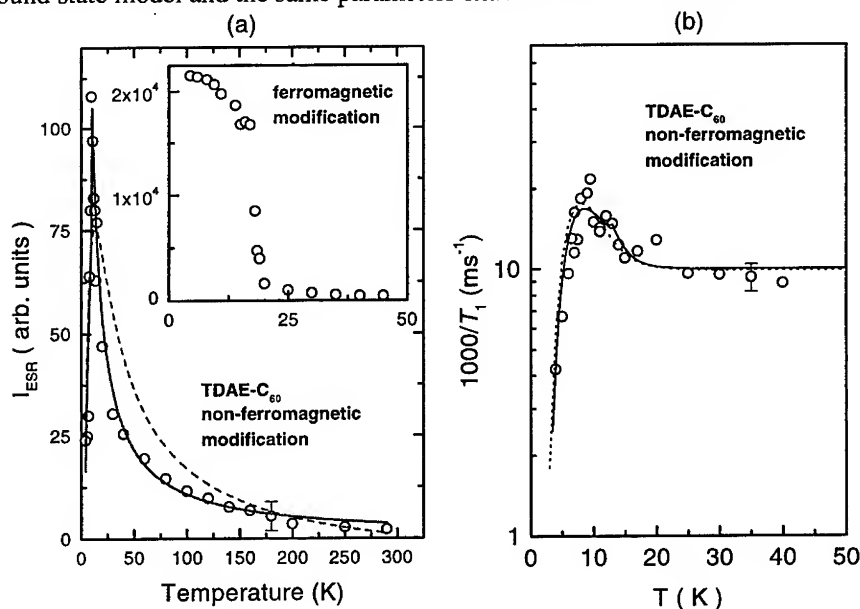


Fig. 3: (a) Temperature dependence of the ESR susceptibility in the non-ferromagnetic modification. The solid line represents the fit assuming the opening of the singlet-triplet gap below 11 K while the dashed line is calculated using the temperature independent gap. The insert shows the increase of the ESR susceptibility in the ferromagnetic modification below the transition temperature $T_C=16$ K. (b) Proton spin-lattice relaxation data confirms the opening of the spin-gap below 11 K. Solid and dashed lines have the same meaning as in Fig. 3a.

CONCLUSIONS

ESR and ^1H NMR results showed that TDAE- C_{60} single crystals can be grown in two different modifications (a) ferromagnetic and (b) non-magnetic with a singlet ground state below 11 K. Non-ferromagnetic modification can be transformed into the ferromagnetic one with the extended annealing at or above the room temperature. So what makes the major difference between the two modifications? Preliminary X-ray diffraction comparative study [11] showed that in the ferromagnetic modification the monoclinic angle β is slightly larger than in the non-ferromagnetic modification. This means that the C_{60} - C_{60} contact is in the non-ferromagnetic modification slightly better thus increasing the overlap between the neighbouring spins. Consequently the non-ferromagnetic modification is more quasi-one-dimensional. It is well known that the low-dimensional systems are often a subject of various types of instabilities. Arovas et al. [12] showed that TDAE- C_{60} in a purely one-dimensional limit would have a non-magnetic singlet ground state. This has been indeed observed in our fresh samples. In their theory they have also shown that switching on the chain-chain interactions would lead to a 3-dimensional ferromagnetic ordering. The ferromagnetic modification indeed possesses this property as demonstrated by ^1H NMR which showed a significant spin density on the methyl protons. TDAE $^+$ ions thus seem to serve as a super-exchange bridge between the two neighbouring C_{60}^- chains and are crucial for the ferromagnetic ordering in this compound.

REFERENCES

- [1] O. Chouvet et al., *Phys. Rev. Lett.* **72**, 2721 (1994).
- [2] Y. Iwasa, et al., *Phys. Rev. B* **53**, R8836 (1996).
- [3] P. M. Allemand, et al., *Science* **253**, 301 (1991).
- [4] A. Schilder et al., *Phys. Rev. Lett.* **73**, 1299 (1994).
- [5] F. Bommelli, et al., *Phys. Rev. B* **51**, 1366 (1995).
- [6] R. Blinc et al., *Appl. Magn. Reson.* **11**, 203 (1996).
- [7] R. Blinc et al., *Phys. Rev. B* **58**, 14416 (1998).
- [8] D. Arčon, et al., *Phys. Rev. Lett.* **80**, 1529 (1998).
- [9] Z. Trontelj et al., unpublished.
- [10] D. Arčon et al., *Phys. Rev. B* **59**, 5247 (1999).
- [11] A. Omerzu et al., to be published
- [12] D.P. Arovas and A. Auerbach, *Phys. Rev. B* **52**, 10114 (1995).

Spin-singlets in metallic cubic quenched CsC₆₀

V. Brouet¹, H. Alloul¹, F. Quéré¹, G. Baumgartner² and L. Forró²

¹*Physique des solides, UMR 8502 CNRS, UPS, 91 405 Orsay (France)*

²*Physique des solides semicristallins, IGA, EPFL, 1015 Lausanne (Switzerland)*

Abstract. We present a discussion of the electronic properties of the quenched cubic phase of CsC₆₀, based on our recent investigation by ¹³C and ¹³³Cs NMR. We conclude that the phase is metallic but that localized spin-singlets are formed on a small fraction of the C₆₀ molecules. We discuss possible mechanisms for the stabilization of these spin-singlets, related to the occurrence of Jahn-Teller distortions of the C₆₀ molecule.

I INTRODUCTION

Two different AC₆₀ cubic phases are known : one at high temperatures ($T > 350$ K) for A = K, Rb or Cs and one below 130 K in CsC₆₀ obtained by quenching this high temperature phase to avoid polymerization. Although the structures of these two phases are very similar (they only differ by the orientational order between the C₆₀ [3]), their electronic properties seem to differ drastically. Therefore, the intrinsic behavior of cubic AC₆₀ is not yet understood, even though it is of crucial interest for a global understanding of fullerenes. The ESR susceptibility of the high-T phase is Curie-like [1] suggesting localization of one electron on each C₆₀ ball, whereas the quenched cubic (QC) CsC₆₀ has a Pauli-like ESR susceptibility [2], suggesting that it is metallic.

Recently, we have detected by NMR the coexistence of *spin-singlets* with the metallic behavior [4]. It was deduced from the unexpected observation of two well resolved ¹³³Cs NMR lines with similar intensities. This indicates the existence of two inequivalent Cs sites, mixed on the microscopic scale, although structural measurements cannot explain the presence of two different sites [5]. Moreover, the local electronic environment of these two sites are very different. NMR measurements of the local susceptibility sensed by the most shifted Cs line (denoted hereafter S for "Shifted", the other line being NS for "Not Shifted") are displayed on figure 1. Both $1/T_1T$ and its shift have a strong temperature dependence, that can be modelled by an activated law, indicating that the electronic spectrum is *locally gapped*. This proves that QC CsC₆₀ is not a simple metal as suggested by ESR and also by the temperature dependence of the ¹³C NMR relaxation rates between 50 K and 110 K, and this is certainly important for the understanding of its ground state.

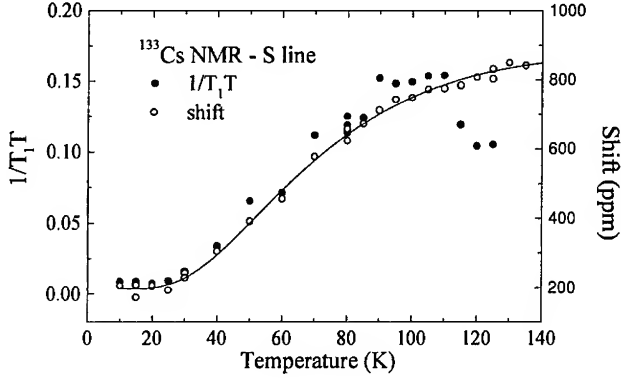


FIGURE 1. $1/T_1T$ and K as a function of temperature for the most shifted ^{133}Cs line. The line is a fit to $K=a+b/T\cdot\exp(-175/T)$. The discrepancy between shift and $1/T_1T$ above 110 K is presumably related to exchange between the two Cs sites.

We present here a more detailed discussion of the properties of this phase together with new experimental observations that supports our analysis.

II DESCRIPTION OF THE MODEL

To reconcile these two sets of experimental facts, we have proposed that the electronic properties of the QC phase are *inhomogeneous on the local scale*. Figure 2 represents a possible solution to this problem. Within a globally metallic phase, we assume that, on a few C_{60} molecules, two electrons are localized and paired into a spin-singlet. Roughly speaking, then we expect two different types of local electronic behavior : a nearly temperature independent susceptibility for the metallic component χ_m and an activated one for the singlets χ_g . The nature of this latter gap could be either related to fundamental excitations of the spin-singlet or to breaking and/or delocalization of the electronic pair.

Only the nearest neighbor Cs sites of a C_{60}^{2-} would sense the spin-gap and they correspond to the observed S sites. More precisely, the NMR shift K of a Cs line is proportional to the local electronic susceptibility of its six C_{60} neighbors through hyperfine coupling. We then expect:

$$K_S = 5A_m \chi_m + A_g \chi_g \quad \text{and} \quad K_{NS} = 6A_m \chi_m \quad (1)$$

where A_m and A_g are the hyperfine coupling to a metallic ball and a C_{60}^{2-} respectively. The small shift observed for the NS sites is typical of metallic fullerenes, where A_m is in fact very small because of the very small hybridisation between C_{60} and Cs^+ . The much larger shift observed for the S sites implies either $A_g \gg A_m$

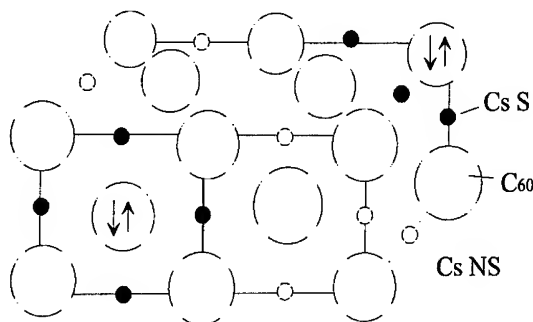


FIGURE 2. Dilution of spin-singlets in the metallic QC CsC_{60} . The neighboring Cs sites of a C_{60} that bears a spin-singlet (C_{60}^{2-}) are “S sites”, the other ones NS sites.

or $\chi_g \gg \chi_m$ or both. Hyperfine couplings are generally very sensitive to small local perturbations, so that it would be reasonable to find that A_g largely exceed A_m .

Within this model, we can deduce the number of C_{60}^{2-} from the relative intensities of the two Cs lines. Experimentally, we observe roughly the same number of S and NS sites, which implies about 10% of C_{60}^{2-} . As this is a small fraction of the C_{60} , measurements like ESR would not be very sensitive to the presence of the singlets. A local probe strongly coupled to the C_{60}^{2-} such as the Cs S site has been necessary to identify them unambiguously.

III ADDITIONAL SUPPORT FOR THE MODEL

Following the lines of this model, it is easy to convince oneself that there is a non-negligible probability of finding a Cs site with two C_{60}^{2-} neighbors. These sites could be called “2S” sites. Their likelihood depends on the distribution of the C_{60}^{2-} , which may be completely random or partially ordered, but is expected to be between 5 and 10 %. It is unlikely that they would behave as S sites; we would instead expect a larger shift for the 2S sites of the order of $K_{2S} = 4A_m \chi_m + 2A_g \chi_g \simeq 2K_S$.

Consequently, we have carefully investigated the high frequency side of the spectra, where we expect such a resonance to occur. Figure 3 shows that such a line clearly exists at 120 K, and it can be followed down to at least 80 K. We estimate its intensity to $6 \pm 2\%$ in very good agreement with our expectations. Its shift is approximately twice the one of the S line, and its relaxation time is shorter : at 80 K, $T_1 = 43 \text{ms} \pm 11 \text{ms}$ to be compared with $110 \pm 10 \text{ms}$ for the S line, in good agreement with the expected ratio $T_{1,2S} / T_{1,S} \simeq 2$. More experiments are needed to establish whether the temperature dependence of K_{2S} and $(1/T_1)_{2S}$ scales with those of the S line.

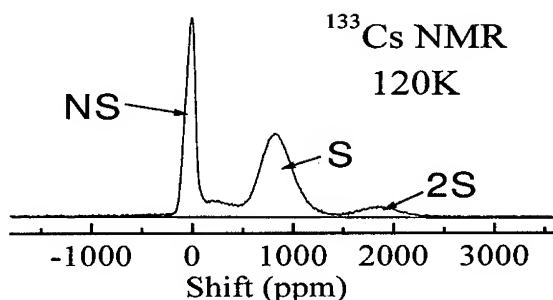


FIGURE 3. ^{133}Cs NMR spectra at 120 K with a repetition time of 100 ms.

The detection of a new Cs “2S” line shows rather unambiguously that the inequivalency between the Cs sites results from a coupling with *zero* (NS), *one* (S) or *two* (2S) “anomalous C_{60} ”. If it were otherwise, it would be hard to explain the presence of a line that senses almost exactly twice the local susceptibility of the S sites.

However, it certainly eliminates the possibility of a symmetry-reducing *collective* effect, such as a small dimerization or a particular arrangement between the different C_{60} orientations. Hence, this new observation strongly supports our model.

IV STABILIZATION OF THE SPIN-SINGLETS

The essential information revealed by the study of ref. 4 is the tendency to electron pairing evidenced by the formation of spin-singlets. This is an unusual behavior for fullerides, and one might have expected QC CsC_{60} to be a superconductor similar to A_3C_{60} . The recent observation of an insulating non-magnetic ground state in polymerized CsC_{60} at 5 kbar [6] is another example of formation of spin-singlets. However, they likely result from a totally different type of interaction related to the 1D character of the polymerized phase.

We suggest that the singlet in the QC phase is stabilized by a Jahn-Teller (JT) distortion of the C_{60} molecule. The energy gain due to a JT distortion is predicted to be larger for a C_{60}^{n-} with even n [7–9], leading to an effective *attractive interaction* between electrons for odd n . It has been argued that this indirect electronic interaction may help to overcome Coulomb repulsion in A_3C_{60} and favor superconductivity. Our study support the idea that JT distortion indeed lead to indirect electron interactions. However, in QC CsC_{60} , the two Cs lines indicate that the singlets are static, at least below 110 K and on the time-scale of the NMR experiment ($\simeq 30$ kHz).

These C_{60}^{2-} could be viewed as local defects in the electronic structure appearing quite independently. The number of singlets will then depend essentially of the

probability for a C_{60} in the metallic phase to be doubly occupied. Structural defects (for example in the orientational order) could play a role in “trapping” these C_{60}^{2-} . In the temperature range of stability of the QC phase, we do not detect a strong variation of the number of singlets with temperature (it increases at most by 20% between 130 K and 10 K). We note that such a situation causes a non-stoichiometric doping of the t_{1u} band, and one can wonder whether the metallic character results from this off-stoichiometry.

Another possibility is that a cooperatively ordered ground state with alternating C_{60}^{2-} and neutral C_{60} is partially formed. Whether these dilute C_{60}^{2-} form a long-range super-structure remains an open question. Incomplete dismutation could be due to frustration in the fcc lattice which cannot be divided into two equivalent sublattices. The energy cost due to electrostatic repulsion between C_{60}^{2-} could also act to limit their concentration. However, this study raises the possibility that such a ground state could be competing with superconductivity in A_nC_{60} with odd n .

V CONCLUSION

We have shown that about 10% of the C_{60} balls behave “anomalously” in the QC phase, this anomaly being characterized by the presence of a *non-magnetic spin-gap*. It could be explained by the presence of a spin-singlet on these balls. The stabilization of C_{60}^{2-} balls is attributed to the larger stability of JT distorted C_{60}^{2-} compared to JT distorted C_{60}^- . Although the role of JT distortions has often been invoked to explain the properties of fullerides - both in the metallic A_3C_{60} and insulating A_4C_{60} compounds - there is no unambiguous evidence of their importance. In this light, these results will aid in reaching a global understanding of the different parameters that influence the electronic interactions in these systems.

We acknowledge financial support from the TMR Programme of the European Commission (Research Network “FULPROP” ERBMRXVT970155).

REFERENCES

1. O. Chauvet *et al.*, Phys. Rev. Letters **72**, 2721 (1994).
2. M. Kosaka *et al.*, Phys. Rev. B **51** 17, 12018 (1995).
3. A. Lappas, M. Kosaka, K. Tanigaki and K. Prassides, J. Am. Chem. Soc. **117**, 7560-7561 (1995).
4. V. Brouet *et al.*, Phys. Rev. Letters, **82**, 2131 (1999)
5. The sample used for NMR has been investigated by X-ray with P.W. Stephens and G. Bendele at the Brookhaven National Synchrotron Light Source. No structural distortion with respect to the structure proposed in ref. 3 could be detected.
6. B. Simovic, *et al.* Phys. Rev. Letters, **82**, 2298 (1999)
7. W. Victoroff and M. Héritier, J. Phys. I France **6**, 2175-2180 (1996)
8. O. Gunnarson PRB **51**, 3493 (1995)
9. N Manini, E. Tosatti and A. Auerbach, Phys. Rev. B **45**, 13008 (1994)

Distinct polymer chain orientations in KC_{60} and RbC_{60}

P. Launois¹, R. Moret¹, S.C. Erwin², J. Hone³, A. Zettl³

¹*Laboratoire de Physique des Solides (UMR 8502 CNRS), bât. 510, Université Paris Sud,
91405 Orsay CEDEX, France*

²*Center for Computational Materials Science, Naval Research Laboratory,
Washington, D.C. 20375, USA*

³*Department of Physics, University of California at Berkeley, and Materials Sciences Division,
Lawrence Berkeley National Laboratory, Berkeley, California 94720, USA*

Polymerized alkali fullerides KC_{60} and RbC_{60} display different electronic properties. Single crystal X-ray diffraction and diffuse scattering studies show that the C_{60} chains possess different relative orientations about their axes. We will discuss this result in relation with electronic band structure calculations. The influence of pressure will also be discussed.

Alkali fullerides AC_{60} ($\text{A}=\text{K}, \text{Rb}$) exhibit a transition around 350K from a high temperature cubic phase towards an orthorhombic one where the molecules form polymer chains (1-3). The unit cell parameters are $a_{\text{K}} \approx a_{\text{Rb}} \approx 9.12 \text{ \AA}$, $b_{\text{K}} = 9.95 \text{ \AA}$, $b_{\text{Rb}} = 10.11 \text{ \AA}$, $c_{\text{K}} = 14.32 \text{ \AA}$, $c_{\text{Rb}} = 14.23 \text{ \AA}$. Polymerization occurs by [2+2] cycloaddition along the shortest a axis (fig.1(a)). Powder diffraction studies showed that: i) the intrachain C-C bond lengths are similar in KC_{60} and RbC_{60} (4,5), and ii) the angle μ formed by the cycloaddition planes of a chain and the c axis, which characterizes the chain orientation, satisfies $|\mu| = 45^\circ \pm 5^\circ$, in both KC_{60} and RbC_{60} (3). No definite structural difference has been evidenced between the two compounds, although the relative chain orientations have not been unambiguously determined in any of them. MAS-NMR studies (6) revealed differences between the spin distributions in KC_{60} and in RbC_{60} , suggesting that orientational chain ordering may differ. The AC_{60} compounds have also been investigated by ESR, μSR , NMR and electrical or optical conductivity measurements, and the electronic properties of KC_{60} and RbC_{60} are different. For instance, between 50K and 25K, RbC_{60} exhibits a magnetic transition, unlike KC_{60} (see e.g. (7,8); the possibility of coexistence with a spin-singlet phase has also recently been reported (9)).

In this paper, we present the results of a single-crystal X-ray diffraction study of KC_{60} and RbC_{60} . The relative chain orientations are different in the two compounds, which probably influences the electronic properties. This is discussed in light of ab-initio band structure calculations.

X-RAY DIFFRACTION RESULTS

KC_{60} and RbC_{60} single crystals (typical volume 10^{-2} mm^3) were obtained by stoichiometric doping of C_{60} crystals at 400°C . A solid state transformation to the polymer phase was obtained by subsequent slow cooling to room temperature. The X-ray diffraction experiments (10) were performed using precession, fixed-film and diffractometer techniques.

Precession photographs, which give a global view of the reciprocal space, were taken first. They reveal the existence of orientational domains, which appear at the transition from the cubic to the polymer phase. These domains are related by the point symmetry operations lost at the transition and their orientational relationships could be determined from analysis of the photographs. Additionally, we have shown that Bragg peaks satisfying the relation $h+k+l$ odd are present in KC_{60} but not in RbC_{60} . Thus, the Bravais lattice of polymerized KC_{60} is primitive, while that of RbC_{60} is body-centered.

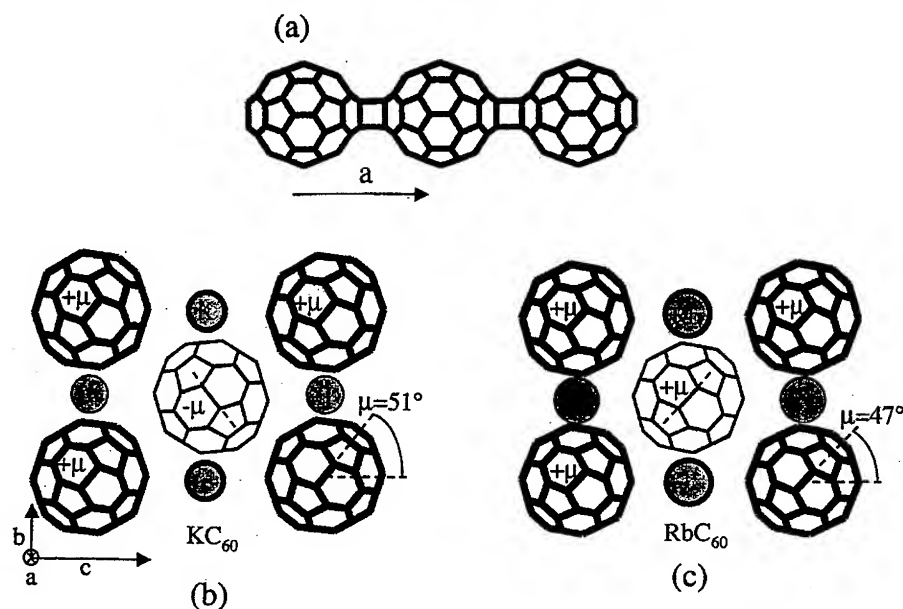


FIGURE 1. (a) Linear polymer chain running along **a**. (b) KC_{60} and (c) RbC_{60} unit cells. In (b) and (c), light lines indicate out of plane C_{60} and alkali ions.

The two orthorhombic space groups compatible with the C_{60} chain symmetry are Pmnn and Immm (3). Thus, one may infer that KC_{60} space group is Pmnn , while RbC_{60} is Immm . For the Immm space group, if the chains are not oriented with their cycloaddition rings in the mirror planes perpendicular to **b** or to **c** ($\mu = 0^\circ$ or 90°), they should take orientations μ and $-\mu$ with equal probability. In a diffraction experiment,

this disorder would produce some diffuse scattering localized between the Bragg reflections. Careful search for such diffuse scattering, using the fixed-crystal fixed-film method under vacuum, to maximize signal-over-noise ratio, was carried out (fig.2). The results showed that there is no diffuse scattering in RbC_{60} , contrary to what would be expected for Immm.

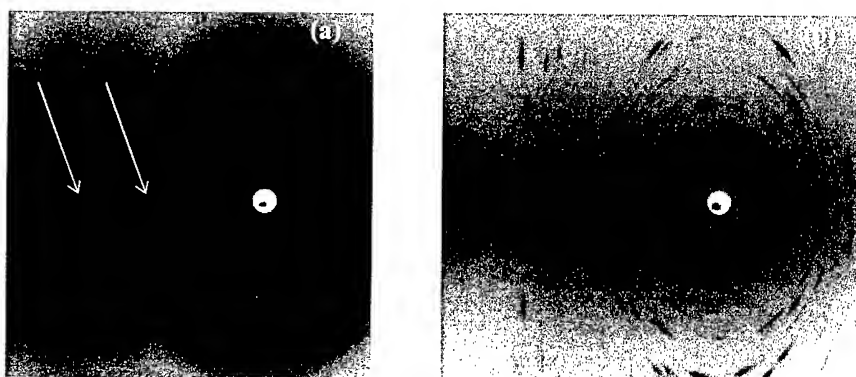


FIGURE 2. Monochromatic fixed-crystal fixed-film photographs from (a) a C_{60} crystal, (b) a RbC_{60} crystal. In (a) and (b), the central ring, from background contributions, should be ignored. In (a), the arrows point toward the diffuse scattering due to the rotating molecules in pure C_{60} at room temperature. The diffuse scattering expected for orientational chain disorder in RbC_{60} , which should be of the same order of magnitude, is absent in (b).

Finally, Bragg peak intensity measurements on KC_{60} and RbC_{60} were performed on a three-circle diffractometer. Despite the existence of orientational variants, we succeeded in measuring a sufficient number of isolated peaks from a single variant. A single crystal structure refinement was then performed, minimizing the reliability factor i.e. the difference between calculated and measured structure factors (fig.2 in ref.(10)). For Pmnn KC_{60} , we obtain a minimum value of the reliability factor $R_{\min} \approx 0.16$ for $\mu \approx 51^\circ$. An attempt to refine the RbC_{60} data for the Immm space group gives $R_{\min} \approx 0.24$ for $\mu \approx 48^\circ$. This configuration is in conflict with the absence of diffuse scattering, so that we were lead to consider a space group of lower symmetry than orthorhombic. The convenient space group compatible with the symmetry of the C_{60} chains is the monoclinic space group I2/m. A refinement within I2/m leads to an improved value of the reliability factor : $R_{\min} \approx 0.06$, for $\mu \approx 47^\circ$. This validates the I2/m structure. We note that no deviation from 90° (allowed by the monoclinic symmetry) has been detected within an experimental resolution of 0.5° . In any case, this deviation is expected to be small due to the rather homogeneous distribution of the C atoms around the chain axes.

In summary, the chain orientation angles are similar in KC_{60} and RbC_{60} (51° and 47°), in agreement with ref.(3), but these compounds are found to possess different space groups, Pmnn and I2/m, respectively. This implies different relative chain orientations; the chain orientations alternate (μ and $-\mu$) in KC_{60} while they are parallel

in RbC_{60} , as shown in fig.1(b) and (c). The single-crystal X-ray diffraction and diffuse scattering study has thus evidenced an important structural difference between KC_{60} and RbC_{60} .

ELECTRONIC BAND STRUCTURE CALCULATIONS

We now address the question of whether the different magnetic properties of KC_{60} and RbC_{60} can be explained by their different relative chain orientations. In ref. (11), first-principles electronic-structure calculations within Local Density Approximation (LDA) were used to calculate the single-particle band structure of the paramagnetic state. A tight-binding fit of the conduction bands (fig.3(a)) was then used as the input to a many-body model Hamiltonian in order to study magnetic fluctuations around the paramagnetic state. The orientational state was taken (for computational simplicity) to be $I2/m$, with $\mu = 45^\circ$, which has now been found to be the correct space group for RbC_{60} ; unit cell parameters were those of RbC_{60} .

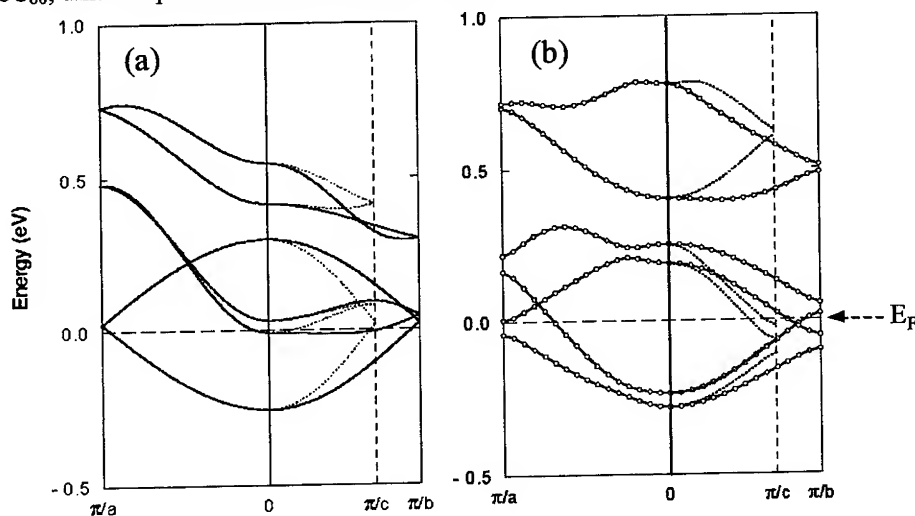


FIGURE 3. (a) Tight-binding fit to the LDA conduction-band structure of RbC_{60} with space group $I2/m$; the bands are folded into the corresponding doubled $Pmnn$ unit cell. (b) Full LDA band structure for the space group $Pmnn$.

To repeat that calculation for the $Pmnn$ space group describing KC_{60} is beyond the scope of this paper. Instead, we examine the input to the many-body calculation - namely, the conduction band dispersion within the LDA. We focus here solely on the differences between RbC_{60} and KC_{60} relative chain orientations. To make the comparison simpler, all other parameters are kept fixed. Fig. 3(b) shows the LDA band structure for the $Pmnn$ space group, appropriate for KC_{60} . The electronic dispersion of the lowest band is three-dimensional (11), despite the quasi-one-dimensional polymer

chains, for both I2/m and Pmnn chain orientations. For the I2/m space group, the rather flat band near the Fermi level (E_F) in fig. 3(a) may contribute to the stabilization of a magnetically ordered ground state, in which a splitting of 0.1 eV results in a pseudo-gap near E_F (fig.3 in ref.(11)). For the Pmnn space group, this flat band at E_F is completely absent. Without the peak at E_F , the energy gain from exchange splitting is considerably reduced. We speculate that it is in fact insufficient to stabilize a magnetic ground state. This is consistent with the experimental findings (7,8).

PRESSURE EFFECTS

KC₆₀ and RbC₆₀ possess different chain orientations while their unit cell parameters are close. This may be related to the strong sensitivity of the orientational potential of the C₆₀ chains with the interchain distances (12). Significant pressure effects may thus be expected. Indeed, resistivity measurements have shown that around 5kbar and 180K, RbC₆₀ exhibits a transition (13); NMR studies also show that the magnetic ground state disappears under pressure (8). Our present results about (i) the influence of the chain orientations on the electronic properties and (ii) the sensitivity of the orientational potential with the interchain distances, suggest that the transition evidenced in ref.(13) may be associated to changes in the chain ordering. Structural investigations under pressure would thus be very interesting.

ACKNOWLEDGMENTS

Fruitful discussions with H. Alloul, V. Brouet, M. Héritier, D. Jérôme, T. Ogitsu, S. Ravy, E. Sandré, B. Simović and W. Victoroff are acknowledged.

REFERENCES

1. Chauvet O. *et al.*, Phys. Rev. Lett. **72**, 2721-2724 (1994).
2. Pekker S. *et al.*, Solid State Comm. **90**, 349-352 (1994).
3. Stephens P.W. *et al.*, Nature **370**, 636-639 (1994).
4. Fox J.R. *et al.*, Chem. Phys. Lett. **249**, 195-200 (1996).
5. Guerrero H.M. *et al.*, Chem. Phys. Lett. **297**, 265-272 (1998).
6. Alloul H. *et al.*, Phys. Rev. Lett. **76**, 2922-2925 (1996).
7. Bommeli F. *et al.*, Phys. Rev. B **51**, 14794-14797 (1995); Brouet V. *et al.*, Phys. Rev. Lett. **76**, 3638-3641 (1996); Bennatti M. *et al.*, Phys. Rev. B **58**, 15603-15608 (1998).
8. Auban-Senzier P. *et al.*, J. Phys. I France **6**, 2181-2190 (1996).
9. Simović B. *et al.*, Phys. Rev. Lett. **82**, 2298-2301 (1999).
10. Launois P. *et al.*, Phys. Rev. Lett. **81**, 4420-4423 (1998).
11. Erwin S.C., Krishna G.V. and Mele E.J., Phys. Rev. B **51**, 7345-7348 (1995).
12. Launois P. *et al.*, to appear in Synthetic Metals (ICSM'98 proceedings).
13. Khazeni K. *et al.*, Phys. Rev. B **56**, 6627-6630 (1997).

LOW SYMMETRY STRUCTURES IN THE Li-Rb-C₆₀ PHASE FIELD

A. Lappas,^{*,‡} E. Aslanis,^{*} K. Prassides,^{*} A. N. Fitch,[#] and M. Hanfland[#]

^{*}*School of Chemistry, Physics and Environmental Science, University of Sussex,
Brighton BN1 9QJ, United Kingdom*

[‡]*Institute of Electronic Structure and Laser, Foundation for Research and Technology – Hellas,
P.O. Box 1527, Heraklion 71110, Greece*

[#]*European Synchrotron Radiation Facility, BP 220, F-38043 Grenoble Cedex, France*

Abstract. We report on the Li_xRbC₆₀ system whose structural behaviour has been explored as a function of Li content ($2 \leq x \leq 6$). Synchrotron X-ray powder diffraction measurements at ambient and high pressures and temperatures reveal the existence of low symmetry Li_xRbC₆₀ phases. Stoichiometric Li₂RbC₆₀ shows a face-centred cubic (*fcc*) structure, whereas increasing Li-content stabilises *hcp* fulleride arrangements. At high temperature, Li_xRbC₆₀ (nominal composition, $x \sim 3.0$) is hexagonal, partially transforming to monoclinic at room temperature. Moderate pressure (>2.5 kbar) also stabilises the monoclinic structure, which is characterised by much shorter interfullerene separations, reminiscent of those encountered in the two-dimensional polymer phase, Na₄C₆₀.

INTRODUCTION

Since the discovery of superconductivity in alkali fullerides, many materials with stoichiometry A₂A'C₆₀ have been synthesised (where A, A' = Li, Na, K, Rb, Cs) [1] and studied in an effort to understand the variation of T_c with interfullerene separation. T_c is suppressed sharply with decreasing lattice size in sodium fullerides in which polymeric phases [2] also form below a critical C₆₀³⁻ – C₆₀³⁻ distance (~ 9.35 Å). These structures are characterised by single C-C bridges [3] in contrast to the AC₆₀ polymers (~ 9.11 Å) [4], in which the C₆₀⁻ – C₆₀⁻ anions link via [2+2] cycloaddition. Here we report on the structural modifications occurring in the Li-Rb-C₆₀ phase field with variation of the Li content. Rietveld refinements of the synchrotron X-ray diffraction data suggest that low-symmetry phases with short interfullerene separations can be stabilised at various temperatures and pressures.

RESULTS AND DISCUSSION

We have synthesised a series of Li_xRbC₆₀ materials with composition between $2.0 \leq x \leq 6.0$. The materials under investigation were prepared by solid state reactions of stoichiometric amounts of C₆₀ and the corresponding alkali metals at high temperatures [5]. Annealing at 703 K was employed for a period of 8-12 weeks. Preliminary X-ray diffraction patterns at room temperature were collected on a Siemens D5000 diffractometer with CuK_α radiation. Fig. 1 shows the results of LeBail refinements of two such samples. The salt with a nominal $x \sim 2.0$ composition adopts a *fcc* structure

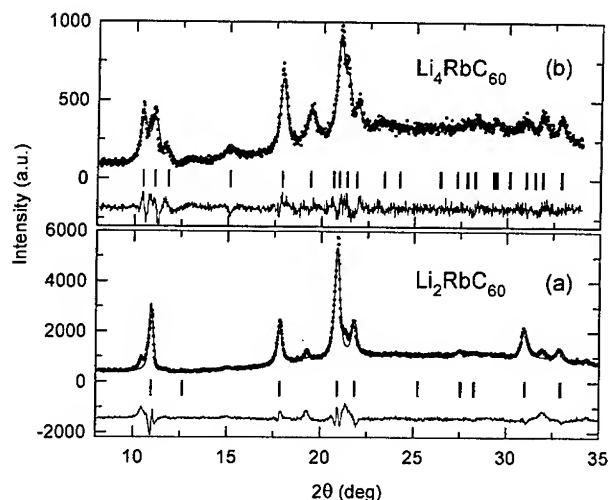


FIGURE 1. LeBail refinements of the room temperature X-ray diffraction patterns for $\text{Li}_x\text{RbC}_{60}$ with nominal $x=2$ (*fcc*) (a) and $x=4$ (hexagonal close packed) (b) compositions.

collected: (i) at ambient pressure and variable temperature on the BM16 beamline ($\lambda=0.83502$ Å) for material loaded in a 0.5-mm diameter glass capillary and (ii) at high-pressure and variable temperature on the ID9 beamline ($\lambda=0.49971$ Å) by employing a diamond anvil cell (DAC). Fig. 2 shows the diffraction pattern from BM16 at room temperature and the corresponding refinement with the LeBail pattern decomposition technique. The high resolution of the instrument allows excellent separation of the Bragg peaks and enables us to index them in a hexagonal (*hcp*) cell ($a=b=10.212(3)$ Å, $c=16.576(4)$ Å). Although the observed extinction conditions ($hh2hl: l=2n$) are consistent with the space group $P6_3/mmc$ or one of its subgroups, there are clearly three observed peaks at $2\theta=8.15^\circ$, 8.52° , and 13.12° , which cannot be described by either the *hcp* or *fcc* extinction rules. Two-phase analysis of the profile leads to the remaining reflections to be indexed on a body-centered monoclinic cell with lattice constants, $a=11.305(4)$ Å, $b=11.754(3)$ Å, $c=10.252(2)$ Å, $\beta=96.05(3)^\circ$. The remarkable improvement of the quality of the fit is reflected in the substantially reduced χ^2 values, from 7.7 to 2.3 in the two-phase model.

This monoclinic structure is reminiscent of that observed before for Na_4C_{60} , in which the fullerene molecules form a two-dimensional network [7] with the nearest neighbour directions defined by the vectors $\frac{1}{2}(\mathbf{a}+\mathbf{b}+\mathbf{c})$ and $\frac{1}{2}(\mathbf{a}-\mathbf{b}+\mathbf{c})$. The nearest inter-

(space group $Fm\bar{3}m$) (Fig. 1(a)) with lattice size, $a\sim 13.9$ Å, similar to that reported before [5]. Peaks that are not accounted for arise from a remnant phase, which indexes on a hexagonal cell. Increased Li-content ($x\sim 4.0$) diminishes the volume fraction of the *fcc* phase with the hexagonal one now becoming the dominant phase (Fig. 1(b)). Reliable quantitative phase analysis of the intermediate nominal $x\sim 3.0$ composition was not possible with laboratory X-ray data. For this purpose, high-resolution synchrotron X-ray powder diffraction measurements were undertaken at the ESRF, Grenoble. The lower symmetry of the structures in the $\text{Li}_x\text{RbC}_{60}$ system contrasts with the behaviour of the $\text{Li}_x\text{CsC}_{60}$ analogues in which increasing the amount of the intercalated Li^+ does not affect the *fcc* structure [6].

Powder diffraction data for $\text{Li}_x\text{RbC}_{60}$ ($x\sim 3.0$) were

fullerene distance in the present case is ~ 9.3 Å, comparable to the singly-bonded $\text{Na}_2(\text{A,A}')\text{C}_{60}$ polymeric fullerides [2,3] and the dimer phases of AC_{60} [8] and $(\text{C}_{59}\text{N})_2$ [9] solids. The thermodynamic stability of $\text{Li}_3\text{RbC}_{60}$ was also addressed by high temperature diffraction measurements. The inset of Fig. 2 displays the synchrotron data at $T = 573$ K. Analysis of the pattern with the LeBail method (space group $P6_3/mmc$) shows a complete transformation to a single phase *hcp* structure with an ideal *c/a* ratio ($a = b = 10.196(2)$ Å, $c = 16.652(2)$ Å).

The low-symmetry monoclinic phase found at room temperature in $\text{Li}_3\text{RbC}_{60}$ was investigated further at high temperature and under applied pressure. Synchrotron X-ray powder diffraction data were collected on the same $\text{Li}_3\text{RbC}_{60}$ sample as before, but now loaded in a DAC, with mineral oil as the pressure medium. We find that even moderate pressure, $P \sim 2.5$ kbar leads to the stabilisation of the body centered monoclinic phase. Fig. 3 presents the results of a two phase Rietveld refinement of the diffraction profile of $\text{Li}_3\text{RbC}_{60}$ at $T = 448(22)$ K and $P \sim 4$ kbar. The two phases used are the body centred monoclinic one ($a = 11.179(3)$ Å, $b = 11.657(4)$ Å, $c = 10.210(3)$ Å, $\beta = 96.10(2)^\circ$; space group $I2/m$) which accounts for $\sim 92\%$ of the volume fraction of the material and the untransformed *hcp* phase ($a = b = 10.165(16)$ Å, $c = 15.994(17)$ Å;

space group $P6_3/mmc$), encountered at high temperature, with the C_{60} electronic density centred at the $2c$ ($1/3, 2/3, 1/4$) site. In view of the similarities of these diffraction data to those of Na_4C_{60} [7], Rietveld refinements of the $\text{Li}_3\text{RbC}_{60}$ X-ray pattern were undertaken both in the $I2/m$ and $P2_1/n$ monoclinic space groups. The limited Q -range of the present data cannot clearly differentiate between these two; however, the refinements at this stage are partially in favour of the former space group. The alkali metals occupy distorted $4i$ ($x =$

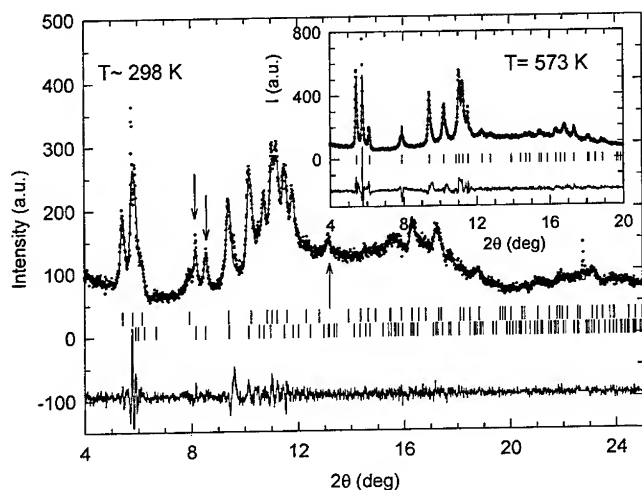


FIGURE 2. Synchrotron X-ray diffraction patterns of $\text{Li}_3\text{RbC}_{60}$ at 298 and 573 K (inset). The arrows indicate Bragg peaks not indexed in the *hcp* cell, but in a body-centered monoclinic one.

$0.649(1)$, $z = 0.481(2)$) and $4h$ ($y = 0.255(2)$) pseudotetrahedral sites, whereas the C_{60} units are centred at the $2a$ site. $I2/m$ also assumes binary disorder of the C_{60} units (instead of the ordered fulleride arrangement in $P2_1/n$) at an orientation, defined by the

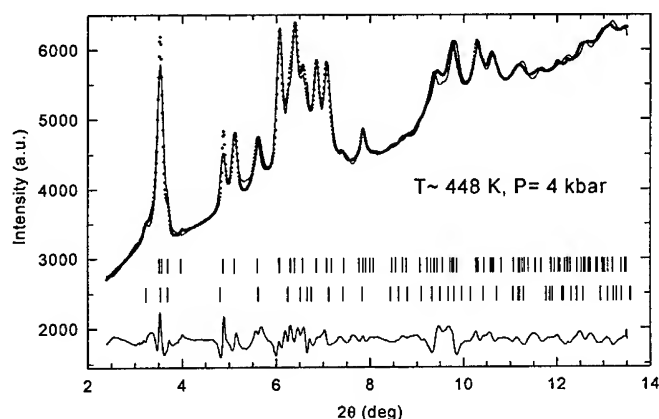


FIGURE 3. Rietveld refinement of the synchrotron X-ray diffraction pattern of $\text{Li}_3\text{RbC}_{60}$ at high pressure and temperature. The top set of ticks mark the reflections of the body-centered monoclinic structure and the bottom those of the minority *hcp* phase.

Euler angles (ψ, θ, ϕ) = $(-55.3^\circ, 25.8^\circ, 49.1^\circ)$. This model gave a good description of the $\text{Li}_3\text{RbC}_{60}$ structure ($R_{\text{wp}} = 13.9\%$, $R_{\text{exp}} = 12.3\%$), which can be viewed as a two-dimensional network of fullerene units, forming short covalent-like (single C-C) bonds along the $(0,0,0)-(\frac{1}{2}, \frac{1}{2}, \frac{1}{2})$ direction ($\approx 9.23 \text{ \AA}$) and longer

interfullerene distances along the $(0,0,0)-(-\frac{1}{2}, \frac{1}{2}, \frac{1}{2})$ direction ($\approx 9.87 \text{ \AA}$) of the unit cell.

CONCLUSIONS

We have presented a brief description of temperature and pressure driven phase-changes observed in $\text{Li}_x\text{RbC}_{60}$. The *fcc* $\text{Li}_2\text{RbC}_{60}$ phase changes to *hcp* modifications at $x \geq 3$, with application of moderate pressure ($> 2.5 \text{ kbar}$) stabilising a body centered monoclinic phase with very short intermolecular distances ($\sim 9.23 \text{ \AA}$), reminiscent of the two-dimensional polymeric structure of Na_4C_{60} .

ACKNOWLEDGEMENTS

We thank G. Oszlanyi for invaluable help in the Rietveld refinements of the polymer phase and S. Margadonna and C.M. Brown for help with the data collection. We acknowledge the support of the EU TMR Programme (FULPROP ERBFMRXCT970155) and the ESRF for provision of synchrotron X-ray beamtime.

REFERENCES

1. Tanigaki K. et al., *Nature* **352**, 222 (1991)
2. Prassides K. et al., *J. Am. Chem. Soc.* **119**, 834 (1997); Prassides K. et al. *Physica C* **282**, 307 (1997).
3. Margadonna S. et al., *Recent Advances in the Chemistry and Physics of Fullerenes and Related Materials*, K.M. Kadish and R.S. Ruoff Eds., Electrochemical Society, Pennington, NJ, 1998, **6**, 650.
4. Chauvet O. et al., *Phys. Rev. Lett.* **72**, 2721 (1994).
5. Tanigaki K. et al., *Chem. Phys. Lett.* **213**, 395 (1993).
6. Kosaka M. et al., *Phys. Rev. B* **59**, R6628 (1999).
7. Oszlanyi G. et al., *Phys. Rev. Lett.* **23**, 4438 (1997).
8. Oszlanyi G. et al., *Phys. Rev. B* **54**, 11849 (1996).
9. Brown C.M. et al., *Chem. Mater.* **8**, 2548 (1996).

Conduction Electron Spin Resonance in the Superconducting State of K_3C_{60}

N. M. Nemes¹, J. E. Fischer¹, G. Baumgartner²,
L. Forró², A. Jánosy³

¹Laboratory on the Research of the Structure of Matter, University of Pennsylvania,
3231 Walnut Str., Philadelphia, PA-19104, USA

²Department de Physique, Ecole Polytechnique Federal de Lausanne,
1015 Lausanne, Switzerland

³Technical University of Budapest, Institute of Physics, H-1521
Budapest, PO BOX 91, Hungary

Abstract. The conduction electron spin resonance (CESR) of K_3C_{60} single crystal and powder samples was studied from temperatures well below the superconducting transition ($T_c=19$ K) to 800 K. Several ESR frequencies were used with corresponding magnetic fields up to 8 T. We observed an anomalous change of the g factor with temperature in the superconducting state which may arise from an anisotropy of the superconducting energy gap. We proved that the change of the g factor is not caused by diamagnetic screening.

In the literature there are only a few attempts to observe the conduction electron spin resonance (CESR) in superconductors below the critical temperature [1,2]. Experimentally, it is rather difficult to observe CESR in the superconducting state. Only type-II superconductors with reasonably high transition temperatures and upper critical fields can be reasonable candidates. However, in most superconductors — e.g. in cuprates — spin lattice relaxation due to impurities or phonons prevent the observation of the CESR in the normal state. Vier and Schultz [1] report a relatively broad CESR in high purity Nb using the transmission technique. Delrieu *et al* [2] report a CESR in the organic superconductor $(TMTSF)_2ClO_4$ at very low fields and below 1 K. In these materials the lines do not follow simple expectations. In particular, the shift to higher field expected from the decrease of the field within the sample due to diamagnetic screening was not observed.

In this contribution we report the observation of CESR in the superconducting state of the fulleride metal, K_3C_{60} . This material is an excellent candidate for testing theories of CESR in the superconducting state. It has a high T_c of 19 K in zero magnetic field, its upper critical field is above 20 T, it consists of light elements and the spin relaxation time is long in the normal state. It has a cubic structure and there is no g factor anisotropy broadening. The main experimental difficulty is the sensitivity of the material to oxygen and the almost inevitable presence of other impurity phases and paramagnetic resonance lines which are apparent in Figure 1.

We studied the CESR of several K_3C_{60} powder and crystalline samples prepared in different ways, in the temperature range of 2 K to 800 K and using several ESR frequencies and corresponding magnetic fields between 0.3 T and 8 T. In the normal state we observed an increase in the g factor and the spin relaxation rate between approximately 50 K and ambient (≈ 300 K) temperature. This g factor anomaly of K_3C_{60} in the normal state was first reported by Petit *et al* [3]. In the superconducting state the linewidth of the resonance showed a well-defined minimum. The initial decrease below T_c was field independent and followed the theory of Yafet [4], which predicts that the impurity spin scattering rate of

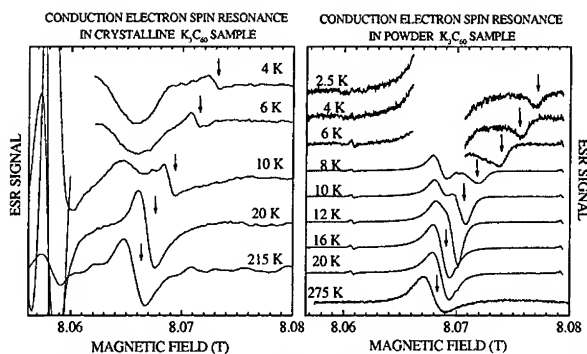


FIGURE 1. CCSR of K_3C_{60} crystalline and powder samples at 225 GHz. The resonance rapidly shifts to higher fields with decreasing temperature in the superconducting state. *Left:* Crystalline sample prepared with KN_3 reaction. Note the intense Curie-like impurity lines in lower fields. *Right:* Powder sample prepared by vapor-phase reaction. Below T_c the resonance splits into two.

normal excitations tends to zero as $T \rightarrow 0$. These effects can be seen in Figure 1.

However, in this contribution we restrict our scope to the anomalous shift of the resonance to higher field in the *superconducting* state with decreasing temperature. We seek to prove that the origin of this shift is a change of the g factor, although there is a smaller contribution from the diamagnetic screening in lower fields.

In the superconducting state, diamagnetic currents decrease the external magnetic field inside the sample; thus one expects the CCSR to shift to higher field from the normal state position. The diamagnetic screening was studied via the static magnetization of the sample using a SQUID magnetometer. At fixed temperature and changing magnetic field the magnetization showed the typical hysteresis loop characteristic of type II superconductors, displayed in Figure 2 *lower panel*. The magnetization decreases with increasing magnetic field; thus we expect the CCSR shift to decrease with field as well. However, we

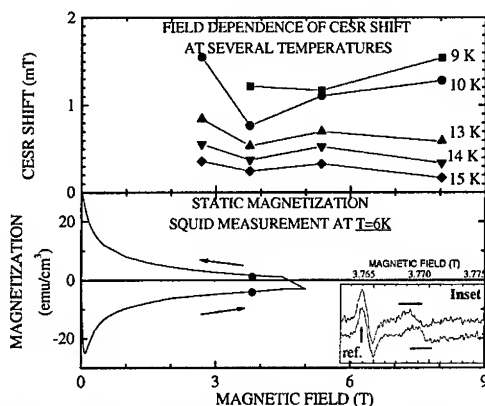


FIGURE 2. *Upper panel:* CCSR shift of K_3C_{60} relative to 20 K position vs. resonance field at constant temperature showed that CCSR shift increased with magnetic field (below 10 K). ESR frequencies used: 75, 105.1, 150 and 225 GHz. *Lower panel:* Hysteresis loop of static magnetization from SQUID measurement of the same crystal showed that diamagnetic screening would cause smaller CCSR shift at higher field. *Inset:* Due to vortex-pinning static magnetization is larger in decreasing than in increasing magnetic field. CCSR at 10 K in 3.77 T field showed opposite irreversible effect.

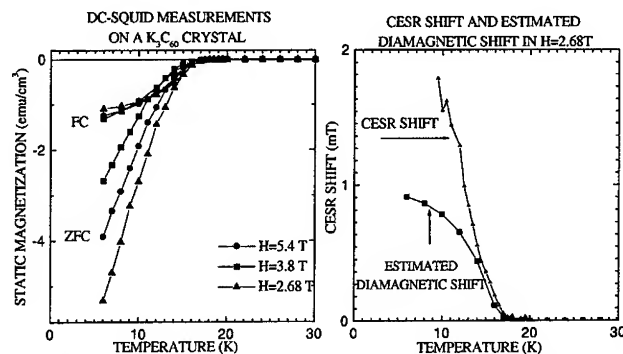


FIGURE 3. *Left:* Field Cooled (FC) magnetization of a K_3C_{60} crystal is much smaller than Zero Field Cooled (ZFC) magnetization because of vortex pinning and superconducting shielding. *Right:* FC magnetization from *left* was converted to ESR-shift scale assuming a demagnetization factor of a sphere ($n_{\text{demag}} = 8\pi/3$). The temperature dependence of the measured CESR shift differs from the expected shift due to diamagnetic screening based on the FC magnetization of the same crystal in the same 2.68 T magnetic field.

observed a larger CESR shift in larger fields as shown in the *upper panel*. This is our first proof that the CESR shift is only partially caused by the diamagnetic screening. Note that in lower fields (2.68 T) we indeed saw a larger CESR shift in accord with the larger expected diamagnetic effect and smaller g factor related shift.

In the SQUID measurements (Figure 3 *left*) there is a large difference in so-called Field Cooled (FC) and Zero Field Cooled (ZFC) magnetization curves [5] due to vortex pinning. ESR experiments almost always follow the FC route. However, we tried a few ZFC experiments (turning off the magnet and then cooling the sample). We observed a minor difference between ZFC and FC sweeps in the ESR, although the SQUID implies a huge difference if the shift is caused by diamagnetic screening. On Figure 3 *right* we show the temperature dependence of the CESR shift in 2.68 T and the rescaled FC magnetization curve in the same field. We calculated the magnetic induction inside the sample from the measured magnetization, assuming the demagnetization factor of a sphere ($8\pi/3$). The figure shows that even in the lowest field, diamagnetic screening alone cannot account for the observed CESR shift.

The demagnetization factor is geometry— and thus sample—dependent. Therefore one expects different CESR shifts at the same temperature and in the same field for different samples if the CESR shift is caused by diamagnetic screening. In Figure 4 *left* we show CESR shifts in 8 T field (225 GHz) from several powder and crystal samples; clearly this difference was not observed. A change in the g factor gives a relative CESR shift proportional to magnetic field, therefore such an effect is most apparent in high field where any diamagnetic effect is small as well. We divided the CESR shifts (relative to the 20 K position) by the resonance field and plotted it against the renormalized temperature — the critical temperature decreases with increasing magnetic field. This renormalized CESR shift should be proportional to the change in g factor and be field independent. As Figure 4 *right* shows, the shifts in higher fields behave similarly. The 2.68 T shifts have a large diamagnetic contribution.

The shift vs. temperature curves did not flatten even approaching the lowest attainable temperature 3 K (see Figure 4 *left*); therefore a model based on a coupled resonance to an impurity phase (e.g. K_1C_{60}) or some other ESR centers inside K_3C_{60} (e.g. vacancies) seems difficult. We propose an anisotropy in the superconducting gap $\Delta(k)$ to explain the shift of the CESR as follows: The g factor depends on k -space position [6]: $g(k)$.

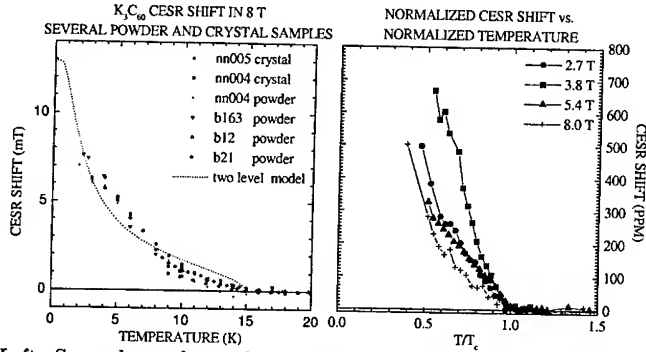


FIGURE 4. *Left:* Several powder and crystal K_3C_{60} samples showed the same temperature dependent CESR shift in the superconducting state in 8 T magnetic field independent of their shape. *Right:* CESR shifts of a K_3C_{60} crystal in four magnetic fields were measured. To prove g factor like behaviour the shifts relative to 20 K position are normalized by the external magnetic field. Temperatures are normalized by the magnetic field dependent critical temperature.

However, in the normal state, conduction electrons scatter rapidly and $\langle g(\mathbf{k}) \rangle$, the average over the Fermi-surface is measured. Below T_c there is a gap for quasi-particle excitations and the \mathbf{k} direction of smallest gap with decreasing temperature becomes increasingly more populated. For an anisotropic gap the resonance shifts towards the g factor for the direction with minimum gap. A crude model of an anisotropic gap is a system with 2 energy levels above the ground state:

$$g(T) = \frac{e\left(-\frac{\Delta+\delta}{k_B T}\right)}{e\left(-\frac{\Delta+\delta}{k_B T}\right) + e\left(-\frac{\Delta}{k_B T}\right)} g_+ + \frac{e\left(-\frac{\Delta}{k_B T}\right)}{e\left(-\frac{\Delta+\delta}{k_B T}\right) + e\left(-\frac{\Delta}{k_B T}\right)} g_-$$

$\delta = 0.12\Delta(T)$ provided a fit to the measured curves as shown in Figure 4 *left* dotted line, and 12% is a crude estimate of the anisotropy required to explain the CESR shift.

In conclusion we observed the conduction electron spin resonance of the normal electron excitations in K_3C_{60} . We found anomalous shifting behaviour of the resonance position. We proved that this shift is partly caused by diamagnetic screening in low field and mostly caused by a change in the g factor. We proposed to explain this g factor change by a 12% anisotropy in the superconducting gap.

We are indebted to C. L. Lin for his help with the SQUID measurements at Temple University. Work in Philadelphia was supported by NSF DMR9730298. Work in Budapest was supported by OTKA T029150 es FKFP 0352/1997.

REFERENCES

1. D. C. Vier and S. Schultz. *Phys. Lett.*, 98A:283, 1983.
2. J. M. Delrieu et al. *J. de Physique*, 44:C3-1033, 1983.
3. P. Petit et al. *Phys. Rev. B*, 54:R3764, 1996.
4. Y. Yafet. *Phys. Lett.*, 98A:287, 1983.
5. V. Buntar et al. *Phys. Rev. B*, 54:14128, 1997.
6. Y. Yafet. *Solid State Phys.*, 14:2, 1963.

Orientational Ordering of Alkali Ammonia Clusters in Ammoniated Alkali Fullerides $(\text{NH}_3)\text{K}_3\text{C}_{60}$ and $(\text{ND}_3)\text{K}_3\text{C}_{60}$

K. Ishii*, T. Watanuki*, A. Fujiwara*, H. Suematsu*,
Y. Iwasa†, H. Shimoda†, T. Takenobu†, and T. Mitani†

*Department of Physics, The University of Tokyo, Hongo, Bunkyo-ku, Tokyo 113-0033, Japan
†Japan Advanced Institute of Science and Technology, Tatsunokuchi, Ishikawa 923-1292, Japan

Abstract. Synchrotron x-ray diffraction measurements of $(\text{NH}_3)\text{K}_3\text{C}_{60}$ and $(\text{ND}_3)\text{K}_3\text{C}_{60}$ have revealed a structural phase transition at $T_s \simeq 150$ K. The low-temperature phase has a unit cell derived by doubling the unit lattice vectors of high-temperature phase, and is characterized as an orientationally ordered state of the K-NH₃ pair at the octahedral site of the C₆₀ lattice. At $100 \text{ K} < T < T_s$, a negative thermal expansion is observed at the *ab*-plane where K-NH₃ pairs lie, which is related to the ordering of K-NH₃ pair.

INTRODUCTION

Some attempts of ammoniation of superconducting $A_3\text{C}_{60}$ (*A* is an alkali atom) have been performed to obtain a compound with larger lattice constant and higher superconducting transition temperature (T_c). While the increase of T_c was observed in the successful case of $(\text{NH}_3)_4\text{Na}_2\text{CsC}_{60}$ [1], $(\text{NH}_3)\text{K}_3\text{C}_{60}$ does not become a superconductor [2], but transits to a magnetic ground state [3,4].

In the viewpoint of the crystal structure, the introduction of ammonia to alkali fulleride brings a displacement of alkali atom to a lower symmetry site with a disorder. The room-temperature crystal structure of $(\text{NH}_3)\text{K}_3\text{C}_{60}$ has been determined as an orthorhombic structure slightly distorted from fcc [2]. K and NH₃ in the octahedral site are oppositely displaced from the site center in the $\langle 110 \rangle$ direction, and the K-NH₃ pair directs randomly in one of four equivalent directions. This directional disorder is plausibly dynamic at high temperatures where ammoniation is carried out (from room temperature to 100 °C), and we expect an ordered state caused by freezing of intercalant motion at a low temperature. Such a structural phase transition was reported in C₆₀-*n*-pentane clathrate [5]. This type of transition has been observed in the case of $(\text{NH}_3)\text{K}_3\text{C}_{60}$ in the present study.

EXPERIMENTAL

The polycrystalline sample of $(\text{NH}_3)\text{K}_3\text{C}_{60}$ was synthesized by the direct reaction of K_3C_{60} and NH_3 gas. The detail was presented in the previous report [3]. The sample was sealed in a thin glass capillary for x-ray diffraction experiments. Synchrotron x-ray diffraction measurements were carried out at Photon Factory (BL6C₁ and BL18C), KEK, Tsukuba. The incident x-ray was monochromatized at wavelength 1.100 Å with a Si double crystal and collimated to 0.2-0.5 mm in diameter. An imaging plate was used for detection of the Debye rings, which was converted in the conventional spectrum by integrating the intensity along the ring. We also measured a deuterated sample, $(\text{ND}_3)\text{K}_3\text{C}_{60}$ in a similar way.

RESULTS AND DISCUSSION

Figure 1(a) shows the powder x-ray diffraction spectra of $(\text{NH}_3)\text{K}_3\text{C}_{60}$ at 300 K and 15 K. The spectrum at 300 K is consistent with the previous report [2]. At 15 K, however, we observed a number of extra peaks and found a structural phase transition. These peaks correspond to the index of half an integer or the forbidden reflections in the face-centered lattice at 300 K. The unit lattice vectors at the low-temperature phase should have a double size of the fundamental ones. From the reflection conditions $h+k, k+l, l+h = \text{integer}$ (here, hkl is the index in the fundamental unit cell) and the absence (100), (010), and (001) peaks, we can determine the space group as $Fddd$.

As the origin of the structural phase transition we can consider some possibilities, such as the C_{60} dimer or polymer formation, the orientational ordering of C_{60} molecules, or the positional ordering of K and NH_3 at the octahedral site. The possibility of dimerization or polymerization is very low because the intermolecular distance of C_{60} , 10.1 Å in the present case, is too large to form a covalent bond. The orientational ordering of C_{60} cannot explain the observed strong intensity of superlattice reflections in the low-angle region. Therefore we proceed the structural analysis on the basis of the positional ordering of K- NH_3 pairs.

In order to satisfy the space group $Fddd$, we should put the off-centered potassium atom on the $32h$ (origin choice 2) position $(\frac{1}{4} + \delta_x, \delta_y, 0)$, where $(\frac{1}{4}, 0, 0)$ is the center of the octahedral site and $(\delta_x, \delta_y, 0)$ is a displacement vector. The NH_3 molecule is placed at an off-centered position in the opposite direction to potassium. All C_{60} molecules were aligned in the same direction following the previous report about the room-temperature structure. Based on this model, we carried out the Rietveld analysis with use of the RIETAN program [6], and obtained a good fit with $R_{wp}=2.63\%$ and $R_I=2.45\%$. All positions of atoms and molecules are reported elsewhere [7]. As shown in Figs. 1 (b) and (c), the crystal structure of the ordered phase is characterized as the alignment of the K- NH_3 pairs in an antiferroelectric fashion. This can be understood in terms of the electrostatic interaction between

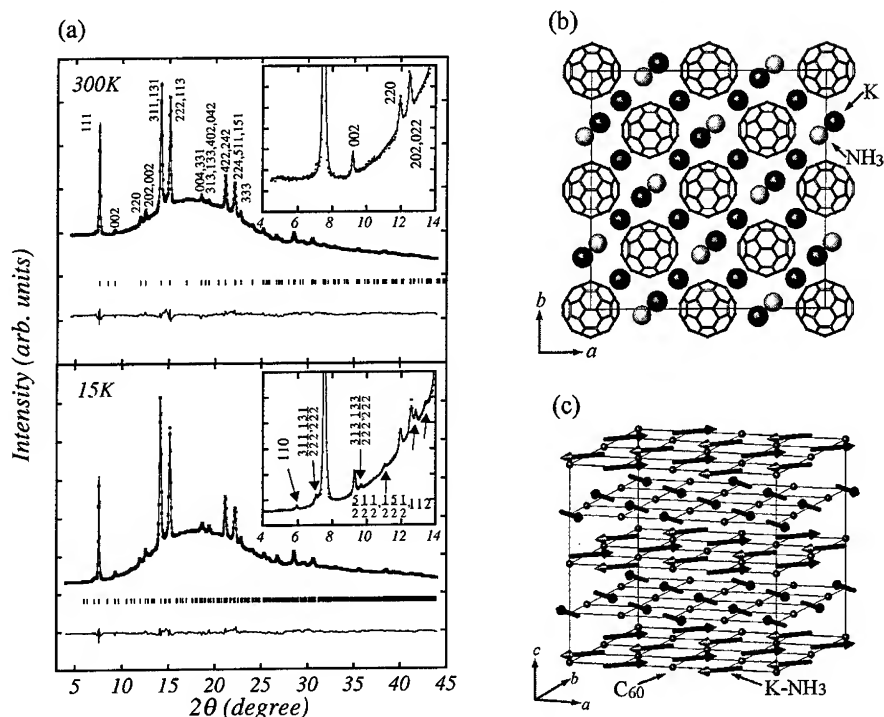


FIGURE 1. (a) Powder x-ray diffraction spectra of $(\text{NH}_3)\text{K}_3\text{C}_{60}$ at 300 K (upper panel) and 15 K (lower panel). The insets are magnifications of the low-angle region. The cross marks represent observed intensity, and solid lines are the results of Rietveld refinement. The arrows indicate the superlattice reflections. (b) Crystal structure of the low-temperature phase near $z=0$. (c) Schematic view of the unit cell. The arrows represent K-NH₃ pairs. Potassium atoms in the tetrahedral site are not shown for simplicity.

K^+ ions at the octahedral site. The pairs on the upper ab -plane are perpendicular to those on the lower plane.

We observed the same transition in $(\text{ND}_3)\text{K}_3\text{C}_{60}$. Figures 2 (a) and (b) show the temperature dependence of superlattice reflection intensity in $(\text{NH}_3)\text{K}_3\text{C}_{60}$ and $(\text{ND}_3)\text{K}_3\text{C}_{60}$, respectively. The reflections appear below $T_s \simeq 150$ K, and the difference between NH_3 sample and ND_3 sample is too small to distinguish in this experiments. Little influence of deuteration to T_s seems to support that the transition occurs mainly by the electrostatic interaction of K^+ ions.

The temperature dependence of the lattice constants in $(\text{NH}_3)\text{K}_3\text{C}_{60}$ is shown in Figs. 2 (c) and (d). The difference between a_0 and b_0 is very small, so that the average value is given in the figure. A most remarkable feature is the negative thermal expansion in a_0 (and b_0) between 100 K and 150 K, whereas we observe no anomaly in c_0 . This temperature region just corresponds to that of the evolution

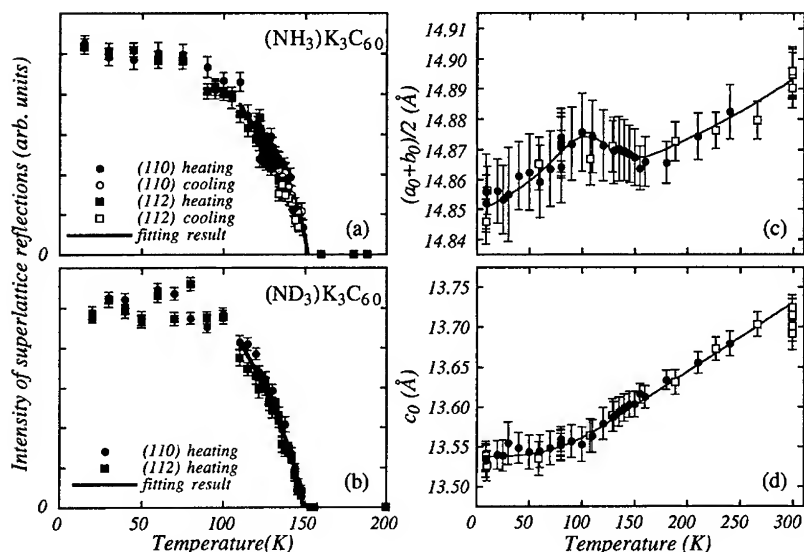


FIGURE 2. (a), (b) Temperature dependence of superlattice reflection intensity of $(\text{NH}_3)\text{K}_3\text{C}_{60}$ and $(\text{ND}_3)\text{K}_3\text{C}_{60}$, respectively. (c), (d) Temperature dependence of the lattice constants in $(\text{NH}_3)\text{K}_3\text{C}_{60}$. Open makes and filled marks represent the data in cooling and heating run, respectively. Solid lines are guide to eyes.

of the superlattice reflections, which suggests that the negative expansion is closely related to the orientational ordering of the K-NH₃ pair in the ab -plane. We found that the distance between K and NH₃ increases below T_s than that above T_s and this could be a reason for this anomaly.

ACKNOWLEDGMENTS

This work was supported by “Research for the Future” of Japan Society for the Promotion of Science (JSPS), Japan. One of the authors, K.I., was supported by JSPS Research Fellowship for Young Scientists.

REFERENCES

1. Zhou, O. *et al.*, *Nature (London)* **362**, 433-435 (1993).
2. Rosseinsky, M. J. *et al.*, *Nature (London)* **364** 425-427 (1993).
3. Iwasa, Y. *et al.*, *Phys. Rev. B* **53**, R8836-8839 (1996).
4. Prassides, K. *et al.*, *Physica C* **282-287**, 307-310 (1997).
5. Faigel, G. *et al.*, *Phys. Rev. B* **49**, 9186-9189 (1994).
6. Izumi, F., *The Rietveld Method*, Oxford: Oxford University Press, 1993, ch. 13.
7. Ishii, K. *et al.*, *Phys. Rev. B* **59**, 3956-3960 (1999).

Electronic properties of the $\text{Na}_2\text{AC}_{60}$ family ($\text{A}=\text{K}, \text{Rb}, \text{Cs}$)

Natasa Čegar^{*}, Ferenc Simon[†], Gabriel Baumgartner, Andrzej
Sienkiewicz[‡], László Forró

*Laboratoire de Physique des Solides Semicristallins, IGA, Departement
de Physique, Ecole Polytechnique Federale de Lausanne 1015, Lausanne
Switzerland*

Barbara Ruzicka, Leonardo Degiorgi

Laboratorium fuer Festkoerperphysik, ETH Zurich, CH-8093 Zurich, Switzerland

László Mihály

SUNY Stony Brook, Department of Physics, Stony Brook, NY 11794 USA

Electron Spin Resonance(ESR) at ambient and under high pressure and optical reflectivity measurements were used to study the consecutive phase transitions in $\text{Na}_2\text{AC}_{60}$ family of fulleride compounds. The high temperature *fcc* phase in all three $\text{A}=\text{K}, \text{Rb}, \text{Cs}$ compounds are found to show *semi-metallic* behaviour. For the first time a peculiar sequence of phase transitions from *semi-metallic* to *metallic* to *superconducting* phases are observed in $\text{Na}_2\text{CsC}_{60}$. The metallic properties of the polymeric phases in $\text{A}=\text{K}, \text{Rb}$ were established.

INTRODUCTION

The steeper dependence of superconducting transition temperature T_c on the lattice constant in $\text{Na}_2\text{AC}_{60}$ compounds¹ with respect to other (not Li or Na based) $\text{A}_2\text{A}'\text{C}_{60}$ ($\text{A}, \text{A}'=\text{K}, \text{Rb}, \text{Cs}$) or A_3C_{60} ($\text{A}=\text{K}, \text{Rb}$) compounds has still not been satisfactorily explained. It is experimentally well established from both physical and chemical pressure studies that the variation of T_c is related to the change in the density of states at the Fermi level, $N(\epsilon_F)$. Therefore, a different dependence of $N(\epsilon_F)$ on the lattice constant a is expected for $\text{Na}_2\text{AC}_{60}$ compounds. The low temperature phase of $\text{Na}_2\text{AC}_{60}$ is *sc* with orientational order^{2,3} in contrast to the merohedrally disordered *fcc* phase of the $\text{A}_2\text{A}'\text{C}_{60}$ compounds. This is ascribed to the smaller size of Na that promotes a configuration where the nearest possible distance between C atoms on adjacent C_{60} balls is achieved. Based on the different structure of $\text{Na}_2\text{AC}_{60}$ compounds it was argued that modified electron hopping is responsible for the different variation of $N(\epsilon_F)$ with a . It has to be pointed out that in their early work Maniwa et al.⁴ indeed found a scaling of T_c with locally measured $N(\epsilon_F)$ in $\text{Na}_2(\text{K},$

^{*} Tragically disappeared in Swissair 111 flight accident on 2nd September, 1998.

[†] Permanent address: Technical University of Budapest, Institute of Physics., H-1521 Budapest, PO.Box 91, Hungary, e-mail: simon@phy.bme.hu.

[‡] Permanent address: Polish Academy of Sciences, Institute of Physics, PL-02668 Warsaw, Poland.

Rb) C_{60} but the values are deduced in the temperature range where a polymer phase is also present, at the time yet unknown. No evidence for a different variation of $N(\epsilon_F)$ on a is found in Na_2CsC_{60} and K_3C_{60} or Rb_3C_{60} in the work of Tanigaki et. al.⁵. Most probably it is the single electron band model which fails to explain for all experimental observations. As already mentioned $Na_2(K, Rb)C_{60}$ undergoes polymerization below 250 K at ambient pressure⁶ whereas Na_2CsC_{60} polymerizes only under pressure⁷. In contrast to the doubly bonded A_1C_{60} polymers⁸, Na_2AC_{60} polymer forms single bonds. In this work we present a comprehensive study of the physical properties of Na_2AC_{60} compounds in all their three structural phases. We show that the *sc* and the *polymer* phases are metallic, whereas the high temperature *fcc* phase shows a *semi-metallic* behaviour, adding a new phase to the already very rich phase diagram of C_{60} fullerenes. We discuss how the observation of this phase might be linked to the peculiar properties of Na_2AC_{60} compounds.

EXPERIMENTAL

Samples were prepared by conventional solid-state reaction method. Phase purity was checked by X-ray diffraction. ESR experiments were performed on commercial ESR spectrometer and cavities in X-band (at 9.5 GHz) in the temperature range of 5 to 800 K. ESR intensities were thoroughly calibrated by $CuSO_4 \cdot 5H_2O$ reference samples and also all experimental conditions were monitored in the full temperature range for a reliable measure of the spin-susceptibility. When studying polymerization, slow cooling rate was imposed (typically 50 K/hour). Quenching was done by immersing the sample from room temperature into liquid nitrogen and putting it in the precooled ESR cryostat, immediately. High pressure ESR studies were performed up to 5 kbar. The infrared reflectivity measurements were performed up to 14000 cm^{-1} in a sealed sample holder with a wedged diamond window described in Ref. 9.

RESULTS AND DISCUSSION

Polymerization in Na_2KC_{60} and Na_2RbC_{60}

At room temperature the ESR signal of Na_2RbC_{60} consists of single relaxationally broadened line with a linewidth of 4 mT. This is the conducting ESR(CESR) signal of the metallic simple cubic (*sc*) phase. As shown in Fig. 1a. when the sample is slowly cooled below 250 K a new line appears with a linewidth of 0.5 mT. Similar signals are observed in Na_2KC_{60} with the only difference in the linewidths (1.2 mT and 0.2 mT for the signal of the room temperature *sc* phase and for the new signal appearing below 250 K, respectively) that is due to the scaling in the CESR relaxation rates which are dominated by the spin-orbit coupling on the alkali (Rb or K). Since this temperature range coincides with the appearance of the *polymer* phase we associate the new signal with that of the *polymer*. Fig. 1b. and 1c. show the intensities and linewidths of the two lines after deconvolution into two derivative Lorentzian lines.

The broader signal corresponds to the *sc* phase while the narrow component to the *polymer*. Unless quenched, $\text{Na}_2\text{KC}_{60}$ was always found to fully polymerize below 200 K whereas polymerization is only partial even for slow cooling for $\text{Na}_2\text{RbC}_{60}$. In the temperature range of 250-200 K intensity of the ESR signal of the *polymer* increases. The signal of the *sc* phase drops at the same time with an amount equal to the increase in the intensity of the *polymer* phase. Therefore the susceptibility of the *polymer* phase is equal to that of the *sc* that is $3 \cdot 10^{-4}$ emu/mol. The *polymer* fraction saturates at 200 K at a ratio of 1:4 *polymer*/cubic. Significantly reduced cooling rate did not enhance polymerization. Hysteresis is observed in the *polymer* fraction in agreement with hysteretic lattice constant data¹⁰. Hysteresis is explained by macroscopic strains in the *polymer* phase. In the temperature range where polymerization is completed, for both compounds the *polymer* phase shows a simple metallic susceptibility and for $\text{Na}_2\text{RbC}_{60}$ the still present *sc* phase is also a metal. Below 50 K susceptibility of the *polymer* appears to increase, an effect explained by an impurity phase which linewidth and g factor are close to that of the *polymer*. This impurity phase was also found in quenched experiments where the polymer was not present. X-band ESR technique is limited at this point and NMR or high-field ESR is required for the study of the single bonded polymer below 50 K. ESR linewidth of Fig. 1c. shows a clear linear, i.e. phonon dominated, relaxation mechanism of both phases. The slight upturn of the linewidth of the polymer is an effect of the impurity phases. The smaller ESR linewidth of the polymer implies that the electronic wave functions in this phase overlap less with the alkali than that of the *sc* phase.

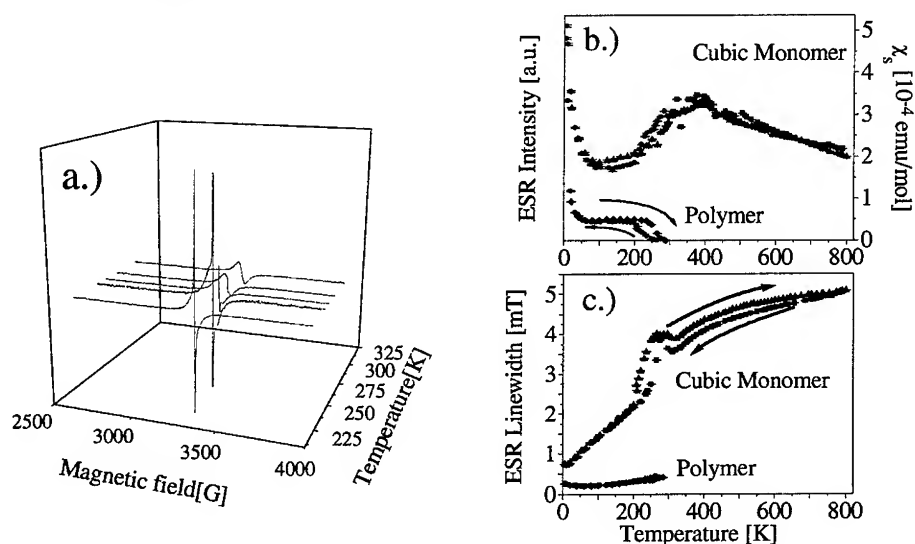


FIGURE 1a. The emerging line in the ESR signal of $\text{Na}_2\text{RbC}_{60}$ below 250 K is from the *polymer* phase. Due to its longer relaxation rate i.e. higher relative *amplitude* the new line dominates the ESR signal. Fig. 1b. and Fig. 1c. show intensity and linewidth of ESR lines. The right hand scale of Fig. 2a shows the spin-susceptibility of the signal normalized by the full amount of sample. It gives a measure of the spin-susceptibility in the presence of one line only.

In Fig. 2. polymerization is shown under pressure for $\text{Na}_2\text{KC}_{60}$. The linewidth for both phases shows a decrease in agreement with a model of a 3D metal by Elliot¹¹. This variation of the linewidth of the *polymer* phase can be contrasted to the behaviour in A_1C_{60} *polymers* where the linewidth *increases* under pressure implying a 1D electronic properties¹².

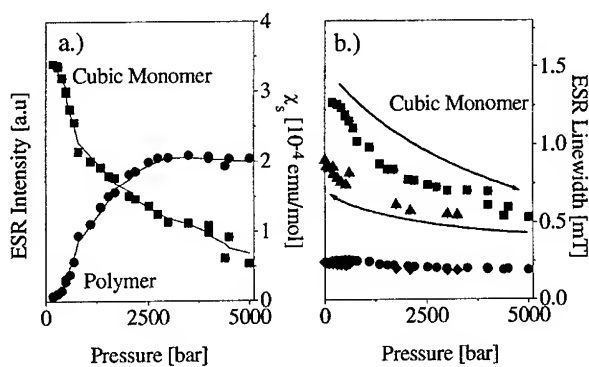


FIGURE 2. High pressure induced polymerization in $\text{Na}_2\text{KC}_{60}$ at ambient temperature (295 K). Solid lines are guides to the eye. Arrows indicate the direction of pressure change. Linewidth of the cubic phase shows hysteresis.

High temperature *fcc* phase in $\text{Na}_2(\text{K, Rb and Cs})\text{C}_{60}$

As is it shown in Fig. 1c. the *sc-fcc* phase transition around room temperature can be traced in the ESR spectra as an extremum in the linewidth. The temperature of the extremum (310 K) is close to the value found by Tanigaki et al.² (313 K) in DSC studies for $\text{Na}_2\text{RbC}_{60}$. Above this transition temperature linewidth shows a non-linear temperature dependence. Also hysteresis in the linewidth is observed after the 800 K heat treatment. For all three compounds through the *sc-fcc* transition temperatures the spin-susceptibility changes continuously with a gradual drop that is most significant for $\text{Na}_2\text{CsC}_{60}$ (not shown), where the spin-susceptibility drops a factor of 2 in the temperature range of 300-800 K. The temperature dependence of the spin-susceptibility variation resembles a Curie-like dependence, although from the Curie constant we obtain only 1/7 spins per C_{60} units. The situation therefore is not at all analogous to the case of CsC_{60} where in its high temperature *monomer* phase the Curie-like susceptibility corresponds to one spin per C_{60} ¹³. Apart from localization, other models like change in the density of states due to lattice expansion or assuming the development of a spin-gap for the conducting electrons would give just the opposite trend in the temperature dependence of the spin-susceptibility. In the *fcc* phase the ESR linewidth is still large therefore spins are not localized on C_{60} balls. To further clarify the nature of this high temperature *fcc* phase we performed IR reflectivity studies. Based on our preliminary results, a *metal to insulator*

transition(MIT) is found through the *sc-fcc* phase transition those nature is discussed in more detail in Ref. 9. All these observations point toward a picture where the experimental results in the *fcc* phase are not explained by a single electron model but electron-electron correlations should be taken into account. This *semi-metallic* phase is believed to arise as a results of close criticality to a MIT due to strong correlation effects. Most probably Anderson-like disorder, due to the free tumbling of Jahn-Teller distorted C_{60} balls, also plays an important role in determining the physical properties. Additional theoretical work is required to further elucidate the nature of this high temperature phase to coherently explain all the observations. We believe that this close proximity to a non-metallic phase is inherited into the low temperature *sc* phase that would explain the difference in response of T_c to the lattice parameter between the *fcc* $A_2A'C_{60}$ and *sc* Na_2AC_{60} compounds.

CONCLUSIONS

ESR and optical reflectivity measurements have shown: i.) polymerization can be followed in Na_2KC_{60} and Na_2RbC_{60} . Down to low temperatures the polymer remains a metal. Its susceptibility is reminiscent to that of the simple cubic metal. ii.) The high temperature *fcc* phase in all Na_2KC_{60} , Na_2RbC_{60} and Na_2CsC_{60} compounds is shown to be *semi-metallic*. This is believed to be linked to the unique properties of Na_2AC_{60} compounds among other $A_2A'C_{60}$ materials.

ACKNOWLEDGEMENTS

This work is supported by the grant of the Swiss National Science Foundation and by OFES in the frame of a European Network "Fulprop". FS acknowledges the Hungarian State Grants OTKA T29150, FKFP 0352/1997 and HAS-TUB Research Team No. 04119 on Solids in Magnetic Fields.

REFERENCES

- ¹ K. Prassides et. al., Phys. C **282** 307 (1997).
- ² K. Tanigaki et. al., Phys. Rev. B **49** 12307 (1994).
- ³ K. Prassides et. al., Science **263** 950 (1994).
- ⁴ Y. Maniwa et. al., Phys. Rev. B **52** 7054 (1995).
- ⁵ K. Tanigaki et. al., J. Mater. Chem. **5** 1515 (1995).
- ⁶ G. Bendele et. al., Phys. Rev. Lett. **80** 736 (1998).
- ⁷ A. Lappas et. al., In this Conference Proceedings.
- ⁸ S. Pekker et al., Solid State Comm. **90** 349 (1994).
- ⁹ B. Ruzicka et al., in preparation.
- ¹⁰ S. Margadonna et. al. Proceedings IWEPNM **97**, 327.
- ¹¹ R. J. Elliott, Phys. Rev. **96** 266 (1954).
- ¹² Gabriel Baumgartner, PhD thesis, EPFL Lausanne, Unpublished.
- ¹³ O. Chauvet et. al., Phys. Rev. Lett. **72** 2721 (1994).

Structure and Physical Properties of Cs_3C_{60} under Ambient and High Pressures

Y. Kubozono,^{1*} S. Fujiki,¹ Y. Takabayashi,¹ Y. Yoshida,¹ S. Kashino,¹
K. Ishii,² A. Fujiwara,² H. Suematsu²

¹ Department of Chemistry, Okayama University, Okayama 700-8530, Japan

² Department of Physics, University of Tokyo, Tokyo 113-0033, Japan

Abstract. Structure and physical properties of a pressure induced superconductor Cs_3C_{60} were studied by X-ray powder diffraction and ESR methods. All X-ray diffraction patterns below 300 K under ambient pressure (1 bar) showed that Cs_3C_{60} took a body-centered orthorhombic (bco) structure as main phase and an A15 structure as minor phase. The ESR at 1 bar showed that Cs_3C_{60} was metallic from 2 to 290 K. The pressure dependence of X-ray powder diffraction showed a disappearance of A15 phase above 20 kbar. The compressibility for the bco phase of Cs_3C_{60} , $3.1 \times 10^{-3} \text{ kbar}^{-1}$, was similar to those of Rb_3C_{60} and K_3C_{60} .

INTRODUCTION

Cs_3C_{60} is a pressure induced superconductor with a superconducting transition temperature T_c of 40 K at 14.3 kbar.¹ A superconducting transition was not observed for Cs_3C_{60} under ambient pressure (1 bar). However, the transition was observed by applying pressure, and the T_c raised with an increase in pressure. This is a contrast to the other fullerene superconductors, which show a decrease in T_c by applying pressure. The increase in T_c for Cs_3C_{60} by applying pressure is inconsistent with the model that a band broadening caused by the increase in pressure reduces the density of state, $N(\epsilon_F)$, and T_c . Palstra et al. proposed three different explanations for the increase in T_c .¹ The first explanation is that the shielding currents are suppressed by a disorder owing to the fine grain and the existence of two phases of a body-centered tetragonal (bct: $I4/mmm$) and an A15 ($Pm3n$) structures at 1 bar.¹ The disorder may reduce T_c by a fluctuation in the phase of the superconducting order parameter Ψ . If one phase is realized under high pressure, applying pressure should reduce the fluctuation and improve the superconducting state. In fact, Palstra et al. found a disappearance of A15 phase under high pressure.¹ As the second explanation, they pointed out that applying pressure should improve the connectivity of material by pressing the grains. The improvement of the connectivity can reduce the phase fluctuation. The third explanation is that Cs_3C_{60} is a Mott-Hubbard insulator. If Cs_3C_{60} is an insulator at 1 bar, applying pressure can lead to a metallic state and further a superconducting state. In this paper, we report the structure and physical properties of Cs_3C_{60} under ambient and high pressures in order to clarify the origin of the

pressure induced superconductivity.

Experimental

The Cs_3C_{60} sample was prepared by a synthesis method using liquid NH_3 .¹ The sample obtained was transferred into a 0.7 mm quartz capillary in a glove box for the Raman, ESR and X-ray diffraction measurements under ambient pressure and into the diamond anvil cell for the pressure dependent X-ray diffraction measurement. The Ag(2) Raman peak of the sample was observed at a center frequency ω_0 of 1449 cm^{-1} , showing that the sample was Cs_3C_{60} . The X-ray diffraction pattern was measured with a synchrotron radiation at the BL-6C in KEK-PF; the wavelength, λ , of X-ray beam was 1.100 and 0.689 Å for the X-ray diffraction measurements under ambient and high pressures, respectively. Rietveld analysis was performed with RIETAN-94 program.² The ESR was measured with an X-band ESR spectrometer (Bruker ESP300).

Results and Discussion

Figure 1 shows the X-ray diffraction patterns for Cs_3C_{60} at 300 and 9 K under ambient pressure. Both X-ray diffraction patterns could not be reproduced with a bct and an A15 structures. Rietveld analysis for X-ray diffraction pattern at 300 K was performed with a body-centered orthorhombic (bco; $Immm$) and an A15 structure ($\approx 5\%$). The bco structure was produced by eliminating a four-fold axis from the bct structure of $I4/mmm$.¹ Recently, Rosseinsky's group reported that Cs_4C_{60} took a bco structure.³ The structure was the same as that of Cs_3C_{60} except for the occupancy of Cs atom. The weighted pattern R factor, R_{wp} , and the pattern R factor, R_p , in the final refinement were 4.85 and 3.77 %, respectively. The lattice constants a , b and c were 11.843(7), 12.220(7) and 11.464(6) Å at 300 K, respectively. The C_{60} molecule is orientationally ordered in the bco structure. The Cs atom occupied 4f and 4h sites with occupancy of 0.75(2). The atomic parameters determined from the X-ray diffraction pattern at 300 K are reported elsewhere.⁴ No new peaks were observed in the X-ray diffraction pattern at 9 K except for a weak peak around $2\theta = 12.8^\circ$; the origin for the weak peak could not be clarified. The X-ray diffraction pattern at 9 K could be reproduced with the bco and the A15 structures ($R_{wp} = 5.68$, $R_p = 4.45\%$). The a , b and c were 11.773(7), 12.160(8) and 11.433(7) Å at 9 K, respectively. The expansion coefficients, α 's, for a , b and c determined from the X-ray diffraction patterns above 70 K were 2.8×10^{-5} , 2.4×10^{-5} , and $1.5 \times 10^{-5}\text{ K}^{-1}$, respectively. Figure 2 shows the temperature dependence of volume, V and the curve based on the Debye approximation (Debye temperature $\theta_D = 439(9)\text{ K}$). A small drop of V was observed around 100 K. However, it could not be concluded whether the drop was related to the structural phase transition. The α for V was estimated to be $6.8 \times 10^{-5}\text{ K}^{-1}$,

which was smaller than that for Rb_3C_{60} ($9.3 \times 10^{-5} \text{ K}^{-1}$).⁵

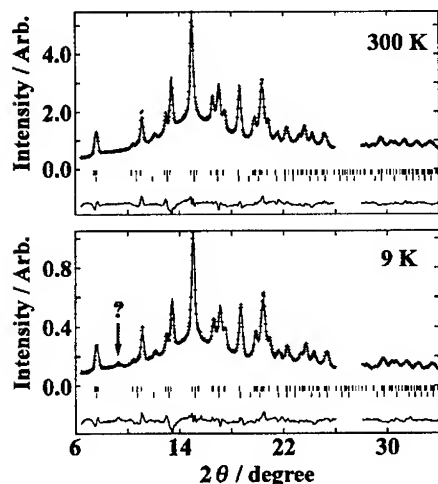


FIGURE 1. X-ray diffraction pattern at 1 bar.

The ESR spectrum at 295 K was composed of three components. Two peaks with a very narrow and a narrow line width were assigned to paramagnetic defects. Figure 3 shows the temperature dependence of ΔH_{pp} for the broad peak. This dependence suggested a metallic property for Cs_3C_{60} below 295 K. Furthermore, the spin susceptibility χ_{spin} estimated from the broad peak showed a Pauli type behavior. The $N(\epsilon_F)$ was evaluated to be 9 state/eV-spin C_{60} from the χ_{spin} , which was smaller than those of Rb_3C_{60} and K_3C_{60} .⁶ The results show that Cs_3C_{60} is not the Mott-Hubbard insulator but the broad band metal.

Figure 4 shows the X-ray diffraction patterns for Cs_3C_{60} under the pressures of 19.5 and 48.8 kbar at 300 K. The X-ray diffraction pattern at 19.5 kbar showed a very weak peak at $2\theta = 7.7^\circ$ due to the A15 phase. The Rietveld analysis was performed with two phases of the bco and the A15 ($\approx 5\%$). The a , b and c for the bco structure were 11.51(2), 11.97(2) and 11.46(2) Å, respectively: $R_{wp} = 4.33$, $R_p = 3.41\%$. The peak assigned to the A15 phase disappeared above 20 kbar. The X-ray diffraction at 48.8 kbar showed no

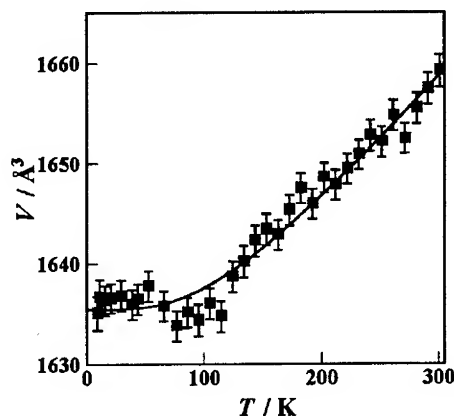


FIGURE 2. Temperature dependence of V .

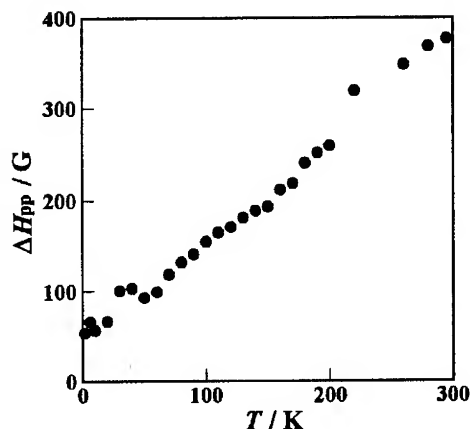


FIGURE 3. Temperature dependence of ΔH_{pp} .

peak due to the A15 phase. The pattern could be analyzed with a bco structure. The a , b and c were determined to be 11.06(8), 11.69(8) and 11.45(8) Å, respectively: $R_{wp} = 2.57$, $R_p = 1.96\%$. The temperature dependence of V are shown in Figure 5. The compressibility κ for a , $2.0 \times 10^{-3} \text{ kbar}^{-1}$, was larger than those for b and c (κ for b : $6.3 \times 10^{-4} \text{ kbar}^{-1}$, κ for c : $1.8 \times 10^{-4} \text{ kbar}^{-1}$). The κ for V was estimated to be $3.1 \times 10^{-3} \text{ kbar}^{-1}$, which was similar to those for K_3C_{60} and Rb_3C_{60} , $4.08 \times 10^{-3} \text{ kbar}^{-1}$.⁷ The fact that only a bco phase exists under high pressure does not exclude the possibility that the phase fluctuation of Ψ by the two phase nature suppresses the superconductivity for Cs_3C_{60} at 1 bar.

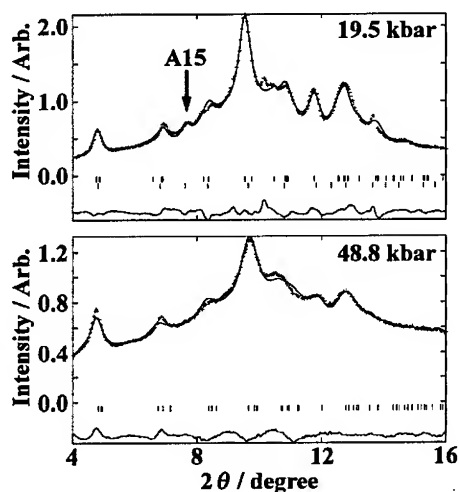


FIGURE 4. X-ray diffraction patterns at 300 K under high pressure.

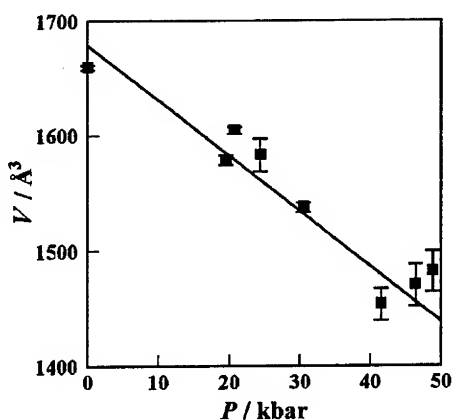


FIGURE 5. Pressure dependence of V .

REFERENCES

1. Palstra, T. T. M. *et al.*, *Solid State Commun.*, **93**, 327-330 (1995).
2. Izumi, F., *The Rietveld Analysis*, Oxford, Oxford Univ. Press, 1993, ch 13, pp. 236-253.
3. Dahlke, P. *et al.*, *J. Mater. Chem.*, **8**, 1571-1576 (1998).
4. Yoshida, Y. *et al.*, *Chem. Phys. Lett.*, **291**, 31-36 (1998).
5. Zhou O., and Cox D. E., *J. Phys. Chem. Solids*, **53**, 1373-1390 (1992).
6. Ramiretz, A. P. *et al.*, *Phys. Rev. Lett.*, **69**, 1687-1690 (1992).
7. Zhou, O. *et al.*, *Science*, **255**, 159-161 (1992).

Structural Studies of Superconducting $\text{Li}_3\text{CsC}_{60}$

Serena Margadonna and Kosmas Prassides

*School of Chemistry, Physics and Environmental Studies, University of Sussex,
Brighton BN1 9QJ, U.K.*

Abstract. The structural features of the novel superconductor $\text{Li}_3\text{CsC}_{60}$ are studied by synchrotron X-ray powder diffraction as a function of pressure and temperature. In contrast with the behaviour of semiconducting $\text{Li}_2\text{CsC}_{60}$, $\text{Li}_3\text{CsC}_{60}$ shows a phase transition at 290 K from *fcc* (space group $Fm\bar{3}m$) to an orientationally ordered primitive cubic phase (space group $Pa\bar{3}$), isostructural with the metastable phases of $\text{Na}_2\text{A}'\text{C}_{60}$. The system does not show any other phase transitions upon both slow cooling and heating protocols. The pressure dependence of the structure of $\text{Li}_3\text{CsC}_{60}$ at ambient temperature was followed up to 8.12 GPa. A phase transition occurs first at 0.38 GPa from *fcc* to primitive cubic, followed by a second one at 0.72 GPa to a low symmetry fullerene-bridged polymer phase (space group $P2_1/a$).

INTRODUCTION

Alkali fullerides with stoichiometry $\text{A}_2\text{A}'\text{C}_{60}$ ($\text{A}, \text{A}' =$ alkali metals) display superconductivity with T_c as high as 33 K at ambient pressure. Exceptions are the Li-intercalated fullerides, $\text{Li}_2\text{CsC}_{60}$ and $\text{Li}_2\text{RbC}_{60}$, which are not superconducting down to 50 mK. The loss of superconductivity has been associated with the presence of strong bonding $\text{Li}^+\text{-C}$ interactions, not encountered in other alkali fullerides.¹ As a result, the formal charge of the C_{60}^{n-} ions in $\text{Li}_2\text{AC}_{60}$ is less than 3, implying a less than full t_{1u} band. Raman measurements have established a value of $n \sim 2.5$. The strong $\text{Li}^+\text{-C}$ interactions control the structural properties of the Li-containing systems that differ markedly from those of the Na analogues. $\text{Na}_2\text{AC}_{60}$ ($\text{A} = \text{K}^+, \text{Rb}^+$) are primitive cubic (space group $Pa\bar{3}$) just below 290 K. On slow cooling, they become monoclinic with a structure comprising of quasi-one-dimensional chains of C_{60}^{3-} ions, bridged by single C-C bonds.² $\text{Na}_2\text{CsC}_{60}$ remains strictly cubic at ambient pressure but polymerises at pressures ≥ 0.7 GPa. In contrast, $\text{Li}_2\text{CsC}_{60}$ shows no structural phase transitions; it remains strictly cubic (space group $Fm\bar{3}m$) at all temperatures, under different cooling/heating procedures, and up to 6 GPa.

In order to overcome the $\text{Li}^+\text{-C}$ interactions and achieve half filling ($n=3$) of the t_{1u} band, the series of fulleride salts, $\text{Li}_x\text{CsC}_{60}$ ($1.5 \leq x \leq 6$) was synthesised. By adjusting the Li content, x , the electron-transfer from the alkali metals to C_{60} and the filling level of the conduction band was controlled. Half filling is achieved for the composition $\text{Li}_3\text{CsC}_{60}$ which is a bulk superconductor with $T_c = 10.5$ K.³ We have

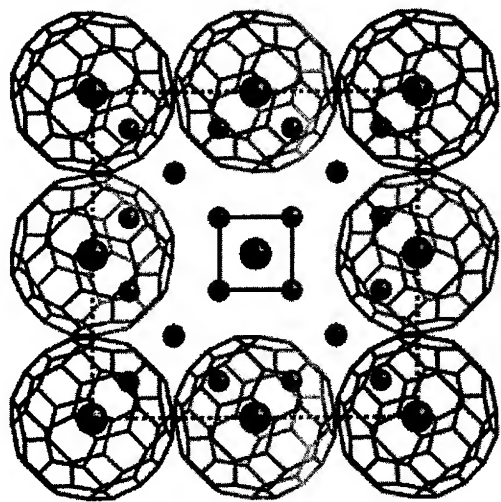
studied the structural properties of this novel superconductor by synchrotron X-ray powder diffraction as a function of both temperature at ambient pressure (down to 4 K) and pressure at room temperature (up to 8.1 GPa).

RESULTS

(a) Structural Results at Ambient Pressure

High resolution synchrotron X-ray diffraction measurements on $\text{Li}_3\text{CsC}_{60}$ were performed at 295, 150 and 4 K ($\lambda = 0.8107 \text{ \AA}$, BM16 beamline, ESRF). Inspection of the room temperature diffraction profile reveals that the structure is *fcc*. Rietveld refinements were initiated using the structural model (space group $Fm\bar{3}m$) developed earlier for $\text{Li}_2\text{CsC}_{60}$.¹ The pronounced orientational disorder of the fullerene units was

Fig.1 Unit cell basal plane projection of the primitive cubic $\text{Li}_3\text{CsC}_{60}$ structure.



modelled by describing the scattering density in terms of symmetry-adapted spherical harmonic (SASH) functions. Refinements proceeded smoothly with the Li^+ and Cs^+ ions placed in the tetrahedral and octahedral sites, respectively, resulting in a lattice constant, $a = 14.1089(4) \text{ \AA}$. The values obtained for the fitted coefficient of the SASH functions ($C_{6,1} = 0.024(4)$ and $C_{10,1} = -0.12(1)$) imply an orientational distribution function for $\text{Li}_3\text{CsC}_{60}$, comparable to that postulated for $\text{Li}_2\text{CsC}_{60}$ with an accumulation of electronic density of the spherical shell along the cubic $\langle 111 \rangle$ direction, but with a considerably weakened $\text{Li}^+\text{-C}$ interaction. In order to locate the excess intercalated Li^+ , a difference Fourier analysis was performed. The results showed the existence of scattered intensity in the vicinity of the $32f$ (0.375, 0.375, 0.375) site of the

unit cell that defines a cube, centred at the $(\frac{1}{2}, \frac{1}{2}, \frac{1}{2})$ octahedral position. Thus the Rietveld refinements were repeated after introducing a Li^+ ion in the (0.375, 0.375, 0.375) position. The occupancy converged to 1.00(1) per C_{60} , implying that the Li^+ defect is disordered over the corners of a cube of size 3.527 \AA with an $\approx 1/8$ occupancy ($R_{\text{wp}} = 7.8\%$, $R_{\text{exp}} = 5.2\%$).

In contrast to the situation encountered for $\text{Li}_2\text{CsC}_{60}$, the diffraction profiles of $\text{Li}_3\text{CsC}_{60}$ collected at 150 and 4 K revealed the presence of a phase transition to an

orientationally ordered primitive cubic structure (space group $P\bar{a}3$; $a = 14.0545(7)$ Å at 150 K; $a = 14.0261(3)$ Å at 4 K) in analogy with the Na-containing systems. In the Rietveld refinements, the structural model developed for $\text{Na}_2\text{CsC}_{60}$ was used. Due to the reduction in symmetry, the Li^+ defect was split over two symmetry inequivalent positions, those at $(x, x, x; x \approx 0.375)$ and $(x, y, z; x \approx y, x \approx z + 1/2, z \approx 0.375)$. Stable refinements of both datasets were achieved with this structural model ($R_{\text{wp}} = 11.7\%$, $R_{\text{exp}} = 8.4\%$ at 150 K; $R_{\text{wp}} = 10.7\%$, $R_{\text{exp}} = 6.7\%$ at 4 K). The geometry of the Li defect is well defined at low temperatures, implying disorder over the corners of a cube with edge size $3.35(19)$ Å at 150 K and $3.14(9)$ Å at 4 K and an $\approx 1/8$ occupancy (Fig. 1).

Synchrotron X-ray powder diffraction profiles were also collected on slow cooling (40 K/h) from 320 and 200 K on the BM1A beamline at the ESRF. The fcc to

primitive cubic phase transition occurs in the vicinity of 290 K in analogy with $\text{Na}_2\text{RbC}_{60}$ and $\text{Na}_2\text{CsC}_{60}$ and no other transitions are evident, despite the slow cooling procedure adopted. Extraction of reliable lattice constants down to 200 K was performed with the LeBail method using the fcc model between 320 and 290 K and the primitive cubic model below 290 K (at 320 K: fcc lattice constant $a = 14.115(1)$ Å). The temperature dependence of the lattice constant of

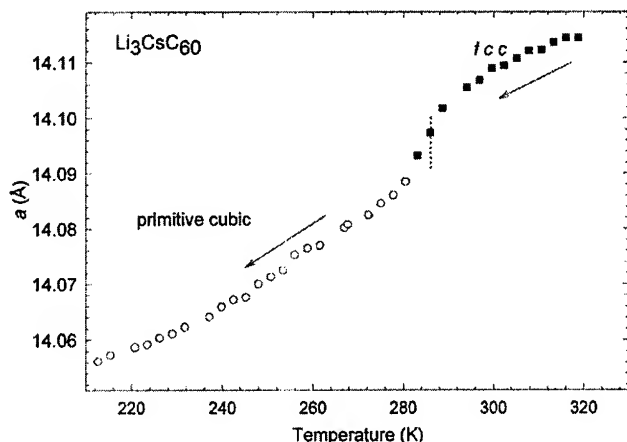


Fig. 2. Temperature dependence of the cubic lattice constant in $\text{Li}_3\text{CsC}_{60}$

$\text{Li}_3\text{CsC}_{60}$ is shown in Fig. 2. The linear thermal expansivity, $\alpha (=d\ln a/dT)$ is calculated to be $3.40(8) \times 10^{-5} \text{ K}^{-1}$ between 285 and 200 K, consistent with the values encountered in other monomeric alkali fullerides ($3.63(3) \times 10^{-5} \text{ K}^{-1}$ for the fcc phase of $\text{Li}_2\text{CsC}_{60}$; $2.20(6) \times 10^{-5} \text{ K}^{-1}$ for the primitive cubic phase of $\text{Na}_2\text{CsC}_{60}$) in the same range of temperatures.

(b) Structural results at high pressure

Synchrotron X-ray powder diffraction profiles of $\text{Li}_3\text{CsC}_{60}$ were collected between ambient and 8.12 GPa (beamline ID9, ESRF, Grenoble). In this range of pressure, two distinct phase transitions are seen, in contrast with the behaviour of $\text{Li}_2\text{CsC}_{60}$.⁴ At

ambient pressure, the structure is *fcc* with $a = 14.111(1) \text{ \AA}$ ($Fm\bar{3}m$). Inspection of the diffraction profiles shows that as soon as a pressure of 0.39 GPa is reached, the

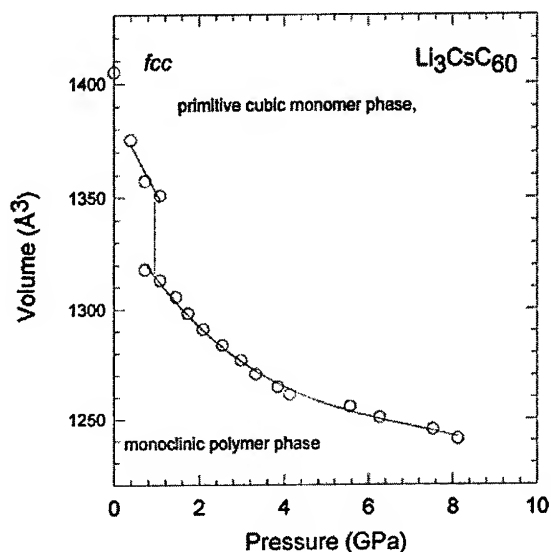


Fig. 3. Pressure dependence of the unit cell volume. V of $\text{Li}_3\text{CsC}_{60}$

positions of the cubic peaks shift to larger 2θ values, indicating the same primitive cubic orientational ordering transition that we already encountered on cooling at 290 K. At a pressure of 0.72 GPa, the diffraction pattern shows new peaks that could not be accounted for by the primitive cubic structural model. Moreover, these appear to grow with increasing pressure at the expense of the peaks assigned to the primitive cubic phase, until they completely dominate the profile at a pressure of 1.08 GPa. These new Bragg reflections could be indexed with the monoclinic space group $P2_1/a$, used before to describe the polymeric phase of $\text{Na}_2\text{RbC}_{60}$ ² and $\text{Na}_2\text{CsC}_{60}$.⁵ The diffraction data collected at 1.08 GPa were refined by the Rietveld method using a monoclinic structural

model based on the quasi-one-dimensional polymeric structure of $\text{Na}_2\text{RbC}_{60}$ described in previous works, in which the fullerene molecules form chains connected via single C-C covalent bonds. The alkali metals, Cs and Li were located at the $(\frac{1}{2}, 0, 0)$ and $(x \approx 0, y \approx \frac{1}{4}, z \approx \frac{1}{2})$ sites, derived from the high symmetry octahedral and tetrahedral positions of the parent cubic structure, respectively. In the same way, we derived the position of the Li^+ defect which is split over four symmetry inequivalent positions; these describe a cube centred at the pseudo-octahedral $(\frac{1}{2}, 0, 0)$ site with an $1/8$ occupancy. A stable refinement was achieved with this structural model and the values obtained for the monoclinic lattice constants are $a = 13.62(1) \text{ \AA}$; $b = 14.061(2) \text{ \AA}$; $c = 9.362(2) \text{ \AA}$; $\beta = 133.48(7)^\circ$ ($R_{\text{wp}} = 12.14\%$, $R_{\text{exp}} = 11.7\%$).

In order to extract reliable values of the lattice constants, we analysed the data at all pressures by the LeBail method. The data collected at ambient pressure were refined with the *fcc* model, while those at 0.38 GPa with the primitive cubic model. The X-ray powder diffraction profiles at 0.72 and 1.08 GPa were treated using a two phase model of co-existing monoclinic and cubic phases, while for those at pressures between 1.08 and 8.12 GPa, a single phase monoclinic model was employed. The pressure evolution of the normalised monoclinic lattice constant a , b , c indicates that

there is a substantial anisotropy in the compressibility along the three axes. The structure is less compressible along c , which defines the polymeric chain and is most compressible along a . This is in contrast with what is observed for the $\text{Na}_2\text{CsC}_{60}$ polymer which is most compressible along the interchain b direction. This can be ascribed to the greatly increased sterical hindrance caused by the Li defect along the b axis. The pressure-volume curve for the monoclinic phase up to 8.12 GPa has been fitted using the Murnaghan EOS (Fig. 3). The average bulk modulus, K_0 of the polymer is ~ 30 GPa, consistent with the value for the $\text{Na}_2\text{CsC}_{60}$ polymer ($K_0 = 28(1)$ GPa).⁵

CONCLUSIONS

The superconducting $\text{Li}_3\text{CsC}_{60}$ phase ($T_c = 10.5$ K) adopts a primitive cubic structure (space group $Pa\bar{3}$) isostructural with the metastable phases of $\text{Na}_2\text{A}'\text{C}_{60}$. The tetrahedral and octahedral interstices of the structure are occupied by the Li and Cs cations, respectively, while the excess Li (one per C_{60} unit) is disordered at the corners of a cube with an edge length of ~ 3.4 Å, centred at the octahedral sites. At room temperature, a phase transition occurs to a fcc structure (space group $Fm\bar{3}m$) which contains orientationally disordered C_{60}^{3-} ions. In addition, $\text{Li}_3\text{CsC}_{60}$ transforms under pressure at room temperature to a monoclinic phase, which comprises of quasi-one-dimensional singly C-C bonded C_{60}^{3-} chains. Increased crowding due to the presence of the Li defects leads to a considerable decrease in compressibility, especially along the monoclinic b axis.

ACKNOWLEDGEMENTS

We thank the ESRF for provision of beamtime. We acknowledge M. Hanfland, K. Knudsen and A. N. Fitch for help with the synchrotron X-ray diffraction experiments and M. Kosaka and K. Tanigaki for the provision of the sample.

REFERENCES

- [1] I. Hirose *et al.*, *Science* **264**, 1294 (1994).
- [2] G. M. Bendele *et al.*, *Phys. Rev. Lett.* **80**, 736 (1998); A. Lappas *et al.*, *J. Phys.: Condens. Matter* **11**, 371 (1999).
- [3] M. Kosaka *et al.*, *Phys. Rev. B* **59**, R6628 (1999).
- [4] S. Margadonna *et al.*, *J. Inorg. Mater.*, submitted.
- [5] S. Margadonna *et al.*, *J. Solid State Chem.*, in press.

Structure of $\text{Ca}_4(\text{NH}_3)\text{C}_{60}$

G. Oszlányi, S. Pekker, G. Faigel, L. Forró

*Research Institute for Solid State Physics and Optics, H-1525 Budapest, POB. 49, Hungary
Département de Physique, EPFL, 1015-Lausanne, Switzerland*

Abstract. Single phase $\text{Ca}_4(\text{NH}_3)\text{C}_{60}$ was prepared by a synthesis in liquid ammonia. X-ray powder diffraction shows that coordinated ammonia is held in the structure by a cage of calcium cations leading to surprisingly high thermal stability. It is likely that a series of similar compounds can be synthesized in which both the charge state and the electronic overlap can be controlled in a systematic manner.

I INTRODUCTION

Despite AE_xC_{60} salts (AE: alkaline-earth metal) show superconductivity at remarkably high charge states they attracted less attention and are less understood than their alkali- C_{60} relatives. This is partly due to their more complicated structure and partly to the high melting point of alkaline-earth metals which makes the direct solid state chemical reaction problematic. Their synthesis in liquid ammonia would make high reaction temperatures unnecessary and offer a new dimension in the AE- C_{60} phase diagram. The inclusion of the NH_3 molecule in the structure could change interfullerene distances and thus alter the physical properties.

The Ca_xC_{60} system was first studied by Kortan et al. [1]. Superconducting Ca_5C_{60} [1] and the vacancy ordered $\text{Ca}_{2.75}\text{C}_{60}$ [2] have complicated structures which need special attention. Therefore we have chosen the simple Ca_4C_{60} composition which is in the middle of a range where solid solution behavior with face centered cubic structures were reported. Our aim was to test the feasibility of the Ca- NH_3 - C_{60} synthesis without controlling the ammonia content.

II EXPERIMENTAL

The liquid ammonia route is now a well established sample preparation technique [3]. In our process liquid ammonia was condensed into a stoichiometric mixture of C_{60} and calcium. The reaction was complete in half an hour and the product precipitated directly from the solution. Then ammonia was removed in a two stage procedure. First the sample was heat treated at 350°C while the cold end was kept at liquid nitrogen temperature. Cryopumping driven by the large

temperature gradient was maintained for one week. After this the cold end of the reaction tube was sealed and a two week annealing at 400°C followed. The original aim of these heat treatments was to remove all traces of ammonia from the system but instead we arrived at the nearly stoichiometric compound $\text{Ca}_4(\text{NH}_3)\text{C}_{60}$.

For structural characterization parallel beam x-ray diffraction data were collected at the X3B1 beamline of the Brookhaven National Laboratory NSLS. The wavelength of 1.1501 Å was selected by a channel-cut Si(111) monochromator and the sample in 1 mm capillary was rocking a 5° range during the data acquisition at room temperature.

III RESULTS

The product is well crystallized and its diffraction pattern differs from literature data for Ca_4C_{60} . The unit cell is still face centered cubic (space group $\text{Fm}\bar{3}\text{m}$) but the lattice parameter is $a=14.084$ Å which is significantly larger than the $a=13.98$ Å value found by Kortan et al. [1]. This unit cell expansion already suggests the inclusion of NH_3 molecules in the structure but an analysis based on intensity distribution is essential.

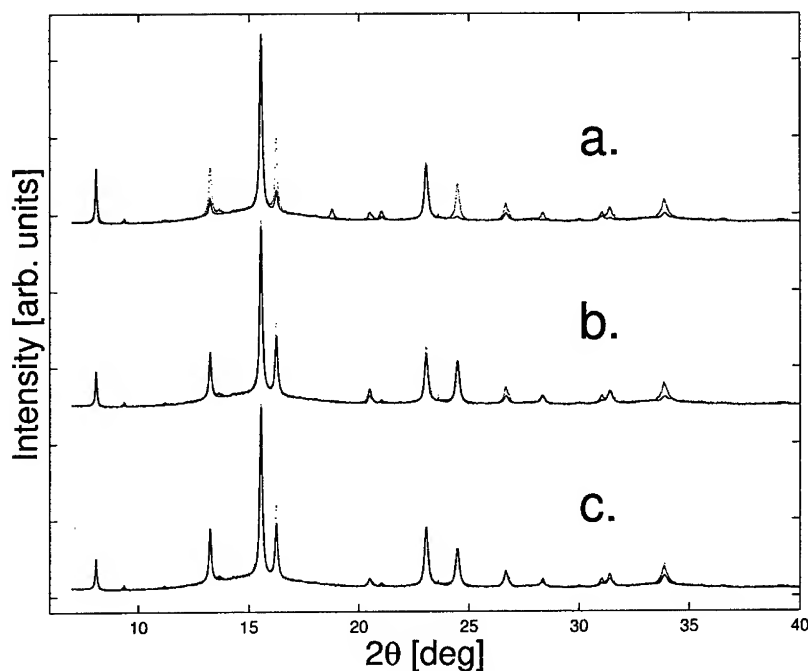


FIGURE 1. Rietveld fits of room temperature powder diffraction data of $\text{Ca}_4(\text{NH}_3)\text{C}_{60}$. Details of the various structural models are given in the text.

Figure 1.a-c show the observed data and Rietveld fits based on various structural models. In all these the scattering of the C_{60} molecule is approximated by a spherical shell. The worst fit (Fig. 1.a, $R_{wp}=17.7\%$) is given by a model in which calcium cations are constrained at ideal tetragonal and octahedral sites (T and O) of the fcc lattice. This model is easily rejected by the eye. The fit is strikingly improved (Fig. 1.b, $R_{wp}=9.8\%$) if the calcium at the O site is free to shift to the off-centered O^* site at (x,x,x) with $x=0.41$. This model is heavily disordered with $\sim 30\%$ occupancy of the eight equivalent vertices of the O^* cube. The size of this cube is also quite large: edge= 2.5 \AA , face diagonal= 3.6 \AA , body diagonal= 4.4 \AA . These dimensions can not be understood without the inclusion of ammonia when the Ca^{2+} radius is just 1.0 \AA and the vertices of the cube are only partly occupied. The model is further improved (Fig. 1.c, $R_{wp}=8.1\%$) by adding charge to the ideal octahedral site again. This charge refines to a value which is very close to the number of electrons in the NH_3 molecule. While the quality of the fit is now improved by a smaller amount, this improvement is still convincing.

The final structural model and parameters are shown in Fig. 2. As the relative size of the NH_3 molecule and the Ca^{2+} cation are nearly identical, now it is obvious

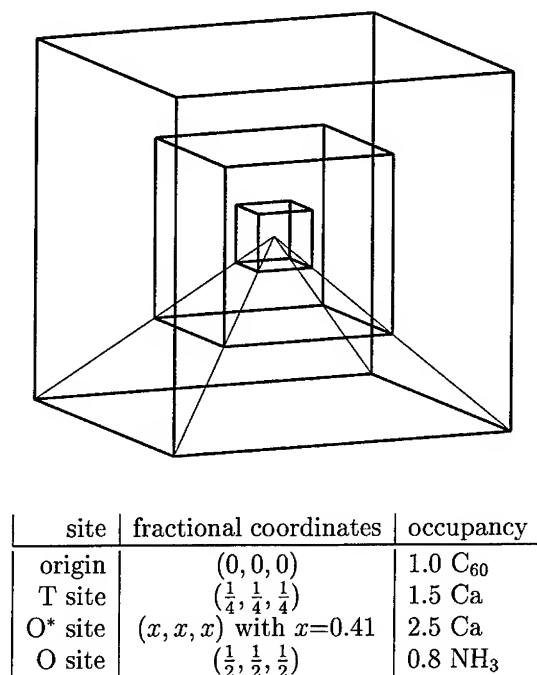


FIGURE 2. Best structural model and parameters of $Ca_4(NH_3)C_{60}$

II. ENDOHEDRAL FULLERENES

Atoms in Molecular Cages

B. Pietzak*, M. Waiblinger*, K. Lips**, A. Weidinger*

* Hahn-Meitner-Institut Berlin, Glienicker Straße 100, D-14109 Berlin, Germany

** Hahn-Meitner-Institut Berlin, Rudower Chaussee 5, D-12489 Berlin, Germany

Abstract. Fullerenes are ideal traps for atomic nitrogen and phosphorus. The inert shell of the fullerenes protects these very reactive atoms from the surrounding and keeps them stable at ambient conditions. Electron paramagnetic resonance (EPR) measurements give clear evidence that the enclosed atoms reside at the centre of the cage and keep their atomic ground state configuration. Quantum-chemical calculations confirm these findings. In this contribution the complexes $N@C_{60}$, $N@C_{70}$ and $P@C_{60}$ will be discussed. Special attention will be paid to: i) the stability of endohedral complexes, ii) the g-factor shift between $N@C_{60}$ and $N@C_{70}$ and iii) the vibrations of the atoms in the cage. A new cage which is able to entrap atomic hydrogen will be shortly described.

INTRODUCTION

We describe here atom-in-cage systems with minimal interaction between the two. The ideal situation would be if the interaction between the atom and the cage would be zero, but this is of course not possible. Thus we search for systems where this interaction is small. An almost ideal system is $N@C_{60}$. It has been shown that the N atom in C_{60} retains its atomic ground state configuration and resides in the centre of the cage (1). The observed very long spin relaxation times are also indicative of an almost uncoupled system (2). On the other hand the hyperfine interaction of N in C_{60} is almost 50% larger than that of free nitrogen. At the first sight this seems to be contradicting what was said before but one has to keep in mind that the ground state hyperfine interaction is extremely small whereas it is quite large in the excited states. Thus an admixture of these states, even if small, can make a large effect in the hyperfine interaction.

In this contribution we present additional evidence for the almost free suspension of N in C_{60} and compare it with $P@C_{60}$ and $N@C_{70}$. We will show N in C_{60} and C_{70} and P in C_{60} are probably the only stable systems in this category of endohedrals. Hydrogen in C_{60} is not stable but recently a new cage became known where it is stable (3,4).

EXPERIMENTAL DETAILS

The endohedral systems are produced by ion implantation. In our set-up, the cage molecules (fullerenes or silsesquioxanes) are continuously evaporated onto a substrate and simultaneously bombarded with ions of the selected species. After several hours of bombardment the material is removed from the substrate, dissolved in toluene or CS_2

and filtered. Only the soluble fraction containing filled and empty cage molecules is used for the subsequent experiment.

The EPR (electron paramagnetic resonance) spectrometer was the model ELEXSYS 580 from Bruker and it was used in the cw and the pulsed mode, respectively.

RESULTS AND DISCUSSION

The stable systems: $N@C_{60}$, $P@C_{60}$ and $N@C_{70}$

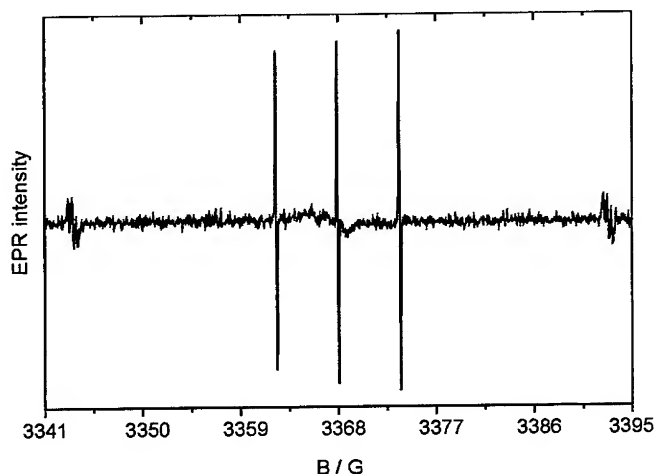


FIGURE 1. EPR spectrum of $N@C_{60}$ and $P@C_{60}$ in solution. In this experiment, N and P were only contaminations in the ion source from previous experiments, the main gas was AsF_5 but no signal from trapped As or F was observed.

Figure 1 shows the EPR spectrum of a mixture of $N@C_{60}$ and $P@C_{60}$. The much larger hyperfine coupling constant of $P@C_{60}$ (outer doublet) compared to $N@C_{60}$ (inner triplet) is clearly seen. This spectrum was obtained when we tried to implant As into C_{60} using AsF_5 as source gas. The signals in Figure 1 result from a contamination in the source, whereas no signal is seen from As, also not in a larger region of the spectrum. We conclude that $As@C_{60}$ is not stable and argue that the larger radius of As is responsible for the instability.

Similarly, when we tried to implant P in C_{70} , only the signal of $P@C_{60}$ due to the C_{60} contamination in the fullerene material was seen. We conclude from this finding that $P@C_{70}$ is not stable. Here the argument can not be the available space for the encapsulation, since C_{70} is larger than C_{60} . Here the reason is probably that the inner wall of C_{70} is less inert than that of C_{60} and therefore allows a bonding from the inside with the consequence that it leaves the cage or at least that it is not detectable by EPR.

We tried also very hard to produce hydrogen in C_{60} but without success. Thus it seems that $N@C_{60}$, $P@C_{60}$ and $N@C_{70}$ are the only stable systems in this category of endohedrals, although, of course, not all combinations have been checked experimentally. It might also be that some systems are stable at low temperatures but not at room temperature where the present survey was performed.

High resolution data and g-factor shift

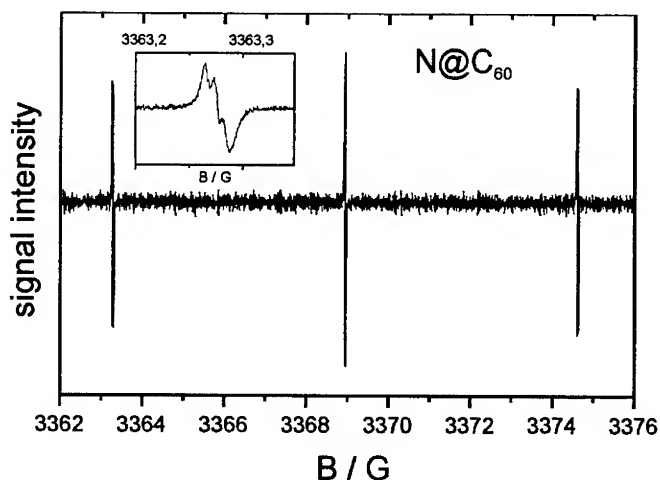


FIGURE 2. EPR spectrum of $N@C_{60}$ in solution. The inset shows a magnification of the low field line where the three components are clearly seen.

Figure 2 shows the EPR spectrum of $N@C_{60}$ in solution. In this experiment special care was taken to obtain the highest possible resolution with the cw spectrometer. The inset shows that the low field line consists of three components with a separation from one another by 9 mG, i.e. less than 3 ppm of the applied field. A similar splitting is observed for the high field line. The splitting of the lines is a consequence of the $S = 3/2$ spin of the system and is further proof for the fact that the three p-electrons of N have their spins aligned parallel as required by Hund's rule for the ground state of a free atom.

The observation of the splitting is only possible since the intrinsic width of the lines is extremely small. It also requires a careful tuning and a high stability of the spectrometer and therefore this line can be used to check the homogeneity and the stability of the magnet.

Figure 3 shows the EPR spectrum of a mixture of $N@C_{60}$ and $N@C_{70}$. The triplet of lines with the slightly smaller intensity belongs to $N@C_{70}$, the others are due to $N@C_{60}$. It can be seen that the splitting and therewith the hyperfine coupling is smaller for $N@C_{70}$ than for $N@C_{60}$. This difference has been discussed before and was attributed

to a slightly different squeezing of the encased atom in the cages with a different size. A remarkable feature of this spectrum is also that the central lines of these two systems due not coincide. This would be the case if the g factors were the same. The shift is only 20 ppm but is clearly visible due to the simultaneous observation of the two systems and since the lines are sharp.

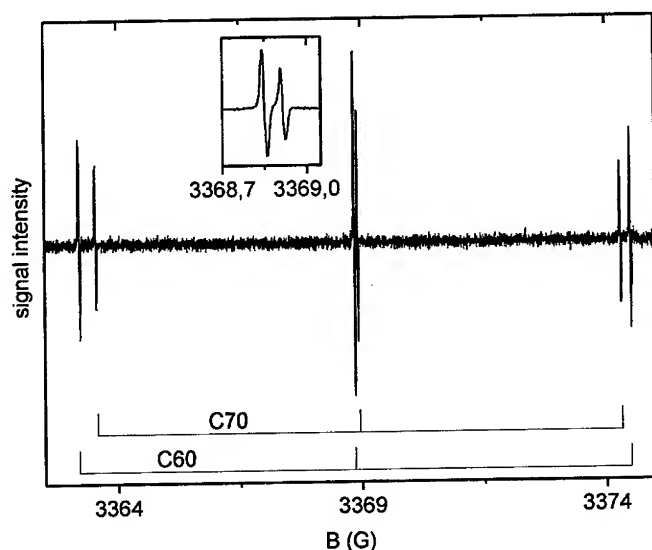


FIGURE 3. EPR spectrum of a mixture of $N@C_{60}$ and $N@C_{70}$ in solution. The hyperfine constant of $N@C_{70}$ is smaller than that of $N@C_{60}$ due to the larger inner volume in C_{70} .

In EPR a g -factor shift is usually attributed to the property of the electronic configuration of the atom in question. In the present case this would be the electron shell of nitrogen. However, it seems that this is not the case here. The argument goes as follows: A shift of similar magnitude (22 ppm) was observed in an NMR experiment for ^3He in C_{60} and C_{70} and was attributed to the diamagnetic ring currents in the hexagons (5). The larger number of these hexagons in C_{70} is therefore responsible for the larger diamagnetic shift of $^3\text{He}@C_{70}$.

Vibrations of the atom in the cage

Total energy calculations (6,7) show that nitrogen is trapped in the centre of the cage. For small elongations, the potential is approximately harmonic and oscillation energies in the order of 20 meV are predicted.

Experimentally, the oscillations can be studied indirectly via the temperature dependence of the hyperfine coupling. Assuming that the hyperfine coupling increases by

a certain amount with increasing excitation energy, one can fit the observed temperature dependence and derive the oscillator strength for each system. In this way we obtained $h\nu \approx 20$ meV for N@C₆₀ and $h\nu \approx 27$ meV for P@C₆₀. The temperature dependence of the hyperfine coupling of N@C₇₀ is clearly more complex and can be fitted only by assuming different oscillator strength along the C₅ axis and perpendicular to that. $h\nu$ in the perpendicular direction is close to that of N@C₆₀, but along the C₅ axis a much lower oscillator strength has to be assumed.

New Cages

Recently we got aware that hydrogen can be trapped in cages built up of Si₈O₁₂-cubes with hydrogen or organic substituents at the corners. This is particularly important since hydrogen can apparently not be trapped in fullerene cages, at least not at room temperature. Different to the production method described in the literature (γ -irradiation) (3,4) we used our implantation technique to incorporate hydrogen in Si₈O₁₂ cages. Subsequent EPR measurements showed that hydrogen is incorporated and stabilised in its ground state in these cages at room temperature.

We also tried to incorporate nitrogen and muonium in the C₂₀H₂₀ cage. In both cases no endohedrals were found.

REFERENCES

1. Almeida Murphy T., Pawlik T., Weidinger A., Höhne M., Alcalá R., Spaeth J. M., *Phys. Rev. Lett.* **77**, 1075-1078 (1996).
2. Knapp, C., Dinse, K.-P., Pietzak, B., Waiblinger, M., Weidinger, A., *Chem. Phys. Lett.* **272** (1997) 433-437
3. Sasamori, R., Okaue, Y., Isobe, T., Matsuda, Y., *Science* **265** (1994) 1691-1693
4. Päch, M., Stössner, R., *J. Phys. Chem.* **101** (1997) 8360-8365
5. Saunders, M., Jiménez-Vázquez, H.A., James Cross, R., Mroczkowski, S., Freesberg, D.I., Anet, F.A.L., *Nature* **367** (1994) 256-258
6. Mauser, H., van Eikema Hommes, N. J. R., Clark, T., Hirsch, A., Pietzak, B., Weidinger, A., Dunsch, L., *Angew. Chem. Int. Ed. Engl.* **36** (1997) 2835-2838
7. Pietzak, B., Waiblinger, M., Almeida Murphy, T., Weidinger, A., Höhne, M., Dietel, E., Hirsch, A., *Chem. Phys. Lett.* **279** (1997) 259-263

IR and Raman analysis of diatomic encapsulates in fullerene cages

M.Hulman^a, M. Krause^a, M. Inakuma^b, J. Dennis^b, H. Shinohara^b and
H. Kuzmany^a

a) Institut für Materialphysik, Universität Wien, Strudlhofgasse 4, A-1090 Wien, Austria

b) Department of Chemistry, University of Nagoya, Nagoya 464, Japan

Abstract. We present IR and Raman measurements of endohedral compounds $\text{Sc}_2@C_{84}$ with D_{2d} symmetry and its empty counterpart C_{84} .

Our main task was to determine mutual carbon cage – Sc vibrations. The attention was therefore concentrated in the region below 300 cm^{-1} in which one expects this type of motions. Comparing spectra for empty and filled isomers with D_{2d} symmetry we identified several candidates for the cage – Sc vibrations. The unexpected high number of such modes can be explained by site and correlation field splittings. Other modes observed in the region we attributed either to fundamental or combination modes of the cage.

The temperature dependence of the spectra gave a better insight into the dynamics of the metallofullerene compounds. We observed a broadening of some modes in the mid-IR region with increasing temperature. From a model describing the interaction between cage modes and reorientational motion we obtained an activation energy for the reorientations.

Introduction

The metallofullerene compound $\text{Sc}_2@C_{84}$ is one of the most investigated endohedral metallofullerenes. Its relatively high yield as compared to other endohedrals enabled important measurements confirming an endohedral nature of the compound. There are 24 isomers obeying so called isolated pentagonal rule. The isomer with D_{2d} (No. 23 in the Fowler- Manolopoulos nomenclature) cage symmetry is the most abundant. As we know from X-ray measurements [1] two scandium atoms are located on the two fold axis leaving the D_{2d} symmetry unchanged. $\text{Sc}_2@C_{84}$ has a monoclinic structure with two molecules in the unit cell. Both Sc atoms are equivalent in the cage of D_{2d} symmetry as shown from ^{13}C -NMR measurements [2].

Calculations on a vibrational structure of C_{84} [3] show a dense distribution of cage modes in relatively narrow range between 200 and 1800 cm^{-1} . The situation changes dramatically by encapsulating two scandium atoms into the cage. One can expect mutual Sc atom – cage vibrations which can fill up a gap between the cage and lattice vibrations. Using a force constant obtained from a measurement of a metal – cage mode in $\text{M}@C_{82}$ [4] we obtain a value of 270 cm^{-1} for the highest metal – cage

vibration in $\text{Sc}_2@\text{C}_{84}$. On the other hand the lattice modes must have energies less than 50 cm^{-1} which is the energy of the highest lattice mode in C_{60} .

Two Sc atoms in the cage mean six additional degrees of freedom which are distributed among two nondegenerated and two twofold degenerated representations of the point group D_{2d} . Since the density of the cage modes decreases towards the far infrared there is a good chance to distinguish between the cage and the Sc – cage modes by comparing the spectra of the empty and filled C_{84} cages.

This scenario can be strongly influenced by another effect which is present in a charged system. Like in exohedrally doped systems a charge transfer from two Sc atoms to the C_{84} cage can lead to the charged phonon effect [5]. Weak or silent cage modes in C_{84} borrow energy from electronic transitions and enhance their intensity considerably in $\text{Sc}_2@\text{C}_{84}$. An identification of the Sc-cage modes requires a careful analysis using both IR and Raman spectra.

The vibrational modes observed in IR and Raman spectra carry also an information on the dynamical properties of the compound. Widths and positions of the lines are determined by interactions of vibrations with themselves or between the vibrations and other excitations. In our case there are several types of vibrations – the cage modes, lattice phonons and mutual Sc- cage vibrations. They can interact with rotational degrees of freedom and this type of interaction is indeed very important in molecular crystals like C_{84} and $\text{Sc}_2@\text{C}_{84}$. Temperature dependent measurements provide a reliable tool to distinguish different types of mechanisms responsible for a linewidth and a lineshift of IR active modes.

Experimental

Thin films of $\text{Sc}_2@\text{C}_{84}$ were prepared by drop coating a gold mirror with fullerene dissolved in CS_2 . The condensed film was baked for several hours in high vacuum to get rid of enclosed solvents. Transmission spectra were taken at 2 and 0.5 cm^{-1} resolution using a Bruker IFS 66v spectrometer with both DTGS and Ge detectors in the far-infrared and with a MCT detector in the mid-IR region. Recorded spectral ranges extended from 80 cm^{-1} to 2000 cm^{-1} . An Oxford cryostat was used to measure the temperature dependence between 80 and 300 K.

Results and discussion

Mid-infrared spectra of three fullerene compounds are shown in Fig.1. As expected from their lower symmetry C_{84} and $\text{Sc}_2@\text{C}_{84}$ have much more lines as compared to C_{60} . We clearly see a gap between 800 cm^{-1} and 1100 cm^{-1} separating radial and tangential vibrations. Both parts are not equally affected by the endohedral doping as seen from a comparison of the spectra for the empty and filled cages.

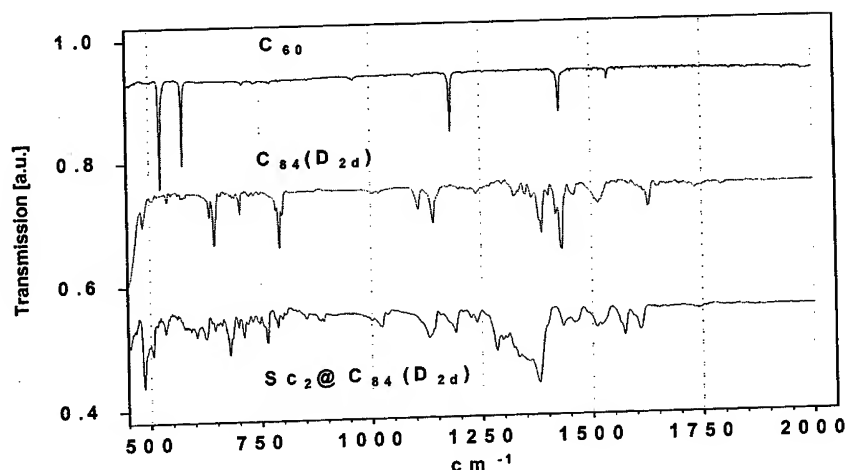


Fig.1. Mid-infrared spectra of C_{60} , $C_{84}(D_{2d})$ and $Sc_2@C_{84}(D_{2d})$

We observed many new and strongly enhanced lines in the radial part below 800 cm^{-1} . Lines above the gap are mainly broadened and up- or downshifted. We attribute the strong enhancement and lineshift to the charged phonon effect

In the far-infrared region, Fig.2, we see an even stronger difference. We found IR lines only above 400 cm^{-1} for the empty cage C_{84} . Intensities most of the weak features

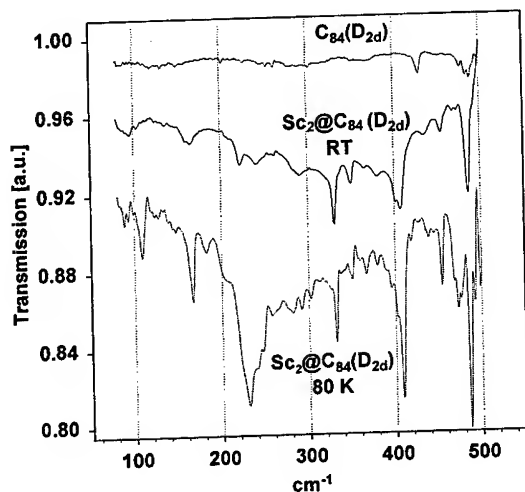


Fig. 2 The same as Fig.1 in the far-IR region

below 400 cm^{-1} are comparable to noise. Thus these features are not considered to be an intrinsic IR lines. The situation changes considerably after the endohedral doping. IR lines are distributed in the whole region between 80 cm^{-1} and 500 cm^{-1} . Silent modes become stronger and visible in the spectrum. Some of them especially those lying below 300 cm^{-1} can belong to the Sc-cage modes. At this stage we cannot exclude the cage modes from the spectrum of $Sc_2@C_{84}$ and identify the Sc-cage modes by comparing of both spectra only. The most likely candidates for the Sc-cage modes are lines at 160 cm^{-1} and a broad band just below 100 cm^{-1} from the RT spectrum.

IR lines become stronger and narrower for the low temperature spectrum at 80 K. We can resolve modes at 90, 110, 145, 165 cm^{-1} and an extended band at 230 cm^{-1} as possible candidates for the Sc-cage modes.

We measured also Raman spectra of $\text{Sc}_2@\text{C}_{84}$ in order to distinguish the Sc-cage modes with a higher reliability. Raman spectra at room temperature and at 96 K are displayed in Fig.3 together with the IR spectrum at 80 K. The Raman spectrum of C_{84} shows no lines below 200 cm^{-1} as expected from the calculations. All lines we observed belong to the cage modes. The broad band at 220 cm^{-1} reappears in the low

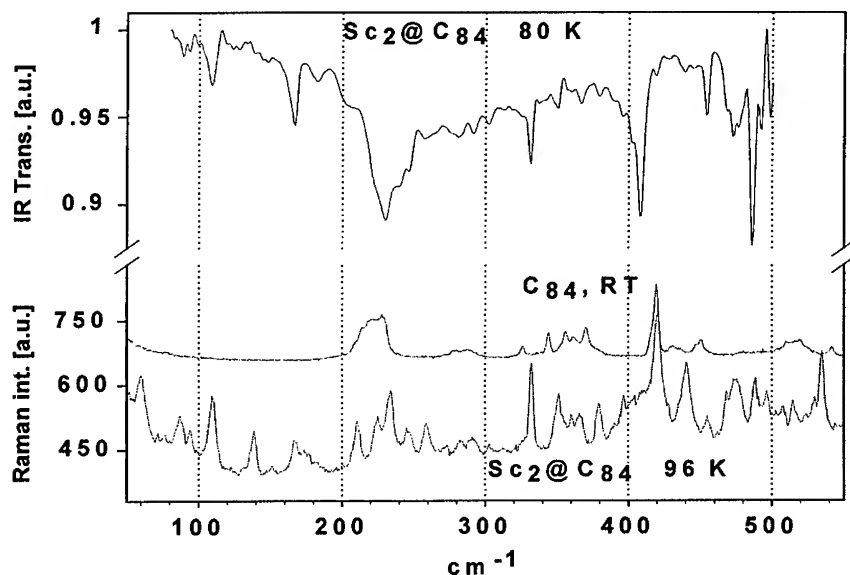


Fig.3 Raman and IR spectra of C_{84} and $\text{Sc}_2@\text{C}_{84}$ with D_{2d} symmetry

temperature spectrum. But the line at 260 cm^{-1} and all the lines below 200 cm^{-1} are really new features in the spectrum of $\text{Sc}_2@\text{C}_{84}$. There are at least 10 additional lines which is more than expected from the degrees of freedom originating from two scandium atoms inside the cage. As mentioned above these six degrees of freedom are distributed on two nondegenerated and two twofold degenerated irreducible representations of the point group D_{2d} . Two $\text{Sc}_2@\text{C}_{84}$ molecules occupy sites with a C_1 symmetry in the unit cell. Thus the twofold degeneration is removed into two nondegenerated states. Additional splitting is caused by a correlation field which doubles a number of modes giving a possible final number of 12 modes. At the moment we assign the following modes to the Sc- C_{84} cage vibrations: 261 (R), 258 (IR,R), 166 (IR,R), 159 (IR), 138 (IR,R), 109 (IR,R), 95 (IR,R), 87 (IR,R) and 60 cm^{-1} (R). Almost all lines are both IR and Raman active in agreement with group theory.

Results of temperature measurements are plotted in Fig. 4. In an Arrhenius plot the logarithm of linewidths is expressed as a function of a reciprocal temperature. Plotted are mid-IR modes of C_{84} at 1108 cm^{-1} and of $Sc_2@C_{84}$ at 1286 cm^{-1} with D_{2d} cage symmetry and of C_{84} at 1382 cm^{-1} with D_2 symmetry. At high temperatures the

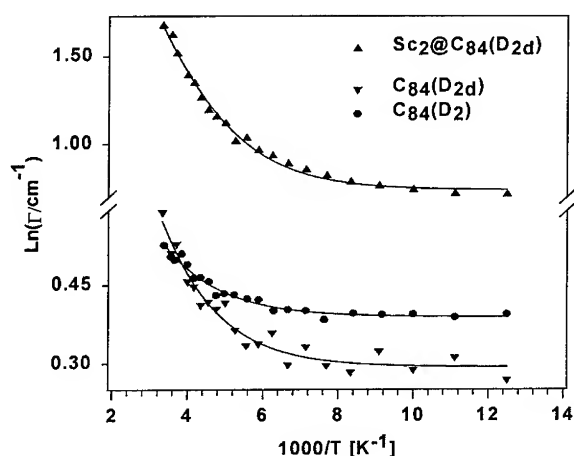


Fig.4. Arrhenius plot for C_{84} and $Sc_2@C_{84}$

linewidths decrease monotonically with increasing temperature. We assume that the temperature dependence is caused by a coupling of the cage modes with a thermally activated rotational motion of the C_{84} molecules. If τ is a characteristic time for a correlation of molecular reorientations then the linewidth is determined directly by $2/\tau$. In the model of rotational diffusion $\tau^{-1} = \Gamma = \exp(-E_a/k_B T)$ where Γ is the linewidth and E_a is an activation energy for the reorientations. The solid lines in Fig. 4 represent a fit of the values measured where we also included a constant term expressing a finite linewidth at low temperatures. The results for the activation energy are 65 meV for C_{84} (D_{2d}), 59 meV for C_{84} (D_2) and 63 meV for $Sc_2@C_{84}$ (D_{2d}). The linewidths are almost temperature independent below 160 K which suggests a suppression of molecular rotations. The observed results are qualitatively similar to the results obtained from measurements of a C_{80} dimetallofullerene [6]. They found an energy of 33 meV for the activation and a temperature independence of the reorientational correlation time below 160 K.

Acknowledgment

Work supported by the FFWF in Austria, Project No. P 11 943 (M.H.) and by the EU TMR project ERBFMRX-C197-0155 (M.K. and H.K.)

References

- [1] M. Takata et al., Phys. Rev. Lett. **78**, 3330, (1997)
- [2] E. Yamamoto et al., J. Am. Chem. Soc. **118**, 9, (1996)
- [3] B.L. Zhang et al., Phys. Rev. B **47**, 1643, (1993)
- [4] S. Lebedkin et al., Appl. Phys. A **66**, 273, (1998)
- [5] T. Pichler et al., Phys. Rev. B **49**, 15879, (1994)
- [6] W. Sato et al., Phys. Rev. B **58**, 10850, (1998)

ENDOHEDRAL FULLERENES WITH LOWER CARBON CAGE SIZES

Lothar Dunsch, Pavel Kuran, Petra Georgi and Andrej Gromow

Institut für Festkörperforschung, IFW Dresden, Abt. Elektrochemie und leitfähige Polymere, Helmholtzstraße 20, D-01069 Dresden (Germany)

While endohedral fullerenes of the type $\text{Me}@C_{82}$ were extensively investigated, the structures with lower carbon cage sizes are of high interest to study the role of the carbon cage on their structure and physical properties. The existence of C_{72} and C_{74} metallofullerene structures differs from the availability of empty fullerenes which were not isolated up to now.

As model structures $\text{La}_2@C_{72}$, $\text{Tm}C_{76}$ and $\text{Tm}C_{78}$ were chosen to study the correlation between the type of the metal incorporated and the metallofullerene cage size. The structures were prepared by the Krätschmer arc burning method and isolated by a multistep HPLC separation technique. UV-Vis-NIR and infrared spectroscopy were used at room temperature. It is shown that some metals which are present in the 2+ redox state in fullerenes (Tm) form stable exohedral structures of C_{78} .

INTRODUCTION

Among endohedral fullerenes those structures with C_{82} cages like $\text{Tm}@C_{82}^{1-3}$, $\text{La}@C_{82}^4$, $\text{Sc}@C_{82}^5$ and $\text{Y}@C_{82}^6$ have been shown to be very stable. Furthermore, it has been recently demonstrated that in the case of $\text{Eu}@C_{74}^7$ an endohedral fullerene with a lower carbon cage size is also a stable structure although the corresponding empty fullerene was not isolated in larger amounts so far. Thus, the aim of this work is to characterize new metallofullerenes existing in a larger variety of structures for Tm, La and Ce. As our recent work⁸⁻¹¹ was focused on the relation between the structure and the physical properties of endohedral fullerenes in presented paper the influence of the type of the carbon cage and of the element on the stability was to be followed. These fullerenes were characterized by mass spectrometry, cyclovoltammetry, *ex situ* and *in situ* ESR as well as UV-Vis-NIR- spectroscopy.

EXPERIMENTAL

The metallofullerenes were prepared by the arc burning method of Krätschmer and Huffman. The mass spectrometric characterisation by a sector field mass spectrometer MAT 95 (FINNIGAN, Bremen) and HPLC separation have been described elsewhere¹².

The electrochemical measurements were carried out at room temperature with a potentiostat PAR 273 (EG&G, USA) including the software PARC M270, version 3.0. A conventional voltammetric cell which was installed in a glovebox under inert conditions was used. As solvent o-dichlorobenzene and as supporting electrolyte tetrabutylammoniumtetrafluoroborate were applied. The working electrode material was platinum, the counter electrode a large platinum sheet and the reference electrode a silver-/silverchloride electrode in the same supporting electrolyte.

UV-Vis-NIR spectra of the fullerenes in solution were measured using an UV 3101 PC spectrometer (Shimadzu, Japan) in suprasil 300 quartz cells of 10 mm path length from 200 to 3000 nm with a resolution of 4 nm.

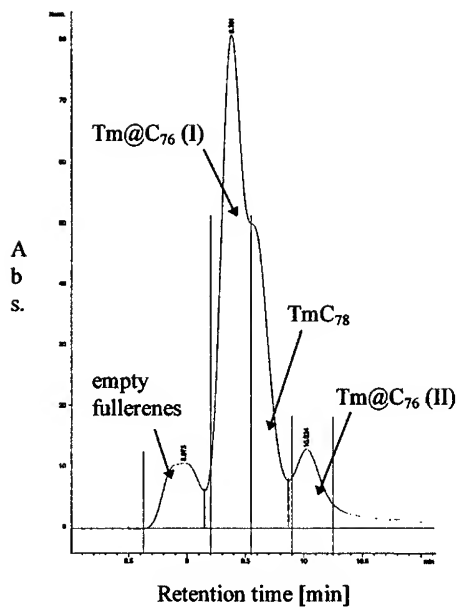
Electron spin resonance spectra were recorded by an EMX X-band spectrometer (Bruker) with 100 kHz modulation at 9.5 GHz microwave frequency and 340 mT medium magnetic field strength. The *in situ* electrochemical technique used in this study was described elsewhere¹³.

RESULTS

Besides Tm@C₈₂ the Tm fullerene soot contains larger amounts of Tm@C₇₆ and TmC₇₈ which have to be separated in a multistep HPLC (Fig. 1). The chromatographic behaviour of both Tm metallofullerene structures demonstrates that the TmC₇₈ exist in one single isomeric structure while Tm@C₇₆ is present in two isomeric forms which differ markedly in their retention times and therefore also in their chemical structure. TmC₇₈ fullerene, being expected to eluate after both Tm@C₇₆ isomers, comes out surprisingly between these structures. This makes the chromatographic separation more complicated. On the other hand it sheds a certain light on the chemical nature of TmC₇₈.

The nature of this metallofullerene is characterized by mass spectrometry in the FAB as well as in the CI mode. As shown in Fig. 2a by the FAB mode it is possible to get highly purified samples by a multistep HPLC separation. The content of other fullerenes than TmC₇₈ is less than 5 %. Thus the TmC₇₈ metallofullerene is a stable structure in solution as well as in the solid state. This is to be pointed out because the same structure shows a strong instability in mass spectrometry using the chemical ionization mode. By this ionization it is possible to detect empty C₇₈ cages. As this cage structure was neither detected by HPLC nor by FAB mass spectrometry it is produced by ionisation of TmC₇₈. As a consequence the structure must have the Tm ion in a position which allows a splitting off without a destruction of the carbon cage. A structure which is consistent with this behaviour is the existence of an exohedral metallofullerene structure. The special case of an exohedral structure which is stable in solution is to be demonstrated by further experimental methods.

1a)



1b)

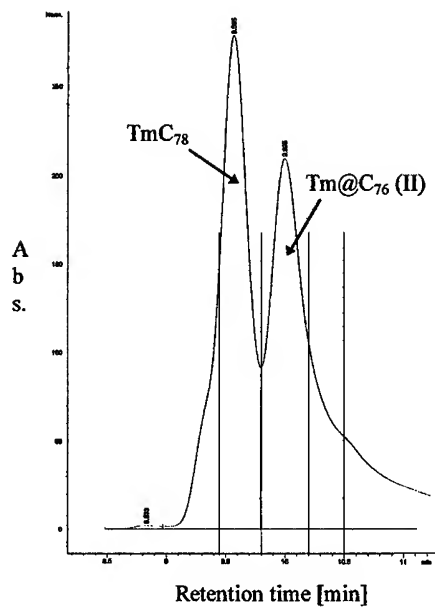
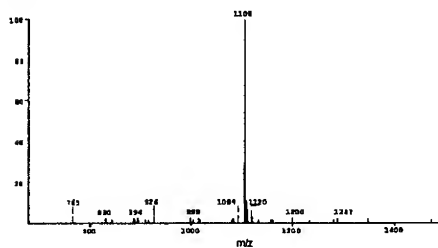


FIGURE 1: HPLC of Tm@C₇₆ and TmC₇₈ on a Buckyclutcher column (10mm x 250mm) with 2 ml toluene per minute

- a) first separation of the thulium couple
b) fourth separation step

2a)



anodic potential range. While the first two cathodic electron transfers are similar to the redox peaks of $\text{Eu}@\text{C}_{74}$ which was previously found to be divalent, the TmC_{78} has in contrast a third reduction step at more negative potentials. This odd number electron transfer is found for metallofullerenes but does not contradict the assumption that even in this structure the Tm is divalent. The two anodic waves are supporting the two valent state of thulium in this special metallofullerene structure.

Furthermore the cyclic voltammogram of TmC_{78} in a solvent mixture of toluene and acetonitrile (not shown here) shows the absence of the anodic peaks after an exhaustive electrochemical oxidation what seems to be a further hint for the split off at the metallofullerene by charge transfer forming the empty fullerene cage. This result is supported by mass spectrometry where the thulium salt of the counter anion of the supporting electrolyte was found.

By *in situ* ESR spectroscopic measurements in o-dichlorobenzene it is shown that at the open cell potential as well as in the first reduction step no ESR signal is found. The original as well as the reduced states of the endohedral fullerene are therefore not detectable by ESR. But in the case of a mixture of toluene and acetonitrile the electron transfer at cathodic potentials gives an ESR signal which is attributed the paramagnetic state of an empty C_{78} cage with a similar g-factor of the reduced state. Thus the ESR signal indicates a split off at the metallofullerene structure

Both isomers of $\text{Tm}@\text{C}_{76}$ eluted on BC column in distinct different retention times (difference 0.7 min), shown in Fig. 1a. In addition, the recovery of the first $\text{Tm}@\text{C}_{76}$ -isomer is dramatically higher than that of the second $\text{Tm}@\text{C}_{76}$ -isomer. Both isomers are of completely different colour, which is confirmed by UV-Vis-NIR spectroscopy. During separation and characterisation both isomers were stable.

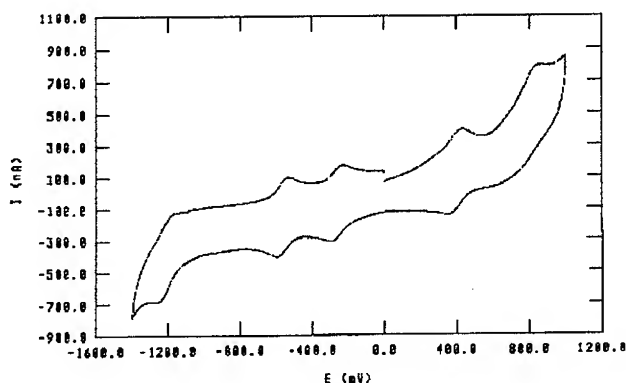


FIGURE 3: Cyclic voltammogram of TmC_{78} in o-dichlorobenzene solution at a platinum electrode. Scan rate: 20 mV/s.

The influence of the carbon cage size on the stability of a metallofullerene was studied at $\text{La}_2@\text{C}_{72}$. The $\text{La}_2@\text{C}_{72}$ was separated by two step HPLC. In the first step a

preparative Buckyprep column and in the second step a semipreparative Buckyclutcher column was used. The structure was stable during separation and characterisation (UV-Vis-NIR and IR).

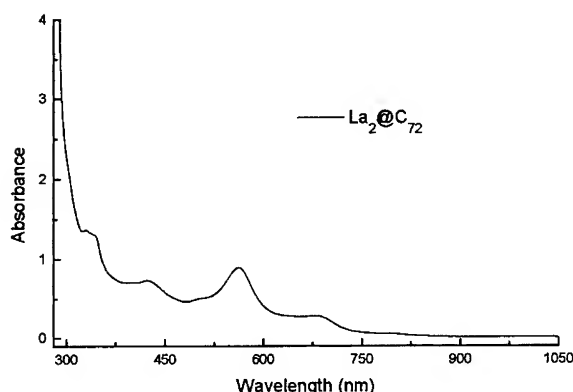


FIGURE 4: UV-Vis-NIR spectrum of $\text{La}_2@C_{72}$ in toluene

Fig. 4 shows the UV-Vis-NIR spectrum of $\text{La}_2@C_{72}$. Absorptions at 330, 424, 564 and 681 nm are found. These absorption bands are similar to the absorptions of the $\text{Ce}_2@C_{72}$ -structure.

CONCLUSIONS

Like endohedral fullerenes of the type $\text{Me}@C_{82}$ the fullerene structures with lower carbon cage sizes are shown to be stable. The role of the metal on the carbon cage structure and their physical properties demonstrate that the existence of C_{72} and C_{74} fullerene is supported by the metals as the cage size of these structures is not available for empty cages.

As model structures $\text{La}_2@C_{72}$, TmC_{76} and TmC_{78} were demonstrated to give rise of new chemical and physical properties of the metal incorporated and the metallofullerene cage size. The structures were prepared by the Krätschmer arc burning method and isolated by a multistep HPLC separation technique. UV-Vis-NIR and infrared spectroscopy were used at room temperature. It is shown that metals which are present in the 2+ redox state in fullerenes form stable exohedral structures of C_{78} .

ACKNOWLEDGEMENT

The support of this work by the *Deutsche Forschungsgemeinschaft*, the German *Bundesministerium für Bildung und Forschung* and EU (TMR-project ERBFMRX-CT97-0155) is gratefully acknowledged. Furthermore thanks to Dr. Anton Bartl for

discussions on ESR-measurements and the technical assistance of Ulrike Feist, Brunhild Schandert, Heidi Zöller and Frank Ziegs.

REFERENCES

1. U. Kirbach and L. Dunsch, *Angew. Chem. Int. Ed. Engl.* 35 (1996) 2380
2. L. Dunsch, P. Kuran, U. Kirbach, D. Scheller, in: "Recent Advances in the Physics and Chemistry of Fullerenes and related materials", Vol. 4 (K. M. Kadish and R. S. Ruoff, Eds.) Pennington, *Electrochem. Soc.* 1997, 523-536
3. M. Krause, P. Kuran, U. Kirbach, L. Dunsch, *Carbon* 37 (1998) 113-115
4. Y. Chai, T. Guo, C. Jin, R. E. Haufler, L. P. F. Chibante, J. Fure, L. Wang, J. M. Alford and R. E. Smalley, *J. Phys. Chem.* 95 (1991) 7564
5. C. S. Yannoni, M. Hoinakis, H. M. S. de Vries, D. S. Bethune, J. R. Salem, M. S. Crowder and R. D. Johnson, *Science* 256 (1992) 1191.
6. J. H. Weaver, Y. Chai, G. H. Kroll, T. R. Ohno, R. E. Haufler, T. Guo, J. M. Alford, J. Conceicao, L. P. F. Chibante, A. Jain, G. Palmer and R. E. Smalley, *Chem. Phys. Lett.* 190 (1992) 460;
S. Bandow, H. Shinohara, Y. Saito, M. Ohkohchi and Y. Ando, *J. Phys. Chem.* 97 (1993) 6101
7. P. Kuran, M. Krause, A. Bartl, L. Dunsch, *Chem. Phys. Lett.* 292 (1998) 580-586
8. A. Bartl, L. Dunsch, J. Fröhner and U. Kirbach, *Chem. Phys. Letters* 229 (1994) 115
9. A. Bartl, L. Dunsch and U. Kirbach, *Appl. Magn. Res.* 11 (1996) 301
10. A. Bartl, L. Dunsch, U. Kirbach, *Solid State Comm.* 94 (1995) 827
11. P. Kuran, M. Krause, A. Bartl, L. Dunsch, *Chem. Phys. Lett.* (1998) in prep.
12. L. Dunsch, U. Kirbach, P. Kuran, in: "Recent Advances in the Physics and Chemistry of Fullerenes and related materials", Vol. 5 (K. M. Kadish and R. S. Ruoff, Eds.) Pennington, *Electrochem. Soc.* 1997, in press
13. L. Dunsch and A. Petr, *Ber. Bunsenges. Phys. Chem.* 97(1993) p. 436
L. Dunsch, in: *Progress in Fullerene Research*; (H. Kuzmany, J. Fink, M. Mehring and S. Roth, Eds.) Singapore, World Scientific 1994, p. 482

Atoms in Fullerene Traps as Probes for Local Fields

C. Knapp, N. Weiden, H. Käß, and K.-P. Dinse

Phys. Chem. III, TU Darmstadt, Petersenstr. 20, D-64287 Darmstadt, Germany

Abstract. The "high spin" state of Nitrogen and Phosphorus atoms encapsulated in Fullerenes by ion bombardment provides a sensitive tool to test the symmetry of the local electric potential via Zero-Field-Splitting (ZFS) interaction. Because of the symmetry-dictated absence of this interaction in case of isolated C_{60} , even small effects resulting for instance by collision-induced cage distortions or by long range ordering in the crystalline phase can be detected. As an example we studied the first-order phase transition of C_{60} at 258 K, by which the site symmetry at the Nitrogen position is lowered from T_h to S_6 , thus allowing for the existence of ZFS with axial symmetry in the low temperature phase. Furthermore, the ability to detect the presence of trace amounts of paramagnetic species via fluctuating magnetic dipole-dipole interaction is also demonstrated.

I INTRODUCTION

Recently, C_{60} molecules could be synthesized in which an additional Nitrogen atom is positioned at the center of the carbon frame. These molecules, which are generated by ion bombardment, are stable at room temperature and it was shown that the encapsulated Nitrogen atom is surprisingly not bound to the carbon cage but rather found in its quartet spin ground state ($^4S_{3/2}$), characteristic for the free atom [1,2]. Obviously, the paramagnetic atom, which is situated at special positions in the C_{60} crystal is an ideal 'spy' to sense a change in site symmetry which might result from phase transitions. Furthermore, hyperfine interaction between the paramagnetic spin at the center and the nuclear spins in the shell can also be used to detect the reorientational dynamics of the cage, which are not directly related to the phase transitions. In this contribution we report on the observation of a non-vanishing Zero-Field-Splitting (ZFS) in the low-temperature phase of crystalline C_{60} sensed via the quartet electron spin state of nitrogen. This interaction is 'seen' by atoms situated at the special sites of the crystal, irrespective of fast tumbling of the carbon cage. Furthermore, the capability of $N@C_{60}$ to sense fluctuating magnetic fields originating from paramagnetic impurities which are not directly detectable by EPR is demonstrated.

II EXPERIMENTAL

N@C₆₀ was prepared by ion bombardment using a low pressure discharge as described elsewhere [3]. The raw product was dissolved in toluene and separated from colloidal particles by micro-filtration (0.05 μ). Polycrystalline material was obtained by slowly evaporating the solvent. The sample was finally sealed off on a high-vacuum line. The relative concentration of N@C₆₀ in C₆₀ was estimated as $3 \cdot 10^{-5}$. All spectra were obtained with a pulse EPR spectrometer (BRUKER ELEXSYS E 580) with integrated pulse ENDOR facility (BRUKER E 560P). Commercial probe heads were used for FT-EPR as well as for the ENDOR experiments, which were inserted in an OXFORD CF 935 cryostat. Signal analysis was performed with the BRUKER Xepr software package.

III RESULTS AND DISCUSSION

A EPR Spectra of N@C₆₀ in Polycrystalline C₆₀

In the high-temperature phase, C₆₀ molecules have their center-of-mass on a face-centered cubic (fcc) lattice (space group $Fm\bar{3}m$) [4]. Accordingly, Nitrogen atoms occupying special positions (4a) in the crystal, will experience a site symmetry of O_h . This high symmetry is the reason for vanishing expectation values of all traceless second-rank tensor operators. Because the effective spin Hamiltonian of a $S = 3/2$ spin system can be described by tensor operators up to rank two, the spectrum can be explained by invoking scalar terms only. Below T_c , long range orientational order is established and the symmetry is lowered to simple cubic (sc) with four molecules per unit cell (space group $Pa\bar{3}$). As a result, the site symmetry at the center positions is lowered from O_h to S_6 . In this group, no higher than two-dimensional irreducible representations exist. The presence of non-vanishing elements of an axially symmetric ZFS tensor therefore is allowed by symmetry. For the first-order phase transition at 256 K this implies that a typical powder spectrum of a quartet spin should be observable just below T_c in the EPR spectrum.

Fig. 1 shows EPR spectra measured a few degrees above and below T_c . In the low temperature phase just below T_c the expected satellites are clearly visible at each hyperfine component (hfc). (Although the spectra were taken in the pulsed mode in order to avoid line broadening by field modulation and/or power broadening, it should be noted that the additional structure can also be observed by conventional c.w. EPR, if very low modulation frequencies are used.) With a least squares fit an axially symmetric ZFS tensor with $D = 0.52$ MHz is obtained. Lowering the temperature, the general feature persists, although the spectral resolution decreases. This can be attributed to additional line broadening by anisotropic ^{13}C hfi which is observable at lower temperature when spinning of the carbon shell is sufficiently slowed down.

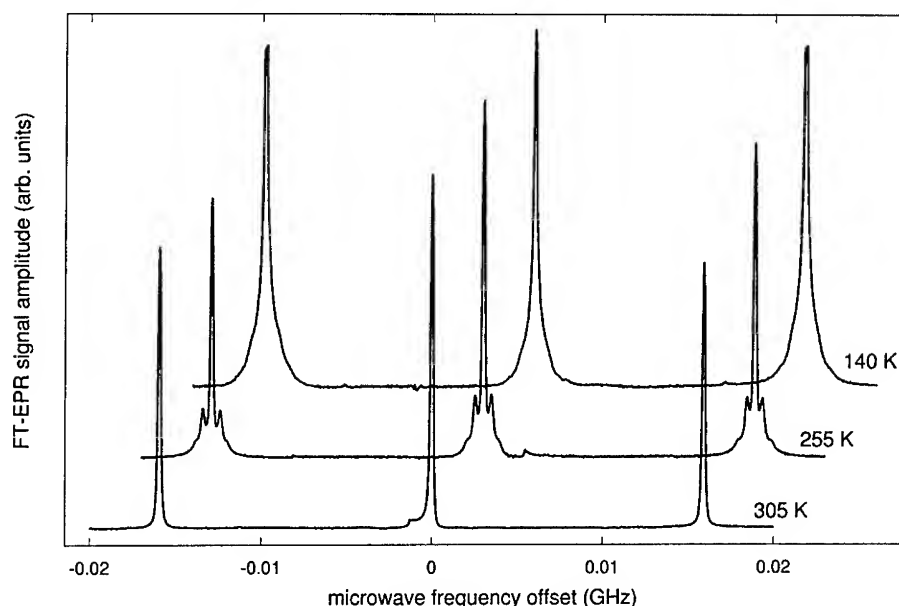


FIGURE 1. FT-EPR spectra of N@C₆₀ in polycrystalline C₆₀. Below the phase transition temperature of 260 K, a characteristic powder pattern appears, which can be simulated by assuming an axially symmetric ZFS tensor with principle value $D = 0.52$ MHz.

B ENDOR Spectra of N@C₆₀ in Polycrystalline C₆₀

Whereas the effects of long-range order are detected by ZFS sensed by the central quartet spin, rotational dynamics instead are best detected by measuring the hyperfine interaction of the Nitrogen electronic spin with the ¹³C nuclear spins on the cage. An estimate of the point dipole interaction leads to a predicted value of 440 kHz for the principle value of the coupling tensor, necessitating the use of ENDOR for an accurate analysis. In case of an isotropically rotating Carbon cage, complete averaging of the anisotropic part of the dipolar interaction is expected, leading to a "solution-like" ENDOR spectrum even in the solid phase, displaying the isotropic part of the hfi only. Slowing down of cage rotation should lead to the appearance of powder like features, resulting from the overlap of contributions of the four m_S sub levels of the electronic quartet spin (see below).

In Fig. 2, ENDOR spectra measured at 80 K and 250 K are depicted, taken at the ¹³C spectral region. For the experiment, a "Davies"-type pulse sequence was utilized ($\tau_\pi(5\mu s) - \tau_{rf}(60\mu s) - \tau_\pi(2.5\mu s) - \tau(15\mu s) - \tau_\pi(5\mu s) - echo$), which is best suited for the detection of small coupling constants. In a quartet electronic spin system, first order ENDOR transitions ($\Delta m_S = 0, \Delta m_I = \pm 1$) for $I = 1/2$

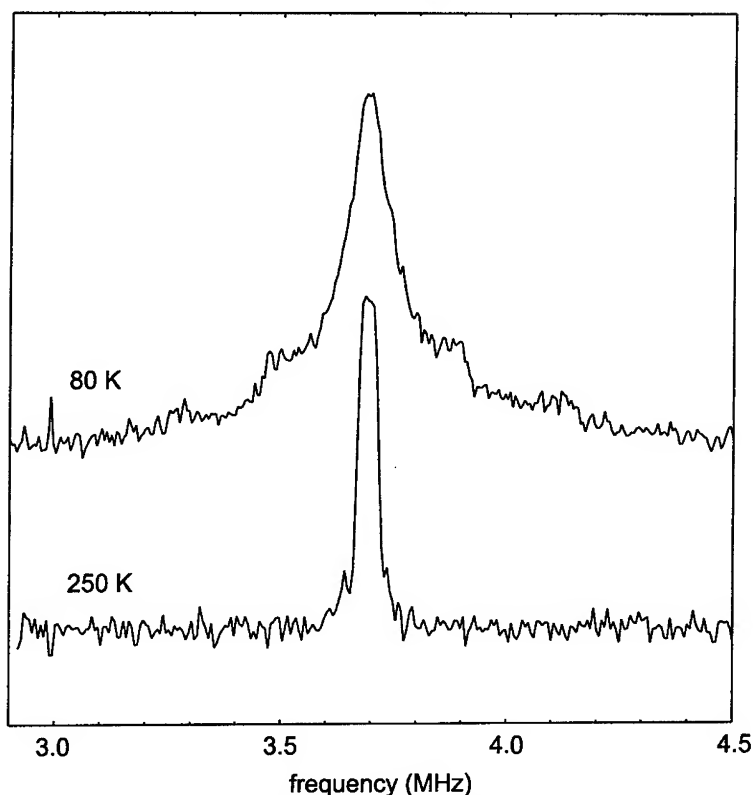


FIGURE 2. Pulse ENDOR spectra of N@C₆₀ in polycrystalline C₆₀ measured close to the ¹³C nuclear Zeeman frequency.

nuclei like ¹³C are expected at $\nu'_{\text{ENDOR}} = |\nu_n \pm A_{zz}(\beta, \gamma)/2|$ and at $\nu''_{\text{ENDOR}} = |\nu_n \pm 3A_{zz}(\beta, \gamma)/2|$, which collapse into single transitions in case of a vanishing hfi. The angular dependence of A_{zz} on the orientation of the molecule with respect to the external field axis, which is denoted by the Eulerian angles β and γ leads to a typical powder pattern if the cage rotation is sufficiently slow. As can be seen in Fig. 2, the broad structure collapses at 250 K into an apparently single line, indicating isotropic rotation of the cage with a correlation time shorter than the reciprocal width of the low temperature spectrum. A quantitative analysis of the ¹³C powder ENDOR which results from coupling to 60 equivalent "local" nuclei in the carbon cage indicates that not only point dipole interaction with the Nitrogen spin but also contributions from spin density delocalized on the cage contributes to the observed pattern.

C Sensing EPR-Silent Paramagnetic Impurities

Taking advantage of the exceptional long spin relaxation times of N@C_{60} , the presence of trace quantities of paramagnetic impurities in solution should be detectable because of fluctuating magnetic fields contributing to spin relaxation. Nitroxide spin labels are used routinely for the detection of paramagnetic molecular Oxygen in biological tissues down to a concentration of a few $\mu\text{mol}/\text{dm}^3$, because in an aqueous solution saturated with air ($[\text{O}_2] = 200 \mu\text{mol}/\text{dm}^3$) the EPR lines are broadened by about $20 \mu\text{T}$. To our surprise we found that the same Oxygen concentration only leads to an increase of the spin relaxation rate of N@C_{60} by $3 \cdot 10^4 \text{ s}^{-1}$, corresponding to a line width increase of bare $2 \mu\text{T}$. Using Nitroxide spin labels as "relaxers", we found a linear dependence of this additional rate on the concentration of the impurity spins. The much weaker proportionality factor compared to the conventional case can be explained by the complete absence of Heisenberg spin exchange, leaving only dipole-dipole interaction as relaxation mechanism for the Fullerene-encased Nitrogen spin. This behavior can be rationalized by the fact that the Nitrogen atom is not only confined in space but because of negligible spin transfer to the Fullerene cage spin exchange during collisions with other spins is prevented. This is in contrast with strong Oxygen-related line broadening observed for Metallo-Fullerenes, for which spin density resides on the Carbon cage and therefore is accessible. Using the calibration obtained from the Nitroxide probes, it could be demonstrated that Ho@C_{82} which is EPR silent at room temperature in solution is paramagnetic as expected from the odd number of electrons in the system.

IV ACKNOWLEDGEMENT

This report was possible because of continuing collaboration with B. Pietzak, M. Waiblinger, and A. Weidinger (HMI Berlin). Financial support from the Deutsche Forschungsgemeinschaft (Di 182/20-1) and a temporary loan of a pulse ENDOR probe head from BRUKER is gratefully acknowledged.

REFERENCES

1. T. Almeida Murphy, T. Pawlik, A. Weidinger, M. Höhne, R. Alcala, J.-M. Spaeth, *Phys. Rev. Lett.* 77 (1996) 1075
2. C. Knapp, K.-P. Dinse, B. Pietzak, M. Waiblinger, A. Weidinger, *Chem. Phys. Lett.* 272, (1997) 433
3. B. Pietzak, M. Waiblinger, T. Almeida Murphy, A. Weidinger, M. Höhne, E. Dietel, and A. Hirsch, *Chem. Phys. Lett.* 279 (1997) 259
4. W. I. F. David, R. M. Ibberson, J. C. Matthewman, K. Prassides, T. J. S. Dennis, J. P. Hare, H. W. Kroto, R. Taylor, and D. R. M. Walton, *Nature* 353 (1991) 147

CERIUM METALLOFULLERENES

Petra Georgi, Pavel Kuran and Lothar Dunsch

*IFW Dresden, Abt. Elektrochemie und leitfähige Polymere
Helmholtzstr. 20, D-01069 Dresden, Germany*

With respect to its redox state cerium is of high interest in metallofullerene research as its preferable redox states are 3+ and 4+. As representative structures of the cerium fullerene family both $Ce_2@C_{72}$ and $Ce@C_{82}$ were prepared by the Krätschmer arc burning method. The metallofullerene $Ce_2@C_{72}$ was isolated for the first time using a two stage HPLC separation technique. The UV-Vis-NIR, IR and ESR spectra were compared with those of other C_{72} cage metallofullerenes. The existence and stability of the $Ce_2@C_{72}$ structure supports the assumption that the C_{72} carbon cage can be stabilised by metal ions.

The endohedral fullerene $Ce@C_{82}$ was also isolated by two stage HPLC and characterised by UV-Vis-NIR, IR and ESR spectroscopy for comparison with other endohedral C_{82} fullerenes. The redox properties of this metallofullerene structure were studied by cyclic voltammetry.

INTRODUCTION

Cerium fullerenes represent the interesting group of endohedral fullerenes¹⁻³, because the redox state of the cerium atom inside the cage can be 3+ or 4+. Besides the structures like $La@C_{82}$ ⁴, $Sc@C_{82}$ ⁵ and $Y@C_{82}$ ^{2,6} the carbon cages with lower sizes are predominately studied. Therefore the influence of compounds containing five-membered rings (for instance decacyclene, see Fig. 1) on the formation and yield of smaller fullerene structures like $Ce_2@C_n$ ($n=72, 76, 78, 80$) was studied. Mass spectrometric, UV-Vis-NIR, IR- and electrochemical measurements were chosen to characterise the dimetallofullerene $Ce_2@C_{72}$ and the monometallofullerene $Ce@C_{82}$.

EXPERIMENTAL

The cerium fullerenes were produced by using the arc vaporisation method by Krätschmer and Huffman. The helium pressure inside the arc burning chamber was 200 mbar.

TABLE 1 Composition of rod filling mixture

graphite	cerium (metallic)	decacyclen	$Ce(NO_3)_3$
6	1	0.25	0.25
6	1	0.125	0.125
6	1	0.5	0.5

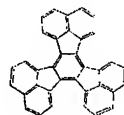


FIGURE 1 Decacyclene

In the first set of experiments the graphite rods for the production cycles were filled with a mixture of graphite, metallic cerium, decacyclene and cerium nitrate in different molar compositions as shown in Table 1. The cerium fullerene structures were extracted from the soot by carbon disulphide and purified by two stage HPLC. After the first HPLC step a long term storage of the $Ce@C_{82}$ containing fraction for seven months under laboratory conditions was undertaken.

In a further preparation cycle the carbon rods were filled with a mixture of graphite and metallic cerium in the ratio of 12.5 to 1 (molar). The fullerenes were again extracted by CS_2 , then dissolved in toluene and passed in one step through HPLC.

RESULTS AND DISCUSSION - CERIUM FULLERENE FAMILY

The mass spectra of the family of cerium fullerene structures produced in both preparation cycles are as follows:

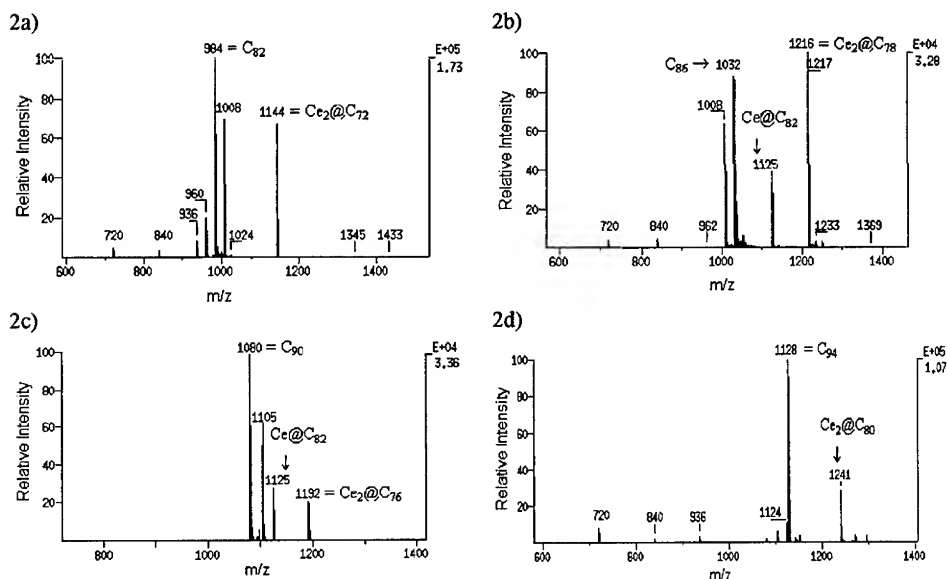


FIGURE 2 Mass spectra of fractions after preparative HPLC

- a) $Ce_2@C_{72}$ containing fraction; b) $Ce_2@C_{78}$ containing fraction;
c) $Ce_2@C_{76}$ and $Ce@C_{82}$ containing fraction; d) $Ce_2@C_{80}$ containing fraction

In Fig. 2a-d the mass spectra of the endohedral cerium fullerene structures $Ce_2@C_{72}$ ($m/z=1144$), $Ce_2@C_{76}$ ($m/z=1192$), $Ce_2@C_{78}$ ($m/z=1216$), $Ce_2@C_{80}$ ($m/z=1241$) and $Ce@C_{82}$ ($m/z=1125$) are shown. The higher dimetallo cerium fullerenes $Ce_2@C_{76}$, $Ce_2@C_{78}$ and $Ce_2@C_{80}$ could also be detected in pre-separated fractions of preparative HPLC separation.

$\text{Ce}_2@\text{C}_{72}$

The stable $\text{Ce}_2@\text{C}_{72}$ structure as well as $\text{La}_2@\text{C}_{72}$ point to the fact that the C_{72} cage can be stabilised by metal ions, because the isolation of the empty C_{72} cage was unsuccessful up to now. Fig. 3 shows the UV-Vis-NIR spectrum of $\text{Ce}_2@\text{C}_{72}$. Absorptions at 340 nm, 556 nm and 677 nm were found. These absorption bands are similar to the UV-Vis-NIR- absorption of the $\text{La}_2@\text{C}_{72}$ structure. This is an indication that the oxidation state of cerium is 3+.

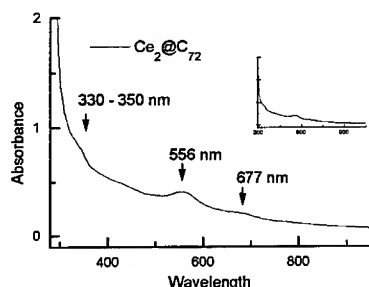


FIGURE 3 UV-Vis-spectrum of $\text{Ce}_2@\text{C}_{72}$

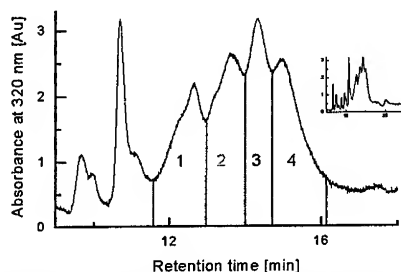


FIGURE 4 HPLC-chromatogram of $\text{Ce}@\text{C}_{82}$ on analytical BC after long-term storage

$\text{Ce}@\text{C}_{82}$

The separation of endohedral $\text{Ce}@\text{C}_{82}$ after a long-term storage was made on an analytical Buckyclutcher column. The HPLC-profile is shown in Fig. 4.

After collecting the fractions at retention times between 11.7 and 16 minutes the UV-Vis-NIR spectra were measured. All four fractions showed the same absorptions at 390, 631 and 1008 nm. As already shown by mass spectrometry all fractions contain $\text{Ce}@\text{C}_{82}$. This behaviour suggests, that a light-induced transformation of the $\text{Ce}@\text{C}_{82}$ -structure has taken place during storage.

SPECTROSCOPY AND STABILITY OF $\text{Ce}@\text{C}_{82}$

The $\text{Ce}@\text{C}_{82}$ structure produced in the second production cycle (without decacyclene and cerium nitrate in the rod filling mixture) was separated by one-step-HPLC.

The purity of the $\text{Ce}@\text{C}_{82}$ is more than 90%. The influence of light on the stability of the $\text{Ce}@\text{C}_{82}$ structure was investigated by using two samples from the same separation batch. One sample was stored for seven days under day light, the other sample was irradiated for 4 hours with light at 200 nm. Both samples have been irreversibly changed. This change was clearly seen in the HPLC-profiles before and after irradiation. To avoid this change it was necessary to measure the UV-Vis-NIR and IR-spectra (Fig. 5a and b) shortly (less than 12h) after HPLC-separation and to store the structure in the

dark. UV-Vis-NIR absorptions at 380 nm, 500 nm, 630 nm and 1010 nm and typical IR-absorptions (in comparison with $\text{La}@C_{82}$ ⁷) are detected.

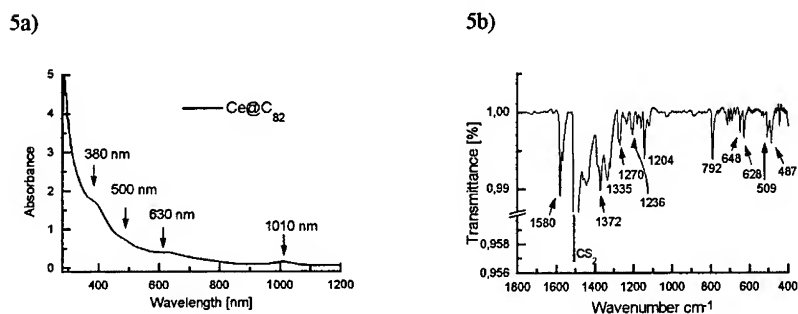


FIGURE 5 UV-Vis-NIR and IR-spectra of $\text{Ce}@C_{82}$

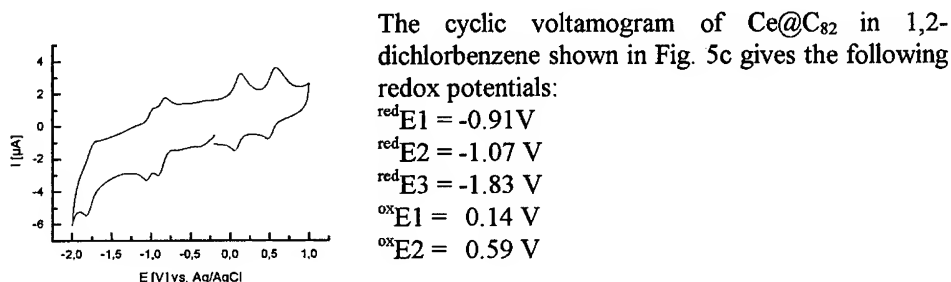


FIGURE 6 Cyclic voltammogram of $\text{Ce}@C_{82}$

In comparison with $\text{La}@C_{82}$ the $\text{Ce}@C_{82}$ shows very similar absorption in the UV-Vis-NIR spectra, the vibrational modes are comparable and also the cyclic voltammograms are similar. These results indicate, that also in the case of $\text{Ce}@C_{82}$ the redox state of the cerium atom is 3+.

CONCLUSIONS

For the first time $\text{Ce}_2@C_{72}$ was isolated by two stage HPLC separation and characterised by UV-Vis-NIR and mass spectrometry. The retention behaviour in HPLC and the UV-Vis-NIR spectrum of $\text{Ce}_2@C_{72}$ are similar to those of $\text{La}_2@C_{72}$. The stable higher dimetallo ceriumfullerenes $\text{Ce}_2@C_{76}$ and $\text{Ce}_2@C_{78}$ were detected in pre-separated fractions of preparative HPLC. The stability of $\text{Ce}@C_{82}$ under irradiation was studied and it was shown that irreversible changes of the $\text{Ce}@C_{82}$ structure under the formation of a new ones eluting at the shorter retention times than $\text{Ce}@C_{82}$ are observed. This new $\text{Ce}@C_{82}$ structures were shown to give completely different HPLC-profiles.

ACKNOWLEDGMENTS

This work was financially supported by *Bundesministerium für Bildung und Forschung, Deutsche Forschungsgemeinschaft (Schwerpunktprogramm Grundlagen der elektronischen Nanotechnologie)* and *EU (TMR-project ERBFMRX-CT97-0155)*.

REFERENCES

1. R. D. Johnson, H. S. de Vries, J. Salem, D. S. Bethune and C. S. Yannoni, *Nature* 355 (1992) 239; R. D. Johnson, D. S. Bethune and C. S. Yannoni, *Acc. Chem. Res.* 25 (1992) 169.
C. S. Yannoni, H. R. Wendt, M. S. de Vries, R. L. Siemens, J. R. Salem, J. Lyster, R. D. Johnson, M. Hoinkis, M. S. Crowder, C. A. Brown, D. S. Bethune, L. Taylor, D. Nguyen, P. Jedrzejewski and H. C. Dorn, *Synth. Metals* 59 (1993) 279.
2. S. Bandow, H. Shinohara, Y. Saito, M. Ohkohchi and Y. Ando, *J. Phys. Chem.* 97 (1993) 6101
3. A. Bartl, U. Kirbach, L. Dunsch, B. Schandert and J. Fröhner, in: *Progress in Fullerene Research*; (H. Kuzmany, J. Fink, M. Mehring and S. Roth, Hrsg.) Singapore, World Scientific 1994, p. 112.
4. Y. Chai, T. Guo, C. Jin, R. E. Haufler, L. P. F. Chibante, J. Fure, L. Wang, J. M. Alford and R. E. Smalley, *J. Phys. Chem.* 95 (1991) 7564
5. C. S. Yannoni, M. Hoinkis, H. M. S. de Vries, D. S. Bethune, J. R. Salem, M. S. Crowder and R. D. Johnson, *Science* 256 (1992) 1191.
6. J. H. Weaver, Y. Chai, G. H. Kroll, T. R. Ohno, R. E. Haufler, T. Guo, J. M. Alford, J. Conceicao, L. P. F. Chibante, A. Jain, G. Palmer and R. E. Smalley, *Chem. Phys. Lett.* 190 (1992) 460
7. M. Krause, P. Kuran, U. Kirbach, L. Dunsch, *Carbon* 37 (1999) 113-115

The electronic properties of charged N@C_{60}

László Udvardi

*Dept. of Theoretical Physics, Institute of Physics, Technical University of Budapest,
H-1521 Budapest, Budafoki út 8, Hungary*

Abstract. The energy of the triplet and singlet states of the N@C_{60}^{-1} have been calculated at ROHF and MCSCF level. The ground state of the anion appeared to be triplet and the nitrogen atom has been found to sit at the centre of the molecule. A possible reason why the endohedral molecule remains neutral in the AC_{60} phase is discussed at the end of the paper.

I INTRODUCTION

N@C_{60} was recently discovered by T. Almeida Murphy et al. [1] and attracted great experimental and theoretical interest. Surprisingly the encapsulated nitrogen atom in the fullerene cage keeps its atomic quartet spin state as it is indicated in several ESR experiments [1–3]. The nitrogen atom sitting in the cage molecule seems to be intact even if the fullerene molecule makes a chemical reaction with some adducts [4], so the ESR signal of the nitrogen atom could be a good indicator of the changes in geometrical and electronic structure of the molecule.

In the case of the alkali doped fullerenes the C_{60} molecule accepts the valence electron of the ionized alkali atom. We expect that with the help of the N@C_{60} molecule we can detect the different charged states in these fullerites.

In the present contribution the electronic structure of the N@C_{60}^{-1} complex is calculated at ab-initio Restricted Open-shell Hartree-Fock (ROHF) and MCSCF levels. The energies of the triplet and the singlet states of the icosahedral and d_{2h} distorted molecules are compared in order to find the ground state of the system.

II RESULTS AND DISCUSSION

The calculations were done using Huzinaga's mini [5] basis on the carbon atoms and 631G^{++} on the nitrogen. Since in the case of the carbon cage the extra electron can be distributed among 60 atoms but if it occupies the N orbitals it is localized

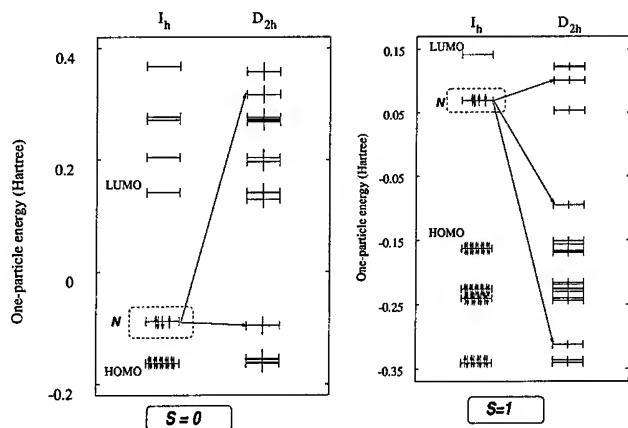


FIGURE 1. The energy of the molecular orbitals of the $N@C_{60}^{-1}$ in the vicinity of the HOMO in the case of the icosahedral and d_{2h} distorted structure.

on one atom diffuse basis was applied only on the nitrogen. However, the difference between the quality of the two basis sets makes the Mulliken charges to be meaningless. The choice of the basis was a compromise due to the size of the system.

In the neutral quartet system the p_x , p_y , p_z valence orbitals of the nitrogen atom are energetically between the HOMO and the LUMO of the C_{60} . According to our expectations the excess electron occupies the p -orbitals of the nitrogen in the icosahedral anion both in triplet and in singlet case. The many-electron ground state of the system was turned out to be $^3T_{1u}$ which is Jahn–Teller active. The geometry of the distorted ion was optimized at Hartree–Fock level prescribing d_{2h} symmetry for the system, however, the application of MCSCF procedure should have been more preferable due to the presence of the quasi degenerate HOMO. This fact was reflected by the huge splitting of the triply degenerate niveous of the nitrogen (see Fig. 1.).

We checked the possibility of the off-centred position of the nitrogen atom in the cage. We have found a minima on a twofold axis about 1.9 Å from the centre of the molecule at 2.9 eV higher then the energy of the centred position. We concluded that in the case of the $N@C_{60}^{-1}$ the nitrogen remains at the centre of the molecule.

In order to get the multiplicity of the ground state at correlated level MCSCF calculations were done on the icosahedral and d_{2h} systems. The active space included all possible configurations of the HOMO and LUMO of the C_{60} molecule and the p -molecular orbitals of the nitrogen. The result of the calculations are summarised in Table 1.

In all the cases the restricted open-shell HF and MCSCF calculation predicted the triplet state to have the lowest energy according to the Hund's rule and the

Off-centred		Central			
C_{2v} (ROHF)		I_h (ROHF)		D_{2h} (ROHF)	
Singlet	Triplet	Singlet	Triplet	Singlet	Triplet
-2310.4978	-2310.4928	-2309.9840	-2310.6014	-2310.5153	-2310.5162
		I_h (MCSCF)		D_{2h} (MCSCF)	
		Singlet	Triplet	Singlet	Triplet
		-2310.5473	-2310.6052	-2310.5849	-2310.5897

TABLE 1. Energies of the different structures at Restricted Open-shell Hartree-Fock and MCSCF level. All values are given in Hartree.

excess electron of the negative ion is localized on the nitrogen atom at the centre of the molecule. The triplet electronic state of the $N@C_{60}^{-1}$ should be seen on the ESR signal of the alkali doped sample and it should be well distinguishable from the lines of the neutral $N@C_{60}$. However, the ESR measurements which were done on thermally doped [6] and electro chemically doped [7] C_{60} did not show the sign of the change of the electronic structure of the nitrogen. The only change which could be detected was the decrease of the signal of the neutral $N@C_{60}$ which can be explained by the fact that the nitrogen can escape from the cage as the temperature is increasing.

So as to give a possible explanation of the contradiction between the results of the calculations and the experiments compare the energetics of charged C_{60} and $N@C_{60}$. The energies of the two systems were calculated with different ionic charges by means of ROHF method supposing always the highest possible multiplicity of the ground state and using Dunning's double zeta basis [8]. In both cases the energy can be well fitted by a parabola which fact can be explained by the spherical structure of the systems. Dropping the unimportant constant terms the two curves are shown by Fig. 2.

One can see that the charging of a $N@C_{60}$ requires always larger energy then the charging of an empty fullerene ball. In the experiments the alkali atoms were put by diffusion into the C_{60} sample containing small amount of $N@C_{60}$. Since the presence of alkali ions in the vicinity of the endohedral complex increase the energy of the system more then if they occupied the interstitial sites close to an empty ball the sites neighbouring to the $N@C_{60}$ remains empty in the AC_{60} phase and the molecule will be neutral. That is why we can not see the signal of the $N@C_{60}^{-1}$ in the ESR spectrum. At higher alkali concentration the statistical probability of the occupation of these sites could be estimated by means of the simple lattice gas model introduced by ref. [9] and it needs further investigations.

III CONCLUSIONS

As the result of ROHF and MCSCF calculations we have found that the ground state of the $N@C_{60}^{-1}$ molecule is triplet and the excess electron is localized on the

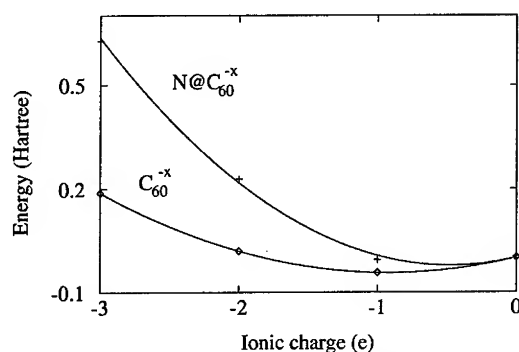


FIGURE 2. The energies of the multiply ionized C_{60} and $N@C_{60}$ as the function of the charge. The constant terms are subtracted from both curves.

nitrogen atom. The nitrogen atom is at the centre of the fullerene cage similarly to the neutral system. The calculation of the energies of the C_{60} and $N@C_{60}$ anions showed that the charging of the endohedral complex is energetically more expensive than the charging of the empty balls. As a consequence the vicinity of the $N@C_{60}$ is not occupied by the alkali ions and it remains neutral in the AC_{60} phase. This fact can explain the lack of the signal of the triplet nitrogen ion in the ESR spectrum.

This research was supported in part by the Hungarian National Research Fund (OTKA) under Grants No. T24137.

REFERENCES

1. Almeida Murphy, T. Pawlik, A. Weidinger, M. Höhne, R. Alcalá, J.M. Spaeth, *Phys. Rev. Lett.* **77**, 1075 (1996)
2. C. Knapp, K.-P. Dinse, B. Pietzak, M. Waiblinger, A. Weidinger, *Chem. Phys. Lett.* **272** (1997) 433-437
3. B. Pietzak, M. Waiblinger, T. Almeida Murphy, A. Weidinger, M. Höhne, E. Dietel, A. Hirsch, *Chem. Phys. Lett.* **279** (1997) 259-263
4. B. Pietzak, M. Waiblinger, T. Almeida Murphy, A. Weidinger, M. Höhne, E. Dietel, A. Hirsch, *Molecular Nanostructures*; eds H. Kuzmany, J. Fink, M. Mehring and S. Roth, (World Scientific, Singapore, 1998), 180-183
5. Gaussian Basis Sets for Molecular Calculations" S.Huzinaga, J.Andzelm, M.Klobukowski, E.Radzio-Andzelm, Y.Sakai, H.Tatewaki Elsevier, Amsterdam, 1984.
6. A. Weidinger, B. Pietzak, S. Pekker, L. Korecz, A. Jánosy, F. Simon, L. Forró, unpublished
7. K.-P. Dinse, private communication
8. T.H.Dunning, Jr., P.J.Hay Chapter 1 in "Methods of Electronic Structure Theory", H.F.Shaefer III, Ed. Plenum Press, N.Y. 1977, pp 1-27.
9. L. Udvardi, G. Szabó, *J. Phys. Condensed Matter* **8** 10959 (1996)

Structural and Magnetic Studies of the Endohedral Metallofullerene Ce@C₈₂

C. J. Nuttall, Y. Watanabe, Y. Inada, K. Nagai, T. Muro, D. H. Chi, T. Takenobu, Y. Iwasa[#] and K. Kikuchi[#]

JAIST, Ishikawa 923-1292, Japan.

[#]Department of Chemistry, Tokyo Metropolitan University, Tokyo 192-0397, Japan.

Abstract: Metal encapsulating fullerenes (endohedral metallofullerenes) are interesting because of their unusual structural properties and possibilities of exotic electronic properties. We report the structural and magnetic properties of the newly isolated endohedral metallofullerene compound Ce@C₈₂. The synchrotron X-ray powder profile, obtained after annealing Ce@C₈₂ in a dynamical vacuum, indexes on a P6₃/mmc cell [$a=11.1544$ Å, $c=18.2256$ Å] which equates to hexagonal close packing (hcp) of the roughly spherical C₈₂ cages. In contrast, the powder profile of sublimed Ce@C₈₂ contains dominantly face centred cubic close packing (fcc) [Fm-3m; $a=15.766$ Å]. Through comparisons of the obtained diffraction profiles with those simulated from structural models we are able to discern that the cerium atom lies approximately 1.8 Å from the centre of the C₈₂ cage. The hcp phase appears to be metastable, formed due close similarity to that of the solvent included structure [assuming isomorphology with La@C₈₂·CH₃C₆H₅]. We present a temperature dependant X-ray diffraction study of the hcp compound. The magnetic behaviour of hcp Ce@C₈₂ has also been investigated.

INTRODUCTION

The endohedral metallofullerene Ce@C₈₂ provides a fascinating case of a metal encapsulating fullerene: Not only is the location and behaviour of the endohedral cerium atom in question; but also the magnetic ground state of the compound is of interest, due to the possible co-existence of localized f-electrons on cerium and delocalized conduction bands within C₈₂. [cf. the case of La@C₈₂ which shows strong indications that charge transfer to [La]³⁺[C₈₂]⁺³ occurs].¹ Such a combination, of dilute localized electrons and conduction bands, is analogous to that in the Kondo effect.² Our research has thus been directed towards the synthesis and structural characterization of pure Ce@C₈₂ samples, wherein delocalization of the fullerene electrons is most likely to occur. Subsequently, we have performed a preliminary magnetic characterization of the compound.

SYNTHESIS

Bulk samples of Ce@C₈₂ containing soot were produced by the DC arc discharge of CeO₂ loaded carbon composite rods, under a partial He atmosphere (200 torr). The soot was then extracted *via* refluxing, firstly, in 1,2,4-trichlorobenzene and then in pyridine

solvents. Ce@C₈₂ was then isolated by HPLC² and characterised using TOF-Mass spectra and UV-vis-NIR absorption spectra. Diffraction quality samples of Ce@C₈₂ were prepared by the slow evaporation of Ce@C₈₂ solutions in CS₂ (or toluene) under anaerobic conditions; yielding crystals of solvent including Ce@C₈₂.CS₂ (or toluene), with predominantly, flat-plate, monoclinic morphology. The included solvent was then removed *via* drying under dynamical vacuum at 250°C. Vacuum sublimation of dried Ce@C₈₂ samples was carried out at 600°C.

DIFFRACTION

Room temperature X-ray powder profiles were collected on Ce@C₈₂ samples at the Photon Factory, KEK, on beam lines BL-1B and BL-6C. Figure 1(a) shows the observed profile for dried Ce@C₈₂ ($\lambda=1.6994$ Å). The profile is single phase and indexes on a hexagonal close packed cell (hcp), space group P6₃/mmc, yielding the refined lattice parameters $a=11.1544$ Å, $c=18.2256$ Å. Figures 1(b,c) show the comparison to simulated hcp Ce@C₈₂ X-ray profiles.³ Model Ce@C₈₂ structures were generated by approximating C₈₂ as a spherical carbon shell of radius 4.2 Å, with appropriately averaged density. An hcp array of C₈₂ is then generated by placing shells at the 2c symmetry positions within P6₃/mmc. Further, by placing the cerium atom at different locations within the C₈₂ shell we were able to conclude the best comparison with experimental data occurred with the cerium atom approximately 1.8 Å from the shell centre, at a site of general symmetry.

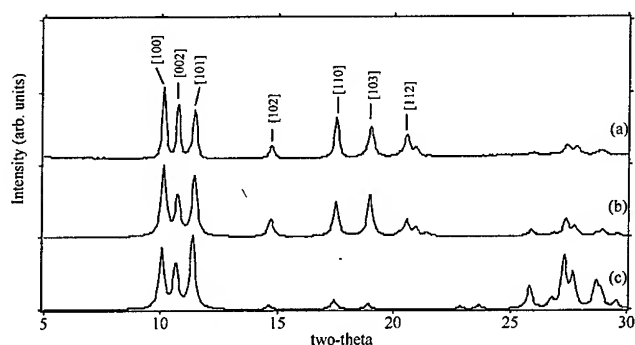


Figure 1: (a) Observed X-ray diffraction profile of dried Ce@C₈₂, indexing on P6₃/mmc; compared to simulated profiles of hcp Ce@C₈₂ with: (b) cerium atom at 1.8 Å from the shell center and (c) cerium atom at the center of the C₈₂ shell.

The X-ray profile obtained on sublimed Ce@C₈₂ was biphasic. The dominant phase indexed on a face centred close packed cell (fcc), space group Fm-3m, with refined lattice parameter $a=15.766$ Å. A minority hcp phase was apparent in the profile

as a few broad asymmetric reflections. These may result from stacking faulting within predominantly fcc crystallites.

Temperature dependant X-ray profiles were collected on the single phase hcp Ce@C₈₂ compound between 8.5K and 300K, on the BL-6C beam-line at the KEK. The refined cell parameters are plotted as a function of temperature in Figure 2. The sharp drop-off in the in-plane *a* lattice constant at around 150K is reminiscent of that seen in a similar study of the hcp phase of C₇₀.⁵ Over the temperature range studied, no evidence of a transition to lower symmetry was observed down to the lowest temperature studied, 8.5K. This is in contrast to the known lower C_{2v} symmetry of C₈₂ when compared to lattice symmetry. Three possibilities present themselves: (i) a rotational ordering of C₈₂ cages occurs but the change is not measurable at this resolution, (ii) C₈₂ maintains a locked-in disorder at low temperatures, (iii) a further possibility of locked-in disorder resulting from multiple C₈₂ isomers in each crystallite. Further experiments are now in progress in order to resolve these issues.

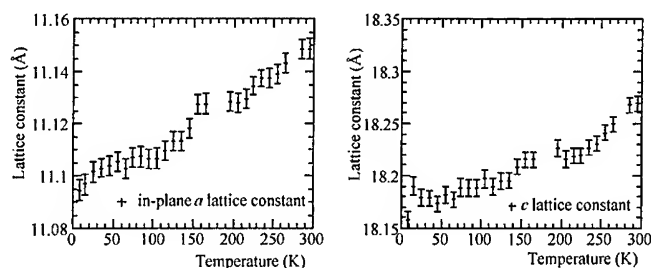


Figure 2: Plots of the refined lattice parameters of hcp Ce@C₈₂ as a function of temperature.

MAGNETISM

The magnetic behavior of hcp Ce@C₈₂ was investigated with a Quantum Design MPMS5 SQUID Magnetometer. The magnetic susceptibility ($\chi_{\text{mol}^{-1}}$) as a function of temperature (plotted in Figure 3(a)) displays paramagnetism down to 2K. The observed paramagnetic moment was mainly attributed to localised 4f-electrons on the endohedral cerium ion (this was inferred by comparison with susceptibility data collected on a sample of hcp La@C₈₂).⁶ The temperature dependence of the effective paramagnetic moment μ_{eff} is plotted in Figure 3(b). At 300K the effective moment, $\mu_{\text{eff}}(300\text{K}) = 2.3\mu_{\text{B}}$, is close to the free-ion value for Ce³⁺ (f^1 , $J=5/2$, $\mu_{\text{eff}} = 2.54\mu_{\text{B}}$); however, the effective moment decreases towards lower temperatures, reaching $\mu_{\text{eff}}(2\text{K}) = 1.0\mu_{\text{B}}$.

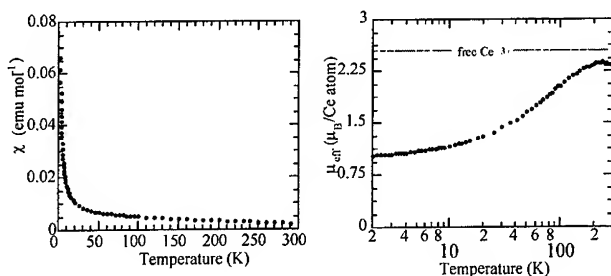


Figure 3: (a) Susceptibility ($\chi \text{ mol}^{-1}$) behaviour of Ce@C₈₂ vs. temperature and (b) Plot of μ_{eff} of Ce@C₈₂ vs. temperature.

DISCUSSIONS

We have prepared bulk quantities of Ce@C₈₂ and reported its structural properties for the first time. We found that we can prepare single phase hcp samples *via* solvent removal and dominantly fcc samples *via* sublimation. The observed crystal chemistry can be rationalised by considering the close similarity between the solvent included structure (e.g. the isomorphous La@C₈₂, toluene structure)⁴ and the hcp phase of Ce@C₈₂. It seems likely that the non-severe conditions of solvent removal facilitate the exclusive formation of a metastable hcp phase. Sublimation yields the thermodynamically favoured fcc phase; including hcp as impurity, possibly in the form of stacking faults.

We investigated the hcp Ce@C₈₂ phase further, finding that the cerium position seemed to be best described in an endohedral position some 1.8 Å from the C₈₂ cage center. Temperature dependent measurements on the phase revealed some evidence of a sharp drop-off in the *a* lattice parameter at around 150K; however, we observed no evidence of symmetry lowering, even at 2K.

Magnetic susceptibility measurements indicate paramagnetic behaviour down to 2K. The paramagnetic moment at 300K is approximately that for free-ion Ce³⁺ ($J=5/2$), indicating 3-electrons have been transferred to the C₈₂ cage. Towards lower temperatures the paramagnetic moment falls, monotonically reaching $1\mu_B$ at 2K. One tentative explanation for the loss of paramagnetic moment with temperature, lies in the disordered cerium ion position at high temperatures, becoming quenched upon cooling. This would result in an increase, in the crystal field within the compound. The ground-state for Ce³⁺ ($J=5/2$) is expected to be $|J_z|=1/2$ giving a $\mu_{\text{eff}}(0\text{K}) = 0.74\mu_B$, close to the observed value at 2K.

We note that the observed sharp drop-off in the *a* lattice parameter, below 150K, co-incides with the onset of the more gradual fall in the paramagnetic moment (μ_{eff}). This structural change most likely represents a freezing of fullerene motion, which may accompany an ordering of the cerium ion positions, which in turn is that required to precipitate the change in magnetic behaviour.

REFERENCES

- (1) Shinohara, H., *et al.*, J. Phys. Chem. **96** 3571-3573 (1992)
- (2) Kondo, J., Solid State Phys. **23** 184 (1969).
- (2) Kikuchi, K. *et al.*, Chem. Phys. Lett. **216**, 67 (1993).
- (3) Profiles were generated using the LAZY-PULVERIX program, Yvon, K.x
- (4) Takata, M., *et al.*, Nature, **377** 46-49 (1995).
- (5) Nakao, H., *et al.*, J. Phys. Soc. Jpn., **67** 12 pp.4117-4123 (1998).
- (6) Iwasa, Y., *et al.*, *unpublished results*.

Dynamic Motion of Ce@C₈₀ — Comparison Study with Ce@C₈₂ —

Wataru Sato, Keisuke Sueki, Koichi Kikuchi, Shinzo Suzuki, Yohji Achiba,
and Hiromichi Nakahara

Graduate School of Science, Tokyo Metropolitan University, Hachioji, Tokyo 192-0397, Japan

Yoshitaka Ohkubo

Research Reactor Institute, Kyoto University, Kumatori, Osaka 590-0494, Japan

Kichizo Asai

*Department of Applied Physics and Chemistry, The University of Electro-Communications, Chofu,
Tokyo 182-8585, Japan*

Fumitoshi Ambe

The Institute of Physical and Chemical Research (RIKEN), Wako, Saitama 351-0198, Japan

Abstract. Characterizable amount of La@C₈₀ was prepared by means of a two-stage HPLC purification of fullerene ingredients which were extracted from carbon soot in macroscopic quantity. In the same way as the investigation of Ce@C₈₂ and CeLa@C₈₀ in our previous work, molecular dynamic behavior of the newly purified species has been studied by means of time-differential perturbed angular correlation measurements. The data analyzed have shown that powder Ce@C₈₀ has somewhat slow rotational motion at room temperature compared with Ce@C₈₂ of the same form and the electric field gradient at the encaged Ce nucleus is almost equal to that at the corresponding atom of Ce@C₈₂.

INTRODUCTION

Physical and chemical properties of endohedral metallofullerenes have widely been investigated by means of various spectroscopic techniques (1) since the achievement of macroscopic production of those species (2). Molecular dynamics has particularly been focused on and the nature of the interaction between the molecules has gradually been unveiled.

Concerning dynamic behavior of endohedral fullerenes, we have already studied molecular and intramolecular motion of Ce@C₈₂ and CeLa@C₈₀, which are β^- decay products of La@C₈₂ and La₂@C₈₀, respectively, by means of time-differential perturbed angular correlation (TDPAC) measurements, and have reported the difference of the rotational motion between the molecules (3, 4). Our next interest was directed to what makes the difference of the mobility of the molecules in order to reach collective

CP486, *Electronic Properties of Novel Materials—Science and Technology of Molecular Nanostructures*,

edited by H. Kuzmany, J. Fink, M. Mehring, and S. Roth

© 1999 American Institute of Physics 1-56396-900-9/99/\$15.00

understanding on molecular interaction of metallofullerenes.

Ce@C₈₀ is considered to be an intermediary species between Ce@C₈₂ and CeLa@C₈₀ because of the cage size and the singly encapsulated atom. Expecting to obtain further information pertaining to the nature of molecular dynamics of monometallofullerene and/or endohedral C₈₀ fullerene, we applied the TDPAC method to a novel metallofullerene Ce@C₈₀ as a β^- decay product of La@C₈₀.

TDPAC METHOD

The angular correlations of successive γ rays emitted from an excited nucleus have a directional anisotropy, which is characteristic of individual nuclear disintegration. In case that there is a certain time interval between the cascade γ -ray emission and if there is some electric and/or magnetic interaction between the nucleus of interest and the extranuclear field, the angular correlation is perturbed depending on the strength of interaction and the reorientational correlation time, τ_c , of the principal axis of the electric field gradient (EFG) produced at the probe nucleus. Information about the physical and chemical surroundings of the probe nucleus can be obtained by observing the way of the perturbation.

Specifically speaking, for the present decay system, perturbation on the probe nucleus can be observed through the time variation of the directional anisotropy [$A_{22}G_{22}(t)$] of the 329-487 keV γ - γ cascade from excited Ce nuclei, whose 2083-keV intermediate level with its nuclear spin and parity of 4^+ has a half life of 3.45 ns, where A_{22} ($=-0.14$ for the present case) is the coefficient which is characteristic of the relevant cascade and $G_{22}(t)$ is the perturbation factor as a function of the time interval, t , between the cascade. For a series of the cerium-fullerene studies, especially in the investigation of solid-state molecular dynamics, we consider that the TDPAC method is one of the most powerful spectroscopies.

EXPERIMENT

A two-stage HPLC method was used to separate the La@C₈₀ fraction from the other fullerene ingredients extracted from the carbon soot generated by a dc arc discharge of lanthanum-carbon composite rods in 250 torr He atmosphere (5). After irradiating the purified sample with reactor neutrons at the neutron fluence rate of $1.0 \times 10^{14} \text{ cm}^{-2}\text{s}^{-1}$ for several hours, an HPLC purification was again performed to get rid of the impurities produced by hot atom effects and/or radiation effects. TDPAC measurements were performed for the powder sample at room temperature and 10 K on the 329-487 keV cascade γ rays from the ^{140}Ce nucleus with a conventional four-detector system (6). The directional anisotropy is defined by $A_{22}G_{22}(t) = 2[N(\pi, t) - N(\pi/2, t)]/[N(\pi, t) + 2N(\pi/2, t)]$, where $N(\theta, t)$ is the number of coincident events observed at angle θ .

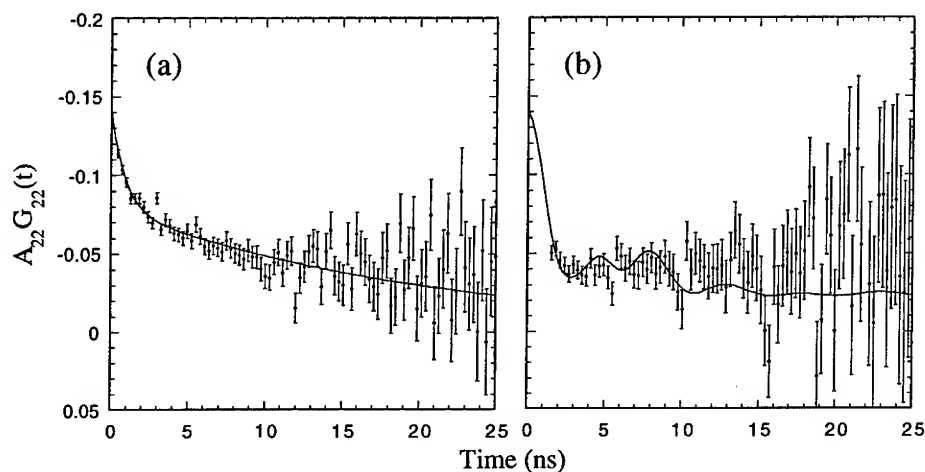


FIGURE 1. Time variation of TDPACs of ^{140}Ce in powder Ce@C_{80} at (a) room temperature and (b) 10 K.

RESULTS AND DISCUSSION

The TDPACs measured at room temperature and 10 K are shown in Figure 1. The directional anisotropy at room temperature indicates gradual relaxation, which is a typical behavior for the case that the principal axis of the EFG at the probe Ce nucleus is dynamically perturbed by the extranuclear field. On the other hand, there is an oscillatory structure in the TDPAC at 10 K indicating static perturbation on the nucleus by an electric quadrupole interaction between the EFG and the nuclear quadrupole moment of the probe nucleus. In a similar way to our previous work (3, 4), two-component analyses were performed for the TDPACs at room temperature and 10 K with the respective equations below:

$$A_{22}G_{22}(t) = -0.14[P \exp(-\lambda_1 t) + (1 - P) \exp(-\lambda_2 t)], \quad (1)$$

and

$$A_{22}G_{22}(t) = -0.14[PG_{22}^{\text{static}}(t)_{\delta\omega_Q} + (1 - P) \exp(-\lambda_2 t)]. \quad (2)$$

Here, P is the fraction of the first component, λ is the relaxation constant proportional to the reorientational correlation time, and the subscripts 1 and 2 represent the first and second components, respectively. Detailed description on the equations appears in reference (4).

The τ_c value for the first component ($=0.91 \pm 0.10$ ns) estimated by the least-squares fit shows that Ce@C_{80} has slow rotational motion at room temperature compared

with Ce@C₈₂ (3). The absolute value of the EFG, $|V_{zz}|$ ($= (1.4 \pm 0.1) \times 10^{23}$ V m⁻²), which is deduced by the value of the nuclear quadrupole frequency, ω_Q , obtained by the fit, is almost equal to that of Ce@C₈₂ (3). From the comparable values of the optimized parameters and similar behavior of TDPACs, it can be inferred that Ce@C₈₀ molecules have thermal molecular motion at room temperature, whereas the motion freezes at 10 K.

CONCLUSION

It has been found from the optimized value of $|V_{zz}|$ that Ce atom encaged in C₈₀ is in a similar electronic surroundings to Ce atom in C₈₂ cage. Accordingly, the valence state of the atom is regarded as trivalent.

Two different components have been observed in each TDPAC taken at room temperature and 10 K. The reorientational correlation time of the principal axis of the EFG at room temperature, which is several times as large as that of Ce@C₈₂, is considered to directly reflect the time scale of the molecular motion at that temperature, although temperature dependence of TDPACs needs to be examined so as to check the plausibility of the interpretation of the molecular motion.

ACKNOWLEDGMENTS

The authors are grateful to Professor Y. Kawase and Dr. S. Uehara for their arrangement for the experiment. The present work was accomplished as part of the Inter-University Program for the Common Use of JAERI (Japan Atomic Energy Research Institute) Facilities and of Visiting Researcher's Program of the Kyoto University Research Reactor Institute (KURRI). This work was partly supported by a grant from the Ministry of Education, Culture, Sports, and Science of Japan.

REFERENCES

1. For example; Takata, M., Nishibori, E., Umeda, B., Sakata, M., Yamamoto, E., and Shinohara, H., Phys. Rev. Lett. **78**, 3330-3333 (1997).
2. Krätschmer, W., Lamb, L. D., Fostiropoulos, K., and Huffman, D. R., Nature (London) **347**, 354-358 (1990).
3. Sato, W., Sueki, K., Kikuchi, K., Kobayashi, K., Suzuki, S., Achiba, Y., Nakahara, H., Ohkubo, Y., Ambe, F., and Asai, K., Phys. Rev. Lett. **80**, 133-136 (1998).
4. Sato, W., Sueki, K., Kikuchi, K., Suzuki, S., Achiba, Y., Nakahara, H., Ohkubo, Y., Asai, K., and Ambe, F., Phys. Rev. B **58**, 10850-10856 (1998).
5. Sato, W. *et al*, to be submitted for publication.
6. Ohkubo, Y., Kobayashi, Y., Asai, K., Okada, T., Ambe, F., Phys. Rev. B **47**, 11954-11961 (1993).

Structural Phase Transitions of Endohedral Metallofullerene La@C₈₂ Studied by Single Crystal X-ray Diffraction

T. Watanuki¹, A. Fujiwara¹, K. Ishii¹, Y. Matsuoka¹, H. Suematsu¹,
K. Ohwada², H. Nakao², Y. Fujii²,
T. Kodama³, K. Kikuchi³, and Y. Achiba³

¹*Department of Physics, The University of Tokyo, Hongo, Bunkyo-ku, Tokyo 113-0033, Japan.*

²*Institute for Solid State Physics, The University of Tokyo, Roppongi, Minato-ku, Tokyo 106-8666, Japan.*

³*Department of Chemistry, Tokyo Metropolitan University, Hachioji, Tokyo 192-0397, Japan.*

Abstract. Recently we have succeeded to synthesize solvent-free single crystals of endohedral metallofullerene La@C₈₂ with the size of 0.5x0.2x0.2mm³ for the first time. We have investigated the low temperature (T) x-ray diffraction measurements (20K-300K), and have revealed that the solvent-free La@C₈₂ crystal takes various structured phases, that is, (I) the face-centered cubic (fcc) phase (300K-180K), (II) the rhombohedral phase (180K-140K), (III) the triclinic phase (140K-20K) and (IV) the simple cubic (sc) phase (132K-20K). The rhombohedral and triclinic phases are characterized by the C₈₂-cage orientational order, and the sc phase is characterized by the molecular electric dipole order, and in the fcc phase both are not in order. As for the two lowest-T phases, with slow cooling below 132K, the crystal remains in the triclinic phase. On the other hand with rapid cooling, the crystal undergoes the phase transition to the sc phase at 115K. Once the phase transition occurs, the sc phase is stable up to 132K, and the sc phase with rapid cooling is more stable than the triclinic phase, contrary to the usual cases. We also revealed that the triclinic phase turns to the sc phase by x-ray irradiation.

INTRODUCTION

The structural feature of the endohedral metallofullerene crystal is attracting much attention, because the metallofullerene has a large molecular electric dipole moment [1] and it should play an important role in contrast to the "empty" fullerene crystals. Actually our previous results of powder x-ray diffraction study showed that the solvent-free crystal of La@C₈₂ has the fcc lattice structure ($a_0=15.78 \text{ \AA}$) at room temperature (T), and the molecules tend to take an orientation that the long axes of the Rugby-ball shaped C₈₂-cage face away each other and simultaneously minimizing the electrostatic interaction between the electric dipoles of the La@C₈₂ molecule, and turn their direction between the

CP486, *Electronic Properties of Novel Materials— Science and Technology of Molecular Nanostructures*,

edited by H. Kuzmany, J. Fink, M. Mehring, and S. Roth

© 1999 American Institute of Physics 1-56396-900-9/99/\$15.00

preferable orientations with jumping motion [2]. We also observed that the lattice shrinks steeply in the T-region of 180K-80K, however no other significant change is observed. So we prepared the solvent-free single crystals of La@C_{82} which enable us to obtain the high resolution data. We also established the method to synthesize the single crystal from a small amount of the powder sample. In this paper, we will report the successive structural phase transition of the solvent-free La@C_{82} crystal.

EXPERIMENTAL

Solvent-free single crystals of La@C_{82} were synthesized by the sublimation method in the following way. First, we isolated the high purity samples from other fullerenes, metallofullerenes and isomers by three-step HPLC technique. We put the dried powder sample of the amount of 0.2mg into a quartz glass tube of 2mm in a diameter, and baked the powder sample in a vacuum ($<1 \times 10^{-6}$ torr) to remove almost all the solvent. Then, we sealed the tube in a vacuum of 3×10^{-7} torr and heated it up to 600°C at the powder sample side and to 580°C at the other empty side. After three weeks, we obtained the single crystals of the largest size of $0.5 \times 0.2 \times 0.2 \text{ mm}^3$ at the lower temperature side (Fig.1).

Low temperature x-ray diffraction experiments (20K-300K) were carried out both at the synchrotron radiation source of Photon Factory (BL6C₁ and BL1B), KEK, Tsukuba ($\lambda=1.1 \text{ \AA}$) and at the ISSP rotating-anode source ($\text{CuK}\alpha$). We used a scintillation counter and an imaging plate for detection.

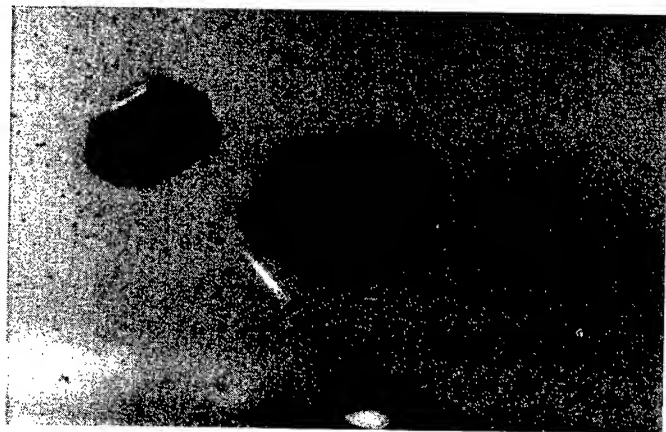


Figure 1. Solvent-free single crystal of La@C_{82}

RESULTS AND DISCUSSION

Figure 2. shows the temperature (T) dependence of the peak intensity of the 022 reflection. All Bragg reflections behave as the same way. We observed an anomaly at 180K. Above 180K, the crystal takes the fcc structure as shown in the rotation photograph (Fig.3a). Below 180K, the peak intensity steeply decreases with T decreasing, and simultaneously we observed the peaks broadening in the tangential direction of the reciprocal space and also splitting in the radial direction (Fig.3b), which means the crystal is divided into the micro-domains. From the splitting width of each reflection, the crystal structure is determined as the rhombohedral structure. And below 150K, furthermore splitting was detected with the high resolution experiment, which means the crystal takes the triclinic structure. We observed two series below 132K. With the slow cooling from 132K to 110K, the crystal remains in the triclinic structure to the lowest-T (20K). On the other hand, with the rapid cooling, the peak intensity jumps up at 115K to the same level as in the fcc phase, and the crystal returns to the single domain, even though once the crystal was divided into the micro-domains. The diffraction pattern is similar to the fcc phase, but we observed the super lattices indicating the sc structure (Fig.3c). This phase transition is accompanied by the large hysteresis, and once turning to the sc phase, the sc phase is stable up to 132K. Such cooling rate dependence appears only in that T-region (132K-110K). In another T-region or in the heating process, the structural feature depends only on T and the above processes are reversible. With respect to the two phase below 132K, we can conclude that the sc phase with rapid cooling is more stable than triclinic phase with slow cooling, contrary to the usual cases, because the triclinic phase can turn to the sc phase as mentioned above, on the other hand, the inverse process cannot occur.

As for the molecular orientation, in the rhombohedral phase, judging from the lattice has a uniaxial type symmetry, we think that the order of the C_{82} -cage long axes occurs and the molecular motion is restricted around its long axis. And also we think that, in the triclinic phase, the order of the C_{82} -cage short axes also occurs and the molecular rotational motion is frozen. In the sc phase, we concluded that the order of the molecular electric dipoles occurs, which is shown by the analysis of the super lattice intensity.

We also revealed the x-ray induced structural phase transition, that is, by the synchrotron x-ray irradiation with the flux of 8×10^{10} photons/mm²s ($\lambda = 1.1 \text{ \AA}$), the triclinic phase gradually turns to the sc phase which is completed about three hours.

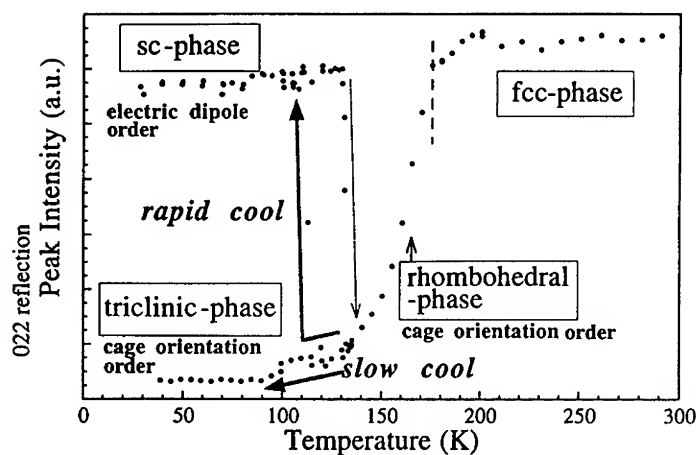


Figure 2. Temperature dependence of the peak intensity of 022 reflection. All Bragg reflections behave in the same way.

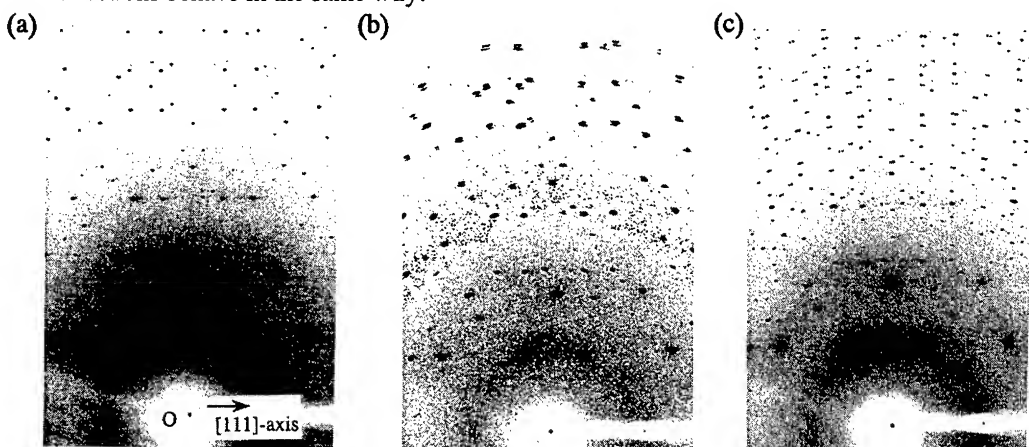


Figure 3. Rotation photograph of the La@C₈₂ single crystal around [111]-axis. (a) the fcc-phase at 300K (b) the triclinic-phase at 135K (c) the simple cubic phase at 100K

ACKNOWLEDGMENTS

This work was supported by "Research for the Future" of Japan Society for the Promotion of Science (JSPS), Japan.

REFERENCES

1. Fuchs, D. et al., Fullerenes and Fullerene Nanostructures, edited by Kuzumany, H et al., (World Scientific, Singapore, 1996) p. 186
2. Watanuki, T. et al., Photon Factory Activity Report 14 (1996) 403

Endohedral rare earth fullerenes — Electronic and dynamic properties

K. Vietze*, G. Seifert†, M. Richter‡, L. Dunsch¶, M. Krause¶

*Max-Planck-Institut für Physik komplexer Systeme, D-01187 Dresden, Germany

†Theoretische Physik, Universität GH Paderborn, D-330998 Paderborn, Germany

‡Institut für Theoretische Physik, TU Dresden, D-01069 Dresden, Germany

¶Institut für Festkörper- und Werkstofforschung, D-01069 Dresden, Germany

Abstract. Experimental studies of endohedral rare earth fullerenes indicate variations of the valence states of the rare earth atoms in these systems and the stabilization of certain fullerene cages, as e.g. in $\text{La}_2\text{@C}_{80}$ or Eu@C_{74} .

Using a semirelativistic Density Functional based Tight Binding formalism (DF-TB) the valence states of rare earth metals in various fullerene cages (e.g. C_{74} , C_{80} , C_{82} , C_{84}) as endohedral complexes were examined in comparison to experimental investigations. The rare earth atoms in a fullerene cage seem to be mostly in a trivalent state. Some elements like Sm and Tm are to be considered borderline cases since they may change their valence state via a $5d \rightarrow 4f$ promotion.

Molecular dynamics simulations indicate a rather high mobility of the rare earth atom(s) in certain endohedrals due to the relatively weak coupling to the cage.

INTRODUCTION

The recent success in the synthesis, extraction and characterization of rare earth endohedral fullerenes has lead to a number of questions to be investigated for a proper understanding of these compounds, as regards growth mechanisms, stabilities, chemical properties for example.

Of special interest is of course the question for the behaviour of the $4f$ -electron systems of the rare earth metals. The strongly localized $4f$ electron subsystem keeps localized in compounds, but its configuration may change, thus changing the effective valency of the endohedral rare earth atom. This valency will essentially affect the properties of the fullerene isomers, like e.g. ground state geometries, cage stabilizations and distortions, chemical reactivity etc. Thus, the valence state of the lanthanides in compounds, trivalent $[\text{Xe}]4f^n5d^16s^2$ or divalent $[\text{Xe}]4f^{n+1}6s^2$, and possible transitions are some of the key questions in this field.

The method applied in the calculations is a non-orthogonal density-functional-based tight-binding scheme (DF-TB) [1,2]. In contrast to other tight-binding

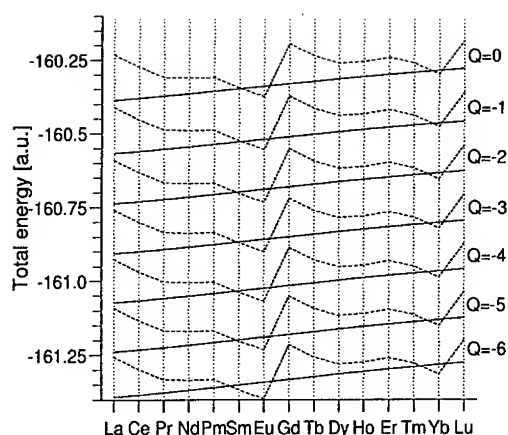


FIGURE 1. Energies of rare earth metals in endohedral RE@C₈₂ for trivalent (solid line) and divalent (dashed line) configurations of the rare earth atoms. Q denotes the total charge of the whole system.

models the Hamiltonian and overlap matrix elements are calculated from first principles. In order to describe the lanthanide atoms properly a scalar-relativistic extension has been used [3].

VALENCE STATES OF RE METALS IN C₈₂

While most of the Lanthanides have a divalent atomic ground state $[\text{Xe}]4f^{n+1}6s^2$ (La, Ce, Gd and Lu are trivalent $[\text{Xe}]4f^n5d^16s^2$, $n=0$ for La), their state in the bulk metal is trivalent except for Eu and Yb. An additional exception is Cerium which is known to occur in a tetravalent configuration ($[\text{Xe}]4f^05d^26s^2$) as well.

To investigate the influence of the enclosing cage on the valence state of the lanthanide atoms various fullerene cages were considered, e.g. C₇₂, C₇₄, C₈₀ and C₈₂. Generally, the 5d-states of the lanthanides form delocalized states with the molecular orbitals of the fullerene cage. Consequently the interaction is not completely ionic but contains a considerable amount of covalent contributions. Also common to all considered systems is the location of the endohedral rare earth atom above a hexagon-hexagon adjacency of the fullerene cage.

The systematic increase of the energy with ascending nuclear charge of the lanthanides in the trivalent case is just the effect of subsequently filling the 4f electron shell (fig. 1). In the divalent case there is not this monotonic behaviour, reflecting the high complexity of the 4f electron subsystem. In the cases of Eu and Yb the HUNDT's rule on maximizing the spin favours a divalent state. Some other elements like Samarium or especially Thulium are considered to be borderline cases since the energetic differences between di- and trivalent states are rather small,

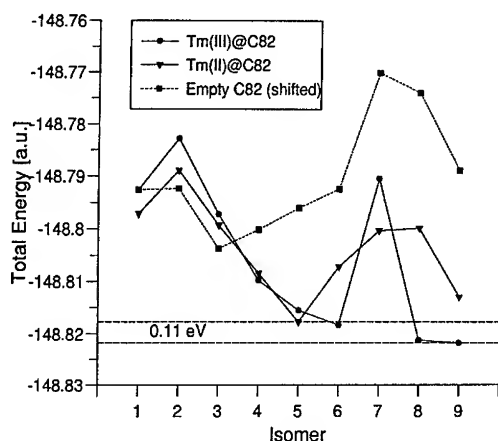


FIGURE 2. Energies of endohedral Thulium in 9 different isomers of C_{82} . III refers to a trivalent atomic configuration $[Xe]4f^{12}5d^16s^2$ of the Thulium atom, II denotes the divalent configuration $[Xe]4f^{13}6s^2$.

so they may change their valence state via a $d \rightarrow f$ promotion according to the environmental conditions like the total cage charge or the cage isomery.

The influence of the cage isomery is shown in fig. 2 for $Tm@C_{82}$ as an example. The total energy of $Tm@C_{82}$ was calculated for trivalent as well as divalent configurations of the Thulium atom in every of the nine IPR isomers of C_{82} . The calculated energy difference between the most stable isomer configurations is only about 0.11eV in favour of the trivalent configuration. I.e., due to this small energy difference the existence of $Tm@C_{82}$ with a divalent Tm, as reported recently [4], cannot be excluded.

Eu@C₇₄

The empty C_{74} fullerene cage (D_{3h} symmetry) has a very small electronic HOMO-LUMO gap indicating a low stability. Indeed the (empty) fullerene could not be isolated yet. On the other hand the isolation of endohedral $Eu@C_{74}$ has been reported recently [5].

As a result of the calculations for the ground state geometry of $Eu@C_{74}$ a C_{2v} configuration was found to be energetically most favourable, where the Eu atom is located above a bonding bridge between two adjacent hexagons. This molecular geometry implies three isoenergetic configurations, i.e. there are three almost equivalent minima on the potential energy surface (PES, fig. 3). The energetic difference between a position at a minimum and the center position is about 2eV, which is large enough to keep the Europium atom off-center.

To study the mobility of the Europium atom in the cage molecular dynamics

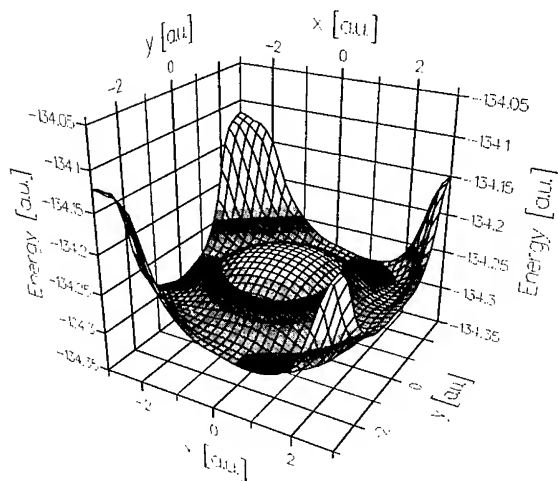


FIGURE 3. Potential energy surface of the Europium atom in endohedral Eu@C₇₄ within the σ_h plane of C₇₄ (D_{3h}).

simulations were performed. Although the PES suggests a possible rotation of the Eu atom in the cage cycling through the three minima the calculations have shown that the Eu atom will be trapped in one minimum, i.e. no rotation occurs.

Nonetheless the Europium atom has a rather high mobility within the cage, showing a strong oscillation around its equilibrium position. Due to this large amplitude oscillations, the harmonic oscillator approximation for the interpretation of molecular spectra is not longer valid. Hence, due to this 'dynamical' symmetry breaking the experimentally obtained spectra may look like there is only low symmetry (C_s) or no symmetry at all (C_1), although the equilibrium geometry should be of higher symmetry (C_{2v}).

REFERENCES

1. G. Seifert, H. Eschrig and W. Bieger
Z. phys. Chemie **267**, 529 (1986)
2. D. Porezag, Th. Frauenheim, Th. Köhler, G. Seifert and R. Kaschner
Phys. Rev. B **51**, 12947 (1995)
3. K. Vietze, M. Richter and G. Seifert
to be published
4. M. Krause, P. Kuran, U. Kirbach and L. Dunsch
Carbon (1998) in press
5. P. Kuran, M. Krause, A. Bartl and L. Dunsch
Chem. Phys. Lett. **292**, 580–586 (1998)

The electronic structure of mono- and dimetallofullerenes by photoemission spectroscopy

T. Pichler¹, M. S. Golden¹, P. Kuran¹, L. Dunsch¹, M. Knupfer¹, J. Fink¹, M.R.C. Hunt², P. Rudolf², M. Inakuma³, H. Shinohara³

¹ *Institut für Festkörper- und Werkstofforschung Dresden, Postfach 270016, D-01171 Dresden.*

² *LISE-FUNDP, Rue de Bruzelles 61, B-5000 Namur, Belgium.*

³ *Department of Chemistry, Nagoya University, Nagoya 464-01, Japan.*

Abstract.

In this contribution we compare the electronic structure of selected mono- and dimetallofullerenes from the viewpoint of high-energy spectroscopy. Particular emphasis will be placed upon the valency of the encapsulated metal ion or ions.

INTRODUCTION

The ability of fullerene molecules to encapsulate one or more metal ions inside their carbon cage has captured the imagination of many researchers. These so-called metallofullerenes represent a truly novel type of matter, which is expected to display remarkable electronic and structural properties in comparison to the empty fullerene cages [1]. Of great importance for the electronic properties is the amount of charge transfer between the metal ions and the fullerene cage. Therefore it is crucial to proof the valency of the encaged metal ions in the metallofullerenes beyond any doubt.

In this contribution, we give an overview what we can learn about the valency of encaged metal ions in selected mono- as well as dimetallofullerenes by high-energy spectroscopy. We will especially show to what extent ultraviolet photoemission spectroscopy (UPS) as well as x-ray photoemission spectroscopy (XPS) can be used as probes to answer this question.

EXPERIMENTAL

The preparation and separation of three different isomers of Tm@C₈₂ [2] and Sc₂@C₈₄ [3–5] has been described previously. After purification by multi-cycle chromatography the metallofullerene sample was filled into an alumina crucible and degassed in the effusion cell in ultra high vacuum (UHV) at 160° C for 48 hours and at 500° C for 30 min. For the photoemission and x-ray absorption experiments, thin films of a thickness of about 200 Å of the D_{2d} isomer of Sc₂@C₈₄ were prepared

by sublimation at 680° C onto freshly evaporated gold films in UHV . The samples were then transferred under UHV conditions into the measuring chamber. The PES experiments were carried out using a hemispherical electron analyser, together with a noble gas discharge lamp providing He I (He II) radiation (21.22 eV (40.8 eV), overall resolution 100 meV) or an x-ray source providing monochromatised Al K α radiation (1486.6 eV, overall resolution 350 meV).

RESULTS AND DISCUSSION

A comparison of the valence band photoemission spectra of three different metallofullerenes and their empty host cages C₈₂ and C₈₄ is depicted in Fig. 1. For the used photon energies ($h\nu = 21.22\text{eV}$) the photoemission spectra are dominated by the carbon $\pi + \sigma$ molecular orbitals (MOs) of the charged fullerene cage. The transport properties of the fullerenes are determined by the π -molecular orbitals (MOs) of the carbon cage (up to about 5 eV BE).

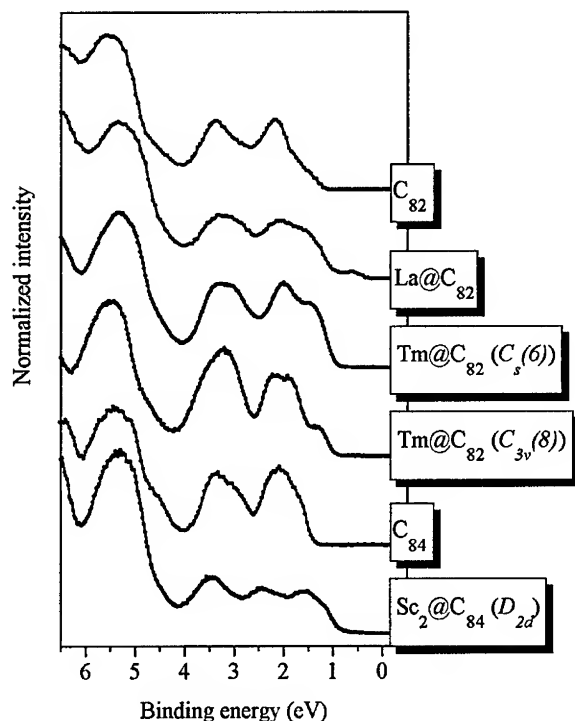


FIGURE 1. Valence band photoemission spectra of C₈₂ (Ref. [8]), La@C₈₂ (Ref. [8]), two isomers of Tm@C₈₂, C₈₄ (Ref. [6]) and Sc₂@C₈₄.

All pristine fullerenes and metallofullerenes shown in Fig. 1 are semiconductors. The onset of the highest occupied molecular orbital (HOMO) is about 1.15 eV,

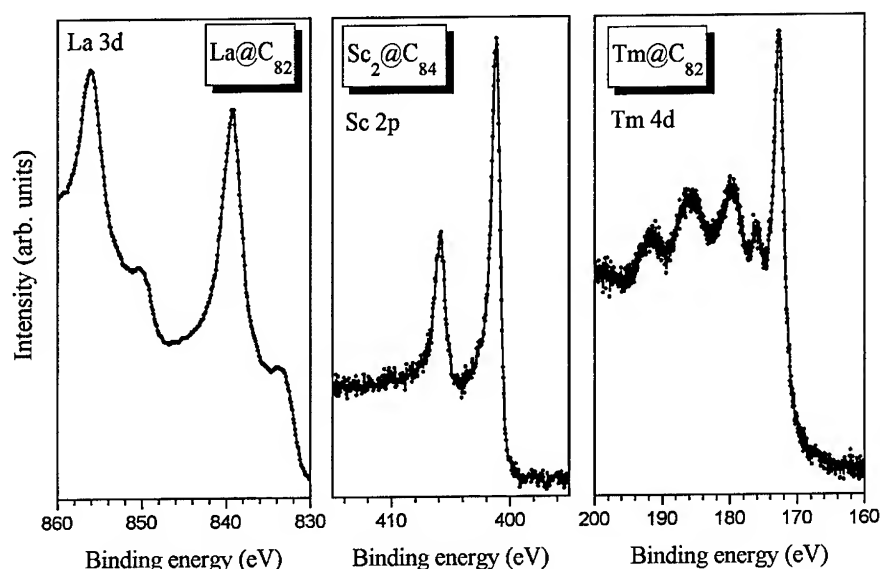


FIGURE 2. XPS photoemission spectrum using monochromatic AlK_{α} radiation of the La 3d levels of La@C₈₂ (Ref. [8]), the Sc 2p levels of Sc₂@C₈₄ and of the Tm 4d levels of Tm@C₈₂.

0.25 eV, 1 eV, 0.9 eV, 1.3 eV, and 1 eV for C₈₂, La@C₈₂, Tm@C₈₂ (with $C_s(6)$ symmetry), Tm@C₈₂ (with $C_{3v}(8)$ symmetry), C₈₄ and Sc₂@C₈₄ (with D_{2d} symmetry), respectively. The observation of an additional structure at low energy in La@C₈₂ is in contrast to the other two metallofullerenes and is a first hint for an open shell configuration with an odd charge transfer to the fullerene cage as predicted by calculations [10]. The observed onset of the HOMO in Tm@C₈₂ as well as in Sc₂@C₈₄ may be explained with a closed shell configuration and a charge transfer of an even number of electrons to the carbon cage. For Sc₂@C₈₄ this result is consistent with the theoretically predicted [10] charge transfer of four electrons, but no proof. In Fig. 2 characteristic XPS lines of encaged metal ions are shown for La@C₈₂, Sc₂@C₈₄ and Tm@C₈₂. This method has been shown to be a suitable indirect probe of the valency of the La in La@C₈₂ [7,8]. In this case, the comparison of the La 3d core level spectrum with those of various La trihalides showed that the La is trivalent, with the (C₈₂)³⁻ providing an environment slightly less electronegative than that in LaBr₃ [8]. In the same way first XPS experiments of the Sc 2p lines on air exposed samples of films of Sc₂@C₈₄ with D_{2d} symmetry were interpreted by a Sc valency between Sc₂O₃ and Sc metal [9]. However the core level shift could also be most likely assigned to a different screening of the core hole. Therefore from those results no values for the effective charge distribution could be extracted and additional experiments using 'fingerprint'-features in the system under investigation had to be performed. For the system La@C₈₂ from the difference in the relative photoionization cross sections of La 5d and C 2p in XPS and UPS it was concluded that there is essentially no contribution of La 5d orbitals

to the valence band at low binding energy [8]. Further experiments using resonant photoemission across the La 3d threshold clearly showed a resonance enhancement of features at low binding energy corresponding to La 5d states pointing out the existence of some hybridisation between La and fullerene derived states [11]. A simple charge transfer model can therefore not be applied for this monometallofullerene as about 1/3 of the electronic charge of the La 5d orbital is localized at the La atom [11]. In the case of the other analysed lanthanide monometallofullerene Tm@C₈₂ valence band high energy spectroscopy clearly showed that the encaged Tm is divalent. Although the Tm 4d XPS lines shown in Fig. 2 lead to a very complicated multiplet structure due to a strong interaction between the 4d and 4f electrons the valency can be probed [12]. A direct proof of a formal Tm²⁺@C₈₂²⁻ charge distribution was found using the characteristic 4f multiplets of the encaged rare earth as a fingerprint of the Tm valency [12].

In summary, we have shown the ability of valence band UPS to get a first hint about the valency of encaged metal ions. However a definite proof from valence band photoemission alone is not possible in most of the cases. XPS has also been shown to give an estimate for the valency of encaged metal ions. A direct proof for the valency by this method is however only possible if strongly localized states are involved that have a characteristic multiplet splitting which can be used as a fingerprint [12]. Otherwise additional methods like x-ray absorption spectroscopy (e.g Tm@C₈₂ [12] or Sc₂@C₈₄ [13]) or resonant photoemission [11] have to be used to get additional information.

We thank the European Union for funding within the TMR Research Network 'FULPROP' (ERBFMRXCRT-970155).

REFERENCES

1. D.S. Bethune et al., Nature(London) **366**, 123 (1993).
2. U. Kirbach, and L. Dunsch, Angew. Chem. Int. Ed. Engl. **35**, 2380 (1996).
3. H. Shinohara et al., J. Phys. Chem. **97**, 500 (1993).
4. H. Shinohara et al., J. Am. Chem. Soc. **97** 4259 (1993).
5. E. Yamamoto et al., J. Am. Chem. Soc. **118** 2293 (1996).
6. J.F. Armbruster et al., Phys. Rev. **B 50**, 4933 (1994).
7. J.H. Weaver et al., Chem. Phys. Lett. **190**, 460 (1992).
8. D.M. Poirier et al., Phys. Rev. **B 49**, 17403 (1994).
9. T. Takahashi et al., Phys. Rev. **B 52**, 13812 (1995).
10. K. Laasonen, W. Andreoni, M. Parinello, Science **258**, 1916 (1992); S. Nagase and K. Kobayasi, Chem. Phys. Lett. **214**, 57 (1993); S. Nagase and K. Kobayasi, Chem. Phys. Lett. **231**, 319 (1994).
11. B. Kessler et al., Phys. Rev. Lett. **79**, 2289 (1997).
12. T. Pichler et al., Phys. Rev. Lett. **79**, 3026 (1997).
13. T. Pichler et al. unpublished.

A Raman study of empty C_{84} isomers D_2 and D_{2d} and three isomers of $Sc_2@C_{84}$

M. Krause¹, M. Hulman¹, H. Kuzmany¹, T.J.S. Dennis², M. Inakuma³, H. Shinohara³

¹ Institut für Materialphysik, Universität Wien, Strudlhofgasse 4, A-1090 Wien, Austria

² Hahn-Meitner Institut, Glienickerstr. 100, D-14109 Berlin, Germany

³ Department of Chemistry, Nagoya University, Nagoya 464-01, Japan

Abstract: The room temperature Raman spectra of the C_{84} isomers 22: D_2 and 23: D_{2d} are shown to resemble a downshifted and split C_{60} spectrum in the range of the radial cage modes below 450 cm^{-1} . Additional Raman lines with a basically similar structure were found for three isomers of $Sc_2@C_{84}$ (C_s , C_{2v} and D_{2d}) below 200 and at 260 cm^{-1} and attributed to (Sc- C_{84})-vibrations. These modes are further specified with respect to their normal coordinates. Factor group splitting in the solid state of the $Sc_2@C_{84}$ D_{2d} isomer explains for the larger number of (Sc- C_{84})-vibrations as found for the other isomers.

INTRODUCTION

The isolation of two C_{84} isomers (22: D_2 and 23: D_{2d}) and three isomers of $Sc_2@C_{84}$ (10: C_s , 17: C_{2v} and 23: D_{2d}) offered the opportunity to study the vibrational structure of two endohedral metal ions in one fullerene cage for the first time (1, 2). In this paper we discuss the Raman spectra of these compounds with particular emphasis on the frequency range below 450 cm^{-1} . We assign (Sc- C_{84}) and pure C_{84} vibrations and distinguish the (Sc- C_{84}) modes with respect to their estimated normal coordinates. The unexpected high number of (Sc- C_{84}) modes for the D_{2d} isomer is explained by solid state effects on the molecular spectrum.

EXPERIMENTAL

Isomer pure C_{84} was prepared by arc burning of graphite electrodes in a He stream, extracted in a soxhlet by CS_2 and isolated by recycling HPLC using a Cosmosil 5PYE column (1). For the production of the $Sc_2@C_{84}$ isomers a composite of Sc_2O_3 , graphite powder and a high-strength pitch stuffed within cavities of the graphite rods was used for the arc burning process. The resulting fullerene soot was soxhlet extracted under totally anaerobic conditions by CS_2 . The isolation of $Sc_2@C_{84}$ was performed by multistage HPLC using two complementary types of columns (2). The final purity of the samples was 99.9% relative to other fullerenes.

The fullerenes were dissolved in toluene, dropped on gold coated silicon substrates, dried to polycrystalline films under ambient conditions and heated in high

vacuum at 525 K for 4 hours. The probes were placed in a cryostat under a high vacuum better than 10^{-6} mbar. Raman spectra were excited with 514 nm radiation of an argon ion laser model 2020-04 (Spectra-Physics, USA) and the 647 nm line of a krypton ion laser CR-500K (Coherent, USA) using a line focus of 0.5×3.0 mm². A prism premonochromator and interference filters were applied to eliminate laser plasma line radiation. Scattered Raman radiation was analysed in a 180° geometry by a triple spectrometer XY 500 (Dilor, France) with a spectral resolution of 3.0 cm⁻¹.

RESULTS AND DISCUSSION

A vibrational structure resembling a downshifted and split C_{60} spectrum was found for both empty C_{84} isomers. Strong Raman bands are grouped around 220, 350 and 420 cm⁻¹ (Fig. 1 and Tab. 1). The centre of gravity of these bands is shifted by a factor of 0.81, 0.81 and 0.85 with respect to the $H_g(1)$, $H_g(2)$ and $A_g(1)$ modes of C_{60} . A correlation between the cage mass and the frequencies from fullerene modes of similar origin seems to be fairly justified by this result.

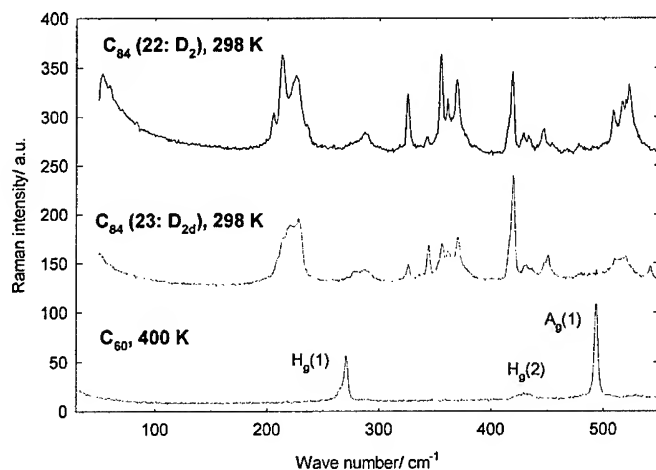


Figure 1: Low frequency Raman spectra of C_{84} (22: D_2), C_{84} (23: D_{2d}) and C_{60} , 514 nm excitation, laser power 3.0 mW for C_{84} and 1.0 mW for C_{60}

The number of pure C_{84} cage modes is preserved in the Raman spectra of the three $Sc_2@C_{84}$ isomers (Fig. 2,3 and Tab. 1). Additional modes were detected around 80, 100, 165 (very weak) and 260 cm⁻¹ for all $Sc_2@C_{84}$ isomers. Their relative intensities depend strongly on the specific cage isomer. The three lower energetic modes have

counterparts in the infrared spectrum (3). Two more Raman lines at 92 and 137 cm^{-1} were found for the isomer 23 only.

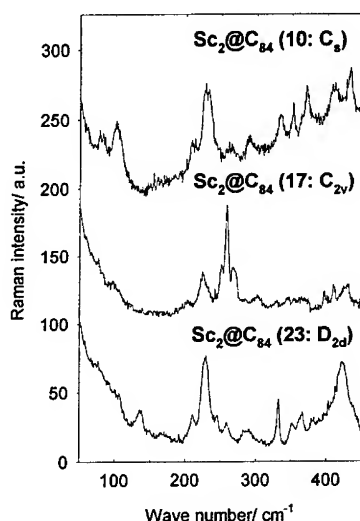


Figure 2: Low frequency Raman spectra of the $\text{Sc}_2@C_{84}$ isomers 10 (C_s), 17 (C_{2v}) and 23 (D_{2d}), 298 K, 514 nm excitation, 3.0 mW laser power

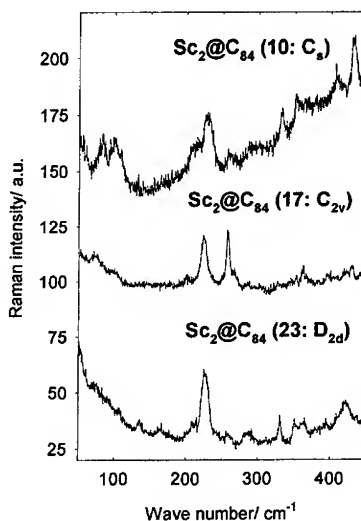


Figure 3: Low frequency Raman spectra of the $\text{Sc}_2@C_{84}$ isomers 10 (C_s), 17 (C_{2v}) and 23 (D_{2d}), 298 K, 647 nm excitation, 1.5 mW laser power

For their frequencies and their absence in the Raman spectra of the empty C_{84} these additional modes are attributed to vibrations between the encapsulated scandium ions and the surrounding fullerene cage. According to a group theoretical treatment the 6 ($\text{Sc}-C_{84}$) modes of the $\text{Sc}_2@C_{84}$ isomer 23: D_{2d} belong to the symmetry species

$$\Gamma_{\text{vib, Sc-C}_{84}} = 1A_1(Ra) + 1B_2(Ra, IR) + 2E(Ra, IR).$$

Normal mode considerations show that the A_1 mode represents a symmetric and the B_2 mode an antisymmetric stretching vibration of the scandium ions against the cage. The displacement of the scandium ions parallel to the cage leads to the E modes which are termed ($\text{Sc}-C_{84}$) deformations. This picture is sufficient to assign the ($\text{Sc}-C_{84}$) modes of the isomers 10 and 17. The two highest energetic modes are attributed to ($\text{Sc}-C_{84}$) stretching vibrations and those at 80 and 100 cm^{-1} to ($\text{Sc}-C_{84}$) deformations (Tab. 1). For the lower reduced mass the Raman mode at 260 cm^{-1} is assigned to the symmetric and that at 165 cm^{-1} to the antisymmetric stretching. This is consistent with

the complementary Raman and infrared intensities (3). As the removal of degeneracy does not split the (Sc-C₈₄) deformations of the isomers 10 and 17 we ascribe the higher number of (Sc-C₈₄) vibrations of the D_{2d} isomer to a factor group splitting in crystalline Sc₂@C₈₄ (tab. 1). This is caused by the interaction of the two molecules in the unit cell of the crystal with the space group P2₁ (4).

Table 1: Raman frequencies and assignments of the C₈₄ and Sc₂@C₈₄ modes between 50 and 300 cm⁻¹, s: strong, m: medium; w: weak, vw: very weak, sh: shoulder, ¹ infrared active only

C ₈₄ (22: D ₂)	C ₈₄ (23: D _{2d})	Sc ₂ @C ₈₄ (10: C _s)	Sc ₂ @C ₈₄ (17: C _{2v})	Sc ₂ @C ₈₄ (23: D _{2d})	Assignment
287 w	287 w	290 w	302 w	290 w	C ₈₄
279 sh, w	279 w	-	270 m	283 w	C ₈₄
-	-	262 w	258 s	259 w-m	v _s (Sc-C ₈₄)
236 sh	229 m	243 sh	251 m	245 w-m	C ₈₄
228 m	224 m	232 m	230 sh	230 s	C ₈₄
220 sh	219 sh, m	227 m	224 m	225 sh, w-m	C ₈₄
214 m	214 sh, m	215 sh	-	210 w-m	C ₈₄
206 m	208 sh, w	208 w-m	202 w	-	C ₈₄
-	-	160 vw	(160) ¹	166 vw	v _{as} (Sc-C ₈₄)
-	-	-	-	137 m	δ (Sc-C ₈₄)
-	-	101 m	100 sh	107 sh	δ (Sc-C ₈₄)
-	-	-	-	92 sh	δ (Sc-C ₈₄)
-	-	80 m	75 sh	77 sh	δ (Sc-C ₈₄)

ACKNOWLEDGEMENT

Financial support was given by the EU, TMR network ERBFMRX-CT97-0155 and the Humboldt foundation.

REFERENCES

1. T.J.S. Dennis, S. Margadonna, K. Prassides, M. Hulman, H. Kuzmany, "Isolation and characterization of C₈₄ isomers", Proc. of the XIII. Int. winterschool on electronic properties of novel materials, Kirchberg, Austria, 1999
2. E. Yamamoto, M. Tansho, T. Tomiyama, H. Shinohara, H. Kawahara, Y. Kobayashi, Am. Chem. Soc. **118**, 2293(1996)
3. M. Hulman, M. Krause, M. Inakuma, T.J.S. Dennis, H. Shinohara, H. Kuzmany, "IR and Raman analysis of diatomic encapsulates in fullerene cages", Proc. of the XIII. Int. winterschool on electronic properties of novel materials, Kirchberg, Austria, 1999
4. M. Takata, E. Nishibori, B. Uneda, M. Sakata, E. Yamamoto, H. Shinohara, Phys. Rev. Lett. **78**, 3330 (1997)

A vibrational spectroscopic structure analysis of Eu@C_{74}

M. Krause^{1,2}, P. Kuran², L. Dunsch²

¹ *Institut für Materialphysik, Universität Wien, Strudlhofgasse 4, A-1090 Wien, Austria*

² *Institut für Festkörper- und Werkstofforschung Dresden, Helmholtzstr. 20, D-01171 Dresden, Germany*

Abstract: Polarization dependent Resonance Raman measurements were used to study the molecular structure of Eu@C_{74} in solution. In total 84 polarized fundamentals with a depolarization ratio of $1/8 \leq \rho < 3/4$ were assigned. This result is discussed as a consequence of the position and the dynamics of the encapsulated europium ion causing a molecular symmetry not higher than C_5 .

INTRODUCTION

Much progress was achieved in the structure analysis of endohedral metallofullerenes like $\text{Sc}_2\text{@C}_{84}$ and Ca@C_{82} in the past few years by ^{13}C -NMR spectroscopy (1, 2). For the paramagnetic lanthanide metallofullerenes interference by NMR line broadening, the shift of the whole spectrum or an expanded shift range is expected. Therefore alternative methods for structure determination are necessary. Resonance Raman spectroscopy seems promising as it combines a low detection limit and structure specific informations like the polarization state of molecular vibrations. We have applied this technique on Eu@C_{74} which has an electronic state $\text{Eu}^{2+}\text{@C}_{74}^{2-}$ (3). The endohedral europium ion shows ideal Curie paramagnetism (4). The vibrational properties are incompatible with a molecular symmetry higher than C_5 . This result is discussed as a consequence of the position and the dynamics of the encapsulated europium ion in the C_{74} cage.

EXPERIMENTAL

Eu@C_{74} was prepared by a modified Krätschmer arc burning method, extracted with a Soxhlet by CS_2 and isolated by a two stage HPLC (high performance liquid chromatography) using a preparative Cosmosil Buckyprep (Nacalai, 25x2 cm) and an analytical Buckyclutcher column (SES, 25x1 cm). A final purity of higher than 98% was obtained (3).

Resonance Raman spectra of saturated Eu@C_{74} solutions in CS_2 were excited with 763 nm radiation of a Ti:Sa laser 899 LC (Coherent, USA) and the 514 nm line of an argon laser Innova 305 (Coherent, USA). The Raman radiation was analysed in a

back scattering geometry with a triple spectrometer T 64 000 (Jobin Yvon, France). For polarization dependent studies subsequently the perpendicular (I_{\perp}) and the parallel scattering intensity (I_{\parallel}) were determined and the ratio of depolarization was calculated by $\rho = I_{\perp} / I_{\parallel}$.

RESULTS AND DISCUSSION

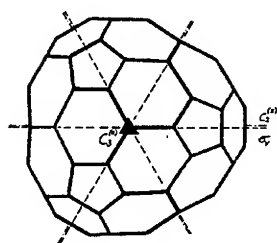


Figure 1: Molecular structure of C_{74} , after (5), with symmetry elements

For the molecular point group D_{3h} the 216 normal modes of empty C_{74} belong to following symmetry species:

$$\Gamma_{vib, C_{74}} = 21A_1'(Ra) + 16A_1''(-) + 16A_2'(RR) + 19A_2''(IR) + 37E'(Ra, IR) + 35E''(Ra).$$

The depolarization ratio ρ for the 21 totally symmetric A_1' modes is given by $0 \leq \rho < 3/4$ for non resonant Raman conditions.

For resonance Raman scattering used here to study endohedral $Eu@C_{74}$ values of $1/8 \leq \rho < 3/4$ are expected for the A_1' modes whereas $\rho = 3/4$ and $3/4 \leq \rho < 2$ for the 37 E' and the 35 E'' Raman modes (6). In contrast to this predictions based on a unperturbed D_{3h} symmetry the experimental vibrational structure of $Eu@C_{74}$ is characterised by 84 Raman modes with $1/8 \leq \rho < 3/4$ and a much lower number of nonpolarized vibrations (Tab. 1, Fig. 2, 3). The spectra excited with 763 nm radiation show only one nonpolarized line of substantial intensity (Fig. 2, indicated by an arrow). A few more anomalously polarized and depolarized Raman lines were found with an excitation wavelength of 514 nm (Fig. 3). These results are definitely incompatible with a molecular symmetry group D_{3h} .

Table 1: Vibrational structure of $Eu@C_{74}$

Fundamentals	145
Polarized Raman modes ($1/8 \leq \rho \leq 3/4$)	84
Depolarized Raman modes ($\rho = 3/4$)	3
Anomalously polarized Raman modes ($3/4 < \rho < \infty$)	16
Inversely polarized Raman modes ($\rho \rightarrow \infty$)	-

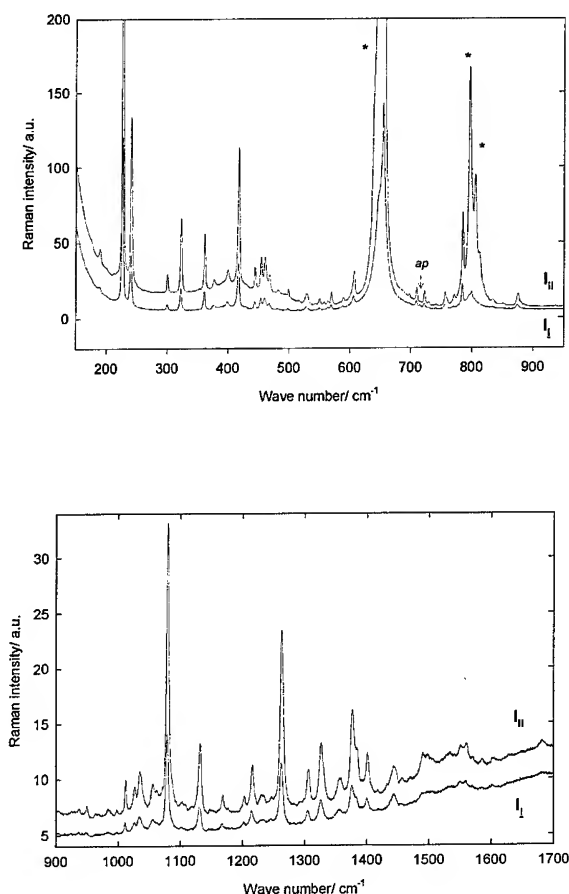


Figure 2: Polarized resonance Raman spectra of a saturated Eu@C_{74} solution in CS_2 , 7fold expanded intensity scale in the lower trace, 763 nm excitation, 40 mW laser power, spectral resolution 1.8 cm^{-1} , integration time 12 min, ap: anomalously polarized lines, * indicates CS_2 lines

By vibrational studies of solid Eu@C_{74} a (Eu-C_{74}) mode was found at 123 cm^{-1} (3) indicating a chemical bond between the encapsulated Eu^{2+} ion and the C_{74} cage which is hidden by the Rayleigh line in the solution spectra. Assuming the validity of the isolated pentagon rule the molecular symmetry of Eu@C_{74} should be determined by the equilibrium position and the dynamics of the encapsulated Eu^{2+} ion only. A subsequent symmetry reduction shows that only a molecular point group lower than C_{2v} i.e. C_s can explain the polarization data of the Eu@C_{74} fundamentals obtained here. This structure could be realized by an asymmetric equilibrium position of the Eu^{2+} ion above a (6,6) double bond or a hexagon in the molecular plane of C_{74} (Fig. 1)

or by an large asymmetric oscillation of the Eu^{2+} ion around the equilibrium position that gives rise to a dynamic symmetry reduction as indicated by theoretical calculations (7).

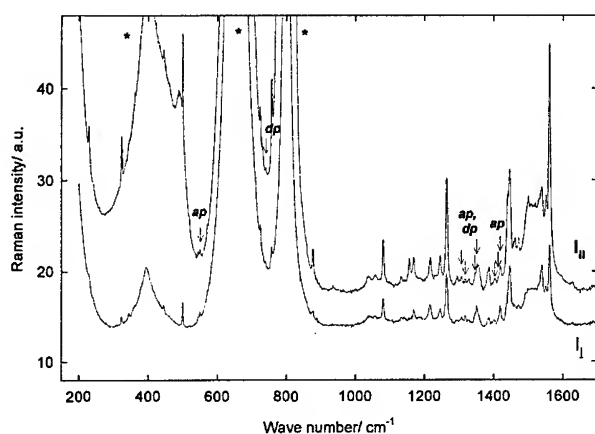


Figure 3: Polarized resonance Raman spectrum of a saturated Eu@C_{74} solution in CS_2 , 514 nm excitation, 25 mW laser power, spectral resolution 1.8 cm^{-1} , integration time 20 min, ap: anomalously polarized lines, dp: depolarized lines, * indicates CS_2 lines

ACKNOWLEDGEMENT

Financial support was given by the EU, TMR network ERBFMRX-CT97-0155.

REFERENCES

1. H. Shinohara, Endohedral metallofullerenes: Structures and electronic properties, *Advances in Metal and Semiconductor Clusters*, Vol 4, 1998, 205-226
2. T.J.S. Dennis, H. Shinohara, *Appl. Phys. A* **66**, 243 (1998)
3. P. Kuran, M. Krause, A. Bartl, L. Dunsch, *Chem. Phys. Lett.*, **292**, 580 (1998)
4. L. Dunsch, D. Eckert, J. Fröhner, A. Bartl, P. Kuran, M. Wolf, K.-H. Müller, "Magnetic properties of endo- and exohedral fullerenes", *Electrochem. Soc. Proc.* Vol 98-8, 1998
5. P.W. Fowler, D.E. Manolopoulos, *An Atlas of Fullerenes*, Clarendon Press, Oxford, 1995
6. R.J.H. Clark, T.J. Dines, *Angew. Chem.* **98**, 131 (1986)
7. K. Vietze, G. Seifert, M. Richter, L. Dunsch, M. Krause, "Endohedral rare earth fullerenes - electronic and dynamic properties", *Proc. of the XIII. Int. winterschool on electronic properties of novel materials*, Kirchberg, Austria, 1999

Light-Induced Release of Nitrogen from Fullerene Cages

B. Goedde, N. Weiden, and K.-P. Dinse

Phys. Chemie III, TU Darmstadt Petersenstr. 20, D-64287 Darmstadt, Germany

Abstract. The release of atomic nitrogen from fullerene cages under irradiation with ultraviolet laserlight has been studied. The experiments show that there is a more favorable decay pathway for $N@C_{60}$ than for $N@C_{70}$, indicating that the lifetime of the metastable triplet state is not controlling the escape.

I INTRODUCTION

Atomic nitrogen can be encapsulated in C_{60} and C_{70} using ion beam implantation techniques. Typical energies giving a maximum of encased species are in the range of 20 to 50 eV, consistent with predictions from quantum chemical calculations. As was demonstrated using EPR detection, the encapsulated nitrogen atoms cannot penetrate the Carbon cage on a time scale of several months at room temperature. 'Thermal release' experiments, have shown that the EPR signal intensity decays irreversibly with a time constant of approximately 200 s at 500 K in case of C_{60} and 450 K for C_{70} cages [1].

Attempts to model the escape mechanism led to the suggestion that the initial escape step occurs via binding to a particular Carbon-Carbon bond [2]. We therefore expected that the escape probability would be influenced by exciting the Fullerene cage to a long-lived metastable electronic state.

II EXPERIMENTAL SET UP

Carefully degassed, sealed-off samples of $N@C_{60}/N@C_{70}$ dissolved in toluene were irradiated at room temperature in the EPR cavity using a frequency-tripled Nd:YAG laser ($\lambda = 355$ nm, ~ 5 mJ pulse energy). Using FT-EPR techniques to monitor the EPR signal before and after irradiation possible effects of saturation in the sample of varying concentration were avoided. EPR signals of the metastable triplet state of C_{60} could be detected and used as internal standard for the photon flux absorbed in the sample. The concentration of intact nitrogen-containing cages was determined by evaluating the integrated EPR signal intensity.

III PROBE CHARACTERIZATION

For a direct comparison of the decay characteristics of C_{60} and C_{70} cages, samples of a mixture of C_{60} and C_{70} were bombarded with nitrogen ions. From the relative EPR signal intensity, a relative initial concentration of C_{60} and C_{70} cages was determined as 11:1. The sample concentration was estimated as 10^{-3} M $C_{60}/9 \cdot 10^{-5}$ M C_{70} in toluene. The relative concentration of fullerenes with encapsulated nitrogen to empty fullerenes was estimated as 10^{-4} to $3 \cdot 10^{-4}$. The total number of Fullerenes in the EPR cavity is derived as $3 \cdot 10^{16}$.

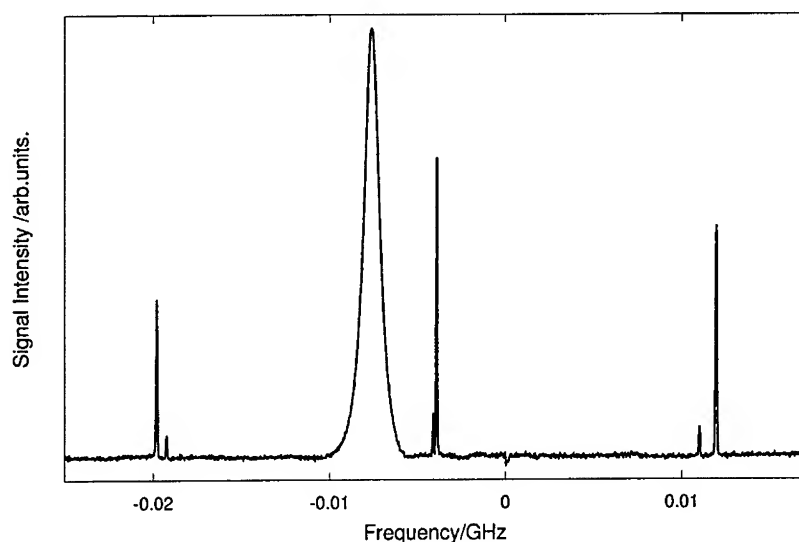


FIGURE 1. FT-EPR Spectrum taken at a delay of 200 ns after laser excitation showing two sets of narrow lines of ground state $N@C_{60}$ and $N@C_{70}$ molecules as well as a single line of $^3C_{60}$

The number of excitation processes can be estimated in analogy to the processes measured for 'empty' fullerenes by two different methods:

1. The total number of photons incident on the sample is estimated. Because of a triplet quantum yield of nearly 1, this number can be converted directly into the number of excitation cycles. Because of missing data for the quantum yield of $N@C_{60}$ and $N@C_{70}$ this value is also used for these molecules: The total number of photons in the excitation beam is $7 \cdot 10^{15}$ (5 mJ/pulse). The total number of photons absorbed in the sample is estimated as 5 % ($3 \cdot 10^{14}$) due to loss by geometric factors like metal grid (50%), multiple reflections on surfaces (sapphire, quartz, toluene), unfocused beam dimension (8 mm 1/e diameter).

2. The transient EPR signal of the triplet state can be compared with the stationary EPR signal of the N@C_{60} molecules. Their number in the cavity is estimated as $3 \cdot 10^{12}$ to $9 \cdot 10^{12}$. Experimentally, a triplet EPR signal with relative intensity ratio of 20:1 is observed, leading to an estimated number of excited molecules of $6 \cdot 10^{13}$ to $1.8 \cdot 10^{14}$.

The results of both estimates agree within a factor of 3(2). Taking the mean value of the EPR-derived value as more reliable, the efficiency of excitation is derived as 1/300.

IV RESULTS

Observed light induced rate constant of $510000 \text{ pulse}^{-1}$ indicates a very low efficiency of light-induced nitrogen release from C_{60} cages: approximately 1700 excitation cycles are necessary for the release of the encapsulated atom. Simultaneous observation of the decay of N@C_{60} and N@C_{70} under identical conditions allows further conclusions about the decay pathway:

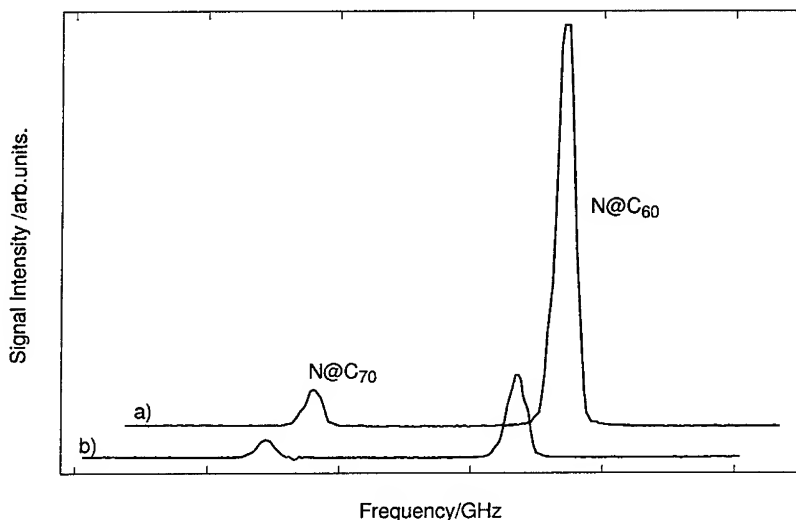


FIGURE 2. Signal intensity of the high frequency hyperfine components measured a) before and b) after $8.6 \cdot 10^5$ laser excitations

Because of nearly identical extinction coefficients of C_{60} and C_{70} at 355 nm ($\epsilon = 17850$ vs. $18500 \text{ M}^{-1} \text{ cm}^{-1}$) we can assume that the incident photons are 'shared' by both molecules in the ratio of their concentrations. Accordingly, the efficiency of the excitation cycle is identical, allowing to compare directly the efficiency of the release process by optical excitation by the measured EPR signal

decay.

The observed decay rate of N@C_{70} is smaller than that of N@C_{60} by a factor of 2. By measuring the relative concentration of C_{60} and C_{70} with HPLC before and after laser excitation was complete, it was established that the relative concentration of 'empty' fullerenes was invariant under our experimental conditions. We therefore exclude that photopolymerization contributes selectively to the decay of the EPR-active species.

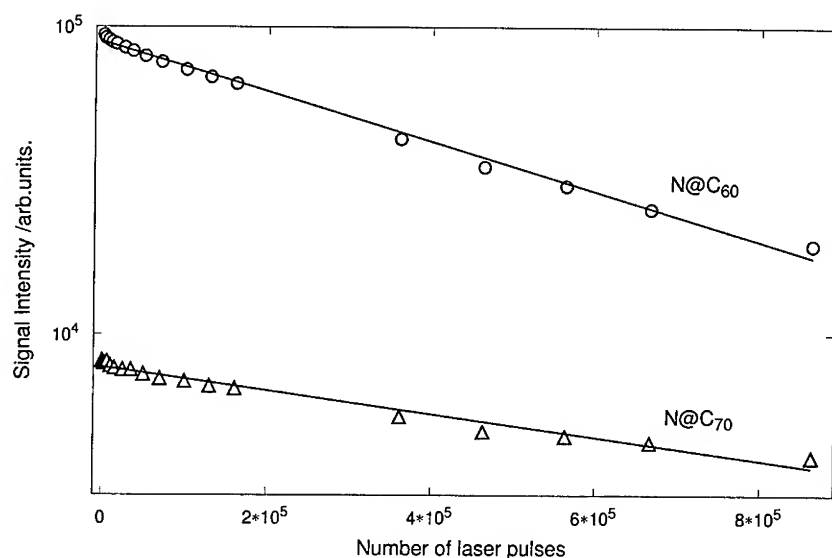


FIGURE 3. EPR signal decay as function of incident laser pulses

We conclude, that the lifetime of the electronically excited triplet state is not the controlling parameter for nitrogen release, because the lifetime of $^3\text{C}_{70}$ is two orders of magnitude larger than that of $^3\text{C}_{60}$, and should therefore lead to an much more pronounced effect on the release rate. We rather propose, that vibrational excitation via local heating by internal conversion and ISC is the dominating release mechanism. The observation of facilitated optical release from the C_{60} cage is at variance with results from thermal release experiments reported by Pietzak, Waiblinger, Lips and Weidinger, who measured a 50 degree lower characteristic decay temperature for the C_{70} cage.

REFERENCES

1. B. Pietzak, M. Waiblinger, K. Lips, and A. Weidinger, private communication.
2. H. Mauser, N. J. R. van Eikema Hommes, T. Clark, A. Hirsch, B. Pietzak, A. Weidinger, and L. Dunsch, *Angew. Chemie Int. Ed. Engl.*, **1997**, *36*, 2835.

Atomic Hydrogen in the Si_8O_{12} Cage

M. Waiblinger*, B. Pietzak*, K. Lips**, T. J. S. Dennis*, A. Weidinger*,
M. Päch***, R. Stösser***

* Hahn-Meitner-Institut Berlin, Glienicker Straße 100, D-14109 Berlin, Germany

** Hahn-Meitner-Institut Berlin, Rudower Chausse 5, D-12489 Berlin, Germany

***Dep. of Chemistry, Humboldt-Universität zu Berlin, Hessische St. 1-2, D-10115 Berlin, Germany

Abstract: Contrary to nitrogen and phosphorous, atomic hydrogen is not stable in C_{60} at room temperature. However, recently it was reported that hydrogen can be stabilized the a cube-like cage of Si_8O_{12} . In the present experiment the endohedral system $\text{H}@\text{Si}_8\text{O}_{12}\text{Et}_8$ (Et = ethyl) was produced by ion implantation using ion implantation on a growing Si_8O_{12} -film.

INTRODUCTION

Attempts of our group to entrap hydrogen in fullerenes by the implantation method (1) failed. $\text{H}@\text{C}_{60}$ with hydrogen in its atomic ground state is not stable at room

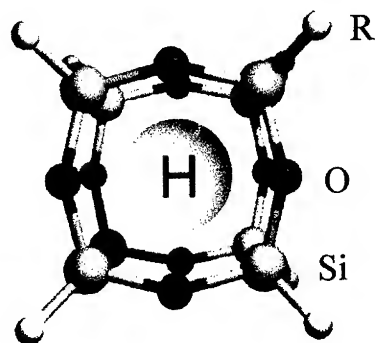


FIGURE 1. Schematic view of an encapsulated hydrogen in a $\text{Si}_8\text{O}_{12}\text{R}_8$ cage. R stands for H or an organic substituent.

temperature. However, recently hydrogen was successfully enclosed in the Si_8O_{12} cage at ambient conditions (2,3). This cage consists of a cube-like Si_8O_{12} core and hydrogen

or organic substituents at the corners of the cube to saturate the remaining bonds (see Fig.1). The entrapment of hydrogen in this cage was achieved in Ref. 2,3 by irradiating this material with γ -rays from a ^{60}Co source. It is shown (3) that the trapped hydrogen originates from hydrogen contained in the substituents at the corners of the cube, but the exact capture process is still unknown. In the present experiment we used ion implantation to encapsulate hydrogen. This procedure has the advantage that the host-guest combinations can be freely chosen and that higher concentrations of filled cages can be obtained.

EXPERIMENTAL DETAIL

The Si_8O_{12} cage material (3) was continuously evaporated onto a substrate and simultaneously bombarded with hydrogen or nitrogen ions. Nitrogen bombardment was used in order to distinguish between direct implantation which is possible only with H ions and an indirect effect due to radiolysis of the substituents. The later effect occurs in both cases. EPR measurements were performed with the Bruker ELEXSYS 580 spectrometer.

RESULTS AND DISCUSSION

Figure 2 shows the solid state EPR spectrum of hydrogen in $\text{Si}_8\text{O}_{12}\text{Et}_8$, i.e. for the ethyl substituted cage. The two main lines correspond to the hyperfine splitting of atomic

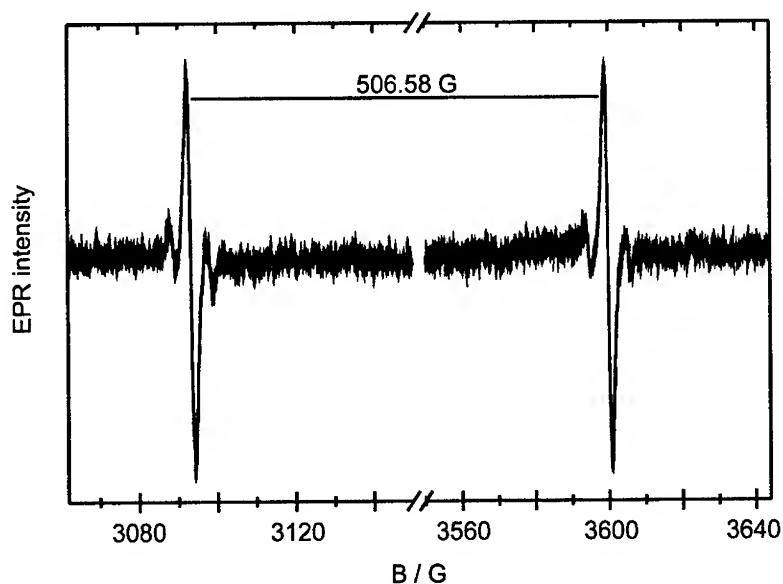


FIGURE 2: Solid state EPR spectrum of hydrogen in $\text{Si}_8\text{O}_{12}\text{Et}_8$, where Et stands for ethyl. The two satellites of each line are due to spin flips of the protons in the substituents.

hydrogen. The satellites on the left and the right of the main lines are due to a simultaneous flip of the spin of a proton in the substituents with the EPR transition (spin-flip satellites). The expected super-hyperfine interaction with ^{29}Si nuclei is small and hidden in the width of the lines in the solid state EPR.

Figure 3 shows a comparison of EPR line intensities obtained with N ion and H ion irradiation, respectively. Approximately the same ion fluences and evaporation rates

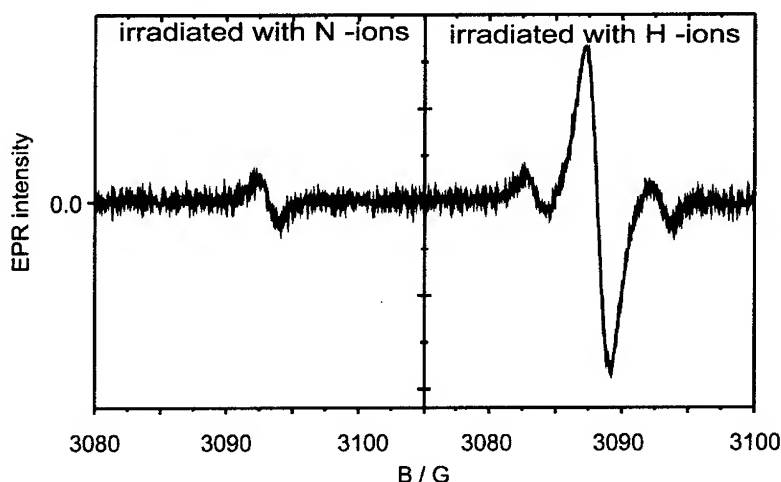


FIGURE 3: Low magnetic field lines of the solid state EPR spectra of hydrogen in $\text{Si}_8\text{O}_{12}\text{Et}_8$ for different production processes (irradiation with N and H, respectively). The irradiation doses and the other experimental conditions were similar, thus the line intensities are direct measure of the produced endohedrals.

were used in the two cases. It can be seen that N bombardment does also produce encaged hydrogen, apparently by mobilizing or displacing H-atoms contained in the substituents. This effect is similar to that reported in Ref. 2,3 for γ -irradiation and will occur also during hydrogen implantation. But in the latter case, in addition, also direct incorporation of the beam particle takes place. This latter process is apparently much more effective as can be seen from the larger intensity of the corresponding EPR line (intensity ratio 20:1).

CONCLUSION

We have shown that ion implantation, using the method of simultaneous evaporation and ion bombardment, offers a good way to produce the recently discovered endohedral hydrogen- Si_8O_{12} cage systems. Ion implantation is very versatile and allows host-guest combinations not accessible with the previously published method. In addition, it seems that high concentrations of filled to empty cages can be reached. This could be of

particular importance if the separation of the two by chemical or other method should turn out to be not possible.

ACKNOWLEDGEMENT

One of us (T.J.S. D.) thanks the Alexander von Humboldt Foundation for support.

REFERENCES

- (1) A. Weidinger, M. Waiblinger, B. Pietzak, T. Almeida Murphy, *Applied Physics A* **66**, 287 (1998)
- (2) R. Samamory, Y. Okaue, T. Isobe, Y. Matsuda, *Science* **265** (1994) 1691
- (3) M. Päch, R. Stösser, *J. Phys. Chem. A* **101** (1997) 8360

III. NEW NANOSTRUCTURED MATERIALS

Oligomer-fullerene dyads and triads as model compounds for bulk-heterojunction PV cells

R.A.J. Janssen^a, E. Peeters^a, B.M.W. Langeveld-Voss^a,
P.A. van Hal^a, J. Knol^b, and J.C. Hummelen^b

a. Laboratory for Macromolecular and Organic Chemistry, Eindhoven University of Technology, PO Box 513, 5600 MB Eindhoven, The Netherlands and b. Stratingh Institute and MSC, University of Groningen, Nijenborgh 4, 9747 AG Groningen, The Netherlands; e-mail: j.c.hummelen@chem.rug.nl

Abstract. Covalent oligomer-fullerene donor-acceptor structures can serve as important model systems for plastic PV cells, based on interpenetrating networks of conjugated polymers and fullerene derivatives. Several series of [60]fullerene-oligomer dyads and triads were prepared. Photoinduced electron transfer phenomena were studied using photoinduced absorption spectroscopy. Measurements in solution and in the solid state reveal that the environment plays a crucial role in the formation and lifetime of the photoinduced charged states in these molecules.

INTRODUCTION

Photovoltaic cells, based on composites of conjugated polymers and fullerene derivatives (1,2), are considered as promising devices for solar energy production. At present, the efficiency of such 'plastic' PV cells is limited because the devices only produce current when a relatively thin active layer is used. As a consequence, only a small fraction of the incoming light is absorbed (3). The ruling paradigm is that the plastic PV devices suffer from low charge carrier mobility because of the random nature of the interpenetrating networks, formed spontaneously upon spin coating of a co-solution of the two constituents of the active layer. It is expected that structural ordering of the constituents will lead to a substantial increase in charge carrier mobility: the concept of a 'molecular electronic highway'. At present, little or nothing is known about the relation between the architecture of molecular (multi-)donor-(multi-) acceptor structures on one side and their material properties such as the efficiency of formation, the mobility, and lifetime of the photo-generated charge carriers on the other. A remarkable feature of conjugated polymer/fullerene blends is the fact that an ultra-fast forward electron transfer reaction occurs (< 1 ps), whereas the recombination of photogenerated charges is slow ($> \text{ms}$). The large difference in electron transfer rates can, in principle, be either an intrinsic property of the structures involved or a material property. In order to gain some insight in these matters, we are investigating model systems for such architectures. We use conjugated oligomers as

model compounds for the polymer. These oligomers have been synthesized, functionalized, and coupled to C_{60} in such a way that well-defined donor-acceptor dyad or triad molecules are obtained that can be studied both as individual molecules in solution and as (ordered) assemblies in the solid state. Plastic PV cells are usually made using either polythiophenes or poly[p-phenylenevinylene]s. Therefore, model systems were constructed that contain oligomer parts of these two types of polymers.

RESULTS AND DISCUSSION

Two types of oligothiophene-fullerene compounds were synthesized using the well-established Prato reaction (4). First, a simple dyad containing a terthiophene donor moiety and one fullerene acceptor moiety was prepared. Terthiophene monoaldehyde (**1b**), N-methyl glycine, and C_{60} were heated in toluene at reflux temperature during 16 hrs to yield a mixture of C_{60} , the desired mono-fulleropyrrolidine **2** and some higher adducts (Figure 1, left). The monoadduct was isolated in 47% yield using standard column chromatography. Dyad **2** was soluble enough in the standard organic solvents to allow for full characterization.

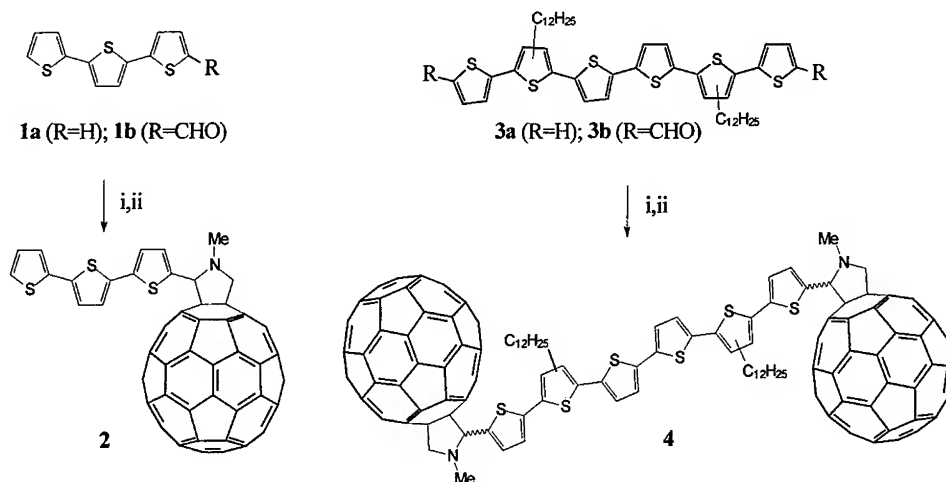


FIGURE 1. Synthesis of oligothiophene-fullerene dyads. Step i: DMF, $POCl_3$; step ii: N-methylglycine, C_{60} , toluene, Δ .

Similarly, triad **4** was prepared by refluxing a chlorobenzene solution of the highly soluble sexithiophene α,ω -bisaldehyde **3b**, N-methyl glycine, and C_{60} during 16 hrs (Figure 1, right). Since the starting oligomer material consisted of a mixture of three isomers and because the Prato reaction yields chiral products in the case of aldehyde starting material, triad **4** is a mixture of (maximally) 10 regio- and stereoisomers. Nevertheless, molecular models indicate that in all of these isomers the donor-acceptor configuration is very similar. 1H -NMR spectroscopy indicates the

presence of a small impurity of isocyanobenzene (PhNC) in benzonitrile (PhCN) which acts as a donor to the triplet state of **5**. This is a bimolecular reaction and

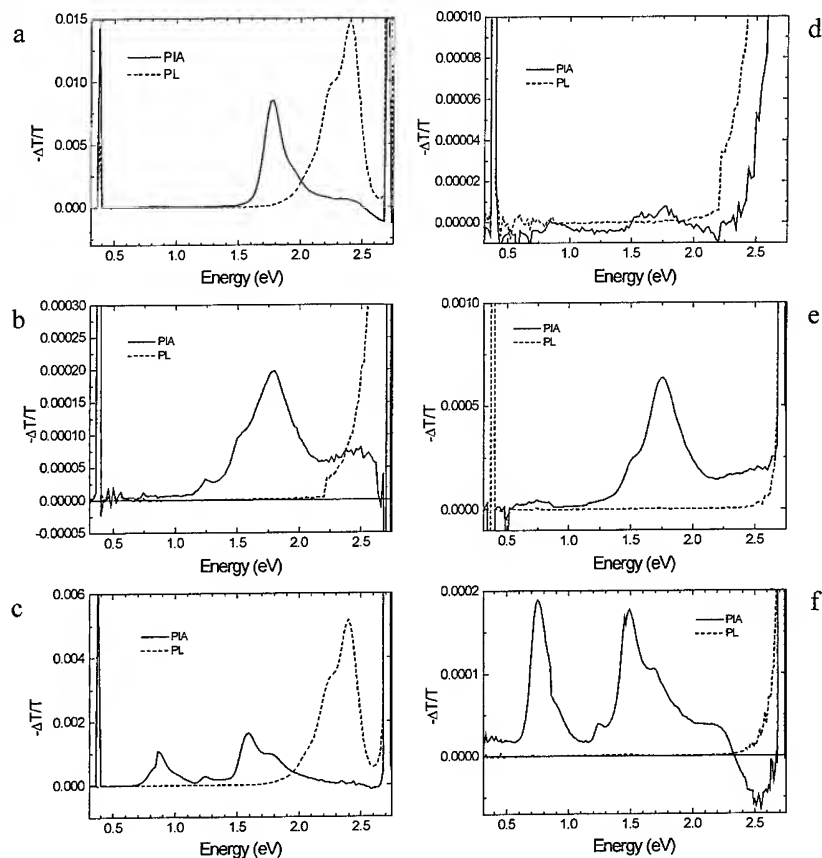


FIGURE 3. PIA and PL spectra of (a) **3a** in benzonitrile; (b) **5** in benzonitrile; (c) **3a** and **5** (1:1 molar ratio) in benzonitrile; (d) **4** in benzonitrile; (e) **4** in toluene; (f) a thin film of **4** on quartz. Spectra a-e were recorded at 295 K, spectrum f was recorded at 80 K. The PL curves shown in spectra b and d-f are mainly due to scattering of the excitation laser beam

the lifetime of the anions formed is long because charge recombination is hampered by follow-up reactions of the isocyano-benzene cation radical, acting as an sacrificial electron donor. When **3a** and **5** are dissolved in benzonitrile in a 1:1 ratio, we find the clear characteristics of the 6T radical cation with bands at 0.87 and 1.60 eV in solution and a band of the radical anion of **5** at 1.24 eV (Figure 3c) (6). The fact that under these conditions the fluorescence of **3a** is not quenched demonstrates that electron transfer does not occur from the S_1 -state of **3a** which is formed preferentially at first. Rather electron transfer occurs from the T_1 triplet state of **3a** which is formed via intersystem crossing from S_1 . The lifetime of the 6T radical cation is on the order of 200-400 μ s. The determination of the lifetime of the radical anion of **5** is hampered by

the isocyanobenzene impurity which remains to act as electron donor to the triplet state of **5**. When **3a** and **5** are photoexcited in an apolar solvent such as toluene, instead of the highly polar benzonitrile, only triplet states are formed. Photoexcitation of the 1:1 mixture in toluene results in triplet energy transfer from 6T(T_1) to **5** rather than electron transfer, similar to previous observations for mixtures of 6T and C₆₀ (6). The reason for a preference for energy transfer in toluene is that the charge-separated state is less stabilized in apolar solvents.

Photoexcitation of a benzonitrile solution of triad **4** results neither in a detectable PIA signal nor in a detectable PL signal (only scattering of pump laser) (Figure 3d). Apparently, the S_1 -state of the 6T moiety is completely quenched. This behavior can be rationalized by assuming that in benzonitrile a fast forward electron transfer reaction occurs resulting in an intramolecularly charge-separated state. The fact that this charge-separated state is not detected with the PIA technique is explained by assuming that the lifetime is less than about 10 μ s, below the detection limit of our near-steady state PIA spectrometer.

When the solvent is changed to toluene (which is less polar) the PL is not restored but a clear PIA signal similar to the triplet state of **4** is observed with a lifetime of about 250 μ s (Figure 3e). This indicates that in toluene an intramolecular energy transfer occurs in which the singlet excitation energy is transferred to the C₆₀ fragment. This singlet C₆₀ photoexcitation subsequently intersystem crosses to a C₆₀ triplet state. When triad **4** is cast from solution on quartz glass a solid film is obtained. PIA spectroscopy of this thin film at 80 K shows that a long-lived charge-separated state is formed (Figure 3f). Characteristic absorption bands of the radical cation of 6T at 0.72 and 1.49 eV and of the radical anion of C₆₀ at 1.24 eV appear in the spectrum. The PIA bands increase with the square root of the excitation intensity, indicative of bimolecular decay. The frequency dependence follows a power law: $\Delta T \propto \omega^{-p}$, with $p = 0.12-0.17$. Such a power-law behavior is often observed for a distribution of lifetimes. We propose that such a long-lived charge-separated state can only exist when the hole and electron are localized on different molecules. The experiments of **4** in benzonitrile show that intramolecular charge recombination occurs with a time constant that must be less than 10 μ s. In solution, a fast intramolecular photoinduced electron transfer reaction may occur in **4**, depending on the Coulombic stabilization of the charge-separated state by the medium. The charge transfer in solution is governed by the Weller equation (7). Intramolecular charge recombination in the photoexcited arrays occurs on short time scales (probably $\ll 10 \mu$ s). This demonstrates that the long lifetime of the charge-separated states in solid blends of 6T and fullerene derivatives (8) or solid films of the C₆₀-6T-C₆₀ array is a material rather than a molecular property. In solvents where electron transfer does not occur, we invariably observe the spectral characteristics of the triplet-state of the fullerene moiety, even when the oligothiophenes are preferentially excited (6). In combination with the absence of oligothiophene fluorescence it can be concluded that in these cases an efficient energy transfer occurs from the excited oligothiophene to the fullerene. Solutions of dyad **2** in toluene and in benzonitrile show similar photoinduced absorption spectra. No signatures of charge separated states were found. Instead, the

typical absorption spectrum, corresponding to triplet C₆₀, is observed. This indicates that in both solvents either highly efficient intramolecular energy transfer occurs from the terthienyl moiety to the fullerene part of the molecule or direct excitation of the fullerene moiety takes place (at 458 nm, **5** has a higher absorption coefficient than terthienyl).

The oligo[p-phenylenevinylene]-fullerene dyads **6-9** are currently being investigated using photoinduced absorption spectroscopy in solutions and as solid films. Preliminary results show that the behavior of **8** and **9** parallels that of triad **4**. For **8** and **9** the photoluminescence is strongly quenched under all conditions. Photoexcitation of **8** and **9** in toluene gives a C₆₀ triplet state, while in benzonitrile a fast forward and fast backward electron transfer reaction occurs. In thin films of **8** and **9** a long-lived charge separated state is observed with the hole localized on the oligo[p-phenylenevinylene] fragment and the electron on the fullerene moiety.

In conclusion, it has been demonstrated that compounds **4**, **8**, and **9** behave photophysically in such a way that they can serve as model compounds for conjugated polymer / fullerene blends. The formation and the lifetimes of photoinduced charge separated states in oligomer-fullerene compounds **4**, **8**, and **9** depend fully on the chemical environment of the molecules. Long lifetimes of charge separated states are only observed in the solid state. Hence, stabilization of the charge-separated state is a material property of these compounds. Based on our experiments, we propose that a rapid diffusion mechanism for a substantial fraction of the photo-generated charges to the corresponding units of neighboring molecules is operating in the solid state.

ACKNOWLEDGMENTS

We thank the Netherlands Organization for Energy and the Environment (Novem) for financial support (Novem 146.120-008.1). EP was supported by the Netherlands Foundation for Chemical Research (NCO) with financial aid from the Netherlands Technology Foundation (STW, 349-3562). PvH was supported by the Ministries of Economic affairs, of the Environment, and of Education (E.E.T. K97115)

REFERENCES

1. Sariciftci, N. S., Smilowitz, L., Heeger, A.J., Wudl F., *Science* **258**, 1474-1476 (1992).
2. Yu, G., Gao, Y., Hummelen, J.C., Wudl, F., Heeger, A.J., *Science* **270**, 1789-1791 (1995)
3. Brabec, C.J., Padinger, F., Dyakonov, V., Hummelen, J.C., Janssen, R.A.J., Sariciftci, N.S., *Electronic Properties of Novel Materials*, World Scientific Publishing, 1998, pp 519-522
4. Maggini, M., Scorrano, G., Prato, M., *J. Am. Chem. Soc.* **115**, 9798-9799 (1993)
5. Janssen, R.A.J., Smilowitz, L., Sariciftci, N. S., Moses, D., *J. Chem. Phys.* **101**, 1787-1798 (1994).
6. Janssen, R.A.J., Moses, D., Sariciftci, N. S., *J. Chem. Phys.* **101**, 9519-9527 (1994).
7. Weller, A., *Z. Phys. Chem. Neue Folge* **133**, 93-98 (1982)
8. Janssen, R.A.J., Christiaans, M.P.T., Pakbaz, K., Moses, D., Hummelen, J.C., Sariciftci, N.S., *J. Chem. Phys.* **102**, 2628-2635 (1995).

Photo-Induced Charge-Transfer Processes in Fullerene-Containing Dyad and Triad Molecules

S. Knorr*, A. Grupp*, M. Mehring*,
G. Grube[†], and F. Effenberger[†]

*2. Physikalisches Institut, Universität Stuttgart,
Pfaffenwaldring 57, 70550 Stuttgart, Germany

[†]Institut für Organische Chemie,
Pfaffenwaldring 55, 70550 Stuttgart, Germany

Abstract. We report on pulsed electron-spin-resonance (ESR) investigations of novel model systems for photo-induced electron-transfer processes. The schematic structures of the molecules are T_5-C_{60} and $A-T_5-C_{60}$, i.e., the fullerene C_{60} is used as the acceptor, and quinquethiophene (T_5) or anthracene (A) act as a donor. In frozen solutions of both the dyad and triad, we find rather long-lived radical signals (lifetime $\approx 2 \mu s$) after laser-pulse excitation. The observed signals can be assigned by the g factor and the linewidth to the anion C_{60}^- and the cation T_5^+ . We have examined the influence of the solvent polarity (toluene or benzonitrile) and of the excitation wavelength (355 nm or 532 nm) on the efficiency of the charge transfer.

INTRODUCTION

The dyad and triad systems presented here (see Fig. 1 for the chemical structures) have been synthesized [1] as novel model systems for charge transfer. The acceptor C_{60} and the potential donors quinquethiophene (T_5) and anthracene (A) are connected in a single supermolecule. We investigated the dependence of the charge-transfer efficiency on the nature of the donor (T_5 or A) and on the excitation conditions.

EXPERIMENTAL

Theoretical calculations basing on the Rehm-Weller equation [2] show that in the triad both final states $A^+-T_5-C_{60}^-$ and $A-T_5^+-C_{60}^-$ are possible from an energetic point of view. For these considerations, we assumed the photo excitation of only one chromophore in the triad. To fortify this conjecture experimentally, we

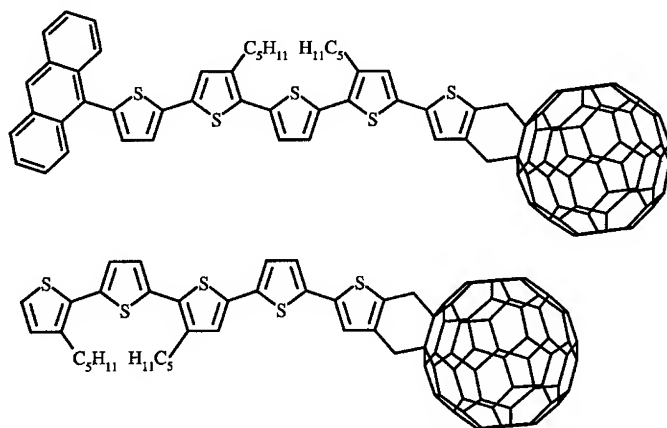


FIGURE 1. Chemical structures of the triad A-T₅-C₆₀ (top) and of the dyad T₅-C₆₀ (bottom); the side chains are introduced to improve the solubility.

measured the optical absorption spectra of the dyad and the triad and compared them with those obtained by a superposition of the single-chromophore spectra (see Fig. 2). We find almost perfect agreement which proves that the C₆₀ acceptor is electronically independent from the donor part.

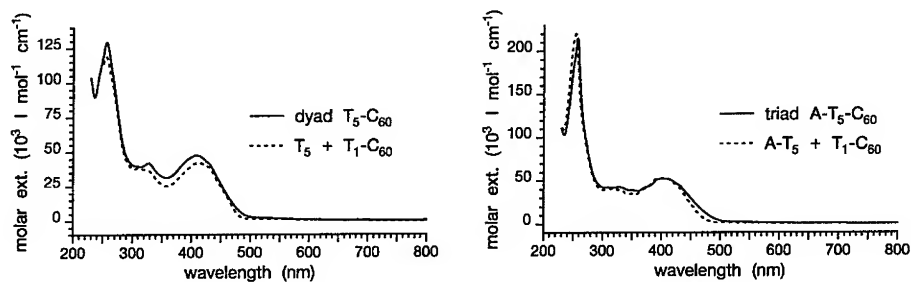


FIGURE 2. Comparison of the optical absorption spectra. The spectra of the dyad T₅-C₆₀ (left) and of the triad A-T₅-C₆₀ (right) are drawn with solid lines; the summed single-chromophore spectra correspond to dashed lines. Note that the spectrum of T₁-C₆₀ is used as the fullerene part for comparison since C₆₀ and C₆₀-monoadducts show some characteristic differences.

For the pulsed ESR investigations we prepared solutions of the supermolecules in the unpolar solvent toluene and the polar solvent benzonitrile. The liquid solutions were shock-frozen at $T=77$ K and subsequently cooled to 5 K. Since a photo-induced charge transfer results in a well-separated radical pair, we expect to observe in our systems the radical anion C₆₀⁻ together with the corresponding radical cation T₅⁺ or A⁺, provided the lifetime of the charge-separated state is long enough compared to the time resolution of the ESR spectrometer.

The radical ions should be identified by their characteristic g factors and the

linewidths. For the C_{60}^- signal we expect only very little line broadening due to hyperfine coupling since ^{12}C nuclei have no spin, and ^{13}C nuclei with $I = 1/2$ are only 1.1% abundant. Hence, a long-lived FID signal is expected for a C_{60}^- state.

For the cation, the situation is different. There are abundant protons on both possible donor parts to cause hyperfine broadening. This results in an FID decaying within the lifetime of the spectrometer. However, since hyperfine interaction broadens the line inhomogeneously, the FID can be refocused in an electron spin echo.

RESULTS

When working in frozen toluene solutions of the supermolecules, we obtain after photo-excitation at $\lambda = 355$ nm and 532 nm $^3C_{60}$ -like triplet spectra [3,4] with high spin polarization. The zero-field-splitting parameters $|D| = 10.6$ mT and $|E| = 1.6$ mT indicate a considerable distortion of the triplet symmetry with respect to pure C_{60} . We assign this to the functionalization of the C_{60} cage, since other monoadducts of C_{60} , e.g. the C_{60} -4,5-dimethoxybenzene-adduct [5], show similar triplet spectra.

The probability of a charge transfer is expected to increase when a polar solvent is used. Therefore, we continued the ESR experiments with frozen benzonitrile solutions applying laser pulses at $\lambda = 355$ nm. For both the dyad and triad molecules, we observe a sharp line centered at $g = 2.0000$ with a lifetime of $2.0 \mu s$ and a broad line centered at $g = 2.0023$ with the same lifetime. These signals are displayed in Fig. 3. The graph on the left hand side represents the Fourier-transformed FID spectra at $g = 2.0000$ for various delays Δt after the laser excitation; the echo-detected magnetic-field spectrum centered at $g = 2.0023$ (right hand side) extends over 4 mT FWHM.

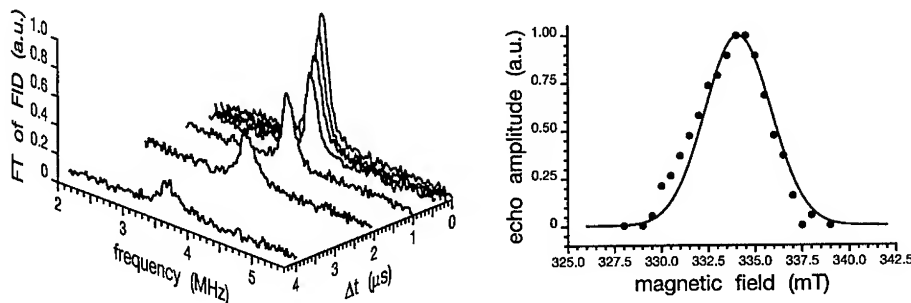


FIGURE 3. Fourier-transformed FID spectra (left) and echo-detected magnetic-field spectrum (right) after laser excitation of T_5-C_{60} in frozen benzonitrile solution.

According to the discussion above, we attribute the FID signal to the C_{60}^- anion and the echo to the T_5^+ cation. The appearance of the charge-separated state in

both supermolecules proves that the dyad is sufficient for allowing photo-induced charge transfer.

When applying the laser excitation at 532 nm, where almost only the C₆₀ part of the supermolecules is absorbing, we find both a ³C₆₀-like triplet spectrum and a rather small FID of the C₆₀⁻ anion. We ascribe this to a competition between charge and energy transfer on the dyad. Hence, photo-excitation of the quinquethiophene part seems to be the starting point for the charge-separation process.

DISCUSSION

In the dyad and triad molecules, the observed appearance of two ESR signals with the same lifetime, the correct *g* factors and linewidths provides strong evidence for a photo-induced charge-transfer process. However, a correlated radical-pair state was not found. For this reason and due to the small linewidth of the C₆₀⁻ signal we conclude that the observed radical signals originate from an intermolecular charge separation. We propose that the electron-transfer process is initiated in the T₅-C₆₀ dyad and similarly in the triad on a time scale < 1 ns. These molecular complexes act in a first step as photo-sensitizers. In a second step, the electron is injected into the matrix where it finds the C₆₀ part of another dyad molecule as acceptor. Thus, recombination on a sub-nanosecond time scale is prevented. The use of a polar solvent enhances the charge-transfer process and stabilizes the charge-separated state. [6]

ACKNOWLEDGEMENT

We acknowledge partial support of this project by the Deutsche Forschungsgemeinschaft (SFB 329) and the Fonds der Chemischen Industrie.

REFERENCES

1. F. Effenberger and G. Grube, *Synthesis*, 1372 (1998).
2. H. D. Roth and G. J. Kavarnos, *Top. Curr. Chem.* **156**, 1 (1990).
3. M. R. Wasielewski, M. P. O'Neill, K. R. Lykke, M. J. Pellin, and D. M. Gruen, *J. Am. Chem. Soc.* **113**, 2774 (1991).
4. M. Bennati, A. Grupp, M. Mehring, K.-P. Dinse, and J. Fink, *Chem. Phys. Lett.* **200**, 440 (1992).
5. M. Bennati, A. Grupp, M. Mehring, P. Belik, A. Gügel, and K. Müllen, *Chem. Phys. Lett.* **240**, 622 (1995).
6. S. Knorr, A. Grupp, M. Mehring, G. Grube, and F. Effenberger, *J. Chem. Phys.* **110**, 3502 (1999).

C₅₉N on silicon surfaces: monomers, dimers and multilayers

M.J. Butcher¹, F.H. Jones¹, P.H. Beton¹, P. Moriarty¹, K. Prassides² and N. Tagmatarchis²

¹School of Physics and Astronomy, University of Nottingham, Nottingham, NG7 2RD, UK

²School of Chemistry, Physics and Environmental Sciences, University of Sussex, Brighton, East Sussex, BN1 9QJ, UK

We have investigated the adsorption of C₅₉N on the Si(111)-7x7 surfaces using ultra-high vacuum scanning tunnelling microscopy. For coverages of C₅₉N close to a monolayer a disordered layer is adsorbed directly on the Si surface. Following the deposition of more C₅₉N small islands are formed indicating that C₅₉N may diffuse on the adsorbed monolayer. There is some evidence for hexagonal ordering in the islands. The higher adsorbed layers may be desorbed by annealing at ~400°C leaving a C₅₉N monolayer. We also discuss the deposition of C₅₉N and C₆₀ on this annealed monolayer.

The formation of heterofullerenes in which atoms other than carbon are incorporated on or within the fullerene cage is a topic of long standing interest [1,2]. One heterofullerene which has attracted particular attention is C₅₉N [3]. In this molecule a group V nitrogen atom replaces a Group IV carbon atom inviting comparison with n-type doping in semiconductors. It was widely recognised that C₅₉N would be a highly reactive species, and when finally synthesised in bulk quantities it was isolated in a dimerised form (C₅₉N)₂ [4]. The availability of C₅₉N through chemical synthesis has enabled the investigation of thick and thin films, and nearly all of the published data to date has confirmed the presence of dimers in such films [5-7]. However, in more recent work based on scanning tunnelling microscopy (STM) of C₅₉N adsorbed on Si surfaces, clear evidence was provided for the presence of C₅₉N monomers [8]. This result indicates that C₅₉N sublimes in monomer rather than dimer form. The presence of C₅₉N monomers was confirmed using photoemission [8]. Sublimation in monomer form was also invoked to account for the morphology of C₅₉N islands grown on unreactive surfaces [9].

The sublimation of C₅₉N monomers may, at first sight, appear to be in contradiction with the presence of dimers in thin films. However, it is possible that

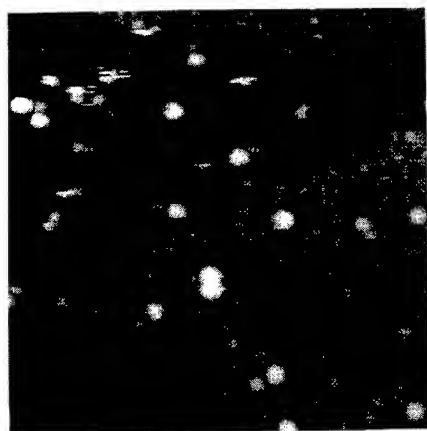


Figure 1. STM image (40nm x 40nm) of near monolayer coverage of $C_{59}N$ on Si(111)-7x7. Scanning parameters - sample voltage -3.5V, tunnel current 0.5nA.

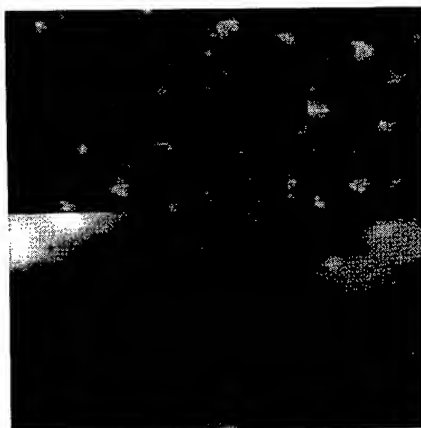


Figure 2. STM images following the deposition of ~10ML of $C_{59}N$. Upper - 200nm x 100nm scanning parameters 3V, 0.2nA; lower - 50nm x 25nm, 2V, 0.05nA.

incident $C_{59}N$ monomers may diffuse and re-form dimers following adsorption. In this paper we present results on the deposition of incident $C_{59}N$ on a $C_{59}N$ monolayer which is strongly adsorbed on a Si surface. $C_{59}N$ monomers which are incident on such monolayers are able to diffuse and form small islands in which some hexagonal ordering may be resolved. These islands may be desorbed by annealing leaving the monolayer in tact. We also discuss the morphology which results following the deposition of $C_{59}N$ and C_{60} on annealed monolayers.

For these experiments pieces of Si(111) (p-type, 1 Ω cm) were loaded into an ultra-high vacuum (UHV) system, outgassed overnight at 600°C, flash annealed at 1200°C then allowed to cool to room temperature. This results in a clean defect free 7x7 reconstruction. $C_{59}N$ is then deposited from a Knudsen cell at a typical deposition rate of 1 monolayer (ML) per hour. STM images of the surface were recorded in constant current mode using electrochemically etched W tips.

Figure 1 shows an STM image of the surface following the deposition of close to 1ML of $C_{59}N$. Individual adsorbed molecules may be resolved in the monolayer (intermediate contrast level). The regions of darker contrast correspond to the underlying Si surface (i.e. gaps in the adsorbed monolayer) and the brightest features are adsorbed 2nd layer $C_{59}N$ molecules. Images such as Fig. 1 show that a $C_{59}N$ monolayer grows to near completion prior to the formation of 2nd layer islands. This implies that $C_{59}N$ incident on a partially completed monolayer is able to diffuse until it is adsorbed at a site on the Si surface. Similar behaviour is observed following the deposition of C_{60} [10]. However one difference between the surface shown in Fig. 1 and the equivalent surface following the deposition of C_{60} is the presence of many

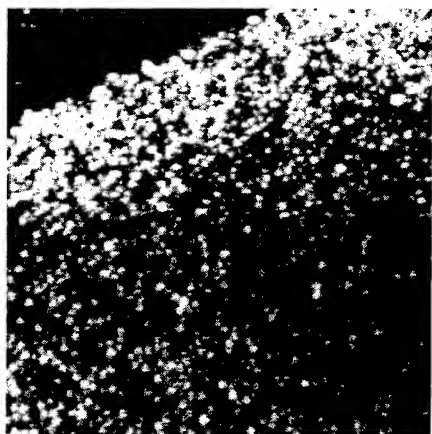


Figure 3. STM image following annealing of sample with multilayer coverage of C₅₉N. Image shows C₅₉N monolayer remaining on surface. Scan size and parameters - 40nm x 40nm, -3.0V, 0.3nA

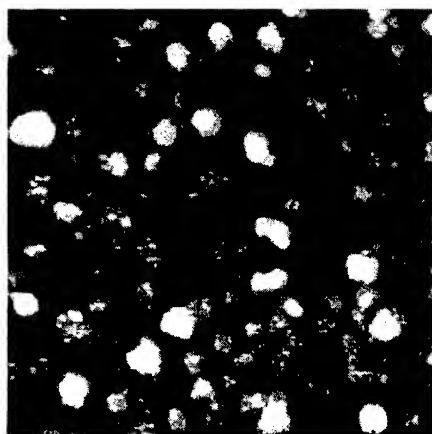


Figure 4. STM image following deposition of ~10ML of C₅₉N on annealed C₅₉N monolayer. Scan size and parameters 300nm x 300nm, -5.0V, 0.1nA

isolated 2nd layer C₅₉N molecules. This implies that there are some sites where C₅₉N is adsorbed sufficiently strongly to inhibit diffusion at room temperature.

Figure 2 shows an image of the surface following the deposition of ~10ML of C₅₉N. This image reveals that that C₅₉N forms islands on the C₅₉N monolayer. These islands have a typical width of 20nm and height 4nm. Higher resolution images (lower part of Fig. 2) reveal that some islands have a smooth top layer and show some evidence for faceting. However there are other islands which appear rather more diffuse in the STM images. Thus it is clear that C₅₉N may diffuse across the adsorbed C₅₉N monolayer at room temperature.

The islands shown in Fig. 2 may be desorbed by annealing the sample at ~400°C. Figure 3 is an STM image of the surface following such an anneal. This image shows that following desorption of the higher layers the C₅₉N monolayer remains adsorbed on the Si surface, confirming that the monolayer is more strongly bonded to the Si than the higher C₅₉N layers. In addition the monolayer seems more ordered following annealing (compare Figs. 1 and 3).

The annealed monolayer may itself be used as a template for further growth of C₅₉N. Figure 4 shows an STM image taken after the deposition of ~10ML of C₅₉N on an annealed monolayer. There are clear similarities with Fig. 2 although the typical island width is larger, 30nm. In addition many more islands display a flat terrace like top surface and more pronounced faceting. It is likely that these differences are

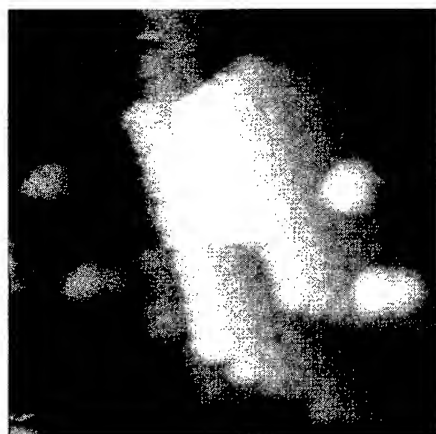


Figure 5. High resolution zoom of Fig. 4 showing hexagonal ordering within a $C_{59}N$ island. Zoomed area $20\text{nm} \times 20\text{nm}$

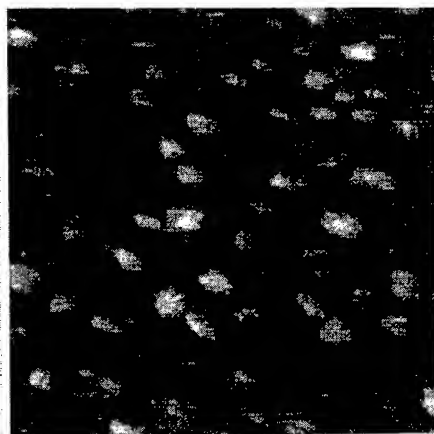


Figure 6. STM image showing surface morphology following the deposition of $\sim 10\text{ML}$ of C_{60} on annealed $C_{59}N$ monolayer. Scan size and parameters - $300\text{nm} \times 300\text{nm}$, -6.5V , 0.1nA .

related to the enhanced order of the annealed monolayer which acts as a substrate for the islands in Fig. 4. A zoom of part of Fig. 4 (see Figure 5) shows a $C_{59}N$ island at higher resolution. In this image the hexagonal ordering of the molecules in the island is very clear. The intermolecular spacing is found to be $1.0 \pm 0.05\text{nm}$, the same value, within experimental error as observed for C_{60} and for bulk $C_{59}N$ [4]. The separation of the cages in dimerised $(C_{59}N)_2$ is 9.4nm [4]. While the resolution limits of our STM preclude the differentiation of intra- and inter-dimer separations with confidence, previous photoemission results provide clear evidence for the presence of dimers in films with this thickness and morphology. It is natural to assume, therefore, that dimerisation has occurred in the ordered islands.

In many respects the island in Fig. 5 resembles a C_{60} island. However one important difference is the presence in Fig. 5 of a number of isolated pairs of molecules - for example the two pairs on the uppermost terrace and several pairs on the left hand side of the image. No such pairs are observed for C_{60} growth. This may be attributed to the fact that the C_{60} - C_{60} interaction is rather weak and so the lifetime of such a pair at room temperature is $\sim 10^{-7}\text{s}$. The presence of $C_{59}N$ - $C_{59}N$ pairs implies a stronger interaction. The centre-centre separation of these pairs varies from $\sim 1.0 \pm 0.2\text{nm}$ to $1.6 \pm 0.2\text{nm}$ and it is possible that some of these pairs correspond to dimerised $(C_{59}N)_2$.

Finally we show in Figure 6 the morphology observed following the deposition of C_{60} on the annealed $C_{59}N$ monolayer. The C_{60} islands are clearly larger

with some terraces extending over 80nm. The islands are very similar to those grown on an equivalent annealed C_{60} monolayer.

Overall we have presented a set of data which reconciles the presence of dimerised $(C_{59}N)_2$ with the impingement on a growing surface of $C_{59}N$ monomers. The $C_{59}N$ first forms a strongly adsorbed monolayer. Further $C_{59}N$ which impinges on this monolayer is free to diffuse and form ordered islands in which dimerisation may occur. In many respects the morphology is similar to that observed for C_{60} growth, although there is clear evidence that, as expected, the intermolecular interactions are greater for $C_{59}N$ than for C_{60} .

This work was supported by the UK Engineering and Physical Sciences Research Council. NT acknowledges support from the EU in the form of a Marie Curie fellowship.

References

1. Y. Chai et.al., J. Phys. Chem. **95** 7564 (1991).
2. R.D. Johnson et.al., Nature **355** 239 (1992); D.S. Bethune et.al., Nature **366** 123 (1993).
3. W. Andreoni, F. Gygi and M. Parrinello, Chem. Phys. Lett. **190** 159 (1992).
4. J.C. Hummelen, B. Knight, J. Pavlovich, R. Gonzalez and F.Wudl, Science **269** 1554 (1995)
5. C.M. Brown, L. Cristofolini, K. Kordatos, K. Prassides, C. Bellavia, R. Gonzalez, M. Keshavarz-K., F. Wudl, A.K. Cheetham, J.P. Zhang, W. Andreoni, A. Curioni, A.N. Fitch and P. Pattison, Chem. Mater. **8** 2548 (1996).
6. T. Pichler, M. Knupfer, M.S. Golden, S. Haffner, R. Friedlein, J. Fink, W. Andreoni, A. Cuironi, M. Keshavarz-K., C. Bellavia-Lund, A. Sastre, J-C. Hummelen and F. Wudl, Phys. Rev.Lett. **78** 4249 (1997).
7. W. Andreoni, A. Curioni, K. Holczer, K. Prassides, M. Keshavarz-K. J-C. Hummelen and F. Wudl, J. Am.Chem.Soc., **118** 11335 (1996).
8. M.J. Butcher et.al., unpublished.
9. Ch. Sommerhalter et.al., paper presented at ICSS-10, Birmingham 1998.
10. D.M. Chen, J. Chen and D. Sarid, Phys. Rev.B**50** 10 905 (1994).

Homonuclear bonds in BN clusters?

P.W. Fowler,^a K.M. Rogers,^a T. Heine,^a and G. Seifert^b

^a School of Chemistry, University of Exeter, Stocker Road, Exeter, EX4 4QD, UK

^b Universität-GH Paderborn, FB6 Theoretische Physik, D-33095 Paderborn, Germany

Abstract. Optimisations starting from fully alternant B_xN_x ($x = 3, 4$) graphs using DFTB and DFT methods often converge to molecules with N–N links, suggesting that such structures may be competitive for boron nitride clusters, cages and molecules.

Introduction. If we are to judge from bulk materials, alternation of atoms will play an important role in the stability of heteronuclear clusters. This has implications for cluster structures as, for example, the odd-membered cycles of a fullerene-like cage preclude its realisation with a heteronuclear pair of atoms on every edge. Topical cases are BN systems, where cages must be built either from even rings only (*e.g.* hexagons and squares) or incorporating BB or NN contacts. In the present note, we explore the role of alternation in small B_xN_x clusters.

Isomer generation. All possible alternant isomers of formula B_3N_3 and B_4N_4 were constructed as graphs obeying selected mathematical rules [1]. It was decided to at first confine attention to alternant isomers (boron atoms bonded only to nitrogens and *vice versa*) as it was assumed that the most stable isomers would be of this nature. A complete study of all alternant and non-alternant isomers becomes impossibly large. The rules for each isomer set are: (i) all graphs must be alternant and fully connected; (ii) there must be equal numbers of vertices in the two alternant sets; (iii) the maximum degree (valency) of each vertex (atom) is three; (iv) if two distinct isomers are generated by swapping the two alternant sets of vertices, then both are considered.

Application of these rules to B_3N_3 and B_4N_4 generates 13 (10) and 56 (38) distinct isomers, respectively, with the numbers of geometrically distinct isomers given in brackets. The isomers are labelled in ascending order of maximum eigenvalue of their adjacency matrices, resulting in an ordering which reflects the amount of branching. Thus, for B_4N_4 , isomer 1 is the unbranched chain and isomer 38 is the cube. Graphs in which swapping of the two sets of atoms results in distinct isomers take the same numerical label but with additional letter *a* or *b*.

Optimisation. All isomer structures were pre-optimised using molecular mechanics, parameterised to the B–N bond length in hexagonal boron nitride. All bond angles were maximised to ensure maximum symmetry of the starting geometry; divalent atoms were made linear, trivalent atoms as near trigonal as possible.

The main tool for the full survey of structures is the DFTB (density-functional

Molecular graph		DFTB results	
		Structure	Energy (eV)
1	$(D_{\infty h} : C_{\infty v})$		1.13
2a	$(C_{2v} : C_{2v})$		1.95
2b	$(C_{2v} : C_{2v})$		6.10
3	$(D_{2h} : C_{2v})$		3.86
4	$(D_{6h} : D_{3h})$		0.00
5a	$(C_{2v} : C_{2v})$		2.67
5b	$(C_{2v} : C_{2v})$	1	—
6	$(C_{2v} : C_s)$	1	—
7	$(D_{2h} : C_{2v})$	4	—
8a	$(C_{2v} : C_{2v})$	5a	—
8b	$(C_{2v} : C_{2v})$		7.15
9	$(D_{2d} : C_{2v})$	5a	—
10	$(D_{6h} : D_{3h})$		6.04

Table: Alternant isomers of B_3N_3 , showing starting and converged structures. Black (white) circles denote nitrogen (boron) atoms. Each graph is labelled $n (x : y)$, where n is the numerical label, x is the maximum symmetry group of the undecorated molecular graph and y is the maximum symmetry group of the B,N-labelled graph. DFTB energies are given relative to the most stable isomer (no. 4) in eV, for those isomers that converged. Structure entries marked with a number indicate that on optimisation the graph converged to a structure already in the list.

tight-binding) method [2,3]. This approach has been applied for carbon clusters [2] and cages [4,5] and is known to give a realistic description of energies and structure for BN systems, both solid state and molecular [6-8]. For a number of structures, more sophisticated full density-functional (gradient-corrected) calculations were performed with the deMon package [9], using the PD91 GGA exchange-correlation functional and TZVP basis set.

Results. All isomers of B_3N_3 and B_4N_4 were optimised with the DFTB method. From the 13 alternant B_3N_3 starting graphs, 8 isomeric minima were found (see Table). Similarly, of the 56 initial alternant isomers of B_4N_4 , 28 optimised to distinct minima with the DFTB model (see Figure 1).

As the table and figure show, many of the isomers rearranged considerably from their starting geometries. In general, the linear and simple branched isomers were found to lie in minima on the potential energy surface, whereas the more highly connected isomers tended to collapse to more open structures. It is often clear how these changes occurred from inspection of their starting geometries (see Table).

Even more striking is the observation that in many cases, two close but unconnected nitrogen atoms have moved together in the DFTB optimisation, thus forming a bond and breaking the alternation rule. Examples of this are isomers 3 and 8b (B_3N_3) and isomers 4, 7, 23b, 25, 27b and 32a (B_4N_4). In these cases, the rearranged clusters contain an odd-membered, non-alternant ring. Other plausible non-alternant structures might also optimise to new minima. This is a strong indication that non-alternant structures have to be considered.

Inspection of the DFTB results for B_3N_3 and B_4N_4 shows that in both cases, the unbranched monocyclic ring is the most stable isomer by a considerable margin. Many other trends can be identified, but it is clear that most isomers are very high in energy and poor candidates for stable cluster structures. Some of the isomers containing N-N bonds are next in stability to the branched ring (8a) and linear chain (1) for B_4N_4 . Of the non-alternants, isomers 32a and 33b that each contain a seven-membered ring are lowest in energy.

Highly-connected, cage-like structures tend to collapse to ring or branched-linear geometries under DFTB optimisation although, *e.g.* the cube (isomer 38) for B_4N_4 does lie in a very shallow minimum. The stabilities of small, *alternant* B_xN_x clusters follow the sequence: monocyclic ring > branched rings > linear chain > chains with branching at N > chains with branching at B > cage-like structures.

In all cases where the starting geometry has collapsed to an odd-membered ring, the resulting homonuclear bond connects two nitrogen atoms, never two boron atoms. Any branching from the rings occurs at nitrogen, satisfying its trigonal preference. Some useful rules for predicting the stability of clusters containing homonuclear bonds can be drawn from the results and were confirmed by further calculations on selected B_5N_5 and B_6N_6 isomers: (i) at fixed nuclearity, unbranched, even-membered rings will generally be more stable than branched, odd-membered rings, regardless of the number of homonuclear bonds; (ii) the stability of even-membered monocyclic rings will decrease with the length of any included homonuclear segment(s).

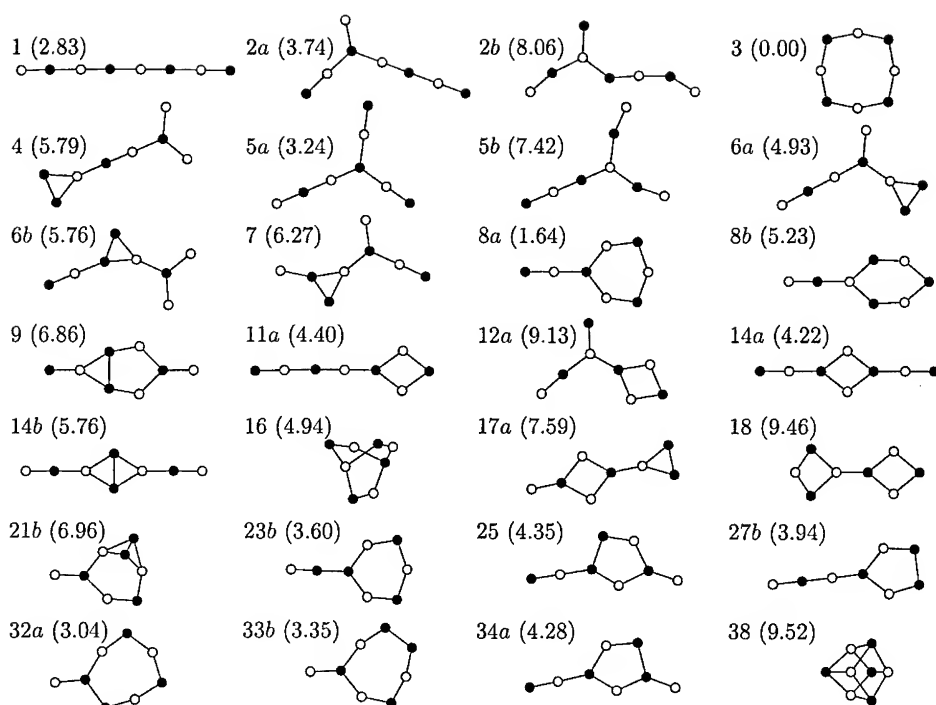


Figure 1: Converged structures for B_4N_4 . DFTB energies are given relative to the most stable isomer (no. 3) in eV. All were started from alternant graphs but 14 formed N–N bonds during optimisation. The numerical label of each structure indicates the starting alternant graph.

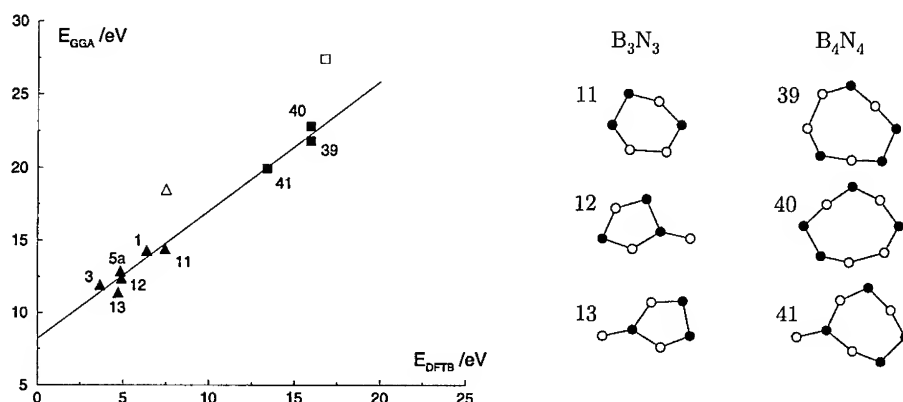


Figure 2: Comparison of DFTB and full DFT (GGA) energies for selected isomers B_xN_x , defined with respect to separated BN pairs. Triangles denote $x = 3$, squares $x = 4$; open symbols correspond to the fully alternant monocycle. Isomer numbers refer to the converged structures of the table (alternant starting geometries) and to the structures at the right for non-alternants. The regression line excludes the two alternant rings.

As a check on the reliability of the results and conclusions drawn from the DFTB calculations, a number of B_xN_x isomers were also optimised in the full DFT approach described above. The test set of isomers comprises several of the structures found within the original generation process, plus a selection of stable non-alternant systems containing one N–N bond (see Figure 2).

The results are displayed as binding energies with respect to dissociation to BN pairs, calculated at the same level of theory. DFTB and DFT (GGA) treatments both give the fully alternant ring as the most stable structure for B_3N_3 and B_4N_4 and the energetic sequence of isomers is in qualitative agreement between the two methods. However, the fully alternant ring appears to be more stable with respect to the other isomers in the full DFT treatment. If we exclude these two rings, there is a good correlation between DFTB and DFT (GGA) binding energies.

An important result of the survey described here is that isomers containing one or sometimes two adjacent N–N bonds could lie in minima on the potential surface. We have seen that such structures are also minima at the full DFT level. It might be thought that isomers of this type would be especially vulnerable to fragmentation by extrusion of N_2 . Simple energy comparisons show that in many cases, there is no gain on direct elimination of N_2 . For example, energy of the fragmentation of isomer 11 of B_3N_3 (Figure 2) to N_2 and linear B–N–B–B is positive in DFTB (+1.02 eV) and higher in full DFT (+3.21 eV).

Conclusion. We have shown that a study confined to alternant structures misses many low-energy forms of B_xN_x and that in particular, homonuclear N–N bonding does not always carry a prohibitive energetic penalty. Although fully alternant rings are dominant in this small size range, non-alternant BN systems may become more important for large clusters and nanotube caps [7]. It will be interesting to see how these findings generalise to other heteronuclear systems, *e.g.* GaN.

REFERENCES

1. The *nauty* program written by B.D. McKay, including the graph generators *makeg* and *makebg* are available from <http://cs.anu.edu.au/people/bdm/nauty/>
2. D. Porezag, T. Frauenheim, T. Köhler, G. Seifert and R. Kaschner, *Phys. Rev. B*, 1995, **51**, 12947.
3. G. Seifert, D. Porezag and T. Frauenheim, *Int. J. Quantum Chem.*, 1996, **58**, 185.
4. P.W. Fowler, T. Heine, D.E. Manolopoulos, D. Mitchell, G. Orlandi, R. Schmidt, G. Seifert and F. Zerbetto, *J. Phys. Chem.*, 1996, **100**, 6984.
5. P.W. Fowler, T. Heine, D. Mitchell, G. Orlandi, R. Schmidt, G. Seifert and F. Zerbetto, *J. Chem. Soc., Faraday Trans.*, 1996, **92**, 2203.
6. P.W. Fowler, T. Heine, D. Mitchell, R. Schmidt and G. Seifert, *J. Chem. Soc., Faraday Trans.*, 1996, **92**, 2197.
7. P.W. Fowler, K.M. Rogers, G. Seifert, M. Terrones and H. Terrones, *Chem. Phys. Lett.*, 1999, **299**, 359.
8. J. Widany, T. Frauenheim, T. Köhler, M. Sternberg, D. Porezag, G. Jungnickel and G. Seifert, *Phys. Rev. B*, 1996, **53**, 4443.
9. A. St-Amant and D.R. Salahub, *Chem. Phys. Lett.*, 1990, **169** 387. See also the website <http://www.cerca.umontreal.ca/deMon/> for a description of the deMon program.

Synthesis and Characterisation of Organometallic Compounds of Fullerene Derivatives

Nikos Tagmatarchis and Kosmas Prassides

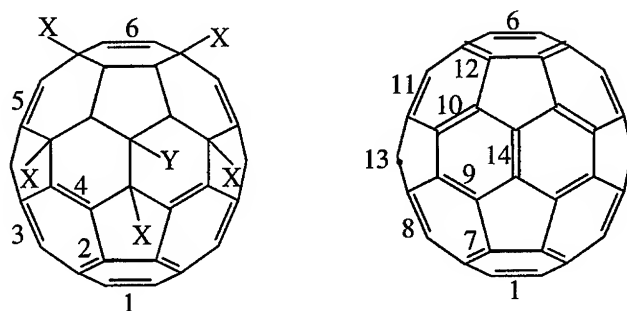
*School of Chemistry, Physics and Environmental Science, University of Sussex, Falmer,
Brighton BN1 9QJ, UK*

The synthesis of a series of platinum and palladium organometallic fullerene derivatives with stoichiometries $[\{M(PPh_3)_2\}_n(\eta^2-C_{60}Ph_5H)]$ and $[\{Pt(PPh_3)_2\}_n(\eta^2-C_{60}Cl_6)]$, ($M = Pt, Pd$; $n = 1, 2$) was achieved upon treatment of $C_{60}Ph_5H$ and $C_{60}Cl_6$ with $M(PPh_3)_4$. Single isomers, retaining the C_s symmetry of the starting hexasubstituted fullerene derivatives are formed in all cases. In addition, the first organometallic complex of azafullerene, $(C_{59}N)_2$ was synthesised and characterised by ^{31}P NMR spectroscopy.

Low-valent transition-metal complexes are well known to react with electron-deficient alkenes. As C_{60} behaves in a similar fashion, Group 10 transition metals provide promising reagents for the facile synthesis of a variety of organometallic fullerene complexes¹. A series of such π -complexes of C_{60} has been already prepared and characterised (*e.g.* $[M(\eta^2-C_{60})(PR_3)_2]$, $[M(\eta^2-C_{60})\{P(OR)_3\}_2]$; $M = Ni, Pt, Pd$; $R = Ph, Et, Bu$)²⁻⁵. As it was expected, the metal was found to add preferentially only to C-C double bonds of the fullerene framework that comprise 6:6 (hexagon-hexagon) ring junctions. Subsequent experiments have also shown that complexes containing up to six metal atoms could be formed and characterised^{1,6}.

Upon the addition of one equivalent of $[M(PPh_3)_4]$ ($M = Pt, Pd$) to $C_{60}Ph_5H$, fourteen possible different isomers may result (Scheme 1). The ^{31}P NMR spectrum of the Pt complex, A shows a singlet with satellites due to coupling of the ^{31}P nucleus to the spin- $1/2$ ^{195}Pt isotope. This implies that the two ligated phosphorus atoms are chemically equivalent. Eleven isomers (2-5, 7-13) among the fourteen possible ones do not retain the C_s symmetry of the molecule and thus can be excluded – they contain non-equivalent phosphorus atoms, which would have led to a pair of doublets in the ^{31}P NMR spectrum, each exhibiting ^{195}Pt satellites. Evidence for the formation of a single isomer is provided by the 1H NMR spectrum of A; this shows clearly a distinct singlet, integrated for one proton at δ 5.04. As a result, we conclude that the resulting complex is formed by binding of the metal to one of the C-C double bonds of the fullerene, numbered 1, 6 and 14 in Scheme 1.

Scheme 1. Sites of possible metal co-ordination on the fullerene skeleton of hexasubstituted derivatives of C_{60} .



1. $X = Y = Cl$
2. $X = Ph, Y = H$

FRONT VIEW

BACK VIEW

Fourteen different double bonds for possible complexation of the m
Double bond 13 is perpendicular to the plane

Possible positions for single co-ordination of metal: 1, 6 and 14
Position for double co-ordination of metal: 1 and 6

Addition of two equivalents of $[M(PPh_3)_4]$ ($M = Pt, Pd$), to $C_{60}Ph_5H$ leads to the formation of an organometallic compound, **B** – in the case where $M = Pt$ – whose ^{31}P NMR spectrum displays the same pattern as that for the singly substituted product, **A** – two singlets together with their ^{195}Pt satellites. The presence of a singlet hydrogen resonance at δ 5.04 in the 1H NMR spectrum again implies the formation of a single isomer. As before, the resulting complex, $[\{M(PPh_3)_2\}_2(\eta^2-C_{60}Ph_5H)]$ is highly symmetric with the possible binding sites of the two metal atoms identified as the C-C double bonds numbered 1 and 6 in Scheme 1.

The complexes, $[Pt(PPh_3)_2(\eta^2-C_{60}Cl_6)]$ (**C**) and $[\{Pt(PPh_3)_2\}_2(\eta^2-C_{60}Cl_6)]$ (**D**) were also synthesised. In contrast, the isolation of the corresponding Pd complexes was not successful as in the previous cases, probably because the resulting complexes are very labile. Again the C_s symmetry of the fullerene derivative is retained upon co-ordination of the Pt metal atom. Presumably in this case, the co-ordination is facilitated by interaction between the Cl atoms and the co-ordinated PPh_3 units.

Complexation of Pt with azafullerene, $(C_{59}N)_2$ is somewhat different. Addition of one equivalent of $[Pt(PPh_3)_4]$ – or half an equivalent per $C_{59}N$ monomer unit – led to a

compound **E**, with low symmetry, as revealed from the ^{31}P NMR. – a pair of doublets, each exhibiting ^{195}Pt satellites. This implies that the two ligated phosphorus atoms are not chemically equivalent.

Examination of the stability of this series of complexes with time shows that they are unstable - the Pd complexes are much less stable than the Pt ones, especially in solution, and they gradually return to the original starting materials.

In conclusion, we have synthesised and characterised by NMR, UV and IR spectroscopy and mass spectrometry a series of highly symmetric organometallic compounds of phenylated and chlorinated fullerene derivatives as well with a platinum complex of the azafullerene with low molecular symmetry.

Experimental Section

Addition of one or two equivalents of $[\text{M}(\text{PPh}_3)_4]$, ($\text{M} = \text{Pt}, \text{Pd}$) to a 0.01 M solution of $\text{C}_{60}\text{Ph}_5\text{H}^{7,8}$ or $(\text{C}_{59}\text{N})_2$ in dry toluene under nitrogen resulted in the formation of a dark brown or deep green mixture, respectively. Following overnight stirring and dilution with dry hexane, the resulting precipitate was immediately washed with small portions of dry hexane and dried in vacuo to leave either a light-brown solid for the Pt derivatives or a dark brown one for the Pd complexes (yield: 88-93%).

Selected spectroscopic data for the Pt complexes **A**, **B**, **C**, **D** and **E**.

A: ^{31}P NMR (121.7 MHz, THF- d_8) δ : 22.0 (s, 2P, $J_{\text{Pt-P}} = 3883$ Hz); ^1H NMR (300MHz, THF- d_8) δ : 5.04 (s, 1H), 7.58-7.46 (m, 6H), 7.36-7.33 (m, 4H), 7.16-6.91 (m, 45H); IR (KBr, cm^{-1}): 2952, 2922, 2835, 1538, 1494, 1434, 1385, 1096, 1030, 846, 802, 743, 691, 661, 619, 515; UV (λ_{max} , nm): 319.8, 367.5, 420.0, 485.3, 615.0; MS (m/z): 1826 (M^+).

B: ^{31}P NMR (121.7 MHz, THF- d_8) δ : 22.2 (s, 2P, $J_{\text{Pt-P}} = 3883$ Hz), 31.1 (s, 2P, $J_{\text{Pt-P}} = 3946$ Hz); ^1H NMR (300MHz, THF- d_8) δ : 5.04 (s, 1H), 7.67-6.95 (m, 85H); IR (KBr, cm^{-1}): 2955, 2920, 2843, 1494, 1480, 1435, 1311, 1213, 1200, 1109, 1094, 1007, 999, 847, 801, 720, 743, 692; UV (λ_{max} , nm): 310.4, 477.6, 615.5; MS (m/z): 2446 (M^+).

C: ^{31}P NMR (121.7 MHz, THF- d_8) δ : 21.1 (s, 2P, $J_{\text{Pt-P}} = 3685$ Hz); ^1H NMR (300MHz, THF- d_8) δ : 7.52-7.44 (m, 12H), 7.38-7.20 (m, 10H), 7.11-6.94 (m, 8H); IR (KBr, cm^{-1}): 2924, 2843, 1480, 1435, 1331, 1310, 1184, 1157, 1119, 1097, 1027, 999, 923, 858, 847, 817, 753, 744, 706, 691; UV (λ_{max} , nm): 328.5 446.8 615.1; MS (m/z): 1544 (M-3Cl^+).

D: ^{31}P NMR (121.7 MHz, THF- d_8) δ : 21.1 (s, 2P, $J_{\text{Pt-P}} = 3685$ Hz), 29.2 (s, 2P, $J_{\text{Pt-P}} = 4050$ Hz); ^1H NMR (300MHz, THF- d_8) δ : 7.49-7.37 (m, 24H), 7.22-7.09 (m, 36H); IR (KBr, cm^{-1}): 2925, 2843, 1664, 1630, 1478, 1431, 1152, 1093, 1026, 997, 923, 860, 850, 823, 744, 705, 689; UV (λ_{max} , nm): 330.3, 406.0; MS (m/z): 2333 (M-Cl^+).

E: ^{31}P NMR (121.7 MHz, THF- d_8) δ : 27.2 (d, 1P, $J = 34.7$ Hz, $J_{\text{Pt-P}} = 4023$ Hz), 26.9 (d, 1P, $J = 34.7$ Hz, $J_{\text{Pt-P}} = 4023$ Hz); ^1H NMR (300MHz, THF- d_8) δ : 7.62-7.02 (m, 30H).

Acknowledgement.

N.T. thanks the European Union for the award of a Marie Curie Fellowship.

References and Notes

1. Fagan, P. J.; Calabrese, J. C.; Malone, B. *Acc. Chem. Res.* **1992**, 25, 134.
2. Brady, F. J.; Cardin, D. J.; Domin, M. J. *Organometal. Chem.* **1995**, 169, 491.
3. Bashilof, V. V.; Petrovskii, P. V.; Sokolov, V. I.; Lindeman, S. V.; Guzey, I. A.; Struchkov, Y. T. *Organometallics* **1993**, 12, 991.
4. Fagan, P. J.; Calabrese, J. C.; B. Malone, B. *Science* **1991**, 252, 1160.
5. Stephens, A. H. H.; Green, M. L. H. *Adv. Inorg. Chem.* **1997**, 44, 1.
6. Fagan, P. J.; Calabrese, J. C.; B. Malone, B. *J. Am. Chem. Soc.* **1991**, 113, 9408.
7. Birkett, P. R.; Avent, A. G.; Darwish, A. D.; Kroto, H. W.; Taylor, R.; Walton, D. R. M. *J. Chem. Soc., Chem. Commun.* **1993**, 1230.
8. Avent, A. G.; Birkett, P. R.; Crane, J. D.; Darwish, A. D.; Langley, G. J.; Kroto, H. W.; Taylor, R.; Walton, D. R. M. *J. Chem. Soc., Chem. Commun.* **1994**, 1463.

Non-IPR Fullerenes: C₃₆ and C₇₂

Zdeněk Slanina,^a Xiang Zhao,^a Filip Uhlík^b and Eiji Ōsawa^a

^a*Laboratories of Computational Chemistry & Fullerene Science
Department of Knowledge-Based Information Engineering
Toyohashi University of Technology, Toyohashi 441-8580, Japan*

^b*Department of Physical and Macromolecular Chemistry
Faculty of Science, Charles University
Albertov 2030, CZ-128 40 Prague 2, Czech Republic*

Abstract. Non-IPR structures can play an important role not only in smaller fullerene systems but also with some higher fullerenes. This paper reports computations on C₃₆ and C₇₂. While for C₃₆ the related cages must be non-IPR structures, C₇₂ in principle allows for one IPR cage. Nevertheless, even for C₇₂ the structure prevailing at high temperatures is still a non-IPR species.

INTRODUCTION

The IPR structures have been considered most frequently in fullerene science (1). However, other than IPR structures can play a role under special circumstances. Hence, we should certainly not consider the IPR conjecture as a rule without exceptions. It was already reported that the rule did not work for a charged C₆₀ (2) and also for Ca@C₇₂ (3). This paper deals with the computed IPR/non-IPR interplay for the pristine C₇₂. There is just one IPR structure, *D*_{6d}, and this isomer is the system ground state. However, at elevated temperatures the equilibrium mixture is dominated by a *C*₂ isomer with one pentagon-pentagon junction. Hence, the IPR rule does not seem to control the C₇₂ relative stabilities at high temperatures. In the region below C₆₀ no IPR structures are possible. Moreover, *quasi*-fullerenes can be of some importance, too, as documented (4) on C₃₂. The ground state of C₃₂ is a *D*_{4d} *quasi*-fullerene (two four-membered rings, eight pentagons, eight hexagons), though at higher temperatures altogether five structures are significantly populated. However, for C₃₆ our computations agree with conclusions (5) of the recent ¹³ NMR spectroscopy. The computations suggest that the computed energetics itself is not always able to produce a good agreement with observations. However, if entropy terms are considered, too, theory-experiment agreement can be obtained.

COMPUTATIONS

At the very first stage, the cages are generated by a topological program (4), then optimized at a molecular mechanics level and finally reoptimized with the semiempirical SAM1 method implemented in the AMPAC package (6)). In the SAM1 optimized geometries, the harmonic vibrational analysis is carried out. The separation energetics is further checked at *ab initio* level, e.g., Hartree-Fock (HF) SCF computations in the 4-31G basis set (HF/4-31G) or density-functional computations at the B3LYP/6-31G* level using the G94 program package (7). Finally, rotational-vibrational partition functions are constructed from the computed data and temperature-dependent relative concentrations are evaluated. A special attention is paid to the symmetry and chirality contributions into the partition functions. Symmetry of the cages is extracted using a procedure developed (8) recently.

RESULTS AND DISCUSSION

Recently, Zettl *et al.* isolated (5) a new solid fullerene, C_{36} , and concluded a D_{6h} cage structure. These C_{36} observations represent an interesting challenge to computations. There are just fifteen conventional fullerene cages for C_{36} , all being non-IPR. In order to reduce the number of pentagon-pentagon junctions, one can consider four-membered and/or seven-membered rings, i.e., *quasi*-fullerenes. If the topological search is limited to conventional fullerenes and to *quasi*-fullerenes with one or two squares (no heptagon), one heptagon (no square), or one square and one heptagon, the total number of generated cages is 598.

Our highest approach to energetics of C_{36} is represented by the B3LYP/6-31G*//SAM1 treatment. We can ignore the structures especially high in the potential energy - only the structures with the separation energy less than 150 kJ/mol are considered further. This bracketing leads to about twelve low-energy structures. Among them, seven are the conventional fullerenes. It is convenient to classify the cages by a ring index, a vector containing the counts n_i of the rings considered: n_4, n_5, n_6, n_7 . Out of the remaining five *quasi*-fullerenes, three isomers are of the 1,10,9,0 type (one square), one is the 1,11,7,1 type (one square, one heptagon), and one is the 2,11,7,0 type (two squares, no heptagon).

It turns out that in the C_{36} system there are a few cases of considerable differences between the SAM1 and B3LYP/6-31G* approaches. Nevertheless, the ground state is always represented by the conventional fullerene with the D_{2d} symmetry. There is also one high symmetry species, a conventional D_{6h} fullerene. In fact, the D_{6h} point group is a topological symmetry, however, our more flexible symmetry diagnostic tool (8) gives only a C_{6v} or even C_{2h} symmetry. We are actually dealing with a Jahn-Teller distortion owing to the degenerate frontier orbitals. While in the SAM1 and HF/4-31G approaches the structure is relatively high in energy, it drops in the B3LYP/6-31G*//SAM1 treatment - namely to

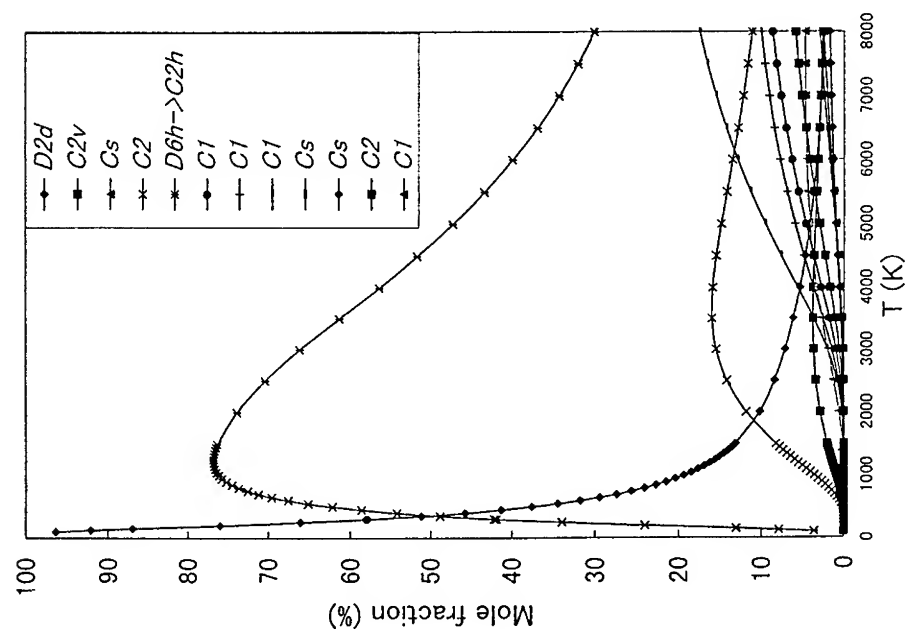


FIGURE 1. The B3LYP/6-31G**/SAM1 computed relative concentrations of the twelve lowest isomers of C_{36} .

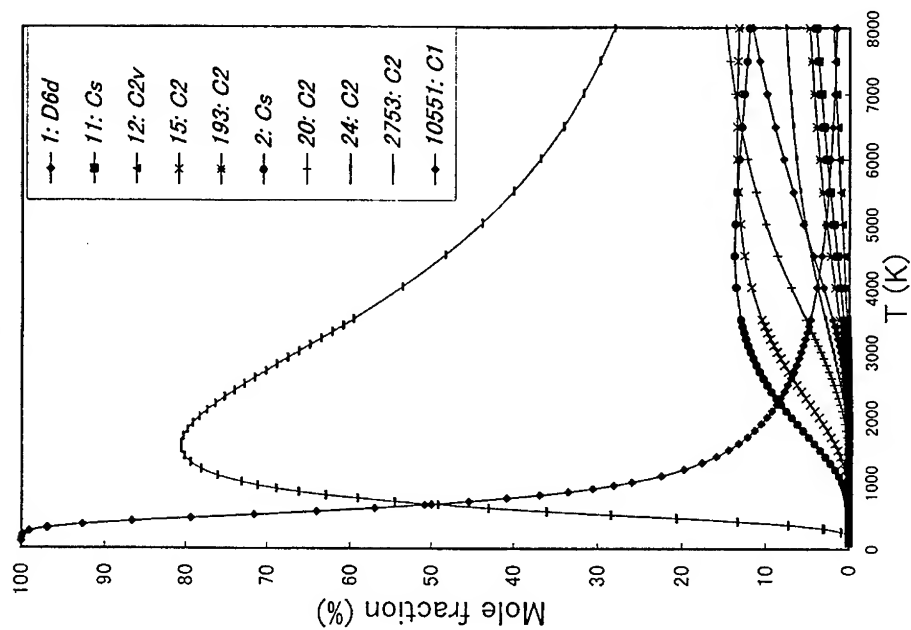


FIGURE 2. The SAM1 computed relative concentrations of IPR (D_{6d}) and selected non-IPR isomers of C_{72} .

only 23 kJ/mol above the ground state. Hence, the structure becomes the second lowest. If we now perform the complete B3LYP/6-31G* geometry optimization, the D_{6h} - D_{2d} separation energy decreases to mere 15 kJ/mol.

As fullerenes are formed at high temperatures, entropy effects are possibly important. It turns out that in the most sophisticated computational approximation used here, just two structures are really important in the region of higher temperatures, the conventional fullerenes D_{6h} and D_{2d} - see Fig. 1. Although the D_{2d} ground state has to prevail at low temperatures, the stability order is reversed at moderate temperatures. Hence, a good agreement with the observation (5) is obtained. Our best treatment predicts a high relative population of the D_{6h} cage, more than two or even three times higher than the population of the second most abundant isomer. The theoretical prediction is however based on the presumption of the inter-isomeric thermodynamic equilibrium. Moreover, an effective synthetic temperature is unclear. In overall, the treatment reveals that *quasi*-fullerenes are not particularly important for C_{36} . The computations also indicate that the separation energies can in some cases be quite method-sensitive. Finally, the entropy contribution actually explains why the species, which is not the system ground state, still comes as the observed isomer.

Let us now move to C_{72} , a not yet isolated species. For this system, there is just one IPR cage, actually exhibiting a high symmetry, D_{6d} . Fig. 2 gives the SAM1 computations of the temperature evolution of the isomeric relative stabilities for the system. The IPR D_{6d} structure, in spite of being the system ground state, decreases its relative population pretty fast. At higher temperatures the equilibrium isomeric mixture is in fact governed by a C_2 isomer with one pentagon-pentagon junction. This result is a further indication that non-IPR structures cannot always be ignored.

ACKNOWLEDGMENTS

Work is supported by the Ministry of Education, Science and Culture in Japan.

REFERENCES

1. Slanina, Z., Zhao, X., and Ōsawa, E., in Computational Studies of New Materials, eds. D. A. Jelski and T. F. George, Singapore: World Sci. Publ., 1999.
2. Fowler, P. W. and Zerbetto, F., Chem. Phys. Lett. **243**, 36 (1995).
3. Kobayashi, K., Nagase, S., Yoshida, M., and Ōsawa, E., J. Am. Chem. Soc. **119**, 12693 (1997).
4. Zhao, X., Ueno, H., Slanina, Z., and Ōsawa, E., Rec. Advan. Chem. Phys. Fullerenes Relat. Mater. **5**, 155-166 (1997).
5. Piskoti, C., Yarger, J. and Zettl, A., Nature **393**, 771 (1998).
6. AMPAC 6.0, Shavnee, KS: Semichem, 1997.
7. Frisch, M. J., *et al.*, GAUSSIAN 94, Revision E.2, Pittsburgh, PA: Gaussian, Inc., 1995.
8. Sun, M.-L., Slanina, Z., Lee, S.-L., Uhlík, F., and Adamowicz, L., Chem. Phys. Lett. **246**, 66 (1995).

Effect of Alkali Doping on the Structural Stability of Solid C₃₆

A. Zettl, C. Piskoti, Jeffery C. Grossman, Marvin L. Cohen,
and Steven G. Louie

Department of Physics, University of California at Berkeley, and
Materials Sciences Division, Lawrence Berkeley National Laboratory,
Berkeley, CA 94720 U.S.A.

Abstract

We demonstrate that alkali-doping C₃₆ solids causes the C₃₆ cage molecules to be bonded less strongly to each other in the solid. Laser irradiation mass spectroscopy experiments show that for pure C₃₆ solid, no isolated C₃₆ subunits are observed in the ablated material, while for potassium-doped C₃₆, isolated C₃₆ molecules are readily produced by laser irradiation. Theoretical modelling shows that charge transfer from the alkali to the C₃₆ molecules greatly hinders C₃₆ dimer formation, consistent with these experiments.

In sharp contrast to the behavior of van der Waals solids formed from the more inert higher fullerenes such as C₆₀, the carbon-cage molecules in solid C₃₆ are tightly held together with covalent-like bonds. This relatively strong bonding configuration may have distinct advantages for practical applications. On the other hand, the same bonding character also makes it difficult to dissociate solid C₃₆ into its constituent C₃₆ molecules. Isolating individual C₃₆ molecular species from each other or from other molecular or atomic units is often desirable if not absolutely necessary for certain purification or characterization purposes.

In the original arc synthesis of C₃₆ molecules and solids, it was found that arc-generated carbon "soot" contained a sizable fraction of C₃₆ molecules¹. These species were identified by time-of-flight mass spectroscopy. In the mass spectroscopy method, a film of the fullerene-containing soot is irradiated by photons from a nitrogen laser, and the ejected material is ionized and accelerated through a mass spectrometer. The fact that this rather "violent" laser ablation works at all for C₃₆ is somewhat surprising; one might expect that the laser photons would break apart the C₃₆ molecules before pulling them intact from the solid. One possible reason for the success of the method is that the substantial amounts of amorphous carbon and higher-order fullerenes surrounding the C₃₆ molecules in the unpurified soot act as an energy absorbing and isolation matrix.

We here investigate the influence of a matrix on the laser-induced dissociation of solid C₃₆. We find that without an isolation matrix, lone C₃₆ molecules cannot easily be extracted from the solid via laser irradiation. We then show that introducing alkali metal into the C₃₆ solid prior to laser irradiation does allow for clean and highly efficient C₃₆ ablation from the solid. A theoretical investigation of C₃₆ intermolecular interactions indicates that uncharged C₃₆ molecules easily bond to one another to form dimers, while negatively charged C₃₆ molecules have a substantially higher energy barrier for dimerization and a higher bound state energy. These findings are consistent with the experimental laser-induced dissociation results on pure and alkali-doped solid C₃₆.

Pure C₃₆ samples were prepared using variations on a previously described method¹. 6mm POCO graphite rods were arced in a 400 torr He atmosphere using approximately 50A DC at 20-25V. The resulting sublimation product was brushed from the walls and loaded into a soxhlet extractor where higher fullerenes (C₆₀, C₇₀, etc) were removed by extraction with toluene. The C₃₆ was then extracted using pyridine. Care was taken to keep all materials under an argon atmosphere throughout all purification steps, and all solvents used were first dried by distilling over sodium.

Fig. 1a shows a laser desorption/ionization mass spectrum (negative ion acceleration configuration) of the purified C₃₆ solid. The laser wavelength is 337.1 nm with intensity close to threshold for observing a signal in the mass spectrum. The observed spectrum shows a very broad mass distribution peaked at about 120 carbon atoms. A sharp rise in the mass peak occurs at about 70-75 carbon atoms, which could be a signature of dimerized C₃₆ units. Conspicuously absent, however, is a peak that would correspond to 36 carbon atoms. Indeed, from Fig. 1 alone one might conclude that this sample contains no C₃₆ molecules whatsoever!

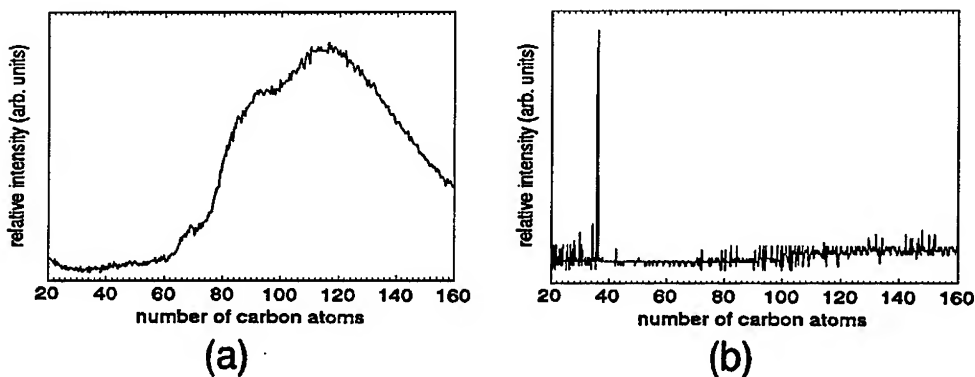


Fig. 1 Mass spectrum for a) pure C₃₆ solid and b) K-doped C₃₆ solid.

Our interpretation is that the sample used for Fig. 1 does contain C₃₆ but that it is simply too pure. The highly reactive C₃₆ molecules have bonded strongly to each other (i.e. the material has polymerized). With no matrix present to isolate the molecules or to aid in energy dispersal, no individual C₃₆ molecules can be readily ablated. This underscores the utility of an additional matrix in mass spectroscopy studies of solid C₃₆.

To further support the conjecture of strong spontaneous bonding in a purified C₃₆ solid, we have prepared a sample exactly as that used for Fig. 1a (i.e. a highly purified sample), but then added potassium to the solid. The potassium insertion was accomplished via a low temperature liquid ammonia technique to be described in detail elsewhere².

Fig. 1b shows the time-of-flight mass spectrum of the K_xC₃₆ compound. The spectrum shows a large reduction in the higher mass distribution of Fig. 1a, as well as a dramatic and very sharp peak at exactly at 36 carbon atoms, i.e. at C₃₆. The introduction of potassium into the C₃₆ solid system clearly allows the solid to give up isolated, in-tact C₃₆ molecules quite readily upon laser irradiation. The absence of a higher mass distribution in Fig. 1b also suggests that this distribution (seen in Fig. 1a) originates from C₃₆ dimers and other fragments of polymerized C₃₆ solid. Potassium-doping of C₃₆ provides the cleanest and most direct source of pure and isolated C₃₆ molecules that we have found.

We now investigate theoretically how potassium or charge transfer may facilitate dissociation of the C₃₆ solid into independent C₃₆ molecules. For simplicity, we examine the related "inverse" problem of C₃₆ dimer formation, both for case of two neutral C₃₆ molecules and for the case of two negatively charged C₃₆ molecules. LDA calculations^{3,4} have been performed for various intermolecular separations. At each point, a full structural optimization was carried out with the constraint of fixed intermolecular bond distance.

Fig. 2 shows the results of the calculation. The solid circles (with solid line) are for the neutral molecules. As the neutral molecules are brought closer together, the onset of an attractive, van der Waals type interaction appears at around 4.5Å. The total energy possesses a shallow minimum at about 3.0Å, and at 2.6Å separation a small barrier of order 0.1eV is encountered before the dimer begins to covalently bond, reaching a stable minimum at 1.6Å. We do not consider the small barrier at 2.6Å to be important; it may be due to technical limitations of the calculations, and in any case it occurs below the reactant energy. For neutral C₃₆ molecules, spontaneous polymerization is favored.

The solid squares (with dashed line) in Fig. 2 represent a similar calculation for two C₃₆⁻ molecules (the resulting dimer thus has a charge of -2). The total energy in this case suggests that extra charge substantially inhibits dimer formation. The two

negatively charged molecules experience an electrostatic $1/r$ repulsion as they approach one another, which accounts for the fact that at 8 Å separation the dimer is more than 1 eV unbound. At the equilibrium distance of 1.6 Å the charged system is energetically bound by roughly 0.4 eV; however, to reach this minimum the system must pass through an unfavorable barrier which is 0.35 eV above the energy at 8 Å separation and 1.5 Å above the energy of two isolated C_{36}^- molecules. These results help account for the experimental findings that charged C_{36} molecules (the charging resulting from alkali introduction) are less likely to be found in a strongly-bonded state. Interestingly, these findings for C_{36} are exactly the opposite to those for C_{60} , where charging the molecules actually enhances polymerization.

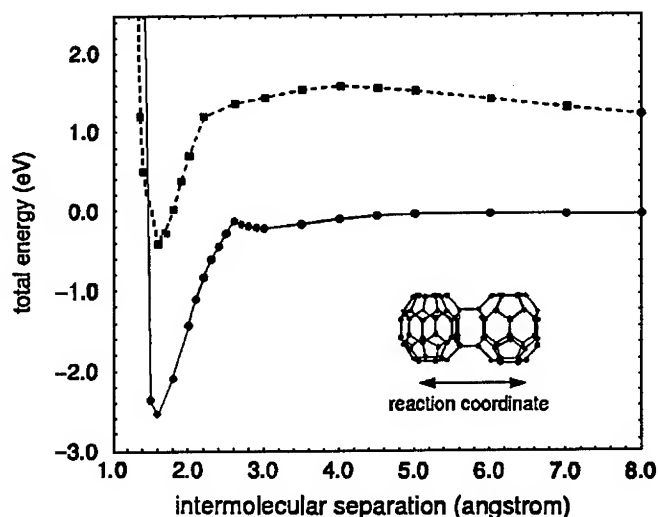


Fig. 2 Calculated total energy for dimer formation for neutral (solid circles) and charged (solid squares) C_{36} molecules.

This research was supported in part by the Director, Office of Energy Research, Office of Basic Energy Sciences, Materials Sciences Division of the U.S. Department of Energy under Contract No. DE-AC03-76SF00098.

References

1. C. Piskoti, J. Yarger, and A. Zettl, *Nature* **393**, 771 (1998); J.C. Grossman, M. Cote, S.G. Louie, and M.L. Cohen, *Chem. Phys. Lett.* **284**, 644 (1998); M. Cote, J.C. Grossman, M.L. Cohen, and S.G. Louie, *Phys. Rev. Lett.* **81**, 697 (1998)
2. C. Piskoti, J. Grossman, M.L. Cohen, S.G. Louie, and A. Zettl (to be published)
3. J.C. Grossman, C. Piskoti, S.G. Louie, M.L. Cohen, and A. Zettl (to be published)

ISOLATION AND CHARACTERISATION OF [84]FULLERENE ISOMERS

T. J. S. Dennis¹, H. Shinohara², S. Margadonna³, K. Prassides³,
M. Hulman⁴, H. Kuzmany⁴,

¹ Hahn Meitner Institute, Glienickestrasse 100, 14109 Berlin, Germany

² Department of Chemistry, Nagoya University, Nagoya 464, Japan

³ C.P.E.S., University of Sussex, Brighton, BN1 9QJ, England

⁴ Department of Materials Physics, Vienna University, Strudlhofgasse 4, 1090, Vienna, Austria.

Abstract We report the isolation of nine isomers of [84]fullerene (C₈₄). Of these minor isomers, six were sufficiently abundant to allow characterisation by ¹³C NMR spectroscopy. These have, in order of decreasing abundance, D₂(IV), D_{2d}(II), C_s(V), D_{2d}(I), D₂(II), and C₂(IV) molecular point group symmetry.

INTRODUCTION

[84]Fullerene (C₈₄) is the third most abundant fullerene solvent extractable from arc-processed soot. Early ¹³C NMR studies¹⁻³ indicated it exists as two isomers with D₂ and D_{2d}(II) symmetry and a 2:1 abundance ratio. The separation of these two isomers was finally achieved only last year.⁴ One of the early studies reported the presence of several minor isomers,³ and Saunders *et al.*⁵ later suggested there are nine extractable isomers based on the ³He NMR spectrum of iHeC₈₄ (isomer mixture). A number of spectroscopic and structural studies have been carried out on [84]fullerene during the last 7 years,⁶ but as the isolation of any isomers had not been achieved, all these experiments were performed on isomer mixtures. Here, we report on the complete isolation of the two major isomers⁴, D₂(IV) and D_{2d}(II), and seven minor isomers⁷ of C₈₄, and characterisation of the two major isomers by temperature-dependent FTIR spectroscopy and temperature-dependent x-ray diffraction.

Production and Isolation

Fullerenes were produced by the contact-arc and Soxhlet extracted. Isolation of the C₈₄ isomers was achieved by multi-stage recycling HPLC using a Cosmosil 5PYE column (21 mm × 250 mm).

¹³C NMR Spectroscopy of the Seven Most Abundant Isomers

The measured ¹³C NMR spectroscopic chemical shifts (ppm) for the seven most abundant isomers are listed in Table 1. There is remarkable agreement between the number of isolated isomers presented here, and the number of isomers reported for *i*HeC₈₄⁵ obtained from high pressure helium capture by a C₈₄ isomer mixture.

D ₂ (IV)	D _{2d} (II)	C ₃ (V)		C ₂ (IV)		C ₂ (V)		D _{2d} (I)	D ₂ (II)
133.81	134.98	134.11	140.19	133.19	139.99	133.03	141.62	131.46	132.05
135.48	138.48	134.43	140.21	134.78	140.00	133.17	141.86	133.44	132.11
137.39	138.87	135.86	140.27	134.84	140.15	134.43	142.06	135.97	133.94
137.50	138.88	136.33	140.44	135.43	140.24	135.01	142.65	142.64	138.03
137.91	139.82	136.40	140.71	135.45	140.41	135.26	142.82	143.18	139.97
138.58	140.00	136.74	140.77	135.47	141.53	135.34	143.30	144.90	140.98
139.63	140.37	136.74	141.17	135.89	141.87	135.35	142.76	145.61	141.14
139.74	140.50	137.03	141.76	135.85	142.39	136.14	143.80	145.80	141.16
139.77	141.37	137.17	141.88	136.45	143.23	137.03	143.84	146.12	141.24
139.79	142.13	137.72	142.30	136.57	143.51	137.14	143.87	146.59	141.60
140.32	144.60	138.09	142.85	136.85	143.55	138.66	144.12	148.39	141.79
140.60		138.80	143.87	137.72	144.97	138.69	144.81	149.44	142.24
141.00		138.93	143.92	137.96	145.31	138.76	145.41		142.49
141.33		139.11	145.36	138.01	145.65	139.07	145.46		142.54
142.58		139.18	145.51	138.26	146.00	140.33	145.63		143.32
142.89		139.22	146.04	138.74	147.66	140.41	145.96		143.76
143.78		139.46	146.23	139.59	147.97	140.44	146.19		143.79
143.81		139.96	147.23	139.69	148.13	140.63	146.52		145.15
143.98		140.04	148.16	139.72	148.18	141.04	146.69		145.28
144.48		140.08	149.15	139.78	148.32	141.15	147.42		145.38
144.58		140.14	149.39	139.84	155.81	141.47	147.94		151.58
			149.40						

Table 1. Chemical Shifts (ppm) for the seven most abundant isomers of C₈₄

Temperature-dependent FTIR and XRD Studies of the Two Major Isomers

The crystal structure of the D₂(IV) and D_{2d}(II) isomers was determined at 300 K and 20 K⁸. Both isomers adopt a FCC structure at room temperature and undergo structural phase transitions at lower temperatures. At 20 K the crystal structure of the D₂(IV) isomer becomes orthorhombic (space group I222: *a* = 11.2934495 Å, *b* = 11.005383 Å, *c* = 15.887341 Å), and the crystal of the D_{2d}(II) isomer becomes monoclinic (space group I2/m: *a* = 15.9260 Å, *b* = 11.139552 Å, *c* = 11.12241 Å, β = 90.9805°). Preliminary results suggest the phase transition for both isomers occurs between 150 K and 170 K on warming. Interestingly, the normal 2:1 mixture of the D₂(IV) and D_{2d}(II) isomers remains FCC at all temperatures down to 20 K⁹.

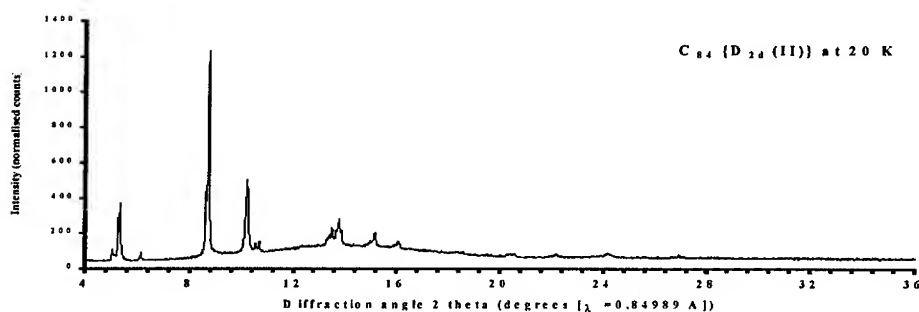


Figure 1. XRD pattern for solid $C_{84}\{D_{2d}(II)\}$ at 20 K

FTIR spectra of the $D_2(IV)$ and $D_{2d}(II)$ isomers were recorded between 300 K and 80 K¹⁰. Figure 2 is the FTIR spectra of these isomers, and Figure 3 shows a plot of HWFM vs. temperature for a, the 1382 cm^{-1} line of the $D_2(IV)$ and b, the 1105 cm^{-1} line of the $D_{2d}(II)$ isomer. The change in slope near 160 K for both isomers is consistent with the structural phase transition temperatures obtained by the XRD study.

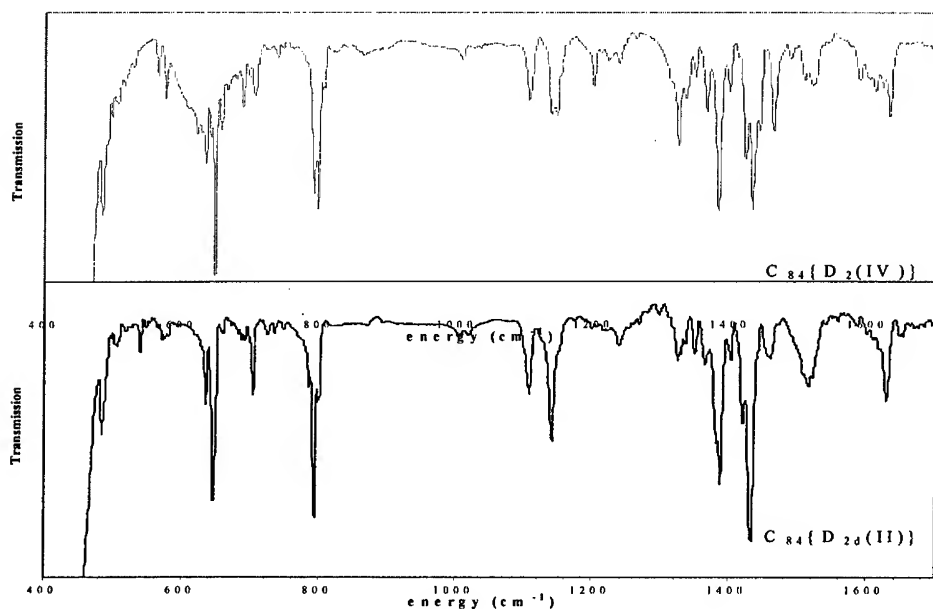


Figure 2. FTIR spectra of purified $C_{84}\{D_2(IV)\}$ and $C_{84}\{D_{2d}(II)\}$

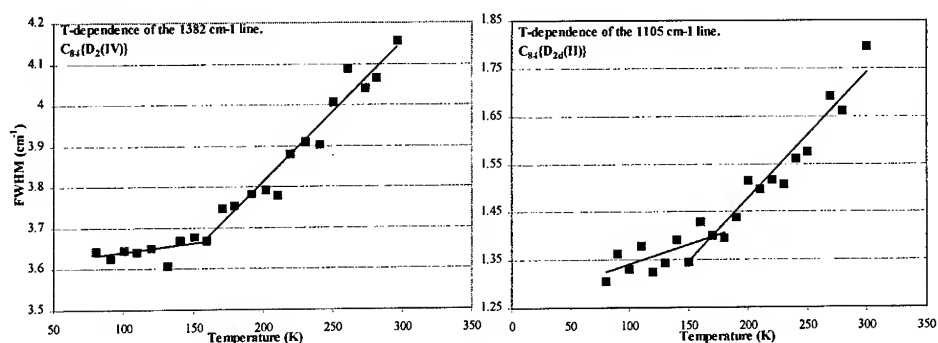


Figure 3 Temperature dependence of the FTIR spectra.

In conclusion, together with the two major isomers, we have isolated nine isomers of the third most abundant fullerene, C_{84} . The present ^{13}C NMR data on C_{84} isomers, which represent almost half of all fullerenes so far isolated, should lead to better theoretical modelling of fullerenes in general.

ACKNOWLEDGMENTS

T.J.S.D. thanks the Humboldt Foundation for a Humboldt Research fellowship, and H.S. thanks the Japanese Ministry of Education, Science, Sports and Culture for Grants-in-Aid for Scientific Research on Scientific Research (A)(2) (No.08554020), for financial support of the present study. S.M., K.P., M.H., and H.K. acknowledge financial support from the European Community project ERBFMRX-C197-0155.

REFERENCES

1. Kikuchi, K.; Nakahara, N.; Wakabayashi, T.; Suzuki, S.; Shiromaru, H.; Miyake, Y.; Saito, K.; Ikemoto, I.; Kainosho, M.; Achiba, Y. *Nature* **1992**, 357, 142.
2. Manolopoulos, D. E.; Fowler, P. W.; Taylor, R.; Kroto, H. W.; Walton, D. R. M. *J. Chem. Soc. Faraday Trans.* **1992**, 88, 3117.
3. Taylor, R.; Langley, G. J.; Avent, A. G.; Dennis, T. J. S.; Kroto, H. W.; Walton, D. R. M. *J. Chem. Soc. Perkin Trans. 2*, **1993**, 1029.
4. Dennis, T. J. S.; Kai, T.; Tomiyama, T.; Shinohara, H. *J. Chem. Soc. Chem. Commun.* **1998**, 619.
5. Saunders, M.; Jimenez-Vazquez, H. A.; Cross, R. J.; Billups, W. E. *J. Am. Chem. Soc.* **1995**, 117, 9305.
6. Dresselhaus, M. S.; Dresselhaus, G.; Eklund, P.C. *Science of Fullerenes and Carbon nanotubes*, Academic Press, New York, **1996**, pp. 730 - 733.
7. Dennis, T. J. S.; Shinohara H, to be published.
8. Margadonna, S; Prassides, K; Fitch, A; Dennis T. J. S.; Shinohara H. To be published.
9. Margadonna, S.; Brown, C. M.; Dennis, T. J. S.; Lappas, A.; Pattison, A.; Prassides, K. *Chem. Materials*, **1998**, 10, 1742
10. Dennis, T. J. S.; Hulman, M.; Kuzmany, H.; Shinohara, H. To be published.

New Three-component Systems Based on C₆₀

Rimma N. Lyubovskaya*, Dmitry V. Konarev, Evgeniya I. Yudanova,
Yury M. Shul'ga, Natalia V. Drichko¹, Yan V. Zubavichus².

Institute of Problems of Chemical Physics RAS, 142 432 Chernogolovka, Russia.

¹*A. F. Ioffe Physical-Technical Institute RAS, 194021, St. Petersburg, Russia.*

²*Institute of Organoelement Compounds RAS, 117334, Vavilov St. 28, Moscow, Russia*

Abstract. For the first time the C₆₀ complex, C₆₀(BEDT-TTF⁺)(I₃⁻), comprising the radical cation of the organic donor BEDT-TTF (bis(ethylenedithio)tetrathiafulvalene) was synthesized. Single crystals of the complex were obtained in benzonitrile. This compound has C-centered monoclinic lattice with the unit cell parameters: $a=17.419(6)$, $b=9.997(4)$, $c=13.499(1)$ Å, $\beta=99.00(1)^\circ$. The bands characteristic of the BEDT-TTF⁺ cation radical and neutral C₆₀ are present in IR- and optical reflectivity spectra of single crystals and optical absorption spectra in KBr pellets. The signal with $g = 2.0074$ and $\Delta H_{pp} = 23$ G is attributed to BEDT-TTF⁺ in the EPR spectrum. The position of I3d_{5/2} peak confirms the formation of the I₃⁻ anion.

INTRODUCTION

Tetrathiafulvalene derivatives are known to be widely used in the design of radical cation salts which manifest metallic and superconducting properties. For example, a family of BEDT-TTF based superconducting radical cation salts, namely, (BEDT-TTF)₂X, X=I₃⁻, IBr₂⁻, AuI₂⁻, ReO₄⁻, Cu(NCS)₂⁻ and (BEDT-TTF)₄Hg_{2.89}Hal₈, Hal. = Cl, Br has been synthesized¹.

However fullerene C₆₀ forms only neutral complexes with tetrathiafulvalene derivatives, namely, with bis(ethylenedithio)tetrathiafulvalene (BEDT-TTF)², dibenzotetrathiafulvalene³, octamethylenetetrathiafulvalene⁴ and others⁵⁻⁶.

To change a neutral state of molecular complexes of C₆₀, we intercalated the D_kC₆₀(Solv)_x (D is donor, Solv is a solvent) compounds by iodine in gas phase. During intercalation the solvent is substituted by iodine and the donor is oxidized in solid state to a radical cation or a dication to form a three-component system D_k⁺C₆₀I_n⁻, $n>5$ ⁷. However, gas-phase intercalation is a diffusion process and homogeneity of the resulting samples is hardly attained.

The present paper reports on the synthesis of the first three-component complex of C₆₀ in solution which contains the (BEDT-TTF⁺) radical cation, namely, C₆₀(BEDT-TTF⁺·I₃⁻). The crystal lattice parameters are determined. IR absorption spectra and polarized electron reflectivity spectra are measured on single crystals. The data on EPR and X-ray photoelectron spectra are presented.

EXPERIMENTAL

BEDT-TTF- I_x , $x \sim 3.4$ was used as a starting compound in the synthesis of $C_{60}(\text{BEDT-TTF} \cdot I_3)$. $C_{60}(\text{BEDT-TTF} \cdot I_3)$ was prepared by cocrystallization of stoichiometric quantities of BEDT-TTF- $I_{3.4}$ and C_{60} in benzonitrile. The compound was prepared as rhomb-like crystals up to 0.5 mm in size. Found, %: C 56.4; H 0.74; S 17.14; I 26.20. $S_8C_{70}H_8I_3$. Calculated, %: C 56.7; H 0.53; S 17.14; I 25.6.

The IR transmission spectrum of the $C_{60}(\text{BEDT-TTF} \cdot I_3)$ single crystals was measured within the $650\text{--}4000\text{ cm}^{-1}$ range on the Perkin-Elmer 1760 IR spectrometer equipped with a microscope. Electron reflectivity spectra of single crystals were measured on a home made double-beam microspectroreflectometer. X-ray photoelectron spectra were excited by Mg-K α -radiation ($h\nu=1253.6\text{ eV}$). The spectra were calibrated as to the peak C1s (285.0 eV). The data of X-ray powder diffraction were obtained on the DRON-3 automatic diffractometer with Cu-K α radiation ($\lambda=1.5418\text{ \AA}$) and graphite monochromator.

RESULTS AND DISCUSSION

Compound $C_{60}(\text{BEDT-TTF} \cdot I_3)$ has the following parameters of monoclinic crystal face-centered unit cell: $a=17.419(6)$, $b=9.997(4)$, $c=13.499(1)\text{ \AA}$, $\beta=99.00(1)^\circ$, $V=2321.8\text{ \AA}^3$. All the observed reflections were indexed and no systematic exclusions

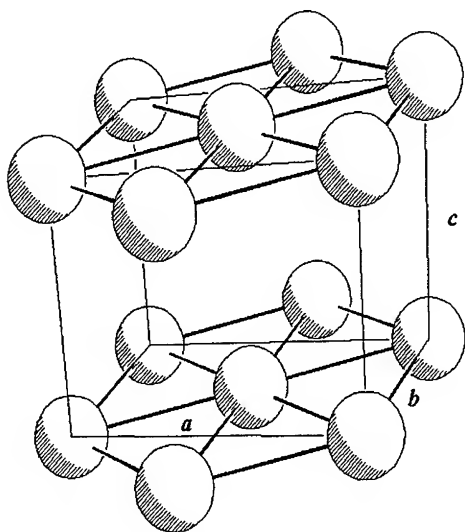


FIGURE 1. The diagram of the position of C_{60} molecules in the crystal lattice of $C_{60}(\text{BEDT-TTF} \cdot I_3)$. C_{60} molecules are marked by spheres, crystallographic directions and the shortest distances between the centers of C_{60} molecules are marked by thin lines.

from the monoclinic face-centered lattice were observed. Therefore, the space groups $C2$, Cm or $C2/m$ are possible for the unit cell. Every fullerene molecule can be surrounded by six almost equidistant neighbouring C_{60} molecules. In this case two fullerene molecules with the 10.00 \AA distances between the centers (translation vectors are $0 \pm 1\ 0$) and the four neighbouring C_{60} molecules with the 10.04 \AA distances between the centers (translation vectors are $\pm 0.5 \pm 0.5\ 0$) can be located in the ab plane (see Fig.1). Therefore, one can assume that fullerene molecules form slightly distorted close-packed layers parallel to the

ab plane. The distances between these layers are 13.5 Å. The BEDT-TTF⁺ radical cations and the I₃⁻ anions can occupy cavities in the interlayer space. Such layered structures are characteristic of C₆₀ complexes with substituted tetrathiafulvalenes, in which donor and solvent molecules are located between close-packed fullerene layers^{4,6}.

The IR transmission spectrum of the C₆₀(BEDT-TTF·I₃) single crystals represents the absorption bands at 1429 and 1182 cm⁻¹ characteristic of C₆₀. Their position remains unchanged as compared with that in the spectrum of initial C₆₀, indicating the absence of noticeable charge transfer to the fullerene molecule. The spectrum also demonstrates the absorption bands characteristic of the BEDT-TTF⁺ radical cation: 1384, 1289, 1021, 927, 899, 882, and 808 cm⁻¹. Their positions are close to those of absorption bands observed earlier for the BEDT-TTF⁺ radical cation in the transmission spectrum of the BEDT-TTF·I₃ radical cation salt⁸.

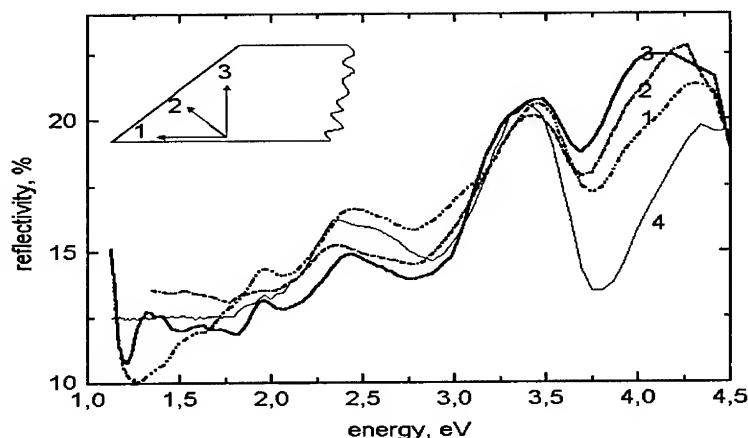


FIGURE 2. Electronic reflectivity spectra of the C₆₀(BEDT-TTF·I₃) single crystals measured from the developed plane for three polarizations (1, 2, 3) and the reflectivity spectrum of the initial C₆₀ crystal (4).

Electron polarized reflectivity spectra of the C₆₀(BEDT-TTF·I₃) single crystals were measured from the larger crystal face for three polarizations (see Fig.2). This spectrum exhibits the peaks at 4.2, 3.6, 2.5, and 1.1 eV and a relatively weak peak at 1.96 eV. The positions of peaks of C₆₀ at 4.2 and 3.6 eV in the complex are close to those of pure C₆₀, however the peaks are essentially broadened. Such a broadening was observed earlier at intercalation of fullerene complexes by iodine⁷. The reflectivity band at 2.5 eV can be attributed mainly to intermolecular charge transfer between HOMO-LUMO of the neighbouring C₆₀ molecules⁹. This band has approximately equal intensity in the spectrum of C₆₀(BEDT-TTF·I₃) and the crystals of pure C₆₀.

A reflectivity band at 1.1 eV can be attributed to BEDT-TTF⁺. This band is weakly polarized, the highest intensity is observed in the polarization «1». The similar band was observed in polarized spectra of the (BEDT-TTF)₂I₃ single crystals¹⁰.

Table 1. Binding energies (E_b) and half-widths (Δ) of XP lines. All the values are in eV and calibrated as to the peak C1s (285.0 eV).

Compound	Δ C1s	S2p	Δ S2p	I3d _{5/2}	Δ I3d _{5/2}
C ₆₀ (BEDT-TTF·I ₃)	2.1	164.1	2.6	619.4	2.3
(BEDT-TTF) ₂ I ₃ ¹¹	2.0	163.8	2.4	619.0	2.1
BEDT-TTF	1.9	163.6	2.4	-	-
(Ph ₄ P) ₂ C ₆₀ ·I ¹²	2.1	-	-	617.7	2.2

Table 1 shows half-widths and positions of the peaks C1s, S2p, and I3d_{5/2} in XP spectra of C₆₀(BEDT-TTF·I₃).

A positive shift of the S2p binding energy is observed at changing from BEDT-TTF to C₆₀(BEDT-

TTF·I₃). This corresponds to the decrease of electron density on sulfur atoms at changing from neutral BEDT-TTF to the radical cation state in C₆₀(BEDT-TTF·I₃).

The position of the peak I3d_{5/2} with E_b =619.4 eV in this compound is close to its position in (BEDT-TTF)₂I₃¹¹. This indicates that the sample under study contains iodine as the I₃⁻ anion since for I⁻ anion essentially lower binding energy is characteristic, for example, in (Ph₄P)₂C₆₀(I⁻) E_b is equal to 617.7 eV¹².

EPR studies of the spectra of C₆₀(BEDT-TTF·I₃) at room temperature showed the presence of an intense EPR signal with g =2.0074 and ΔH_{pp} =23 G corresponding to the BEDT-TTF⁺ radical cation. With the temperature decrease the position of g -factor and the width of the EPR signal remain almost unchanged and g =2.0074, ΔH_{pp} =20 G (77 K). Such a behaviour is different from that of (BEDT-TTF)₂I₃ which is characterized by a noticeable narrowing of the EPR signal with the temperature decrease¹. The integral intensity of the signal in C₆₀(BEDT-TTF·I₃) increases 2.2 times with the temperature decrease from 300 down to 77 K. Such a behaviour of the EPR signal is the most probably associated with electron localization over the BEDT-TTF⁺.

Conductivity of C₆₀(BEDT-TTF·I₃) measured on a pressed pellet amounts to 2·10⁻⁴ Ohm⁻¹cm⁻¹. This value is two orders of magnitude higher than conductivity of the (BEDT-TTF)₂C₆₀ complex (10⁻⁶ Ohm⁻¹cm⁻¹) measured under the same conditions. The low value of conductivity is assumed to be due to integer-valued charge on the BEDT-TTF molecule (+1) and is characteristic of other BEDT-TTF radical cation salts with full charge transfer¹.

ACKNOWLEDGEMENTS

This work is supported by the Russian program «Fullerenes and Atomic Clusters» and Russian Foundation for Basic Research, project N98-02-18303.

REFERENCES

1. Williams J.M., Ferraro J.R., Thorn R.J., Carlson K.D., Geiser U., Wang H.H., Kini A.M., and Whangbo M.-H., *Organic Superconductors (including Fullerenes). Synthesis, Structure, Properties and Theory*, Prentice Hall, Englewood Cliffs, New Jersey, 1992.
2. Izuoka A., Tachikawa T., Sugawara T., Suzuki Y., Konno M., Saito Y., Shinohara H., *J.Chem.Soc.,Chem.Comm.*, 1472 (1992).
3. Konarev D.V., Zubavichus Y.V., Slovokhotov Yu.L., Shul'ga Yu. M., Semkin V.N., Drichko N.V., and Lyubovskaya R.N., *Synth.Met.*, **92**, 1 (1998)
4. Saito G.,Teramoto T., Otsuka A., Sugita Y., Ban T., Kusunoki M., and Sakaguchi K.-I., *Synth. Met.*, **64**, 359 (1994).
5. Konarev D.V., Valeev E.F., Slovokhotov Yu.L., Shul'ga Yu.M., et.al. *Synth.Met.*, **88**, 85(1997)
6. Llacay J., Tarres J., Veciana J., Rovira C., Veciana J., Mas M., and Molins E., *J.Phys.Chem.Solids*, **58**, 1675 (1997)
7. Lyubovskaya R.N., Konarev D.V., and Yudanov E.I., et.al., *Synth. Met.*, **84**, 741 (1997).
8. Kozlov M.E., Pohodnia K.L., and Yurchenko N.M., *Spectrochimica Acta*, **45A**, 437 (1989).
9. Saeta P.N., Greene B.I., Kortan A.R., Kopylov N., and Thiel F.A., *Chem.Phys.Lett.*, **190**, 184 (1992).
10. Vlasova R.M., Prie S.Ya., Semkin V.N., et.al., *Fizika Tverdogo Tela (in Russian)*, **32**, 448 (1990).
11. Konarev D.V., Lyubovskaya R.N., Shul'ga Yu.M., *Dokladii RAS (in Russian)*, **346**, 490 (1996).
12. Shul'ga Yu.M., Spitsyna N.G., and Yagubskii E.B., *Dokladii RAS (in Russian)*, **348**, 502 (1996)

Cluster-assembled amorphous carbon nano-foam synthesised by high-pulse-rate laser ablation

A. V. Rode*, E. G. Gamaly†, R. G. Elliman*, A. S. Kheifets*, and B. Luther-Davies*

**Research School of Physical Sciences and Engineering,
Australian National University, ACT 0200, Canberra, Australia*

*†Departamento de Fisica, Universidad Autonoma Metropolitana -Iztapalapa,
Apartado Postal 55-534, 09340, Mexico D.F., Mexico*

Abstract. We report on a new fractal amorphous carbon nano-foam with a large fraction of tetrahedrally-bonded atoms. The material was produced by high-repetition-rate laser ablation in an argon-atmosphere which resulted in a high collision frequency between carbon atoms and ions in the laser plume and argon atoms in the chamber. This creating the optimal vapour temperature and density for the efficient formation of 4-membered sp^3 bonds typical of diamond. The bulk density of various foam samples is in the range $(2-10) \cdot 10^{-3}$ g/cm³, whilst the specific surface area is 300-400 m²/g comparable to that of carbon aerogels. At low temperatures the as-deposited foam exhibits a strong positive electrostatic charge and non-linear current-voltage characteristics with strong hysteresis, indicative its insulating nature. After annealing, the resistivity of the foam measured at low-voltage (± 30 V) is $(1-3) \cdot 10^9$ Ohm-cm at room temperature and $(1-10) \cdot 10^{13}$ Ohm-cm at 80 K, with virtually no hysteresis. The DC conductivity of this low-density carbon foam and its temperature dependence appears to be very close to that of RF-sputtered solid amorphous diamond-like carbon films.

Carbon nanometer-size porous structures such as carbon aerogels and activated carbon fibres exhibit unique electrical, optical, mechanical, and thermal properties, which are different from those of bulk precursors [1-3]. Many of these physical properties can be attributed to the fact that the structures have a significant fraction of the surface carbon atoms with different co-ordination from that of internal atoms.

In this paper we report a new form of nanometer-size granular carbon material, a low-density carbon nano-foam, which has been produced by a recently developed ultrafast laser ablation technique described elsewhere [4,5]. The high-repetition-rate laser evaporation uses a 10 kHz Q-switched Nd:YAG laser to evaporate a carbon target in a 1-100 torr Ar atmosphere. This produces a higher evaporation rate of carbon atoms and ions than conventional laser ablation techniques, resulting in an increased average temperature and density of the carbon/argon mixture in the experimental chamber and increased probability for the formation of higher energy carbon-carbon bonds. The increased collision frequency resulting from these deposition conditions encourages diffusion limited aggregation of carbon atoms into fractal structures.

Scanning and transmission electron microscopy show that the deposited carbon foam consists of interconnected carbon clusters with size ~ 6 nm, assembled into one-dimensional chains which, in turn, form foam-like (or web-like) structures (Fig. 1). The web looks like a

capricious mixture of “strings of pearls”. The $sp^3/(sp^2+sp^3)$ bonding ratio determined by electron energy-loss spectra is in the range from 0.15 to 0.5. Preliminary mass spectroscopy of the carbon foam shows a broad peak around 35,000-60,000 a.m.u. with the maximum at $\sim 50,000$ a.m.u., i.e. the dominant cluster contains $\sim 4 \cdot 10^3$ carbon atoms. Attributing this weight to a 6-nm cluster one obtains the average cluster density of ~ 0.73 g/cm³, assuming the clusters are closed structures. The bulk density of the *a*-C foam samples, determined from He⁺ ion backscattering measurements of the areal carbon density and scanning electron microscopy measurements of the film thickness, is in the range $(2-10) \cdot 10^{-3}$ g/cm³, while the measured specific surface area of the foam is 300 – 400 m²/g.

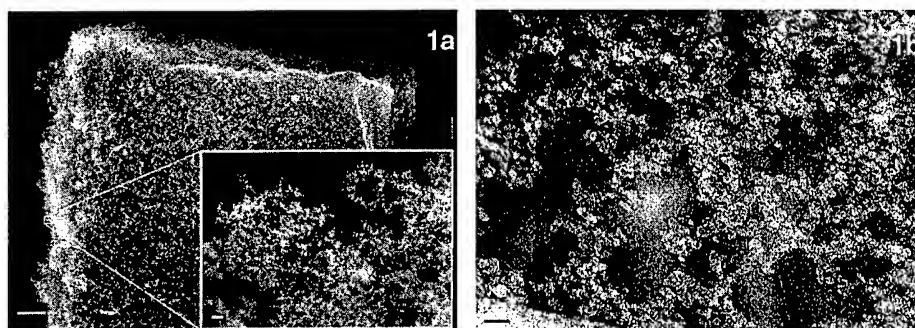


FIGURE 1. Scanning (a) and Transmission Electron Microscope (b) images showing the free-standing carbon foam. The bars in the images are 10 μ m (Fig.1a); 100 nm (inset in Fig.1a); and 10 nm (Fig. 1b). The fractal structure is clearly seen in the high-resolution inset (a) and in (b), which consists of a network of interconnected carbon clusters of ~ 6 nm in size.

The process of carbon cluster formation takes place in several stages. A flow of carbon atoms and ions is created by laser ablation of the target surface. The measured temperature of the carbon atoms in the laser plume is ~ 2 eV. As the carbon cloud expands, the carbon atoms collide with the ambient gas and with each other, exchanging their energy via collisions. As they diffuse through the gas, they bond into various structures, and finally attach to the substrate surface and to carbon structures already on that surface. Estimates of the diffusion time t_{diff} of a single carbon atom from the target to the substrate suggest $t_{diff} = 0.1$ s for 1 torr and $t_{diff} = 10$ s for 100 torr of Ar pressure. Using the measured evaporation rate $1.4 \cdot 10^{26}$ C-atoms/(cm²s) [5] we obtain that after 30 s of evaporation at 1 torr of Ar the number density of carbon atoms in the chamber reaches the density of Ar atoms. From this it follows that in a typical 30 mins deposition experiment the temperature of Ar in the chamber grows continuously during the evaporation process, reaching the average carbon vapour temperature in a few minutes. Similarly, the average carbon density approaches the Ar density in about an hour for 100 torr Ar pressure. This combination of the carbon/argon temperature and the partial carbon density provides the conditions for efficient sp^2 and sp^3 bonding [6].

In order to elucidate the electronic structure of the foam, optical absorption spectra, Raman spectra, and high-resolution electron energy loss spectra (EELS) were measured at room

temperature, together with electrical resistivity in the temperature range from 80 K to 450 K. The optical absorption measurements provide an estimate of the optical band-gap, which is in the range from 0.5 to 0.7 eV: this being typical for sp^2 dominated amorphous carbon (*a*-C) films [7]. The measured Raman spectra (632.8 nm excitation) are similar to those obtained for laser-evaporated amorphous diamond-like carbon (DLC) films, and show broad peaks centred at $(1341-1353) \text{ cm}^{-1}$ (D-peak) and at $(1569-1579) \text{ cm}^{-1}$ (G-peak) which are attributed to graphitic sp^2 bonding. To achieve a reasonable fit to the experimental results it was always necessary to add the third peak with maximum at $\sim 1160 \text{ cm}^{-1}$, which is attributed in the literature to regions of sp^3 -bonded amorphous diamond within an amorphous carbon matrix [8,9].

Examples of the current-voltage (I-V) characteristics of the foam in the applied DC voltage range of $\pm 100 \text{ V}$ at various temperatures from 85 K to 130 K are presented in Fig. 2. The I-V curves are symmetric with respect to voltage sign reversal. They are non-linear and demonstrate a voltage-dependent resistivity: the differential resistivity being approximately 10 times higher in the low-voltage region ($\pm 30 \text{ V}$) than in the high voltage region ($\pm 100 \text{ V}$). The resistivity of the foam measured in the low-voltage region decreases with temperature from $\sim 10^{11} \text{ Ohm-cm}$ at 85 K to $\sim 10^8 \text{ Ohm-cm}$ at room temperature (297 K) for the as-deposited foam, and from $\sim 10^{14} \text{ Ohm-cm}$ at 85 K to $\sim 10^9 \text{ Ohm-cm}$ at 297 K for the foam annealed at 450 K for 18 hours. The temperature dependence of the DC conductivity on a double logarithmic scale is presented in Fig. 3. For comparison, results for an RF-sputtered *a*-C film [10] are shown on the same graph. Fitting the conductivity $\sigma(T)$ over a wide temperature range with a power law T^n gives $n = 9.5 - 9.7$ for the foam, compared to $n = 15 - 17$ for the *a*-C films.

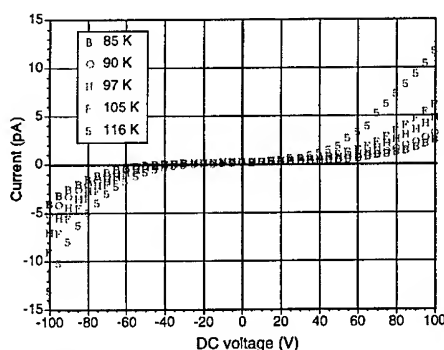


FIGURE 2. Nonlinear current-voltage (I-V) curves of the annealed carbon foam at various temperatures. The differential resistivity is about ten times higher in the low-voltage range $\pm 30 \text{ V}$ than that at $\pm 100 \text{ V}$.

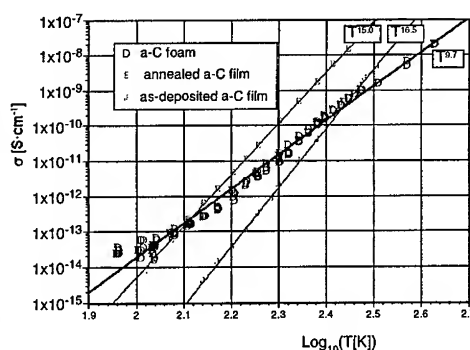


FIGURE 3. Logarithmic temperature dependence of the *dc*-conductivity of the carbon foam (crosses). For comparison, the same dependence is shown for as-deposited (closed circles) and annealed (open circles) sputtered *a*-C films from Ref. [10]. The T^n values for empirical description of the conductivity in the form $\sigma_{dc} \propto T^n$ are shown for each curve.

In conclusion, it has been shown that a new form of carbon, a cluster-assembled nano-foam, can be produced by high repetition rate laser ablation in an Ar ambient. The foam consists of interconnected C clusters of ~6nm diameter and has an average sp^3 fraction in the range from 0.15 to 0.5. It has a surface area 300 – 400 m²/g comparable to that of the sp^2 -bonded carbon aerogels but a bulk density which is one hundred times lower, and a resistivity which is several orders of magnitude larger.

ACKNOWLEDGMENTS

We are very thankful to S. T. Hyde, B. Altshuler, Koung-An Chao, R. F. Haglund, Jr., and D. R. McKenzie for valuable and stimulating discussions. We gratefully acknowledge our colleagues who helped us to perform a number of measurements: S. Bulcock (electron energy loss spectroscopy), J. Fitz Gerald (transmission electron microscopy), N. J. Welham (surface area measurements), and T. J. Senden (mass-spectrometry). A.V.R. acknowledges support from the Australian Research Council through a Queen Elizabeth II Fellowship, and E.G. G. acknowledges support from CONACYT of Mexico.

REFERENCES

1. Dresselhaus, M. S., *Annu. Rev. Mater. Sci.*, **27**, 1-34 (1997).
2. Fung, A. W. P., Wang, Z. H., Lu, K., Dresselhaus, M. S. and Pekala, R. W., *J. Mater. Res.*, **8**, 1875-1885 (1993).
3. Fung, A. W. P., Wang, Z. H., Dresselhaus, M. S., Dresselhaus, G., Pekala, R. W., and Endo, M., *Phys. Rev. B*, **49**, 17325-17335 (1994).
4. Gamaly, E. G., Rode, A. V., and Luther-Davies B., *J. Appl. Phys.*, **85**, xxx-xxx (1999).
5. Rode, A. V., Gamaly E. G. and Luther-Davies B., *J. Appl. Phys.*, **85**, xxx-xxx (1999).
6. Pierce, H. O. *Handbook of carbon, graphite, diamond and fullerenes*, Park Ridge, NJ, Noyes Publications, 1993.
7. Robertson, J. and O'Reily, E. P., *Phys. Rev. B*, **35**, 2946-2957 (1987).
8. Mergulov, V. I., Lannin, J. S., Munro, C. H., Asher, S. A., Veerasamy, V. S. and Milne W. I., *Phys. Rev. Lett.*, **78**, 4869-4872 (1997).
9. Wang, C. Z. and Ho K. M., *Phys. Rev. Lett.*, **71**, 1184-1187 (1993).
10. Shimakawa, K. and Miyake K., *Phys. Rev. B*, **39**, 7578-7584 (1989).

Self-Formation of Nanostructures from Hydrated Aggregates and Nanocrystals of $(C_{60})_n$ Molecules on the Liquid Crystal Layer

E. Buzaneva, A. Gorchinskyi, A. Benilov, Yu. Kirghisov,
F. V. Pogorelov, Yu. Astashkin, V. Bukalo, Yu. Prilutski,
G. S. Durov (*), P. Scharff (**), G. Andrievsky (***)

* *National T. Shevchenko University, Vladimirskaya St. 60, 252022, Kiev, Ukraine,*

** *Institut für Anorganische und Analytische Chemie, TU Clausthal, Paul-Ernst-Strasse 4, D-38670 Clausthal-Zellerfeld,*

*** *Institute for Therapy of the Academy of Medical Sciences of Ukraine, Postysheva St. 2a, 310116, Kharkov, Ukraine*

Abstract. The formation of $(C_{60})_n$ molecular systems of nanostructures from C_{60} hydrated aggregates/nanocrystals on the surface of p-aminoxybenzylidene/p-toluidine liquid crystal layer with self-assembling of one-dimension polymerized $(C_{60})_n$ ($n=13, 33$) chains and C_{60} bridged molecules is predicted and experimentally confirmed by AFM, UV-vis, IR and Raman spectroscopy.

INTRODUCTION

The principal direction in the C_{60} molecular engineering is their coating on the surface of metals and semiconductors. In these works, it was made by coating in a UHV system. We have developed the new method of the formation of the C_{60} molecular nanostructures from $(C_{60})_n$ hydrated aggregates/nanocrystals by coating from C_{60} water solution which consists of the self-assembled building blocks. The formation in water of highly stable cluster/crystallite structures from fullerene C_{60} has been theoretically predicted and experimentally confirmed at [1,2]. It is shown, that in water solution of C_{60} fullerenes the formation of highly stable hydrated spherical aggregates $(C_{60})_n$ and the cubic nanocrystals takes place. The diameters of $(C_{60})_n$ ($n=13$ and 33) molecular clusters are 25 and 36 Å corresponding. The size of cubic nanocrystals is 28.6 Å [2].

Our idea is to initiate self-organization of a nanostructure systems from $(C_{60})_n$ hydrated aggregates/nanocrystals creating of the molecular roughness surface of

p-aminoxylbenzylidene/p-toluidine (ABT) solid Liquid Crystal (LC) layer. We concerned that C_{60} molecules in adsorbed agglomerates has a low reorganization energy and the intermolecular interaction of C_{60} and LC molecules can provide the self-assembling of $(C_{60})_n$ hydrated agglomerates/nanocrystals.

EXPERIMENTAL

The C_{60} molecular water solution with different fullerene clusters concentration were prepared as described at [1]. The ABT powder was deposited on quartz and TiBr-TiJ monocrystal substrate, heated to temperature 343 K corresponding to liquid isotropic state and slow cooled to $T=293K$. The fixed volume of C_{60} water solution was used for covering of the surface ABT layer with area 0.25 cm^2 . Then, the cover was dried in the dark at $T=293K$ and under laser illumination ($\lambda=514.5\text{nm}$).

The $(C_{60})_n$ molecular clusters images was investigated by AFM (NANOTOP-203). The $(C_{60})_n$ molecular clusters composition and electronic structure on ABT layer was determined by UV-vis, IR and Raman spectroscopy with $\lambda_{\text{ex}}=514.5\text{ nm}$ and step $0.5\text{-}1\text{ cm}^{-1}$ at $T=293K$, using the theoretical calculations [2,3].

RESULTS AND DISCUSSION

The Images of the $(C_{60})_n$ Molecular Clusters on LC Layer

The comparison of the AFM images of the ABT surface before (fig. 1a) and after (fig. 1b) $(C_{60})_n$ molecules clusters coating was performed with taking into account of calculation results [4,5].

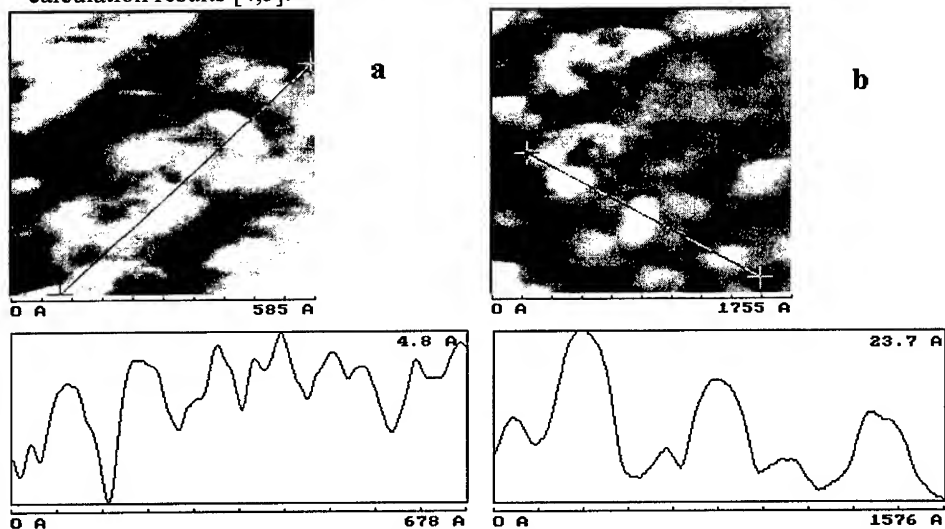


Figure 1. AFM images of the ABT surface before (a) and after (b) $(C_{60})_n$ molecules clusters coating. A

height scan along line on images is presented below.

As the results we defined: on surface of ABT layer with roughness 2.5 Å corresponding to one-layer LC molecules with planar orientation agglomerates with length up 135 Å from four $(C_{60})_{33}$ molecular clusters with the diameter up 36 Å is self-organized; between these agglomerates small agglomerates with length up 50 Å from two $(C_{60})_{13}$ molecular clusters with the diameter 25 Å and/or crystallites C_{60} with linear size up 28.6 Å is inserted; these cluster systems form one-dimensional chains as the result of photopolymerization at laser excitation. It is possible that more less agglomerates creating networks between ordered agglomerates consist from individual C_{60} molecules or from them small groups. The obtained results are not contrary to experimental results [1].

The Bonding and Charge State of $(C_{60})_n$ on LC Layer

Raman scattering, optical absorption and IR transmissions spectra was compared in order to be able to determine interball bonding patterns and charge state in the $C_{60}/(C_{60})_n$ adsorption layer on various substrates and LC layer. We took into account that the splitting and new bands in the spectra as it is demonstrated by theory [3] contain the information about symmetry of the balls and the frequency shift of the $T_{1u}(1-4)$ and $A_{1g}(2)$ fundamentals correlate with the charge state and the interball bonding.

The first step of our investigation is evidence of the formation of polymerized C_{60} agglomerates on base of analysis of Raman spectra in region of wavenumber 80-600 cm^{-1} . As soon from Raman spectra on Fig. 2. The splitting of the bands nearly 270 cm^{-1} and new band at 117, 126 cm^{-1} confirm polymerization of C_{60} molecular layer in particularly formation of $(C_{60})_2$ [3]. The observed bands lie at the region of calculated intermolecular frequencies of the $(C_{60})_{33}$ clusters: 42-227 cm^{-1} [2]. These frequencies are lower vibrational spectrum for individual C_{60} molecule (296-1590 cm^{-1}) which is observed in self-organized $(C_{60})_{33}/C_{60}$ on LC layer. From optical absorption spectra in region 2-6.5 eV of C_{60} agglomerates we defined that it is characterized for crystalline fullerene C_{60} and identified electronic transitions: $h_u \rightarrow t_{1g}$ ($E=2.75$ eV), $g_g + h_g \rightarrow t_{1u}$ ($E=3.52$ eV), $h_u \rightarrow h_g$ ($E=4.5$ eV), $g_g + h_g \rightarrow t_{2u}$ ($E=5.5$ eV). These transitions are concerned to coated C_{60} nanocrystallites.

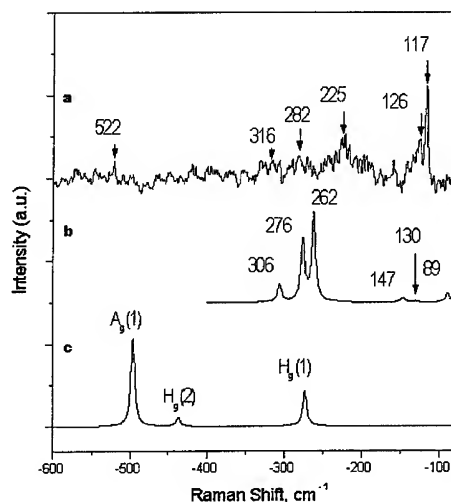
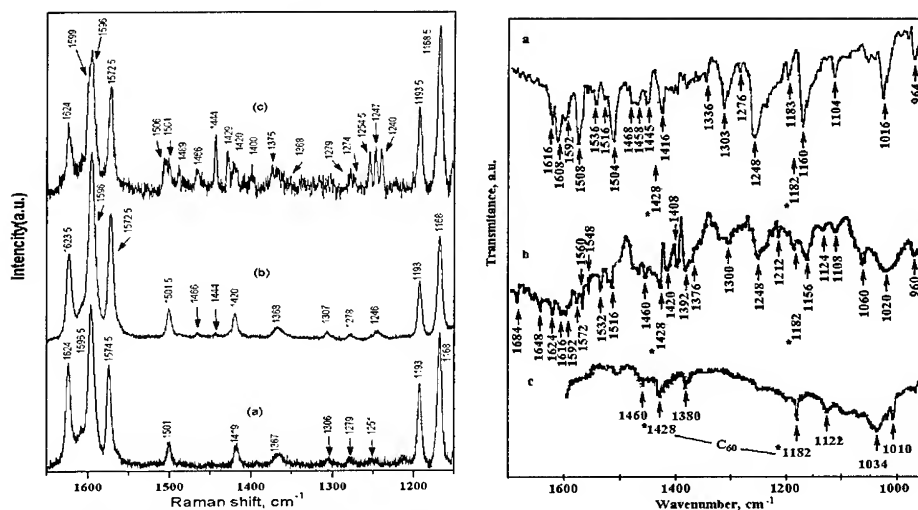


Figure 2. Raman spectra of $(C_{60})_n$ on LC layer (a) in comparison to the calculation Raman spectra [6] (b) and experimental spectra of C_{60} molecules (c).

The next step is detection of molecular bonds (C_{60})_n in agglomerates which depend from LC layer with detecting photoinduced electron transfer between molecules: C_{60}



and C14H14N2O (NH₂-O-C₆H₄-CH=N-C₆H₄-CH₃).

Figure 2. Left panel: Raman spectra of the LC layer on quartz substrate (a), the (C_{60})_n on LC layer/quartz substrate with thickness of (C_{60})_n 20 Å (b) and 30 Å (c), Right panel: IR spectra of LC layer on TiBr-TiJ (a), surface (C_{60})_n agglomerates on LC layer (b) and C_{60} layer on substrate (c).

The direct evidence of the charging of C_{60} molecules on LC layer as a result of photoinduced electron transfer is observing of the shifting of the IR bands: from 1429 to 1380 cm⁻¹ ($T_{1u}(4)$) and from 527 to 524 cm⁻¹ ($T_{1u}(1)$) for (C_{60})_n (20 Å) and 488 cm⁻¹ (30 Å). The such intermolecular interaction with 3 e⁻ transferred is possible in complex. In the Raman and IR spectra bands correspond to the vibration all modes of both individual C_{60} molecules and LC molecules. Besides in spectra of (C_{60})_n/LC layer the appearance of molecular conformations of LC is observed. It is manifested in splitting of vibrational bands 1596, 1501 cm⁻¹. The three new strong vibrational bands in the region of (1240-1255)cm⁻¹ are connected with peculiarity of interaction between the C_{60} , (C_{60})_n and LC molecules. As a result the formation of complex (C_{60})_n/LC is possible.

REFERENCES

1. G.V.Andrievsky, M.V.Kosevich, O.M.Vovk, V.S.Shelkovsky, L.A.Vashchenko, J. Chem. Soc., Chem.Comm. 12, 1281-1285 (1995).

2. Yu.Prilutski, S.Durov, L.Bulavin, V.Pogorelov, Yu.Astashkin, V.Yashchuk, T.Ogul'chansky, E.Buzaneva, G.Andrievsky, *Mol.Cryst. Liq.Cryst.* **324**, 65-70 (1998).
3. Porezag D., Pederson M.R., Frauenheim T., Kohler T., *Phys. Rev.* **B 52**, 4963-4968 (1995).
4. T.Picher, R.Winkler, H.Kuzmany. *Phys.Rev.B, Solid State* **49**, 15879-15884 (1994).

Chains of Carbon Nanoparticles from the Interaction of Fullerenes with Thin Metal Films

H. Kanzow^a, A. Ding^a, H. Sauer^b, T. Belz^b and R. Schlögl^b

^aTechnische Universität Berlin, Optisches Institut, Sekr. P 1-1, Str. d. 17. Juni 135, D-10623 Berlin

^bFritz-Haber-Institut der Max-Planck-Gesellschaft, Faradayweg 4-6, D-14195 Berlin, Germany

Abstract. Different fullerene blacks were produced by the arc-discharge vaporization of graphite in various experimental conditions. Pressed pellets of these materials were sputtered with thin metal films. After the subsequent pyrolysis up to 1200°C the samples were studied with SEM. Wormlike nanostructures arose from the nickel covered parts of the fullerene containing pellets. TEM and EELS showed that chains of hollow elongated carbon nanostructures were generated with outer diameters usually between 35 and 90 nm. A model for the formation of the chains is proposed considering diffusion of carbon through a metal particle and surface melting of the metal.

1. Introduction

In the last years methods for the covaporization of carbon and metal were optimized to produce carbon nanostructures. A first approximation of the reactions outside the carbon-metal plasma is given by the phase diagram: Considering the diagrams¹ for Co or Ni with carbon we expect carbon-metal vapors to condense as liquids after having left the hot plasma. When the melt is further cooled, a metal free carbon phase will be segregated. Finally a metal rich phase deposits on these carbon particles.

2. Experimental

To simulate this system we produced different samples of fullerene black by vaporizing pure graphite in helium². Samples containing carbon blacks FI 101, CN 220 and FW2 (Degussa), pieces of glassy carbon (Sigradur G, HTW) and graphite (Edelgraphit) were also used for comparison. The soot materials were pressed into pellets. All samples were covered with thin sputtered films of Co, Ni or Mo and subsequently pyrolyzed in argon between 400 and 1200°C. The surfaces of the samples were examined with SEM. A few samples were also prepared for TEM and EELS analysis.

3. Results

In many cases only minor changes of the surface structure of the soot pellets were observed with SEM. The most significant change took place with the only fullerene containing material using Ni as a catalyst: Before the pyrolysis the material consisted of round carbon particles (Fig. 1). After sputtering of Ni and the subsequent pyrolysis at $T \geq 850^\circ\text{C}$ the surfaces became always completely covered with wormlike nanostructures (in Fig. 3.) TEM tilting experiments demonstrated that the nanostruc-

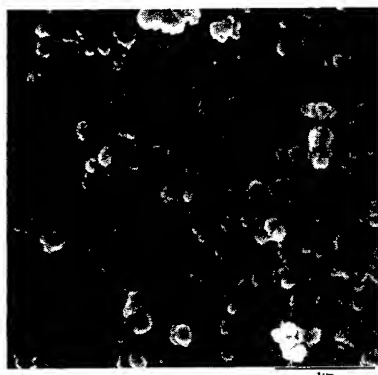


Fig.1 SEM: Surface of the fullerene black before the pyrolysis

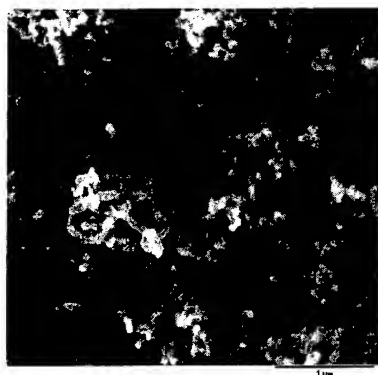


Fig.2 SEM: Surface of fullerene black sputtered with 25 nm nickel and subsequently pyrolyzed at 1000 °C for 3 min.



Fig.3 TEM: The worm-like material are chains of multi-walled carbon nanoparticles

tures are chains of hollow elongated carbon nanoparticles (Fig. 3). They often contained graphitic planes orientated in different directions with respect to the walls. The diameters of the chains were usually between 35 and 90 nm

although diameters as low as 30 nm and as high as 430 nm have been found. They did not change significantly along one chain. The walls are formed by up to 100 highly graphitic planes. The high degree of graphitisation in the walls is also observed by the EELS spectra, which are comparable with the ones we obtained from HOPG. On rare occasions encapsulated Ni particles were also observed using TEM. No fibers were generated, when Co or Mo was used instead of Ni. Most of the results with the fullerene containing soot and Ni are shown in Tab. 1. When we changed the parameters above 850°C, we did not observe any trends in the structure of the nanochains (NCs). We believe the reaction always occurred at the same temperature, immediately after the sample was

varied parameter	range	other parameters	results
time of pyrolysis	1 - 20 min	1000°C, 25 nm Ni	always worms
film thickness Ni	2 - 100 nm	1000°C, 3 min	always worms
oven temperature	400 - 1200°C	3 min, 25 nm Ni	T ≥ 850°C worms

Tab. 1 Experiments with the nickel covered fullerene black pellets

introduced into the hot reactor. Finally experiments were done to determine if the nanostructures were generated because of the fullerene content in fullerene black or the reaction of Ni with the solid amorphous carbon: Therefore we evaporated all volatile compounds like fullerenes from the soot at 1200°C in 15 min. Some of the fullerene free pellets were sputtered with Ni and subsequently pyrolyzed at 1000°C. No change in the sooty surface structure was observed. Pellets of this material mixed with 8 %wt. of C₆₀ (Hoechst) were sputtered with Ni and pyrolysed as before. The latter showed the same typical wormlike nanostructures as shown in Fig.2. The role of the

fullerenes as a feedstock in the formation of these NCs was also confirmed by our latest experiments, where we reacted C_{60} with metal films on different substrates.

The generation of similar NCs in electric carbon-metal arcs was also reported by Y.Saito et al.³ and S.Seraphin⁴. They found NCs of hollow graphitic particles with outer diameters of 10 - 20 nm in the cathode deposit using Ni or Fe as a catalyst. S. Seraphin observed (partly) encapsulated metal particles at one end of the chains. As in our experiments Co failed to produce NCs.

The Ni films on glassy carbon became only slightly roughened when pyrolyzed for 3 min. at 600°C. Between 700 and 1000 °C the glassy carbon was transformed into polycrystalline graphite⁵, indicated by the roughening of the surface. Above 1100 °C a process resembling melting resulted in the formation of metal droplets prior to the formation of graphite. We believe that the particles melted and lost the contact with the substrate. So it was impossible to absorb enough carbon to reach supersaturation, which would have resulted in the precipitation of graphite. We also observed melting processes of sputtered Ni and Co films on graphite starting at temperatures as low as 900°C.

4. Discussion:

A model for the growth of multi-walled carbon nanotubes (MWCNTs) from carbon containing gases is well established⁶: The idea originates from the vapor-liquid-solid-mechanism (VLS) for the formation of whiskers⁷. In this theory gaseous molecules are decomposed on the surface of a catalytic metal droplet. After diffusion of a compound, the local supersaturation causes the solute to precipitate continuously in the form of cylinders.. Tibbetts' equations⁸ explain why such carbon nanofibers are MWCNTs.

Our experiments proved that volatile fullerenes are the feedstock for generating NCs. It is reasonable to assume that they react as gaseous compounds with the metal in a VLS way. However, the precipitation of carbon is not continuous, as chains of nanoparticles were generated rather than MWCNTs. In the experiments with graphite melting processes of the Ni and Co films were observed at temperatures close to the point where the NC formation takes place. It is possible that the large carbon fluxes and the high temperatures involved in the formation of the NCs cause surface melting of the metal particles involved. Surface melting⁹ can be observed even below the already drastically reduced melting temperatures of small metal particles^{10,11}.

The model adapted from the VLS-model is shown in Fig. 4: (1)-(2): The heat converts the polycrystalline metal film into metal islands. (2)-(3): The exothermic decomposition and absorption of fullerenes can cause the metal to melt (a). Due to the surface tension the droplet loses contact with the substrate and the fullerenes can attack from all directions. No cooler region exists for fiber growth. This is hypothesized for Co films. (2)-(4): Alternatively, the diluted carbon may only cause surface melting of the particle (b). The carbon diffuses into the cooler regions near the substrate, where supersaturation leads to the segregation of carbon. More carbon can be stored in a molten phase than in a solid phase. (4)-(5): Graphitic planes are generated. The subsequent planes bend the previous one. The bending of the graphitic planes will stabilize the unsaturated sp^2 -orbitals of the border of graphene sheets by the overlap with the d-orbitals of the metal. (5)-(6): This contact then serves as a crystallization seed for the following segregation of carbon, initializing a cylindrical growth. (6)-(7):

The surface of the whole system grows as the reaction continues. The increased surface intensifies the cooling of the particle by the surrounding gas atmosphere and through radiation. This may cause the interface between metal and carbon fiber to solidify. The extra carbon stored on this side is segregated at once. (7)-(8): The new graphitic planes will close the previously built multi-walled cylinder. Excess planes will serve as the starting point for the next nano-unit to be formed in the same way.

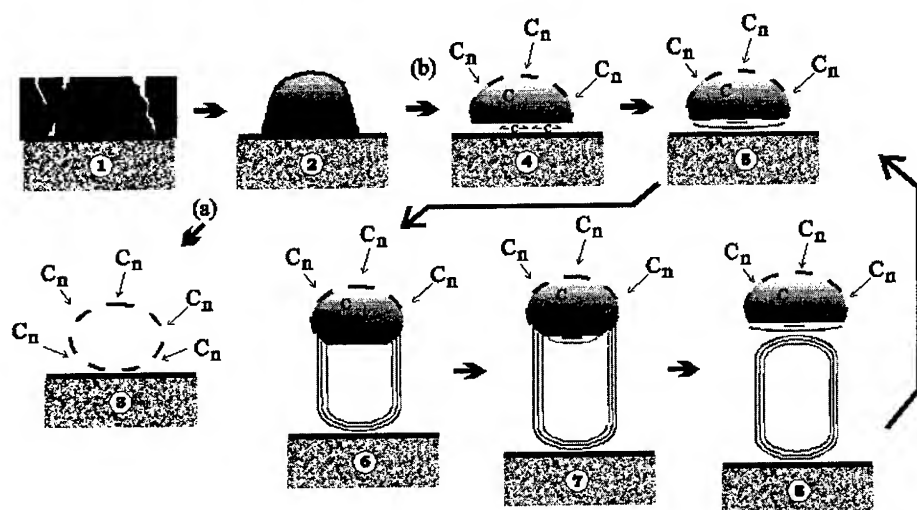


Fig. 4 Possible mechanism of nanochain formation, metal: dark \rightarrow cold, light \rightarrow hot, dashed line \rightarrow molten surface, solid line \rightarrow solid surface

Acknowledgement

This work has been funded by the German Ministry of Science and Technology and the SFB 337. The SEM pictures were taken by J. Nissen, ZELMI, TU Berlin. We received helpful information about cluster melting from Prof. Haberland.

Literature

- 1 T.B.Massalski, Binary Alloy Phase Diagrams, ASM International 1996
- 2 T.Belz et al. Ber. Bunsenges. Phys. Chem. **101** (1997) 712
- 3 S.Saito et al., J. Phys. Chem. Solids **54** (1993) 1849
- 4 S.Seraphin, Chem Phys. Lett. **228** (1994) 506
- 5 W.Weisweiler, Ber. Deut. Keram. Ges., **48.12** (1971) 519
- 6 N.M.Rodriguez, J. Mater. Res. **8.12** (1993) 3233
- 7 R.S.Wagner and W.C.Ellis, Trans. AIME **233** (1965) 1053
- 8 G.G.Tibbetts, J. Crystal Growth **66** (1984) 632
- 9 K.F.Peters et al., Appl. Phys. Lett. **71** (1997) 283
- 10 K.F.Peters et al., Phys. Rev. B, **57.21**(1998)13430
- 11 M.Schmidt et al., Phys.Rev. Lett. **79** (1997) 99

Electrochemical Preparation of Carbon Chains and Nanoparticles

Ladislav Kavan

J. Heyrovský Institute of Physical Chemistry, Dolejšková 3, CZ-182 23 Prague 8

Abstract. The composite of carbon with alkali metal fluoride, C-MF (M = Li, Na) was prepared by cathodic defluorination of perfluorinated hydrocarbons at room temperature. Raman spectra of C-MF from PTFE indicate carbon chains (oligoynes, 1974-2024 cm⁻¹) in addition to graphite-like carbon (1300-1500 cm⁻¹). The oligoyne-containing carbon is partly selforganized by cross linking towards graphene. Highly-organized carbons were prepared from friction-deposited PTFE films. AFM confirms perfect ordering of the precursor molecules (up to atomic resolution), but the corresponding carbonization product is rapidly reconstructed upon contact to air. Raman spectra of oriented carbons display high conjugation lengths (up to 18 *sp*-bonded carbon atoms). Cyclic perfluorinated precursors are also smoothly defluorinated to elemental carbon. TEM indicates that these carbons contain about 1 % of carbonaceous nanoparticles, i.e. nanotubes and onions. Also small quantity of fullerene C₆₀ (≈0.01 %) was detected in the toluene extract.

INTRODUCTION

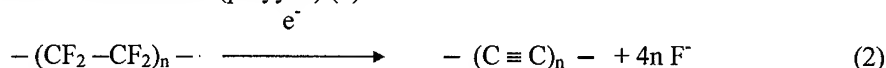
All-carbon molecules (oligoynes and fullerenes) and nanoparticles are usually prepared at high temperatures *via* controlled condensation of carbon vapor or by pyrolytic processes. However, elemental carbon can also be prepared at room temperature by chemical or electrochemical redox reactions of suitable precursors, CY_n (Y denotes general substituent(s)) (1):



These reactions might be thermodynamically very favored. For instance, the standard potential of reductive defluorination of poly(tetrafluoroethylene) (PTFE) is as high as 1 V (1). The electroreduction of PTFE proceeds either on a metal cathode in aprotic electrolyte solutions, or, to advantage, in a cell with alkali metal (M) amalgam anode. The latter is formed spontaneously at the PTFE/amalgam interface (1):



C-MF denotes the reaction product, i.e. a mixture of carbon with the alkali metal fluoride (1). According to an idealized scheme, the defluorination of PTFE may lead to *sp* bonded carbon chains (polyynes) (1):



Polyynes manifest themselves by a Raman line at about 2000 cm^{-1} (2,3). The defluorination (Eq. 2) is accompanied by a small over-reduction, i.e. n-doping of the formed carbon; the doping level equals about $0.2 \text{ e}^-/\text{C-atom}$ (1). Carbon from stretch-oriented PTFE foil shows the presence of partly oriented oligoynes with a maximum conjugation length of 16 carbon atoms (8 conjugated triple bonds) in the direction of alignment (2).

This paper aims at two targets:

1. To explore whether or not more organized carbon chains can be prepared from highly oriented PTFE films made by friction deposition ("hot-dragging") (4).
2. To employ the same strategy for carbonization of low-molecular weight fluorocarbons, which may serve as precursors for fullerenes and nanotubes.

EXPERIMENTAL SECTION

PTFE films were prepared from commercial foils (Goodfellow, 1 mm thick) by friction deposition on Si or glass (4). Perfluorocyclopentene, C_5F_8 , perfluorodecalin, $\text{C}_{10}\text{F}_{18}$ and perfluoronaphthalene, C_{10}F_8 (Fluorochem, Ltd.) were purified from trace humidity and oxygen, and distilled or sublimed in vacuum. The PTFE films were contacted at room temperature with the Li or Na amalgam (0.9-1.2 at%). Alternatively, the amalgam was exposed to a saturated vapor of purified low-molecular weight fluorocarbon at room temperature. In some cases, the preparation took place in an evacuated quartz optical cell (Hellma 220 QS), which served for *in-situ* Raman measurements (3). The prepared materials were studied by AFM (TopoMetrix 2010), XPS (VG Scientific ESCA 3 Mk II), Raman spectroscopy (T64000, Jobin/Yvon, Ar^+ laser, 1.5 – 2.0 mW, $\lambda = 488 \text{ nm}$) and TEM (Jeol, JEM-1200EX II). The carbons were extracted by toluene in a Soxhlet extractor for 20-40 hours, and the extracts were analyzed for fullerenes by HPLC and UV-Vis spectroscopy.

RESULTS AND DISCUSSION

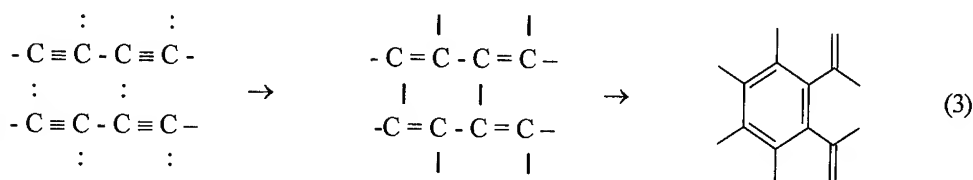
Carbon chains

The highly oriented PTFE films display the AFM patterns of perfectly aligned fluorocarbon macromolecules. These are defluorinated quantitatively (at least within the probing depth of XPS). Upon carbonization with Li-amalgam, the F 1s signal at 689.2 eV (CF_2) disappears completely, being replaced by a signal at 684.8 eV (LiF).

The carbonized film is sensitive to oxidation in air, which is reflected by C1s features of surface oxides at 284.6, 284.8, 286.7, 289.4 eV. Experiments failed, up to now, to see in C-MF also the highly ordered molecular structure of the precursor. This is probably due to the sample degradation during the AFM measurement in air.

Raman spectroscopy evidences a partial formation of *sp* bonded carbon chains in C-MF. The conjugation length is higher for oriented C-MF as compared to non-oriented C-MF and for C-NaF as compared to C-LiF. The frequencies of the C≡C stretching mode equal (in cm⁻¹): 2024 (ordinary C-LiF), 1988 (oriented C-LiF), 1996 (ordinary C-NaF) and 1974 (oriented C-NaF). Consequently, in terms of the conjugation length model (3), the oriented C-NaF shows about 18 carbon atoms in an unperturbed *sp*-chain. This is the best so far reported value for *ex*-PTFE carbons (1).

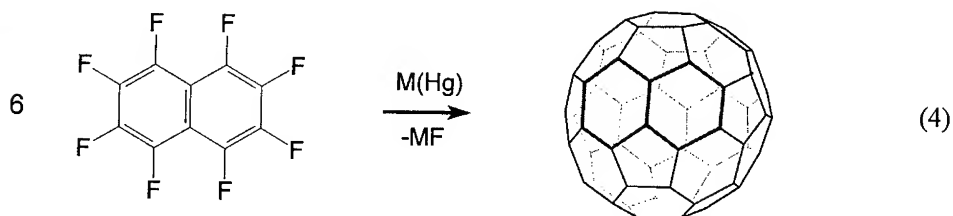
The products also contain *sp*² structures (with Raman features at 1300-1500 cm⁻¹), which are formed by subsequent intermolecular cross linking of the oligoynes:



Generally, no solid carbon material reported up to now contains *sp*-carbon chain in pure form, and discussions about its existence are still contradictory (5). Kawase et al (6) have recently shown that oligoynes in the electrochemical *ex*-PTFE carbon can be transformed to carbon nanoscale tubules upon electron irradiation at 600-800 °C. No such nanotubes were observed in our (as-received) carbons (C-MF). Also, there was no detectable amount of fullerene in the toluene extract from C-MF.

Fullerenes and Nanotubes

According to some hypotheses (7) the condensation of C₆₀ in carbon vapor starts from naphthalenoctyl radical (totally dehydrogenized naphthalene). This presents a challenge to generate the same precursor electrochemically by the amalgam-driven defluorination of perfluorodecalin or perfluoronaphthalene. Hence, the C₆₀ would be formed from six C₁₀ units according to the overall reaction scheme:



Analogous reasoning leads to a hypothesis that C_{60} may condense from twelve C_5 units, which can be derived from (perfluorinated) cyclopentane.

As in the case of PTFE (see above), chemical analysis confirmed a quantitative transformation of perfluorocyclopentene, perfluorodecalin and perfluoronaphthalene into a mixture of alkali metal fluoride and elemental carbon. The actual consumption of $M(Hg)$ was again by about 10-15% higher than the stoichiometrically requested amount, which is due to n-doping of the electrochemical carbon (1)

The HPLC and UV-Vis analyses revealed the presence of fullerene, C_{60} in toluene extracts. Hence, the model reactions (cf. Eq. 4) do occur in reality, and - to the best of our knowledge - this is the first evidence that fullerenes can be prepared by a simple chemical process at room temperature. However, the yield of C_{60} was poorly reproducible, and usually below 0.01% of the total amount of carbon produced¹.

TEM and electron-diffraction studies revealed the presence of graphitic carbon nanotubes, both straight and curly. The straight nanotubes were typically about 15 nm in diameter and 100-200 nm long. The yield of carbon nanotubes was *ca.* 1-2 % in the best samples. Spheroidal graphitic carbon grains of about 20-100 nm size were also occasionally detected; they are similar to onion-like particles. This is again a first indication that carbon nanotubes and onions can be prepared by "soft chemistry" at room temperature.

ACKNOWLEDGMENTS

This work was supported by the Grant Agency of the Czech Republic (contracts Nos. 203/98/1168 and 203/99/1015). Thanks are due to Prof. Asao Oya (University of Gunma) for TEM analyses and to Dr. Lothar Dunsch (IFW Dresden) for Raman measurements.

REFERENCES

1. Kavan, L., *Chem.Rev.* **97**, 3061-3082 (1997).
2. Kavan, L., Hlavaty, J., Kastner, J. and Kuzmany, H., *Carbon* **33**, 1321-1329 (1995).
3. Kastner, J., Kuzmany, H., Kavan, L., Dousek, F.P. and Kürti, J., *Macromolecules* **28**, 344-353 (1995).
4. Wittmann, J.C. and Smith, P., *Nature* **352**, 414-417 (1991).
5. Heimann, R.B., Evsyukov, S.E. and Kavan, L. (Eds.), *Carbyne and Carbynoid Structures, Physics and Chemistry of Materials with Low-Dimensional Structures, Vol. 21* Dordrecht: Kluwer Academic Publ., 1999.
6. Kawase, N., Yasuda, A., Matsui, T., Yamaguchi, C., Matsui, H., *Carbon* **37**, 522-524 (1999).
7. Goeres, A. and Sedlmayr, E., *Chem.Phys.Lett.* **184**, 310-317 (1991).

¹⁾ The best observed yield of C_{60} was 0.36 % (according to HPLC and UV-Vis) in one batch from C_5F_8/Li -amalgam, but we failed to reproduce this value in subsequent experiments.

Preparation of Carbyne-Like Films by Dehydrochlorination of Poly(Vinylidene Chloride)

Tetsuya Danno, Kaori Murakami and Ruriko Ishikawa

*Department of Lifestyle Design, Kochi Women's University
5-15 Eikokuji-Cho, Kochi 780-8515 JAPAN*

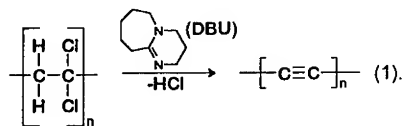
Abstract. Films of conjugated carbyne-like system was obtained by dehydrochlorination of poly(vinylidene chloride) (PVDC) by the two step treatments with 1,8-diazabicyclo[5,4,0]undec-7-ene (DBU). Amorphous region of PVDC was dehydrochlorinated in the proper swelling solution at the first step treatment and the crystalline region was treated in the pure solvent at the second step, so that the film shape was kept after the whole treatments. Two characteristic IR absorption bands were observed at ca. 2000 and ca. 1650 cm^{-1} which are assigned to stretching vibration of polyne structure($\nu_{\text{C}\equiv\text{C}}$) and that of polyene structure($\nu_{\text{C}=\text{C}}$), respectively. The intensity of $\nu_{\text{C}\equiv\text{C}}$ decreased with time upon storage even under the inert atmosphere.

INTRODUCTION

Carbyne has attracted the particular interest of researchers from the point of view of the simplest linear chains of carbon atoms and the fourth allotrope of carbon[1]. In spite of the effort of synthesis, *e.g.*, catalytic and electrochemical polycondensation of acetylene compounds[2,3], the suitable size of samples, especially single crystal, have not been available. The most known route to obtain the carbyne system is the polymer reaction, *e.g.*, dehydrohalogenation[4,5] or reductive defluorination of PTFE[6].

We have obtained polyene films with high content of conjugated Sp^2 carbon by dehydrochlorination of solid poly(vinyl chloride) using 1,8-diazabicyclo[5,4,0]undec-7-ene (DBU), which is the strongest organic base so far known, in polar solvents[7]. The film shape was kept by the two step treatments, each amorphous and crystalline region is dehydrochlorinated stepwise.

In this paper we prepared the carbyne-like film system from the poly(vinylidene chloride)(PVDC) under the similar working hypothesis to the previous work as following equation:



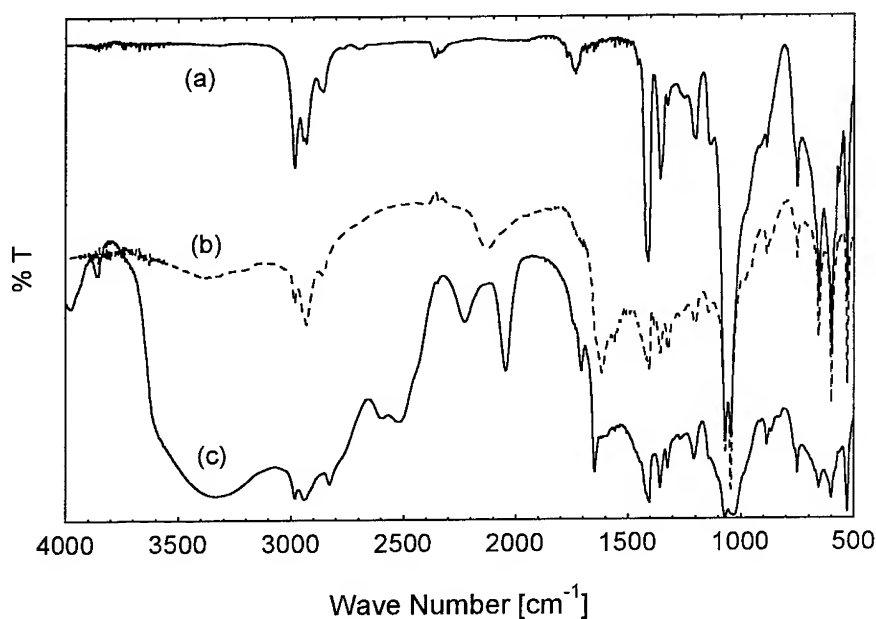


FIGURE 1. IR spectra of (a) PVDC; (b)(c) dehydrochlorinated PVDC(after 2nd-step treatment).

EXPERIMENT

Commercially available food-wrapping grade PVDC(Saran, copolymer of vinylidene chloride (VDC) and vinyl chloride (VC) (VDC/VC = ca.9/1)) was chosen as a starting material. Additives were removed from raw material by usual extracting manner. Films about half μm thick were spin-coated on the KBr single crystal cleavages(ca. 1 cm^2) from THF solutions and annealed at 120°C in air for 4 hr thereafter. Dehydrochlorination was carried out under the Schlenk flask techniques, inert atmosphere, and vacuum line techniques. In the first-step treatment, acetone was used as a swelling solvent and THF was chosen in the second-step. Typical concentration of DBU in the solvents was ca. 1 vol.%. Dehydrochlorination was carried out at 50°C for 12 hr in each step. Specimens were rinsed with MeOH and dried *in vacuo*. Infrared spectra and optical absorption spectra were recorded in inert atmosphere with transmittance mode.

RESULTS AND DISCUSSION

As spin-coated specimen without annealing was easily dissolved into the reaction solution even in the 1st-step treatment. From the DSC thermal analysis the morphology of the crystalline region in PVDC was much arranged after annealing, so that the treatment could be possible in the swelling medium. Thus in the 1st-step treatment,

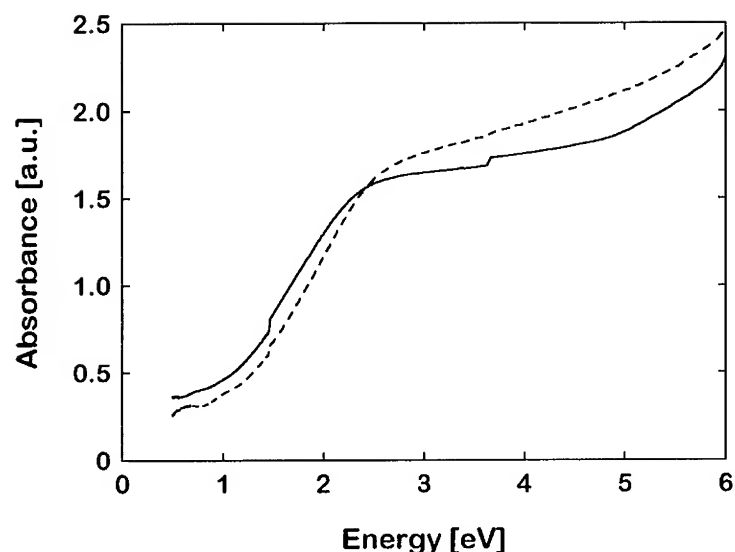


FIGURE 2. Optical absorption of dehydrochlorinated PVDC films. Broken line: after 1st-step treatment; solid line: after 2nd-step treatment.

amorphous region of PVDC was swollen and dehydrochlorinated, and crystalline region played as a cross link point to keep the film shape. Similarly in the 2nd-step treatment, crystalline region was swollen and dehydrochlorinated, and carbyne-like species already formed from the amorphous region played a role to keep the film shape.

FIGURE 1. shows the IR spectra of starting PVDC and two different dehydrochlorinated specimens treated under the same condition. Although the specimens were treated in the pure solvent system (DBU/THF) at the 2nd-step treatment, characteristic band from starting PVDC around 1000 cm⁻¹ is still observed, which means that the dehydrochlorination in the crystalline region was not enough carried out.

From the reproducibility check most of dehydrochlorinated specimens showed the similar spectra to type (b) in FIGURE 1. and very few showed as type (c). In type (b) a weak and broad absorption band around 2100 cm⁻¹ was observed, whereas the strong and sharp absorption band at ca. 2040 cm⁻¹ in type (c). Both two absorption bands were assigned to $\nu_{C\equiv C}$ stretching vibration in polyene structure[2,3,4]. In analogy with the observed and calculated Raman shifts for the conjugated carbon triple bonds[8], frequency of IR $\nu_{C\equiv C}$ stretching vibration band corresponds to the conjugation length, *i.e.*, lower frequency means the longer conjugation length. Therefore the conjugation length in type (c) is longer than the one for type (b), and such longer conjugated sample is difficult to obtain with good reproducibility.

Relatively sharp absorption bands at ca. 1640 cm⁻¹ are observed in both IR spectra. This band attributed to $\nu_{C=C}$ stretching vibration in polyene structure[4]. Thus the sample consists of both Sp² and Sp carbon. Although the starting material is the

copolymer of VDC and VC, the minor component of VC comonomer was inserted randomly into the chain during polymerisation. Therefore the isolated carbon double bond formed from the VC component plays as a terminating defect for conjugated carbon triple bonds. Polyene structure is proposed as the reaction products owing to incomplete or inter chain dehydrochlorination, as well as side reactions of cross linking[9]. The intensity of $\nu_{C=C}$ decreased with time upon storage even under the inert atmosphere. These changes also suggest the aging and cross linking of chains.

There are many arguments that IR bands from 1000 to 1600 cm^{-1} are attributed to the polycumulene[2,5] combining the experimental data with the quantum calculations[10]. In this study, however, no significant evidence was observed about this kind of argument, since the absorption bands from the remaining starting PVDC lap over the one for carbyne-like material.

FIGURE 2. shows the optical absorption of dehydrochlorinated PVDC films. Similar results were observed in the previous works[4,8], but no clear absorption maximum was observed in the present study. Absorption edge shifted downwards about 0.2 eV (from 0.8 eV to 0.6 eV) after 2nd-step treatment compared with the one after 1st-step treatment. Furthermore, clearer plateau region around 3eV is observed in the curve after 2nd-step treatment. These features suggest that carbyne-like species formed from crystalline region after 2nd-step treatment have narrower HOMO-LUMO transition energies, which means existence of the longer conjugated carbon-carbon bonds[8].

ACKNOWLEDGEMENTS

The authors acknowledge Dr. M. Goto for his kind help in the DSC measurements. The financial support from Ms. N. Danno to one of the authors (T.D.) is highly appreciated.

REFERENCES

- [1] Kudryavtsev, Yu.P., Heimann, R.B., in *Carbyne and Carbynoid Structures*, eds R.B. Heimann, S.E. Evsyukov, L. Kavan, Dordrecht/Boston/London, KLUWER ACADEMIC PUBLISHERS, 1999, Ch. 1, pp. 1-7.
- [2] Kijima, M., Sakai, Y., Shirakawa, H., *Chemistry Letters*, 2011-2014(1994).
- [3] Kijima, M., Sakai, Y., Shirakawa, H., *Synthetic Metals*, **71**, 1837-1840(1995).
- [4] Akagi, K., Nishiguchi, M., Shirakawa, H., *Synthetic Metals*, **17**, 557-562(1978).
- [5] Evsyukov, S.E., in *Carbyne and Carbynoid Structures*, eds R.B. Heimann, S.E. Evsyukov, L. Kavan, Dordrecht/Boston/London, KLUWER ACADEMIC PUBLISHERS, 1999, Ch. 3, pp. 55-74.
- [6] Kavan, L., *Carbon*, **36**, 801-808(1998).
- [7] Danno, T., Kondoh, H., Furuhashi, K., Miyasaka, K., *J. Appl. Poly. Sci.*, **29**, 3171-3184(1984).
- [8] Kastner, J., Kuzmany, H., Kavan, L., Dousek, F.P., Kürti, J., *Macromolecules*, **28**(1), 344-353(1995).
- [9] Kavan, L., Kastner, J., in *Carbyne and Carbynoid Structures*, eds R.B. Heimann, S.E. Evsyukov, L. Kavan, Dordrecht/Boston/London, KLUWER ACADEMIC PUBLISHERS, 1999, Ch. 6, pp. 343-356.
- [10] Kürti, J., Magyar, C., Balázs, A., and Rajczy, P., *Synthetic Metals*, **71**, 1865-1866(1995).

X-ray emission spectroscopy study of C_2F intercalated with benzene

A.V. Antich¹, A.V. Okotrub², L.G. Bulusheva², V.M. Paasonen²

¹ - 2 Pirogova St., Novosibirsk State University, Novosibirsk, Russia

² - 3 Lavrenteva Ave., Institute of Inorganic Chemistry SB RAS, Novosibirsk, Russia

Abstract. We have studied $(C_2F)_n \bullet C_6H_6$ intercalation compound by means of x-ray fluorescence spectroscopy "as is" and after heat treatment at 150 °C *in situ*. Differential spectrum of these two in general represents electronic state of carbon atoms in benzene molecules contained within C_2F matrix. Observed changes in the obtained spectrum compared with the spectrum of pure solid benzene result from interactions between C_6H_6 molecules and graphite fluoride (GF) layers.

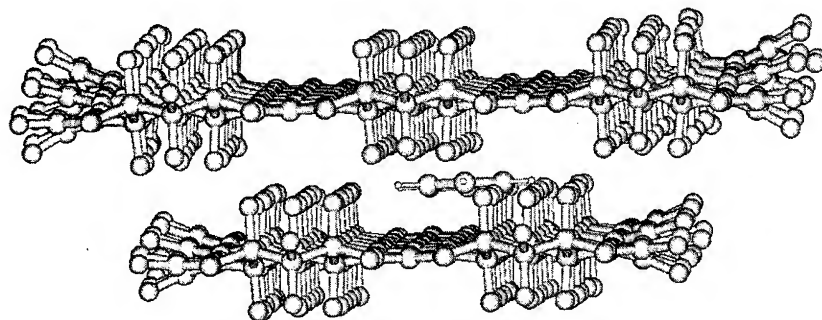
I INTRODUCTION

Chemical treatment of graphite with halogen fluorides (BrF_3 , ClF_3) at room temperature leads to formation of graphite fluoride intercalated compounds C_nHalF_m , where $Hal = Br, Cl$. Along with fluoridation, another process occurs - inclusion of some amount of molecules between the GF layers. The resulting composition of the compound is given as $C_xFHal_y \bullet zR$, where $x \approx 2$, $y \approx 0.1(0.02)$ for $Hal=Cl(Br)$, R denotes molecules of different possible intercalants [1,2]. Molecules R can be easily substituted for different organic or inorganic molecules [3] that afterwards remain for long periods of time inside the C_2F matrix with extremely low vapor pressure ($10^{-4} - 10^{-5}$ torr) even in case of volatile compounds [4].

Distribution of fluorine atoms on graphene sheets in C_2F is still known, as well as the nature of interactions between inserted molecules and GF layers. One of the most developed models suggests the structure of C_2F layer composed of fully fluorinated stripes alternating with the areas of aromatic carbon hexagons (Fig.1).

In order to investigate the electronic structure of benzene molecules intercalated into GF we have used high resolution x-ray fluorescence spectroscopy. $CK\alpha$ spectrum originates from electron transitions from occupied orbitals to $C1s$ vacancies of a compound. In framework of Koopman's theorem distance between the lines in $CK\alpha$ spectrum on energy scale corresponds to one electron energies difference. Line intensity is proportional to 2p-AOs contribution to the orbital from which the transition occurs.

FIGURE 1. Suggested model of the $C_2F \bullet C_6H_6$ intercalation compound

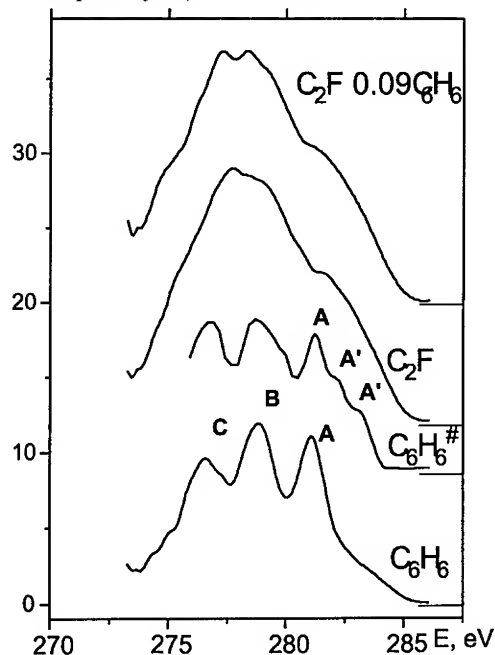


Both benzene and GF carbon atoms contribute to the formation of x-ray spectrum creating a necessity to exclude benzene carbon atoms contribution to the spectrum. GF intercalated compounds present a possibility to remove inserted molecules by means of heat treatment. Mass-spectrometry measurements have demonstrated that vacuum heat treatment of the studied compound leads to extraction of the most of C_6H_6 molecules at 130-150 °C. This fact allows to suppose that the difference between original and heat-treated samples' spectra would be characteristic of, to a large degree, benzene electronic structure.

II EXPERIMENTAL

Synthesis of $C_2F \bullet C_6H_6$ compound was performed as described in [3]. Product composition is $C_2F_{0.85} \bullet (C_6H_6)_{0.1} \bullet Br_{0.05}$. $CK\alpha$ spectra have been obtained with the laboratory x-ray spectrometer "Stearat" as described below. Original $C_2F \bullet C_6H_6$ sample was placed on the copper support and cooled down to the liquid nitrogen temperature in the x-ray tube vacuum chamber. After we had measured the spectrum of the original compound (1) the sample was heated to 150 °C inside the vacuum chamber during 45 minutes. Finally, heat-treated sample (2), that we expect to contain minimal amount of benzene molecules, was cooled down again and its x-ray fluorescence spectrum was recorded. Spectrum of the pure solid benzene was obtained by method described elsewhere [5]. Spectra were recorded at a pressure of 10^{-4} Pa, anode voltage of 6 kV and 0.5 A cathode current. Resolution of the spectra is about 0.4 eV. Gas proportional counter with methane filling at 0.1 atm was used for x-ray radiation registration. Ammonia biphthalate (NH_4AP) mono-crystal was used as crystal-analyzer. Reflection efficiency of this crystal near the CK absorption edge decreases 30-40 times over a region of 10-15 eV. To correct this behavior a special mathematical procedure was used [6].

FIGURE 2. X-ray emission spectra of (from top to bottom): initial sample; heat treated sample; difference between them multiplied by 10; solid benzene.



III RESULTS AND DISCUSSION

Spectral profiles of both samples (Fig.2) are similar and present two major features: peak A in the short-wave region (280-284 eV) and more intensive band B that occupies the interval from 274 to 280 eV. Differential spectrum obtained by subtraction of heated sample's spectrum from the original one corresponds to x-ray fluorescence spectrum of benzene molecules removed during the heating procedure. This spectrum multiplied by 10 is plotted in Fig.2. It should be noted that this spectrum is affected by the change in C_2F matrix structure as well. However we have reasons to believe that the effect associated with matrix deformation can be neglected in comparison with the contribution by benzene molecules.

X-ray spectrum of pure benzene (Fig.2) has three clearly distinguished peaks A, B and C. Low statistics of the experiment does not allow to obtain valid information of the energy region below 280 eV (area occupied by B and C peaks) in the differential spectrum. However, comparing this spectrum to solid benzene line one can easily observe short-wave peak A splitting into three: A, A' and A". We consider this to be a result of the change in electronic structure of benzene, which originates from interaction with GF layers.

First peak splitting in the x-ray spectrum of benzene may and actually does have

two roots: 1) due to low symmetry of the layers HOMO of benzene splits into two orbitals, producing two lines in the spectrum; 2) core 1s levels of different carbon atoms in a benzene molecule have different energy, producing up to six different lines. The latter effect takes place if the charge distribution within a benzene molecule is asymmetric due to either a chemical bond formation or presence of electric field gradient. This may easily be the case in $C_2F \bullet C_6H_6$ compound if a benzene molecule is inclined under a certain angle with respect to a GF layer. Which of these two effects has major contribution in the spectrum is subject to further theoretical investigations. However, since one observes *three* and not *two* peaks, electric field influence on core levels seems to be the most likely candidate responsible for the spectrum alteration.

IV CONCLUSION

X-ray fluorescence spectroscopy study of electronic state of benzene molecules intercalated into C_2F matrix has been done. It was shown that differential spectrum associated with inserted benzene molecules has significant differences in comparison to the spectrum of solid benzene. Obtained spectrum profile can be explained by the assumption that benzene molecules do not form chemical bond with fluorine atoms of GF but are situated under an angle to a GF layer that creates electric field.

V ACKNOWLEDGEMENTS

This work is supported by grant no. 4.14.99 of "Modern directions in condensed matter physics" program, direction "Surface atomic structures".

REFERENCES

1. Nikanorov Yu.I., Gornostaev L.L., *Russ.Chem.Bull.*, **9**, v.4, 55-59 (1979)
2. Makotchenko V.G., Nazarov A.S., Yakovlev I.I., *Zh.Neorg.Khim.*, **42**, no.4, 584-587 (1997)
3. Yudanov N.F., Yakovlev I.I., *Russ.Chem.Bull.*, **2**, v.1, 66-69 (1988)
4. Makotchenko V.G., Nazarov A.S., Yur'ev G.S., Yakovlev I.I., *Zh.Neorg.Khim.*, **36**, no.8, 1950-1955 (1991)
5. Okotrub A.V., Yumatov V.D., Mazalov L.N. et al, *Zh.Struktur.Khim.*, **29**, no.2, 167-170 (1988)
6. Yumatov V.D., Okotrub A.V., Mazalov L.N. et al, *Zh.Struktur.Khim.*, **26**, no.4, 59-64 (1985)

Vandium pentoxide nanowires

J. Muster, V. Krstic, M. Burghard, and S. Roth

Max-Planck-Institut für Festkörperforschung, Heisenbergstr. 1, D-70569 Stuttgart, Germany

Abstract. Colloidal vanadium pentoxide sols consist of individual V_2O_5 fibres which are uniformly 1.5 nm high and 10 nm wide. Their length depends on the age of the sol and can reach up to several μm . Fibres were deposited on chemically modified electrode structures with electrode separations of 3 μm and about 150 nm, respectively. Position and shape of the nanowires on the electrodes were determined by Scanning Force Microscopy. Electrical transport measurements revealed non-linear characteristics at room temperature and 4.2 K. In addition, the transport behaviour of networks of V_2O_5 fibres is interpreted in terms of one-dimensional variable range hopping.

1 INTRODUCTION

Vanadium pentoxide sols have been known since the beginning of this century (1). A sol is a colloidal suspension of solid particles in a liquid (2). In the case of vanadium pentoxide sols, V_2O_5 fibres, 1.5 nm in height and 10 nm wide, are dispersed in water. The length of the fibres depends on the age of the sol and can reach up to several μm (3). There are various synthetic routes to prepare these sols, which all are based on polycondensation of molecular precursors such as vanadates or vanadium alkoxides (3). Despite the knowledge of V_2O_5 sols for a long time, it has been only a decade since the internal structure of the fibres was resolved by cryo-Transmission Electron Microscopy (TEM) and X-ray diffraction (3, 4). The basic structural units of a fibre are VO_5 square pyramids, which are assembled into 2.5 nm wide fibrils. Eight of these

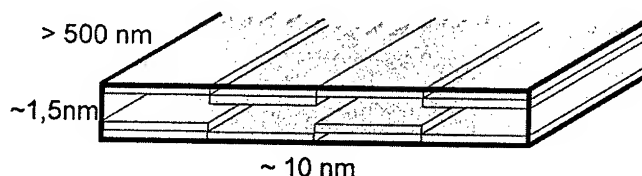


FIGURE 1. Schematic representation of an individual V_2O_5 fibre consisting of 8 fibrils in a double layer structure. The length of the fibres depends on the age of the sol and can reach up to several μm .

fibrils, arranged in a double layer structure as shown in Fig. 1, form a V_2O_5 fibre. Consequently, each fibre consists of only two layers of vanadium atoms and represents a wire of molecular dimensions.

It is known from electrical studies on amorphous and crystalline V_2O_5 bulk material, that transport proceeds via hopping between vanadium(V) and vanadium(IV) impurity centres (3, 5, 6). Until now, to the best of our knowledge, electric transport measurements on thin V_2O_5 networks or on individual V_2O_5 fibres have not been reported. Especially the latter are of great interest, because their conductivities might be compared with the electrical behaviour of other molecular wires such as carbon nanotubes.

2 EXPERIMENTAL

V_2O_5 sols were prepared from 0.2 g ammonium(meta)vanadate (NH_4VO_3) and 2 g acid ion exchange resin (DOWEX 50WX8-100) in 40 ml water. After a few hours, the formation of an orange coloured sol is observed. Longer fibres (up to a few μm) are obtained after a few days.

Electrode arrays were created on Si wafers with a 1 μm thick thermally grown SiO_2 layer. Electrode structures with 3 μm gaps were fabricated by conventional optical lithography, the structures with 150 nm gap using conventional e-beam lithography.

Both bare Si/ SiO_2 substrates and the electrode arrays were chemically modified with 3-aminopropyltriethoxysilane (3-APS) (6 μl in 10 ml water) for about 15 min, which creates positively charged ammonium-groups on the SiO_2 surface.

V_2O_5 network samples were prepared as follows: a droplet of a several day old, undiluted V_2O_5 sol was deposited on the electrode structure with the larger gaps. After 15 min, the sample was rinsed with water and blown dry with air. For deposition of individual fibres on the electrodes separated by 150 nm, the whole substrate was dipped into a mixture of V_2O_5 sol/water (1:10) for 3 s. Afterwards, the substrate was rinsed with water and blown dry.

The samples were characterised before electrical transport measurements with a Scanning Force Microscope (SFM, Digital Instruments, Nanoscope IIIa) in Tapping Mode. The transport experiments were performed with Keithley current and voltage sources at room temperature (RT) and liquid He temperature (4.2 K).

3 RESULTS AND DISCUSSION

To investigate the electrical transport behaviour of an individual V_2O_5 fibre, a way had to be found to deposit the fibres onto electrode structures without aggregation. In these experiments, bare Si/ SiO_2 substrates were used to optimise the adsorption parameters. If a droplet of the V_2O_5 sol is just dried on a SiO_2 surface, a so-called xerogel is obtained, which forms ordered colloidal phases (tactoids), as shown by the

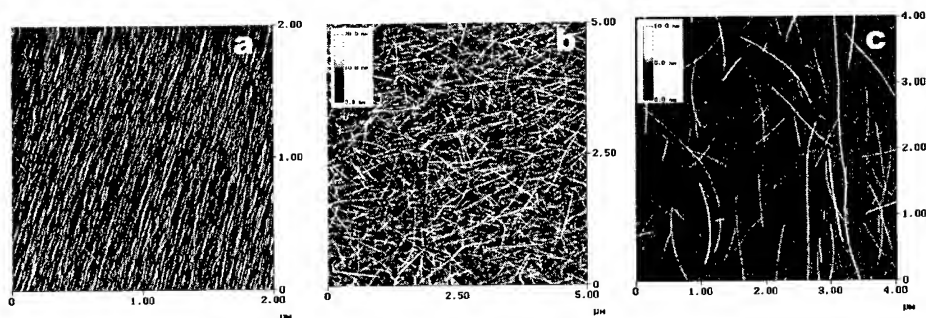


FIGURE 2. SFM images of (a) V_2O_5 xerogel forming an ordered tactoid, (b) dense V_2O_5 network, and (c) individual V_2O_5 fibres adsorbed on a chemically modified SiO_2 surface.

SFM image in Fig. 2a. This ordering results from the increased interaction between the fibres upon drying (3). In contrast, a disordered, but dense network of V_2O_5 fibres is obtained if the sol is adsorbed on SiO_2 for a couple of minutes and afterwards the excess rinsed away with water (Fig. 2b). Obviously both procedures do not yield well-separated, individual fibres. The situation is improved by taking advantage of the negative surface charge of the V_2O_5 fibres (3), which can interact with the positively charged ammonium-groups on the 3-APS treated SiO_2 surface. Using optimised parameters like concentration of the sol and adsorption time, we succeeded in the deposition of individual fibres, as exemplified in Fig. 2c. In this sol, the average length of V_2O_5 fibres was about $1\text{ }\mu\text{m}$. The measured height of 1.5 nm is in accordance with the value for individual fibres known from TEM investigations (4). However, the observed width of about 25 nm appears to be too large for individual fibres, but can be explained by tip convolution of the SFM.

After successful deposition of individual fibres onto bare substrates, a similar procedure was applied to deposit individual fibres on electrode arrays. SFM investigation revealed in most cases up to 10 individual fibres in contact with the gold electrodes. Nevertheless, further optimisation of the adsorption process should allow the deposition of only one individual fibre onto one electrode array.

To get a first impression of the conductivity of the V_2O_5 fibres, electrical measurements on thin networks adsorbed on electrode structures with gaps of about $3\text{ }\mu\text{m}$ were performed (Fig. 3a). The current/voltage (I/V) characteristic of these networks was found to be non-linear at RT (Fig. 3b). Figure 3c shows that the network resistance increases with decreasing temperature. Bullot et al. reported transport measurements on amorphous V_2O_5 films revealing thermally activated hopping between vanadium IV- and V-centres (5). In general, the amount of vanadium(IV) and hence, the resistivity, depends on the preparation method of the V_2O_5 . Vanadium in oxidation state IV forms localised states in the band gap. In the following, we evaluate our data in terms of variable range hopping (VRH), which is well known from, e.g.,

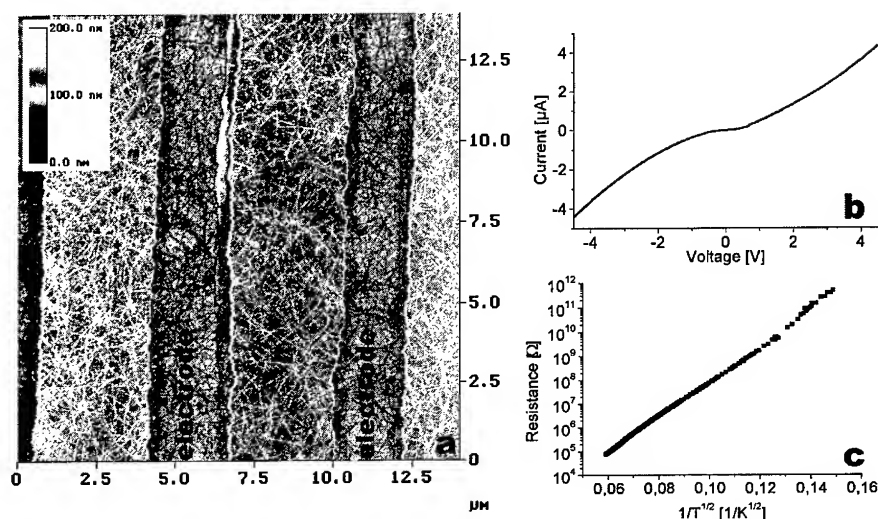


FIGURE 3. (a) SFM image of a V_2O_5 network deposited on an electrode array with $3\ \mu\text{m}$ gaps. (b) I/V characteristic of the sample at RT. (c) MOTT plot for one-dimensional variable range hopping.

conducting polymers (7). For VRH, the temperature dependence of the resistance is described by the MOTT law:

$$\ln \frac{R_0}{\rho} = - \left(\frac{T_0}{T} \right)^{\frac{1}{1+d}}, \quad (1)$$

where ρ is the resistance at temperature T , ρ_0 the resistance at temperature T_0 , and d the dimensionality of the hopping process. The data could be fitted best with $d=1$ (Fig. 3c). This result might be related to a dominant electron transport along the quasi one-dimensional V_2O_5 fibres.

Following the investigation of network samples, individual fibres were adsorbed on electrode arrays with an electrode distance of about $150\ \text{nm}$. In the specific example shown in Fig. 4a, about seven individual V_2O_5 fibres have contact with the middle electrode pair. As observed for the network, the I/V characteristic is non-linear at RT (Fig. 4b). When applying a bias of about $1\ \text{V}$, a current in the nA range was obtained. At $4.2\ \text{K}$, a bias larger than $3.5\ \text{V}$ was needed to obtain currents exceeding $1\ \text{pA}$ (Fig. 4c). Thus, the conductivity of the sample is strongly frozen out and/or the contact between the fibres and the electrodes is strongly temperature dependant. Nevertheless, even for a few V_2O_5 fibres, as in Fig. 4a, electrical transport measurements are still possible.

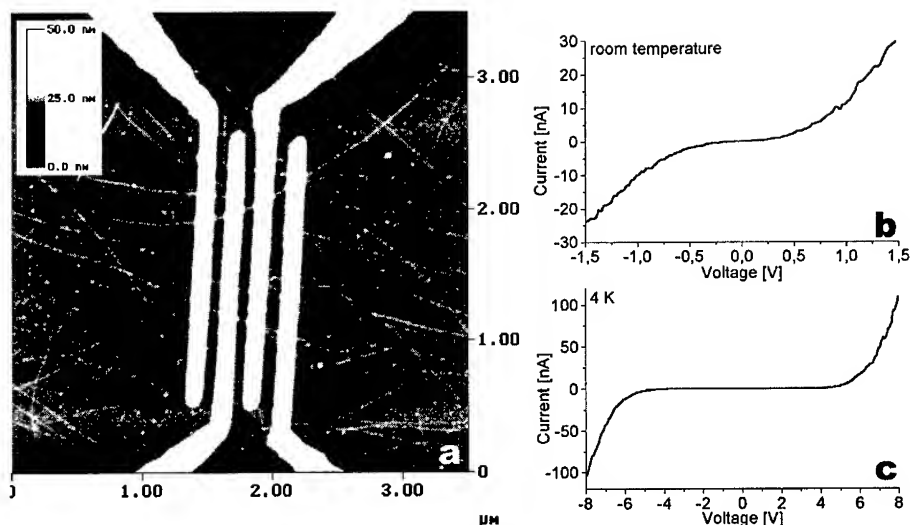


FIGURE 4. (a) SFM image of individual fibres adsorbed on an electrode array with 150 nm electrode separation. I/V characteristic obtained from the middle electrode pair at RT (b) and at 4.2 K (c).

CONCLUSION

Individual V_2O_5 fibres can be adsorbed on chemically modified SiO_2 surfaces and electrode arrays. Transport measurements on dense networks of V_2O_5 fibres revealed one-dimensional hopping conductivity. A few individual V_2O_5 fibres adsorbed on an electrode array are sufficiently conducting to allow electrical measurements. By optimising the adsorption process, transport experiments on only one individual fibre should become possible.

ACKNOWLEDGMENTS

The authors are grateful to G.-T. Kim (Seoul National University, Korea) and M. Wagenhals, who performed measurements on the V_2O_5 networks.

REFERENCES

1. Biltz, W., *Ber. Dtsch. Chem. Ges.* **37**, 1098 (1904).
2. Brinker, C. J., Scherer, G.W., *Sol-Gel science*, New York: Academic Press, 1990.
3. Livage, J., *Chem. Mater.* **3**, 578-593 (1991).
4. Bailey, J. K., Pozarnsky, G. A., McCartney, M. L., *J. Mater. Res.* **7**, 2530-2537 (1992).
5. Bullot, J., Gallais, O., Gauthier, M., Livage, J., *Appl. Phys. Lett.* **36**, 986-988 (1980).
6. Perlstein, J. H., *J. Solid State Chem.* **3**, 217-226 (1971).
7. Roth, S., *One-dimensional metals*, Weinheim: VCH, 1995.

Production and Investigation of Vanadium Pentoxide (V_2O_5) Nanostructures Grown in IR Laser-Field

R. Vajtai¹, J. Janicskó-Csáthy¹, L. Thiên-Nga², L.-M. Bonard² and L. Forró²

¹Department of Experimental Physics, JATE University, H-6720 Szeged, Dóm tér 9., Hungary

²Physics Dept./IGA, Ecole Polytechnique Federale de Lausanne, CH-1015 Lausanne, Switzerland

Abstract. The synthesis of nanometer-sized vanadium-pentoxide structures by continuous IR laser induced oxidation under air is reported. In these experiments the beam of a Nd:YAG laser was slightly focused onto the surface of a $8 \times 8 \times 0.3 \text{ mm}^3$ vanadium sheet in order to reach a controlled temperature region of 900–1100 °C. During oxidation of the vanadium sample and after the cooling-off period different vanadium oxide nanostructures are formed. The size of the crystallites (measured by SEM) lays on 10 nm scale in width and on μm scale in length. SEM images clearly show a tubular structure in some samples. The dependence of the formation of different structures on external parameters (oxygen, electric field etc.) is studied.

INTRODUCTION

At the moment of the discovery of the first carbon fullerenes [1] and, a few years later, carbon nanotubes [2], attention of theoretical and experimental scientists was drawn to prospect new structures. We have discovered a lot of unbelievable properties and features, but this story hasn't ended. Every new structure and every new material in the nanometer range can help us make optimally designed (tailored) nanostructures for micro-(nano)mechanics, micro-(nano)electronics, micro-(nano)optics and micro-(nano)biology. Quasi one-dimensional structures showing big length/width ratio are of particular importance. As derived from ab-initio calculations, nanotubes not only of carbon, but of boron, boron nitride and similar materials are stable, too. Microtubules generated by laser assisted oxidation of vanadium [3] and nanotubes on a carbon nanotube template [4] made of vanadium pentoxide has been reported. The laser-generated oxide micro-crystallines have a rectangular shape and the free surface of thin laser-fabricated material is 1000 times higher than the free surface of vanadium-pentoxide micro-powder used in the industry. In this work we investigated

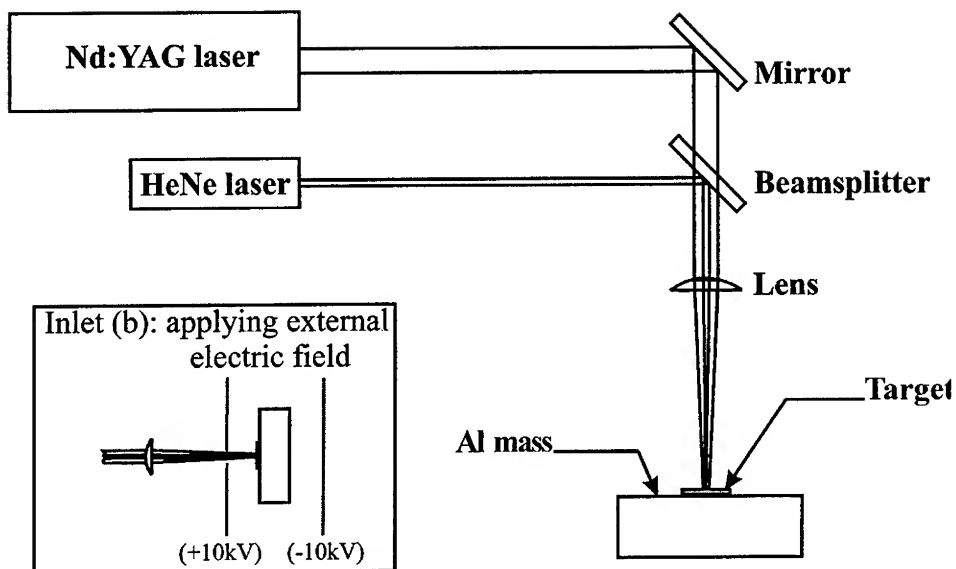


FIGURE 1. Experimental setup

experimentally whether the laser generated micro-crystas can be shrunk down into the nanometer region by changing the illumination parameters.

EXPERIMENTAL

The experimental setup of laser illumination is given in Fig 1. Metallic vanadium samples were illuminated by a continuous wave Nd:YAG laser ($\lambda=1.060 \mu\text{m}$) in ambient air and oxygen atmosphere. Several targets were illuminated in the presence of external electric field (Fig. 1(b)). The optical alignment procedure was helped by a HeNe laser. The IR beam was directed perpendicularly to the target and focussed slightly onto the sample surface by a plano-convex lens. The size of vanadium sheets were $8 \times 8 \times 0.3 \text{ mm}^3$ and the diameter of laser beam reaching the target was typically 3 mm. Our samples were chemically cleaned before illumination, and cemented onto the surface a bigger ($m=300\text{g}$) aluminum mass in order to increase their heat capacity.

RESULTS AND DISCUSSION

It is easy to recognize the fact that most nanostructures are generated under strongly nonstationary (and far from equilibrium) conditions. The keyrole of these conditions in nanotube formation processes and a model to describe their general usefulness

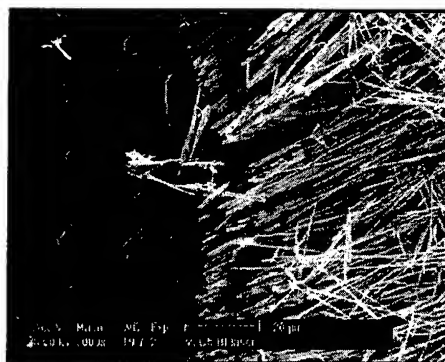
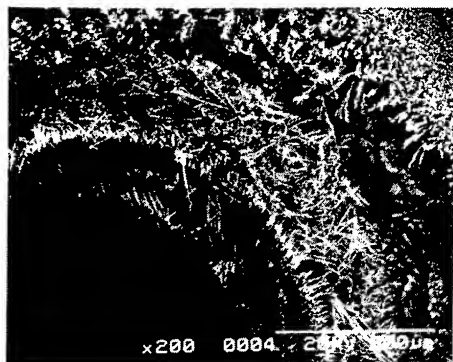


FIGURE 2. Electron micrographs (SEM and TEMs of the edge region of the oxide crater with different magnitudes, the white size-lines represent 200 μm and 20 μm on the left and right pictures, respectively. The left photo shows the concentric structure of the crater, while the right one shows microtubules, near the clear metal surface, having great aspect ratio. The microtubes have a macroscopic orientation, the radial direction is distinguished by the temperature gradient.

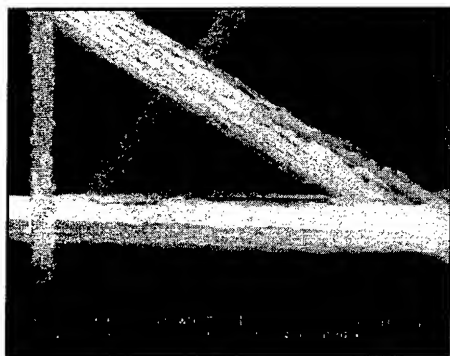
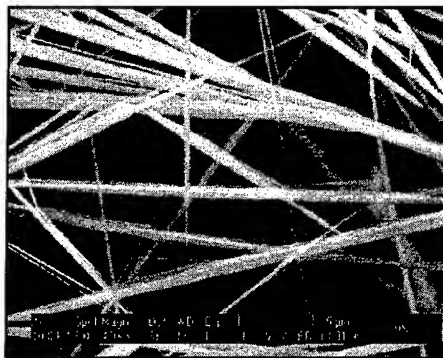
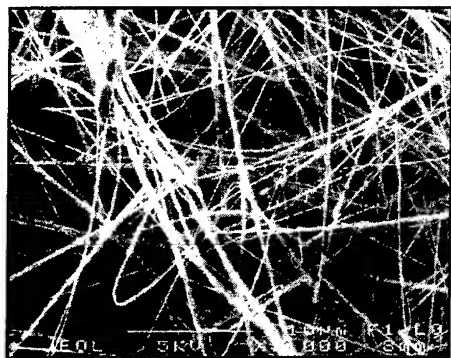


FIGURE 3. SEM pictures taken from the straggly bundle of vanadium oxide fibres. The white lines represent 10 μm , 5 μm and 2 μm on upper-left, upper-right and lower photographs, respectively. The sub-structure of rods with sizes laying in the micrometer and submicron scale is also distinguishable. The aspect ratios of the rods derived from SEM measurements were 100-500.

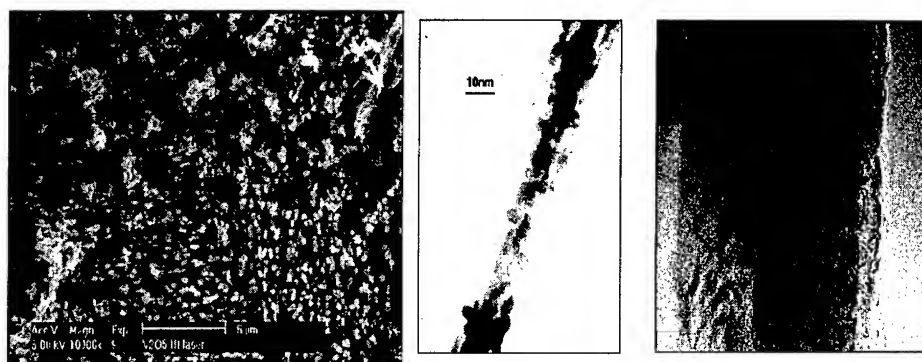


FIGURE 4. Electronmicrographs (SEM and TEM) of isotropic and very anisotropic structures of laser-generated vanadium oxide. The left photograph is taken from the sample surface near but out of the illuminated area (the bar represents 5 μ). The middle and right pictures show the mesoscopic (middle) and atomic (left) structure of grown nanorods (bars represent 10nm). Both $\langle 010 \rangle$ and $\langle 001 \rangle$ planes may be identified on TEM pictures.

is described elsewhere [5]. In our case the sources of nonequilibrium processes are the laser heating, the exothermal oxidation process itself and the external electric field. The preilluminated vanadium targets covered with well-developed oxide structures were subjected investigations by SEM and TEM microscopy. Results of these investigations are presented in Figs. 2-4. The different symmetrical and crystallographic features are caused by the oxidation and crystallization processes. Generally, the laser assisted chemical processes lead to development of “far from equilibrium” circumstances because of the high input per volume ratios we used. In laser induced oxidation of metals there are a few extra features causing further special instabilities even in the case of low power ($P=10-100$ W) continuous lasers effecting only “thermal changes”:

- The process is of Arrhenius type. The rate equation for an $A + B \rightarrow C$ form chemical reaction is $v=k[A][B]$, where v is the reaction rate, k the reaction rate constants, $[A]$ and $[B]$ are parameters of reagents. $k=c \exp(E_a/RT)$, c and E_a are the Arrhenius parameters of the reaction, c is the preexponential constant and E_a is the activation energy.
- A feedback appears between the chemical and thermal degrees of freedom. The process normally has a positive feedback, namely the absorption of laser light in the case of clean metal surfaces is relatively low (these surfaces serve as good mirrors), but after the beginning oxide formation the absorption of this complex system can grow up or can oscillate. The typical absorption efficiency of a vanadium metal surface covered by a native oxide layer is under 10% (at $\lambda=1,060$ μ m) and absorption efficiency of a thick vanadium-pentoxide layer is above 70%. So, when the oxidation process begins the efficiency grows up causing higher temperature, with higher reaction rate and addition of an extra term (the energy of the exothermal reaction) to the energy balance.

- Macroscopic “far from equilibrium” states appear when the laser driven temperatures change faster than the relaxation of the system into a quasi-equilibrium state.
- In the special case of vanadium oxidation the melting point of grown oxide is low (670 °C), so it is in liquid phase in the duration of the process causing different hydrodynamic type of instabilities such as Marangoni and Taylor vortices as well as hot filaments.

In the present experiments series we changed the illumination parameters (the power of the laser and the focal spot on the target), the chemical environment (lab air and oxygen-enriched) and the effect of an extrinsic electric field was also tested.

Dissipative structures resulted by nonlinearities arising in the system has control parameter C of $\left[C = \frac{P}{mr^2} \right]$, where P is the coupled power of the laser source, m is the mass of the sample and r is the radius of the focal spot in case of nonuniform illumination. Optimization of these parameters betided by morphological investigation of grown oxide layers with an optical microscope.

The change in the oxygen concentration from normal (28%) to enriched (>99%) atmosphere seems to be negligible, taking into account its linear role in the rate equation and in comparison to the exponential effect of the temperature. However, this smaller amount, but extra energy caused by oxygen-rich atmosphere can be important because of its special location under the oxide layer (“internal heat source”).

By applying an external electric field the ionic transport of the metal and oxygen through the oxide layer can be modified. In the investigated parameter range (1-10 kV/cm) V_2O_5 production wasn't observed, but some fine VO_2 powder covered the electrodes.

ACKNOWLEDGEMENTS

The authors are indebted to the Hungarian Foundation of Scientific Development Foundation (Contract No. F022264).

REFERENCES

1. Kroto, H.W., Heath, J.R., O'Brien, S.C., Curl R.F. and Smalley, R.E., *Nature* **318**, 162-164 (1985).
2. Iijima S., *Nature* **354**, 56-58 (1991).
3. Nánai L., George T.F., *J. Mater. Res.* **12**(1), 283-284 (1997).
4. Ajayan P.M., Stephan, O, Redlich, P, Colliex, C, *Nature* **375**, 564-567 (1995).
5. Kiss, L.B., Vajtai, R., Ajayan, P.M., under publication

Perfect Nanospheres from Polymerized Lipofullerenes

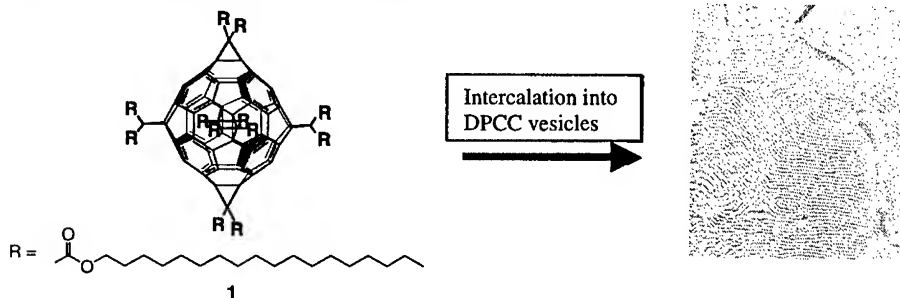
Otto Vostrowsky,^a Xavier Camps,^a Andreas Hirsch,^a Michael Hetzer,^b
Hauke Clausen-Schaumann,^b Sybille Bayerl^b and Thomas Bayerl^b

^aInstitute of Organic Chemistry, University of Erlangen-Nürnberg, D-91054 Erlangen, Germany

^bInstitute for Physics, University of Würzburg, D-97074 Würzburg, Germany

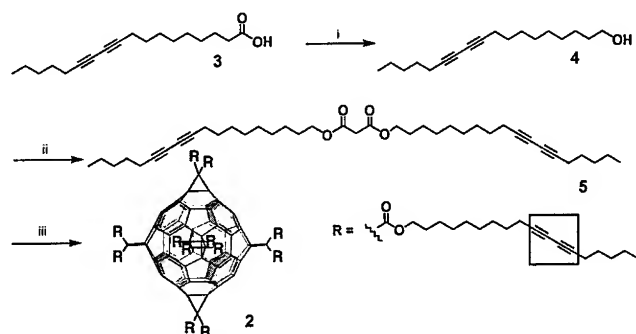
Perfect hollow and filled nanospheres are formed upon intercalation of hexakisadduct **2** into multilamellary DPCC vesicles and subsequent photopolymerization by UV-irradiation.

We recently have shown, that lipophilic hexakisadducts of buckminsterfullerene C₆₀ (**1**) upon intercalation into synthetic multilamellar vesicles [MLVs] of dipalmitoylphosphatidylcholine [DPPC], the widely used model of natural membranes, tend to self-assemble into rod-like structures of up to 30 nm diameter and of several μm length.^[1,2] As a result, a composite of colloidal dimensions is formed with interesting micromechanical properties. An enhancement of membrane stiffness was observed and a decoupled lateral diffusion of lipids and lipofullerenes within the bilayer found.^[1,2,3] For a fluid-like bilayer, the rods show a lateral mobility and flexibility within the fluid bilayer plane, leading to collisions between adjacent rods.



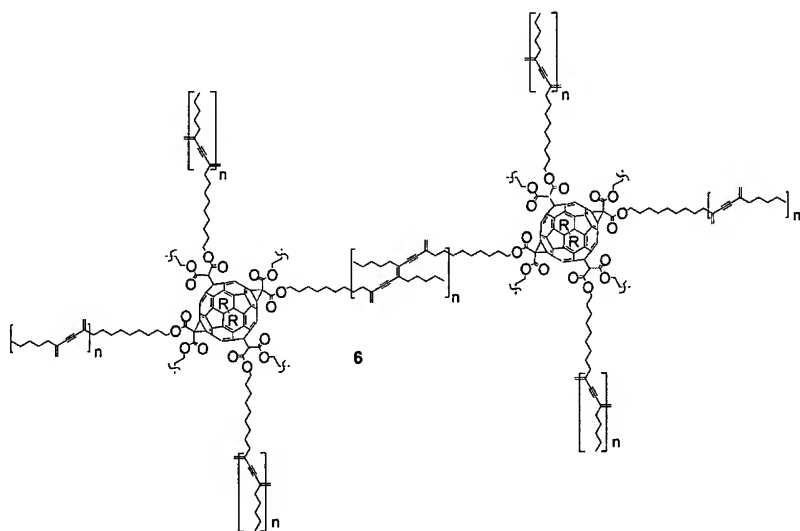
To investigate this phenomenon, the polymerizable hexakisadduct **2** was synthesized, intercalated into phospholipid vesicles and subjected to UV-initiated polymerization. Commercially available octadecadiynoic acid **3** was reduced and the alcohol **4** formed reacted with malonyl dichloride to give dioctadecadiynyl malonate **5**. From **5** and

[60]fullerene the T_h -symmetrically hexakisadduct **2** was obtained *via* template activation and exhaustive cyclopropanation^[4] (scheme 1).



Scheme 1. Synthesis of polymerizable lipofullerene hexakisadduct **2**. i) LiAlH_4 , ether; ii) $\text{ClCOCH}_2\text{COCl}$ /pyridin, CH_2Cl_2 ; iii) [60]Fullerene, DMA, CBr_4 , DBU, toluene.

From polymerization of **2** in the solid state a polymer of possible structure **6** is obtained, which was characterized by MAS spectroscopy.



The DPCC-lipofullerene composite system formed showed significant changes after UV-treatment with respect to the lipid molecular order and dynamics. Lineshape analysis and numerical deconvolution of ^2H NMR spectra using chain perdeuterated DPCC- d_{62} shows that the molecular order along the DPCC tails is increased and the bilayer becomes less flexible. Furthermore, a significant reduction of the ^2H NMR transverse relaxation time t_2 is found (Fig. 1).

Perfect nanospheres are formed within the DPPC bilayer under fluid bilayer conditions, as is revealed by freeze fracture electron microscopy (Fig.3). While the sample before the polymerization (Fig. 3a) shows the above mentioned rod-like structure, we

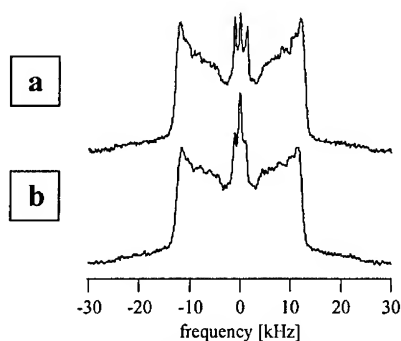


Fig. 2.: Deuterium NMR spectra of chain perdeuterated dipalmitoyl-phosphatidylcholine (DPPC- d_{61}) multilamellar vesicles containing 15 mol-% **2** prior (a) and after (b) UV irradiation at 50°C.

observe perfectly spherical objects (diameter range 100 nm - several μm), essentially consisting of polymerized **6** (Fig. 3b). The smaller spheres are hollow (Fig. 3c), whereas the larger ones enclose other spheres in a onion-like fashion (Fig. 3d), rendering the core regions impenetrable to the electron beam.

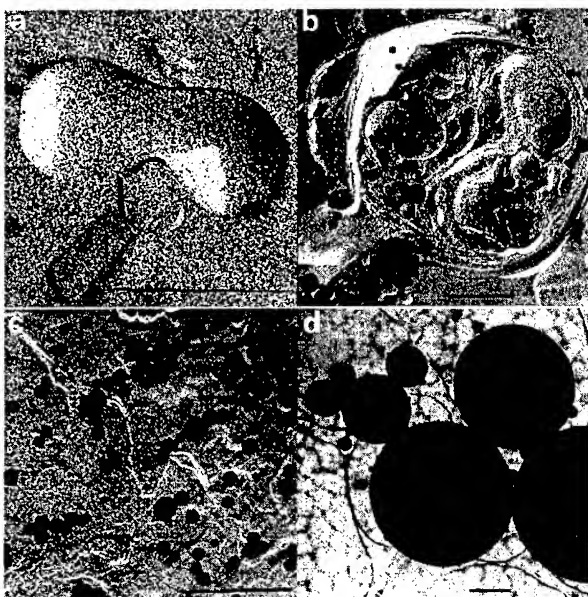


Fig. 3: Freeze fracture transmission electron micrographs (TEM) of 15 mol% of polymer **6** in DPPC multilamellar vesicles before (a) and after (b,c,d) polymerization.

An extraction of the templating DPPC by solvents and subsequent vacuum drying (Fig. 3d) allows their transmission EM-inspection in absence of the freeze fracture replica.

Atomic Force Microscopy (AFM) was used for an assessment of the surface of the spheres at a molecular scale after the extraction of the lipid. The surface of the spheres is surprisingly smooth with maximum amplitudes in height of 1.5 nm (Fig. 4).

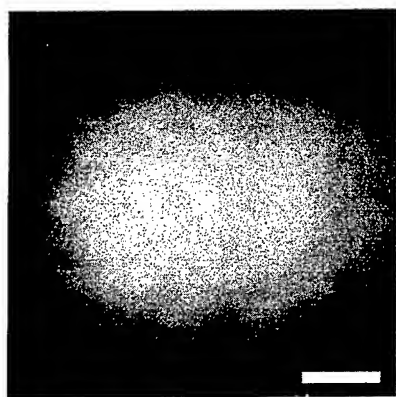


Fig. 4: Atomic Force Microscopy of the polymerized lipofullerene hollow spheres after extraction of the DPPC; the bar represents 50 nm.

The lipofullerene hollow beads seem to exhibit an unusually high mechanical strength. We expect that such a two-dimensional configuration may exhibit a very high elasticity modulus, which may explain why we did not observe any mechanically damaged spheres. Furthermore, the the wall thickness of the beads must be below the resolution limit of our microscope (below 10 nm).

- [1] M. Hetzer, S. Bayerl, X. Camps, O. Vostrowsky, A. Hirsch, T.M. Bayerl, *Adv. Mater.* **1997**, 913.
- [2] M.. Hetzer, S. Bayerl, T.M. Bayerl, X. Camps, O. Vostrowsky, A. Hirsch, in *Molecular Nanostructures* (H. Kuzmany, J. Fink, M. Mehring, S. Roth, eds.), S. 528, World Scientific Publishing Company, 1997.
- [3] M. Hetzer, T. Gutberlet, M.F. Brown, X. Camps. O. Vostrowsky, H. Schönberger, A. Hirsch, T.M. Bayerl, *Journ. Phys. Chem. A* **1999**, A 103, 637 - 642.
- [4] I. Lamparth, C. Mössmer, A. Hirsch, *Angew. Chem.* **1995**, 107, 1755; *Angew. Chem. Int. Ed. Engl.* **1995**, 35, 1607.
- [5] M. Hetzer, H. Clausen-Schaumann, S. Bayerl, Th.M. Bayerl, X. Camps, O. Vostrowsky, A. Hirsch, *Angew. Chem.* **1999**, 111, im Druck.

**IV. PREPARATION AND
CHARACTERIZATION OF
CARBON NANOTUBES**

A continuous wave CO₂ laser reactor for nanotubes synthesis

J-L. Cochon¹, J. Gavillet², M. Lamy de la Chapelle¹, A. Loiseau²,
M. Ory¹, D. Pigache¹

¹ONERA, ²LEM, UMR 104 ONERA-CNRS,
29 avenue de la Division Leclerc, BP 72, 92322 Châtillon, France

We present here the first results obtained with a reactor specially designed for studying and modelizing the conditions and the parameters of synthesis of different kinds of nanotubes. The principle of the reactor is derived from that developped by Maser et al [1] and uses for the species vaporization a 1500 W continuous wave CO₂ laser which avoids the use of a furnace. The ablation of pure carbon leads to a deposit which consists mainly of aggregates of single- and multi-wall tubular cages. When doping the target with catalysts such as Ni and Co, we obtain bundles of single-wall nanotubes similar to those produced by other methods.

INTRODUCTION

Within the last three years, much effort has been done for finding new routes to the synthesis of self assembled single-wall nanotubes (SWNT). Except the catalytic decomposition of hydrocarbons [2], all the methods currently developped - laser ablation [1, 3], electric arc discharge [4], solar energy [5] - have in common to induce the simultaneous sublimation of graphite and metallic catalysts at high temperature - 3000K or more - under an inert gas atmosphere and subsequent aggregations of carbon atoms or clusters. It is therefore likely that the formation and the growth of SWNT should occur through a general scheme independent of the technique used for sublimating the chemical species. However the mechanisms driving the SWNT growth and their self-assembling are far from being understood. In order to have a better knowledge of the synthesis conditions, we have built a reactor, derived from that developped by Maser et al [1]. It offers the advantage of its simplicity for varying, controlling and measuring the different relevant parameters and studying in situ the conditions of synthesis. We present here the first results obtained with this technique.

EXPERIMENTAL

The experimental set up is shown in Fig.1. The reactor is a cylindrical, metallic and water-cooled chamber (255 mm in height and 180 mm in diameter). The target is a rod of 5 mm in diameter placed along the axis of the chamber. During the experiment, it is

continuously rotated around its axis and is translated upward by a step-motor mechanism when ablated by the laser. The laser is a continuous wave CO₂ laser, for avoiding the use of a furnace. Its power can be varied up to 1500W allowing one to heat the target at a temperature above the vaporization of the graphite and to vary the density of the carbon vapor. The laser beam enters the chamber through a ZnSe window and a ZnSe lens focuses it on the top of the target with an incidence angle of 45° with respect to the chamber axis. The spot size of the beam on the target can be adjusted between 1 and 3 mm by moving the lens along the optical axis. The target temperature is measured by optical pyrometers as indicated in Fig.1. An argon flow is introduced at the bottom of the chamber and extracted through a silica pipe (20 mm in diameter) placed above the target. The argon pressure is 0,5 bar and the flow rate is 50 cc/s at normal temperature and pressure. The gas is heated only by contact with the hot target. The ablation products are carried away by the argon flow through the pipe and collected on a filter.

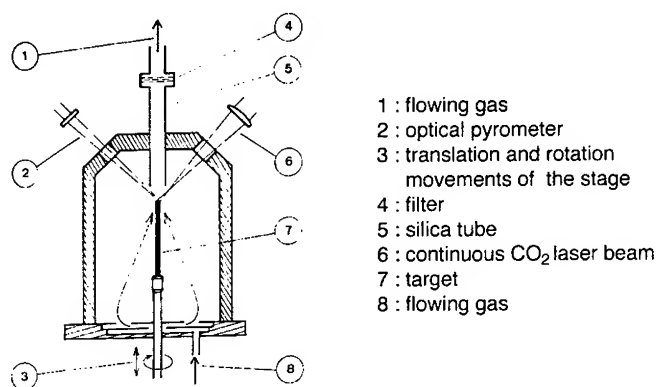


FIGURE 1. Experimental set-up of the laser reactor.

We have studied the ablation of two kinds of target: high purity graphite and graphite doped with a mixed Ni-Co catalyst. In this latter case, an hole of 4 mm in diameter is drilled in a pure graphite target and filled up with the appropriate Ni:Co:C powder.

The collected soot has been characterized first by field emission gun scanning electron microscopy (FEG SEM), using a Zeiss Gemini working at a tension between 1 and 3 kV, and second by transmission electron microscopy (HRTEM), using a JEOL 4000FX working at 400 kV. For SEM observations, the powder was dispersed on a conducting and adhesive strip and metallized by evaporating a very thin layer of carbon. For TEM observations, the soot was ultrasonically dispersed in ethanol and deposited onto holey carbon grids.

RESULTS AND DISCUSSION

We have first analysed the soot resulting of the ablation of the pure graphite target. It consists of almost spherical carbonaceous aggregates with sizes ranging between 50 and 300 nm (fig.2). SEM images (fig.2a) exhibit a typical granular surface contrast suggesting mimosa flowers. Their detailed structures have been revealed by HRTEM

observations (fig.2b,c). The aggregates consist of a packing of graphitic nanocages irradiating from the centre to the outer surface of the aggregate. Three kinds of aggregates have been recognised depending on the structure of the nanocages. *In the first type*, the cages are very small and can be assimilated to large fullerene molecules. *In the second type*, which constitutes the majority of the aggregates, the cages involve a single graphene layer and are tubular in shape: their length is typically a few tens nm whereas their diameter is a few nm. They are terminated by characteristic elongated conical tips suggesting petals of flowers. Tip angle is equal to 19° in most cases (Fig.2c) indicating a structure involving five pentagonal rings as in nanotubes. Furthermore, the frequent observation of a separation between adjacent cages of roughly 0.34 nm is relevant of a self organisation of these cages in close packed arrangements [6]. It is worth mentioning that this kind of aggregates has also been observed by Iijima who described the cages as « nanohorns » [7]. Finally, *in the third kind* of aggregates [6], the nanocages are multiwalled and display entangled features typical of mesoporous carbon [8].

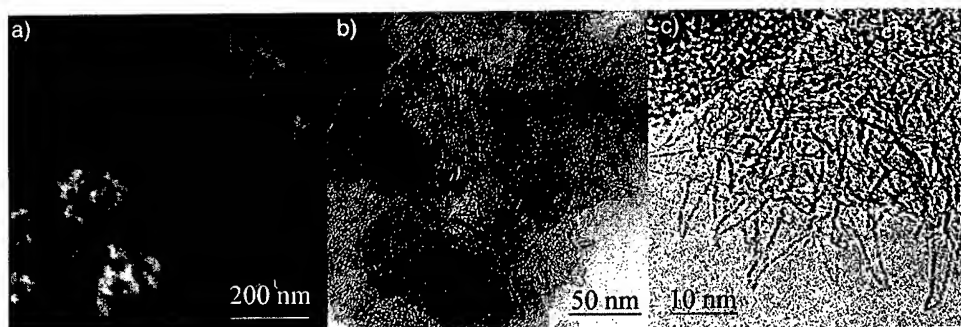


FIGURE 2. Carbon structures obtained when ablating a pure graphite target. a) SEM image, b) TEM image c) HRTEM images of the tubular cages emerging at the surface of the aggregates seen in b).

These three kinds of aggregates can be associated to three stages of graphitization of the carbonaceous structures arising at different temperatures. Their formation is certainly due to temperature inhomogeneities in the reactor chamber.

We have then analysed the soot arising from a Ni:Co:C (4:4:92 %at) target. Fig.3 attests that we have achieved the production of ropes of SWNT's presenting the same structural characteristics than those obtained by other techniques yet reported [1, 3-5]. At low scale (Fig.3a,b), the ropes display entangled networks. HRTEM observations (Fig.3c) provide structural details on the self-organisation of SWNT in bundles. The analysis of the fringe contrast shows that the tubes are well periodically packed and twisted along the rope axis. Cross section like views as the example in the inset of Fig.3c reveal that the bundles contain a reduced number of SWNT ranging from a few units to 20. The lattice parameter which can be deduced from both section views and fringe images ranges from 1.5 to 1.6 nm with a peak at 1.54 nm, which is significantly smaller than the value found for electric arc and pulsed laser bundles. This could indicate that ropes are formed at a somewhat lower temperature. The second inset of fig.3c reveals an interesting feature. Bundles are very frequently embedded or covered by aggregates of C₆₀ molecules. Sometimes row of molecules aligned along the fringes are observed but there is presently no evidence of molecules nesting the tubes as in the pea-pods recently found for pulsed laser tubes [9].

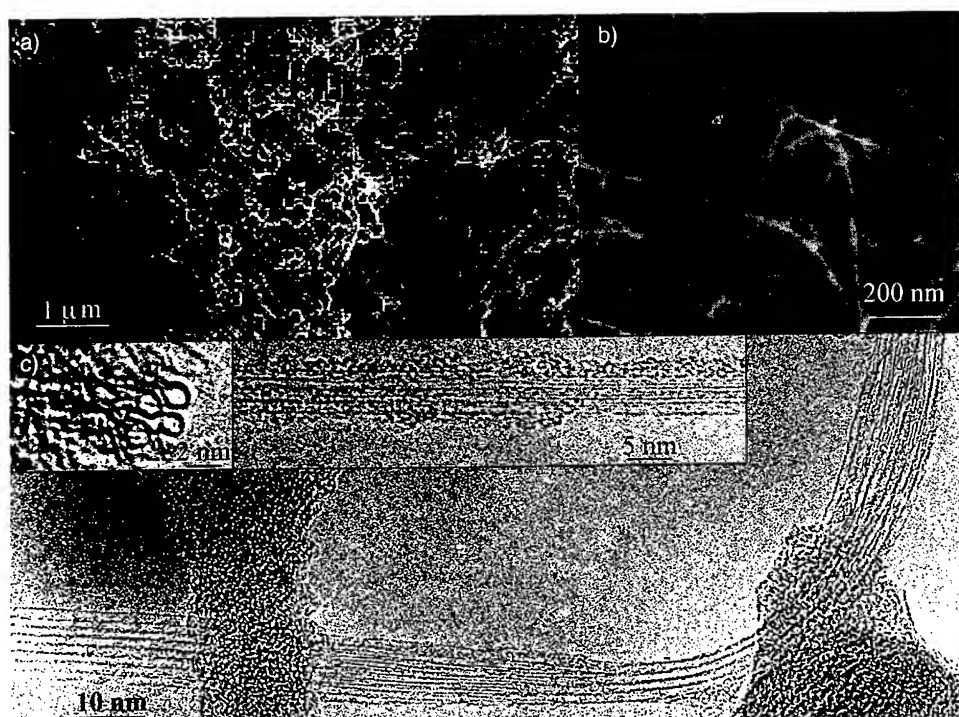


FIGURE 3: soot produced by the ablation of a Ni:Co:C (4:4:92 %at) target. a) and b) SEM images, c) HRTEM images of bundles projected along and perpendicular to the electron beam.

Bundles are observed along with metallic particles and important amounts of carbonaceous structures (fig.3a) similar to those obtained when ablating pure graphite. It is likely that their formation is due to an insufficient homogeneity of the metals and carbon mixture in the target, to the detriment of the yield of bundles. Work is currently in progress for optimizing this yield by improving the homogeneity of the target and by studying the influence of different adjustable parameters.

- [1] Maser, W. et al, *Chem. Phys. Lett.* **292** 587 (1998)
- [2] Cheng, H.M., *Chem. Phys. Lett.* **289** 602-610 (1998)
- [3] Thess, A. et al, *Science* **273** 483-487 (1996)
- [4] Journet, C. et al, *Nature* **388** 756-758 (1997)
- [5] Laplaze, D. et al, *Carbon* **36** 685-688 (1998)
- [6] Cochon, J. - L. et al, submitted to *Appl. Phys. A*
- [7] Iijima, S., communication at the MRS fall meeting, Boston, 1998
- [8] Dresselhaus, M.S., Dresselhaus, G., and Ecklund, P.C., *Science of fullerenes and carbon nanotubes*, San Diego: Acad. Press, 1996, pp 15-59
- [9] Smith, B. W. et al, *Nature* **396** 323 - 324 (1998).

Synthesis, purification and characterisation of multi- and single-wall nanotubes produced by catalytic decomposition of hydrocarbons

J.-F. Colomer, P. Piedigrosso, I. Willems, Z. Konya,
A. Fonseca and J. B. Nagy

Laboratoire de Résonance Magnétique Nucléaire
Facultés Universitaires Notre-Dame de la Paix
61, Rue de Bruxelles, B-5000 Namur, BELGIUM

Abstract. The catalytic process is the third method, with laser evaporation and electric arc techniques, to produce carbon nanotubes. By this way, multi-wall carbon nanotubes can be synthesised by catalytic decomposition of acetylene over supported catalyst Co/Zeolite NaY. The tubes produced are purified in two steps: first, separation of nanotubes and catalyst particles are carried out by fluorhydric acid treatment; then, the amorphous carbon elimination is made following two oxidative treatments. Multi-wall carbon nanotubes are obtained quasi-pure with high yield. Recently, single-walled nanotubes can be also synthesised by the catalytic pyrolysis of hydrocarbons. Typical TEM images of multi- and single-wall carbon nanotubes are given: for multi-wall nanotubes, after each step of production and purification, and for single-wall nanotubes after synthesis.

1. Introduction

In addition to the laser evaporation and electric arc discharge techniques, the catalytic process is a very efficient method to produce carbon nanotubes. Until now, only multi-wall carbon nanotubes (MWNTs) was produced by this way^(1,2). But recently, many reports^(3,4) have shown that this process could be used to synthesise single-wall carbon nanotubes (SWNTs).

In the present work, we describe the synthesis and the purification of MWNTs by catalytic decomposition of acetylene on Co/zeolite NaY supported catalyst. This catalyst has been chosen because many works carried out in our laboratory have shown the efficiency and the reproducibility of the nanotubes formation^(1,2). Moreover, the purification of nanotubes obtained on this support seems be easier than those obtained on other supports such as silica⁽¹⁾.

The nanotubes so-produced are purified in two steps: first separation of nanotubes and catalyst particles are carried out by fluorhydric acid treatment; then, the elimination of the amorphous carbon is made by oxidation in air or by potassium permanganate oxidation in acidic solution. Multi-wall carbon nanotubes are obtained quasi-pure with high yield⁽⁵⁾. After production and purification, the quality of the multi-wall nanotubes was checked by transmission electron microscopy (Philips CM 20 and Jeol 200CX) and typical images after each step are given.

The synthesis of SWNTs by the catalytic way is also reported : SWNTs can be produced by the catalytic pyrolysis of hydrocarbons (ethylene, methane) over different supported metal catalysts, at 1080°C. Different supports (alumina and silica) and different metals or mixtures of metals (Co, Ni, Fe, Co-Fe,...) are used in the preparation of the catalysts. After reaction, the quality of material obtained is also characterised by TEM.

2. Experimental

2.1 Synthesis of MWNTs

Zeolite NaY supported catalyst was synthesised by impregnation of zeolite with an aqueous solution of cobalt salt in the appropriate concentration to obtain 2.5%wt of metal.

The production of nanotubes was carried out in a fixed-bed reactor (quartz tube of 50 mm diameter, 80 cm in length in a carbolite horizontal oven), at 600°C, with a reaction time of 60 min. The reaction parameters used for the nanotubes synthesis are the following: acetylene flow 20ml/min, nitrogen flow 110 ml/min, and amount of catalyst 1.5g.

After reaction, the yield of carbon deposit was calculated as follows : *carbon yield (%)* = $100(m_{tot} - m_{cat})/m_{cat}$, where m_{cat} is the initial amount of catalyst and m_{tot} is the total weight of the sample after reaction

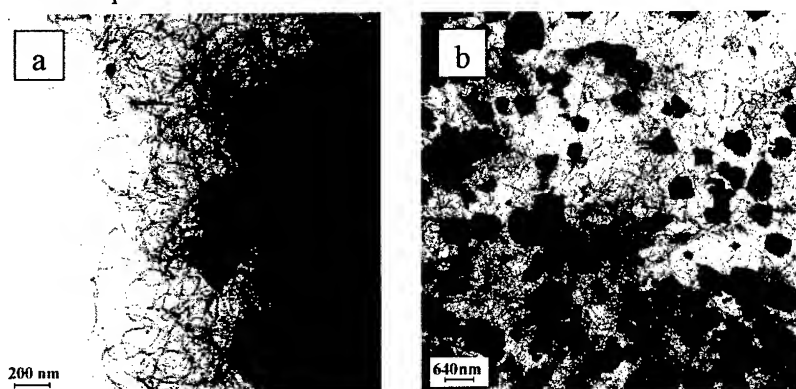


Fig. 1 : Low resolution TEM images of (a) carbon nanotubes produced at 600°C over Co/NaY catalyst and (b) nanotubes and amorphous carbon recovered by filtration after HF treatment.

2.2 Purification of MWNTs

After removing the catalyst by dissolution of the zeolitic support and metal particles using fluorhydric acid (38-40%) during 48h under vigorous stirring, the residue was filtered, washed with distilled water and dried for 12h at 130°C. After this treatment, the aggregates of amorphous carbon released from the inner pores of the zeolite (Fig. 1b), must be eliminated by oxidative treatments to obtain pure nanotubes. Also, the material, recovered after HF treatment, was oxidized (100 mg) at 500°C using an air

flow of 12 ml/min, during 210 min, or by 526.3 mg (0.3eq.) of KMnO_4 in 50 ml of 0.5 M sulfuric acid at 80°C during 1 h.

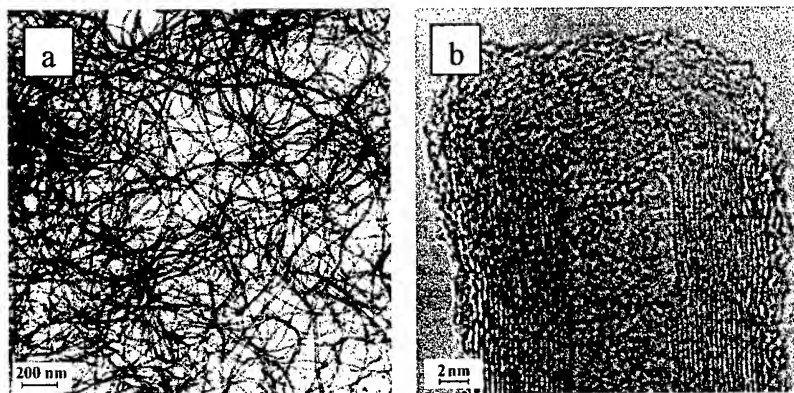


Fig. 2 : Low resolution TEM image of pure carbon nanotubes (a) and high resolution TEM image of a nanotube opened tip after oxidative treatment (b).

2.3 Synthesis of single-wall nanotubes (SWNT)

Various supported metal catalysts are prepared by impregnation on different supports (alumina and silica) using different metals (Co, Ni, Fe) and mixture of metals (Co-Fe, Ni-Co,...). The synthesis is carried out in a fixed-bed reactor (quartz tube of 25mm diameter, 80 cm in length in a carbolite horizontal oven), at 1080°C, with a reaction time of 60 min and an amount of catalyst 200 mg. The flows of different gases used were for the mixture of ethylene/nitrogen 30/80 ml/min, and for the mixture of methane/hydrogen 90/20 ml/min. The quality of material obtained was checked by TEM (Fig. 3).

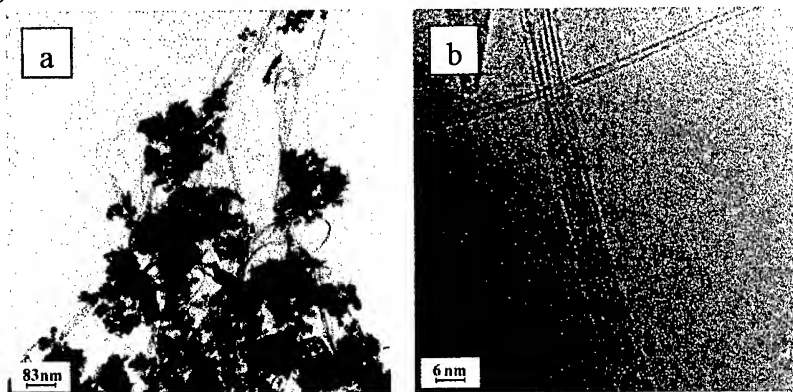


Fig. 3 : Low (a) and high (b) resolution TEM images of SWNTs produced over Co-Ni-Fe catalyst supported on alumina.

3. Results and discussion

The cobalt impregnated NaY zeolite catalyst is an effective catalyst for the catalytic formation of MWNTs. The yield of carbon deposit was around 18%, which is not very high but the quality checked by TEM is very good (Fig 1a). After the HF treatment to remove the support and the metal particles, pure MWNTs are obtained by the two different purification methods in 27-40% yield, with air or low temperature KMnO_4 oxidation, respectively (Fig. 2a). Moreover, by these treatments, the nanotubes are uncapped (Fig. 2b) and ready to be filled by gases or metals. Some chemical functionalisations (hydroxy groups, etc..) are also introduced on the nanotube surface which could be interesting for future applications.

SWNTs are obtained with more or less efficiency depending on the catalyst and/or the hydrocarbon gas used. Moreover, the reaction yield is hard to estimate but the results are based on the abundance of SWNTs in each sample as measured from TEM observations.

The nature and the concentration of metal or mixture of metals, the nature of support play a role in the formation of SWNTs. The best catalysts found are the mixture of metal (Co-Fe, Co-Ni-Fe..) on alumina as support to give abundant bundles of SWNT, using ethylene as hydrocarbon.

4. Conclusion

Multi- and single-wall nanotubes can be easily produced by catalytic decomposition of hydrocarbons. Pure multi-wall carbon nanotubes can be obtained by the different purification methods described above with interesting yields. The production of SWNTs by the catalytic method seems to be attractive to produce SWNTs in a large scale.

Acknowledgment. The authors are grateful to European Commission, TMR contract NAMITECH, ERBFMRX-CT96-0067 (DG12-MIHT) and thank the Belgian Programme on Inter University Poles of Attraction initiated by the Belgian State, Prime Minister's Office of Science Policy Programming (4/10).

5. References

1. V. Ivanov, A. Fonseca, J. B. Nagy, A. A. Lucas, D. Bernaerts, X. B. Xang, **Carbon**, **33**, 1727 (1995)
2. K. Hernadi, A. Fonseca, J. B. Nagy, D. Bernaerts, A. Fudala, A. A. Lucas, **Zeolites**, **17**, 416, (1996)
3. J. Kong, A. M. Cassell, H. Dai, **Chem. Phys. Lett.**, **292**, 567, (1998)
4. J. H. Hafner, M. J. Bronikowski, B. R. Azamian, P. Nikolaev, A. G. Rinzler, D. T. Colbert, A. Smith, R. E. Smalley, **Chem. Phys. Lett.**, **296**, 195, (1998)
5. J.-F. Colomer, P. Piedigrosso, I. Willems, C. Journet, P. Bernier, G. Van Tendeloo, A. Fonseca, J. B. Nagy, **J. Chem. Soc., Faraday Trans.**, **94**, 3753 (1998)

Production of bundles of single walled nanotubes by a simple laser ablation technique

W.K. Maser¹, E. Muñoz¹, A.M. Benito¹, M.T. Martínez¹,
G.F. de la Fuente², E. Anglaret³ and J.-L. Sauvajol³

¹Instituto de Carboquímica, CSIC, Marfa de Luna 12, E-50015 Zaragoza (Spain)

²ICMA, CSIC-Universidad de Zaragoza, Marfa de Luna 3, E-50015 Zaragoza (Spain)

³GDPC, Université de Montpellier II, F-34095 Montpellier Cedex (France)

Abstract. High yield single-walled nanotube (SWNT) material has been obtained by using a very simple laser-ablation experimental set-up. It significantly differs from the usually employed ones in three main points: a) Use of a CO₂-laser (in continuous wave mode), b) a simple vertical evaporation-chamber with rotating graphite/metal composite rods, and c) the absence of a furnace around the graphite targets. The obtained SWNT material is characterized by electron microscopy (SEM, TEM) and Raman spectroscopy. We show that our simple laser system creates very favorable growth conditions and discuss the importance of certain experimental parameters during the formation of SWNTs.

INTRODUCTION

Single-walled nanotubes (SWNTs) can be synthesized by the evaporation of a graphite/bi-metal target under an inert atmosphere of gas. Two efficient methods are currently employed in order to produce this material in high yields: the electric arc discharge method (1) and the laser ablation technique (2). The best results with the latter procedure have been obtained by using a double-pulsed laser system operating at 532 nm and 1064 nm, and an additional furnace around the graphite/bi-metal target which is kept at around 1200°C.

Here, we show that high yield SWNT material can be obtained by a much simpler laser-ablation set-up. It significantly differs from the usually employed one in three main points: a) use of a CO₂-laser (in continuous wave mode), b) a simple vertical evaporation chamber with rotating graphite/bi-metal composite rod and c) the absence of a furnace around the graphite targets. This set-up produces a fruitful laser-target-gas interaction leading to conditions favorable for the growth of SWNTs. Furthermore, we found that argon and nitrogen can equally be used as buffer gas leading to maximum SWNT yields for the pressure range between 200 and 400 Torr. No difference in quantity and quality of the SWNT material could be observed when working under static instead of dynamic conditions. However, no SWNT material was produced when working with helium as buffer gas.

EXPERIMENTAL

A CO₂ laser (Laser Quanta Optoelectrónica) operating in continuous wave mode at 10.6 μm was focused onto a graphite/bi-metal composite target rod (spot-size 0.8 mm², power density 12kW/cm²) which is placed inside a stainless steel chamber (Figure 1). In order to obtain a relatively uniform evaporation rate the target rod is continuously rotated around its axis and up-or downward translated by a step-motor mechanism. The evaporation chamber is evacuated and filled from its bottom side with inert gas flowing at 1 l/min. The experiments were carried out under argon and nitrogen atmospheres ranging from 50 to 500 Torr and under helium atmospheres at 400 Torr. During the evaporation process (about 200 mg of the target material is evaporated per hour) the up-wards flowing gas sweeps the produced soot inside the quartz-tube. Here a large amount of it condenses on an entangled copper-wire system, which has been placed inside. Static gas conditions also have been employed.

The following metal concentrations (in at%) have been used in order to press the graphite/metal target rods (6 mm in diameter and about 5 cm in length): Ni (2), Co (2), Fe (2), Y (0.5), Ni/Y (4/1, 2/0.5, 1/0.25, 0.6/0.6, 0.5/0.13), Ni/Co (4/1, 2/2, 2/0.5, 1/0.25, 0.6/0.6, 0.5/0.13, 0.4/0.4), Ni/Fe (4/1, 2/0.5, 0.6/0.6).

The produced carbonaceous materials have been investigated using scanning electron microscopy (SEM) (JEOL JSM-6400), transmission electron microscopy (TEM) (Philips, CM30, 300 kV) and micro-Raman spectroscopy (argon ion laser with $\lambda = 515.5 \text{ nm}$, power density < 50 mW/mm², Jobin Yvon T6400 spectrometer, resolution: 2 cm⁻¹).

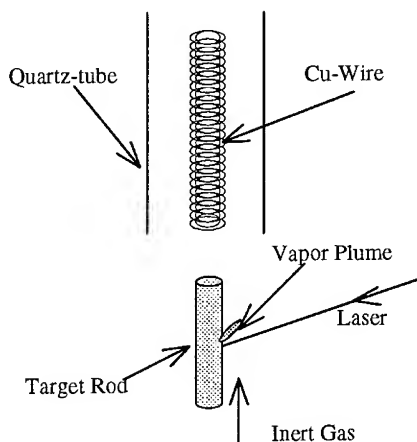


FIGURE 1. Experimental set-up: The target rod is placed inside the center of an evaporation chamber. The CO₂-laser beam is guided into the evaporation chamber and focused via a parabolic mirror onto the target rod. The target rod is continuously rotated and translated up- or down-wards in order to get a relatively uniform evaporation. During the evaporation the target rod is heated up to 1200°C in a zone 1 cm around the focal spot. The inert gas is passing along the hot target rod and then flowing through the quartz-tube.

RESULTS AND DISCUSSION

Powderous soot material obtained with the mono-metal mixtures (Ni, Co and Fe) contained only a few and, in most cases only isolated SWNTs, while no tubes were found with Y as catalyst. However, the use of bi-metal mixtures, leads to the formation of web-like soot material consisting of very fine and long filaments, which are deposited on the copper wire system inside the quartz-tube. Highest amounts of web-material were obtained with the catalyst mixtures Ni/Y (4/1 and 2/0.5 at%) and Ni/Co (2/2 and 0.6/0.6 at%). This web-like structure certainly is a first hint for the existence of high yield SWNT material as can be seen by the following microscopy studies. SEM characterization of this material shows a high density of entangled and cross-linked carbon filaments homogeneously distributed over the whole sample (Figure 2a). From several SEM images the yield of these filaments is estimated to be of the order of 80% (with respect to the total volume of the solid material) and because of their high yield, they can be easily seen in TEM. Figure 2b shows the large abundance of the filaments which are bundles composed of individual SWNTs. These bundles are frequently passing through areas of amorphous /glassy carbon in which additionally are distributed spherical metallic nano-particles (5-25 nm in diameter). No obvious link between these particles and the bundles of SWNTs has been observed. It is important to note that argon and nitrogen atmospheres can be used equally as inert gas without any major differences concerning quantity and quality of the SWNT produced material. This also can be confirmed by micro-Raman spectroscopy. In all our web-samples one easily finds a broad peak consisting of five to nine components between 140 and 185 cm^{-1} (Figure 3). This clearly indicates the presence of SWNTs with a diameter distribution ranging from 1.1 to 1.6 nm consistent with the TEM observations. For both gases the 'best' results were obtained between 200 and 500 Torr. Below 200 Torr the obtained soot material is dominated by amorphous carbon. Furthermore, it is important to note that the experiments performed under helium atmospheres did not lead to the formation of SWNT material. A detailed analysis of the gas and pressure effects can be found in (3).

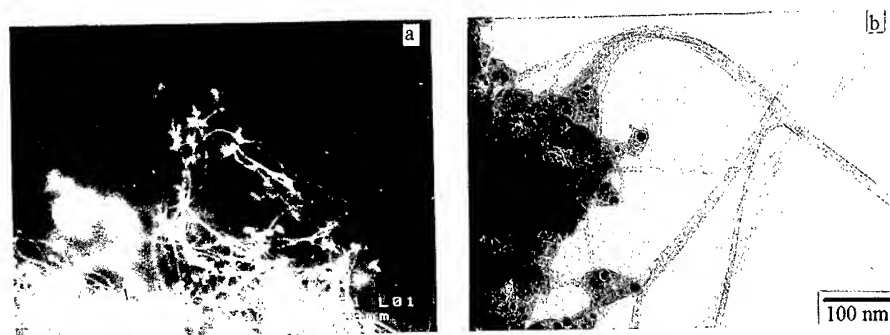


Figure 2. a) SEM image of SWNT material catalyzed with Ni/Y (4/1 at%) shows a high density of entangled filaments. b) TEM image shows the arrangement of SWNTs into bundles (Ni/Co (2/2 at%)).

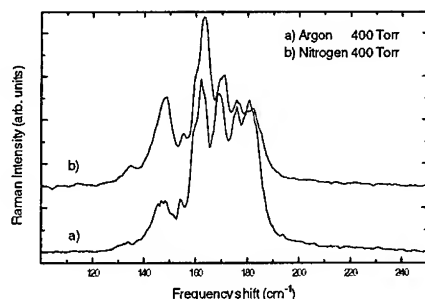


Figure 3. Raman spectra of SWNT material produced under Argon (a) and Nitrogen (b) at 400 Torr.

The obtained results show that our CO₂ laser system induces favorable local conditions for the formation of SWNTs. With a wavelength of 10.6 μm , the laser radiation forms a hot target surface of about 1000-1200°C (pyrometric measurements). This acts as a local furnace preventing a too rapid cooling of the evaporated particles. Furthermore, the pressure range between 200 and 500 Torr seems to be sufficient for keeping together the critical concentration of carbon seed structures and metal catalysts necessary for forming SWNTs.

CONCLUSIONS

High yield SWNT material can be produced by a simple laser-ablation set-up using a CO₂-laser. The CO₂ laser has the advantage that it not only leads to the evaporation of the target material but also heats efficiently at the same time the target rod around the focal spot. In this way, the temperature gradient is reduced and the 'freshly' evaporated species are passing for a sufficient long time a hot zone with the up-wards directed gas-flow. Therefore, our system leads to fruitful laser-target-gas interactions, favorable for the growth of SWNTs without the use of an additional external furnace.

ACKNOWLEDGEMENTS

One of us (EM) acknowledges funding from the Departamento de Educación y Cultura de la Comunidad Autónoma de Aragón.

REFERENCES

1. Journet, C., Maser, W.K., Bernier, P., Loiseau, A., Lamy de la Chapelle, M., Lefrant, S., Deniard, P., Lee, R., Fischer, J.E., *Nature* **388**, 756 (1997)
2. Thess, A., Lee, R., Nikolaev, P., Dai, H., Petit, P., Robert, J., Xu, C., Hee Lee, Y., Gon Kim, S., Rinzler, A.G., Colbert, D.T., Scuseria, G.E., Tománek, D., Fischer, J.E., Smalley, R.E., *Science* **273**, 483 (1996)
3. E. Muñoz, W.K. Maser, A. Benito, M.T. Martínez, G.F. de la Fuente, Y. Maniette, A. Righi, E. Anglaret, J.-L. Sauvajol, submitted to *Chem. Phys. Lett.*

Metal mixtures catalysed carbon nanotube synthesis

Z. Kónya^a, N. Nagaraju^b, A. Tamási^c, K.M. Mukhopadhyay^a, A. Fonseca^a
and J. B.Nagy^a

^a*Facultés Universitaires Notre-Dame de la Paix, Laboratoire de R.M.N., Département de Chimie, 61 rue de Bruxelles, B- 5000, Namur, Belgium.*

^b*St. Joseph's College, Department of Chemistry, Residency Road, 560-025, Bangalore, India.*

^c*József Attila University, Department of Applied and Environmental Chemistry, Rerrich ter 1, H-6720, Szeged, Hungary.*

Abstract - Catalytic activity of iron, cobalt and its mixtures supported on alumina in the formation of carbon nanotubes by the decomposition of acetylene is reported. Two different samples of alumina - ie. Al_2O_3 , prepared from aluminium isopropoxyde and $\text{Al}_2\text{O}_3(\text{com})$, a commercial low BET area sample - are used as supports for the catalysts. The decomposition of the hydrocarbon is carried out at 600 and 700 °C and the effect of flowrate and time of reaction are also studied. All the catalysts were analysed for their XRD pattern, surface area and porosity. Transmission Electron Microscopy (TEM) is used to follow the formation of carbon nanotubes. All the catalysts were active towards the production of carbon nanotubes at 700 °C, but at 600 °C only the Co-Fe mixtures supported on alumina showed activity. High resolution TEM (HREM) analysis showed that the tubes are multilayered and the number of the layers strongly depends on the Fe content.

INTRODUCTION

Since their discovery[1], more and more interest appears towards the chemistry and physics of single and multiwall carbon nanotubes (SWNTs and MWNTs, respectively). Following from their unique molecular structure, the nanotubes have very interesting chemical and physical properties. The mechanical strength, the strong capillarity, the structure-dependent electronic properties and further attributes make the carbon nanotubes very promising materials for potential industrial applications[2,3]. For the synthesis of MWNTs several methods have been proposed[4,5], however for the large, industrial scaling preparation the catalytic way[6] seems to be the most adaptable.

In this short communication, we report interesting new catalysts for the large scale synthesis of MWNTs. This family of catalysts can be perhaps the base of the industrial MWNT preparation.

EXPERIMENTAL

I. Preparation of catalyst supports and supported catalysts

a. Alumina support

Alumina was synthesised starting from aluminium isopropoxyde (Aldrich). About 100 g of aluminium isopropoxyde powder was spread over a wet filter in a petri dish and slowly hydrolysed completely using distilled water. $\text{Al}(\text{OH})_3$ gel thus obtained was kept aside overnight and then placed in a hot air oven at 140 °C for 24 hours. The dry solid was ground into a fine powder and labelled as Al^s . The commercial alumina was labelled as Al^c .

b. Cobalt supported alumina

10 g of the alumina (as prepared above and the commercial sample, respectively) were wetted with 10 ml of cobalt(II)-acetate solution (1.055 g $\text{Co}(\text{CH}_3\text{COO})_2 \cdot 4\text{H}_2\text{O}$ in water) so as to obtain 2.5% metal on the support. It was homogenised thoroughly and placed in a hot air oven at 140 °C for 24 hours. The solids were then ground well in a pestle and mortar into a fine powder. The samples thus obtained were labelled as Co-Al^s , Co-Al^c , respectively.

c. Iron supported alumina

10 g of the alumina (as prepared above and the commercial sample, respectively) were wetted with 10 ml of iron(II)-acetate solution (0.778 g $\text{Fe}(\text{CH}_3\text{COO})_2$ in water) so as to obtain 2.5% metal on the support. The followed drying procedure was the same as in the case of Co. The samples were labelled as Fe-Al^s and Fe-Al^c , respectively.

d. Cobalt and Iron supported alumina

10 g of the alumina (as prepared above and the commercial sample, respectively) were wetted with 10 ml of iron(II)-acetate/Co-acetate solution so as to obtain 2.5% Co and 2.5% Fe metal on the support. The samples are labelled as CoFe-Al^s and CoFe-Al^c , respectively.

II. Production of carbon nanotubes

Acetylene was used as the source of carbon for the production of carbon nanotubes. The decomposition of acetylene was carried out at atmospheric pressure in a fixed bed flow reactor. In a typical experiment about 5g of the exactly weighted supported catalyst was spread over a quartz plate as a thin layer and placed into the furnace which has been preheated to the desired temperature. After flushing with nitrogen gas (120 ml/min) for 15 minutes, the acetylene stream was opened for 1 hour. The decomposition of acetylene was carried out at different temperatures, 600 °C and 700 °C, respectively, and two different rates of acetylene flow (15 and 25 ml/min).

III. Characterisation of the catalysts and the obtained carbon materials

The samples were analysed before and after the reaction by XRD (Phillips P.W. 1349/30 diffractometer). The surface area and the porosity of the different samples at different stages were determined by the conventional BET method at the temperature of liquid nitrogen.

The formation of carbon nanotubes was followed using Transmission Electron Microscopy. The samples for TEM analysis were prepared by glue technique as described earlier[7]. Both low (Phillips CM20) and high resolution (JEOL 200CX) TEM analysis have been made.

RESULTS AND DISCUSSION

The XRD spectra of the used catalysts have not shown any formation of new phases compared to the original samples.

Carbon yield data are summarized in Table 1. It is obvious that the amount of carbon deposit is increasing with the temperature, with the longer reaction time and with the increasing hydrocarbon flow (the latter two are not shown in the table). The difference between the acetylene and the ethylene in the formation of carbon deposit is also evident. However, an interesting new feature appears in the case of the metal mixture containing catalysts (marked lines in the Table 1.).

Table 1. Formation of carbon deposit (%)* in different conditions

Catalyst	600 °C		700 °C	
	C ₂ H ₂	C ₂ H ₄	C ₂ H ₂	C ₂ H ₄
Co-Al ^s	23.5	6.4	26.8	6.6
Fe-Al ^s	17.6	4.2	33.3	7.2
CoFe-Al^s	18.7	4.2	43.1	6.5
Co-Al ^c	2.4	4.5	2.4	1.1
Fe-Al ^c	19.8	4.4	21.1	4.4
CoFe-Al^c	21.2	4.3	64.8	6.3

* Carbon yield (%) = $(m_{cat, before} - m_{cat, after}) / m_{cat, before} * 100$

In Fig. 1., a representative set of pictures is shown. On Co-Al^c sample, nanotube formation is hardly noticeable both at 600 °C and at 700 °C (Fig. 1. A). Although on Fe-Al^c catalyst at 700 °C we can also find nanotubes (Fig. 1. B), the CoFe-Al^c catalyst shows marvellous activity in the investigated reaction (Fig. 1. D-F).

The corresponding HREM pictures from the Al^c-based catalysts are depicted on Fig. 2. In the case of Co, the rare nanotubes formed are well-graphitized with some 10-20 parallel layers and there is almost no amorphous carbon on the outer surface (Fig. 2. A). Oppositely to this, the tubes formed on Fe-containing catalysts are thinner with some 5-12 layers but the number of the defects is much higher (Fig. 2. B). The CoFe-mixture catalysts give even thinner tubes, 2-7 graphitic layers, and in these samples the amount of amorphous carbon is negligible (Fig. 2. C).

In order to investigate more deeply this abnormal feature, the specific surface area and porosity values were determined for both the original and the used catalysts. Nevertheless the results obtained cannot explain the observations.

CONCLUSION

Summarizing the results obtained in the catalytic synthesis of MWNTs, we can state that the metal mixtures containing catalysts can produce MWNTs with high activity and selectivity. Furthermore, with these mixtures we can control some physical properties of the MWNTs. The abnormal increase of the carbon deposit compared to the single metal containing catalysts can indicate the presence of a new reaction center or a modified nanotube formation mechanism. The quasi-parallel running bunches and the sheets nicely denote the presence of a new, presumably alloy-like "micro-phase" on the surface.

ACKNOWLEDGEMENT

The authors are gratefully acknowledged to the Inter University Poles Attraction on Reduced Dimensionality Systems (PAI-IUAP n° 4/10) and the NAMITECH [contract no NAMITECH, ERBFMRX-CT96-0067 (DG12-MIHT)] for the financial support.

REFERENCES

-
- [1] S. Iijima, *Nature*, **354** (1991) 220
 - [2] T.W. Ebbesen, *Phys. Today*, **49** (1996) 26
 - [3] W. A. de Heer, A. Chatelain, D. Ugarte, *Science*, **270** (1995) 1179
 - [4] D. Ugarte, *Nature*, **359** (1992) 707
 - [5] S. Iijima, P.M. Ajayan, T. Ichihashi, *Phys. Rev. Lett.*, **69** (1992) 3100
 - [6] V. Ivanov, J. B.Nagy, Ph. Lambin, A. Lucas, X.B. Zhang, X.F. Zhang, D. Bernaerts, G. Van Tendeloo, S. Amelinckx, J. Van Landuyt, *Chem. Phys. Lett.*, **223** (1994) 329
 - [7] A. Fonseca, K. Hernadi, J. B.Nagy, D. Bernaerts and A. A. Lucas, *J. Mol. Cat.*, **107** (1996) 159

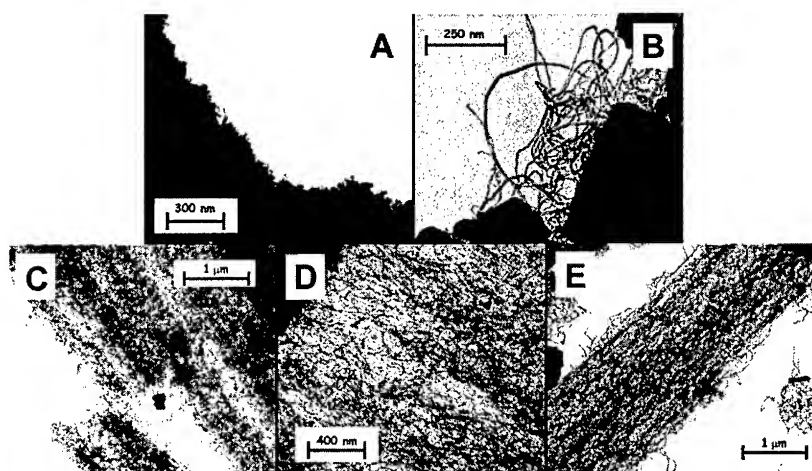


FIGURE 1. TEM images of carbon nanotubes formed at 700 °C over different Co-, Fe- and CoFe-containing catalysts

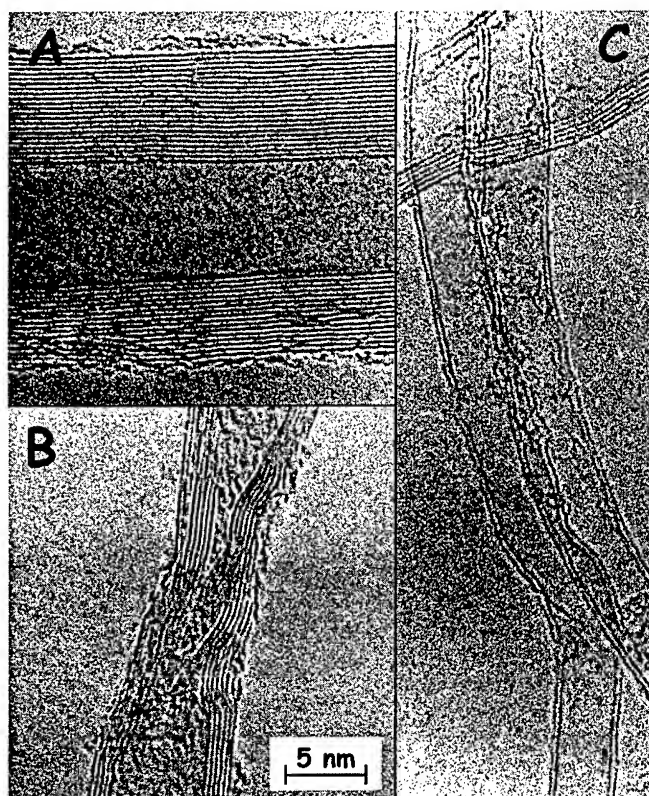


FIGURE 2. HREM images of carbon nanotubes formed on different catalysts (all with the same scale)

Solar synthesis of single wall carbon nanotubes

L. Alvarez (1), T. Guillard (2), E. Anglaret (1), J.L. Sauvajol (1),
P. Bernier (1), G. Flamant (2), G. Olalde (2), D. Laplaze (1),
M.T. Martinez (3), A. Benito (3), and W.K. Maser (3)

1) Groupe de Dynamique des Phases Condensées, U.M.R.5581, 34095 Montpellier, France

(2) Institut de Sciences et de Génie des Matériaux et Procédés, UPR 8521, 66125 Font-Romeu, France

(3) Instituto de Carboquímica, CSIC, Zaragoza, Spain

Abstract: We discuss here the influence of some synthesis parameters in the production of single wall carbon nanotubes (SWNT) with a 2 kW solar furnace at the Odeillo Institute. We first study the specific role of catalysts like nickel or cobalt on the SWNT formation process. SEM and TEM pictures show significant differences in the yield of production and suggest different growth mechanisms. Furthermore, we report Raman spectra for samples produced using lanthanum or sulfur as catalysts. These samples provide very striking results in the low frequency range (in term of distribution in diameter) with a good correlation with the graphite-like modes region.

I Introduction

Although single wall carbon nanotubes are now routinely produced (1,2) and have been extensively studied, the growth mechanisms are still not well understood. With the 2 kW solar furnace of the Odeillo Institute, we can produce carbon nanotubes by direct vaporization of a carbon-bimetal target in argon atmosphere (3) and study the influence of the synthesis parameters on the structure and yield of nanotubes to get a better understanding of the formation mechanisms. Another challenge is the determination of SWNT structures and the relation between the structure and physical properties of these nanostructures. Raman spectroscopy is a powerful technique to study structure, diameter and electronic properties of SWNT. In this paper we discuss the role of catalysts on the SWNT properties and the influence of the temperature gradient in the growth zone on the rate of production.

II Gas flow rate and pressure

The formation of carbon nanostructures was first studied as a function of gas flow rate and pressure using nickel and cobalt as catalysts (4) (Ni 2% at, Co 2% at). For pressure below 120 mbar, only nano-particles or carbon fibers are observed on SEM pictures whereas near 250 mbar, one essentially obtains multiwalled nanotubes. Between 400 and 600 mbars the production of single wall carbon nanotubes is favored. Carbon nano-particles are found in greater amount when the gas flow rate increases. The best yield for SWNT synthesis is obtained for a gas flow rate around 0.2 m³/h and under a pressure close to 500 mbar. An increase of the pressure improves the dilution of vaporized carbon atoms and favors the growth of ordered structures whereas a low gas flow rate allow the annealing of these carbon

nanostructures. The samples synthesized under various gas flow rates and pressures were characterized by Raman spectroscopy. The distribution of tube diameters is generally found to be large (3) and independent of the gas flow rate and pressure.

III The temperature gradient

In the experimental set-up usually used, a graphite pipe surrounds the crucible and acts both as a thermal screen and condensing zone. By placing this pipe in the focus area one increases the temperature in the annealing zone and decreases the temperature gradient in the condensing zone. The produced samples contain a large amount of SWNT. By contrast, changing the gas flow direction to avoid the vapor phase pass through the hot channel formed by the graphite pipe greatly increases the temperature gradient. In this case only a few isolated SWNT are observed. This confirms that the gradient temperature is a very important synthesis parameter.

IV The role of catalyst

The mixture of Ni and Co catalysts is often used in the SWNT synthesis, especially in solar method. The purpose was to determine the specific role of each component by using them separately. Generally a better yield is obtained with the use of both catalysts rather than using only one. In the last case the samples are rather inhomogeneous even if Ni seems more efficient than Co. TEM. images clearly show significant differences between the growth mechanisms of tubes from nickel or cobalt particles.

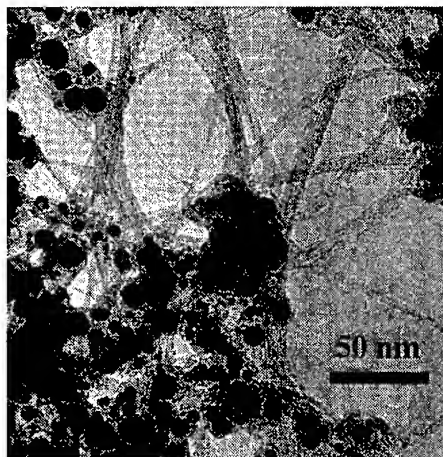
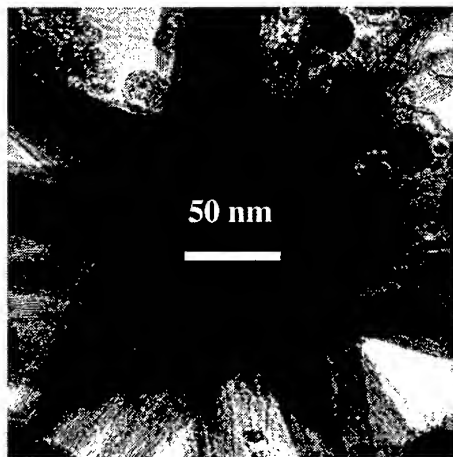


Figure 1: TEM image of sample made with Ni

Figure 2: TEM image of sample made with Co

In the case of Ni (figure1), large number of bundles containing more than 100 SWNT escape radially from a large particle (80 nm in diameter). The model proposed by Y.Saito and al. (5) can account for the growth mechanisms from Ni particles. This model suggests that Ni and C are mixed in the liquid phase where the carbon solubility is larger than in the solid phase. During cooling, carbon atoms segregate to the surface of the drop and form nanotubes or graphitic layers (depending on the cooling rate). By contrast the vaporization of a graphite / cobalt mixture gives many small particles (10

nm in diameter) and bundles formed by few nanotubes (figure 2). For a mixture of Ni and Co TEM pictures look like those observed with Co only. This suggests that the presence of Co limits the self-association of metal particles. The difference between Ni and Co may arise from the catalyst particle size. The larger diameter for Ni particles leads to a higher carbon / catalysts atoms ratio so that a great number of SWNT can be formed.

Samples prepared by the solar route were characterized by Raman spectroscopy, especially in the radial breathing modes low frequency range where the peaks positions directly relate to the tube diameters (6,7). The modes in the intermediate frequency range (300-1000 cm^{-1}) are calculated to depend on the SWNT chirality (8,9). The spectra for samples synthesized with only one catalyst (Ni or Co) are quite similar and display strong peaks between 150 and 180 cm^{-1} corresponding to a diameter range from 1.25 to 1.5 nm. Using a mixture of Ni and Co, these peaks are more intense but we also observe additional peaks located between 220 and 260 cm^{-1} , corresponding to smaller tube diameters.

The use of lanthanum or sulfur as catalysts changes the structure and diameter of SWNT. Figure 3 displays a low frequency Raman spectra recorded on a sample synthesized with lanthanum oxide.

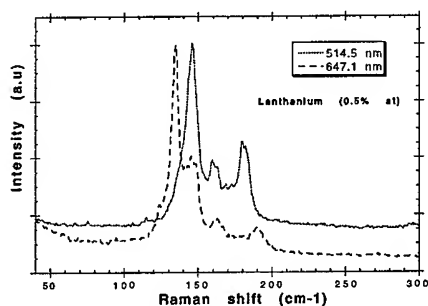


Figure 3: Radial breathing modes region

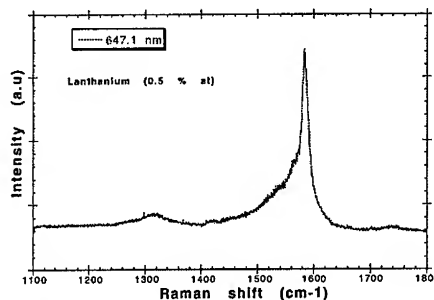


Figure 4: Graphite-like modes region

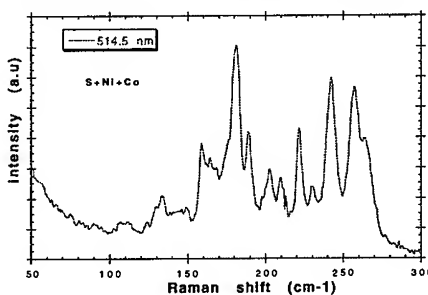


Figure 5: Radial breathing modes region

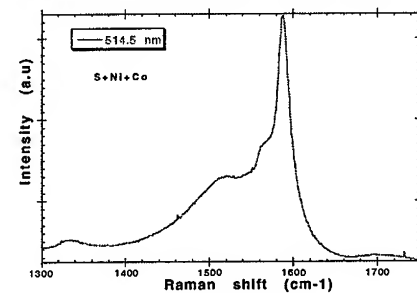


Figure 6: Graphite-like modes region

Note the strong peaks located between 135 and 160 cm^{-1} , corresponding to SWNT with diameters from 1.4 to 1.66 nm. These peaks were already observed but with an intensity smaller than that of the peak located at 180 cm^{-1} . The profile of the Raman spectra in the graphite-like modes region with a 647.1 nm excitation wavelength

usually exhibits the Breit-Wigner-Fano resonance assigned to metallic SWNT (10). With lanthanum this resonance is not observed (figure 4) and we also assign the Raman signal in this case to semiconducting SWNT.

Considering SWNT produced with sulfur as catalyst, the Raman results are different from those obtained with lanthanum (figures 5,6). The main peaks in the radial breathing modes range are located around 240 and 260 cm^{-1} , corresponding to a large distribution of very small SWNT (0.8 to 0.9 nm). Furthermore, the Raman spectrum (recorded with the 514.5 nm laser line) in the graphite-like modes region (figure 6) displays a very broad peak around 1500 cm^{-1} assigned to the Breit-Wigner-Fano resonance, suggesting that those narrow SWNT have a metallic character.

The results obtained with lanthanum or sulfur are consistent with studies by Kataura et al. (11) who calculated the electronic energy gap of SWNT with diameters from 0.8 to 1.8 nm. Metallic SWNT having diameter from 0.8 to 1 nm are expected to exhibit a resonant Raman behavior with a 514.5 nm excitation wavelength (as observed with S in fig.6) whereas the 647.1 nm excitation wavelength emphasized semiconducting behavior of SWNT with large diameter (as seen with La in fig.3).

V Conclusion

We discussed the specific role of some synthesis parameters on the structure, diameter and electronic properties of SWNT. We find that the pressure, the gas flow rate and the temperature gradient act only on the yield of production. The characterization by Raman spectroscopy in the low frequency range allows to estimate the SWNT diameters and we find that the distribution of diameters can be shifted by a convenient choice of catalysts. The Raman spectra profile in the graphite-like modes give some insight in electronic properties of SWNT.

REFERENCES

- (1) A.Thess, R.Lee, P.Nicolaev, H.Dai, P.Petit, J.Robert, C.Xu, Y.H.Lee, S.G.Kim, D.T.Colbert, G.Scuseria, D.Tomanek, J.E.Fischer, R.E.Smalley, *Science*, **273**, 493-487, (1996)
- (2) C.Journet, W.K.Maser, P.Bernier, A.Loiseau, M Lamy de la Chapelle, S.Lefrant, P.Deniard, R.Lee, J.E.Fischer, *Nature*, **288**,756-758, (1997)
- (3) T.Guillard, S.Cetout, L.Alvarez, J.L.Sauvajol, E.Anglaret, P.Bernier, G.Flamant, D.Laplaze, *European Phys.J.*, **5**, 251-256, (1999)
- (4) D.Laplaze, P.Bernier, W.K.Maser, G.Flamant, T.Guillard, A.Loiseau, *Carbon*, **36**, 685-688, (1998)
- (5) Y.Saito, M.Okuda, N.Fujimoto, T.Yoshikawa, M.Tomita, T.Hayashi, *Jpn.J.Appl.Phys.*, **33**, 526-529, (1994)
- (6) A.M.Rao, E.Richter, S.Bandow, B.Chase, P.C.Eklund, K.A.Williams, S.Fang, K.R.Subbaswamy, M.Menon, A.Thess, R.E.Smalley, G.Dresselhaus, M.S.Dresselhaus, *Science*, **275**, 187-191, (1997)
- (7) S.Bandow, S.Asaka, Y.Saito, A.M.Rao, L.Grigorian, E.Richter, P.C.Eklund, *Phys.Rev.Letters*, **80**, 3779-3782, (1998)
- (8) P.C.Eklund, J.M.Holden, R.A.Jishi, *Carbon*, **33**, 959-972, (1995)
- (9) E.Anglaret, N.Bendiab, T.Guillard, C.Journet, G.Flamant, D.Laplaze, P.Bernier, J.L.Sauvajol, *Carbon*, **36**, 1815-1820, (1998)
- (10) M.A.Pimenta, A. Marucci, S.D.M.Brown, M.J.Matthews, A.M.Rao, P.C.Eklund, R.E.Smalley, G.Dresselhaus, M.S.Dresselhaus, *J.Mater.Res.*, **13**, 2396-2404, (1998)
- (11) H.Kataura, Y.Kumazawa, Y.Maniwa, I.Umez, S.Susuki, Y.Ohtsuka, Y. Achiba, proceedings ICSM 98, to be published in Synthetics Metals

Carbon Arc Plasma Doped with Fe and Co/Ni: Spectroscopy and Formation of Carbon Nanostructures

Andrzej Huczko*, Hubert Lange*, Przemysław Byszewski†,
Akira Koshio‡ and Hisanori Shinohara‡

*Dept. of Chemistry, Warsaw University, 02-93 Warsaw, Poland

†Institute of Vacuum Technology, 00-241 Warsaw, Poland

‡Institute of Physics PAS, 02-668 Warsaw, Poland

‡Dept. of Chemistry, Nagoya University, 464-01 Nagoya, Japan

Abstract. Carbon nanostructures (fullerenes and nanotubes) have been effectively produced using carbon arc technique with homogenous Fe- and Co/Ni-doped anodes. The emission spectroscopy of the arc plasma with evaporated dopants was carried out and temperatures and concentrations of active species were evaluated. The solid products were characterized by MS and SEM techniques.

INTRODUCTION

Arc plasma produced carbon vapors showed to be the source of novel fascinating carbon nanostructures - fullerenes (1) and nanotubes (2). The carbon arc co-evaporation of different elements and compounds is also known to produce other various interesting carbon nanomaterials (3). Some published results, regarding those syntheses are, however, inconclusive and even contradictory, mostly due to the poor repeatability and flaws in experimental techniques applied. This is the case, for example, of the synthesis of tubules catalyzed by Cu (4). Also in the production of single-wall carbon nanotubes different catalysts and/or process parameters are claimed to be the best. When Fe was used, single-walled nanotubes grew efficiently in He atmosphere (5). However, Bethune et al. (6) argued that Fe, Ni and Ni-Cu mixture (50:50) do not catalyze the process while Co does. Iijima and Ichihashi (7) claimed that the synthesis using Fe is successful only when methane is present in the reactor.

In the present study we report the results of optical emission studies of C-Fe and C-Co/Ni arc plasma under conditions of fullerene nanostructure formation. Such an approach can give new insights into the process mechanism and was positively tested earlier (8) in the case of pure fullerene formation in carbon arc. The composition of solid products (soot, web, and cathode deposits), in relation to the process operating parame-

ters, is discussed.

EXPERIMENTAL

The reaction system and the arcing procedure have been described in detail elsewhere (8,9). Homogenous anodes (6 mm dia, 0.6 at% of Fe or Co/Ni) were d.c. arced at He pressure within 8 - 80 kPa. Graphite sublimation rate ranged between 2 and 5 mg/s. C_{60} content in the resulting soot was determined spectrophotometrically, while the products (soot, web and deposits) were analyzed by LD-TOF-MS and SEM techniques. Web-like soot was found in the reactor mostly in the case of Co/Ni.

RESULTS AND DISCUSSION

Spectral diagnostics of interelectrode gap

The temperatures and C_2 column densities were determined from the emission Swan (0,0 - 516.5 nm) band taking into account and using the self-absorption phenomenon (9). Some examples of the distributions are shown in Figure 1. From Figure 1A it follows that He pressure strongly influences C_2 concentrations, and thereby the other carbon species, in the arc. Therefore at higher pressure, despite the higher power input, the anode erosion rate is lower comparing to the lower pressure case. By the same reason even a small increase in sublimation rate under higher pressure causes a significant increase in C_2 content (Figure 1B).

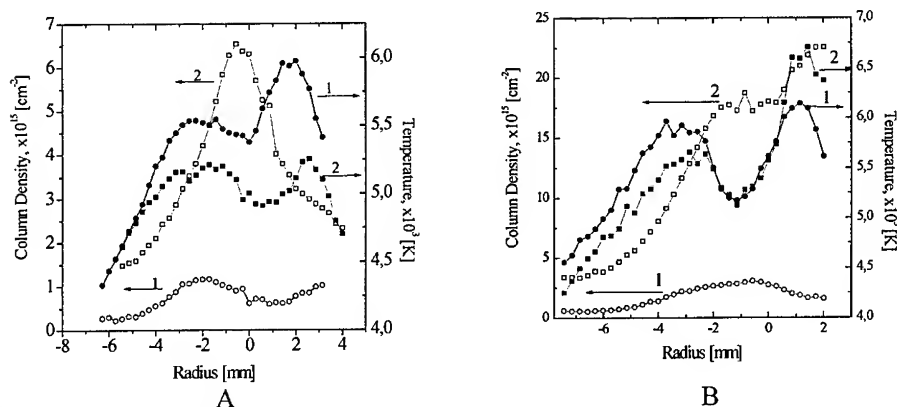


Figure 1. Plasma column density of $C_2(a^3\Pi_u, v=0)$ and temperature distributions.
 (A) C - Fe; pressure: 8 (1) and 80 (2) kPa; power input: 1940(1) and 2470 (2) W; erosion rate: 4 (1) and 2.2 (2) mg s^{-1} .
 (B) C - Co/Ni; power input: 3200 (1) and 4340 (2) W; pressure: 70 (1) and (2) kPa, erosion rate: 3.2 (1) and 4.8 (2) mgs^{-1} .

Obviously partial pressures of He in the reactor chamber and of carbon species in the arc influence the mechanism and kinetics of the carbon vapor nucleation process. It is worth to note that minima in temperature distributions (a few hundred degrees) on the axis are observed. This effect may be related to the arc spot movement around the cathode edge.

Laser-Desorption TOF-MS analyses

LD-TOF-MS analyses revealed that the arcing of homogenous Fe-doped anodes enhanced the formation of some higher fullerenes (C_{72} , C_{74} and C_{80} ; Figure 2), the abundance of which in the case of pure graphite is normally very meager. Particularly, C_{72} and C_{74} are so called "missing fullerenes" (10). Thus, Fe atoms or clusters may play a catalytic role in generating of these, otherwise missing, fullerenes. In the case of Co/Ni this effect is much less pronounced. C_{60} content in soot is lower (within 2 - 7 wt% for Fe-doping and 1 - 6 wt% for Co/Ni-doping), as compared with pure graphite sublimation (11-20 %wt).

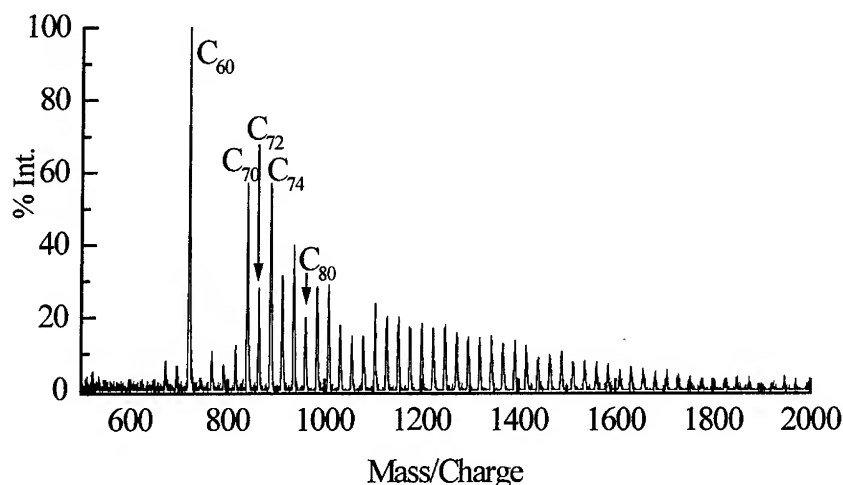


Figure 2. MS of soot produced under pressure 80 kPa (C - Fe anode).

SEM analyses

SEM observations revealed that arc sublimation of Co/Ni-doped anodes produced significant amount of bundles of single-wall nanotubes in "webs", but not in normal soot (Figure 3). The chamber soot contained high density SWNTs together with amorphous carbon and catalyst particles. The catalytic activity of Fe for SWNTs production is rather weak in general. However, the soot resulting from our Fe/C arcing at high pressure (80 kPa) also contained a lot of SWNTs. The above mentioned enhancement of C_{72} and C_{74}

may be closely related to the early stage of the growth of the corresponding SWNTs since the fullerene "cap structure" and some of the nanotube cap structures are the same with each other.

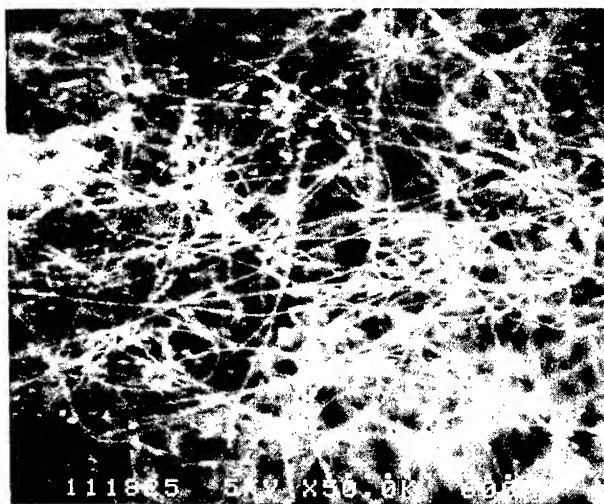


Figure 3. SEM of web-like soot produced under pressure 65 kPa (C - Co/Ni anode).

ACKNOWLEDGMENTS

The work was supported by the Committee for Scientific Research (KBN) through the Dept. of Chemistry, Warsaw University, under Grant No. BW-1418/16/98 (to H.L.). H.S. thanks for the financial support of "New Carbon Processes for Nanomaterials" of JSPS.

REFERENCES

1. Kroto, H. W., Heath, R., O'Brien, S. C. Curl, R.F., and Smalley, R.E., *Nature* **318**, 162-165 (1985).
2. Iijima, S., *Nature* **354**, 56-58 (1991).
3. Banhart, F., Redlich, Ph., and Ajayan, P. M., **292**, 554-558 (1998).
4. Botton, G. A., Burnell, G., Humphreys, C. J., Yadav, T., and Withers, J.C., *J. Phys. Chem. Solids* **58**, 1091-1095 (1997).
5. Cassel, A.M., Scrivens, W. A., and Tour, J. M., *Chem. Mater.* **8**, 1545-1549 (1996).
6. Bethune, D. S., Kiang, C. H., De Vries, M. S., Gorman, G., Savoy, R., Vazquez, J., and Beyers, R., *Nature* **363**, 605-609 (1993).
7. Iijima, S., and Ichihashi, T., *Nature* **363**, 605-609 (1993).
8. Huczko, A., Lange, H., Byszewski, P., Popławska, M., and Starski, A., *J. Phys. Chem.*

A. **101**, 1267-1270 (1997).

9. Lange, H., Huczko, A., and Byszewski, P., *Spectroscopy Letters* **29**, 1215-1221 (1996).

10. Wan, T. S. M., Zhang, H.-W., Nakane, T., Xu, Zhude, Inakuma, M., Shinohara, H., Kobayashi, K. and Nagase, S., *J. Am. Chem. Soc.* **120**, 6806-6807 (1998).

Large Arrays of Well-Aligned Carbon Nanotubes

Z. F. Ren,^{*} Z. P. Huang,^{*} J. W. Xu, D. Z. Wang,^{*} J. H. Wang

Department of Chemistry, State University of New York at Buffalo, Buffalo, NY 14260-3000

^{}Permanent Address: Department of Physics, Boston College, Chestnut Hill, MA 02467*

L. E. Calvet, J. Chen, J. F. Klemic, and M. A. Reed

Department of Electrical Engineering, Yale University, New Haven, CT 06520-8284

Abstract. Large arrays of well-aligned carbon nanotubes on glass, silicon, nickel, platinum, etc. have been successfully synthesized by plasma enhanced chemical vapor deposition at temperatures below 500°C. Either a uniform layer of nickel made by magnetron sputtering or patterns of nickel dots made by e-beam lithography and e-beam evaporation or thermal evaporation was used as the catalyst. Acetylene and ammonia gases were used as the carbon source and dilution gas. Ammonia was also found to act as catalyst. Without ammonia, there was no growth of carbon nanotubes at that low temperature. The diameters of the carbon nanotubes range from a few nanometers to a few hundred nanometers depending on the catalytic nickel size. The length is in a range of a few thousand angstroms to a few hundred micrometers depending on the growth time. In the case of uniform nickel layer used for catalyst, the site density of carbon nanotubes range between 10^9 to $10^{12}/\text{cm}^2$ depending on the diameters of the nanotubes. Whereas in the case of patterned nickel dots used for catalyst, the site density can be controlled at any number.

INTRODUCTION

Since the first observation of carbon nanotubes (1), numerous papers have reported studies on the yield of well-graphitized nanotubes, their diameter and wall thickness, growth mechanisms, alignment (2-5), electron emission properties, and potential applications. Alignment of the carbon nanotubes is particularly important to enable both fundamental studies and applications, such as cold-cathode flat panel displays and vacuum microelectronics. Recently, we have successfully grown large arrays of well-aligned carbon nanotubes on glass (3) and nickel foils (4) at temperatures below 600°C. Besides flat panel displays, applications such as the tips of scanning tunneling microscope (STM) and atomic force microscope (AFM) require selective positioning and growth of a single carbon nanotube. Limited progress has been reported in the controlled placement of nanotubes before our successful demonstration of the growth of single carbon nanotube on each nickel dot (6).

EXPERIMENTAL

Large area growth of carbon nanotubes: A thin nickel layer of 10 – 40 nm was first sputtered onto substrates such as glass, silicon, nickel, platinum, etc. by radio frequency (rf) magnetron sputtering, then large arrays of well-aligned multi-wall carbon nanotubes are grown on the nickel-coated substrates by plasma enhanced hot filament chemical vapor deposition (3,4). **Patterned growth of single carbon nanotube on each nickel dot:** Thin film nickel (Ni) patterns were first fabricated on a p-type boron doped 9.5 Ω -cm (100) silicon substrate by electron beam lithography and metal evaporation. The patterned growth of single carbon nanotube on each nickel dot was carried out the same way as the growth of large arrays.

The base pressure was pumped to below 10^{-6} Torr. A flowing gas mixture of acetylene and ammonia in the ratio of 1:2 – 1:4 was used during growth. The growth time depends on the requirement of nanotube length. Normally it is between 1 – 10 minutes, which yields a length of 0.1 – 20 μ m. After growth, the samples were examined by SEM, TEM, XPS, etc. techniques.

RESULTS AND DISCUSSIONS

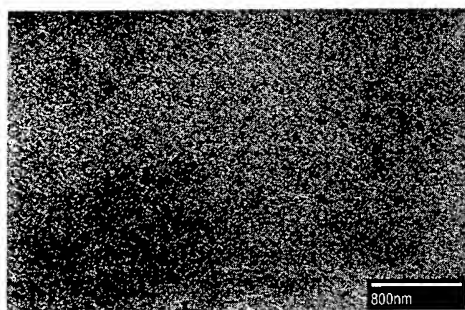


FIGURE 1A. SEM image of the as-sputtered nickel surface. The featureless surface indicates that the nickel layer is smooth and uniform.

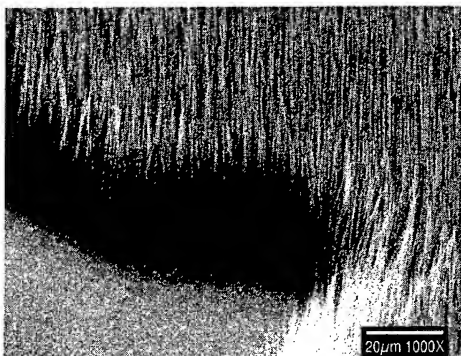


FIGURE 1B. SEM image showing the large area growth of well-aligned carbon nanotubes on glass.

Figure 1A shows the surface of the as-sputtered nickel layer. It is clearly shown that the surface was smooth. Figure 1B shows one of the samples grown on glass. The growth was about 10 minutes. The excellent alignment of the carbon nanotubes is clearly seen. The length of the carbon nanotubes is up to 50 μ m. The diameters were estimated to be in the range of 100 – 150 nm (See Figure 3B).

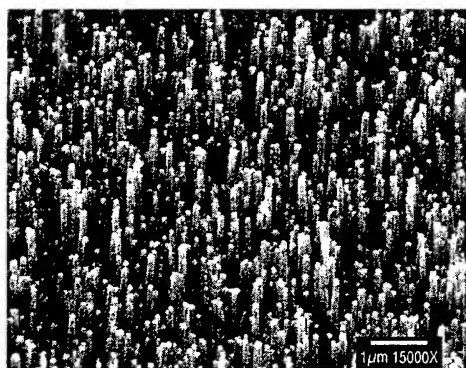


FIGURE 2A. SEM image of well-aligned carbon nanotubes on silicon.



FIGURE 2B. SEM image of very short carbon nanotubes grown on silicon for only 2 minutes.

Figure 2A and 2B show the growth of carbon nanotubes on single crystal silicon for 5 and 2 minutes respectively. From Figure 2A, it is clearly seen that the alignment is very good. On the top of each carbon nanotube, there is a nickel cap which act as the catalyst to keep the growth going. The site density of carbon nanotubes is determined by the thickness of the nickel layer. The thinner the nickel layer, the denser the site. The smallest diameter obtained so far is about a few nanometers. Figure 2B shows the early stage of the growth since the growth was stopped at 2 minutes. The shortest ones are about 0.1 μm.

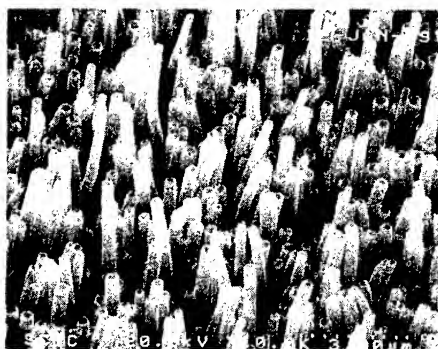


FIGURE 3A. SEM image showing that the nickel caps are etched away by HNO₃ for 1 minute.

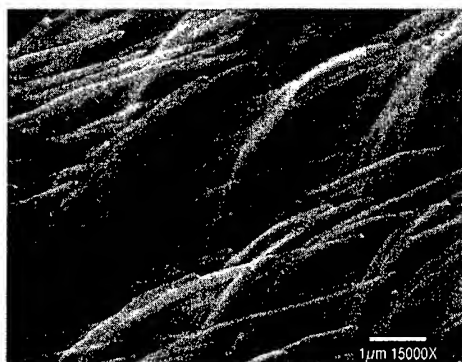


FIGURE 3B. SEM image of the sample which was used in Figure 1B after Ar ion sputtering.

Figure 3A and 3B show the SEM image of the samples after removal of nickel caps by HNO₃ solution etching and Ar ion sputtering respectively. The solution etching by HNO₃ only took about one minute and the removal of nickel caps is

complete. All the ends of the carbon nanotubes are open after etching. Morphologically, there was no observable damage by the HNO_3 etching. In Figure 3B, all the nanotubes were bent by the Ar ions sputtering and the nickel caps were not completely removed. Obviously HNO_3 etching is better than Ar ion sputtering.

In order to study the mechanism of alignment, we put the substrates differently. Figure 4A and 4B show the SEM image taken from side and top on a sample sit tilted a certain angle during growth. It is apparent that the alignment is no longer perpendicular to the substrate surface, but tilted a certain angle. The tilt direction is closely related to the electrical field direction. This demonstration strongly suggests that carbon nanotubes can be grown lying in the plane, which might be very useful to the fabrication of devices.

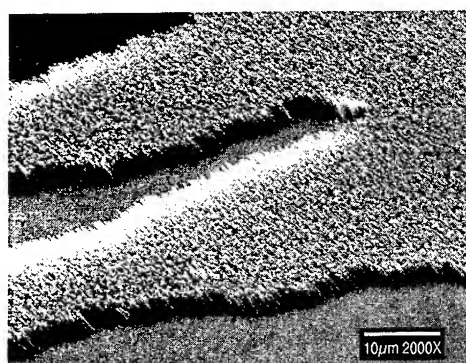


FIGURE 4A. An SEM side view of a sample with carbon nanotubes grown with a tilted angle to the substrate surface.

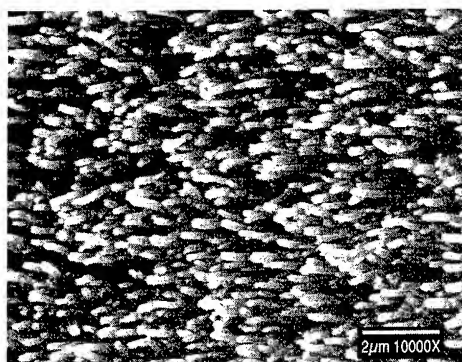


FIGURE 4B. An SEM top view of the carbon nanotubes grown with a tilted angle to the substrate surface.

In some applications, a single carbon nanotube or patterns with controlled site density is desired. In Figure 5A and 5B, we show growth of a single carbon nanotube on each nickel dot in a pattern with spacings of 1 and 2 μm (Figure 5A) and 5 μm (Figure 5B). The site and spacing are precisely controlled. The non-uniformity on height for this sample was believed that the electron beam lithography and electron beam evaporation of nickel was not uniform. With a better control of the e-beam lithography, we can make all the carbon nanotubes almost uniform in height (7). This demonstration is very important in the sense that applications requiring a single or multiple carbon nanotubes with controlled site density could be achieved. The applications involve the direct growth of a single carbon nanotube on the probe tip of scanning tunneling microscope (STM), atomic force microscope (AFM), etc. Another important possible application using multiple carbon nanotubes with well-defined spacing is multi-electron beam lithography which can improve the patterning ability by $10^4 - 10^6$ times.

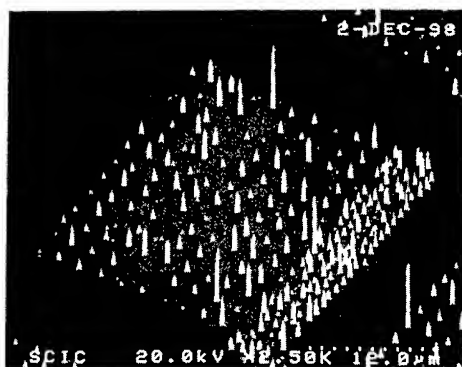


Figure 5A. Growth of single carbon nanotubes on each nickel dot spaced by 1 or 2 μm .



Figure 5B. Growth of single carbon nanotubes on each nickel dot spaced by 5 μm .

CONCLUSIONS

Large arrays of well-aligned carbon nanotubes have been grown on glass, silicon, nickel, platinum, etc. with the diameter, length, site density, growing angle controlled in the way we want them to be.

ACKNOWLEDGMENTS

This material is based on work supported in part by the U.S. Army Research Office under grant number DAAG55-97-1-0139. The management of this program by R. R. Reeber is greatly appreciated. The work performed at Yale was supported in part by DARPA. The authors also thank G. Sagerman for his technical support.

REFERENCES

1. Iijima, S., *Nature* **354**, 56-58 (1991).
2. Li, W. Z., Xie, S. S., Qian, L. X., Chang, B. H., Zou, B. S., Zhou, W. Y., Zhao, R. A., and Wang, G., *Science* **274**, 1701-1703 (1996).
3. Ren, Z. F., Huang, Z. P., Xu, J. W., Wang, J. H., Bush, P., Siegal, M. P., and Provencio, P. N., *Science* **282**, 1105-1107 (1998).
4. Huang, Z. P., Xu, J. W., Ren, Z. F., Wang, J. H., Siegal, M. P., and Provencio, P. N., *Appl. Phys. Lett.* **73**, 3845-3847 (1998).
5. Fan, S. S., Chapline, M. G., Franklin, N. R., Tomblor, T. W., Cassell, A. M., and Dai, H. J., *Science* **283**, 512-514 (1999).
6. Ren, Z. F., Huang, Z. P., Xu, J. W., Wang, D. Z., Wang, J. H., Calvet, L. E., Chen, J., Klemic, J. F., and Reed, M. A., *Appl. Phys. Lett.*, (submitted).
7. Ren, Z. F., Huang, Z. P., Xu, J. W., Wang, D. Z., Wang, J. H., Calvet, L. E., Chen, J., Klemic, J. F., and Reed, M. A., (unpublished results).

Sulfur : the key for filling carbon nanotubes with metals

A. Loiseau², N. Demoncy^{1,2}, O. Stéphan³, C. Colliex³, H. Pascard¹

¹LEM, UMR n° 104 ONERA-CNRS, Onera, B.P. 72, 92322 Châtillon Cedex, France,

²LSI, CEA-CNRS, Ecole Polytechnique, 91128 Palaiseau Cedex, France

³LPS, CNRS URA 002, Université de Paris Sud, Bât 510, 91405 Orsay Cedex, France

It is shown, using combined structural and chemical analysis modes of transmission electron microscopy, that various filled elements can be produced by arcing a graphite cathode and a graphite anode doped with the filling element and a small quantity of sulfur. A growth mechanism based on a catalytic process involving carbon, a metal and sulfur is proposed.

INTRODUCTION

Filling carbon nanotubes is highly attractive for the development of nanomaterials with new electronic or magnetic properties. Different methods of filling have been explored [1-4] but in most cases, they work for a limited range of materials or in low yields. Recently we succeeded in synthesizing a large variety of micron-long nanowires coated by carbon using an arc-discharge experiment in which the anode was successively doped with various elements among transition metals (Cr, Ni, Co, Fe, Pd), rare earth metals (Sm, Gd, Dy, Yb) and covalent elements (S, Ge, Se, Sb) [5]. We investigated both their structure and their chemical composition by Transmission Electron Microscopy (TEM) (diffraction patterns (SAED) and high resolution imaging (HRTEM)) and Electron Energy-Loss Spectroscopy (EELS), using the line-spectrum mode implanted on a dedicated scanning transmission electron microscope which provides elemental concentration profiles [6]. This technique was proved to be essential and particularly adapted for characterizing filled carbon nanotubes and understanding their formation [7].

STRUCTURAL AND CHEMICAL ANALYSIS

We first analysed the nanowires obtained in the conditions described in [5]. Surprisingly, the EELS nanoanalysis revealed that the nanowires obtained with metals were not carbon-rich as initially assumed but contained sulfur. The source of sulfur was found to be the graphite electrodes (99.4 %) whose major impurities are Fe (0.3 %) and S (≈ 0.25 %). Analysis of different cases is presented in [7]. As representative examples, the cases of Cr and of Ni are shown in Fig.1 and 2.

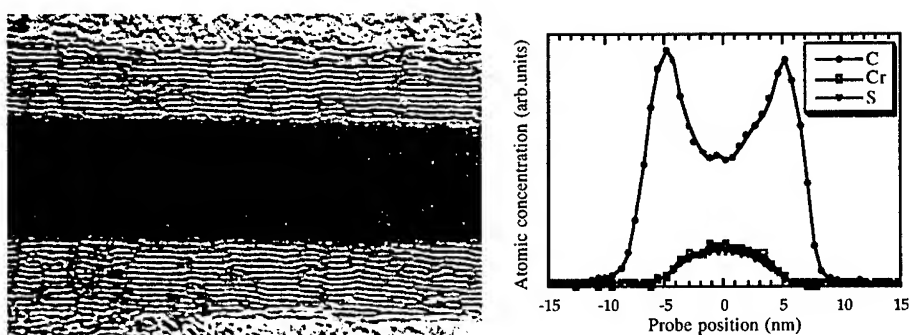


FIGURE 1. Analysis of a filled nanotube obtained with a 99.4% graphite anode doped with Cr. up: Concentration profiles of C, Cr and S deduced from the intensities of the C-K, Cr-L2,3 and S-L2,3 edges as the beam is scanned across the nanotube. down: HRTEM image of the nanowire which is a single crystal having a trigonal structure consistent with that of Cr_5S_6 or Cr_2S_3 . The crystal is epitaxed on the graphitic layers in such a way a $\langle 100 \rangle$ direction is along the tube axis.

Cr-based nanowires are very long single crystals and a majority of them was found to contain sulfur in a ratio close to 1:1, excluding any other element. The structure of these sulfides was identified from SAED and HRTEM analyses to be the trigonal compounds Cr_5S_6 or Cr_2S_3 .

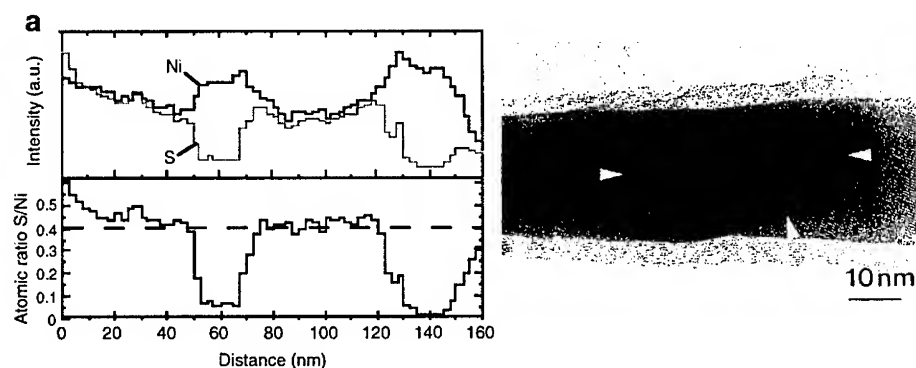


FIGURE 2: Analysis of a filled nanotube obtained with a 99.4% graphite anode doped with Ni. a): Longitudinal concentration profiles along the tube axis of C, Ni and S deduced from the intensities of the C-K, Ni-L2,3 and S-L2,3 edges. The filling material is alternatively pure Ni and a nickel sulfide. b): HRTEM image of a nanowire showing a succession of 3 different crystallites. Grain boundaries are arrowed.

Ni-based nanowires are also very long and contain sulfur. However the concentration in sulfur is not homogeneous along the tube axis as shown in Fig.2. The filling consists of a succession of crystallites alternatively pure Ni and nickel sulfides with a S/Ni ratio ≈ 0.4 . The pseudo cubic compound Ni_3S_2 was identified in certain cases from SAED analyses.

The only exception to this spectacular concentration phenomenon of sulfur inside the nanotubes was observed for Ge. In that case, nanowires are very thin and encapsulated in only 2 or 3 graphitic layers. They are frequently polycrystalline and the crystallites contain typical microtwins or stacking faults. Furthermore, when the doping element was sulfur itself, EELS analysis revealed that the nanotubes were filled with iron sulfides. These results show a spectacular concentration phenomenon of sulfur (or of iron) inside the nanotubes and suggest that the growth of nanowires results from the presence in the arc of three elements : carbon, a metal and sulfur.

ANALYSIS OF THE ROLE OF SULFUR

In order to understand the roles played by sulfur and the metal, we performed two kinds of experiments. First we used high purity carbon rods (99.997%) and we successively doped the anode with Co (99.99%), Ni (99.9%), Cr (99.95%), Dy (99.9%) and S (sublimed). The other experimental conditions [5] were unchanged. It is striking that no filled nanotube was found in the cathode deposit. Co and Ni yielded to the formation of single-walled nanotubes as usually observed [8] whereas only empty multi-walled nanotubes were produced with Cr, Dy and S.

In the second kind of experiments, we focused on the case of Cr which produced the longest nanowires and we added sulfur to Cr in a S/Cr = 0.5% atomic ratio (i.e. S/C = 0.1% in weight). This doping resulted in the abundant formation on the cathode of true nanowires encapsulated in carbon nanotubes. The images of Fig.3 attest that the structural characteristics of these nanowires are similar to those reported in [5]. EELS nanoanalysis

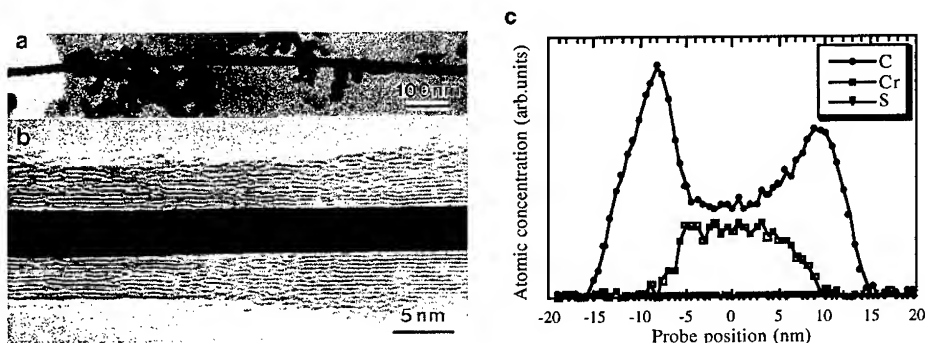


FIGURE 3 : a) HRTEM image of a nanowire coated by carbon obtained with a high purity graphite anode doped with Cr and S in a S/Cr=0.5% atomic ratio. b) Magnification showing the lattice image of the carbon layers and of the filling crystal. c) Concentration profiles of C, Cr and S across a carbon nanotube filled with pure Cr

revealed that some nanowires contained S as those obtained with the 99.4% graphite rods but for a majority of them, the fraction of S was below the limit of detection of the spectrometer. The concentration profiles were thus consistent with nanotubes filled with pure Cr as shown in Fig.3c and in a few cases with a chromium carbide. These results definitely prove that S is crucial for filling carbon nanotubes with Cr and that pure Cr nanowires are formed when S is added in catalytic quantity.

DISCUSSION: GROWTH MECHANISM

Using HRTEM and EELS, we have shown that sulfur is essential for the production of nanotubes filled with a large variety of materials. It is worth noting that filled nanotubes, in particular those partially filled [5], display morphological similarities with carbon nanofibres catalytically grown by chemical vapor deposition (CVD) [9]. Based on these similarities, we propose that the growth of our filled nanotubes follows a catalytic process as for carbon nanofibers [10], which is sketched in Fig.4. However this process arises at much higher temperatures, that is between 1000° and 2000°C, such as the metallic particle is almost in a liquid state [7]. In such a way the catalyst particle can flow inside the tube as it grows. The solid or molten state of the catalyst makes the difference between filled and tubes or nanofibers capped by a particle.

The specific role of sulfur in this process is the following. Below 2000°C, sulfur is known to promote the graphitization of carbon materials by acting as a cross-linker and being then released from the graphitic structure [11]. It is likely that C and S easily combine in the vapor phase, maybe forming S-rich clusters. Sulfur enhances the catalytic activity of the metal as far as graphitization is concerned. Then it is trapped in the filling material because of its strong affinity with metals as sketched in Fig.4. Since it reduces melting points of metals, it helps the filling material to remain in the liquid state and to flow inside the growing nanotube. This process results in a progressive increase of the S concentration in the nanowire. The total amount of S is therefore directly related with the length of the nanotube and the number of carbon layers.

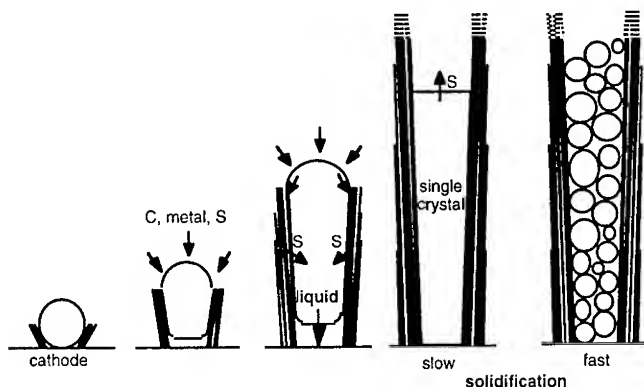


FIGURE 4: Schematic growth mechanism proposed for the formation of a carbon nanotube filled with a metal on the cathode of an arc-discharge experiment in presence of sulfur.

The final microstructure and the chemical composition of the nanowires are determined by the solidification process and the cooling conditions as shown in Fig.4. A rapid quench will lead to a microcrystalline filling. On the contrary if the solidification is slow enough, a solidification front can be established so that the formation of long single-crystals will be possible. Since sulfur is generally not soluble in metals, segregation phenomena occur at the solid-liquid interface and will determine the structure and the composition of the crystallites.

Let us first discuss the case of nickel. S is soluble in liquid Ni but not in solid Ni. Therefore as the solidification front moves, the sulfur is rejected in the liquid state and a pure metal will first grow. In the same time, the composition in sulfur of the liquid phase will increase until the growth of a definite sulfide replaces that of the pure metal. This provokes a rapid decrease of the concentration of sulfur in the liquid state and the growth of the pure metal takes place again. The nanowire will be a succession of pure metal crystals alternating with metallic sulfides. This is what we have effectively observed.

The case of Cr is more complex due to the existence in the Cr-S phase diagram of a miscibility gap in the liquid state between a pure Cr liquid and a S-rich liquid. The cooling of these two liquid phases will lead to the formation of either pure Cr crystals or CrS compounds. The same situation occurs for Ge. However in that case, GeS compounds are not formed because the number of the encapsulating carbon layers and their length are not sufficient to obtain sulfur rich liquid particles of Ge.

CONCLUSION

In conclusion we have shown that the presence of sulfur in catalytic quantity is crucial for the production using an electric arc of abundant metal based nanowires which can be free of sulfur. The role of sulfur is certainly not unique and it is likely that elements like selenium, hydrogen, oxygen probably can act in a similar way on filling processes. It is striking that recently using an hydrogen arc, very similar Ge nanowires have been produced [12]. Furthermore the discussion of the growth mechanism has shown that the metallurgy of the nanowires can be understood by considering the thermodynamical data of the corresponding metal-S systems. One can therefore think that a nanometallurgy can be developed in the electric arc chamber and that it would be possible to control the formation of definite nanowires in the future.

- [1] Ajayan, P.M. and Iijima, S., *Nature* **361** 333-334 (1993).
- [2] Seraphin, S., Zhou, D., Jiao, J., Withers, J.C. and Loufty, R., *Nature* **362** 503 (1993).
- [3] Ajayan, P.M., Colliex C., Lambert, J.M., Bernier, P., Barbedette, L., Tencé, M. and Stéphan, O., *Phys. Rev. Lett.* **72** 1722 (1994).
- [4] Tsang, S.C., Chen, Y.K., Harris, P.J. and Green, M.L.H., *Nature* **372** 159 (1994).
- [5] Guerret-Piécourt, C., Le Bouar, Y., Loiseau, A. and Pascard, H., *Nature* **372** 761 (1994); Loiseau, A. and Pascard, H., *Chem. Phys. Lett.* **256** 246 (1996).
- [6] Tencé, M., Quartuccio, M. and Colliex, C., *Ultramicroscopy* **58** 42 (1995).
- [7] Demoncey, N., Stéphan, O., Brun, N., Colliex, C., Loiseau, A., Pascard, H., *EPJB* **4**, 147 (1998)
- [8] Bethune, D.S. et al, *Nature* **363** 605 (1993).
- [9] Audier, M., Oberlin, A., Coulon, M.J., *J. of Cryst. Growth* **55** 549 (1981).
- [10] Rodriguez, N.M., *J. Mater. Res.* **8** 3233 (1993).
- [11] Oberlin, A., *Carbon* **22** 521 (1984); Bourrat, X., Oberlin, A., Escalier, J.C., *Fuel* **542** 521 (1987)
- [12] Dai, J.Y., Lauerhaas, J.M., Setlur, A.A., Chang, R.P.H., *Chem. Phys. Lett.* **258** 547 (1996).

Alkali-metal intercalation in carbon nanotubes

F. Béguin, L. Duclaux, K. Méténier, *E. Frackowiak, **J.P. Salvetat,
J. Conard, S. Bonnamy and P. Lauginie

CRMD, CNRS-University, 1B rue de la Férollerie, F-45071 Orléans Cedex 2, France

*ICTE, Poznan University of Technology, ul. Piotrowo 3, 60-965 Poznan, Poland

**EPFL, IGA/DP, 1015 Lausanne, Switzerland

Abstract. We report on successful intercalation of multiwall (MWNT) and single wall (SWNT) carbon nanotubes with alkali metals by electrochemical and vapor phase reactions. A LiC_{10} compound was produced by full electrochemical reduction of MWNT. KC_8 and CsC_8 -MWNT first stage derivatives were synthesized in conditions of alkali vapor saturation. Their identity periods and the $2 \times 2 \text{ R } 0^\circ$ alkali superlattice are comparable to their parent graphite compounds. The dysonian shape of KC_8 EPR line and the temperature-independent Pauli susceptibility are both characteristic of a metallic behavior, which was confirmed by ^{13}C NMR anisotropic shifts. Exposure of SWNT bundles to alkali vapor led to an increase of the pristine triangular lattice from 1.67 nm to 1.85 nm and 1.87 nm for potassium and rubidium, respectively.

INTRODUCTION

Intercalation is expected to be a powerful tool to tailor the electronic properties of graphitic materials (1). It has already been shown that doping of SWNT bundles increases noticeably the electrical conductivity (2). Intercalation between the individual nanotubes within the bundles was suggested to explain the structural disorder that is observed by TEM when the SWNT bundles are exposed to alkali-metal vapor (3). Alkali atoms can also be inserted between the layers of MWNT produced by the electric arc discharge method, but a large amount of structural defects is introduced during the process (4). Catalytic MWNT, which are less graphitized than arc-grown MWNT, may be suitable for reversible intercalation in the van der Waals gap between the adjacent shells (5,8). In this paper, we report on the intercalation of catalytic MWNT and arc-grown SWNT bundles with lithium and heavy alkali metals. The modification of the electronic properties was monitored by EPR and NMR spectroscopies. A direct evidence of the expansion of the triangular lattice of SWNT ropes was provided, for the first time, by X ray diffraction.

EXPERIMENTAL

MWNT samples were produced by the catalytic decomposition of acetylene at 900°C on supported cobalt (6). A "fishbone" arrangement of the aromatic layers along the tube axis was observed by TEM. Support and catalyst were eliminated by 72 % HF

and 3 mol.l⁻¹ HNO₃ treatments. MWNT were heat-treated under argon flow above 2400°C in order to eliminate residual cobalt. As an effect of the heat treatment, their aromatic layers became straight and continuous. The corrugated fishbone structure was replaced by a zigzag structure, made of a succession of straight multiwall segments separated by boundaries. SWNT bundles were extracted from raw collarets produced by the electric arc discharge method (7).

Electrochemical intercalation of lithium into MWNT was performed in a two electrode cell. A lithium disk played the role of counter and reference electrode. The working electrode was prepared by pressing a mixture of MWNT (85 %), acetylene black (10 %) and polyvinylidene fluoride (5 %). The electrolyte was LiPF₆ (1 mol.l⁻¹) in a 1:1 mixture of ethylene carbonate and diethyl carbonate (Merck). Lithium insertion/deinsertion curves were obtained with a Mac Pile generator (Biologic) at a constant current density of 20 mA per gram of MWNT in the potential range from 3 V to -0.02 V vs Li/Li⁺.

Saturated intercalation compounds of SWNT and MWNT were prepared in vapor phase using the classical two-bulb method with a small temperature gradient. Composition was determined by measuring the weight uptake after reaction. To obtain 2nd stage MC₂₄ derivatives of MWNT (M=alkali metal), stoichiometric amounts of 1st stage MC₈ compounds and nanotubes were mixed and annealed under vacuum for 2 weeks at 250 °C. The samples were investigated by X ray diffraction in the transmission mode at a wavelength of 0.15405 nm using a position sensitive detector (INEL CPS 120). EPR and NMR spectra were recorded on Bruker spectrometers: EPR at a frequency of 9.47 GHz; ¹³C-NMR (natural abundance) and ⁷Li-NMR on a DSX-360.

RESULTS AND DISCUSSION

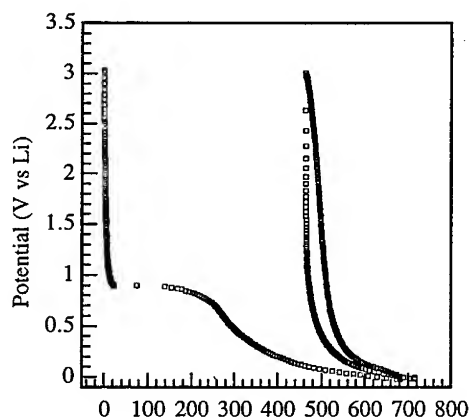


FIGURE 1. Potential vs. specific capacity (mAh/g) curve illustrating electrochemical insertion-desinsertion of Li in annealed MWNT.

Electrochemical insertion-desinsertion of Li in MWNT proceeded almost without hysteresis, i.e. without any overvoltage between the two processes (Fig. 1). This behavior is characteristic of a carbon surface free of functional groups. Reversible and irreversible capacities were 220 and 460 mAh/g, respectively. The high amount of Li irreversibly inserted in MWNT has to be attributed to the relatively large BET surface area of about 100 m²g⁻¹. From the quantity of electrical energy needed for a complete reduction of MWNT in a MWNT/Li cell, we deduced that a LiC₁₀ compound was formed.

This is less than in graphite for which, at saturation, the composition is LiC_6 (the capacity is 372 mAh/g in that case). ^7Li NMR measurements, performed on fully lithiated MWNT samples, confirmed a shift of 12 ppm similar to that of a LiC_9 graphite compound. From these differences between graphite and MWNT, it is likely that the rigid arrangement of coaxial layers in MWNT is a hindrance for reaching a high lithium uptake electrochemically.

Using the vapor phase method, brown first stage MC_8 ($M = \text{K}, \text{Cs}$) intercalation compounds of MWNT were obtained in the conditions of saturation. The identity periods of 0.537 and 0.593 nm for KC_8 and CsC_8 , respectively, are quite comparable to the values measured for their homologous graphite derivatives (0.541 and 0.595 nm, respectively). Asymmetric (h,k) bands in the X ray diffractogram can be attributed to the $2 \times 2 \text{ R } 0^\circ$ alkali superlattice characteristic of a MC_8 arrangement (Fig. 2).

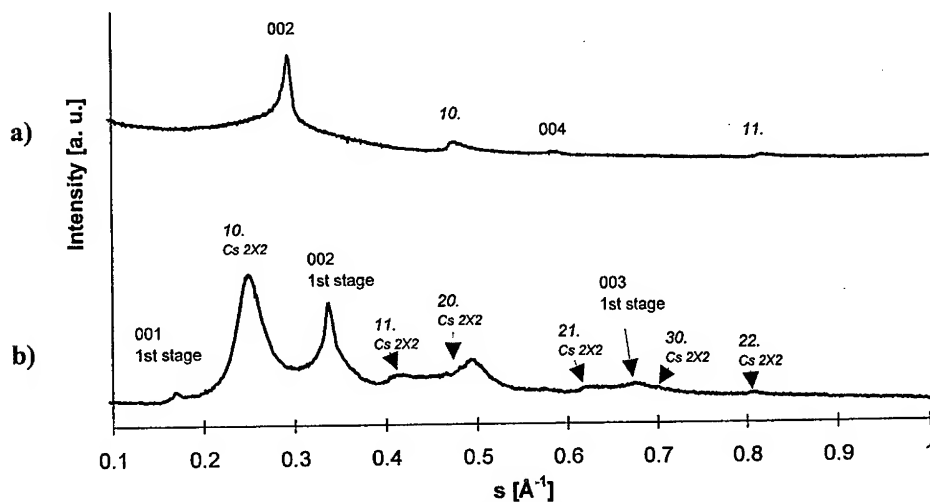


FIGURE 2. X ray diffractograms of: (a) MWNT annealed at 2500°C; (b) CsC_8 from MWNT

MC_8 derivatives have been diluted by the stoichiometric amount of nanotubes in order to get MC_{24} -MWNT. After annealing, the compounds had the characteristic blue color of a second stage intercalation compound; the identity period was 0.875 nm for the K-compound, very close to that of the parent graphite derivative (0.876 nm).

The temperature dependence of the EPR signal of the 1st stage KC_8 derivative was studied and compared with that of annealed MWNT (8) (Fig. 3). The susceptibility of MWNT, roughly estimated from line intensity, reveals a small Curie component, attributed to localised defects, associated to a Pauli term becoming dominant above 50 K. The effective number of spins of about 2.5×10^{18} per gram (0.5×10^{-4} per C) is similar to the spin density of graphite.

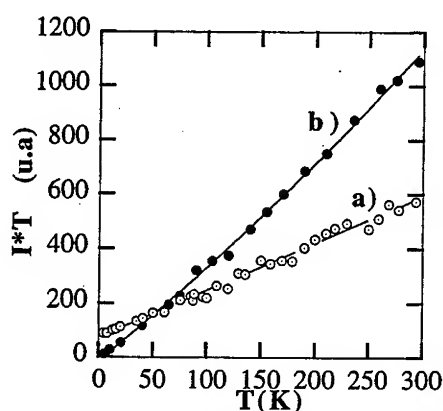


FIGURE 3. Temperature dependence of the intensity (I) of the EPR signal of undoped MWNT (a); KC_8 -MWNT (b), expressed by $I \cdot T$ vs T . For the undoped sample the ordinate scale has been strongly amplified.

The line of the KC_8 -MWNT compound is typically dysonian-asymmetric, as in good conductors. The effective number of spins is 40 times higher than in pristine MWNT, illustrating an important charge transfer like in alkali GIC (9). No Curie term was detected and the slight increase of the susceptibility with temperature might result from skin depth increasing with resistivity (Fig. 3). Whereas g factor was T -dependent in the pristine material, it is independent of temperature in KC_8 -MWNT, denoting a charge-transfer shift of the Fermi level away from the quasi-degeneracy region of the π bands.

EPR line of CsC_8 -MWNT was not observed, due to the strong spin-orbit interaction with increasing the intercalant atomic number.

As compared to MC_8 -MWNT, the EPR line of MC_{24} -MWNT ($M = K, Cs$) is more narrow. Charge transfer is almost total in 2nd stage compounds, and the strong broadening due to spin-orbit interaction of conduction electrons on alkali atoms is reduced (9). EPR lines were observed in 2nd (and likely higher) stage MWNT-Cs derivatives due to this effect.

A further evidence of intercalation was given by ^{13}C -NMR, showing anisotropic metallic shifts, similar to those of alkali-GIC. As for many aromatic-like carbon materials, the signal of pristine nanotubes exhibits a main peak (maybe a doublet) centered at the graphene (a,b) position, and a broad distribution tail (over 500 ppm) (10). Two peaks were observed for KC_8 -MWNT; their shifts relative to the standard graphene $\delta_{a,b}$ and δ_c positions are similar to those observed for KC_8 -GIC. This results mainly from the anisotropic dipolar interaction with conduction electrons, which is proportional to the density of states at the Fermi level (9).

SWNT intercalation compounds were characterized by X ray diffraction. After being exposed to K or Rb vapor, the (100) line characteristic of the triangular lattice of the SWNT bundles was shifted, proving that the alkali metal was inserted between the tubes (Fig. 4). The lattice parameter increased from 1.67 nm for pristine SWNT to 1.85 nm and 1.87 nm, respectively, for the tubes intercalated by potassium and rubidium. This expansion is in agreement with nesting of more than one alkali atom (possibly up to 3) in the (1/3, 2/3) interstitial site of the expanded lattice. To our knowledge, it is the first direct evidence of alkali metals intercalation in the bundles (2-3).

The fact that Zhou et al. did not detect any TEM contrast nor clear electron diffraction could be due to structural disorder caused by partial decomposition of the compounds under vacuum in their microscope chamber (3).

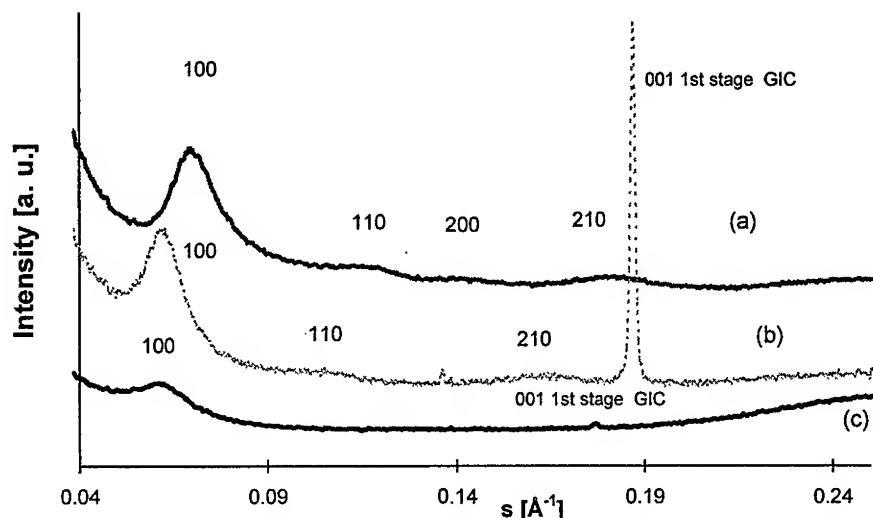


FIGURE 4. XRD of (a) collaret containing SWNT; (b) SWNT doped by K; (c) SWNT doped by Rb

ACKNOWLEDGMENTS

The authors are grateful to C. Journet and P. Bernier (Montpellier) for supplying SWNT collarets. This work was financially supported by the E. C. TMR program NAMITECH, ERBFMRX-CT96-0067.

REFERENCES

1. M.S. Dresselhaus and G. Dresselhaus, *Adv. Phys.* 30, 139 (1981).
2. R.S. Lee, H.J. Kim, J.E. Fischer, A. Thess and R.E. Smalley, *Nature* 388, 255-257 (1997).
3. S. Suzuki, C. Bower and O. Zhou, *Chem. Phys. Letters* 285, 230-234 (1998).
4. O. Zhou, R.M. Fleming, D.W. Murphy, C.H. Chen, R.C. Haddon, A.P. Ramirez and S.H. Glarum, *Science*, 263 1744-1747 (1994).
5. E. Frackowiak, S. Gautier, H. Gaucher, S. Bonnamy and F. Béguin, *Carbon* 37, 61-69 (1999).
6. A. Hamwi, H. Alvergnat, S. Bonnamy and F. Béguin, *Carbon* 35, 723-728 (1997).
7. C. Journet, W.K. Maser, P. Bernier, A. Loiseau, M. Lamy de la Chapelle, S. Lefrant, P. Deniard, R. Lee and J.E. Fischer, *Nature*, 388, 756-758 (1997).
8. K. Metenier, L. Duclaux, H. Gaucher, J.P. Salvetat, P. Lauginie, S. Bonnamy and F. Béguin, "Characterization of heavy alkali metals intercalation in carbon nanotubes", in *Proceedings XII IWEPM-Progress in Molecular Nanostructures*, ed. H. Kuzmany et al., pp 51-54 (1998).
9. P. Lauginie, A. Messaoudi and J. Conard, *Synth. Metals* 56, 3002-3007 (1993).
10. Y. Maniwa, M. Sato, K. Kume, M.E. Kozlov and M. Tokumoto, *Carbon*, 34, 1287-1291 (1997).

About the composition of single wall carbon nanotube bundles: An Analysis from Optical, Raman, and IR Experiments

J. Kürti*, M. Milnera[†], M. Hulman[‡], O. Zhou[†], and H. Kuzmany[†]

*Dept. of Biological Physics, Eötvös University, H-1117 Budapest, Hungary

[†]Dept. of Physics and Astronomy, University of North Carolina, USA

[‡]Institut für Materialphysik, Universität Wien, A-1090 Wien, Austria

Abstract. Optical absorption, resonance Raman scattering, and IR reflectivity were used in combination with tight binding and LDA calculations to investigate the distribution and the quality of single wall carbon nanotubes. Experimental results are found to be consistent with a quasi-continuous distribution of tube species in a certain diameter range.

INTRODUCTION

Single-wall carbon nanotubes (SWCNTs) attract great interest nowadays from both experimental and theoretical point of view. Individual SWCNTs exhibit different electronic structure depending on the way they were rolled up from a graphene sheet. The tubes can be characterized by two integers (n, m) which are the components of the wrapping- or Hamada-vector on the hexagonal lattice of the sheet [1,2]. Tubes with $n = m$ are called armchair, tubes with either $n = 0$ or $m = 0$ are called zigzag, all other tubes are chiral. Armchair tubes are always metallic. Tubes with $n - m = 3r$, r arbitrary integer, exhibit a small gap due to the curvature of the graphene sheet. All other tubes are semiconducting.

There is a continuing discussion concerning the question how many different types of tubes are in a SWNT composite. The name 'composite' indicates that all samples prepared so far are assumed to be mixtures of tubes with different helicities.

In early work on SWCNTs grown from laser ablation it was claimed that samples consist mainly of (10,10) tubes, forming bundles or ropes with a triangular structure [3]. From more recent research there is growing evidence that such nanotube composites are polydisperse with respect to (n, m) . The existence of individual tubes with varying helicity was demonstrated by STM [4] as well as from HRTEM

[5] investigations. One of the most efficient methods for investigating the distribution of the diameter – and in some extent even that of (n, m) – in the bulk material is Raman spectroscopy [6–8].

We carried out Raman, UV-visible and IR investigations on SWCNTs obtained by dual pulse laser evaporation. The experimental results were backed up by *ab initio* calculations of the frequencies for the radial breathing mode and by evaluation of the Raman cross section. Our main result is that all observations are consistent with a quasi-continuous distribution of different SWCNTs in the samples.

EXPERIMENTAL AND CALCULATIONS

Four different types of samples were used, as grown, thin films prepared by microfiltration from tubes suspended in a solution of alcohol and SDS, thin films prepared from tubes treated with nitric acid (bucky paper), and same type of films but after vacuum annealing for 3 hours at 600 °C. The thickness of the bucky paper was only of the order of a micron and appeared slightly transparent in the visible.

For the optical, Raman and IR analysis standard equipment was used.

Calculation of the joint density of states was performed within the tight binding approximation for a graphene sheet. Results for the tubes were then derived by the zone folding technique. For the chiral tubes approximations in the form of Taylor expansions in k -space were applied to reduce computer time. For the evaluation of the Raman intensities resonance excitation was assumed with energy independent transition matrix elements as described previously [8].

RESULTS

UV-visible: Figure 1 shows results from optical absorption. The upper curve is as measured for a thin film grown from the alcohol/SDS suspension. The absorption exhibits several well expressed structures in the low energy regime but becomes rather smooth in the visible and beyond. The lower curve is a calculated overall density of states.

The density of states of a SWCNT is dominated by the 1D van Hove singularities. This means each tube has several characteristic sharp peaks in the UV-vis spectrum. One would expect that these peaks smear out completely in a mixture of many different tubes leading to a spectrum similar to graphite or amorphous carbon. The expected smearing is indeed observed in the energy range above 2 eV. The two well expressed peaks in the low energy part of the spectrum originate from semiconducting tubes because the first transition energies for such tubes are usually between 0.5–1 eV and from the metallic tubes where the first transition energy is between 1–1.5 eV.

In order to check on the origin of these structures we calculated the DOS for all nanotubes with diameters from 1.1 to 1.53 nm. There are 3 armchairs (from (9,9) to (11,11)), 6 zigzags (from (14,0) to (19,0)), and 51 chirals (from (11,5) to (15,7))

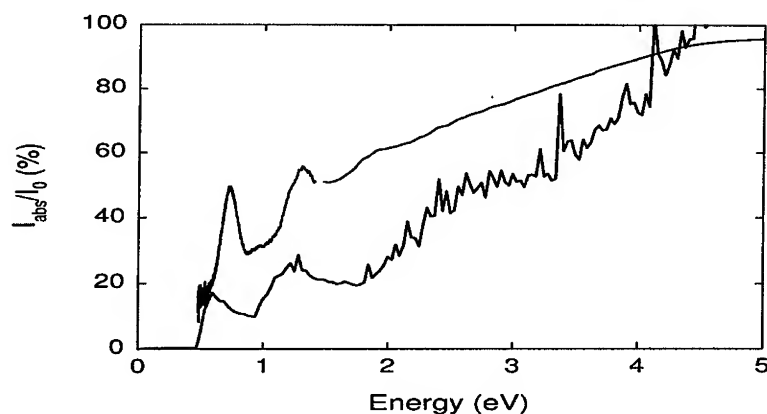


FIGURE 1. Optical absorption of SWCNTs prepared as a thin film (upper curve) and calculated joint density of states averaged over all tubes with diameters between 1.1 nm and 1.53 nm. The tube concentration was weighted with a 0.3 nm wide Gaussian distribution centered at 1.36 nm.

in this diameter range. For the nearest neighbor overlap integral γ a value of 2.7 eV was used. The lower curve of Fig. 1 shows the total joint density of states, calculated as the sum of the contributions of all 60 tubes weighted by a Gaussian distribution. Good correlation with the measured UV-vis spectrum was obtained, although no transition matrix elements were considered. Obviously even for such a large number of tubes the two low energy peaks in the UV-vis spectrum do not smear out in consistence with the experiment.

Raman: SWCNTs have two regions in the Raman spectrum with strong signals. One is around 1600 cm^{-1} where the graphite like modes are expected, the other one is the radial breathing mode (RBM) region between 140 and 220 cm^{-1} . The vibrational frequencies depend on the indices (n, m) of the tube. For the RBM, where the dependence is especially strong, the frequency ν is to a good approximation determined by $\nu = A/D$ where D is the diameter of the tube and A is a constant which can be evaluated from a LDA calculation. A was found to be slightly different for armchair and zigzag tubes [9] and is thus assumed to depend weakly on the helicity of the tubes. The electronic resonance excitations of the nanotubes in the visible spectral range scale also with the tube diameter. These two facts make Raman spectroscopy an excellent tool for the investigation of the diameter distribution. For a mixture of various SWCNTs a given laser excites only a part of the material in resonance. By changing the laser frequency other parts in the same volume are excited and the Raman band shape which is the envelope of the contributions of the various individual SWCNTs changes.

Raman spectra of various samples were recorded in the range of the RBM. For the excitation 10 different laser lines were used from near IR (1064 nm) to the deep blue (457.9 nm). The spectra showed a characteristic fine structure. This structure was changing dramatically with changing the laser excitation. We first tried to fit all observed spectra with a well selected set of oscillators with fixed positions and line widths but varying amplitude. 14 oscillators were required to fit the 10 spectra. The details of the fitting procedure can be found in [8]. To obtain an assignment for the oscillators we performed first principle LDA calculations for armchair and zigzag tubes in the required diameter range. The details of the calculations are in [9]. The analysis revealed that an unique assignment is not possible even if the evaluated resonance cross sections are considered.

The alternate route to obtain an understanding for the recorded variance of the spectra is to anticipate that all geometrically allowed tubes in the relevant diameter range contribute to the shape of the RBM line. This is in full analogy to the procedure described above for the optical experiments. RBM frequencies for the chiral tubes with arbitrary (n, m) , $n \geq m$ were obtained from the results for the armchair and zigzag tubes by interpolation according to $\nu = (239 - 5(1 - m/n))/D$, where ν is in cm^{-1} and D in nm.

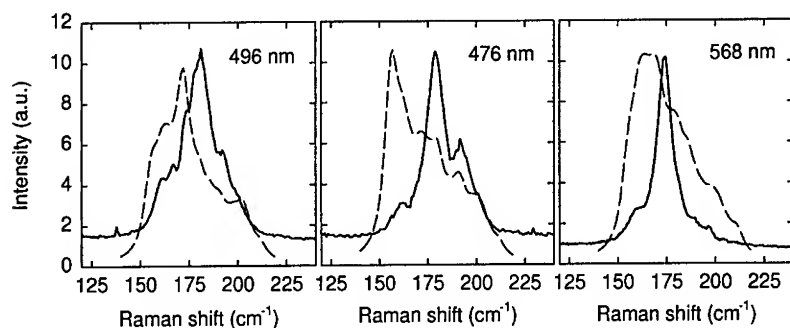


FIGURE 2. Calculated Raman spectra obtained as a sum of the contributions from 60 different SWCNTs for three different laser excitations (dashed lines). The full drawn lines are as measured with a laser of the same wavelength.

To proceed we calculated the Raman cross-section for all 60 SWCNTs mentioned above from the same joint density of states and with the same Gaussian distribution used to explain the optical data. Figure 2 shows the resulting overall RBM Raman band for three different laser excitations.

The shape of the calculated bands changes dramatically with changing laser energy even though it results from an overlap of 60 components. The shape is also in reasonable agreement with experimental observations. The misfit between the absolute value for the calculated and observed bands originates most probably from a neglect of inter-tube interactions in the bundles.

The shape of the Raman band for the RBM is sensitive to chemical and annealing treatment.

The nitric acid treatment used to prepare the bucky paper [10] leads to an upshift of the line. The samples can recover from the upshift by heat treatment in high vacuum but the fine structure in the spectra is lost.

The upshift and the recovery of the Raman band after the acid treatment can be interpreted as a consequence of the reversible oxidative intercalation of the acid molecules between the tubes within the bundles [10,11].

Infrared: Figure 3 shows the reflectivity of bucky paper before and after annealing for a frequency range between 80 and 4000 cm^{-1} .

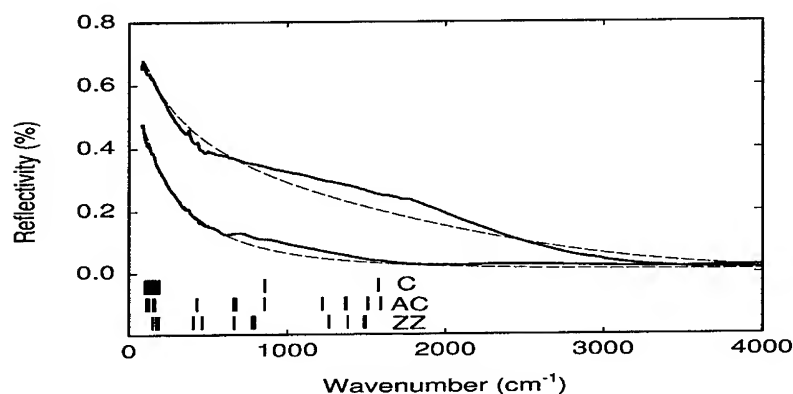


FIGURE 3. Reflectivity of as prepared bucky paper (upper line) and after annealing at 600 °C (lower line). The dashed line is a Drude fit. The spectral regions marked by black bars represent the regions where the IR active phonons are expected for armchair, zigzag, and chiral tubes from a force field calculation.

The overall increase of the reflectivity with decreasing wavenumber can be explained by the metallic nanotubes in the sample. The Drude fits with $\omega_p = 4200 \text{ cm}^{-1}$, $\tau_p = 9.5 \times 10^{-15} \text{ s}$, $\epsilon_\infty = 1.5$ for the etched sample and with $\omega_p = 3000 \text{ cm}^{-1}$, $\tau_p = 5 \times 10^{-15} \text{ s}$, $\epsilon_\infty = 1.5$ for the annealed sample represent the behavior very well. The parameters for the annealed samples may be lower than their

intrinsic values since the sample surface was roughened by the annealing process. The ripples in the reflectivity curve are interpreted as contributions from the IR active phonons. Considering the fact that the frequencies were evaluated from a very rough semiempirical calculation [12] the agreement between observed ripples and calculated frequencies is acceptable. The structure in the reflectivity at low energies may as well have contributions from electronic transitions of the tubes with narrow gaps. Some small features around 1360 cm^{-1} in the unannealed sample may originate from NO_3^- . The broad maximum spread out over the frequency range from 1000 cm^{-1} to 2000 cm^{-1} for the unannealed and from 2000 cm^{-1} to 3000 cm^{-1} for the annealed sample are most probably interference fringes appearing as a consequence of the low thickness of the film.

SUMMARY

We have demonstrated, that the structure of the Raman band for the radial breathing mode as well as the optical absorption spectrum of SWCNT samples grown from laser deposition can be described as a sum of the contributions from all geometrically allowed SWCNTs in the relevant diameter range. Chemical treatment leads to shifting and smearing of the RBM Raman band indicating the introduction of defects by the treatment. The far-IR and mid-IR spectra of a bucky paper sample exhibit a Drude-type metallic behavior and phonon modes representative for a large number of different tubes.

ACKNOWLEDGMENTS

Work was supported by the grants OTKA T022980 and OTKA T030435 in Hungary and by the FWF project P12924 in Austria.

REFERENCES

1. Jishi R.A. *et al.*, *Chem. Phys. Lett.* **209**, 77 (1993).
2. Hamada N. *et al.*, *Phys. Rev. Lett.* **68**, 1579 (1992).
3. Thess A. *et al.*, *Science* **273**, 483 (1996).
4. Wildöer J.W.G. *et al.*, *Nature* **391**, 59 (1998).
5. van Tendeloo G. *et al.*, *Carbon* **36**, 487 (1998).
6. Rao A.M. *et al.*, *Science* **275**, 187 (1997).
7. Kasuya A. *et al.*, *Phys. Rev. Lett.* **78**, 4434 (1997).
8. Kuzmany H. *et al.*, *Europhys. Lett.* **44**, 518 (1998).
9. Kürti J., Kresse G., and Kuzmany H., *Phys. Rev. B* **58**, R8869 (1998).
10. Rinzler A.G. *et al.*, *Applied Phys. A* **67**, 29 (1998).
11. Bower C. *et al.*, *Chem. Phys. Lett.* **288**, 481 (1998).
12. Eklund P.C., Holden J.M., Jishi R.A., *Carbon* **33**, 959 (1995).

Polymers of Single Wall Nanotubes: Geometry, Diffraction Pattern, and Electronic Spectrum Modelling

Leonid A. Chernozatonskii ^a, Elena G. Gal'pern ^b, Nadezhda R. Serebryanaya ^c, Ivan V. Stankevich ^b

^a Institute of Biochemical Physics, Moscow 117977, ^b Institute of Organoelement Compounds, Moscow 117813, ^c Center of Superhard Materials, Troitsk 142092, Russia

Abstract. Results of modelling of linear polymer chains of carbon single-wall nanotubes. It is possible that such polymers could be synthesized under high pressures and temperatures. Their geometry parameters are computed by MM2 and MNDO/PM3 methods, X-ray diffraction patterns of different NT polymer crystals are simulated and compared with known ones. Model of transformation of SWNT rope into a graphite via NT chain polymerization is also considered.

INTRODUCTION

Carbon single-wall nanotubes (SWNT) are obtained usually as ropes (1). Tubes of virtually identical diameter tubes are organized in triangular close-packed molecular lattice with 0.32 nm intertube carbon-carbon distance. Recently we modelled crystals of close-packed covalent bonded nanotubes (2,3). There we consider structures of linear polymerized SWNT analogous to polymer chains of barrelenes - cage clusters with a central nanotube fragment (4). We suppose that such SWNT polymerization could be achieved more easily by partial hydrogenation of nanotubes rather than by action of high pressure and temperature. That is why we have examined at first hydrocarbon nanotubes which may be precursors for SWNT polymers, and then constructed and investigated linear polymers of (n,0) zigzag and (n, n) armchair nanotubes.

RESULTS AND DISCUSSIONS

Hydrocarbon nanotubes

We consider the case when hydrogen atoms are attached to carbon atoms situated on opposite elements of a tube cylinder. Examples of MNDO/PM3 calculations of such hydrocarbon give following parameters (in nm): D_x , D_y = 0.601, 0.410 - for a (6,0) tube, 0.684, 0.456 - for a (7,0) one, 0.824, 0.489 for a (8,0) nanotube. Hydrocarbon "chains" cause the carbon circular cylinder to transform to oval one with typical

diameters $D_x/D_y \approx 1.5$. Thus such partial hydrogenation of nanotubes leads to distortion of SWNT form and appearance of two rows of sp^3 atoms at opposite sides of a nanotube. During annealing of hydrocarbon SWNT we may expect linear polymerization of carbon nanotube radicals after hydrogen desorption.

Zigzag nanotube chain structures

Three types of SWNT linear polymerization are possible: tube coupling via "2+2" cycles of sp^3 atoms located in the (x, y) symmetry plane that contains nanotube axes (Figure 1a); "4" polycondensation bonding of tubes with coupling quarters of sp^3 atoms located in the plane perpendicular to the (x, y) plane (Figure 1b); "2+4" type bonding which connect two rib hexagon atoms of one tube with two top hexagon atoms of a neighbor tube (4). We have present computation results for first and second polymerization types for example of (6, 0) tubes. First, geometry of a linear tube trimer was optimized by MM2 and MNDO/PM3 methods. The following parameters of the middle trimer fragment unit cell were obtained (in nm): D_x , D_y , h = 0.601, 0.410, 0.429 ($d_{C-C'} = 0.156$ - bond length between neighbor tubes) - for the first type; D_x , D_y , h = 0.736, 0.274, 0.426 - for the second type. These parameters were used to construct of a linear SWNT chain polymer structure with 0.32 nm interchain carbon-carbon distance. Two such structures of $Pnnm$ space group are shown at Figure 1. Their parameters are: a, b, c = 7.57, 12.85, 4.29 (nonequivalent atoms: C1: 0.397, 0.0, 0.178; C2: 0.296, C3: 0.161, C4: 0.0, 0.159, 0.335) - for the first structure; a, b, c = 7.36, 11.30, 4.26 (nonequivalent atoms: C1: 0.5, 0.069, 0.18; C2: 0.321, 0.099, 0.334, C3: 0.162, 0.115, 0.164; C4: 0.0, 0.121, 0.333) - for the second type of structure. The latter may be obtained by reforming the first structure under the action more higher pressures and temperatures than those required for to form the first structure of the first type.

Armchair nanotube chain structures

Among (n, n) SWNT linear polymer structures we focus on (10,10) ones, because these tubes are predominant in ropes synthesized with a high yield (1). Usually they are packed in a triangular molecular lattice (Figure 2a). Energy optimization of geometry of a linear tube trimer gives following parameters of middle fragment unit cell (in nm): D_x , D_y , h = 0.179, 0.869, 0.429, $d_{C-C'} = 0.154$, and - The length of "cross" sp^3 bond between atoms of the same tube is $d_{C-C} = 0.156$. We used these parameters to construct a linear polymer structure of $Pnnm$ space group (Figure 2b). Parameters of this structure are: a, b, c = 19.48, 20.69, 2.48 (nonequivalent atoms: C1: 0.461, 0.382, 0.0; C2: 0.425, 0.061, 0.5; C3: 0.366, 0.100, 0.5; C4: 0.337, 0.118, 0.0; C5: 0.275, 0.151, 0.0; C6: 0.242, 0.163, 0.05; C7: 0.175, 0.187, 0.5; C8: 0.141, 0.196, 0.0; C9: 0.071, 0.208, 0.0; C10: 0.059, 0.210, 0.5). It is interesting to remark that polymerization process during pressure action may be stopped at the nanotube dimer formation stage. Subsequent heating can transform these dimer (for example in a (10,10) SWNT) to a dumbbell-like (20, 20) cylinder after breaking of "cross" bonds in the dimer. Its straightening gives usual (20, 20) nanotube. Similar mechanism of

SWNT transformation can explain diameter doubling of SWNT experimentally observed by R. Smalley's group (5).

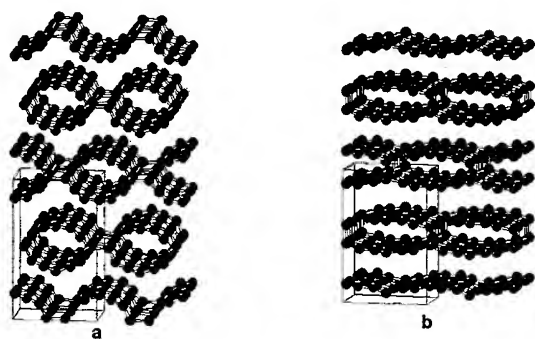


FIGURE 1. Structures of polymerized (6,0) carbon nanotube chains: "2+2" cycloaddition type (a), and "4" polycondensation type (b). Unit cells are marked by thin lines.

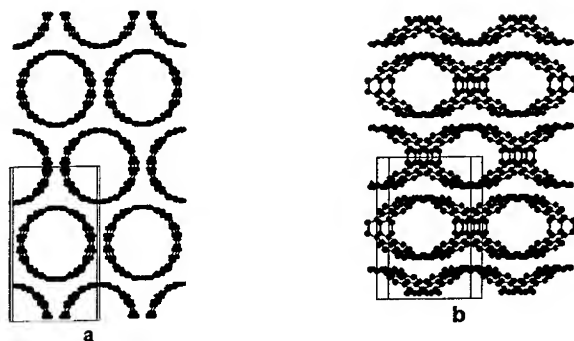


FIGURE 2. Structures of (10,10) nanotubes: usual molecular crystal (a), polymer chain crystal (b).

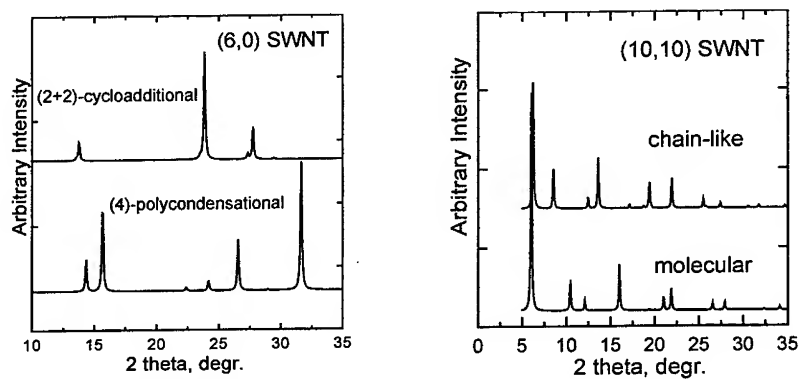


FIGURE 3. Diffraction pattern simulations of considered polymer structures

Diffraction Patterns of SWNT Structures

X-ray diffraction pattern measurements may be used to find boundaries between SWNT phases on (P, T) diagram. Carbon diffraction patterns for above structures simulated by CRYSTALLOGRAPHICA program are shown in Figure 3. In spite of the same symmetry of the crystals their diffractograms for two (6, 0) nanotube structures are substantially different. Computed diffraction patterns of usual molecular (10,10) SWNT structure and its linear polymer are different too. Thus X-ray diffraction patterns may be used of SWNT polymer formation during heating material to predominately containing (10, 10) nanotubes under pressure.

Electronic spectra of SWNT polymer chains

Energy spectra $E(k)$ of SWNT linear chains have been calculated by the crystalline orbital method in valence approach. In the case of (6, 0) and (10, 10) tube chains we have semimetal-like spectrum part in $X' - M$ and $M - \Gamma$ directions of Brillouin zone and semiconductor-like spectrum part in $\Gamma - X'$ direction. Thus, electronic properties of such SWNT chains look like properties of semimetal-semiconductor superlattice. On the other hand, (7, 0) and (8, 0) carbon nanotube chains have semiconductor spectra with energy gaps about 1 eV.

Transformation SWNT polymer chains in graphite

Structures at Figures 1b and 2b may be looked at from another point of view. Such a chain may be considered as a pair of graphene sheets with "cross" sp^3 bonding of atoms located in periodically repeated atomic rows. This structure is in essence a quasi two-dimensional superlattice with periods $a \equiv D_x$ and $b \equiv h$. However neighbor pairs in the crystal structures (see Figures 1b and 2b) are shifted on 1.5 carbon-carbon distance. One may suppose that such structures will be transformed into graphite by breaking of "cross" bonds in each chain under non-hydrostatic pressure and high temperature conditions. This graphite structure may be classified as AADD one of $P6_3mc$ space group. There are new peaks in its diffraction pattern that are absent in diffraction pattern of usual ABAB structure.

ACKNOWLEDGMENTS

This work was supported by Russian Fund for Fundamental Research (grant 99-02).

REFERENCES

1. Rinzler, A.G. et al., *Appl. Phys. A* **67**, 29-37 (1998).
2. Chernozatonskii, L.A., *Mol. Mat.* **7**, 41-48 (1996).
3. Chernozatonskii, L.A., Gal'pern, E.G., Stankevich, I.V., *JETP Lett.* **67**, 712-719 (1998).
4. Chernozatonskii, L.A., *Chem. Phys. Lett.* **297**, 257-260 (1998).
5. Nikolaev P., et al., *Chem. Phys. Lett.* **266**, 322-426 (1997).

The characterization of SWNT containing soot by optical spectroscopy

O. Jost*, R. Friedlein#, A. A. Gorbunov*, T. Pichler#,
M. Reibold#, H.-D. Bauer#, M. Knupfer#,
M. S. Golden#, L. Dunsch#, J. Fink#, W. Pompe*

* *Institut für Werkstoffwissenschaften der TU Dresden, D-01062 Dresden, Germany*

Institut für Festkörper- und Werkstofforschung, D-01171 Dresden, Germany

Abstract. We show optical spectroscopy to be fast and useful for the analysis of the relative diameter distribution and nanotube yield in SWNT soot. The optical spectra revealed a fine-structure consisting of several overlapping absorption bands. While the energy positions of these sub-peaks remained constant upon variation of the synthesis conditions, their relative intensities varied considerably. This allowed the determination of SWNT diameters grouped around preferred values and related, the determination of variations of the fractional abundance.

INTRODUCTION

Critical to a better understanding of physical phenomena related to single-wall carbon nanotubes (SWNT) are methods, which provide information about their mean characteristics such as nanotube yield and SWNT diameter. High resolution electron energy loss spectroscopy (EELS) [1] and optical absorption spectroscopy [2] have shown the existence of several, equally spaced peaks in the energy range between 0.6-3 eV, related to interband transitions between van-Hove-singularities of SWNT [1]. Recent STM/STS observations [3,4] have confirmed the predicted [5,6] dependence of gap transition and nanotube diameter $E \propto 1/d$. Both methods, EELS and optical spectroscopy have the potential to provide information about the above-mentioned mean characteristics of the nanotubes in the soot. In contrast to EELS, optical spectroscopy is easy to use and fast. Here, we present results of the evaluation of optical spectroscopy for the simultaneous determination of relative nanotube yield and relative diameter distribution of SWNT.

EXPERIMENTAL DETAILS

The SWNT were synthesized by the laser ablation procedure [7]. The deposition system consisted of a quartz tube ($d_i = 17$ mm) inside a tube furnace. A Q-switched Nd:YAP laser ($\lambda = 1080$ nm, pulse duration 20 ns, pulse repetition frequency 15 Hz,

pulse energy 300 mJ, run duration 2 min, circular ablation area 16 mm²) was used to ablate the targets. These consisted of intimately mixed and pressed >99.97% purity starting materials (charcoal, metal catalysts Co and Ni with a mixing ratio of unity), the total catalyst content was varied between 0 and 4 at. %. Freshly prepared targets were initially cured (1100 °C, <10³ Pa Ar) for 4 h. The tube wall temperatures were varied between 800-1260 °C. The ablation products were transported by the Ar gas stream ($p = 0.66 \times 10^5$ Pa, $v = 1.6$ l/h) and deposited on a water-cooled copper collector. The preparation for and characterization of the soot with optical spectroscopy was derived from the procedure, proposed by Kataura et al. [2]. The optical absorption spectra were measured with a commercial spectrophotometer (wavelength range 200-3200 nm, resolution 5 nm). The whole time needed for the preparation and characterization of one sample made up only 20 minutes. The highest nanotube yield in our samples has been estimated by TEM to be up to 40 %.

RESULTS AND DISCUSSION

All SWNT-containing samples showed optical absorption spectra with the shape and the number of peaks in general analogous to that reported by Kataura et al. [2]. After a background correction, three broad peaks are visible as shown in Fig. 1.

The pronounced peak at the lowest energy has been chosen for the semi-quantitative determination of the nanotube yield. After an appropriate background subtraction and an additional correction to account for different film-thicknesses, the relative yield is represented by the area below the peak (see Fig. 1). Even for samples with an estimated SWNT abundance of approx.

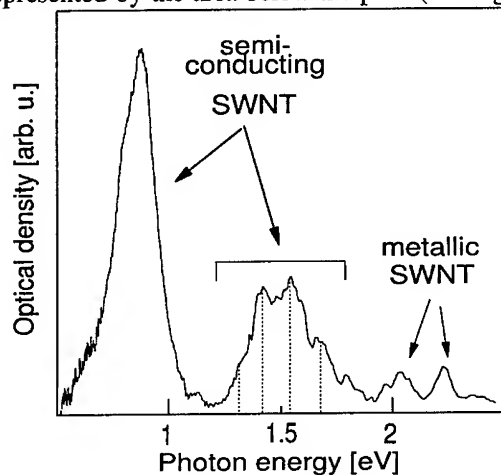


FIGURE 1. Optical absorption spectrum of SWNT soot after background correction. The peaks give several levels of information. The peak area of the peak at the lowest energy represents the relative SWNT abundance; after line shape analysis of the second peak, the sub-peak positions (dotted lines) and the fractional yield (sub-peak area) can be determined.

1% (from TEM observations), the nanotube yield could still be determined. Fig. 2a shows optical spectra for samples with varied total catalyst content in the target and Fig. 2b the corresponding relative nanotube abundance. The results indicate that the maximum of the nanotube abundance takes place for a total catalyst content between 1.2-1.8 %. This is in good agreement with reported values [8].

As can be seen in the Figs. 1, 2a and 3a, all peaks clearly show a fine-structure. This fine-structure was related to the appearance of several resolvable sub-peaks as could be determined by peak shape analysis of the second peak (see dotted lines in Fig. 1). These sub-

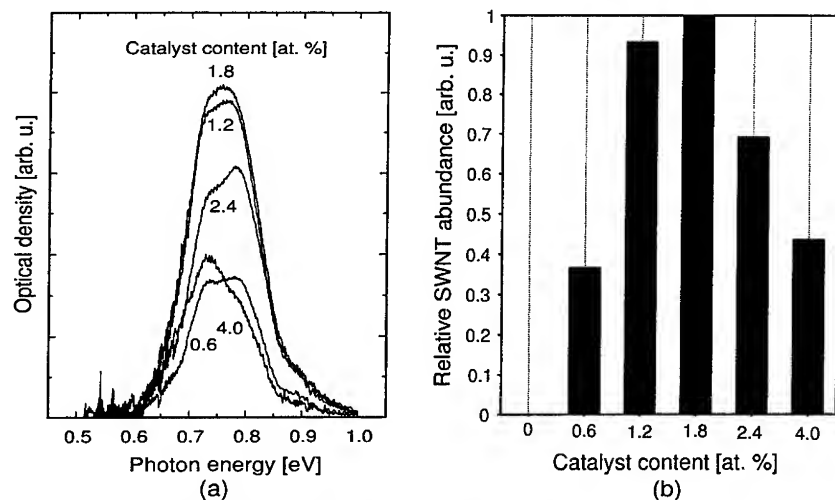


FIGURE 2. Variations of the total catalyst content ($T=1150\text{ }^{\circ}\text{C}$); optical absorption spectra after background correction (a), related normalized total SWNT abundance (b).

peaks remained at the same energy position (within 2-5 meV) despite of changes of the applied synthesis conditions.

Whereas the positions of the sub-peaks remained constant with variations of the synthesis parameters, the shift of the mean energy position of the peaks took place only through relative variations of the intensities of the sub-peaks. Further analysis revealed that these sub-peaks are related to the existence of groups of nanotubes, indicating the existence of preferred nanotube diameters. The nanotube vector map allows the grouping of nanotubes around several diameters even without any preferred chirality with a period of 0.07 nm. This should result in distinguishable sub-peaks in the optical absorption spectra as observed. The effect would occur more pronounced, if the existence of nanotubes of preferred chirality in the vicinity to the armchair axis is assumed, as follows from Raman investigations [9].

The sub-peak area of the sub-peaks below the second peak can be used as a measure for the relative fractional yield. This has been applied to the peaks in Fig. 3a, the resulting fractional yield of the sub-peaks is shown in Fig. 3b. For the calibration of energy positions against the corresponding nanotube diameters shown in Fig. 3b, a sample with a well known and narrow SWNT diameter distribution with a mean diameter of 1.2 ± 0.05 nm has been used [10].

The highest nanotube yield (approx. 40 % from TEM data) was found between 1150-1200 $^{\circ}\text{C}$. The results shown in Fig. 3a and 3b are fully analogous to the TEM data presented by Ref. [9].

To conclude, the obtained results demonstrate the effectiveness and efficiency of optical absorption spectroscopy. The method can be used as a fast and easy to use alternative especially to TEM observations with respect to yield and diameter distribution determinations.

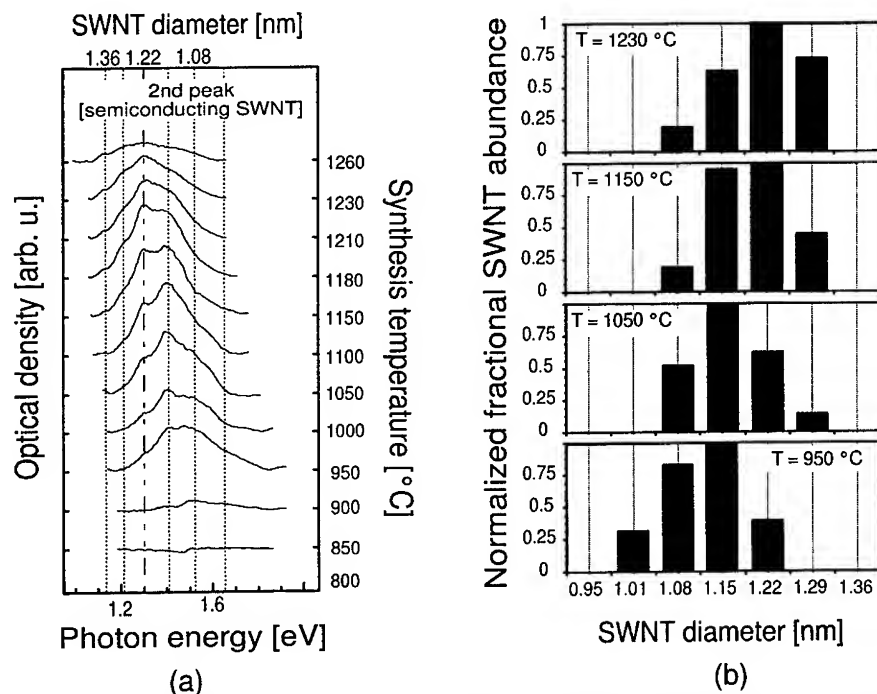


FIGURE 3. Variations of the synthesis temperature (total catalyst content 1.2 at. %); optical absorption spectra after background correction (a), related normalized fractional SWNT abundance (b).

ACKNOWLEDGMENTS

This work was supported in part by the SMWK and by the DFG.

REFERENCES

- [1] T. Pichler et al., Phys. Rev. Lett. **80**, 4729-4732 (1998)
- [2] H. Kataura et al., Synth. Metals (in press)
- [3] T.W. Odom et al., Nature **391**, 62-64 (1998)
- [4] J.W.G. Wildöer et al., Nature **391**, 59-62 (1998)
- [5] M.S. Dresselhaus, G. Dresselhaus, P.C. Eklund, *Science of Fullerenes and Carbon Nanotubes* (Academic Press, San Diego, 1996)
- [6] C.T. White, J.W. Mintmire, Nature **394**, 29-30 (1998)
- [7] T. Guo et al., Chem. Phys. Lett. **243**, 49-54 (1995)
- [8] A. Thess et al., Science **273**, 483-487 (1996)
- [9] S. Bandow et al., Phys. Rev. Lett. **80** (17), 3779-3782 (1998)
- [10] A.G. Rinzler et al., Appl. Phys. **A67**, 29-37 (1998)

Evolution of carbon singlewalled nanotubes diameter as a function of the synthesis parameters : a Raman study.

M. Lamy de la Chapelle^{1,2}, J. M. Benoit¹, S. Lefrant¹,
C. Journet³, P. Bernier³

¹*Laboratoire de Physique Cristalline, Institut des Matériaux de Nantes,
BP 32229, 44322 Nantes, France*

²*ONERA, BP 72, 92322 Châtillon, France*

³*Groupe de Dynamique des Phases Condensées, Université Montpellier 2,
34095 Montpellier cedex 5, France*

Raman spectroscopy is used to characterize the diameter distribution of carbon singlewalled nanotubes (SWNT's) produced by electric arc discharge [1] in order to clarify their growth mechanism. We discuss the diameter distribution evolution as a function of different synthesis parameters : distance to the cathode, inert gas pressure, helium versus argon as the pressure medium, etc. For instance, we show that while the gas pressure does not influence significantly the diameter distribution, using argon instead of helium favours the formation of low diameter nanotubes.

Introduction

These last few years, new methods of synthesis of carbon nanotubes have been presented leading to the formation of large quantities of singlewalled nanotubes (SWNT's). At present time, the techniques reported are based on catalytic sublimation of graphite by several ways : laser ablation [2,3], electric arc discharge [1] and solar energy [4] which allow the production of SWNT's in high yield (> 70%). Whatever the techniques used, the growth mechanisms of such carbon species are far to be completely elucidated. In this way, we propose in this paper a study of the influence of macroscopic parameters such as the pressure and the nature of the inert atmosphere, as well as the localisation where the sample is extracted in the chamber. Indeed, the collection of several samples relevant of the change of these parameters and their analysis by Raman spectroscopy have allowed us to compared the nanotubes structure and more specifically their diameter distribution as a function of each parameter.

Preparation of samples

SWNT's were produced by creating an electric arc discharge between two graphite rods. The anode was drilled and filled with a mixture of nickel and yttrium used as catalysts. The synthesis was performed in a water-cooled chamber first evacuated and then filled with a static pressure of 660 mbar of helium. A current of 100 A was applied and a voltage of about 35 V was maintained constant by continuously translating the anode towards the cathode. Details on the synthesis can be found in Ref. 1. After the synthesis, the extracted product characterized is the

« collaret » found around the deposit on the cathode, where the concentration of tubes is given to be near 70%.

These experimental conditions are standard ones. The systematic study of the collaret reported here has been carried out using there specific conditions. When the atmosphere was changed from helium to argon, we imposed different pressures inside the synthesis chamber, by steps of 100 mbar from 100 mbar to 1200 mbar.

Raman experiments

In all cases, spectra have been recorded at room temperature and in ambient air. With a spectrophotometer Jobin Yvon T64000, the use of a microprobe has allowed us to focus the laser spot in a micrometer scale leading to a great sensitivity to its localisation on the sample. Then, spatially resolved features can be obtained providing clear indications on the distribution of tubes at several spots on the samples as it will be shown later. Otherwise, we used more of the time the 514.5 nm excitation wavelength issued from an argon laser.

The main information derived from the analysis of the Raman spectrum of SWNT's is their diameter [1,5-7]. Indeed, it has been shown that the low frequency A_{1g} mode ($100-300 \text{ cm}^{-1}$) can be resolved into several bands and that for each band, we can associate one diameter. Then, focusing in this range of frequency, we can know both from the position and the relative intensities of each band the diameters of the SWNT's present in the studied spot, as well as we can derive an estimation of the concentration of tubes with a specific diameter.

Localisation parameter

In a first step, we have performed experiments on one splitted collaret. We have studied several spots on each part as shown in the example of figure 1. A gradual evolution of the diameter distribution can be seen on this part with the low frequency group of bands. Then it is clearly observed that along the sample from point 1 to point 6, the diameter distribution changes continuously from low diameters to higher ones.

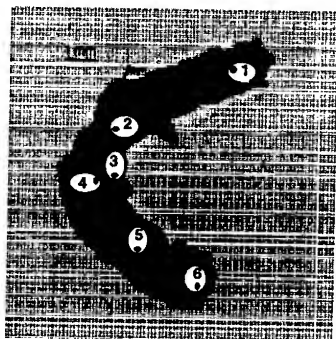


Fig 1 : Part of the collaret

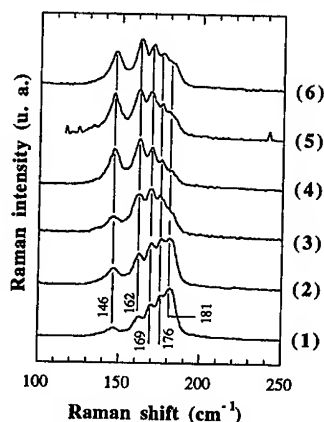


Fig 2 : Evolution of the Raman spectrum

from the point 1 to 6

In a second step, we have studied a whole collaret. In this way, we have recorded the spectra of several points which are located at the same distance from the center of the cathod. As it is shown on figure 3, all spectra obtained from the points located on the same line present the same profile of bands in the low frequency range (see below the image of the collaret). This signifies that all points located at the same distance from the center contain the same diameter distribution and that this distribution is shifted from the higher diameter (13-14 Å) to the lower one (11-12 Å) when this distance increases.

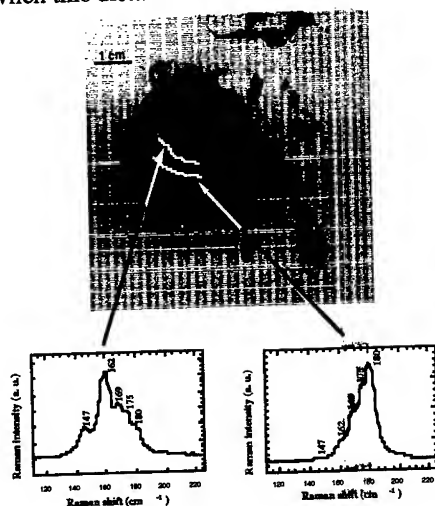


Fig 3 : Evolution of the Raman spectrum with the distance from the center of the cathod

So, it seems from these two experiments that the diameter of tubes evolves continuously inside the collaret increasing with the distance from the center of the cathod.

This is an indication that the conditions in the synthesis chamber are not homogeneous and that the tube production changes from one point to the other. Then specific diameters are presumably favoured compared to others. As a consequence, we can conclude that the location of the extracted sample in the synthesis chamber is of real importance on the production of tubes with a specific diameter.

We can try to relate this parameter to the temperature. Indeed, we can easily suppose that the temperature decreases from the center of the cathod where the electric arc is formed to the border regions of the chamber. In this case, the decrease of temperature deals with the synthesis of tubes of lower diameters.

Inert atmosphere parameter

This second parameter has been studied by changing the pressure and the gas nature. We have performed Raman experiments on several samples produced both with different pressures and with two different gases : helium and argon. Related Raman spectra are shown on the figures 4 and 5.

First, in the case of helium atmosphere, we can notice that whatever the pressure used, we always observe the same peaks with the same positions. But the number of spots on the samples where we obtained Raman spectra of SWNT's decrease for other pressures than 660 mbar. As a consequence, the quantities of SWNT's produced are less important for pressures different how 660 mbar. Whatever the pressure used, the diameters of tubes do not change. We can then conclude that the pressure has only an influence on the rate of the production with the existence of an optimum pressure whereas it has no influence on the structure of the tubes.

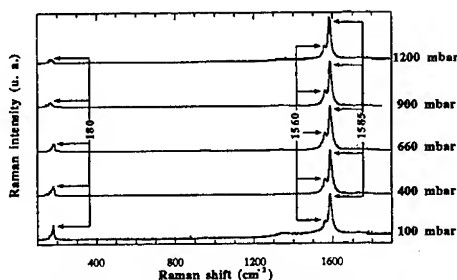


Fig 4 : Raman spectra of SWNT's as a function of the helium pressure

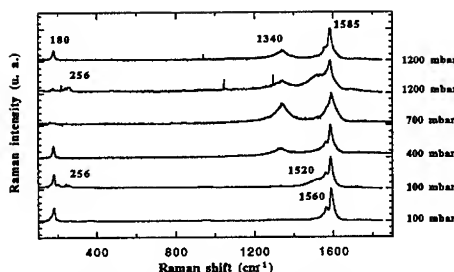


Fig 5 : Raman spectra of SWNT's as a function of the argon pressure

Second, in the case of the argon atmosphere, we can make the same observation with no change on the tube diameter and the existence of an optimum pressure. But, in comparing the two gases, two differences can be put in evidence. Indeed, the optimum pressure is near 100 mbar for argon versus 660 mbar for helium. Then the case of argon, Raman spectra exhibit peaks between 200 and 260 cm^{-1} which could be associated to tubes with diameters comprised between 8 and 10 Å. The first aspect can be associated with the cross section of the atoms of these gases. As the argon one is higher than the helium one, this implies that a fewer number of atoms of argon is needed compared to helium to induce the same number of collisions between the atoms of the inert atmosphere and the particules confined in the chamber. The second aspect can be related to the temperature influence presented above. Indeed, argon has a lower thermal conductivity than helium. So when argon is used, the temperature decreases more quickly as the distance from the cathod increases. In this way, as the lower temperatures favour lower diameters, argon induces lower temperature near the cathod and favours lower diameters. This could explain why we observe SWNT's with diameters between 8 and 10 Å.

Conclusion

In this paper, we have given evidence of the influence of some production parameters on the structure of the SWNT's. First, it seems that the lower temperatures favour lower diameters as it is shown by the location study. Second, we can say that the pressure of the inert atmosphere have only an influence on the rate of the synthesis whereas the nature of the gas favours some specific diameter (helium : 11-15 Å, argon : 8-15 Å).

Acknowledgements:

Research partly supported by EEC TMR program NAMITECH (ERBFMRX-CT96-0067)

References

- [1] C. Journet et al, *Nature*, **388** (1997) 756
- [2] A. Thess et al, *Science*, **273** (1996) 483
- [3] Maser et al, *Chem. Phys. Lett.*, **292** (1998) 587
- [4] D. Laplaze et al, *Carbon*, **36/5** (1998) 685
- [5] A. M. Rao et al, *Science*, **275**, (1997) 187
- [6] M. Lamy de la Chapelle et al, *Carbon*, **36/5** (1998)
- [7] S. Lefrant et al, *Mol. Cryst. Liq. Cryst.*, **322** (1998) 71

V. PROPERTIES OF CARBON NANOTUBES

Neutron scattering studies of carbon nanotubes

E. Anglaret*, S. Rols*[#], J.L. Sauvajol*

* *Groupe de Dynamique des Phases Condensées, UMR 5581, Université Montpellier II, France*

[#] *Institut Laue-Langevin, Grenoble, France*

Abstract. We report on neutron scattering studies of single wall carbon nanotubes (SWNT). Small angle scattering was used to investigate the structure of SWNT suspensions. Diffraction data were compared to calculations on finite-size bundles of SWNT in order to estimate the distribution of tube diameters. Lastly, we present an inelastic neutron scattering study of the density of phonon states in SWNT. In the frequency range of intramolecular modes, the measured spectrum is found to be in good agreement with that calculated on an isolated (10,10) nanotube.

INTRODUCTION

Single wall carbon nanotubes (SWNT) have recently been the matter of intensive studies (1). Many of their physical (mechanical, electronic) and chemical (gas adsorption) properties are expected to depend both on their molecular structure and intermolecular interactions. Mass production techniques are nowadays available (2-5), and this is an actual challenge to probe the structure and dynamics of SWNT both at the molecular scale (diameter and polydispersity, helicoidal pitch) and at the bundle scale (cell parameter, bundle size) in order to relate the structural informations to the intrinsic properties.

Neutron scattering techniques are efficient tools for the study of the structure and vibrational dynamics of SWNT (6). Elastic scattering allows to investigate the structure of SWNT over a large range of length scales. The mean-size of the bundles can be estimated in small angle neutron scattering (SANS) investigations and the study of the crystalline packing of the SWNT can be achieved in neutron diffraction (ND). In the frequency space, the energy of low-frequency excitations (both molecular and intermolecular) are very sensitive to the tubes diameter and helicoidal pitch and to interactions between tubes (6). Raman, and especially micro-Raman, scattering has been used as an efficient tool (7-12) to characterize SWNT because of the small quantities required and the intense resonant signals measured. The phonon density of states can be studied by inelastic neutron scattering (INS). This especially allows to probe optically silent modes, as well as intermolecular excitations at low energy transfers. We discuss hereafter some neutron scattering results on SWNT. A review of our neutron results will be reported elsewhere (6).

SAMPLE DESCRIPTION

SWNT were prepared at Montpellier by the electric arc discharge (EA) technique (3) and in Zaragoza by the laser ablation (LA) technique (4). The EA samples were prepared under a 600 *mbar* He atmosphere using the catalyst mixture Ni-Y (4.2/1 *at.%*) (3). The LA samples were prepared using a cw CO₂ laser operating at 10.6 μm in a 530 *mbar* Ar atmosphere using the catalyst mixtures : Ni-Y (2/0.5 *at.%*).

EXPERIMENTS

The SANS experiments were performed on the spectrometer PACE at Laboratoire Léon Brillouin (LLB), Saclay, France. EA samples were poured and stirred in some water/surfactant (triton X100) suspensions to form suspensions. A water/heavy water mixture was used to kill the contrast between the water and surfactant so that nanotubes can be considered as the scattering particles in an homogeneous solvent.

The ND spectra were measured on the G6-1 spectrometer at LLB and D20 at Institut Laue-Langevin (ILL), Grenoble, France, over a range of wave-vectors transfers 0-4 \AA^{-1} . Diffraction spectra were calculated for finite-size bundles and various distribution of tube diameters and successfully used to fit the data (13,14).

The INS measurements were performed on the spectrometers Mibemol at LLB and IN6 at ILL over a range of energy transfers 0-200 meV. In order to avoid the large contribution from the residual catalyst particles (especially nickel) to the DOS, this is essential to work on nickel-free samples prepared with small amounts of catalysts. Scattering from adsorbed water was also eliminated by carefully heating the samples over 200°C under a dynamic vacuum and storing them in air-free containers. A detailed discussion of the phonon DOS of SWNT, especially in the low-frequency range, will be published elsewhere (15).

RESULTS AND DISCUSSION

Small angle neutron scattering

A typical SANS spectrum for a nanotube suspension (about 1 wt% SWNT) is displayed in figure 1. The main feature is the observation of a $I \sim q^{-4}$ power-law dependence of the signal at large q . This is the so-called Porod signature of isotropic scatterers (particles) with a neat interface between the particles and the solvent. The low- q limit of the Porod law is inversely proportional to the mean-radius of the

scattering particles. We find a particle diameter of about 200 Å and assign the SANS signal to bundles of some hundreds tubes, in good agreement with TEM results (2,3).

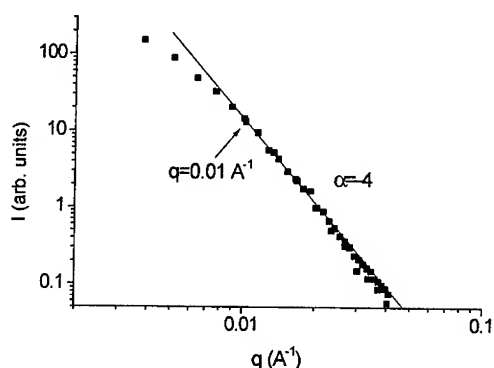


FIGURE 1. Typical SANS spectrum of a water/heavy water/surfactant/SWNT suspension.

Neutron diffraction

Figure 2 presents ND spectra for the EA and LA samples. The main features are the difference in the position of the main peak, corresponding to the (1 0) Bragg reflexion on the hexagonal bidimensional network formed by the tubes (2,13), that shifts from 0.42 Å^{-1} for EA to 0.32 Å^{-1} for LA, as well as a broader profile for the LA spectrum. Calculation of the diffraction spectra for finite-size bundles of SWNT are presented elsewhere (13,14). The general shape of the spectra, and especially the position, width and intensity of the (1 0) peak are found to depend on the distribution of tube diameters and the size of the bundles. Note that no diffraction signature of residual nickel particles is observed for the LA sample (no intense peaks about 3.1 and 3.6 Å^{-1}), because of the smaller amount of catalysts used in the synthesis. The broad signal recorded around 3 Å^{-1} is assigned to some (1 0 0)-like reflections on the curved graphene sheets forming the nanotubes (13). The peaks about 1.87 and 1.84 Å^{-1} correspond to diffraction by graphite and graphite nanoparticles respectively. The amount of these carbon impurities is estimated to be smaller than 15% in the two samples. The spectra are found to be very close to those presented in figure 5 of reference 13. By comparison with calculations (not shown), we estimate for the two samples a mean-diameter of the nanotubes about 13.6 Å but a much larger distribution of tube diameters in case of LA samples ($\pm 5 \text{ Å}$) as compared with EA samples ($\pm 3 \text{ Å}$).

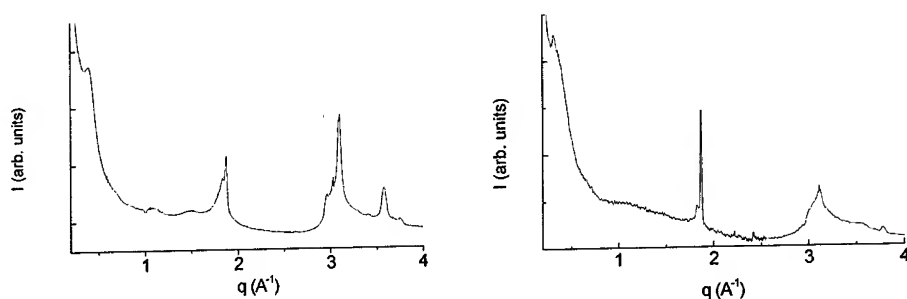


FIGURE 2. Neutron diffraction measurements on EA (left) and LA (right) samples.

Inelastic neutron scattering

The generalized phonon density of states (GDOS) of the LA sample is reported in figure 3. We also report the GDOS of graphite and nickel for comparison, in order to emphasize the high quality of the samples (15). The spectra of graphite and SWNT are very close one from each other above 50 meV, as expected (1). On the other hand, the position of the second maximum in the GDOS of nickel corresponds to a minimum in the GDOS of the SWNT sample.

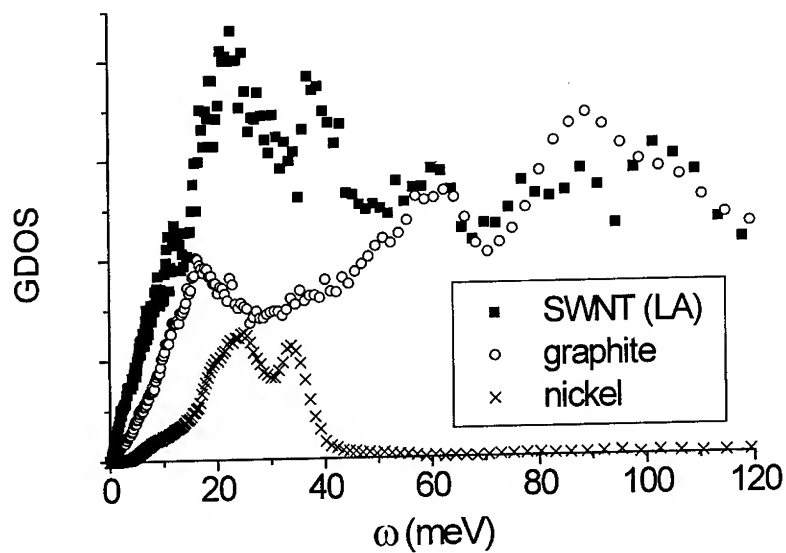


FIGURE 3. Generalized density of phonon states for a LA sample

This confirms that the amount of residual nickel in the sample is negligible (see figure 2) and this allows to assign definitely the peak measured about 22 meV in the SWNT spectrum to the contribution of A_{1g} radial breathing modes to the density of states, in very good agreement with Raman measurements (7-12) and calculations on bundles of SWNT (15). At least two other maxima are observed below 50 meV. We assign that at about 40 meV to the contribution of optically silent modes to the GDOS and that at about 12 meV to E_{1g} Raman-active modes (never observed in Raman). Both are expected in calculations. An extended discussion of the INS spectra, including the description of the low-frequency part of the GDOS, is reported elsewhere (15).

ACKNOWLEDGEMENTS

The neutron experiments were performed at Laboratoire Léon Brillouin, Saclay and Institut Laue-Langevin, Grenoble. We acknowledge our collaborators on the neutron studies, G. Coddens, J.P. Cotton and I. Mirebeau (LLB) and P. Convert and A.J. Dianoux (ILL). We acknowledge P. Bernier, C. Goze, V. Micholet, in Montpellier and A.M. Benito, G.F. de la Fuente, M.T. Martinez, W.K. Maser, E. Munoz in Zaragoza for providing high quality samples and fruitful discussions. One of us (SR) acknowledges the Région Languedoc-Roussillon for financial support.

REFERENCES

1. Saito, R., Dresselhaus, G., Dresselhaus M.S., *Physical properties of carbon nanotubes*, London : Imperial College Press, 1998.
2. Thess, A. *et al*, *Science* **273**, 483 (1996).
3. Journet, C., Maser, W.K., Bernier, P., Loiseau, A., Lamy de la Chapelle, M., Lefrant, S., Deniard, P., Lee, R., and Fischer, J.E., *Nature* **388**, 756 (1997).
4. Maser, W.K., Munoz, E., Benito, A.M., Martinez, M.T., de la Fuente, G.F., Maniette, Y., Anglaret, E., and Sauvajol, J.L., *Chem. Phys. Lett.* **292**, 587 (1998).
5. Guillard, T., Cetout, S., Alvarez, L., Sauvajol, J.L., Anglaret, E., Bernier, P., G. Flamant and D. Laplaze, *Euro. Phys. J.*, in press.
6. Rols, S., Anglaret, E., Sauvajol, J.L., to be published in *Appl. Phys. A*.
7. Eklund, P.C., Holden, J.M., and Jishi, R.A., *Carbon* **33**, 959 (1995).
8. Rao, A.M *et al*, *Science* **275**, 187 (1997).
9. Lamy de la Chapelle, M., Lefrant, S., Journet, C., Maser, W.K., Bernier, P., and Loiseau, A., *Proc. SPIE* **2854**, 296 (1996).
10. Anglaret, E., Bendiab, N., Guillard, T., Journet, C., Flamant, G., Laplaze, D., Bernier, P. and Sauvajol, J.L., *Carbon* **36**, 1815 (1998).
11. Pimenta, M.A., *et al*, *Phys. Rev. B* **58**, R16016 (1998).
12. Alvarez, L., *et al*, this issue.
13. Rols, S., Almairac, R., Henrard, L., Anglaret, E., Sauvajol, J.L., *Euro. Phys. J.*, in press.
14. Anglaret, E., Rols, S., Sauvajol, J.L., *Phys. Rev. Lett.* **81**, 4780 (1998).
15. Rols, S. *et al*, to be published.

Statistical Analysis of the Electronic Structure of Single Wall Carbon Nanotubes in Buckypaper

S. Eisebitt, I. Wirth, G. Kann, and W. Eberhardt

Forschungszentrum Jülich, IFF, D-52425 Jülich, Germany

Abstract. The electronic structure of single wall carbon nanotubes (SWNTs) in intact, undissolved buckypaper has been studied using STM and STS at 23 K. STS allows to distinguish between metallic, narrow gap semiconducting, and wide gap semiconducting SWNTs. In a statistical analysis we find a distribution ratio of $34\pm 6\% : 15\pm 4\% : 51\pm 7\%$, respectively. These ratios indicate that metallic SWNTs are preferentially generated in the buckypaper production process.

ELECTRONIC STRUCTURE OF SWNTs

To a certain degree of approximation, the electronic structure of SWNTs can be deduced from the graphene bandstructure by investigating which electronic states in graphene are allowed in SWNTs, given the boundary conditions in a specific tube. Since the graphene bands are crossing E_F at the K point at the corner of the Brillouin Zone, only those nanotubes whose bandstructure contains this point are metallic. It turns out that a SWNT characterized by the chirality vector (n_1, n_2) is metallic if $(n_1 - n_2)$ is an integer multiple of 3 and semiconducting otherwise. Beyond the graphene approximation, *i.e.* including curvature induced hybridization effects, it turns out that only $(n_1 = n_2)$ and equivalent SWNTs (armchair type) are strictly metallic, whereas small bandgaps form in all other SWNTs which have been classified as metallic in the graphene approximation [1-3]. These latter SWNTs are often referred to as narrow gap SWNTs in contrast to the wide gap SWNTs with $(n_1 - n_2) \neq 3q$.

SWNT samples can be produced by a variety of different techniques, such as arc discharge, laser vaporization or chemical vapor deposition. While the resistivity of the macroscopic sample is often used to for characterization, there is usually no direct information on the content of metallic vs. semiconducting SWNTs. Transport measurements on single SWNTs using electrode structures can only be performed on a few SWNTs and are thus not representative of a macroscopic sample. An indirect determination of the electronic structure via the SWNT topology using theoretical models is only possible for ideal SWNT tubes without *e.g.* defects or interactions in a rope and is thus inherently limited. Due to these difficulties, very different values

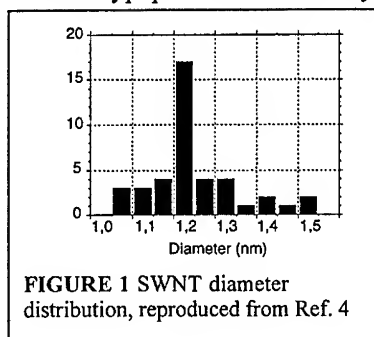
regarding the content of metallic vs. semiconducting SWNTs in a given type of sample have been reported in the past.

In this paper, we report on a statistical analysis of the electronic structure of SWNTs in a buckypaper sample [4], performed by scanning tunnelling spectroscopy on intact, free standing buckypaper at 23 K. The aim of this work is to characterize the amount of metallic vs. semiconducting SWNTs and to characterize the bandgap distribution observed in the buckypaper sample.

EXPERIMENTAL

The sample investigated here is buckypaper prepared by the Smalley group as described in Ref.4 (4'' oven material). The nanotubes were produced by pulsed laser vaporization (PLV) and subsequent purification. The final cleaning step is a vacuum bake at 1200 °C. The overall production process including the purification has been shown to produce a material with a high degree of SWNTs, with a diameter distribution as reproduced in Fig.1 [4]. The final product is a paper-like felt, called buckypaper. The investigations were carried out in a UHV STM chamber with a base pressure $<10^{-10}$ Torr. After exposure to air for the transport, the buckypaper was cleaned by heating to 1200 °C in UHV in our system.

Scanning tunneling spectroscopy (STS) and imaging were performed at a temperature of 23 °K. The buckypaper was investigated as free-standing sheet and was neither disentangled nor dissolved and hence the distribution of SWNTs is unchanged from the freshly purified sample. 114 STS I(V) curves were recorded at random positions on SWNT ropes in the sample, after stable topography imaging had been achieved.



RESULTS AND DISCUSSION

Before a discussion of the spectroscopy results, we show a scanning tunneling microscopy (STM) image from the intact buckypaper in Fig.2. The individual SWNTs are seen to form microbundles of about 30 nm in diameter. In the microbundles, the SWNTs are organized in a parallel fashion and seem to start/end in the same region, *i.e.* the microbundle is not fuzzy at the end. The microbundles aggregate to ropes of about 70-100 nm diameter, which in turn can aggregate to larger superstructures.

The investigation the electronic structure of the SWNTs has been carried out by STS. I(V) curves were recorded at 114 randomly chosen positions on different SWNT ropes. Internal tunnel junctions *e.g.* between different SWNT ropes do not influence our I(V) curves, as I(V) curves recorded with the tip in contact with the buckypaper show perfectly metallic behavior. Apparently the conductivity through the network is always high enough to short out internal tunnel junctions.



FIGURE 2 UHV STM image of a free standing sheet of buckypaper. The fine diagonal lines correspond to single SWNTs, which in turn aggregate to micro-bundles and larger superstructures such as ropes. Image size: 250x250nm.

In order to study the electronic structure of the SWNTs we investigate the shape of the normalized differential conductivity, $(dI/dV)/(I/V)$, which represents in good approximation the shape of density of states (DOS) of the sample. An example is shown in Fig.3. In agreement with the theoretical expectations [1], we observe pronounced peaks in the DOS corresponding to the typical singularities in the DOS for 1D systems. However, even at 23 K these structures appear as fairly broad. As a consequence, a direct and accurate determination of the bandgap size from the $(dI/dV)/(I/V)$ shape around $V=0$ seems impossible.

Nevertheless, the energy positions of the singularities can be measured with reasonable accuracy. As we will demonstrate in the following, these energy positions can be used to distinguish metallic SWNTs from wide gap semiconducting nanotubes.

In metallic SWNTs, a pseudogap region of low DOS is bordered by the first pair of DOS singularities. For simplicity, we will refer to the *pseudogap* in metallic SWNTs as „gap“ as well. In a wide gap semiconducting SWNT, a real DOS gap is bordered by the singularities. For SWNTs of approximately the same diameter, the pseudogap in the metallic SWNT is three times as large as the gap in a wide gap semiconducting SWNT [2]. In both cases, the gap is inversely proportional to the SWNT diameter. The gap can now be measured by energy positions of the singularities in the $(dI/dV)/(I/V)$ signal. In general, it is not possible to distinguish between metallic and wide gap semiconducting SWNTs on this basis, as a metallic SWNT with three times the diameter of a given wide gap semiconducting SWNT will have a gap of the same size as the latter. In our special case of the buckypaper sample, however, a distinction is nevertheless possible. From TEM measurements, the diameter distribution of the SWNTs in the sample is known (Fig.1). It is important to note that the distribution certainly does not span a factor of three in the SWNT radius. Consequently, metallic and wide gap semiconducting SWNTs can be separated. For our diameter range, metallic SWNTs will exhibit gaps of about 1.5 eV to 2 eV, while the gaps for wide gap semiconducting SWNTs are in the region 0.5 eV to 0.7 eV. Narrow gap semiconducting SWNTs have a pseudogap with the same magnitude/diameter dependence as metallic SWNTs and in addition a very small, real DOS gap. They can not be distinguished

from strictly metallic SWNTs by this technique. However, the distinction between metallic and narrow gap SWNTs on one hand and wide gap semiconducting SWNTs on the other hand on the basis of the measured gap is easily possible.

On this basis we determine the metallic & narrow gap to wide gap ratio of SWNTs in the sample to be $49 \pm 7\%$: $51 \pm 7\%$.

While the bandgaps in near gap SWNTs are small and can not be quantified directly with reasonable accuracy with our STS resolution, we observe the presence of weak spectral

features close to zero bias in some STS spectra which show a singularity spacing consistent with metallic or narrow gap SWNTs. We use the presence of this feature as a fingerprint to distinguish metallic from narrow gap SWNTs. On this basis we determine the (metallic : narrow gap : wide gap) ratios at the surface of our buckypaper sample to be $(34 \pm 6\% : 15 \pm 4\% : 51 \pm 7\%)$. The errors indicate the statistical error only. While the distinction between metallic & narrow gap SWNTs vs. wide gap SWNTs is unambiguous, the distinction between metallic and narrow gap SWNTs is qualitative in nature and hence less reliable. The detailed bandgap distributions within the three groups will be published elsewhere.

This result indicates that metallic SWNTs are *preferentially* produced in the PLV/purification process. „Preferential production“ is meant in the following way: within a given diameter interval, we find more metallic tubes than one would expect, if all suitable (n_1, n_2) SWNTs with diameters in this interval would contribute equally to the diameter distribution in Fig.1. In this case one would expect a (metallic : narrow gap : wide gap) distribution of $(4 \pm 1\% : 35 \pm 3\% : 61 \pm 3\%)$. Our experimentally observed values clearly deviate from this distribution. In particular, we find an enrichment of metallic SWNTs in the sample.

Acknowledgement: We thank J.E. Fischer and the authors of Ref. 4 for the buckypaper sample.

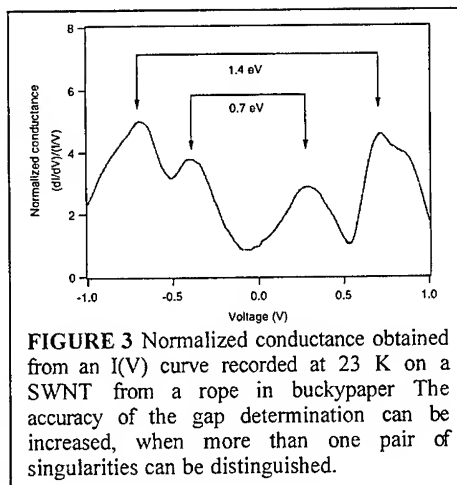


FIGURE 3 Normalized conductance obtained from an $I(V)$ curve recorded at 23 K on a SWNT from a rope in buckypaper. The accuracy of the gap determination can be increased, when more than one pair of singularities can be distinguished.

REFERENCES

1. *Science of Fullerenes and Carbon Nanotubes* by M.S. Dresselhaus, G. Dresselhaus, and P. Eklund, (Academic Press, San Diego, 1996).
2. J.W. Mintmire and C.T. White, *Phys. Rev. Lett.* **81**, 2506 (1998).
3. S. Eisebitt *et al*, *Appl. Phys. A* **67**, 89 (1998).
4. A.G. Rinzler *et al*, *Appl. Phys. A* **67**, 29 (1998).

Characterization of Single Wall Carbon Nanotubes by Scanning Tunneling and Scanning Force Microscopy

W. Clauss*, M. Freitag†, D.J. Bergeron†, and A.T. Johnson†

* *Institute of Applied Physics, University of Tuebingen, Germany,*

† *Department of Physics and Astronomy, and LRSM, University of Pennsylvania
Philadelphia, Pennsylvania*

Abstract. In high-resolution scanning tunneling microscopy images of single-wall carbon nanotubes we often find complex superstructures superimposed onto the simple atomic pattern. They can be interpreted as a result of elastic scattering of the Fermi states at defects or impurities. A new combination of scanning tunneling and scanning force microscopy enables near-atomic point resolution in the resulting images. Using the force interaction as a feedback signal, the tubes can be identified without the need of a conducting substrate. This imaging mode is a crucial step for the characterization of electronic devices based on individual single-wall tubes. First results are presented showing that it is possible to obtain current images from tubes which are only locally connected to electrical contacts defined on insulating substrates.

ELECTRONIC SUPERSTRUCTURES

Single-wall carbon nanotubes (SWNT) can be either metallic or semiconducting, depending on the orientation of the atomic lattice with respect to the tube axis, as defined by the wrapping vector [1]. Recently, the relation between atomic and electronic structure was confirmed by combined STM/STS (scanning tunneling microscopy/spectroscopy) [2] measurements [3–5]. Highly oriented pyrolytic graphite (HOPG) has nearly identical surface properties as carbon nanotubes, and it is well-known from a large number of STM studies that the observed contrast cannot be interpreted straightforward in terms of the atomic lattice structure. The images are strongly influenced by the intrinsic low-dimensional electronic structure and the particular tip-sample interaction conditions. In accordance with these studies, we have observed a variety of contrast patterns on SWNT where the limiting cases are (i) the full honeycomb lattice and (ii) the triangular lattice from normal HOPG images [6]. Moreover, in addition to patterns based on the primitive graphite lattice, we reproducibly obtained other cases with dominating longer wavelength structures. An example of a one-dimensional superstructure is shown

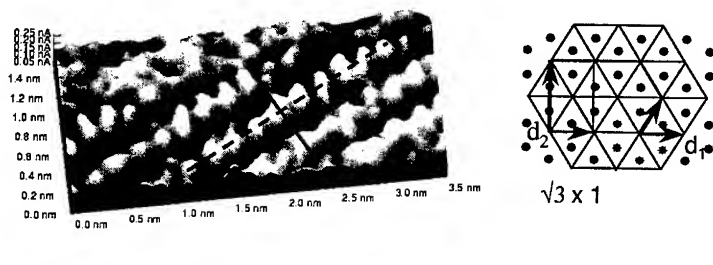


FIGURE 1. a) Flattened high-resolution image of a SWNT oriented along the horizontal image axis. The periodicity along the dashed line is equal to the primitive lattice unit. Along the perpendicular direction (solid line) the period is larger by a factor $\sqrt{3}$. b) Geometrical sketch of the $\sqrt{3} \times 1$ superstructure as defined by the primitive vector d_1 and the vector d_2 connecting every second zig-zag row.

in Fig. 1a. The sketch in Fig. 1b illustrates the geometrical construction of the $\sqrt{3} \times 1$ pattern superimposed onto the primitive lattice. In Fig. 2, we present an example of a two-dimensional $\sqrt{3} \times \sqrt{3}$ pattern. It is clearly visible that the distorted electron wave evolves from the defects visible along the tube [7]. We argue that these patterns have to be distinguished from "normal" structures influenced by the particular tip-sample interaction conditions. We note that in order to get a reliable determination of the chirality of tubes, it is important to understand the

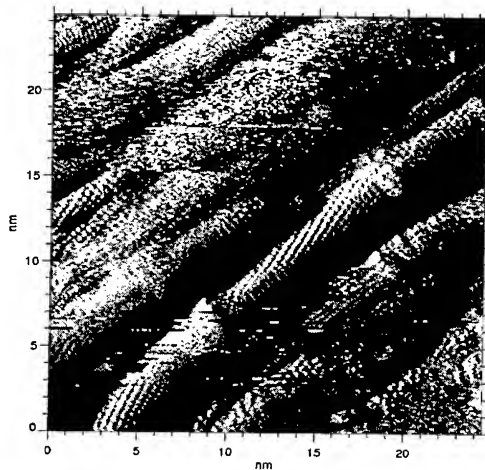


FIGURE 2. Large-scale image (25 x 25 nm) of a tube bundle with various diameters and chiralities. In the upper left corner a part of a tube is visible with a primitive lattice pattern. The tube which runs diagonally through the image exhibits a $\sqrt{3} \times \sqrt{3}$ superstructure. Two localized defects are visible on the tube which are identified as the source of the modulation along the axis.

nature of these patterns. They can be interpreted as interference patterns that are sensitive to coherence between electronic states propagating "forward" and "backward" along a tube. In contrast to a conventional metal, each of the Fermi points at the Brillouin zone corners has both a forward and backward propagating branch of electron eigenstates, so the low energy states can be represented by a small number of plane wave eigenstates. For perfect tubes the charge density of each plane wave has the full periodicity and symmetry of the graphite plane. However, tube defects and ends reflect the incident plane wave states, breaking the symmetry of the charge density distribution probed by the tunneling current. Numerical calculations show that, among others, $\sqrt{3} \times \sqrt{3}$ superstructures are typical features resulting from this type of coherent scattering [8].

COMBINATION OF TUNNELING AND FORCE MICROSCOPY ON NON-CONDUCTING SUBSTRATES

STM, with its ability of spatial resolution down to the atomic scale, can only be used on homogeneously conducting substrates. For the fabrication of electronic devices, tubes have to be attached to partly insulating substrates. In order to regain the ability to characterize the atomic structure, we have combined non-contact scanning force microscopy (SFM) with simultaneous measurements of the tunneling current. The force detection in our SFM is done with a needle-sensor [9] rather than a conventional cantilever. The needle-sensor consists of a piezoelectric resonator

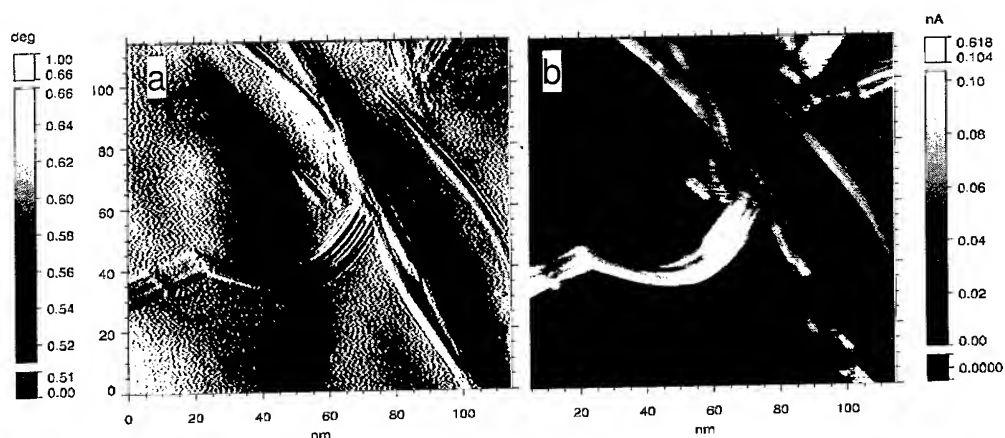


FIGURE 3. a) Force error image as given by the phase deviation between excitation and sensor signal and b) tunneling image obtained simultaneously on SWNT ropes on a Au(111) substrate. The strong contrast between tubes and gold substrate is probably due to the differences of the elastic properties of the materials (see text).

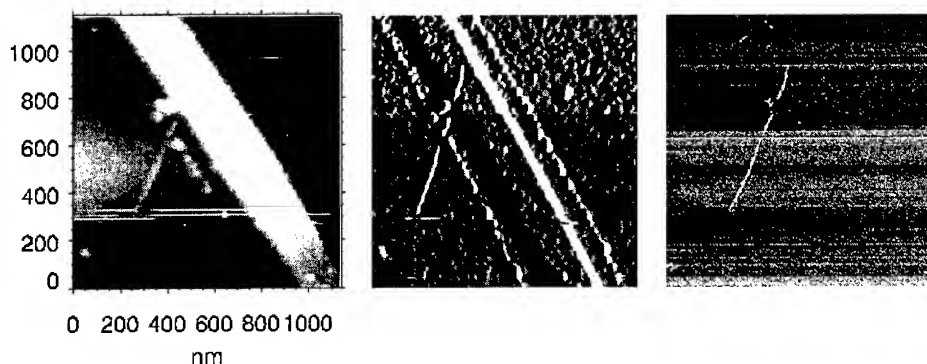


FIGURE 4. A SWNT rope crossing a lithographically defined metal electrode on a SiO_2 substrate. a) Topography image, b) error signal (phase deviation), c) current image.

driven in its resonance near 1MHz by an AC voltage with an SFM tip glued to its end. By applying voltages with amplitudes of the order of 1 mV, we get typical vertical oscillation amplitudes of a few nm [10]. The current through the resonator is extremely sensitive to mechanical damping due to tip-sample interaction. We use the phase-shift of the current signal with respect to the excitation voltage as a measure of the exerted forces. No additional laser-detection scheme is needed. In order to do simultaneous tunneling measurements with SFM feedback, a dc bias is applied to the conductive tip along one of the needle sensor electrodes. If the setpoint of the feedback is high enough to reach the tunneling distance range on a conductive sample area, a current image can be obtained in addition to the SFM topography and phase images. First results have shown that this mode allows atomic resolution imaging of SWNT [6]. Fig. 3 shows a typical set of images of nanotubes dispersed on an annealed gold surface. The images are obtained under force control, and the error signal and the tunneling current are displayed in parts a and b, respectively. The tubes are imaged with a much higher current than the gold substrate. We can explain this image contrast by the different hardness of gold as compared to tubes, taking into account the mechanical oscillation of the tip. On hard areas of the sample, i. e., on clean gold, most of the current flows in the instant of the smallest tip-sample distance. During the remaining part of the cycle, the current is strongly reduced due to the exponential dependence of the current on the tip-sample distance. In contrast to gold, the hollow nanotubes can be squeezed considerably by the tip even under moderate forces. Therefore, the tip is in close contact with the tube for a larger fraction of the cycle, so a considerably higher current can flow in this case.

SFM is routinely used to image tubes on insulating substrates, but the image contrast is usually very poor. On partly insulating substrates, the combination of SFM and STM is of great value to overcome this limitation. Fig. 4 shows an example of a small SWNT rope that crosses from a gold electrode into the non-conducting

area of the substrate. If the tip is scanned where the rope is attached to the gold surface, the current is just passed through the nanotubes into the underlying gold. On the other hand, if the tip is above the rope on the insulating part of the sample, the current is flowing along the nanotubes into the contact. On both sites, the image contrast between the substrate and the nanotubes is very high.

In future experiments, this STM/SFM combination setup will allow detailed electrical characterizations of individual tubes which are connected to electrodes in more realistic device configurations.

ACKNOWLEDGMENTS

This research was supported by grants from the U.S. NSF, Deutsche Forschungsgemeinschaft (W.C.), David and Lucile Packard Foundation (A.T.J.), and the LRSM (D.J.B.). We thank the Smalley group for the nanotube material and C. J. Kane, E.J. Mele, and J.E. Fischer for useful discussions.

REFERENCES

1. J.W. Mintmire, B.I. Dunlap, C.T. White, Phys. Rev. Lett. **68**, 631(1992); N. Hamada, S. Sawada, A. Oshiyama, Phys. Rev. Lett. **68**, 1579 (1992); R. Saito, M. Fujita, G. Dresselhaus, M.S. Dresselhaus, Appl. Phys. Lett. **60**, 2204 (1992).
2. R. Wiesendanger, Scanning Probe microscopy and spectroscopy, Cambridge 1994.
3. J. W. G. Wildoer et al., Nature **391**, 59 (1998), L. C. Venema, et al., Appl Phys. **A66**, S153, (1998).
4. T. W. Odom et al., Nature, Nature **391**, 62 (1998).
5. A. Hassanien et al., Appl. Phys. Lett. **73**, 3839 (1998).
6. W. Clauss, Scanning Tunneling Microscopy of Carbon Nanotubes, Appl. Phys. A, accepted.
7. W. Clauss et al., Europhys. Lett., submitted.
8. E. J. Mele, C. Kane, Phys. Rev. B - Rap. Comm., submitted.
9. OMICRON Instruments, Taunusstein, Germany.
10. W. Clauss, J. Zhang, D. J. Bergeron, and A. T. Johnson, J. Vac. Sci. Technol., submitted.

STM Investigation of Single-Wall Carbon Nanotubes at Room Temperature

A. Hassanien^{a)}, * M. Tokumoto^{a)}, Y. Kumazawa^{b)}, H. Kataura^{b)},
Y. Maniwa^{b)}, S. Suzuki^{b)} and Y. Achiba^{b)}

^{a)} *Electrotechnical Laboratory, 1-1-4 Umezono, Tsukuba, Ibaraki 305-8568, Japan*

^{b)} *Tokyo Metropolitan University, Minami-osawa, Hachi-oji, Tokyo 192-0397, Japan*

Abstract. We have used scanning tunneling microscope (STM), operated in ambient conditions, to investigate the atomic structure of single walled-carbon nanotubes (SWNT). The microscopic scale images show tubes condensed in ropes as well as tubes which are separated from each other. For a single-wall nanotube rope, the outer portion is composed of highly oriented nanotubes with nearly uniform diameter and chirality. On separated nanotubes, atomically resolved images show variable chirality ranges between 0-30°, and variable diameter (1-3 nm), with no one type dominant. From STM and scanning tunneling spectroscopy (STS) measurements we confirmed the correlation between the structural parameters and the electronic properties, namely the tuning from metallic to semiconducting. We also observed a rectifying behavior correlated with the chiral angle of 25°, an important observation for nano-devices application.

INTRODUCTION

Carbon Nanotubes (1), produced by the arc discharge of carbon rods, has attracted increased interest in research to control their growth and quality for practical applications as nanoscale devices (2). Among carbon nanotubes a special attention is focused on the single walled carbon nanotubes (SWNTs) particularly because of the one dimensional nature of conduction within the nanotubes. However, calculations (3,4) predicated that the electronic transport of SWNTs depends very strongly on their structural parameters (chiral angle and diameter) which tune their band gap from metallic to moderate semiconductors. Wildoer *et al.* (5) and Odom *et al.* (6) made the first observation of the atomic structure of SWNTs and confirmed the relation with the electronic properties, namely that they can be either metallic or semiconducting depending on their diameters and chiralities. However, both groups used scanning

* Permanent address: Physics Dept. Faculty of Science Ain Shams University, El-Abbassia, Cairo 11566, Egypt. Electronic mail: hasanien@etl.go.jp

tunneling microscope (STM) at low temperature, 4K and 77K respectively, to test these predications. In this report we show the first measurements of atomic resolution together with the electronic properties of SWNT at room temperature in air using scanning tunneling microscope. For separated nanotubes the images show various diameters (1-3 nm) and chiralities (0-30°) with no one type dominant. On the outer portion of a single wall nanotube rope we have observed highly uniform chirality and/or diameter among the nanotubes.

EXPERIMENTAL PROCEDURE

SWNTs were produced using the conventional arc-discharge method where carbon rod including Ni and Y catalyst (Ni:Y=4.2:1 at.%) was used. A mat of randomly oriented SWNTs fibers were immersed in ethanol and ultrasonically agitated to separate the tubes. The STM samples were prepared by casting a few drops of the nanotubes on freshly cleaved highly oriented pyrolytic graphite (HOPG) substrates and left to dry in a glove box. The STM images were taken by a Digital Instruments nanoscope IIIa operated at room temperature in ambient conditions. High quality atomic resolution images were obtained by recording the tip height at constant current with a tunnel current of $I=300$ pA and a bias voltage $V_{\text{bias}}=40$ mV. The images presented here have not been processed in any way. The STS measurements were performed by interrupting the lateral scanning as well as the feed back loop and measuring the current (I) as a function of tip-sample voltage at a fixed tip-sample distance. The distance between the sample and the tip during the STS $I(V)$ measurements was approximately 8 Å.

RESULTS AND DISCUSSION

The images we obtained show tubular features with lengths on the order of one micrometer and diameters between 1 and 35 nm. The 1-3 nm diameter features are individual single wall nanotubes, whereas the larger diameters are ropes of parallel SWNT nanotubes in which the nanotubes are closely spaced and show high orientational order among each other.

Fig. 1 shows atomically resolved images of chiral SWNTs with diameters; a) 1.2 nm, b) 2.9 nm c) 1.8 nm and d) 2.5 nm obtained by STM in the topographic mode. The dark spots represent hexagon rings on the nanotube wall, which show a lattice on the surface of a cylinder. The images allows us to calculate the chiral angle, that is, the angle between the hexagon rows and the tube axis, which is 11° for the SWNT in a); 23°, 10° and 16° for b) and c) and d) respectively. Fig. 2a) shows atomic resolution for a zigzag tube, the orientation of the hexagons is highlighted for clarity, where carbon-carbon bonds are parallel to the tube axis. We also observed an armchair structure, Fig. 2b), in which the carbon-carbon bonds orient perpendicular to the tube axis. Fig.3 shows an atomically resolved image on the outer portion of a single

nanotube rope. The dark spots, which represent the center of the hexagons, mark homogeneous chirality for all the nanotubes.

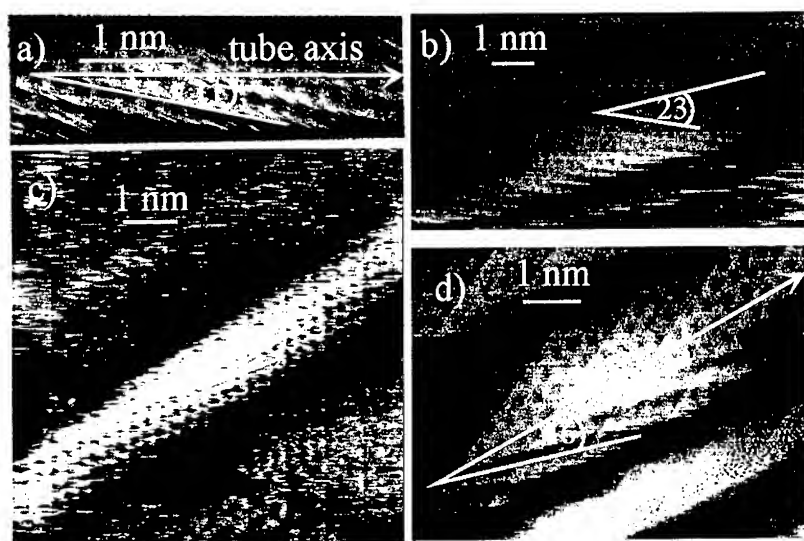


FIGURE 1. Atomic resolution images of single wall carbon nanotubes, the dark spots represent the carbon hexagon centers located on the cylindrical surface of the nanotube wall. The lattice spacing of this triangular lattice is of the order of 0.25 nm, which compares nicely with the expected value of the graphite lattice. The diameter and the chiral angle are: a) 1.2 nm, 11° b) 2.9 nm, 23° c) 1.8 nm 10° and d) 2.5 nm, 16° respectively.

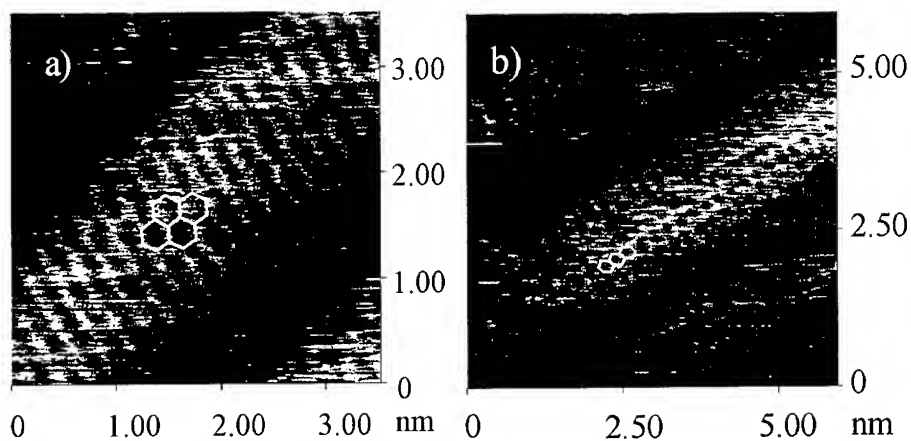


FIGURE 2. Atomic resolution STM images of carbon nanotubes. The hexagons highlight the underlying lattice of the tube wall; a) is a zigzag SWNT where C-C bonds orient parallel to the tube axis; b) is an Armchair SWNT in which C-C bonds orient perpendicular to the tube axis. The background shows less visible features of tubes, which are located near the main highlighted tube.

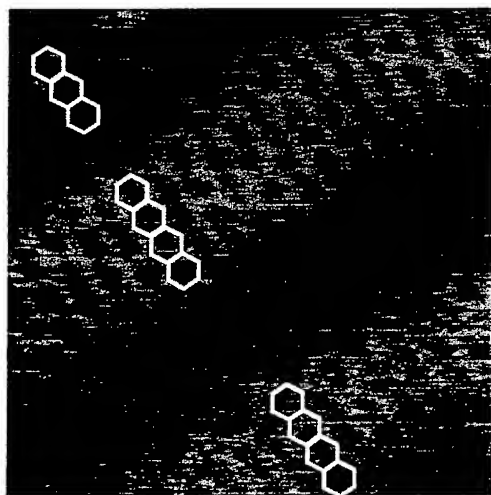


FIGURE 3. 3.5 nm \times 3.5 nm atomic resolution STM image of a SWNT rope. The hexagons, which highlight the underlying zigzag lattice of the nanotubes wall, indicate that the SWNTs are having the same chirality

It is important to note that we only found this homogeneous chirality on the single wall nanotube ropes, other separated tubes (Fig. 1) showed different chirality with no one type dominant. We have checked 12 ropes of SWNTs, and found only one rope feature armchair structure while the rest were zigzag and chiral.

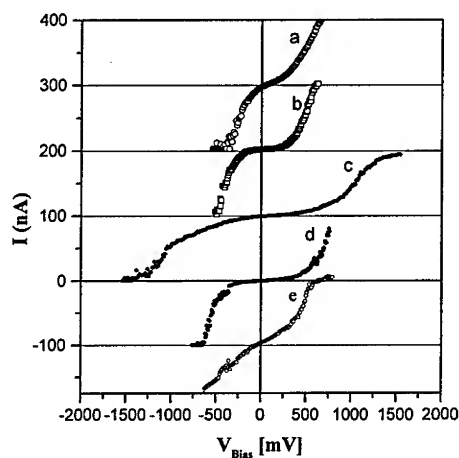


FIGURE 4. I-V STS measurements for separated SWNTs. The curves are off-set vertically in units of 100 nA for clarity. a) is a zigzag with diameter 1.6 nm; The tubes in b), c) and d) has chiral angles of 18°, 21° and 11° with diameters of 1.7 nm, 1.5 nm and 1.8 respectively ; e) is armchair with diameter 1.4 nm.

We have performed our STS experiments far from the tube end to avoid the topology related changes in the local density of states (both theory and experiments showed near the tube cap, the density of states differ markedly from elsewhere on the tube due to topological defects, such as pentagons). The STS $I(V)$ measurements for various SWNTs are shown in Fig. 4. Tube a) is zigzag, b)-d) are chiral, e) is armchair. The low conductance at low bias followed by a gradual increase in the current indicate a semiconductor behavior for the chiral SWNTs. The armchair and zigzag show metallic and narrow gap semiconducting behavior respectively, see Fig.4. We have investigated 40 separated SWNTs nanotubes in this study and only 2 were found to be armchair while the rest were chiral and zigzag.

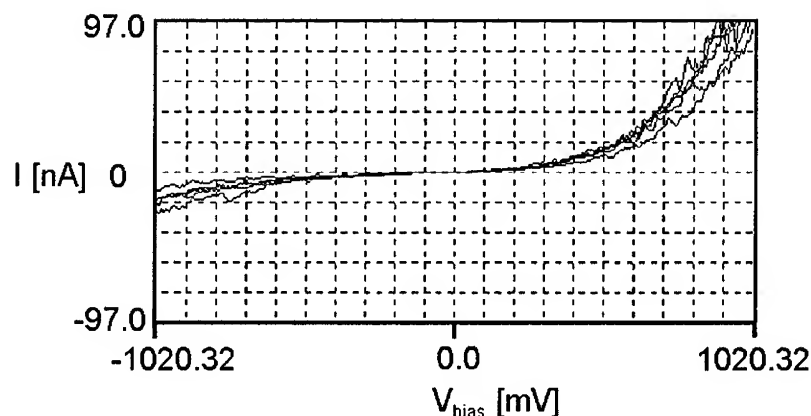


FIGURE 5. I-V spectroscopy of a semiconducting nanotube with a chiral angle of 25° at different location on the nanotube wall. A rectifying behavior is clearly seen as more current flows in the forward direction than the reverse one.

Fig. 5 shows STS $I(V)$ measurements for a semiconducting nanotube with diameter of 1.7 nm and 25° chiral angle. Different curves correspond to different locations on the tube wall and show the reproducibility of the STS spectra. The I-V rectifying behavior is clearly observed as a larger current at a positive voltage than at negative voltage.

One possible mechanism to account for the observed rectifying behavior is electric field enhancement of the barrier: when the sample is at positive polarity the barrier height is slightly decreased and this will enhance the current flow. A negative polarity will increase the potential barrier thereby decreasing the transmission probability and hence the tunneling current. Another mechanism might be due to band bending induced by the tip states. However band bending is strongly related to the distance between the tip and the sample and experiments carried out at different tip-distance, showed that this is not the case. STS measurements with same parameters on different nanotubes with different chirality showed no rectifying behavior. We conclude that this rectifying behavior is unique feature of the chirality of 25° . Beside its occurrence at room temperature the switching of this new electronic states of SWNT vs chirality

is quite striking. However, it is not yet clear how such chirality would modify the electronic structure to yield a rectifying behavior.

CONCLUSION

We have employed an STM at room temperature to investigate the structure and the electronic properties of SWNTs. The images show that most of the nanotubes are chiral with no one type of SWNTs dominant. Homogenous chirality and/or diameter were only observed on the outer portion of single wall nanotube ropes. From STS measurements and atomically resolved images we could verify that the electronic properties are very strongly correlated with the chiral angle and tube diameter. Specifically, a slight changes in these parameters tune their electronic states and causes a shift from metallic to semiconducting behavior. A rather remarkable rectifying behavior correlated with chiral angle of 25° is also observed. It is not quite understood yet how such chirality would promote distinct electronic states. Further study of this new electronic behavior, especially the stability vs temperature would be very helpful. We believe that the room temperature STM and STS characterization of the structure (helicity and nanotube diameter) and its relation to the electronic properties (local density of states) of SWNTs is an important step toward their application in nano devices.

REFERENCES

1. Iijima S., *Nature* **354**, 56 (1991).
2. Sander J. T., Alwin R. M. Verschuere and Dekker C., *Nature*, **393**, 49-52 (1998).
3. Hamada, N., Sawada, S. and Oshiyama *Phys. Rev. Lett.* **68**, 1579-1581 (1992).
4. Saito R., Fujita M., Dresslehaus G. and Dresslehaus M. S. *Appl. Phys. Lett.* **60**, 2204-2206 (1992).
5. Wildoer J. W. G., Venema L. C., Rinzler A. G, E. Smalley R. E. and Dekker C, *Nature*, **391**, 59-62 (1998).
6. Odom T. W., Huang J., Kim P. and Lieber C. M., *Nature*, **391**, 62-64 (1998).

Scanning tunneling microscopy of carbon nanotubes: simulation and interpretation

V. Meunier and Ph. Lambin

*Département de Physique, Facultés Universitaires Notre-Dame de la Paix
61 Rue de Bruxelles, B-5000 Namur, Belgium*

Abstract. Scanning tunneling microscopy (STM) and scanning tunneling spectroscopy (STS) are powerful techniques to investigate electronic and topographical properties of carbon nanotubes. The growing availability of experimental data enables us to study perfect tubules and to probe particular features of nanotubes such as topological (twists) or non-topological (pentagonal and heptagonal rings) modifications of the hexagonal lattice and ending caps structures. We have recently proposed a general approach to interpret and predict STM and STS observations. Our formalism, which is based on a tight-binding framework, is sufficiently precise to be used routinely for various carbon sp^2 geometries. Confronted with experimental results, our approach reveals to be a useful tool to help in the interpretation and prediction of STM and STS measurements.

INTRODUCTION

In 1991, Iijima reported the first observation of carbon nanotubes, long uni-dimensional molecules which can be viewed as the result of the rolling-up of a graphene shell into a tubular object [1]. At that time, no one could have been aware of the exploding “nanotube story” which followed that discovery. Nothing could have been possible without the tremendous work which have been devoted to the production of carbon nanotubes. Often called “ultimate fibers”, carbon nanotubes have spectacular mechanical properties [2,3]. Moreover, carbon nanotubes have very special electronic properties: they are either semi-conductor or metallic depending on the value of their radius and helicity [4]. In order to determine both radius and helicity, only a few experimental techniques are available, namely electron diffraction [5] and scanning tunneling microscopy [6–13]. STM and STS are the only experimental techniques to probe locally the arrangement of carbon atoms and the electronic density of states (DOS) [14]. If, *carbon nanotubes seem to have been made for the STM technique*, interpretation of experimental results is tough and has to be performed very carefully. The tube’s diameter is determined by taking tip-tube convolution effects into account [15] and by considering various geometrical effect. Moreover, transversal distortion due to the 3-dimensional nature

of carbon nanotube affects the determination of the correct value of the so-called chiral angle [16].

In this paper, after giving briefly the main points of our formalism, we present the application of our theoretical method to a twisted carbon nanotube and one carbon nanotube junction.

THEORY

A general first-order expression of the tunneling current between the tip(t) and the substrate(s) has been derived [16].

$$\mathcal{I} = (2\pi)^2 \frac{e}{h} \int_{-eV}^0 dE \sum_{I,I' \in t} \sum_{J,J' \in s} v_{IJ} v_{I'J'}^* \times n_{II'}^t(E_F^t + eV + E) n_{JJ'}^s(E_F^s + E), \quad (1)$$

where V is the tip-sample bias potential ($e > 0$), the E_F 's are the Fermi levels of the unperturbed systems and v_{IJ} are the tip-sample coupling elements. This equation accounts for the electronic properties of both unperturbed tip and substrate. Indeed, diagonal ($I' = I$) elements of $n_{II'}^\lambda(E) = \sum_{\beta \in \lambda} \psi_I^{\beta*} \delta(E - E_\beta) \psi_I^\beta$, where λ stands for t or s respectively, represent the local densities of states (DOS) on site I . When $I \neq I'$, $n_{II'}(E)$ is a quantity which describes the bonding or anti-bonding nature of the $I - I'$ bond. These quantities are computed recursively from a π -tight-binding Hamiltonian with constant first-neighbor interactions ($\gamma_0 = -2.8\text{eV}$) via a continued fraction. In the present study, we have used 200 recursion coefficients. A small imaginary part ($\eta = 0.1\text{eV}$) had to be introduced in order to describe accurately the one dimensional systems we have examined. The tip-tube coupling matrix elements v_{IJ} are described as Slater-Koster sp like hopping interactions decaying exponentially with the separation distance d_J [17].

SIMULATION

Experimentally, observations of perfect carbon nanotubes as well as ending caps have been reported [7,8,13]. Twisted carbon nanotubes have also been imaged at the border of a rope by STM [11]. We have reported in a previous work that much attention must be paid to compute the chiral angle correctly [16]. Now, one can wonder whether a twisted achiral nanotube is different structurally from a non distorted chiral one. The answer is yes. For the purpose of examining that question, let us consider Fig. 1. STM images of a twisted armchair (10,10) and an untwisted chiral (12,9) nanotubes are presented. In a twisted armchair nanotube, one third of the bonds remain perpendicular to the axis whereas there are no such bonds in a chiral structure. The corrugation is about the same (1Å) and the images look the same, although the shape of the hexagonal holes of the twisted (10,10) nanotube are slightly distorted as compared with the elliptical shapes found in (12,9). As

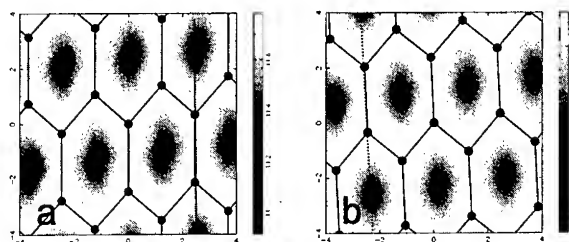


FIGURE 1. Constant current STM images simulated for (a) an armchair (10,10) nanotube twisted by 4.7° and (b) a chiral (12,9) untwisted nanotube (chiral angle $\phi = 4.7^\circ$) ($V=0.5V$). The nanotube axis is along the horizontal direction and the distance tip-tube axis is represented..

shown experimentally, the lines joining second-neighbor hexagon centers along the circumference clearly remain perpendicular to the nanotube axis in the twisted (10,10) nanotube, whereas they do not in the (12,9).

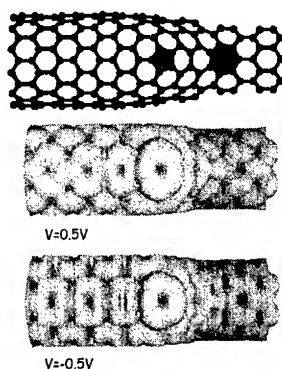


FIGURE 2. Top: schematic view of the (12,0)/(9,0) junction (the 5- and 7-membered rings are shaded); bottom: STM image simulated for bias voltages of $+0.5V$ and $-0.5V$ respectively.

The number of atomically resolved STM images is increasing, at low temperature [8,7] as well as at room temperature [12] and the wish to image features like pentagonal or heptagonal rings is stronger than ever. Recent results have shown that cap structures can be determined with the help of STS measurements [13]. Furthermore, we have shown that it is really difficult to image such defects with STM. This is particularly due to the fact that scattering of electron by the odd-membered rings takes place, making the spatial resolution of the rings very difficult. In this section, we extend our study of 5-7 pair defects with the case of the (12,0)/(9,0) junction [18]. In this junction, the defects are separated by 2 hexagons along the junction axis (top of Fig. 2). In this metal-metal connection, the pentagon is seen as an important protrusion whereas the heptagon can not be easily identified. The (un-)occupied states of the nanotube are visited for (negative) positive bias poten-

tials. Since the DOS shows a relatively large asymmetry around the Fermi level, the maps calculated for opposite potentials display different features. The STM image of the nanotube right before and after the 5-7 defect is also perturbed. This, we believe, is due to the partial reflection of the Bloch waves by the 5-7 conical section [19].

To conclude, we have proposed the application of the tight-binding simulation of STM images technique to a twisted nanotube and a metal-metal carbon nanotube junction. We have firstly shown that the STM signature of a twisted armchair carbon nanotube is different structurally from a chiral one, which confirm the experimental observation. On the other hand, we have shown that pentagonal and heptagonal rings can not be easily identified in carbon nanotube junctions [14]. To help in the identification of such topological defects, it is worth to use STS measurements, as we will describe in a future paper.

This work has been realized under the auspices of the inter-university research program on systems of reduced dimensionality (PAI-IUAP N. P4/10) funded by the Belgian federal government. V.M. thanks the Fund for the Agricultural and Industrial Research (F.R.I.A) of Belgium.

REFERENCES

1. S. Iijima, *Nature* **354**, 56 (1991).
2. E. Hernandez, C. Goze, P. Bernier, and A. Rubio, *Phys. Rev. Lett.* **80**, 4502 (1998).
3. N. Yao and V. Lordi, *J. Appl. Phys.* **84**, 1939 (1998).
4. J. Mintmire, B. Dunlap, and C. White, *Phys. Rev. Lett.* **68**, 631 (1992).
5. D. Bernaerts, A. Zettl, N. Chopra, A. Thess, and R. Smalley, *Sol. State. Comm.* **105**, 145 (1998).
6. M. Ge and K. Sattler, *Appl. Phys. Lett.* **65**, 2284 (1994).
7. J. Wildoer, L. Venema, A. Rinzler, R. Smalley, and C. Dekker, *Nature* **391**, 59 (1998).
8. T.W.Odom, J. Huang, P. Kim, and C. Lieber, *Nature* **391**, 62 (1998).
9. L. Venema, J. Wildoer, C. Dekker, G. Rinzler, and R. Smalley, *Appl. Phys. A* **66**, 153 (1998).
10. L. Biro, S. Lazarescu, P. Lambin, P. Thiry, A. Fonseca, J. B.Nagy, and A. Lucas, *Phys. Rev. B* **56**, 12490 (1997).
11. W. Clauss, D. Bergeron, and A. Johnson, *Phys. Rev. B* **58**, 4266 (1998).
12. A. Hassanien, M. Tokumoto, Y. Kamazawa, H. Kataura, Y. Maniwa, S. Suzuki, and Y. Achiba, *Appl. Phys. Lett.* **73**, 3839 (1998).
13. P. Kim, T. Odom, J.-L. Huang, and C. Lieber, *Phys. Rev. Lett.* **82**, 1225 (1999).
14. A. Rubio, *Appl. Phys. A* **68**, 275 (1999).
15. G. Mark, L. Biro, and J. Gyulai, *Phys. Rev. B* **58**, 12645 (1998).
16. V. Meunier and P. Lambin, *Phys. Rev. Lett.* **81**, 5888 (1998).
17. J. C. Slater and G. F. Koster, *Phys. Rev.* **94**, 1498 (1954).
18. J. Charlier, T. Ebbesen, and P. Lambin, *Phys. Rev. B* **53**, 11108 (1996).
19. R. Tamura and M. Tsukada, *Phys. Rev. B* **55**, 4991 (1997).

The use of computer simulation to investigate tip shape and point contact effects during scanning tunneling microscopy of supported nanostructures

Géza I. Márk^{*,†}, László P. Biró^{*,‡}, József Gyulai^{*}, Paul A. Thiry[‡],
and Philippe Lambin[‡]

^{*}Research Institute for Technical Physics and Materials Science, H-1525 Budapest, P.O.Box 49,
Hungary, E-mail: mark@sunserv.kfki.hu, URL: <http://www.phy.bme.hu/mg/index.html>

[‡]Laboratoire de Physique du Solide, Facultés Universitaires Notre Dame de la Paix, 61, Rue de
Bruxelles, B-5000 Namur, Belgium

[‡]Laboratoire de Spectroscopie Moléculaire de la Surface, Facultés Universitaires Notre Dame de
la Paix, 61, Rue de Bruxelles, B-5000 Namur, Belgium

Abstract. A recently developed computer code [1] is used to investigate effects which may arise during the STM investigation of supported nanostructures, like carbon nanotubes. The effects of tip geometry and point contact imaging are studied. The calculations show that while the magnitude of the tunnel current is determined by the tip-nanotube tunnel gap, the asymmetry of the tip $-/+$ current is influenced by the nanotube-support tunnel gap. The results obtained from simulation are compared with experimental data.

INTRODUCTION

Recently several groups reported asymmetric I-V curves on carbon nanotubes [2–4]. In these experiments STM (scanning tunneling microscopy) was used for recording the I-V curves. Most frequently, a topographic image is recorded first, from which the location of the point(s) where the I-V curves will be measured is decided. STM may generate the image of an object in pure tunneling regime, or in point contact regime; experiments show that the point contact regime induces modifications in the I-V curves [5] as compared with pure tunneling. We studied the STM-tip/nanotube(s)/support system by the wave packet dynamical method to investigate the influence of point contact between the STM- tip and the nanotube, and(or) of the point contact between the carbon nanotube(s) and the support. The point contact was simulated as a 0.2 nm wide conducting channel. The computer simulation is based on the method reported elsewhere [1]. Possible effects arising

from inter-tube contact in "rafts" or "ropes" of carbon nanotubes were investigated too.

WAVE PACKET DYNAMICAL CALCULATION OF THE TUNNELING PROBABILITY

Tunneling probability of an electron scattered [6] on a potential modelling the tip-tube-support system [1] is calculated from the time dependent scattering of a wave packet [7,8] approaching the tunnel interface from the bulk of the tip (support) for the tip negative (positive) case. For the study of nanotube rafts a special initial wave packet has to be applied, which has a plateau of constant probability density larger than the lateral size of the raft. For this purpose we used a truncated plane wave shaped wave packet which is given as the convolution of a Gaussian wave packet with a square lateral window function:

$$\Psi_0(x, z) = N \cdot \exp\left(-\frac{(z - z_0)^2}{a^2} + ik_z z\right) \cdot P_{t_0} \left[\int_{d_1}^{d_2} \exp\left(-\frac{(x' - x)^2}{a^2}\right) dx' \right]$$

where $d_1 = -1.52 \text{ nm}$, $d_2 = 1.52 \text{ nm}$, $a = 0.529 \text{ nm}$, and N is a normalization constant. By the P_{t_0} free space propagator the truncated plane wave is backward propagated in time by an amount of $t_0 = (z_0 - z_{\text{interf}})/k_z$ where z_0 is the desired initial z position of the center of the wave packet and z_{interf} is the z position of the first tunneling interface. The z_0 initial position was chosen to make the probability density of the initial wave packet negligible in the interface region. For the case of infinitesimally small bias a wave packet with momentum $k_z = k_F$ was used where k_F is the Fermi momentum corresponding to the $E_F = 5 \text{ eV}$ Fermi energy.

DISCUSSION AND CONCLUSIONS

Time averaged probability density of the scattered wave packet is shown on *Fig. 1* for the case of one nanotube in the STM gap and for infinitesimally small negative and positive tip potentials.

The effect of point contacts at the tip/nanotube or nanotube/support interface is clearly seen on the figure. The asymmetry of a particular tunneling situation (represented by the corresponding geometry, marked by white lines in *Fig. 1*) is defined as the ratio of the tunneling probabilities for $-/+$ tip polarity. The asymmetries are summarized in *Fig. 2* together with the results of similar calculations for a nanotube raft and an STM junction without nanotubes. In order to enhance the effect of different factors (point contact setup, number of nanotubes) the asymmetries were *normalized* (divided) with respect to the asymmetry of the empty STM junction without point contact (panel *a1* in *Fig. 2*).

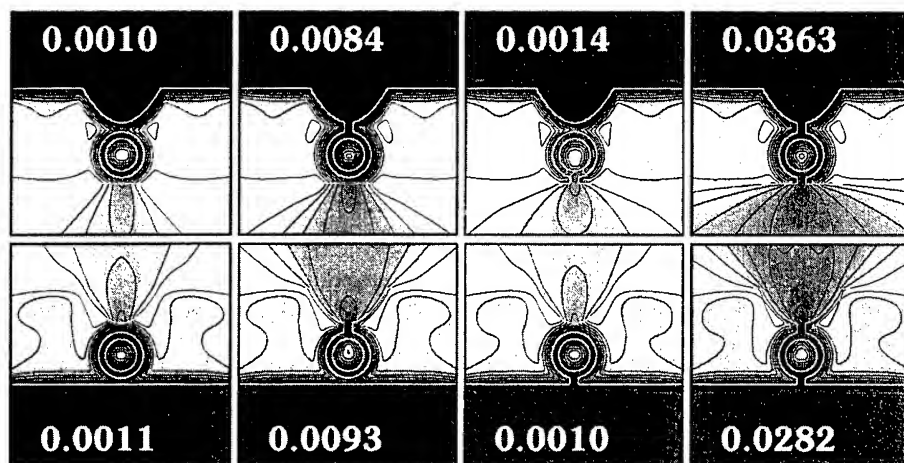


FIGURE 1. Time averaged probability density of the scattered wave packet. Size of each window is 5.76 nm . Contour lines are drawn on logarithmic scale. Darker grey shades are for higher probability density. Thick white lines show the vertical cross section of the effective surface of STM tip, nanotube, and support. The necks between the tip/nanotube and nanotube/support show the point contacts modelled as 0.2 nm wide conducting channels. Upper (lower) figures: tip negative (positive) infinitesimal bias. White numbers indicate the transmission probability. Parameters of the potential are the same as was used in Ref. [1].

A carbon nanotube is not integral part of its support; the consequences of this can not be neglected in the interpretation of STM data [8]. When placed on highly oriented pyrolytic graphite (HOPG), passivated Si, or other substrate, the carbon nanotube will "float" on the van der Waals potential [9]. The interlayer spacing of graphene sheets in HOPG and the distance of single wall carbon nanotubes in bundles are roughly similar, 0.34 nm , therefore it is justified to expect the same distance between the carbon nanotube and the HOPG substrate, or other, underlying nanotubes. During STM measurements, when the STM tip scans across the nanotube, depending on the value of the tunneling current flowing through the substrate-nanotube-tip system as compared with the direct tunneling (in the absence of the nanotube), the tip comes closer to the nanotube than the usual tunneling gap, usually estimated to be around 1 nm . The actual tube-tip distance can be estimated from the lateral distortion [10] of the atomic corrugation of the nanotube. The tip may even come into mechanical contact with the carbon nanotube, as seen in Fig. 3, where the depression in the topmost part of the cross section through the nanotube clearly shows the deformation of the nanotube by the STM tip. The contact resistance measured at the Au/carbon nanotubes interface when no special treatment is done is of the order of $10\text{ M}\Omega$ [11], i.e., of similar magnitude as the resistance of the tunneling gap between HOPG and a Pt tip. This resistance may drop to $k\Omega$, if e-beam is used to modify the contact [11]. This suggests transi-

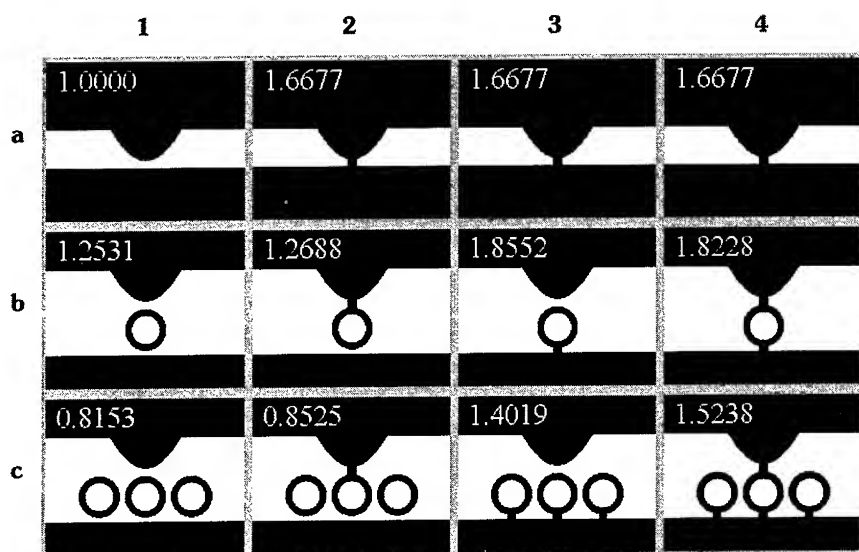


FIGURE 2. Normalized asymmetries for different tunneling potentials.

tion from tunneling to contact regime. During the compression of the nanotube by the STM tip similar phenomena may occur, the tunneling contact of the free tube may switch to (point)contact. It is reasonable to admit that in this case there are two simultaneous point contacts due to the fact that the STM tip is pressing the nanotube towards the support.

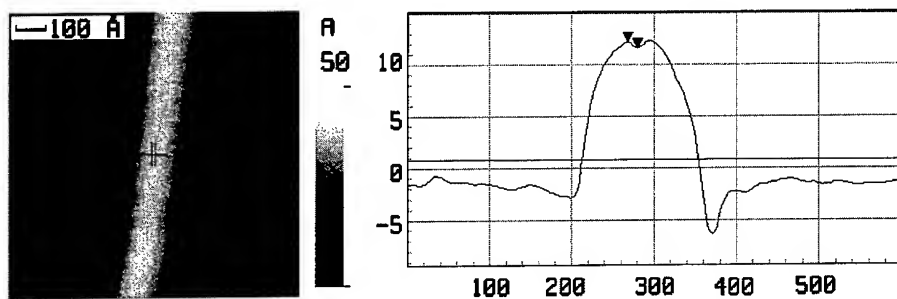


FIGURE 3. *left*) Topographic STM image of a nanotube; *right*) line cut marked in the image.

The comparison of simulation with experimental results reported in [3] shows:
i) regular STS spectrum is obtained when there is **no point contact** between the nanotube and the STM tip, and the contact resistance of the measured nanotube to the support is small - **a-type** curve in [3] (panels *b1* and *c1* in *Fig. 3*); *ii*) when the free nanotube/support contact resistance is high (region with defects,

impurities inside the raft, etc.) the reduction of the transmission coefficient of the system will make the STM tip to descend till point contact is achieved on the topmost part of the nanotube. This will lead to mechanical deformations of the tube, and point contact at the nanotube/support interface, too. The transmission through the system will be controlled by point contact(s), the tunneling current will show a strong increase and a pronounced asymmetry - **b-type curve** in [3], as shown in panels b4 and c4 in *Fig. 3*. The asymmetry being 1.8 means an easy current direction from the negative tip to the positive support, in agreement with experiment [3].

Conclusions: the simulations based on the wave packet scattering technique showed that first: the magnitude of the tunneling current is determined by the carbon nanotube/STM-tip tunneling gap. This is to some extent analogous with mounting in series two resistances, the equivalent resistance will be dominated by the larger one. Second: the asymmetry in the tunneling current will be determined by the contact between the free carbon nanotube and the support. If this contact is a low resistance, ohmic contact, the I-V characteristic will be symmetric, if this contact is dominated by tunneling than asymmetry may show up in the I-V curves due to point contacts at the STM tip/carbon nanotube, carbon nanotube/support interfaces. The adding of point contacts - in a plane normal to the orientation of the tunneling channel - between the nanotubes building up the raft, has no significant influence as compared with the case of point contacts at the nanotubes/support interface. Our preliminary calculations for non vanishing bias show that in agreement with experiments the magnitude of the asymmetry increases with increasing bias.

Acknowledgements: this work was carried out within the framework of PAI/IUAP N. P4/10 on *Reduced Dimensionality Systems*, the work in Hungary was supported by OTKA grants T 030435 and T 025928. G.I.M. and L.P.B. gratefully acknowledge support from the Belgian OSTC.

REFERENCES

1. G. I. Márk et al., *Phys. Rev. B* **58**, 12645 (1998).
2. Ph. G. Collinset al., *Science* **278**, 100 (1997).
3. L. P. Biró et al., *Appl. Phys. Lett.* **73**, 3680 (1998).
4. A. Hassanien et al., *Appl. Phys. Lett.* **73**, 3839 (1998).
5. N. Agrait et al., *Ultramicroscopy* **42-44**, 177 (1992).
6. A. A. Lucas et al., *Phys. Rev. B* **37**, 10708 (1988).
7. <http://www.phy.bme.hu/pub/emrs97/index.html>
8. L. P. Biró et al., *Carbon* **36**, 689 (1998).
9. T. Hertel et al., *Phys. Rev. B* **58**, 13870 (1998).
10. V. Meunier et al., *Phys. Rev. Lett.* **81**, 5588 (1998).
11. A. Bachtold et al., *Appl. Phys. Lett.* **73**, 274 (1998).

Optical Absorption and Resonance Raman Scattering of Carbon Nanotubes

H. Kataura^a, Y. Kumazawa^a, N. Kojima^a, Y. Maniwa^a, I. Umezumi^b,
S. Masubuchi^c, S. Kazama^c, X. Zhao^d, Y. Ando^d,
Y. Ohtsuka^e, S. Suzuki^e and Y. Achiba^e

^a Department of Physics, Tokyo Metropolitan University, Hachiohji, Tokyo 192-0397, Japan

^b Department of Applied Physics, Konan University, Higashinadaku, Kobe 658-8501, Japan

^c Department of Physics, Chuo University, Kasuga Bunkyo-ku, Tokyo 112-8551, Japan

^d Department of Physics, Meijo University, Shiogamaguchi Tempaku-ku, Nagoya 468-8502, Japan

^e Department of Chemistry, Tokyo Metropolitan University, Hachiohji, Tokyo 192-0397, Japan

Abstract. Four kinds of single-walled carbon nanotubes (SWNTs) with different diameter distributions were synthesized using NiY, NiCo, Ni and RhPd catalysts. Optical absorption and resonance Raman spectra were measured. For all the samples, three large absorption peaks were observed from the infrared to visible region. From the band calculation, it was found that they could be explained by the optical transitions between mirror image spikes in density of states caused by the one-dimensional van Hove singularities. Lower two peaks are originating from the semiconductor phases and the third one is from the metallic phases. In the Raman spectra, indeed, broad and asymmetric Fano line shape was observed when the excitation was at the optical transition of metallic SWNTs. Preliminary results about resonance Raman scattering of multi-wall carbon nanotubes that have small core diameter and of Br₂ doped SWNTs are shown.

INTRODUCTION

Recently, Wildöer *et al.* have directly measured electronic density of states of individual single-walled carbon nanotube (SWNT) by scanning tunneling spectroscopy and have shown a good agreement with the tight-binding zone-folding calculation. (1) This is the evidence of one-dimensional van Hove singularity. (2,3) In this system, due to a selection rule, optical transitions between mirror-image spikes are dominant. (4) Thus, it is very interesting to measure the optical absorption spectra (5,6) of the SWNTs. In this report, the optical absorption spectra of four kinds of pristine SWNTs with different diameter distributions will be shown. Furthermore, resonance Raman spectra from infrared to visible region will be shown. Also we will show preliminary results about resonance Raman scattering of multi-wall carbon nanotubes (MWNT) and Br₂ doped SWNTs.

EXPERIMENTAL

SWNTs were prepared by both laser vaporization (7) and electric arc methods. Used catalysts for formation of SWNTs are NiY (4.2-1 at.%), NiCo (0.6-0.6 at.%), Ni (0.6

CP486, *Electronic Properties of Novel Materials— Science and Technology of Molecular Nanostructures*,
edited by H. Kuzmany, J. Fink, M. Mehring, and S. Roth

© 1999 American Institute of Physics 1-56396-900-9/99/\$15.00

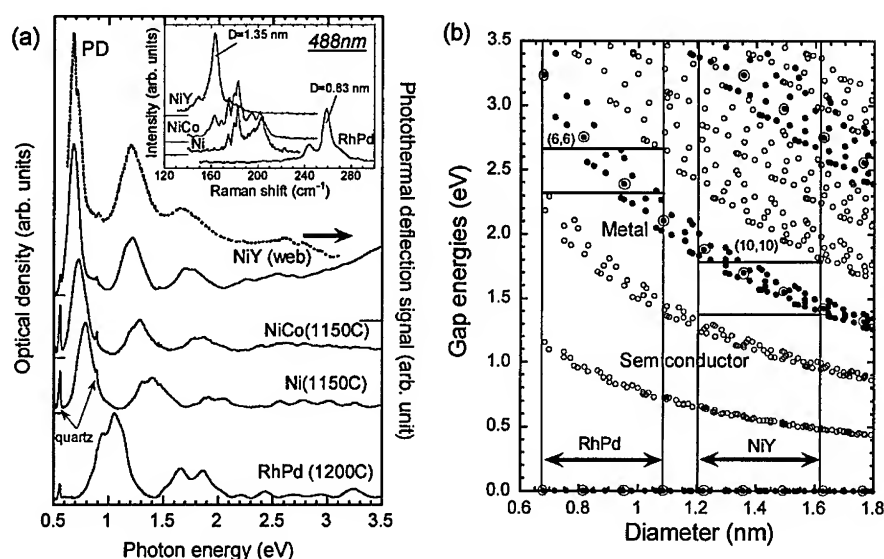


FIGURE 1. (a) Optical absorption spectra of SWNTs. Solid curves show optical density of SWNTs film on quartz plate. Peaks at 0.55 and 0.9 eV are absorption by the quartz substrate. Dotted curve show PD signal of purified SWNTs (NiY). Inset shows Raman spectra of the breathing mode. (b) Gap energies between mirror image spikes in density of states calculated for all chiral indexes larger than (5,5) by zone folding method for $\gamma = 2.75$ eV.

at.%) and RhPd (1.2-1.2 at.%). From the transmission electron microscope (TEM) observation and A_{1g} breathing mode frequencies in Raman spectra, (8) it was found that diameters of SWNTs were distributed from 1.24 to 1.58 nm for NiY catalyst, from 1.06 to 1.45 nm for NiCo and Ni, and from 0.68 to 1.00 nm for RhPd. A thin film of SWNTs was prepared by a painting method. (9) High-grade MWNTs sample was synthesized by carbon arc in hydrogen gas. (10) Br₂ doped SWNTs was prepared in a quartz ampoule which was evacuated after full doping.

RESULTS AND DISCUSSION

Solid curve in Fig.1 (a) shows optical absorption spectra of four kinds of SWNTs with different diameter distributions. For a convenience, large background absorption was subtracted. Diameter distribution of each sample can be estimated from the breathing mode frequencies with a rule, $\omega \propto 1/D$, where D is a diameter of SWNT. (8) In the case of NiY catalyst, three large absorption peaks at 0.68, 1.2 and 1.7 eV are observed. To confirm that these peak structures are characteristics of SWNTs, we measured optical absorption and photothermal deflection (PD) (11) of purified SWNTs. We did not observe any significant difference between spectra before and after the purification in conventional measurement. In the PD, quite similar absorption structure to the conventional one was observed. These results indicated that the absorption structures are not due to the metal particles, amorphous carbon and surface light scattering. We concluded that these absorption peaks are originating from optical

transitions between spike like density of states in SWNTs considering the selection rule (4) of optical transition. For the other catalyst case, very similar absorption structures were observed, but peak positions are considerably different from each other. For example, in the NiCo case, the first peak lies at 0.72 eV and in the case of Ni catalyst, it lies at 0.8 eV. In the thinnest case of RhPd, the first peak is observed around 1 eV. The differences in the peak positions are probably due to the differences in the energy gaps that depend mainly on the diameter of SWNT.

To interpret these absorption spectra, band structure of SWNT was calculated using zone-folding method. (3) In Fig. 1 (b), gap energies between the mirror-image spikes are indicated as a function of the diameter. In the figure, solid circles indicate the energy gap of the metallic SWNTs and open circles indicate the semiconducting SWNTs. Arrows indicate diameter distributions of SWNTs for NiY and RhPd. If each sample contains both types of SWNTs, the semiconducting SWNTs form the first and the second lowest energy-gap groups and the metallic SWNTs form the third group. By considering the dispersion of gap energies and the diameter distribution of the sample, the higher absorption peak should have the wider half width. This theoretical prediction shows very good correspondence with experimental result shown in Fig. 1 (a) for the peak positions and half widths. Of course, each absorption peak consists of much narrow absorption peaks of constituent SWNTs. Indeed, observed each absorption peak has fine structures. Farther, we found that only solid circles are seen in rectangles in the figure. We call it "metallic window". If the laser wavelength is tuned in metallic window, resonance Raman spectrum of metallic SWNTs must be observed.

We have measured resonance Raman spectra of four kinds of samples for wide energy range and it was confirmed that the integrated Raman intensity of breathing mode is roughly proportional to the magnitude of optical absorption. At the high

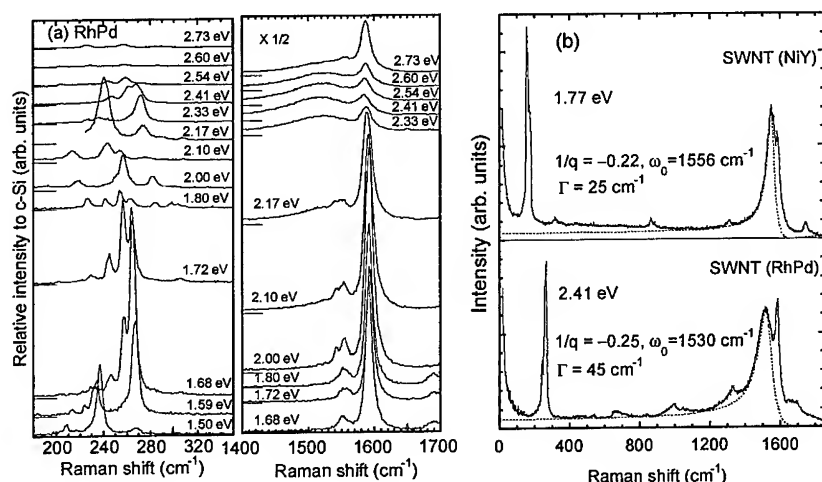


FIGURE 2. (a) Resonance Raman spectra of SWNTs using RhPd as a catalyst. (b) Raman spectra of SWNTs excited by the laser lines in the "metallic window". Dotted curves show Breit-Wigner-Fano line shapes, which is given by $I(\omega) = I_0 \{1 + (\omega - \omega_0) / q\Gamma\}^2 / \{1 + ((\omega - \omega_0) / \Gamma)^2\}$. Fitting parameters are indicated in the figure.

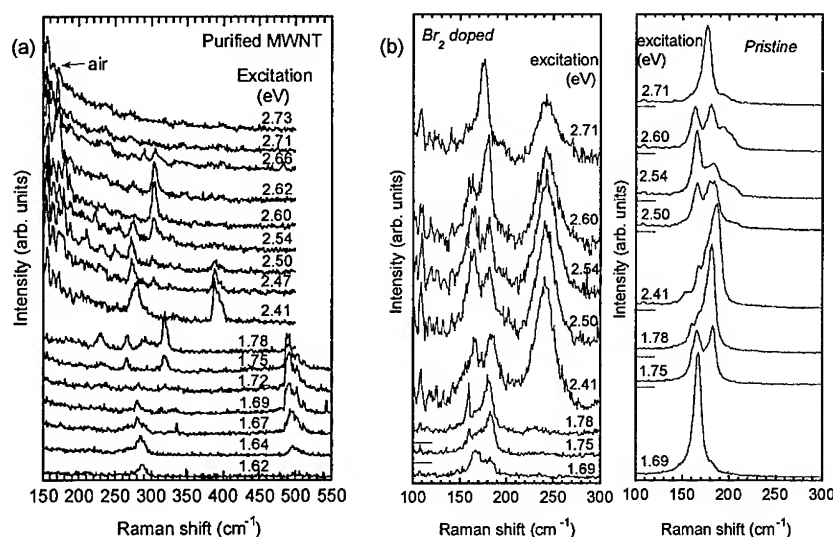


FIGURE 3. Resonance Raman spectra of (a) MWNTs synthesized by the electric arc in hydrogen gas and (b) Br_2 doped SWNTs. Doped SWNTs were sealed in quartz ampoule after evacuation. Raman spectra of pristine sample are shown as a reference.

frequency region, broad and asymmetric Raman peak was observed around 1.7 eV for NiY case and around 2.4 eV for RhPd case, which just correspond to the "metallic window" of each sample. For example, Raman spectra of the SWNTs using RhPd catalyst are shown in Fig. 2 (a). Similar line shape was already reported by Rao *et al.* in K and Rb doped SWNT bundles. (12) They assigned that as a Breit-Wigner-Fano (BWF) interference. We also tried to fit the spectra with BWF line shape. Fig. 2 (b) shows the typical example of the fitting. Fitting parameters are indicated in Fig. 2 (b). In both cases, BWF line shapes could successfully fit the main part of Raman spectra. This means that metallic SWNTs are selectively resonated by the excitation in "metallic window". This result is consistent with the result of optical absorption.

Preliminary result about resonance Raman scattering of MWNTs is shown in Fig. 3 (a). Because the resonance feature of Raman peaks from 200 to 328 cm^{-1} are quite similar to that of SWNTs (13), we concluded that all of them are breathing mode. Frequency of each peak is higher than that of SWNTs about 4%, which is probably due to inter-layer interactions. We also found two large peaks around 390 and 490 cm^{-1} which also show strong resonance features. If these peaks are breathing mode, corresponding diameters are 0.57 and 0.45 nm, respectively. From the TEM observation, indeed, we found that some MWNT have very small core diameter such as 0.5 nm. Clearly, these nanotubes are the core tubes in MWNT. Diameters of the second layer of them are 1.25 and 1.13 nm and breathing mode frequencies are 177 and 196 cm^{-1} , respectively. It is very interesting that we did not observe any Raman peaks around these frequencies. This result suggests that only the core tubes have considerable Raman intensity.

Resonance Raman spectra of Br₂ doped SWNTs are shown in Fig. 3 (b). Rao *et al.* (12) have shown that the breathing mode is terribly shifted to higher frequency by Br₂ doping. In our result, consistently, the breathing mode of doped SWNT bundles is observed at 240 cm⁻¹. Furthermore, it is clearly seen that the breathing mode of doped SWNTs was observed only in a visible region. In the infrared, observed breathing mode is originating from the undoped portions in the doped sample. This result is basically explained by a lack of density of states at the first peak of metallic SWNTs caused by the charge transfer from SWNT to bromine. This is consistent with the previous work about the optical absorption of Br₂ doped SWNTs solution. (5) On the other hand, the resonance feature of undoped portions in doped sample is slightly different from that of pristine sample. Because the Raman signal from the undoped portions is observed only in the case of evacuated sample, it is presumed that they are individual SWNTs. Since the Raman signal of pristine sample comes mainly from the undoped SWNT bundles, the difference in resonance feature of them is probably due to the bundle effect. (14)

ACKNOWLEDGEMENTS

The authors thank Prof. R. Saito for fruitful discussion about phonon mode in SWNT. The authors thank Mr. Misaki for TEM observations. This work was partially supported by Japan Society for the Promotion of Science Research for the Future Program and was partially supported by the Grant-in-Aid for Scientific Research on the Priority Area "Fullerenes and Nanotubes" by the Ministry of Education, Science, and Culture of Japan.

REFERENCES

- 1 J. W. G. Wildöer, L. C. Venema, A. G. Rinzler, R. E. Smalley and C. Dekker, *Nature* **391**, 59 (1998).
- 2 N. Hamada, S. Sawada and A. Oshiyama, *Phys. Rev. Lett.* **68**, 1579 (1992).
- 3 R. Saito, M. Fujita, G. Dresselhaus and M. S. Dresselhaus, *Appl. Phys. Lett.* **60**, 2204 (1992).
- 4 T. Ando and H. Ajiki, *High Magnetic Fields in Semiconductor Physics II*, World Scientific, Singapore (1997) pp. 915-926.
- 5 J. Chen, M. A. Hamon, H. Hu, Y. Chen, A. M. Rao, P. C. Eklund, R. C. Haddon, *Science* **282**, 95 (1998).
- 6 T. Pichler, M. Knupfer, M. S. Golden, J. Fink, A. Rinzler and R. E. Smalley, *Phys. Rev. Lett.* **80**, 4729 (1998).
- 7 T. Wakabayashi, D. Kasuya, H. Shiromaru, S. Suzuki, K. Kikuchi and Y. Achiba, *Z. Phys. D* **40**, 414 (1997).
- 8 R. Saito, T. Takeya, T. Kimura, G. Dresselhaus and M. S. Dresselhaus, *Phys. Rev. B* **57**, 4145 (1998).
- 9 H. Kataura, Y. Kumazawa, Y. Maniwa, I. Umezu, S. Suzuki, Y. Ohtsuka and Y. Achiba, *Syn. Metals*, in press (1999).
- 10 X. Zhao, M. Ohkohchi, M. Wang, S. Iijima, T. Ichihashi and Y. Ando, *Carbon* **35**, 775 (1997).
- 11 I. Umezu, M. Daigo and K. Maeda, *Jpn. J. Appl. Phys.* **33**, L873 (1994).
- 12 A. M. Rao, P. C. Eklund, S. Bandow, A. Thess and R. E. Smalley, *Nature* **388**, 257 (1997).
- 13 H. Kataura, A. Kimura, Y. Ohtsuka, S. Suzuki, Y. Maniwa, T. Hanyu and Y. Achiba, *Jpn. J. Appl. Phys.* **37**, L616 (1998).
- 14 Y. K. Kwon, S. Saito and D. Tománek, *Phys. Rev. B* **58**, R13314 (1998).

***In situ* Raman Investigations of Single-Wall Carbon Nanotubes Pressurized in Diamond Anvil Cell**

E.D. Obraztsova¹, H. Th. Lotz², J.A. Schouten², M.E. Kooi²,
A.V. Osadchy¹, V.L. Kuznetsov³, V.I. Zaikovskii³

¹ Natural Sciences Center of General Physics Institute, RAS, 38 Vavilov street, 117942, Moscow, Russia, elobr@kapella.gpi.ru

² Van der Waals-Zeeman Institute of the University of Amsterdam, Valckenierstraat 65-67, 1018 XE, The Netherlands

³ Boreskov Institute of Catalysis, RAS, 5 Lavrentieva street, 630090, Novosibirsk, Russia

Abstract. The Raman spectra of single-wall carbon nanotubes under the pressures up to 10 GPa have been measured *in situ* in diamond anvil cell. The “breathing” mode was clearly seen at pressures below 2 GPa and disappeared at higher pressures. The splitting of TO mode was kept at all steps of pressurizing. This mode shifted from the position 1592 cm⁻¹ (at ambient pressure) toward high frequencies almost linearly with the pressure. The shift rate (4.9 cm⁻¹/GPa) appeared to be very close to that of graphite. The irreversible broadening and overlapping of the split components of TO mode at pressures above 2.5 GPa have been observed. A polymerization of nanotubes inside ropes followed by the graphite needles formation is discussed as a possible mechanism of the tube structure transformation under the pressure.

INTRODUCTION

The bulk characteristics of single-wall carbon nanotubes (SWNT) change substantially under the pressure. For instance, the temperature dependence of SWNT's resistance is metallic at ambient pressure, but shows a semiconducting behavior at pressures higher than 2 GPa [1]. Which structural transformations do influence to the electronic properties of the material? The best way to answer this question is to monitor “*in situ*” the pressurizing process. It is too complicate to combine a pressure cell with instruments possessing a high spatial resolution. So in this work we used *in situ* Raman diagnostics of SWNT pressurized up to 10 GPa in a diamond anvil cell. Observing changes in the lattice dynamics under the pressure we got indirect information about the material structure.

EXPERIMENTAL

The experiments have been performed with a bucky-paper produced by a double-pulse laser ablation technique followed by an efficient purification procedure [2]. The similar data have been obtained also with a disperse SWNT material.

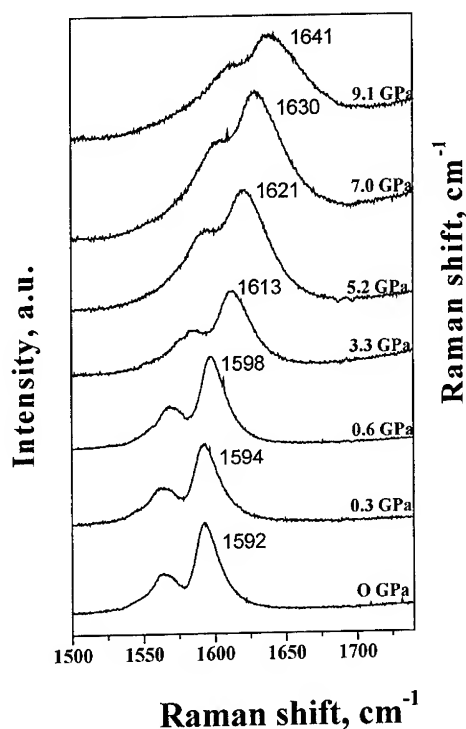


FIGURE 1. Transformation of TO-band contour in the Raman spectrum of SWNT pressurized in diamond anvil cell.

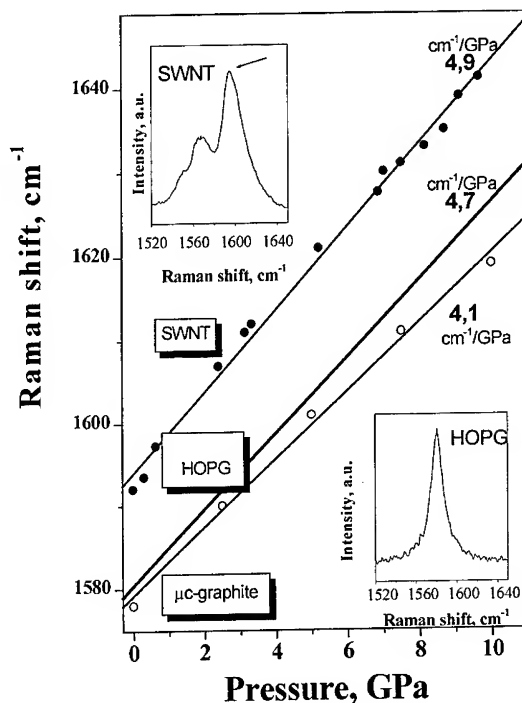


FIGURE 2. The pressure-induced shift of TO-band in the Raman spectra of bucky-paper (*our data*), HOPG [5] and polycrystalline pyrolytic graphite [6].

The pressure was generated with a diamond anvil cell (DAC) of the wedge-type [3], with diamonds selected on low fluorescence. For the pressure calibration the position of fluorescence bands of a ruby chips [4] admixed to SWNT were measured. Due to a high compressibility of SWNT the cell was filled with a buffer gas N_2 .

The Raman spectra were registered with a double monochromator and CCD-matrix. The radiation of Ar^+ -laser with $\lambda=488$ nm was used for excitation.

RESULTS AND DISCUSSION

We have observed two main trends in the pressure-induced transformation of tangential Raman band of SWNT (observed at 1592 cm^{-1} at ambient pressure): (i) the band position shifted toward high frequencies (Fig.1) almost linearly with the pressure (Fig.2). Comparing our data with ones for highly oriented pyrolytic graphite (HOPG) [5] and microcrystalline pyrolytic graphite (μ c-G) [6] we have revealed almost no influence of the curvature of nanotube surface on the coefficient of the pressure-induced TO-band shift. Its value is $4.9\text{ cm}^{-1}/\text{GPa}$ for SWNT, $4.7\text{ cm}^{-1}/\text{GPa}$ for HOPG and $4.1\text{ cm}^{-1}/\text{GPa}$ for μ c-G.

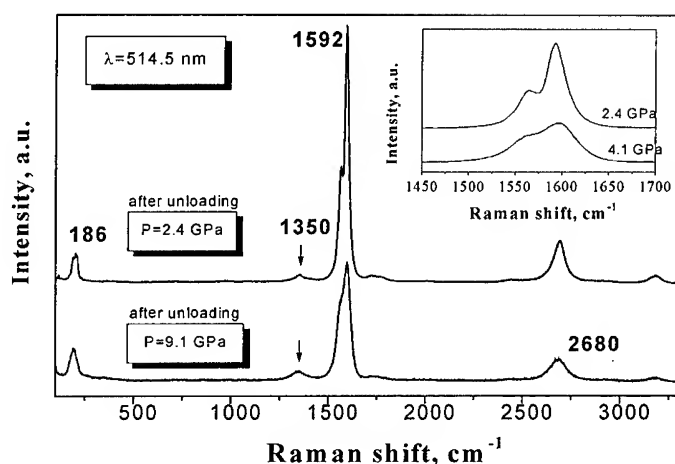


FIGURE 3. The Raman spectra of SWNT treated at different pressures measured after unloading. The insert shows the shape of TO-band in detail. The arrows indicate the position of «D» (disorder-induced) Raman peak.

(ii) The characteristic splitting of TO-mode kept at all steps of SWNT pressurizing. This confirmed the SWNT survival. However after loading with pressures higher than 2.5 GPa the split components of TO-mode began to broaden and to overlap (Fig.3). As a result after the pressure release TO-band returned to the initial frequency position keeping the broadening, while after the treatment at lower pressures no changes of the band shape occurred (Fig.4). The similar trend was observed in the Raman spectra of SWNT removed from a Bridgman-type anvil apparatus [7]. The band broadening increased at higher pressures while the disorder degree of the material didn't change remarkably since the contribution of a disorder-induced Raman peak «D» at 1350 cm^{-1} was small at all pressures (Fig.3).

The polymerization of nanotubes in each rope under the pressure [8] may be considered as a possible mechanism of the observed Raman band transformations. In case of polymerization the dispersity of nanotubes over diameter substantially increases. It should broaden the summary TO-contour which integrates the contributions from tubes of different diameter. The idea of polymerization is not contradictive with our HRTEM observations (Fig.5). The graphitic needles with a perfect structure have been found in the material removed from the anvil after the treatment at 8-9 GPa. Each needle seemed to be formed on the base of individual SWNT rope. Probably, the separate tubes in the rope initially form a polymerized conglomerate, which easier transforms into graphitic platelet at higher pressure.

A «breathing» Raman band with the maximum at 186 cm^{-1} (at ambient pressure) [9] could be more informative for the tube diameter estimation. This band was observed clearly and demonstrated the upward frequency shift while the pressure increased up to 2 GPa. At higher loading the band disappeared. This may happen if the

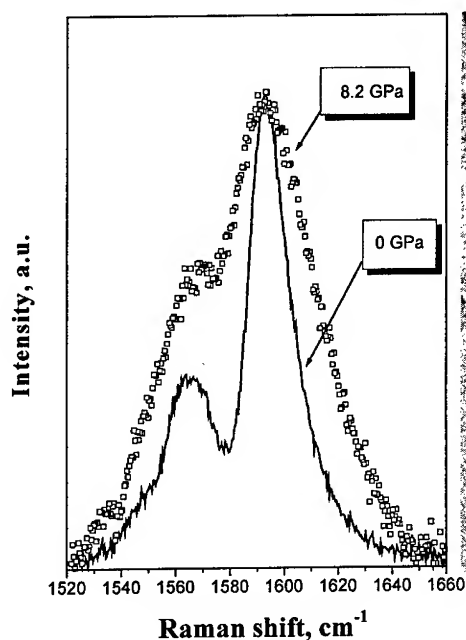


FIGURE 4. Irreversible broadening of TO-band observed in the Raman spectra of SWNT treated under the pressure above 2.5 GPa.

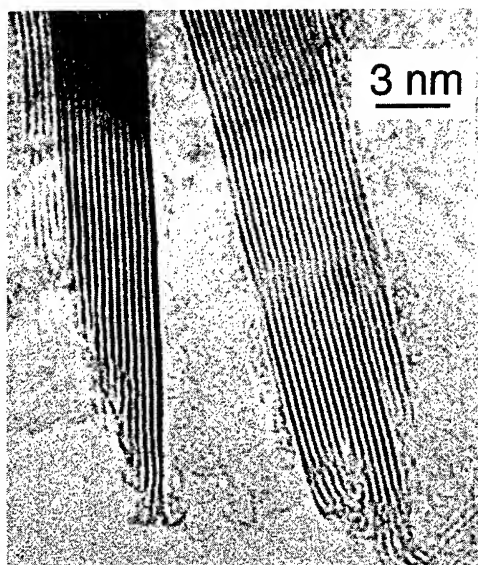


FIGURE 5. The HRTEM image of nanoscale graphite platelets (needles) arising on the base of individual SWNT ropes under the pressure

Raman scattering loses its resonance character due to modification of the electronic structure of SWNT under the pressure or if the polymerization takes place. Our experiments are in progress to monitor in detail the «breathing» Raman mode behavior under the pressure and to clarify the graphitization mechanism of SWNT.

ACKNOWLEDGMENTS

The authors are grateful to V.A. Nalimova and D.E. Sklovsky for the idea of these experiments, A. Rinzler and R. Smalley for the bucky-paper samples, J. Fisher for the fruitful discussion. The work is supported in part by RFBR grant 97-2-17282, by INTAS grant 97-1700, by Federal programs «Integration» (K1129) and «Fullerenes and Atomic Clusters» (99034).

REFERENCES

1. A.D. Bozhko, D.E. Sklovsky, V.A. Nalimova, A.G. Rinzler et al., *Appl. Phys. A* 67 (1998) 75.
2. A.G. Rinzler, J. Liu, H. Dai et al., *Appl. Phys. A* 67 (1998) 29.
3. H. Wieldraaijer, J.A. Schouten, N.J. Trappeniers, *High Temp. High Press* 15 (1983) 87.
4. H.K. Mao, J.Xu, P.M. Bell, *J Geophys. Res.* 91 (1986) 4673.
5. M. Hanfland, H. Beister, K. Syassen, *Phys. Rev. B* 39 (1989) 12 5984.

-
6. T.L. Schindler, Y. K. Vohra, *J. Phys.: Condens. Matter* 7 (1995) L6372.
 7. E.D. Obraztsova, G.N. Bondarenko, V.A. Nalimova et al., *Proceeding of "EuroCarbon'98"*, p. 851.
 8. L.A. Chernozatonskii, *Chem. Phys. Letter* 297 (1998) 257.
 9. E.D. Obraztsova, V.Yu. Yurov, V.M. Shevluga et al., *Nanostruct. Materials* 11 (1999) N3 (in press)
 10. U. Venkateswaran, A.M. Rao et al., *Proc. of American Phys. Soc. Meeting (March 1998)*, Q19.02.

Surface Enhanced Raman Spectroscopy of single wall carbon nanotubes

G. S. Duesberg¹, J. Muster², M. Burghard², H. J. Byrne³, S. Roth²

¹*Trinity College, Dublin, Ireland*

²*Max-Planck-Institut für Festkörperforschung, Heisenbergstr. 1, 70569 Stuttgart, Germany*

³*Dublin Institute of Technology, Kevin St. Dublin 2, Ireland*

Abstract. Raman Microscopy has been performed on single wall carbon nanotubes (SWNTs). For that purpose chromatographically purified SWNTs were adsorbed onto substrates for Surface Enhanced Raman Spectroscopy. Investigations by Scanning Electron and Atomic Force Microscopy of the substrates revealed, that there are only a few objects in the Raman active area. Spectra with a distinct sharp peak in the region of the radial breathing mode (RBM) and four C-C stretching modes centred at 1580 cm^{-1} were recorded. The extremely narrow line width indicates that the spectra originate from individual SWNTs or ropes of SWNTs with a unique diameter.

1 INTRODUCTION

Raman spectroscopy has become a powerful tool for the characterisation of nanotubes. For different SWNTs, defined in diameter and chirality by their roll-up vector (n,m) , variations in the Raman spectra have been theoretically predicted [1,2]. From the frequency of the radial breathing mode (RBM), in which the carbon atoms undergo an uniform radial displacement, the diameter of a SWNT can directly be estimated [3]. Several C-C bond motions contribute to G-line of SWNTs centred at 1580 cm^{-1} , which are only weakly dependent on diameter and helicity of the SWNT.

Until now, however, most of the Raman investigations have been performed on samples containing a variety of SWNTs. The spectra obtained are always a superposition of various types of tubes, causing broad unresolved peaks, which makes a straightforward assignment of modes in bulk samples impossible [4].

Chromatographic purification yields highly pure and length separated carbon nanotubes in aqueous suspension [5], allowing their controlled adsorption on substrates for Surface Enhanced Raman Spectroscopy (SERS). These samples make it possible to obtain Raman spectra from individual SWNTs or a small bundle of SWNTs [6].

2 EXPERIMENTAL

The SWNT soot, produced by the arc discharge method [7], was subjected to chromatography as described previously [8]. The purified SWNTs were deposited on silver substrates produced by the reduction of Tollen's reagent as described by Ni et al. [9]. The adsorption times ranged between 30 sec to 30 min. Finally the substrates were

immersed into distilled water to remove the surfactant. The samples were characterised with AFM (Digital Instruments, Nanoscope IIIa) and by field emission SEM (Gemini DSM 982).

The Raman microscope (Instruments SA Labspec 1B) was equipped with a 20 mW He/Ne laser ($\lambda=632.8$ nm) and a manual X-Y stage. The spot of the incident laser beam is specified to be 1 μm in diameter.

3 RESULTS AND DISCUSSION

Unlike other purification techniques, chromatographic separation yields individual SWNTs and thin ropes of 2-5 nm diameter in aqueous suspension. Approximately 50% of the objects are individual tubes while the other half are ropes as estimated from the analysis of AFM height profiles of the SWNTs adsorbed on silicon wafers [19]. In a similar way, SWNTs were adsorbed onto SERS substrates for Raman investigations. The SEM image in Fig. 1 shows the rough surface structure, made of silver dots approximately in 100 nm diameter, of a typical substrate. A few, spatially separated SWNTs or ropes of SWNTs can be seen on the surface. Detailed SEM and AFM investigations revealed that on average only a small number of objects is present in an area of 1 μm^2 . Hence, the use of SERS substrates makes it possible to detect a small number or even individual tubes, if a Raman microscope with a laser spot of approximately 1 μm^2 is used.

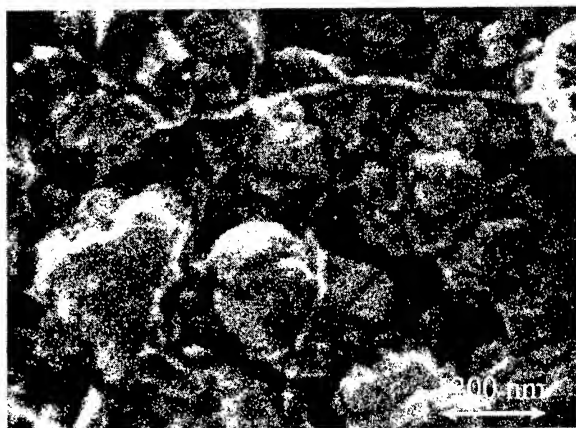


Fig. 1 SEM image of SWNTs on a substrate suitable for SERS investigations. A few tubular structures are recognised on the rough silver surface, indicating the presence of only a few objects in the area of the incident laser spot ($d \approx 1$ μm) of the Raman microscope.

At various spots, spectra with only a single line in the low frequency area could be obtained. Three examples of such spectra are displayed in Fig. 2. The inset of Fig. 2 the single lines in the RBM region can be clearly recognised (the sharp line at 181 cm^{-1} is an instrumental artefact).

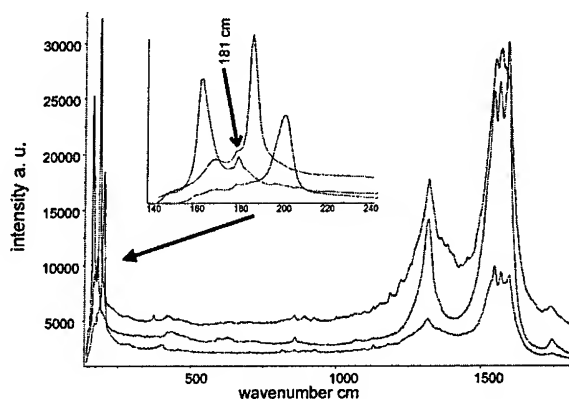


Fig. 2 Three Raman spectra recorded on different location of a SERS substrate. The spectra exhibit a well resolved G-line and only one narrow mode in the RBM region (see inset).

The lorentzian line shape of the RBMs indicates that scattering originates from single objects. The obtained FWHMs below 10 cm^{-1} are consistent with the natural linewidth of this mode expected from the electron - phonon broadening in graphite [10, 11]. The RBM is related to the diameter of the tube by the relation [3]:

$$d = \frac{223.75}{\omega}$$

where d is the diameter of the tube in nanometers and ω is the RBM in wavenumbers. Assuming a resolution of 5 cm^{-1} the diameter of a tube can be derived with an accuracy of approximately $\pm 0.05 \text{ nm}$. However, in the view of deformations of adsorbed nanotubes due to interaction with the surface [12], an influence of the substrate or of surrounding tubes (in case of ropes) on the position of the RBM can not be ruled out.

The G-line could be fitted by four lorentzians ranging between $1510 - 1595 \text{ cm}^{-1}$ with FWHMs smaller than 30 cm^{-1} . The fits match the results of Pimenta et al. [13] who reported broadened and downshifted G-line modes for metallic SWNTs. Only the position of the highest frequency mode does not appear to be downshifted. Selective resonant enhancement of metallic SWNTs of diameters between $1.1 - 1.6 \text{ nm}$ has been reported for red laser light [12]. This is because the energy gap between the first van Hove singularities of these SWNTs is similar to the photon energy exciting laser. Only a limited number of (n, m) combinations fulfil the conditions for diameter and metallic behaviour and therefore an assignment of the modes to specific SWNTs becomes possible.

The change in relative intensities of the RBM relative to the G-line can be explained with calculations performed by Saito et al. [8], who showed that the polarisation and intensity of Raman scattered light depends on the position of the tube with respect to the polarisation of the incident laser beam. A selective surface enhancement of various modes might also take place.

Even though a small residue of amorphous carbon attached to SWNTs may still remain after purification, the intense peak at 1270 cm^{-1} can not be explained by the presence of impurities. It is more likely that the peak originates from the same object as the G-line

since the intensities are directly correlated. There could be selective surface enhancement of the rather weak Raman modes calculated in this region. Another possible explanation is that modes in this region are induced by symmetry breaking effects such as bending or the interaction with the substrate [14].

4 CONCLUSIONS

Raman spectra of individual SWNTs or ropes of SWNTs are presented. The spectra obtained from SWNTs adsorbed on SERS substrates show a single RBM and well defined G-line modes. More detailed investigations with different laser lines and polarisation dependent Raman microscopy should allow the assignment of the modes to specific SWNTs. The effect of the orientation of the tube relative to the polarisation of the laser line and the role of the surface-tube and tube-tube interaction may also be clarified in further experiments.

ACKNOWLEDGEMENT

This work was supported by the European Community TMR project NAMITECH (ERBFMRX-CT96-0067 (DG12-MIHT)). I would like to thank C. Journet and W. Maser for supplying SWNT samples.

REFERENCES

- ¹ M.S. Dresselhaus, G. Dresselhaus, P.C. Eklund, *Science of Fullerenes and Carbon Nanotubes*, Academic Press, New York, 1996
- ² R. Saito, T. Takeya, T. Kimura, G. Dresselhaus and M.S. Dresselhaus, *Phys. Rev. B* 57 (1998) 4145.
- ³ S. Bandow, S. Asaka, Y. Saito, A.M. Rao, L. Grigorian, E. Richter, P.C. Eklund, *Phys. Rev. Lett.* 80 (1998) 3779.
- ⁴ S. Lefrant, M. Lamy de la Chapelle, I. Baltog, C. Journet, P. Bernier, E. Munoz, A. Benito, W.K. Maser, M.T. Martinez, G.F. de la Fuente, D. Laplaze, A. Loiseau, *Mol. Cryst. Liq. Cryst.* 322 (1998) 71.
- ⁵ G.S. Duesberg, M. Burghard, J. Muster, G. Philipp, S. Roth, *Chem. Commun.* 3 (1998) 435.
- ⁶ G.S. Duesberg, W. J. Blau, H. J. Byrne, J. Muster, M. Burghard, S. Roth, *Chem. Phys. Lett.*, in print
- ⁷ C. Journet, W.K. Maser, P. Bernier, A. Loiseau, M. Lamy de la Chapelle, S. Lefrant, P. Deniard, R. Lee, J.E. Fischer, *Nature* 388 (1997) 756.
- ⁸ G.S. Duesberg, J. Muster, V. Krstic, M. Burghard, S. Roth, *Appl. Phys. A* 67 (1998) 117.
- ⁹ F. Ni, T.M. Cotton, *Anal. Chem.* 58 (1986) 3159
- ¹⁰ M.S. Dresselhaus, G. Dresselhaus, *Adv. Phys.* 30 (1981) 139.
- ¹¹ A.M. Rao, E. Richter, S. Bandow, P.C. Eklund, *Thin Solid Films* 331 (1998) 141.
- ¹² T. Hertel, R.E. Walkup, P. Avouris, *Phys. Rev. B* 58 (1998) 13870.
- ¹³ M. Pimenta, A. Marucci, S.D.M. Brown, M.J. Matthews, A. Rao, P.C. Eklund, R.E. Smalley, G. Dresselhaus, M.S. Dresselhaus, *J. Mater. Res.* 13 (1998) 2396.
- ¹⁴ R. Saito, G. Dresselhaus and M.S. Dresselhaus, *Physical Properties of Carbon Nanotubes*, Imperial College Press, London, (1998).

Disorder Effects on Density of States and Electronic Conductance in Carbon Nanotubes

Kikuo Harigaya

Electrotechnical Laboratory, Umezono 1-1-4, Tsukuba 305-8568, Japan

Abstract. Disorder effects on the density of states and electronic conduction in metallic carbon nanotubes are analyzed by a tight binding model with Gaussian bond disorder. Metallic armchair and zigzag nanotubes are considered. We obtain a conductance which becomes smaller by the factor $1/2 \sim 1/3$ from that of the clean nanotube. This decrease mainly comes from lattice fluctuations of the width which is comparable to thermal fluctuations. We also find that suppression of electronic conductance around the Fermi energy due to disorder is smaller than that of the inner valence (and conduction) band states. This is a consequence of the extended nature of electronic states around the Fermi energy between the valence and conduction bands, and is a property typical of the electronic structures of metallic carbon nanotubes.

INTRODUCTION

Recently, carbon nanotubes with cylindrical graphite structures have been intensively investigated (1,2). Many interesting experimental as well as theoretical researches have been performed, and the fundamental metallic and semiconducting behaviors of single wall nanotubes predicted by theories (3-8) have been clarified in tunneling spectroscopy experiments (9,10).

In this paper, we would like to try to apply the Thouless formula (11,12) in order to look at possible decrease of the electronic conductance by a bond disorder potential. The origin of the bond disorder potential is the thermal fluctuations of phonons mainly. This idea has been used in the discussion of disorder effects on the polaron excitations in doped C_{60} systems (13). We use a tight binding model with the nearest neighbor hopping integral t and the Gaussian bond disorder, and finite systems with quite large metallic carbon nanotubes are diagonalized numerically in real space. The electronic conductance calculated by the Thouless formula is averaged over random samples of disorder. The strength of bond disorder is changed within the width whose magnitude is typical to thermal fluctuation of phonons as estimated in C_{60} and carbon nanotubes (8,13).

This paper is organized as follows. In the next section, we consider disorder effects on the density of states. In the third section, the average conductance at the Fermi energy is discussed. The paper is summarized in the last section.

DENSITY OF STATES

Figure 1 shows one example of the density of states (DOS) and electronic conductance of the (5,5) nanotube with the disorder strength $t_s = 0.15t$. In Figs. 1 (a) and (b), the strong one-dimensional peaks in the DOS are broaden and suppressed. However, the flat DOS near the Fermi level does not change so much, because the DOS in these energies is nearly the same. Figure 1 (c) shows the conductance in the energy region $-1.5t \leq E \leq 1.5t$. The conductance at the energies less than $-0.6t$ and larger than $0.6t$, i.e. in the inner conduction (valence) band regions, is around

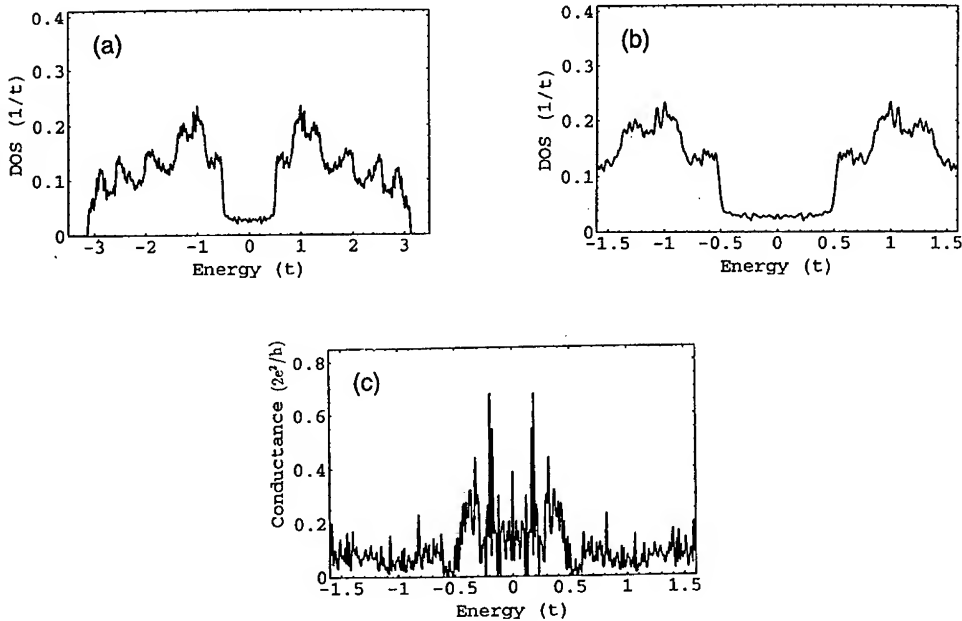


FIGURE 1. Density of states (DOS) and electronic conductance of one sample of the (5,5) nanotube with the disorder strength $t_s = 0.15t$. Figures 1 (a) and (b) show the entire DOS and the enlarged DOS of the energy region $-1.5t \leq E \leq 1.5t$, respectively. Figure 1 (c) shows the electronic conductance in units of $2e^2/h$ of the low energy regions.

0.1 in the unit of $2e^2/h$. This magnitude is one order smaller than that in the clean system. On the other hand, the conductance is around the value 0.3 ($2e^2/h$) in the energy region $-0.6t \leq E \leq 0.6t$. This value is of the same order of magnitude as that of the clean system. Therefore, we find that the conductance in the inner valence (conduction) band regions is easily suppressed by the disorder. However, the conductance near the Fermi level is not suppressed so much, since conduction and valence bands are mutually connected in the metallic carbon nanotube, and therefore the Fermi level is located just at the center of the whole energy bands. Then, the disorder effects are smallest at the center of the entire energy bands, which means the extended nature of electronic states around the Fermi energy.

ELECTRONIC CONDUCTANCE

In this section, we look at the conductance at the Fermi energy $E = 0$ and dependence on the disorder strength t_s .

Figure 2 shows the average conductance at $E = 0$ as a function of t_s . The squares, circles, and triangles are for (5,5), (10,10), and (9,0) nanotubes, respectively. The conductances at $t_s = 0$ are about 0.5, 0.6, and 0.9, in units of $2e^2/h$ for (5,5), (10,10), and (9,0) nanotubes. The magnitude at $t_s = 0.15t$ is at about 0.3 ($2e^2/h$) for the three plots. Therefore, the conductance of (5,5) nanotube decreases by the factor about 1/1.6. The conductance of the (10,10) nanotube decreases by the factor about 1/2. The conductance of the (9,0) nanotube decreases by the factor about 1/3. Thus, the electronic conductance of the realistic system with thermal fluctuations of phonons might be decreased by the factor $1/2 \sim 1/3$, naturally.

The extended nature of electronic states at the Fermi energy will contribute to several interesting transport properties observed in experiments. The ballistic

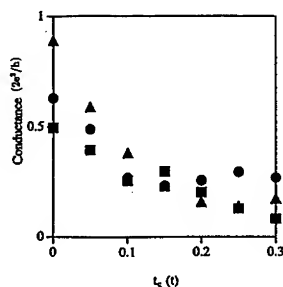


FIGURE 2. The average conductance at the Fermi energy $E = 0$ as a function of t_s . The squares, circles, and triangles show the numerical data of (5,5), (10,10), and (9,0) nanotubes, respectively.

conduction and the quantum single electron tunneling are several examples of the recent experiments of carbon nanotubes. We expect further developments of experimental transport studies, which will promote theoretical investigations of carbon nanotubes as well.

SUMMARY

Disorder effects on density of states and electronic conduction in metallic carbon nanotubes have been analyzed by a tight binding model with Gaussian bond disorder. Metallic armchair and zigzag nanotubes have been considered. We have obtained a conductance which becomes smaller by the factor $1/2 \sim 1/3$ from that of the clean nanotube. This decrease mainly comes from lattice fluctuations of the width which is comparable to thermal fluctuations. We have also found that the suppression of electronic conductance around the Fermi energy due to disorder is smaller than that of the inner valence (and conduction) band states. This is due to the extended nature of electronic states around the Fermi energy

REFERENCES

1. M. S. Dresselhaus, G. Dresselhaus, and P. C. Eklund, "Science of Fullerenes and Carbon Nanotubes", (Academic Press, San Diego, 1996).
2. R. Saito, G. Dresselhaus, and M. S. Dresselhaus, "Physical Properties of Carbon Nanotubes", (Imperial College Press, London, 1998).
3. J. W. Mintmire, B. I. Dunlap, and C. T. White, Phys. Rev. Lett. **68**, 631 (1992).
4. N. Hamada, S. Sawada, and A. Oshiyama, Phys. Rev. Lett. **68**, 1579 (1992).
5. R. Saito, M. Fujita, G. Dresselhaus, and M. S. Dresselhaus, Appl. Phys. Lett. **60**, 2204 (1992).
6. K. Tanaka, K. Okahara, M. Okada, and T. Yamabe, Chem. Phys. Lett. **193**, 101 (1992).
7. K. Harigaya, Phys. Rev. B **45**, 12071 (1992).
8. K. Harigaya and M. Fujita, Phys. Rev. B **47**, 16563 (1993).
9. J. W. G. Wildöer, L. C. Venema, A. G. Rinzler, R. E. Smalley, and C Dekker. Nature **391**, 59 (1998).
10. T. W. Odom, J. L. Huang, P. Kim, and C. M. Lieber, Nature **391**, 62 (1998).
11. J. T. Edwards and D. J. Thouless, J. Phys. C **5**, 807 (1972).
12. D. C. Licciardello and D. J. Thouless, J. Phys. C **11**, 925 (1978).
13. K. Harigaya, Phys. Rev. B **48**, 2765 (1993).

Electronic structure studies of carbon nanostructures using electron energy-loss spectroscopy in transmission

T. Pichler¹, R. Friedlein¹, M. Knapfer¹, M.S. Golden¹, J. Fink¹, K. Mukhopadhyay², T. Sugai², H. Shinohara², Th. Cabioch³

¹ *Institut für Festkörper- und Werkstofforschung Dresden, Postfach 270016, D-01171 Dresden.*

² *Faculty of Science, Department of Chemistry, Nagoya University, Nagoya 464-8602, Japan*

³ *Université de Poitiers, Laboratoire de Métallurgie Physique, UMR 6630 CNRS, Bâtiment SP2MI, Teleport 2, Bd 3, BP 179, 86660 Futuroscope Cedex, France.*

Abstract. In this contribution we present a comparative study of pristine and potassium intercalated carbon nanostructures such as bundles of single-wall carbon nanotubes (SWNTs), multi-wall carbon nanotubes (MWNTs) and carbon onions using electron energy-loss spectroscopy in transmission. Upon potassium doping a maximal intercalation of $C/K \approx 7$ (SWNTs), 8 (MWNTs) and 10 (onions) was found. From the low energy loss function we analysed the optical properties of the investigated material. However only in the intercalated SWNT-bundles a charge carrier plasmon could be identified.

INTRODUCTION

Carbon nanostructures are a promising new member of the growing family of novel fullerene-based materials, and represent model building blocks for nanoengineering as a result of their special electronic [1] and mechanical [2] properties. Nanotubes can be envisaged as rolled-up graphene sheets which are capped with fullerene-like structures. Their electronic properties are predicted to vary depending upon the wrapping angle and diameter of the graphene sheet, thus giving either metallic or semiconducting behavior [3]. However, macroscopic samples generally contain a distribution of tubes with different diameters and chirality and thus the experimentalist measures an averaged picture of their properties. Therefore most of the work has been performed on individual nanostructures. The optical properties have been analysed using spatially-resolved electron energy-loss spectroscopy (EELS) of individual single bundle of SWNTs [4], MWNTs [5] and carbon onions [6]. However, these measurements with high spatial resolution are hindered by the low energy and momentum resolution. Recently, measurements of purified SWNTs using high resolution EELS in transmission have been performed and allowed for the first time to identify and assign the low energy excitations in a bulk sample [7].

In this contribution, we present a comparative study of the electronic structure of pristine and fully intercalated carbon nanostructures such as SWNT-bundles, MWNTs and carbon onions using EELS in transmission.

EXPERIMENTAL

SWNT-bundles were produced by the laser vaporization of graphite [8]. The material was purified as described in Ref. [9] and consists of SWNT-bundles with approximately 1.4 nm mean diameter of the SWNTs and a diameter of the bundles of 5-20 nm. MWNTs (inner diameter of 2.5-3 nm, outer diameter 8-10 nm) were prepared by the catalytic decomposition of acetylene as described in Ref. [10,11]. Carbon Onions (mean diameter 10 nm) were synthesized by carbon ion implantation into thin silver films deposited onto fused silica substrates [12]. Free-standing films for EELS with an effective thickness about 1000 Å were prepared on standard copper electron microscopy grids via three different methods: A) Vacuum filtration of a SWNT suspension in a 0.5 % surfactant (Triton X100) solution in de-ionised water, with a SWNT concentration of ~ 0.01 mg/ml. The surfactant was then rinsed off and the grid was transferred into the spectrometer. B) Using an airbrush to spray a MWNT/ethanol suspension onto KBr single crystals. After subsequent dissolution of the KBr in distilled water the thin film was floated off, captured by a TEM grid and transferred into the spectrometer. C) Recorporation of carbon onions with TEM grids from the fused silica surface after removing the silver.

EELS was carried out in a purpose-built high-resolution spectrometer [13] which combines both good energy and momentum resolution. For the data shown here, an energy and momentum resolution of 115 meV and 0.05 Å^{-1} (valence band excitations) and of 160 meV and 0.06 Å^{-1} (core excitations) were chosen. Unlike many electron spectroscopies, EELS in transmission is volume sensitive, which in the context of the inhomogeneous nature of bulk samples of the nanostructures is a crucial point. All spectra were recorded at room temperature.

RESULTS AND DISCUSSION

By setting the energy-loss to zero, we can carry out electron diffraction experiments in-situ in the EELS spectrometer. Fig. 1 shows electron diffraction data for purified bundles of SWNT, MWNTs and carbon onions in comparison to graphite and C_{60} . The data of the SWNT bundles are consistent with the published x-ray diffraction results which were interpreted in terms of a triangular lattice formed by the individual SWNTs in the ropes [8]. The electron diffraction of MWNTs and carbon onions show that the samples are highly disordered. Similar to amorphous carbon very broad maxima at 1.8 Å^{-1} (reflection from graphite planes) and at about 3 Å^{-1} (reflection corresponding to the distance between planes) are observed.

In Fig 2. the EELS C1s excitation spectra as well as the K2p excitation spectrum of pristine and fully intercalated samples of purified SWNT bundles, MWNTs, carbon onions and highly oriented pyrolytic graphite (HOPG) are depicted. The C1s spectra of the pristine nanostructures strongly resemble that of polycrystalline

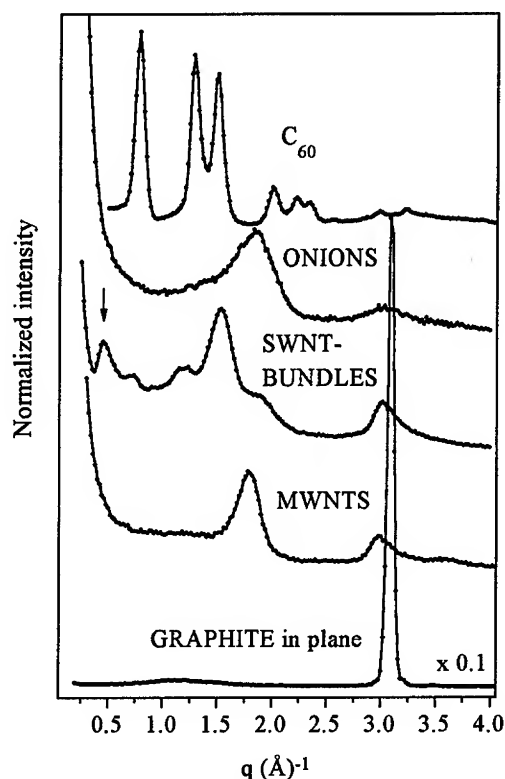


FIGURE 1. Electron diffraction profiles for graphite ((100) direction), SWNT-bundles, MWNTs and carbon onions. The arrow points out the peak corresponding to the triangular SWNT rope lattice.

graphite as can be seen by comparison with directional-dependent C1s excitation measurements [14,15]. To estimate the intercalation level the carbon to potassium ratio for the intercalated nanostructures was derived from the relative intensity of the C1s and the K2p absorption lines [16]. Intercalation up to C/K \approx 7, 8 and 10 is observed for SWNT bundles, MWNTs and carbon onions, respectively. This shows that in all these carbon nanostructures intercalation up to about the same level is possible.

In Fig. 3 the optical properties of the three different nanostructures are analysed. The left-hand panel of Fig. 3 shows the loss function ($\text{Im}(-1/\epsilon(\mathbf{q}, E))$) of purified SWNT bundles, MWNTs and carbon onions for $q=0.15 \text{ \AA}^{-1}$. The position of the π plasmon, which is corresponding to the collective response of the π electron system under investigation, is lowest for the SWNT-bundles (5.4 eV with a shoulder at 6.4 eV). In MWNTs the π -plasmon line is at 6.3 eV, for the carbon onions at 6 eV. In the low energy region the loss function of the SWNTs shows distinct peaks that are related to the interband transitions between characteristic DOS singularities on

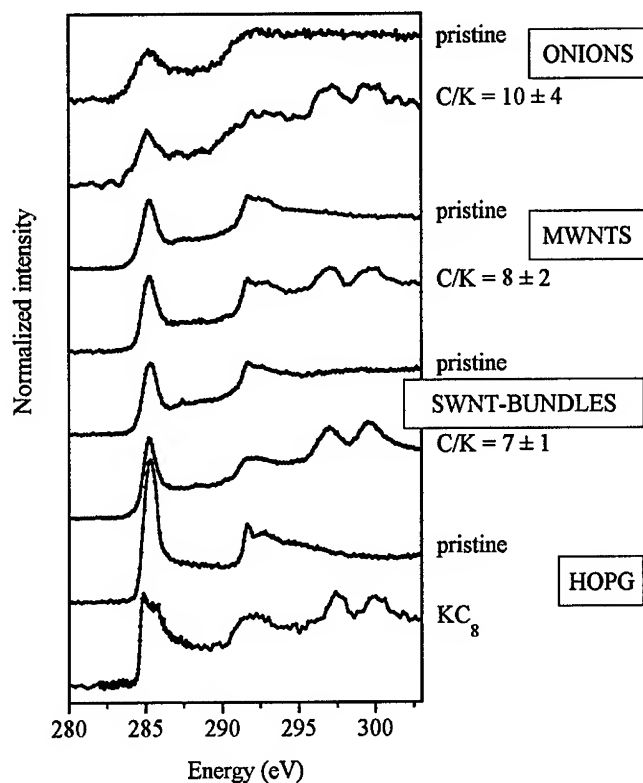


FIGURE 2. C1s excitation spectra of pristine samples and for K-doped samples with saturated intercalation of HOPG (in plane), SWNT-bundles, MWNTs and carbon onions.

the individual tubes [7]. No features are resolvable in this region for the MWNTs and carbon onions. In the case of the MWNTs this can be explained by the small energy separation between the optical allowed interband transitions. The right-hand panel of Fig. 3 shows what happens upon intercalation. In all compounds a small downshift of the position of the π plasmon as well as a broadening is observed. For the carbon onions a splitting into two components at 6.2 eV and at 5.3 eV occurs. However in the low energy region only in the case of the intercalated SWNT-bundles a charge carrier plasmon could be identified and has been used recently to calculate the optical conductivity in the SWNT intercalation compound [16]. For the intercalated MWNTs and intercalated onions the absence of this charge carrier plasmon can be explained in a similar way as for pristine graphite. The plasmon is strongly overdamped by the huge number of decay channels into interband transitions.

The financial support of the DFG (FI 439/8-1) and the SMWK (4-7531.50-03-823-98/5) is appreciated. K.M. thanks the 'Advance Process Research for the Future' program of the JSPS for a fellowship.

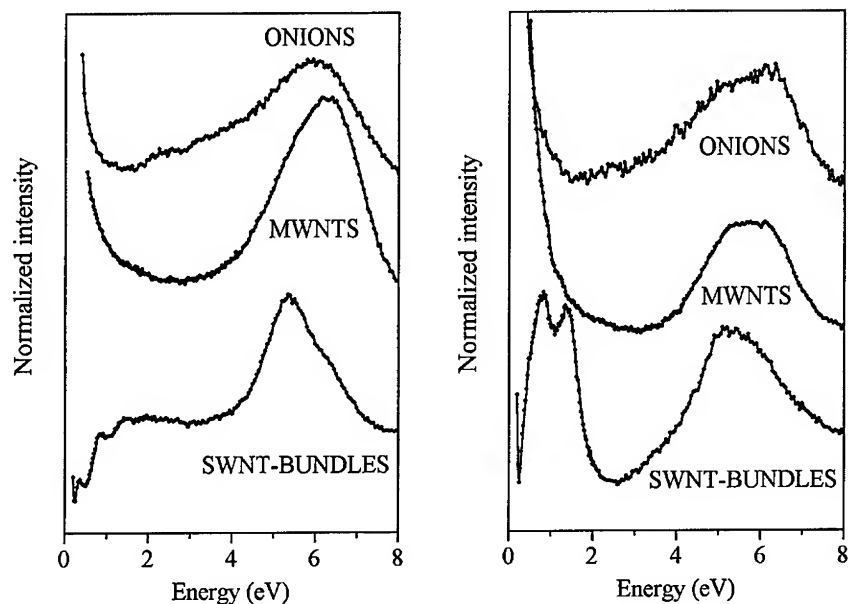


FIGURE 3. Left panel: The loss function of pristine bundles of SWNTs, MWNTs and carbon onions for $q=0.15 \text{ \AA}^{-1}$. Right panel: The loss function of fully intercalated bundles of SWNTs, MWNTs and carbon onions for $q=0.15 \text{ \AA}^{-1}$.

REFERENCES

1. S. Saito, *Science* **278**, 77 (1997); L. Chico et al., *Phys. Rev. Lett.* **76**, 971 (1996).
2. E.W. Wong, P.E. Sheehan and C.M. Lieber, *Science* **277**, 1971 (1997).
3. e.g. M. S. Dresselhaus, G. Dresselhaus and P. C. Eklund, *Science of Fullerenes and Carbon Nanotubes*, (Academic Press Inc., San Diego, 1996).
4. R. Kuzuo et al., *Jpn. J. Appl. Phys.* **33**, L1316 (1994).
5. R. Kuzuo, M. Terauchi and M. Tanaka, *Jpn. J. Appl. Phys.* **31**, L1484 (1992); P. M. Ajayan, S. Ijima and T. Ichihashi, *Phys. Rev. B* **49**, 2882 (1994); A. Bursill et al., *Phys. Rev. B* **49**, 2882 (1994).
6. T. Stöckli et al., *Phys. Rev. B* **57**, 15599 (1998).
7. T. Pichler et al., *Phys. Rev. Lett.* **80**, 4729 (1998).
8. A. Thess et al., *Science* **273**, 483 (1996).
9. A. G. Rinzler et al., *Appl. Phys. A* **67**, 29 (1998).
10. K. Mukhopadhyay et al., *Jpn. J. Appl. Phys.* **37**, L 1257 (1998);
11. K. Mukhopadhyay et al., *Chem. Phys. Lett.* **303**, 117 (1999)
12. Th. Cabioch et al., *Appl. Phys. Lett.* **73**, 3096 (1998).
13. J. Fink, *Adv. Electron. Electron Phys.* **75**, 121 (1989) and references therein.
14. P. E. Batson, *Phys. Rev. B* **48**, 2608 (1993).
15. Y. Ma et al., *Phys. Rev. Lett.* **71**, 3725 (1993).
16. T. Pichler et al., *Solid State Communic.* **109**, 721 (1999).

The effects of dimensionality on the π -plasmon-dispersion in multi-wall carbon nanotubes

R. Friedlein¹, T. Pichler¹, M. Knupfer¹, M. S. Golden¹,
K. Mukhopadhyay², T. Sugai², H. Shinohara², and J. Fink¹

¹*Institut für Festkörper- und Werkstofforschung Dresden, Postfach 270016, D-01171 Dresden*

²*Faculty of Science, Department of Chemistry, Nagoya University, Nagoya 464-8602, Japan*

Abstract.

In this contribution we present the momentum-dependent dielectric response function of multi-wall carbon nanotubes (MWNTs) measured using electron energy-loss spectroscopy (EELS) in transmission. Of particular interest here is the dispersion relation of the π -plasmon, which represents the collective excitation of the π -electron system. At high momentum transfer the plasmon dispersion in the MWNTs parallels that of graphite, whereas in the long-wavelength-limit a significant reduction of the plasmon energy is observed. This can be understood as a consequence of the one-dimensionality of the π -electron system in the MWNTs indicating a suppression of the electron-electron Coulomb interaction at low momenta due to the spatial confinement of the electrons.

INTRODUCTION

Both single- and multi-wall carbon nanotubes exhibit interesting electronic properties which are known to be related to the low-dimensional nature of the electronic system. Prominent examples are van-Hove singularities in the density of states [1,2] and Luttinger liquid behaviour being recently found to influence the transport properties of single-wall nanotube (SWNT) bundles [3]. Electron transport through bundles is imagined to occur through individual metallic tubes embedded in other semiconducting and metallic tubes [4] implying a negligible hopping between the tubes. However, the influence of the environment on the 1D electronic states is still under debate and also not well known for multi-wall nanotubes which are imagined to consist of individual sheets stacked into each other.

Electrons on individual tubes interact via the Coulomb interaction that can modify properties compared to those of individual tubes. Due to the spatial electron confinement in a one-dimensional solid the electron-electron Coulomb interaction is thought to be strongly altered in comparison to a free electron gas or for electrons in a 3D solid without crystal local field effects [5–7] where the Fourier-transformed Coulomb potential is proportional to $1/q^2$ (q is the momentum of the electron). The

modified interaction can then be called an effective Coulomb interaction $v_{q,eff}$. The dielectric function $\epsilon(\omega, \vec{q}) = \epsilon_\infty - v_{q,eff} \cdot \chi(\omega, \vec{q})$ is partly determined by $v_{q,eff}$. In this expression ϵ_∞ is the background dielectric constant and $\chi(\omega, \vec{q})$ is the response function of the many-body system (see e.g. [8]).

In this contribution we report on a study of the collective excitation of the π -electrons in MWNTs by measuring the energy-loss function $\text{Im}(-1/\epsilon(\omega, \vec{q}))$ in which plasmons are identified as pronounced peaks. Our attempt was to extract information on $v_{q,eff}$ of the π -electrons using the assumption that the screening of the σ -electrons can be included in ϵ_∞ . We used momentum-dependent electron energy-loss spectroscopy (EELS) in transmission which allows the determination of the dispersion relation of electronic excitations. It was already successfully applied to a variety of materials, among them 1D and quasi-1D systems like oriented trans-polyacetylene [9], SWNTs [2] and $(\text{TaSe}_4)_2\text{I}$ [10].

EXPERIMENTAL

We investigated MWNT material of a high purity and of a narrow distribution of an inner diameter of 2.5-3 nm and an outer diameter of 10-12 nm thus consisting of 10 to 14 layers. They were synthesized by catalytic decomposition of acetylene at 700°C over cobalt and vanadium particles embedded in zeolite [11]. Thin films of a thickness of about 100 nm as needed for electron spectroscopy in transmission were made by airbrushing [12] from a clear brownish suspension in methanol onto a sodium chloride single crystal using hot nitrogen as carrier gas. The films could be floated off in distilled water and fished on standard gold microscopy grids. The measurements were performed in UHV with a purpose-built high-resolution spectrometer with a primary electron energy of 170 keV [8] by choosing an energy resolution of 115 meV and an momentum resolution of 0.05 \AA^{-1} .

RESULTS AND DISCUSSION

The loss spectra recorded for various momentum transfers are plotted in the left panel of Fig. 1. Two dominant features can be recognized which represent the π -plasmon at about 5-7 eV and the $\sigma + \pi$ -plasmon at about 22 eV. These values are consistent with reported values from EELS measurements on spatially resolved MWNTs [13]. At any q the π -plasmon energy $\omega_\pi(q)$ of MWNTs lays in between those of graphite (parallel to the graphene layers) and non-oriented SWNTs arranged in bundles [2]. This is expected since MWNTs consist of a few rolled-up graphene layers. It can be seen in the right panel of Fig. 1 that the slope of the dispersion relation of MWNTs shows a strong reduction of $\omega_\pi(q)$ at low momentum transfer $q < 0.2 \text{ \AA}^{-1}$.

In a cylindrical system like nanotubes the momentum transfer perpendicular to the tubes, q_\perp , is related to an angular momentum $l = rq_\perp$ that depends on the radius of the tube. It was predicted [6,14] that plasmon excitations in tubes can be classified with respect to the angular momentum by discrete values $L = 0, 1, \dots$

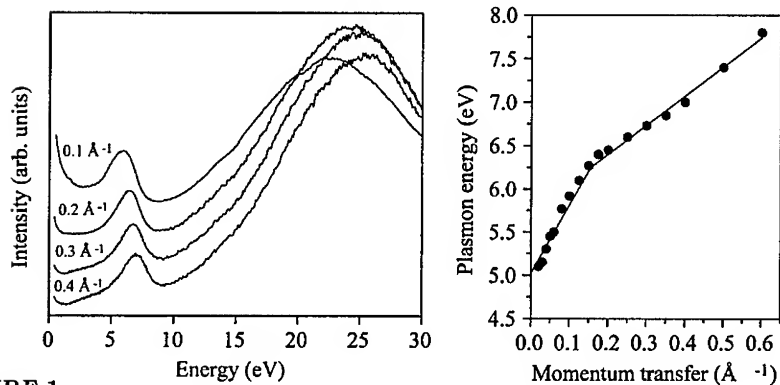


FIGURE 1.

Left: Electron energy-loss function for various q of non-oriented MWNTs.

Right: π -plasmon position of MWNTs (full line is a guide for the eye) as a function of q .

These plasmon modes $\omega_\pi(L, q_\parallel)$ have generally different dispersion relations. But for large diameter tubes ($d > 7$ nm) like the outer shells of the MWNTs they merge [14]. Therefore we were able to conclude that inspite of the non-orientation of the tubes the slope of the measured MWNT dispersion relation is determined by changes connected with the momentum transfer projected onto the tube axis, q_\parallel . To understand the behaviour of $\omega_\pi(L, q_\parallel)$ one can consider a simple Lorentz model without damping where the dielectric function is given by $\epsilon(\omega, \vec{q}) = \epsilon_\infty - f/(\omega^2 - \omega_0^2)$. The plasmon position ω_π is then $\omega_\pi = (\omega_0^2 + f)^{1/2}$. Comparing this with the expression of $\epsilon(\omega, \vec{q})$ as given in the introduction one can see that the effective Coulomb potential $v_{q,eff}$ alters the oscillator strength, f , of the excitation, i.e. a smaller $v_{q,eff}$ also means a reduction of f . Thus, the plasmon energy ω_π also has a lower value when $v_{q,eff}$ is smaller. The Coulomb potential for an individual tube was derived to be $\sim I_L(q_\parallel r)K_L(q_\parallel r)$ [15] with I_L and K_L as the L -dependent modified spherical Bessel functions. As an example for a tube with a diameter of 4 nm this potential for various L is plotted in Fig. 2 in comparison to the bare potential. Fig. 2 demonstrates that the modification of $v_{q,eff}$ compared to the 3D case is largest at small momentum, q_\parallel . Especially for high L the effective Coulomb potential at low q_\parallel is decreased by orders of magnitude (as it is the case for the investigated MWNTs). The observed dispersion of the π -plasmon in MWNTs can therefore be related to this strong reduction of $v_{q,eff}$ at low q . In the limit $q \rightarrow 0$ one would expect the π -plasmon to be near $\omega_0 = 4.5$ eV because the matrix-element-weighted joint density of states of all kinds of nanotubes shows a broad maximum at this energy (e.g. [2]).

We conclude that the measured MWNT π -plasmon dispersion relation shows a typical behaviour for a 1D electronic system indicating a suppression of the electron-electron Coulomb interaction in the long-wavelength limit due to the localization

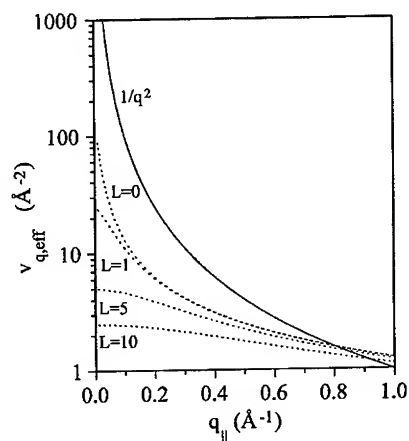


FIGURE 2.

The calculated effective electron-electron Coulomb potential $v_{q,eff} \sim I_L(q_{||}r)K_L(q_{||}r)$ for various modes L in an individual tube with an diameter of 4 nm in comparison to the bare potential $v_q \sim 1/q^2$ (following [15]).

of the electrons within the one-dimensional structures.

This work was supported in part by the SMWK (4-7531.50-03-823-98/5) and by the DFG (FI 439/8-1). K. M. thanks the advance process research for the future programme of JSPS for a fellowship.

REFERENCES

1. e.g. J. W. G. Wildöer et al., *Nature* **391**, 59 (1997).
2. T. Pichler et al., *Phys. Rev. Lett.* **80**, 4729 (1998).
3. M. Bockrath et al., *Nature* **397**, 598 (1999).
4. M. Bockrath et al., *Science* **275**, 1922 (1997).
5. S. Das Sarma and E. H. Hwang, *Phys. Rev. B* **54**, 1936 (1996).
6. C. Yannouleas, E. N. Bogachev, and U. Landman, *Phys. Rev. B* **53**, 10225 (1996).
7. R. Egger and A. O. Gogolin, *cond-mat/9803128*.
8. J. Fink, *Adv. Electron. Electron Phys.* **75**, 121 (1989) and references therein.
9. J. Fink and G. Leising, *Phys. Rev. B* **34**, 5320 (1986).
10. M. Sing et al., *Phys. Rev. B* **59**, 5414 (1999).
11. K. Mukhopadhyay et al., *Jpn. J. Appl. Phys.* **37**, L34 (1998); K. Mukhopadhyay et al., *Chem. Phys. Lett.* **303**, 117 (1999).
12. H. Kataura et al., *Synth. Metals*, in press.
13. R. Kuzuo, M. Terauchi, and M. Tanaka, *Jpn. J. Appl. Phys.* **31**, L1484 (1992).
14. M. F. Lin et al., *Phys. Rev. B* **53**, 15493 (1996).
15. M. F. Lin, and K. W.-K. Shung, *Phys. Rev. B* **50**, 17744 (1994).

Molecular Mechanics Study of Carbon Nanotubes

István László

*Department of Theoretical Physics, Institute of Physics
Technical University of Budapest, H-1521 Budapest, Hungary*

Abstract. The deformation of graphite surface and carbon nanotube under nanotube tip was examined with the help of a molecular mechanics calculation. We have used Brenner's potential for the covalent interactions. The tip-surface and interlayer interactions were described by a Lennard-Jones potential. The 21 nm long tip contained 1680 carbon atoms and had the form of a (5,5) nanotube closed by two halves of a C_{60} molecule at the ends.

INTRODUCTION

Since the invention of the scanning tunneling microscope (STM) [1] and the related atomic force microscope (AFM) [2] it is possible to build structures on atomic scale. The crucial element of these tools is the probe tip [3]. Usually the end of the tip is hundreds of angströms in diameter and in most of the cases the chemical composition and the shape are completely unknown. Ideally the tip should be as precisely defined as the object under investigation, and should maintain its integrity after repeated use. Dai et al. [4] attached individual nanotubes several micrometers in length to silicon cantilevers of conventional atomic force microscope. This nanotube tip could gain access to deeper recesses of surface structure than the conventional tips.

I THE METHOD

In our molecular mechanics simulation the tip was a 21 nm long (5,5) nanotube closed by two halves of a C_{60} molecule at the ends. It contained 1680 carbon atoms. First we studied the tip-graphite (Figure 1 a.), then the tip-nanotube (Figures 1 b. and 1 c.) interactions. The nanotube under study was a (10,10) tube of 520 carbon atoms with a length of 3.3 nm. It was on a graphite layer of 474 atoms. The covalent carbon-carbon interaction was given by a Brenner potential [5]. In the case of tube-layer, tube-tube and layer-layer interactions a 6-12 Lennard-Jones

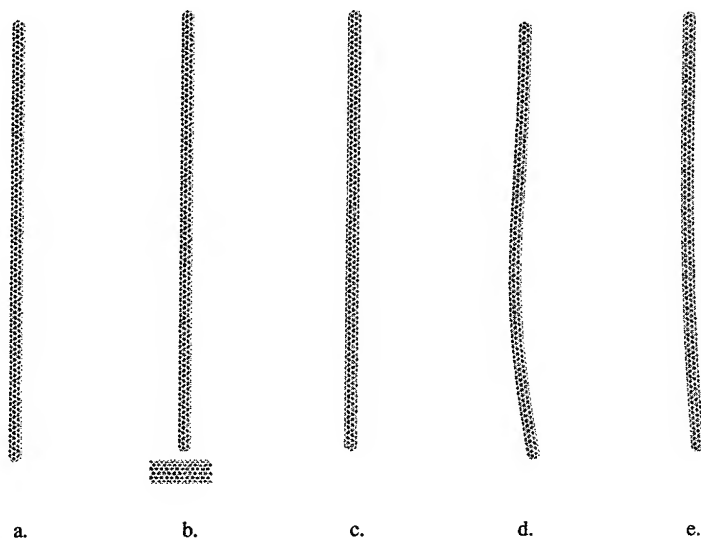


FIGURE 1. Tip-surface interaction. In each molecular mechanics relaxation the initial positions of the 474 carbon atoms in the lower graphite layer and that of the 30 upper carbon atoms in the tip-tube were kept. The graphite layer is parallel with the X-Y plane. The Z axis is directed upward and parallel with the tip. The (10,10) tube is placed along the X axis. The tip-graphite (a.), the tip-nanotube (b. front view and c. side view) interaction. The distortion of the (5,5) nanotube-tip after sliding on the graphite layer (d.) and on the (10,10) nanotube.(e.)

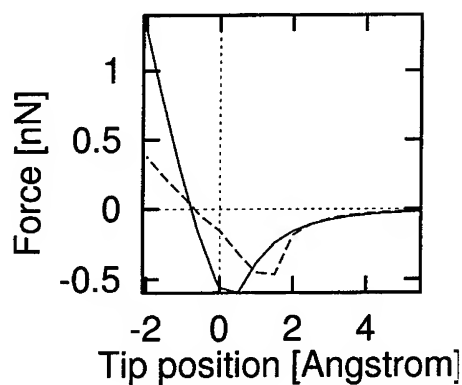


FIGURE 2. The force acting on the tip in the function of the tip position. The tip-graphite (solid line) and tip-tube interaction (dashed line). The tip position is described by the relative Z coordinate of the upper tip atom.

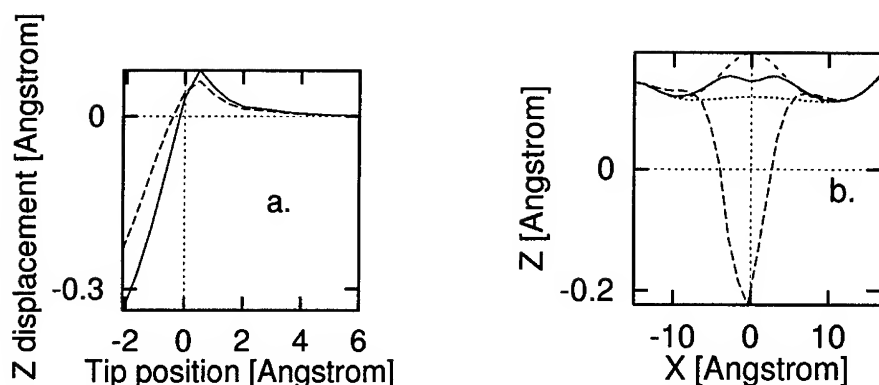


FIGURE 3. The relative displacement of the central atom (solid line) and a side atom (dashed line) on the graphite layer. The central atom is just on the tip axis and the side atom is 3.6\AA from it. (a.). The graphite layer deformations. Deformations at 0.0\AA tip position (solid line). Maximal deformation in the attraction region (upper dashed line). Deformation at -2.0\AA tip position (lower dashed line). (b.)

potential was used with Girifalco's parametrization [6,7]. The energy minimization was based on conjugate gradient method.

II RESULTS AND DISCUSSIONS

Figure shows the force on the tip in the function of the tip position. In the tip position 0.0\AA , the tip-surface distance was 3.35\AA for the unrelaxed case. In the relaxation processes the positions of the carbon atoms were not changed in the lower graphite layer and on the top 30 carbon atoms of the tip. When the tip approaches the surface there is a small attraction between the tip and the surface. This attraction changes to repulsion at smaller distances. There is a significant difference between the repulsion steepness of graphite-tip and tube-tip interaction. The repulsion part of the tip position-force function can be used to make differences between single and multi wall nanotubes. We can see the results for the tip-graphite interaction in Figure 3, and the tip-tube calculations are presented in Figure 4. The most interesting is the relative stiffness of the graphite surface and the radial deformation of the nanotube. It is in accordance with Ref. [8] This work has been supported by the Országos Tudományos Kutatási Alap (Grant No. T025017, T024138, T029813).

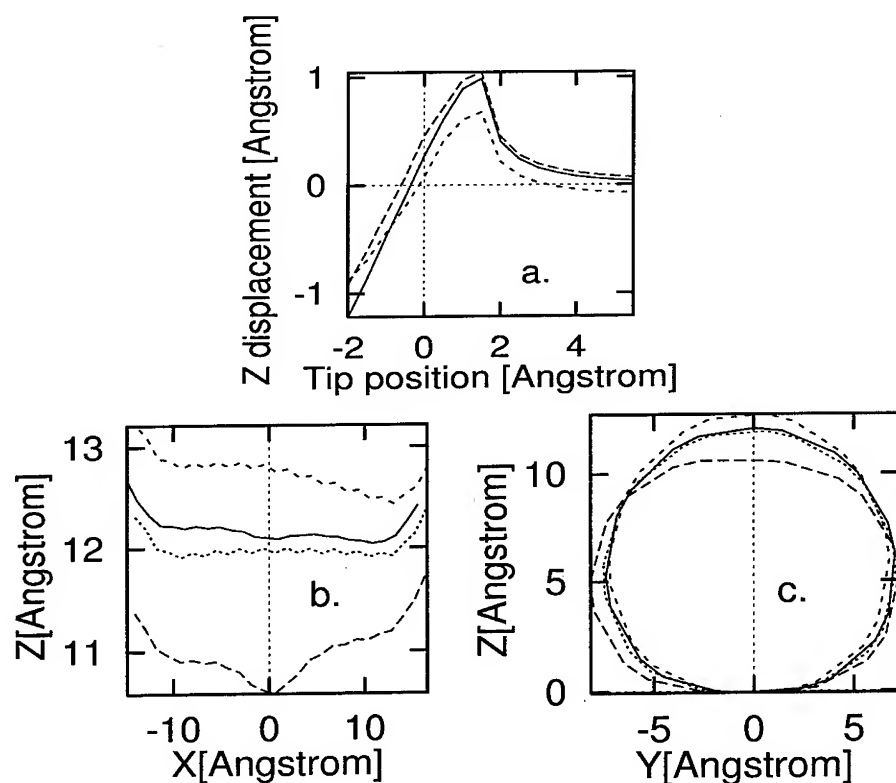


FIGURE 4. The relative displacement of the central atom (solid line), the side atom1 (upper dashed line) and the side atom2 (lower dashed line) on the (10,10) tube. The central atom is just on the tip axis and the side atom1 is 3.6\AA from it in the X direction. The side atom2 is 3.6\AA from the tip axis in the Y direction. (a.) The (10,10) tube deformation under the tip side in the X-Z plane. Deformations at 0.0\AA tip position (solid line). Maximal deformation in the attraction region (upper dashed line). Deformation at -2.0\AA tip position (lower dashed line). Deformation at 4.0\AA tip position in the repulsion region (dotted line). (b.) The (10,10) tube deformation in the Y-Z plane. The $X = 0.0\text{\AA}$ point is on the tip axis. Deformations at 0.0\AA tip position (solid line). Maximal deformation in the attraction region (upper dashed line). Deformation at -2.0\AA tip position (lower dashed line). Deformation at 4.0\AA tip position in the repulsion region (dotted line). (c.)

REFERENCES

1. Bining G., Rohrer H., Gerber Ch. and Weibel E., *Phys. Rev. Let.* **49**, 57 (1982).
2. Bining G., Quate C. F. and Gerber Ch., *Phys. Rev. Let.* **56**, 930 (1986).
3. Keller D., *Nature* **384**, 111 (1996).
4. Dai H., Hafner J. H., Rinzler A. G., Colbert D. T. and Smalley R. E., *Nature* **384**, 147 (1996).
5. Brenner D. W., *Phys. Rev. B* **42**, 9458 (1990).
6. Girifalco L. A. and Lad R. A., *J. Chem. Phys* **25**, 693 (1956).
7. Girifalco L. A., *J. Phys. Chem* **96**, 858 (1992).
8. Hertel T., Walkup R. E. and Avouris Ph., *Phys. Rev. B* **58**, 13870 (1998).

Knock-on Damage in Single Wall Carbon Nanotubes by Electron Irradiation

Brian W. Smith, David E. Luzzi

*Department of Materials Science and Engineering, University of Pennsylvania,
3231 Walnut Street, Philadelphia, PA 19104-6272, USA*

Abstract. We determine with high resolution transmission electron microscopy the effect of electron irradiation on isolated single wall carbon nanotubes. Observations of *in-situ* irradiation at electron energies of 80-400 keV suggest that a nanotube is preferentially damaged on surfaces that lie normal to the electron beam, and the threshold energy for knock-on damage is determined to be ~85 keV. Empirical results are corroborated by calculations based on established anisotropic ejection thresholds.

INTRODUCTION

High resolution transmission electron microscopy (HRTEM) is essential for the study of carbon nanotubes due to their small size. However, low atomic number materials are highly sensitive to electron irradiation, and carbon nanotubes are easily damaged during observation. Damage is believed to occur primarily by knock-on ejection, where an essentially elastic interaction between an incident electron and a carbon nucleus causes displacement of the corresponding atom from the lattice. Determination of the threshold electron energy below which knock-on damage does not occur facilitates the non-destructive characterization of these structures.

EXPERIMENTAL

The nanotubes for this investigation were synthesized by pulsed laser vaporization, acid purified, and vacuum annealed at Rice University (1). Individual single wall nanotubes (SWNTs) were irradiated and imaged in a JEOL 4000EX transmission electron microscope at an electron flux of $\sim 2.3(10)^{19}$

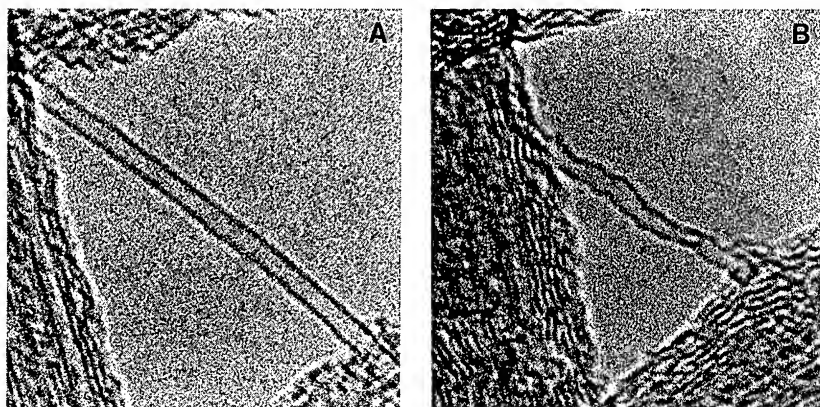


FIGURE 1. HRTEM images of an isolated SWNT (a) before irradiation, and (b) after irradiation with 100 keV electrons.

electrons $\text{cm}^{-2} \text{s}^{-1}$. An image of a SWNT is a projection of the specimen potential and consists of two dark parallel lines whose separation is equal to the tube's diameter. These lines correspond to where the beam is tangent with the tube.

Results and Discussion

The images in Figure 1 were recorded during irradiation of an isolated SWNT with 100 keV electrons. Figure 1a shows the unirradiated tube, whose walls are straight and parallel, suspended between two nanotube ropes.

Figure 1b shows the tube after a moderate electron dose. The imaged walls are distorted, and their separation is no longer uniform. Evolving lattice fringes are seen in the image of the surrounding microstructure, which suggests a graphitic ordering having basal planes oriented parallel to the beam. This is not further addressed in this article, although similar behavior has been observed in other carbonaceous systems (2).

In this instance, the imaged walls of the tube retain strong contrast even after prolonged irradiation. This suggests that carbon atoms are not ejected from surfaces that are tangent with the electron beam, such that the tube is not damaged on its sides. The observed distortion is attributed to knock-on damage to the top and bottom of the tube, thereby destroying the cylindrical rigidity of the molecule. Consequently, the sides are less constrained and can adopt different conformations, with the sp^2 hybridized carbon atoms easily accommodating large out-of-plane bond angle distortions.

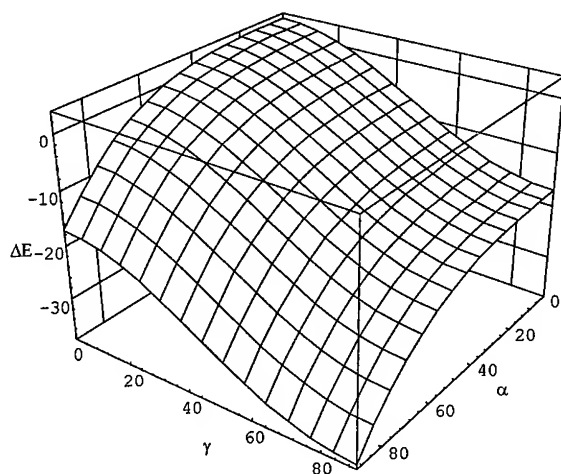


FIGURE 2. ΔE versus (α, γ) for $V = 100$ keV. $\Delta E > 0$ only for small α, γ .

Different behaviors are observed if higher or lower energy electrons are used. Irradiation with 200 keV electrons produces an amorphous-like structure whose image has less contrast than that of the unirradiated tube. The imaged walls are seen to segment during irradiation, suggesting no anisotropic selectivity.

Conversely, irradiation with 80 keV electrons produces essentially no change in the tube's image, even after high total electron dose. This indicates that the knock-on threshold energy is greater than 80 keV. It is estimated from the empirical results that this threshold is ~ 85 keV.

THEORY AND CALCULATIONS

The experimental observations are explained by considering the energy transferred to a carbon atom during a scattering event and the energy barrier that the atom must overcome to escape from the nanotube. To facilitate this discussion, the following geometries are defined: \mathbf{n} is the normal vector to the tangent plane containing the atom; \mathbf{r} is the direction of impulse to that atom; \mathbf{b} is the direction of the electron beam; α is the angle between \mathbf{n} and \mathbf{r} ; γ is the angle between \mathbf{b} and \mathbf{r} . It can be shown that:

$$\Delta E = E_{\text{transfer}} - E_{\text{escape}} = \frac{2V(V + 2m_0c^2)}{m_0c^2} \cos^2 \gamma - f(\alpha) \quad (1)$$

(3) where m_C is the mass of the carbon atom, V is the incident electron energy, and $f(\alpha)$ is a monotonically increasing function fit using a least squares method to established escape thresholds (4).

An ejection can occur for those (α, γ) having positive ΔE . For each such condition, the position of the corresponding atom relative to the beam can be described by the angle $\delta = \alpha + \gamma$ between \mathbf{n} and \mathbf{b} . The largest possible δ for a certain V is denoted $\delta_{\max, V}$ and is obtained by maximizing δ along the intersection of the ΔE surface with the plane $\Delta E = 0$.

The plot of ΔE versus (α, γ) for $V = 100$ keV is shown in Figure 2. It is calculated that $\delta_{\max, 100 \text{ keV}} \sim 55^\circ$, indicating that only those atoms within $\pm 55^\circ$ of \mathbf{b} are susceptible to knock-on damage. The selective destruction of the top and bottom surfaces of a SWNT is predicted, corroborating the empirical results.

It is similarly calculated that $\delta_{\max, 200 \text{ keV}} = 90^\circ$ and $\delta_{\max, 80 \text{ keV}} = 0^\circ$, indicating that every atom comprising a SWNT can be ejected by 200 keV electrons while no atom can be ejected by 80 keV electrons. The threshold energy is determined to be ~ 86.3 keV, corresponding to where the ΔE surface is tangent to the $\Delta E = 0$ plane.

CONCLUSION

We conclude, with excellent agreement between calculation and experiment, that the threshold energy for knock-on damage to a SWNT is approximately 85 keV. More energetic electrons can eject carbon atoms located within $\pm \delta_{\max, V}$ of the beam, where $\delta_{\max, V}$ increases rapidly with increasing electron energy.

ACKNOWLEDGEMENT

The material for this study was provided by R.E. Smalley's group at Rice University. Funded in part by NSF DMR-98-02560.

REFERENCES

1. Rinzler, A.G. *et al.*, *Appl. Phys. A* **67**, 29 (1998).
2. Ugarte, D., *Nature* **359**, 707-709 (1992).
3. Averbach, R.S., and Diaz de la Rubia, T., *Solid State Physics*, New York: Academic Press, 1997, vol. 51, pp. 287.
4. Crespi, V.H. *et al.*, *Phys. Rev. B* **54**, 5927-5931 (1996).

Sliding, stretching, and tapering: recent structural results for carbon nanotubes

Vincent H. Crespi, Peihong Zhang and Paul E. Lammert

*Department of Physics and Center for Materials Physics, The Pennsylvania State University,
104 Davey Lab, University Park, PA, 16802-6300*

Abstract. Typical multiwalled carbon tubes have interlayer incommensuration both azimuthally and axially. Finite size effects then imply that the maximal energetic barrier to interlayer sliding in nanoscale multiwalled carbon nanotubes is, surprisingly, independent of the size of the system. Turning attention from post-synthesis interwall interactions to interwall fluctuations during growth, we note that certain thermal fluctuations during multiwalled nanotube growth and tapering are locked into the final structure. The thermal dispersion in the diameters of tube endcaps reveals that multiwalled nanotubes grow at temperatures much lower than the maximum plasma temperatures for the arc discharge. Finally, considering only noncatastrophic structural distortions (i.e. plastic as opposed to brittle failure under tensile load), the onset of plastic deformation in carbon nanotubes depends very strongly on the wrapping index, as can be understood from a simple model of index-dependent defect-induced lengthening of the tube.

Several unusual properties combine to produce a barrier to interlayer sliding in multiwalled carbon nanotubes [1] which is subextensive. The difference in radii between successive layers forces the interlayer registry to shift constantly as one moves around the circumference. The axial period of a single layer is $3\sqrt{n^2 + nm + m^2}/\text{GreatestCommonFactor}(2n + m, n + 2m)$ bond-lengths, so that when two layers have $n_1/m_1 \neq n_2/m_2$, the two axial unit cells are incommensurate. The barrier to sliding is zero for perfect incommensuration, since the system averages over all possible interlayer registries. Finite incommensurate structures have only approximate averaging; the barrier to sliding then arises from the fluctuations in the finite-sampled registry-averaged interlayer binding energy, (i.e. the finite sampling of a periodic function at an incommensurate period). The upper bound on the error scales inversely with size. The corrugation in the interlayer interaction energy per atom then scales as $1/N$ and the total interlayer corrugation is independent of N . Except for the fluctuations about the overall trend, the energetic barrier in axial and azimuthal interlayer sliding of perfectly rigid multiwalled tubes with walls at different helical angles is roughly independent of the radius and length of the nanotube. This contrasts with the intrinsic linear scaling of the corrugation in

more typical commensurate systems without external load.

Incommensurate systems undergo distortions which improve registry within finite domains. While the elastic cost of an in-plane distortion is second order in the displacement, a generalized in-plane coordinate Q exists for which the energy gain due to enhanced interlayer registry is linear; $E(Q) = -AQ + BQ^2$. The extreme structural anisotropy of graphite ($Ba/A \sim 10^3$) implies that the equilibrium distortion is roughly $a/2000$, yielding an energy of $E \sim 0.002$ meV/atom, a thousand times smaller than the raw interlayer corrugation. This finite-domain registry is then important only for graphitic structures containing many atoms. Deviations from circular cross-section or end-of-tube edge effects can hinder interlayer rotation or sliding. Although the distortions induced by pentagons at closed nanotube ends could also hinder interlayer sliding, nanotube endcaps can be removed.

Not only do the multiple walls on certain nanotubes produce interesting inter-wall structural effects, but they also provide multiple structural events which shed light on local conditions during growth. Multiwalled carbon nanotubes are synthesized in an arc discharge wherein strong temperature gradients obscure the local temperature during tube growth. A careful thermodynamic analysis of structural features visible after tube growth can reveal the conditions necessary to produce these features. A single pentagonal defect in one wall of a nanotube initiates a taper [2,3], which can provide a well-controlled natural laboratory for studying the dynamics of the growth edge as a function of tube diameter. Tapering multiwalled nanotubes typically end in a series of blunt endcaps, each cap containing 5 additional pentagonal rings. The near-periodicity of these caps implies a well-defined crossover radius from exclusive hexagon formation (when the tapering walls are straight) to pentagon formation in the endcap. Therefore the dispersion in cap diameters can reveal the thermal fluctuations during growth. Transmission electron microscopy images of seven such tapers [2-4] yields average endcap diameters of 12.1 ± 1.4 , 12.5 ± 1.4 , 22.8 ± 2.0 , 15.8 ± 2.0 , 15 ± 1.7 , 13.9 ± 1.3 , and 13.7 ± 2.2 Å. When combined with calculations for the energetics of cap formation as a function of the cap diameter [5], these dispersions in diameter can measure the temperature during growth.

A tight-binding total energy [6] calculation shows that the most-favored configuration for pentagon addition becomes degenerate with hexagon addition in a tapering tube at a diameter of ~ 18 Å [5,7]. The slope of the pentagon-hexagon energy difference versus diameter links the dispersion in cap diameters to the temperature during growth. As a function of the diameter, the energy difference between hexagon and pentagon addition near the crossover region has the form $E_{\text{hexagon}} - E_{\text{pentagon}} \approx 0.072(18 - D[\text{Å}])$ eV [5].

We connect this result with the growth temperature by modelling the addition of successive polygons (i.e. hexagons and pentagons) to a tapering tube. Fig. 1 shows a simulation which adds successive polygons to a tapering tube under quasiequilibrium conditions. The dotted lines show the 68%-likelihood interval for closures surrounding the most-likely closure diameter. Using the experimental variation in cap diameter of $2.6 - 4.4$ Å, the temperature of the taper during

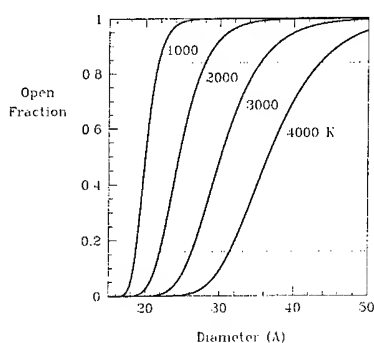


FIGURE 1. Theoretical probability for a tapering nanotube to contain exclusively hexagons as a function of the diameter of the growth edge. In other words, one minus the probability that a nanotube will cap abruptly at a given diameter, assuming that it was open at a diameter of 6 nm.

growth is in the range 850 — 1450 K, well below the commonly quoted ~ 4000 K temperature in the center of the arc discharge. This discrepancy is consistent with the large transverse temperature gradients around the arc. The theoretical endcap sizes are somewhat larger than those observed, because interwall covalent “spot welds” [8–10] enhance the stability of the inner wall. Since the theoretical closure diameters at the temperatures of interest are 0 — 10 Å larger than those observed, the interwall interaction provides a stabilization of $(0.072 \text{ eV/Å})(0 \leftrightarrow 10 \text{ Å}) \approx 0 - 0.7 \text{ eV}$, in reasonable agreement with the calculations [8,9], since formation of a single pentagon should break zero or one spot welds. This interwall interaction decreases the crossover diameter by suppressing pentagon formation, but most likely does not strongly affect the extraction of the growth temperature, since the energetics of spot welds is expected to depend only weakly on the tube diameter [8]. To be conservative, the analysis was repeated for slopes of 0.054 and 0.1 eV/Å, yields a 700 — 1800 K window of possible growth temperatures. Additional sources of fluctuations would only increase the variations in cap diameter; therefore our analysis in terms of thermal fluctuations is an *upper bound* on the temperature for these tubes.

In addition to the information they provide into synthesis conditions, nonhexagonal defects also play a critical role in determining the structural properties of carbon nanotubes such as the limiting stress before plastic distortion. Suggested nanotube structural applications rely upon their high elastic moduli [11]. A $\pi/2$ bond rotation in a graphitic network transforms four hexagons into two pentagons and two heptagons and lengthens the structure along the axis connecting the pentagons, thereby lowering the Gibbs free energy when under external tension. The efficiency of this strain release depends sensitively on the alignment between the

defect and the tube axis. Certain bonds in an (n,n) tube are aligned with the circumference, the optimal orientation from which to rotate for the release of strain. In contrast, the most favorable bonds in an (n,0) nanotube are misaligned by $\pi/6$ from the circumference.

We use tight binding molecular dynamics [6] to investigate the plastic deformation of carbon nanotubes under strain. To separate the effects of tube radius from those of wrapping indices, we study two sets of tubes: (n,0) tubes of different radius and (n,m) tubes of nearly equal radius. Since the critical tension for transformation to a defective phase is roughly proportional to the radius R , we define the reduced transition tension $f_c \equiv F_c/R$ which should vary weakly amongst nanotubes of identical wrapping angle. The C_{2v} symmetry of a bond rotation defect implies that physical quantities are well approximated by $a(R) + b(R) \cos 2\chi$ with radius-dependent coefficients $a(R)$ and $b(R)$ (χ is the angle between the circumference and the best bonds to rotate). We obtain a nearly linear dependence of transition tension on $\cos 2\chi$ for the family of approximately equal-radius tubes. The plastic limit varies widely from about 100 nN/nm for the (6,6) tube to about 180 nN/nm for the (12,0) nanotube. The radial dependence of the reduced transition tension is significant only for the smallest tubes [12].

The reduced transition tension is well approximated by $\frac{F_c}{R} = \frac{1}{R} \frac{\delta E}{\delta L} \Big|_{F=0}$. Since the length change δL depends upon only R and the integrated strain of the defect (with units of length squared), δL scales as R^{-1} . The $\frac{1}{R}$ dependence cancels the normalization prefactor and implies that the radial dependence of the critical tension f_c arises only through the defect energy δE . The defect energy in tubes of moderate radius is a weak function of the wrapping angle (4.0 ± 0.1 eV for the family $\{(12,0), (10,2), (9,3), (8,4), (6,6)\}$). Therefore the angular dependence of the plastic limit arises mainly from the angular dependence of the defect-induced elongation. These defect densities as a function of strain are interesting not only for the mechanical response: the bond rotation defect is also a plausible route towards modulating the electronic properties of carbon nanotubes [13]. The repulsive defect-defect interaction may tend to favor periodic defect arrangements and thereby minimize the random component of the defect-induced potential felt by the electronic states.

We examine the barrier to defect formation at critical external tension by calculating energy as a function of bond orientation. Of the kinetic pathways examined, the lowest barrier for bond rotation in a (6,6) tube occurs when the bond is tilted roughly 15 degrees out of plane, which yields an upper bound of approximately 4.0 eV for the barrier at the transition, decreasing with increasing strain (i.e. it is 8.5 eV at zero strain). This is substantially less than the barriers for the related Stone-Wales transformation in C_{60} or flat graphite [14]. The barrier at zero tension to return to the pure hexagonal state is 5.5 eV, so that the defects can be metastable. The pair of pentagon-heptagon defects (5-7 and 7-5) can be separated by additional bond rotations; under external stress the gliding of these defects is favored [15]. However, the local curvature energy is minimized when the oppositely directed curvature dipoles are adjacent, producing a barrier of 4.5 (8.0) eV for separation by

one (two) intervening layers of hexagons, although in certain situations this barrier may be lower [16]. This large energetic barrier will help suppress fission of the bond rotation defect. Recent experiments on nanotubes securely fixed at each end (e.g. embedded within blobs of solid material) and pressed transversely in the middle of the free section, give a 6% extension for the onset of plastic distortion [17], in accord with our theoretical results for the minimal extension for plastic distortion.

We acknowledge the Packard Foundation, Research Corporation, the National Science Foundation (DMR-9876232), the Penn State Center for Academic Computing, and the NPACI Supercomputer Center.

REFERENCES

1. S. Iijima, *Nature* **354**, 56 (1991).
2. S. Iijima, *Mater. Sci. & Eng.* **B19**, 172 (1993).
3. S. Iijima, T. Ichihashi, Y. Ando, *Nature* **356**, 776 (1992).
4. The last three data are from N. G. Chopra and A. Zettl, unpublished. The first two are from Ref. [2] and the middle two from [3].
5. V. H. Crespi and M. L. Cohen, unpublished. Outer walls were omitted from the simulation. Related calculations using a classical Tersoff potential [7] yielded a larger crossover diameter; apparently the classical potential overestimates the relative importance of dangling bonds.
6. C. H. Xu, C. Z. Wang, C. T. Chan, and K. M. Ho, *J. Phys. Condens. Matter* **4**, 6047 (1992).
7. A. Maiti, C. J. Brabec, C. Roland, J. Bernholc, *Phys. Rev. B* **52**, 14850 (1995); C. J. Brabec, A. Maiti, C. Roland and J. Bernholc, *Chem. Phys. Lett.* **236**, 150 (1995).
8. J.-C. Charlier, A. De Vita, X. Blase, R. Car, *Science* **275**, 646 (1997).
9. Y.-K. Kwon, Y. H. Lee, S.-G. Kim, P. Jund, D. Tománek, R. E. Smalley, *Phys. Rev. Lett.* **79**, 2065 (1997).
10. M. Buongiorno Nardelli, C. Brabec, A. Maiti, C. Roland, J. Bernholc, *Phys. Rev. Lett.* **80**, 313 (1998).
11. J. Tersoff and R. S. Ruoff, *Phys. Rev. Lett.*, **73**, 676(1994); T. W. Ebbeson, *Phys. Today*, **6**, 26 (1996); M. M. J. Treacy, T. W. Ebbeson and J. M. Gibson, *Nature*, **381**, 678 (1996); D. H. Robertson, D. W. Brenner, and J. W. Mintmire, *Phys. Rev. B* **45**, 12592 (1992); B. I. Yakobson, C. J. Brabec, and J. Bernholc, *Phys. Rev. Lett.* **76**, 2511 (1995); C. F. Cornwell and L. T. Wille, *Solid State Comm.* **101**, 555 (1996); J. P. Lu, *Phys. Rev. Lett.* **79**, 1297 (1997).
12. P. Zhang, P. Lammert, and V. H. Crespi, *Phys. Rev. Lett.* **81**, 5346 (1998).
13. V. H. Crespi, A. Rubio, and M. L. Cohen, *Phys. Rev. Lett.* **79** 2093 (1998).
14. A. J. Stone and D. J. Wales, *Chem. Phys. Lett.* **128**, 501 (1986); J.-Y. Yi and J. Bernholc, *J. Chem. Phys.* **96**, 8634 (1992); T. Kaxiras and K. C. Pandey, *Phys. Rev. Lett.* **61**, 2693 (1988)).
15. B. I. Yakobson, *Appl. Phys. Lett.* **72**, 918 (1998).
16. M. B. Nardelli, B. I. Yakobson, J. Bernholc, *Phys. Rev. B* **57**, 4277 (1998).
17. C. M. Lieber, personal communication.

VI. ELECTRONICS OF MOLECULAR NANOSTRUCTURES

Temperature Dependence of the Resistivity of Individual Multi-Walled Pure/Boron Doped Carbon Nanotubes at Elevated Temperatures

Bingqing Wei^{a)}, Ralph Spolenak, Philipp Kohler-Redlich,
Manfred Rühle, and Eduard Arzt

Max-Planck-Institut für Metallforschung, Seestraße 92, D-70174, Stuttgart, Germany

^{a)} Also with Department of Mechanical Engineering, Tsinghua University, Beijing 100084, China

Abstract The resistivities of individual multi-walled pure/boron doped carbon nanotubes have been measured in the temperature range from 25 to 300°C. The connection patterns were formed by depositing two-terminal tungsten wires on a nanotube using focused-ion-beam lithography. A semiconductor-like behavior was found for both B-doped and pure carbon nanotubes. B-doped nanotubes have a reduced room-temperature resistivity (7.4×10^{-7} - 7.7×10^{-6} Ωm) as compared to pure nanotubes (5.3×10^{-6} - 1.9×10^{-5} Ωm). The activation energy derived from the resistivity vs. temperature Arrhenius plots was found to be smaller for the B-doped (58 - 78 meV) than for the pure multi-walled nanotubes (190 - 290 meV).

INTRODUCTION

The electrical properties of carbon nanotubes have attracted much attention since their discovery in 1991¹. Ebbesen et al.² pioneered transport measurements of individual multi-walled nanotube (MWNT) by contacting the nanotubes using focused-ion-beam (FIB) lithography. Tans et al.³ deposited individual single-walled nanotube (SWNT) onto metallic electrode structures and measured electrical resistivities from cryogenic to room temperature. Resistivity measurements have also been reported for arc-produced MWNT bundles⁴ and pellets⁵, oriented films of MWNTs⁶, single ropes of SWNTs⁷ and individual MWNTs as the needle of a scanning-force microscope⁸. Lee et al. were the first to study the effect of doping on the conductivity of bulk samples of SWNTs⁹. Vapour-phase reaction with Br or K was found to increase the conductivity at RT by up to a factor of 30. This exohedral doping by intercalation is distinctively different from the substitutional doping which is investigated in this paper. The surface electronic structure of B-doped MWNTs has already been investigated using scanning tunnelling spectroscopy (STS)¹⁰. This study revealed that the doped tubes show semimetallic character with vanishing or narrow band gap. However, there are no reports concerning direct electronic transport measurements of individual boron doped tubes. The present measurements were performed from room temperature to higher temperatures, thereby covering the range of typical operating temperatures of potential practical applications of carbon nanotube based electronic devices.

EXPERIMENTAL DETAILS

The pure/boron doped MWNTs, with average outer and inner diameters about 20 nm and 2 nm, respectively, were prepared by arc-discharge method. The nanotube powder was dispersed in chloroform using ultrasonic agitation. A drop of this solution was then deposited on an oxidized Si wafer. The tungsten pads and the nanotube connecting tungsten leads were prepared by focused-ion-beam lithography (for details see Wei et al [11]). A typical contacting pattern for a two-terminal resistance measurement of an individual tube is shown in Fig.1. The temperature dependence measurements were carried out in air in the temperature range from 25 to 300°C. The current was measured for input voltages ranging from 5 to 25 V for each selected temperature.

RESULTS

Resistance for four individual pure nanotubes and four B-doped nanotube is measured with different distances between two contacts. The resultant resistivities at room temperature for individual pure and B-doped MWNTs are listed in Table 1. At room temperature the resistivity of B-doped tubes is found to be in the range 7.4×10^{-7} - $7.7 \times 10^{-6} \Omega\text{m}$, about one order of magnitude lower than that of the pure tubes (5.3×10^{-6} - $1.9 \times 10^{-5} \Omega\text{m}$). Hence, the conducting properties of B-doped tubes reach those of graphite along the basal plane. With the temperature increasing the resistivity decreases for both pure and B-doped tubes. This semiconductor-like signature suggests thermal activation of electrons from valence to conduction states separated either by a band gap or a dopant induced Fermi level depression as it was observed for B alloys of graphite¹². This behaviour could also be interpreted as thermally activated interlayer hopping of electrons from inner to outer nanotube walls¹³. The applied current density for B-doped tubes reached values of 10^7 Acm^{-2} at RT and more than 10^9 Acm^{-2} at 300°C, exceeding the values reported for metallic nanotubes given by Ebbesen et al. [2]. These values suggest possible applications of carbon nanotube devices at very high current densities.

TABLE 1. Resistivities at Room Temperature and the Activations Energies of Different Carbon Nanotubes measured in This Paper. The Values for Graphite and Diamond are Also Given.

Material		resistivity at room temperature ($\mu\Omega\text{cm}$)	activation energy (meV)
B-doped MWNT	1	3.3×10^2	71 ± 5
	2	4.9×10^2	65 ± 8
	3	7.7×10^2	78 ± 23
	4	7.4×10^1	58 ± 4
undoped MWNT	1	9.3×10^2	193 ± 20
	2	7.7×10^2	281 ± 13
	3	5.3×10^2	235 ± 28
	4	1.9×10^3	292 ± 6
diamond ¹⁴		$\sim 10^{26}$	$\sim 5.47 \text{ eV}$
graphite (basal plane) ¹⁴		5×10^1	-40^{a}

^a) A negative band gap implies a semimetallic behaviour (band overlap).

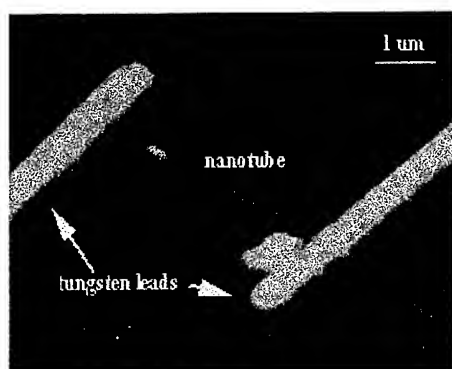


FIGURE 1 Contacting pattern prepared by focused ion-beam (FIB) lithography for electrical transport measurements of individual carbon nanotubes (AFM image).

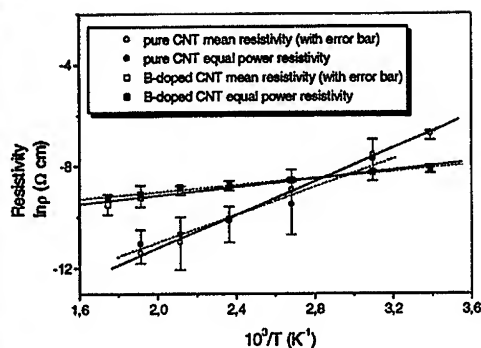


FIGURE 2 Temperature dependence of the electrical resistivities of pure and boron doped nanotubes. The mean resistivity at each temperature (with error bars) are given. The equal power resistivity takes Joule heating into account (The lines are linear fits to the data).

Fig.2 demonstrates that the temperature dependence of the electrical resistivities of the pure and the boron doped nanotubes can be well approximated by the Arrhenius-type relation. An Arrhenius-type behavior is expected for semiconductors in the temperature range where intrinsic conductivity dominates. Both the pure and the B-doped tubes perform semiconductor-like with a different slope of the Arrhenius plot, i.e. with different activation energy, E_a . The decrease of resistance with increasing input voltage can be partially explained as an effect of Joule heating. Therefore, besides the mean resistivities we also compare data for equal input power (i.e. 10 mW). The data corrected thereby for possible Joule heating effects is given for both the doped and the pure tubes by the dashed lines in Fig. 2 yielding only a small correction. For the B-doped CNT the activation energy ($E_a = 58 - 78$ meV) was found to be smaller than that for the pure CNT ($E_a = 190 - 290$ meV). Strong effects of the doping on the electric transport behaviour of nanotubes are expected in the lower temperature range, where charge carrier generation from dopant levels will dominate the temperature dependence of electric transport.

B-doped tubes, having a negative temperature coefficient of resistivities above room temperature, have almost the same RT resistivity as graphite along the basal plane (see Table 1). However, graphite has a positive (metallic) temperature coefficient¹⁴. Most resistivities for pure CNTs reported by other groups are in the order of $10^{-6} - 10^{-5}$ Ωm, confirming that our measurements should yield reasonable results. The resistivity data for different tubes measured in this work lie in a narrow range, indicating good reproducibility of the experiments. Due to the ion beam metal deposition we expect the contact resistances to be much lower than the values measured for the tubes.

Furthermore, a meaningful comparison of the data for pure and B-doped tubes should be possible regardless of the unknown contact resistances. The effects of Ga^+ ion beam, the properties of the metal-nanotube contact and possible systematic deviation in the cross-section of tubes on the electrical transport properties are currently under investigation.

CONCLUSION

Semiconductor-like temperature dependence of resistivity was found in all our resistivity measurements performed on either B-doped or pure MWNTs. B-doped nanotubes as compared to pure CNTs have a reduced resistivity at room temperature (by about one order of magnitude). The possibility to operate carbon nanotube devices at very high current densities could lead to new strategies of nanotube applications in electronics industry. The application of the FIB is shown to have a high potential in exploring the electrical properties of nanostructural devices and in the engineering of nanotube based devices.

ACKNOWLEDGMENTS

One of the authors (B. W.) is grateful for a Scholarship from the Ministry of Science, Research and Art of Baden-Württemberg and from the Max-Planck Society during his visit in Germany. Support of this project by the German Science Foundation, DFG (Ru 342/11-1) is acknowledged.

REFERENCES

- 1 Iijima, S., *Nature* **345**, 56 (1991).
- 2 Ebbesen, T.W. Lezec, H.J. Hiura, H. Bennett, J.W. Ghaemi, H.F. and Thio, T., *Nature* **382**, 54 (1996).
- 3 Tans, S.J. et al, *Nature* **386**, 474 (1997).
- 4 Song, S.N. Wang, X.K. Chang, R.P.H. and Ketterson, J.B., *Phys. Rev. Lett.* **72**, 697 (1994).
- 5 Terrones, M. et al, *Appl. Phys.* **A66**, 307 (1998).
- 6 de Heer, W.A. et al, *Science* **268**, 845 (1995).
- 7 Thess, A. et al, *Science* **273**, 483 (1996).
- 8 Dai, H. Wong, E.W. and Lieber, C.M., *Science* **272**, 523 (1996).
- 9 Lee, R.S. Kim, H.J. Fischer, J.E. Thess, A. and Smalley, R.E., *Nature* **388**, 255 (1997).
- 10 Carroll, D.L. et al, *Phys. Rev. Lett.* **81**, 2332 (1998).
- 11 Wei, B.Q. Spolenak, R. Kohler-Redlich, Ph. Rühle, M. and Arzt, E., *Appl. Phys. Lett.*, (submitted).
- 12 Klein, C. A., *Physics and Chemistry of Carbon*, Vol.2., edited by Walker, P.L. Marcel Dekker, Jr., NY (1966).
- 13 Carroll, D.L., *personal communication* (1998).
- 14 Dresselhaus, M.S. Dresselhaus, G. and Eklund, P.C., *Science of Fullerenes and Carbon Nanotubes*, Academic Press, San Diego (1996) 17.

Temperature Dependent Resistivity of Large Ropes of Single Walled Carbon Nanotubes

J. Lefebvre, M. Radosavljevic, J. Hone and A. T. Johnson

*Department of Physics and Astronomy and LRSM,
University of Pennsylvania, Philadelphia, PA 19104*

Abstract. The electrical resistance of ropes of single walled carbon nanotubes is presented as a function of temperature, magnetic field and electrostatic doping. The entire set of data obtained on many samples can be understood on the basis of data already published for individual nanotubes. The main conclusion is that a rope is well described on the basis of two independent parallel channels, one of semiconducting and one of metallic nanotubes.

The study of the electrical transport properties of single walled carbon nanotubes (SWNTs) is of great interest since simply upon geometrical factors, a nanotube can be either a metal or a moderate gap semiconductor [1]. So far, electrical transport measurements have been performed on bulk material (random network of ropes, a rope being a crystal of individual tubes) and on individual SWNTs. In both cases, the intrinsic properties of the SWNTs is hardly accessible due to "non-intrinsic" effects such as variable range hopping, weak localization and the Coulomb blockade. In this paper, individual ropes of SWNTs have been studied using a standard four-probe method. The electrical resistivity as a function of temperature, electrostatic doping and magnetic field is reported. The data are explained on the basis of published results obtained on individual nanotubes.

The sample preparation goes as follow. First, raw unpurified material produced from the laser ablation method is sonicated in ethanol (or isopropanol) for six hours and then spun on an oxidized (150 nm) silicon chip (degenerate Si) with predefined gold pads and alignment marks. Large ropes of SWNTs are first located using an optical microscope (1000X) and fully characterized with an AFM (tapping mode). Typically, the chosen ropes are 20 to 50 nm high and 10 to 20 μm long. Electron-beam lithography with a beam energy of 40 keV is used to define the current and voltage leads. Usually, gold covered chrome is the metal of choice. The distance between the current probes (outer probes) is typically 3 μm thus making sure that a significant portion of the rope is covered with the large current pads. This maximizes the number of connected tubes and insures as much as possible

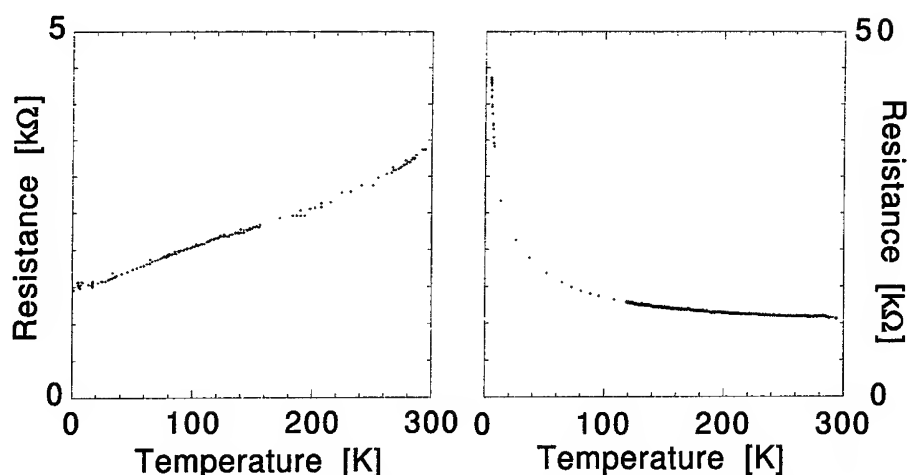


FIGURE 1. Resistance versus temperature of ropes of SWNTs showing the metallic and non-metallic behaviors respectively.

that the current flows uniformly in the bulk of the rope.

Figure 1 shows the four-probe resistance as a function of temperature for two different ropes of similar dimensions. In Both cases, the contact resistance was about 5 to 10 times larger than the four-probe value. The striking feature is that these two ropes have opposite signs of $\delta\rho/\delta T$. One is metallic with a positive $\delta\rho/\delta T$. Its low temperature resistivity is estimated to be $60 \mu\Omega cm$ with a $\delta\rho/\delta T$ equal to $0.3 \mu\Omega cm/K$, similar to what has been reported previously [2]. However, this is likely an overestimate of ρ since we represent the rope as a bulk cylinder and suppose that all the tubes are conducting. The other sample in Figure 1 has a non-metallic behavior with $\delta\rho/\delta T < 0$. In some samples, a minimum resistance was observed between 4.6 and 300 K. In the case of the metallic rope, the four-probe I - V s remain linear down to 4.6 K while they show a small gap (1 to 10 meV) for the non-metallic one. It is not clear at this moment what is the origin of this small gap.

In order to get more clues on the origin of such differing behaviors, the effect of electrostatic doping was studied through the use of a back gate. The electrostatic doping allows to tune the Fermi energy inside the rope. Figure 2 shows the most spectacular behavior observed so far. At high temperature, this sample presents an overall "p-type" behavior with a positive $\delta\rho/\delta V_g$. This is a common result in all the samples measured in this work and seems to be similar to what is seen on individual SWNTs [3,4]. At 160 K, a step is seen around $V_g = 0$ V that becomes more pronounced as the temperature drops to 4.6 K. For $V_g < 0$, a metallic behavior is observed with $\delta\rho/\delta T > 0$ and linear four-probe I - V s. This side of the gate voltage dependence remains more or less featureless down to low temperature. For $V_g > 0$, a non-metallic behavior is observed with $\delta\rho/\delta T < 0$ and non-linear four-probe I - V s. In contrast with negative V_g , the low temperature positive V_g dependence

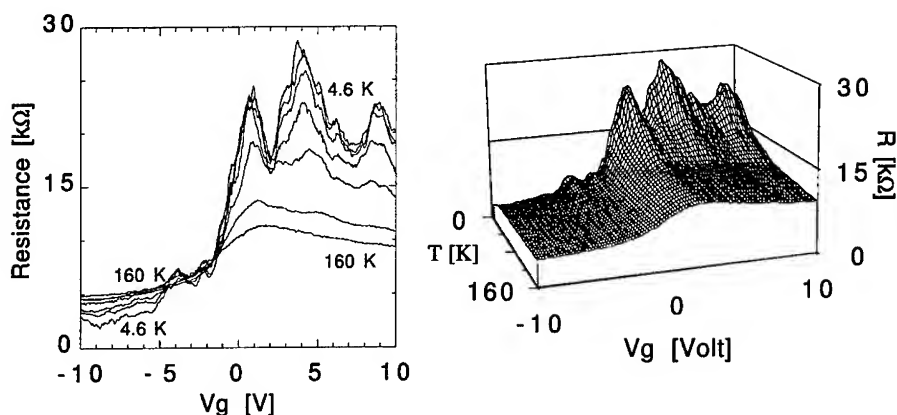


FIGURE 2. Effect of electrostatic doping on the electrical resistance of a rope of SWNTs. Left and Right are the same data sets presented differently. Depending on V_g , a metallic and a non-metallic behavior is observed. The different temperatures on the left figure are 160, 82, 40, 25, 15, 11 and 4.6 K.

show strong oscillations with weaker temperature dependence in the local resistance minima.

The entire set of data gathered on ropes of SWNTs can be understood by considering that a rope is made of tubes with a random distribution of chiralities. It has been shown by electron diffraction that a rope consists of tubes with a narrow distribution of diameters but with a random distribution of chiralities [5]. In a transport experiment, this can be modeled as two independent (parallel) channels of conduction, one of metallic and one of semiconducting tubes. For the metallic channel, one expects a $\delta\rho/\delta T > 0$ for the entire temperature range and a weak $\delta\rho/\delta V_g$. For the semiconducting channel, the behavior is more complicated and depends on where the Fermi energy lies. It has been shown by STM [6] and transport on individual tubes [3,4] that semiconducting tubes show “p-type” behavior with the Fermi energy pinned at the edge of the valence band. In the so-called TUBEFET experiment, the resistance of a semiconducting tube was changed by six orders of magnitude with most of the change arising around $V_g = 0$ V [3]. If the Fermi energy sits in the valence band (or the conduction band), one expects metallic behavior while non-metallic behavior should be observed if the Fermi energy sits in the gap. By reducing the contribution of each tube in a rope to two channels, one metallic and one semiconducting, we can understand the opposite behaviors in the temperature dependence of Fig.1 and the tuning effect of Fig.2. We believe

that a strong metallic behavior in a rope is the result of the metallic channel being dominant. This extreme case doesn't seem to be the most frequently occurring one, as one might expect for a random distribution of chiralities. The situation of Fig.2 is probably a better illustration of an equal contribution from each channel. Here, the gate voltage dependence is similar to that of the TUBEFET. The effect is obviously smaller because of the constant contribution of the metallic channel. But similarly, a step is seen at $V_g = 0$ V and the increase of resistance at positive V_g shows that the Fermi energy is pinned at the valence band edge.

The results of Fig.1 and 2 could also be understood in terms of disorder induced localization. A metallic behavior down to low temperature would be associated with a "clean" sample and inversely for the non-metallic one. As for the gate voltage dependence of Fig.2, a negative V_g would correspond to tuning the Fermi energy away from a mobility edge. As the Fermi energy moves far from the "impurity band" the metallic behavior would be recovered. Attempts have been made to fit the data using various models but no satisfactory results have been obtained. In order to unambiguously separate the two effects, we performed magnetoresistance measurements up to 8 T at different V_g (not shown). In a disordered system, a negative magnetoresistance is expected due to a suppression of scattering processes by the magnetic field. Our data show an amazingly flat magnetoresistance (less than 1 %), strong evidence that disorder is not responsible for results shown here. Moreover, the absence of magnetoresistance could be an evidence that tubes in a rope are weakly coupled. If a 20 – 50 nm rope behaved like a bulk wire, an 8 T field should be large enough to induce orbital effects and associated with it, a positive magnetoresistance.

SWNT material was provided by the Smalley group at Rice University. Financial support for this work came from LRSM, NSF, Packard Foundation, Sloan Foundation and Fonds FCAR (Québec). We would like to thank E. J. Mele and C. Kane for enlightening discussions.

REFERENCES

1. Ajayan P. M. and Ebbesen T. W., Rep. Prog. Phys. **60**, 1025 (1997).
2. Kane C. L., Mele E. J., Lee R. S., Fischer J. E., Petit P., Dai H., Thess A., Smalley R. E., Verschuere A. R. M. and Tans S. J., Europhys. Lett. **41**, 683 (1998).
3. Tans S. J., Verschuere A. R. M. and Dekker C., Nature **393**, 49 (1998).
4. Antonov R. and Johnson A. T., to be submitted.
5. Loiseau A. *et al.*, presentation made at University of Pennsylvania.
6. Wildöer J. W. G., Venema L. C., Rinzler A. G., Smalley R. E. and Dekker C., Nature **391**, 59 (1998).

Manipulation of the Transport Properties of Single-Walled Nanotubes by Alkali Intercalation and Local Charge Transfer

J. Hone, Radoslav Antonov, and A. T. Johnson

*Department of Physics and Astronomy and LRSM,
University of Pennsylvania, Philadelphia, PA 19104*

Marc Bockrath, Paul L. McEuen, and A. Zettl

*Department of Physics, University of California, Berkeley, and Materials Science Division
Lawrence Berkeley National Laboratory, Berkeley, CA 94720*

Abstract. We have studied the effects of charge transfer on the transport properties of individual single-walled nanotubes. This was done in two ways. In the first, we expose devices made of individual nanotubes to alkali metal vapor. This causes no change in the conductance of devices made of metallic tubes, while it increases the conductance of semiconducting tubes and causes them to change from p-type to n-type. In the second method, we examine a single semiconducting nanotube over three leads with an impurity particle near one lead. Local charge transfer from the impurity to the tube causes the region with the impurity to act as a diode, while the other, 'clean', half displays symmetric transport behavior.

Single-walled nanotubes (SWNT's) hold great promise as candidates for molecular-level electronic components. One possible route to construction of nanotube-based devices is through manipulation of their Fermi levels through charge transfer. It has been shown that the electronic properties of bulk 'mats' of tubes can be significantly altered by alkali-metal intercalation [1]. These bulk measurements are only the first step in understanding the details of how charge transfer affects the electronic structure of single tubes. Therefore, we have undertaken studies of the effects of charge transfer on single nanotubes. We will first describe studies of charge transfer by potassium intercalation, and then describe a device constructed of a single semiconducting nanotube that displays rectifying behavior due to the effects of a local impurity particle.

The samples used in this study are prepared by deposition of SWNT's out of suspension onto pre-prepared Au leads on a degenerately-doped Si wafer with a 1 μm oxide layer. This geometry allows for application of both a bias voltage and an electrostatic gate voltage through the conductive silicon substrate. Examination of the samples by atomic force microscopy (AFM) shows that they are 1.4 nm in height, consistent with their being composed of a single nanotube, although it is also possible that a given sample comprises a few nanotubes lying flat in parallel.

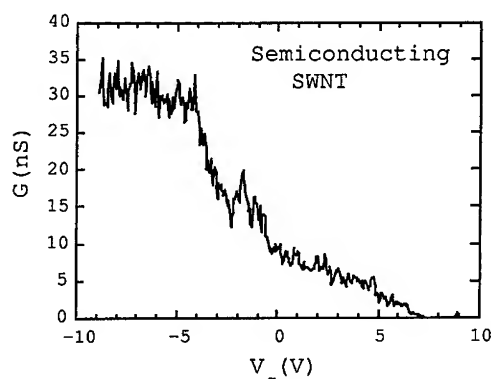


FIGURE 1. Low-bias conductance of a semiconducting nanotube as a function of gate voltage. The decrease in conductance with positive gate voltage shows that the dominant carriers are holes. The saturation at negative gate voltage is most likely due to contact resistance.

After deposition, the samples are characterized by room-temperature transport measurements, primarily by examining low-bias conductance as a function of gate voltage. The samples display behavior that falls into two classes. 'Metallic' devices display a relatively high conductance ($\sim 1 \mu\text{S}$) which is independent of gate voltage. 'Semiconducting' devices, on the other hand, display a much smaller conductance, which is strongly gate-voltage dependent. We choose samples that are clearly in either the semiconducting or metallic limit, and are thus most likely to be dominated by a single metallic or semiconducting nanotube.

Figure 1 shows the low-bias conductance of a semiconducting device as a function of gate voltage. As has been shown in earlier work [2,3], the conductance decreases dramatically as the gate voltage is swept from negative to positive. This behavior can be attributed to a depletion of p-type carriers from the area of the nanotube away from the contacts. Consistent with published results, all of the semiconducting nanotubes we observed displayed p-type behavior.

To 'dope' the nanotube devices with potassium, each chip containing a device was mounted into a pyrex tube with a feedthrough so that electrical measurements could be performed *in situ*. The apparatus was then baked out under dynamic vacuum and transferred to an inert-atmosphere glove box, where a small amount of potassium was inserted into the open end of the tube, which was then evacuated and sealed off. To expose the sample to potassium vapor, each end of the apparatus was heated independently; the sample side was kept hotter than the potassium side to prevent condensation of the potassium onto the sample.

When we first attempted to dope nanotube circuits in this way, we found that the semiconducting devices seemed to 'disappear' after baking out, while metallic ones were relatively unaffected. Therefore, we began to monitor the conductance of devices during the bake-out. The inset to figure 2 shows the conductance of a semiconducting nanotube as a function of time during bake-out at 100°C . Over

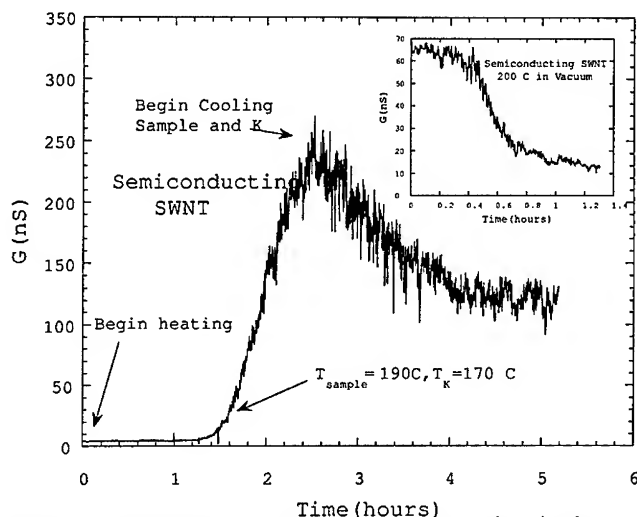


FIGURE 2. Potassium-intercalation of a semiconducting nanotube. As the sample and K reach 190 and 170 °C, respectively, the conductance begins to increase. As the sample and K are held at fixed temperature, the conductance continues to increase. After 1 hour, the sample and K are slowly cooled; the conductance decreases with cooling, but remains significantly larger than the initial conductance. The inset shows the drop in conductance during bake-out prior to intercalation.

a period of two hours, the conductance of the nanotube drops to near zero. It is not known whether this drop in conductance is due to removal of carriers (i.e. that the tube is already doped in air) or a reduction in the mobility of carriers, perhaps due to a removal of species which may passivate local charged defects on the chip surface.

Figure 2 shows the conductance of the same semiconducting tube as a function of time during exposure to potassium vapor. Initially, the conductance of the nanotube was quite low (~5 nS). As the sample and potassium temperatures reached 190 and 170 °C, respectively, the conductance of the device began to increase. At this point, the temperatures were fixed. After one hour, the conductance had risen to 250 nS, and the sample and potassium were slowly cooled. Upon cooling the conductance decreased but remained significantly higher than the initial conductance. It is likely that this increase in conductance is due to charge transfer from the potassium to the nanotube. In subsequent studies of other devices we discovered that the doping process was reversible; heating only the sample side drives off the potassium and causes a reduction in conductance to a level similar to that of the undoped tube, at which point the tube can be doped again. Similar efforts were undertaken to dope metallic tubes, but no effect was observed.

To further examine the electronic structure of the doped semiconducting nanotube, we studied its conductance as a function of gate voltage, as shown in figure

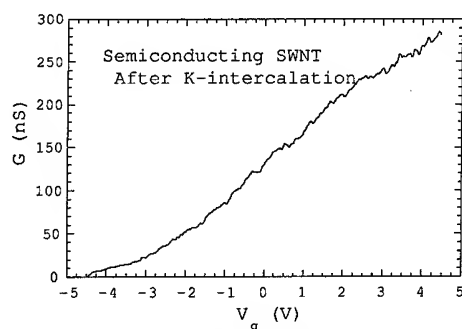


FIGURE 3. Low-bias conductance of a potassium-doped nanotube as a function of gate voltage. Charge transfer from the K to the nanotube has caused the tube to display n-type behavior: the conductance increases with increasing positive gate voltage.

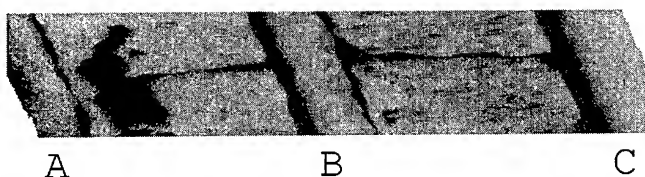


FIGURE 4. AFM image of a single nanotube (1.4 nm in height) lying across three gold electrodes. An impurity particle can be seen near electrode A.

3. In contrast to the behavior seen in the as-prepared samples, the conductance of the alkali-doped device increases as the gate voltage is swept from -5 V to 5 V. The doped device is now n-type, consistent with transfer of electrons from the potassium to the tube.

The above results show that it is possible to dope single semiconducting nanotubes and change their behavior from p-type to n-type. One logical extension of this work would be to try to locally dope a tube, in order to make a p-n junction. Although we have not yet attempted to do this in a controlled fashion, below we describe a device in which this process seems to have occurred by chance.

Figure 4 is an AFM image of what is most likely a single nanotube lying across three gold electrodes, labeled A, B, and C. The segment of the tube lying across leads B and C seems to be 'clean,' i.e. there are no large impurities touching it. The segment across leads A and B, on the other hand, has a large impurity particle lying on top of it about 50 nm from lead A. As will be shown below, this impurity seems to have significant effects on the transport through the tube.

The left side of figure 5 shows the transport characteristics of the 'clean' segment of the nanotube. It shows a symmetric I-V curve characteristic of a semiconducting nanotube: low conductance at low bias and increasing conductance at high positive and negative biases. In addition, the gate voltage dependence (not shown) of the low-bias conductivity shows p-type behavior, as with previous devices.

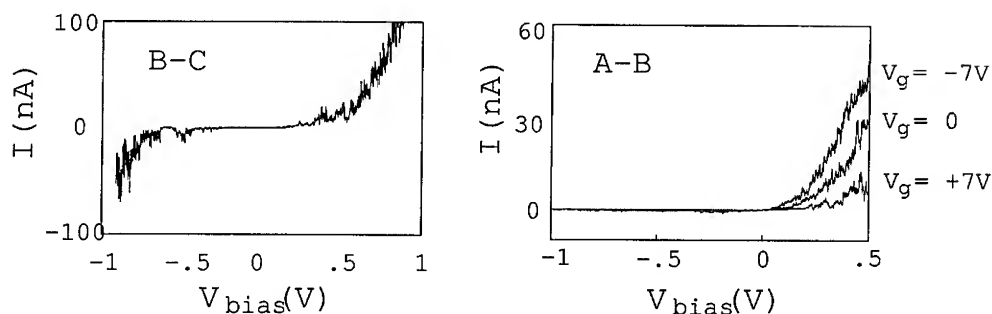


FIGURE 5. (left) Current vs. bias voltage of the nanotube between leads B and C. (right) I-V relation for the nanotube between leads A and B, at gate voltages of -7, 0, and 7 volts.

The right side of figure 5 shows the transport characteristics of the nanotube between leads A and B. The impurity seems to be causing a drastic change in the I-V behavior: the device behaves as between B and C when a positive bias is applied, but does not conduct at any applied negative bias (where here A is biased and B is grounded). Thus the tube with a local impurity acts as a diode. We can understand its rectifying behavior as a result of local transfer of electrons from the impurity to the nanotube, using the TubeFET model of Tans et al. In the TubeFET, the difference in work functions between the leads and the tube pins the Fermi energy of the tube to the valence band edge at the contacts. The bands bend downward between the leads; application of a gate voltage increases or decreases this bending, reducing or enhancing the hole transport across the barrier created by the bent bands. In the nanotube diode, local charge transfer near the impurity creates a depression in the bands which interacts with the effects of the contact. The two effects combine to produce a larger barrier to hole transport at contact A than at contact B. At forward bias, the current is only limited by the barrier near contact B, and current flows as in the intrinsic device. At negative bias, on the other hand, transport is limited by the (now larger) barrier at contact A, and no current flows. It is interesting to note that, in this interpretation, the rectifying behavior depends on the interaction between the impurity and the contact: if the impurity were too far from the contact they would not 'see' each other and there could be no symmetry-breaking. Based on this idea, we can set a minimum characteristic screening length in the tube of about 50 nm, the distance between the impurity and lead A.

REFERENCES

1. Lee R.S. *et al.*, Nature **388**, 255-7 (1997)
2. Tans S.J. *et al.*, Nature **393**, 49 (1998)
3. Martel R., Schmidt T., Hertel T., and Avouris P., Appl. Phys. Lett. **73**, 2447 (1998)

Femtosecond Time-Resolved Photoemission as a Probe of Electronic Transport in Single Wall Carbon Nanotubes

Tobias Hertel and Gunnar Moos

*Department of Physical Chemistry, Fritz-Haber-Institut der Max-Planck-Gesellschaft,
Faradayweg 4-6, 14195 Berlin, Germany*

Abstract. We have performed the first time-domain measurements of the electron-electron ($e-e$) and electron-phonon ($e-ph$) dynamics in single-wall carbon nanotube samples (bucky paper) using time-resolved two-photon photoemission. In these room temperature experiments the absorption of a visible femtosecond pump pulse creates a non-equilibrium electron distribution whose evolution in time can be probed by a second UV-pulse. The decay of the excited electron distribution is characterized by a fast channel on the subpicosecond time-scale — associated with thermalization of the non-equilibrium distribution — and a slower channel which can be attributed to $e-ph$ interaction. Once thermalized the electron distribution cools down to the lattice temperature as determined by the electron-phonon coupling constant g which was found to be $1 \times 10^{15} \text{ W m}^{-3} \text{ K}^{-1}$.

INTRODUCTION

The interaction of electrons with other charge-carriers, phonons and lattice inhomogeneities is crucial to the mean characteristic lengths for electron momentum and phase relaxation L_m and L_φ . The magnitude of these lengths with respect to the Fermi wavelength and the size of the sample determines if electronic transport in a certain experimental arrangement is ballistic, diffusive or classic and if localization effects or universal conductance fluctuations may be observed [1]. Knowledge of L_m and L_φ would, therefore, help to understand electronic transport through carbon nanotubes better. Femtosecond time-resolved photoemission has previously been used to study charge-carrier dynamics in metals and semiconductors [2,3]. Here we apply this technique to study the dynamics in single wall carbon nanotubes at room temperature.

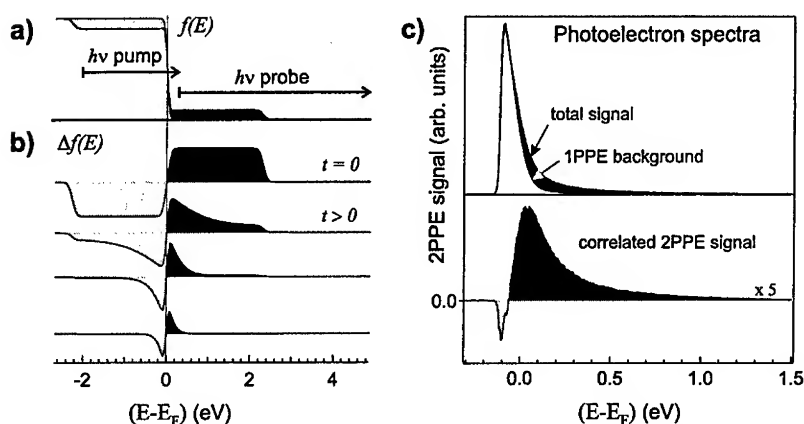


FIGURE 1. a) Perturbation of the Fermi-Dirac distribution by the femtosecond pump pulse. b) Change of the difference of the non-equilibrium with respect to the equilibrium distribution as a function of time. c) Uncorrected and background corrected photoelectron spectra

RESULTS AND DISCUSSION

Single wall carbon nanotube (bucky paper) samples were produced from commercial nanotube suspension (tubes@rice, Houston, Texas) following the procedure described by Rinzler *et al.* [4]. Samples obtained in this manner were attached to a tantalum block which could be resistively heated to 1200° C. The nanotube sample was outgassed thoroughly by repeated heating and annealing cycles under UHV conditions. Two-photon photoelectron (2PPE) spectra were obtained by means of the time-of-flight technique with an improved energy resolution of 10 meV [5]. The visible pump pulses with a duration of less than 90 fs were focused nearly collinearly onto the sample together with the frequency doubled probe pulses. The pump pulse fluence was kept below 10^9 Wcm^{-2} .

In order to study charge carrier dynamics in the vicinity of the Fermi level we used a probe photon energy $h\nu_{\text{probe}}$ of 4.60 eV, slightly above the work function of the nanotube samples $e\Phi$ of 4.5 eV. The pump photon energy was 2.30 eV. Fig. 1a) and b) shows a schematic illustration of the experiment together with a typical photoelectron spectra in Fig. 1c). The intermediate state energy of the electrons ($E - E_F$) is calculated from the electron kinetic energy E_{kin} via the relation $(E - E_F) = E_{\text{kin}} + e\Phi - h\nu_{\text{probe}}$. 2PPE spectra from these samples show no sign of Van Hove type singularities. Such features are probably broadened and smeared out due to tube-tube interactions and averaging effects.

To obtain the correlated 2PPE signal which reflects the changes induced in the electron distribution by the pump pulse, we have to subtract the time independent one-photon photoemission background from the UV probe pulse. The resulting correlated 2PPE signal at zero pump-probe delay is shown in Fig. 1c). This spectrum reflects the excitation-induced depletion of charge carriers below the Fermi

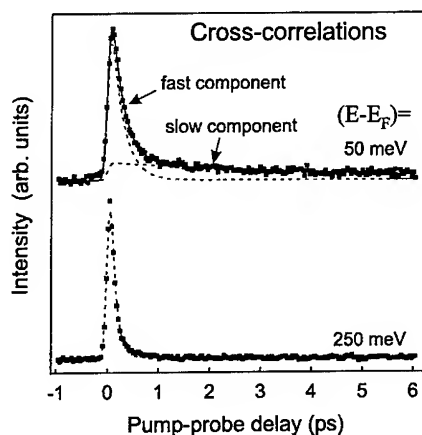


FIGURE 2. Cross-correlations at two different intermediate state energies. The upper trace was recorded at an energy of 50 meV and the lower one was recorded at 250 meV above the Fermi level.

level (negative signal) and the increase in the electron population at energies above the Fermi level (positive signal).

If the intensity at a particular energy in these spectra is recorded as a function of the pump-probe delay we obtain cross-correlations like the ones shown in Fig. 2. The upper cross-correlation in Fig. 2 shows that the electron dynamics is characterized by a slow and a fast component. In analogy to our results obtained on highly oriented pyrolytic graphite the fast component can be attributed to carrier-carrier interactions which lead to a rapid thermalization of the non-equilibrium electron distribution [6,7]. This thermalization can be observed directly from the time dependence of 2PPE spectra which can be described by a thermal Fermi-Dirac distribution after about 500 fs [7]. For the fast channel the characteristic time for relaxation of the electron or hole population at 50 meV above or below the Fermi level is found to be (250 ± 50) fs. Using a Fermi velocity v_F of 8 \AA fs^{-1} this yields an e - e mean free path of 200 nm. Due to the contribution of secondary electron cascades to the 2PPE signal this decay-time should be considered as an upper limit of the actual e - e scattering time. At higher electron energies the relaxation time decreases continuously to less than 20 fs at 2 eV above the Fermi level.

For the pump pulse fluence used in these experiments the temperature of the electronic system has equilibrated after 500 fs at about 850 K. The slow component in the cross-correlations and the dynamics of the 2PPE spectra can then be used to follow the cooling of the electronic system down to the lattice temperature T_l via e - ph interaction. If approximated by an exponential decay $\frac{dT_e}{dt} = -\tilde{c}(T_e - T_l)$ the characteristic rate \tilde{c} at which the electronic temperature T_e decreases is found to be $\sim (2 \text{ ps})^{-1}$.

Such a coupling of the electronic system to the lattice is frequently discussed in the framework of the two-temperature model introduced by Anisimov *et al.* [8]. This model has been used extensively to study e - ph coupling in metals using transient reflectivity measurements (see for example ref. [9]). According to Anisimov *et*

al. the flow of energy between the electronic system and the lattice can be described by the two coupled heat equations:

$$C_e(T_e) \frac{\partial T_e}{\partial t} = \nabla(\kappa \nabla T_e) - g(T_e - T_l) \quad (1)$$

$$C_l(T_l) \frac{\partial T_l}{\partial t} = g(T_e - T_l). \quad (2)$$

Here C_e and C_l are the specific electron and lattice heat capacities respectively. Since C_l is much greater than C_e in graphite (and nanotubes) we can neglect the heating of the lattice and use equation 1 alone to determine the coupling constant g . In the absence of diffusive transport ($\nabla(\kappa \nabla T_e) \approx 0$) a fit of equation 1 to the experimental temperature evolution yields a coupling constant g of $1 \times 10^{15} \text{ Wm}^{-3} \text{ K}^{-1}$. Here we have used the electronic heat capacity of graphite γ of $2.4 \text{ J m}^{-3} \text{ K}^{-1}$. Using the formalism originally developed for e - ph dynamics in metals the coupling constant g can be related to the electron-phonon coupling parameter λ from the BCS theory of superconductivity via $g = (3\gamma\hbar\lambda\langle\omega^2\rangle)/(\pi k_B)$ [10] which is also related to the characteristic time for emission of a phonon by $\tau_{e-ph} = (\pi\lambda\langle\omega\rangle)^{-1}$ ($\langle\omega\rangle$ being the mean phonon frequency) [11]. Using the fit to equation 1 we obtain a value of $\lambda = 0.0025$ which is about 2 orders of magnitude smaller than values typically found in metals [9]. The corresponding e - ph scattering time is 0.85 ps and the e - ph mean free path becomes $0.7 \mu\text{m}$.

Assuming that electron momentum and phase relaxation lengths L_m and L_φ are dominated by e - ph and e - e interactions respectively [1] these results yield a momentum relaxation length $L_m = [3^{-1/2} v_F \tau_{e-ph}]$ of $0.4 \mu\text{m}$ and a phase relaxation length L_φ of 115 nm. In the presence of other momentum or phase changing scattering events these relaxation lengths give an upper limit for the respective processes.

We thank M. Wolf and G. Ertl for fruitful discussions and generous support.

REFERENCES

1. R. Saito, G. Dresselhaus, and M. Dresselhaus, *Physical Properties of Carbon Nanotubes*, London, Imperial College Press, 1998.
2. S. Ogawa, and H. Petek, *Prog. Surf. Sci.* **56**, 239 (1998).
3. R. Haight, *Surf. Sci. Rep.* **21**, 275 (1996).
4. A.G. Rinzler, J. Liu, H. Dai *et. al*, *Appl. Phys. A* **67**, 29 (1998).
5. T. Hertel, E. Knoesel, M. Wolf, and G. Ertl, *Phys. Rev. Lett.* **76**, 535 (1996).
6. S. Xu, J. Cao, C.C. Miller *et. al*, *Phys. Rev. Lett.* **76**, 483 (1996).
7. T. Hertel, and G. Moos, in preparation.
8. S.I. Anisimov, B.L. Kapeliovich, and T.L. Perel'man, *Sov. Phys. JETP* **39**, 375 (1974).
9. S.D. Brorson, A. Kazeroonian, D.W. Face *et. al*, *Phys. Rev. Lett.* **64**, 2172 (1990).
10. V.E. Gusev, and O.B. Wright, *Phys. Rev. B* **57**, 2878 (1998).
11. P.B. Allen, *Phys. Rev. Lett.* **59**, 1460 (1987).

One-dimensional transport in bundles of single-walled carbon nanotubes

David H. Cobden*, Jesper Nygård*, Marc Bockrath[†]
and Paul L. McEuen[†]

* Ørsted Laboratory, Niels Bohr Institute,

Universitetsparken 5, DK-2100 Copenhagen, Denmark

[†] Department of Physics, University of California at Berkeley

and Lawrence Berkeley National Laboratory, Berkeley, CA 94720, USA

Abstract. We report measurements of the temperature and gate voltage dependence for individual bundles (ropes) of single-walled nanotubes. When the conductance is less than about e^2/h at room temperature, it is found to decrease as an approximate power law of temperature down to the region where Coulomb blockade sets in. The power-law exponents are consistent with those expected for electron tunneling into a Luttinger liquid. When the conductance is greater than e^2/h at room temperature, it changes much more slowly at high temperatures, but eventually develops very large fluctuations as a function of gate voltage when sufficiently cold. We discuss the interpretation of these results in terms of impurity scattering within the Luttinger liquid.

The strength and extended length of single-walled carbon nanotubes makes it quite straightforward to attach metallic electrodes to them. This has enabled several recent studies of the transport properties of individual tubes and ropes (ordered bundles of tubes) [1–5]. In most of these studies the conductance at low temperatures is found to be dominated by Coulomb blockade (CB), while at higher temperatures a variety of behavior has been reported. Here we analyse the temperature dependences and other characteristics of a number of devices, in the light of recent predictions that the electrons in nanotubes should form Luttinger liquids.

Each device consists of an individual nanotube rope [6], containing between 1 and ~ 20 tubes lying on a thermally grown SiO_2 surface and contacted with gold electrodes patterned by electron beam lithography. The electrode separation is 0.2 or 0.5 μm , and the metallically doped silicon substrate beneath the 0.3- or 1.0- μm thick SiO_2 is used as a gate electrode. We have two varieties of devices: ‘end-contacted’, where the electrode metal is deposited on top of the rope; and ‘bulk-contacted’, where the rope is deposited on top of prefabricated electrodes. An atomic force microscope (AFM) image of a typical device is inset to Fig. 1. In all the measurements reported here, the two-terminal dc current-voltage (I - V)

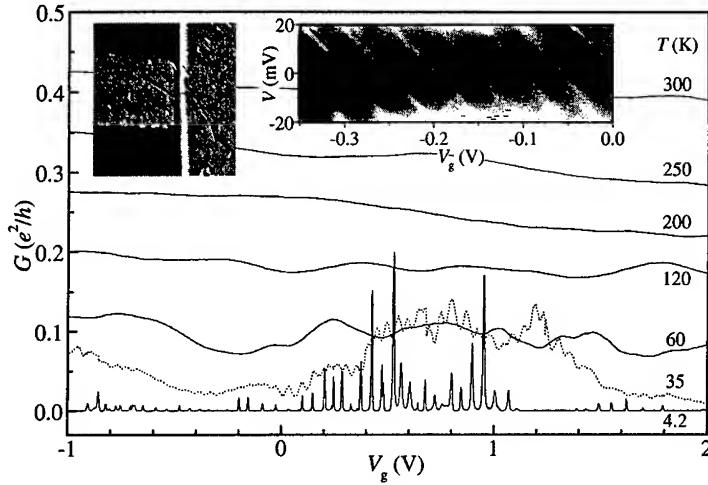


FIGURE 1. Conductance G vs gate voltage V_g at temperatures T from 300 K to 4.2 K for a end-contacted device. Right inset: grey scale plot of dI/dV vs V_g and V at 4.2 K (lighter = more positive). Left inset: AFM image of a nanotube rope lying over two electrodes separated by a 0.2 μm gap.

characteristics were measured in a cryostat with the device bathed in helium.

Although transistor-like behavior is sometimes seen [4], we consider here only devices whose conductance G is approximately independent of gate voltage V_g at room temperature. Fig. 1 illustrates the behavior of a typical (end-contacted) device as it is cooled down. As T decreases, G drops steadily, and below $T \sim 50$ K, Coulomb blockade (CB) peaks develop in G vs V_g [1,2]. The right inset is a grey scale plot of dI/dV vs V_g and V at 4.2 K. A standard analysis of this bias spectroscopy plot [2,7] yields $C_g/C \sim 0.15$ and a charging energy $U = e^2/C \sim 10$ meV, where C_g is the capacitance to the gate and C is the total capacitance. The excitation spectrum for each charge state is resolved here at 4.2 K, allowing us to estimate a mean level spacing $\Delta \sim 2$ meV. From the regularity of this plot we infer that the conductance is largely determined by a single quantum dot. We consider in this paper only devices which show such regularity in their spectroscopy plots. The values of U and Δ are consistent with charging a rope segment of length L roughly equal to the contact separation (in this case $L = 0.5 \mu\text{m}$). This is usual for end-contacted ropes. For bulk-contacted devices on the other hand, U is smaller and corresponds to charging the full length of the rope. This implies that in both cases the electrode-tube interfaces act as tunnel contacts to the rope which form the dot. Our terminology was chosen to reflect this: end-contacted means that the current flows from the metal into the end of the active rope segment, and bulk-contacted means it flows into the bulk.

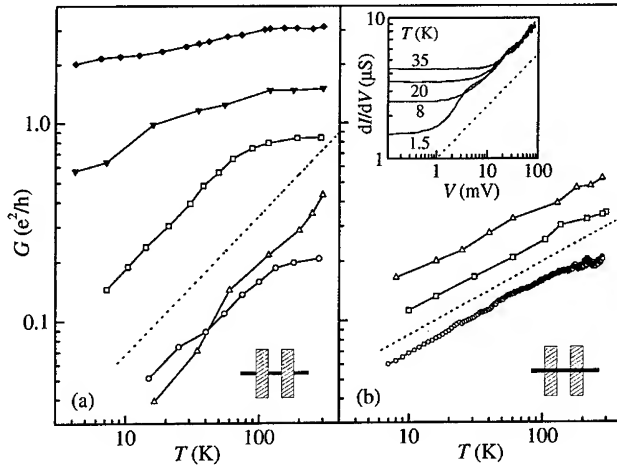


FIGURE 2. Conductance (averaged over V_g) vs temperature for several devices. The data plotted with open symbols have been corrected for Coulomb blockade [3], while the others have not. (a) End-contacted ropes. The dashed line indicates $G \propto T^{0.7}$. The open up triangles correspond to the data in Fig. 1. (b) Bulk-contacted ropes. The dashed line here indicates $G \propto T^{0.37}$. Inset: dI/dV vs V at several temperatures for a bulk-contacted rope. The dotted line here indicates $dI/dV \propto V^{0.37}$.

In Fig. 2 the average conductance G_{av} is plotted against T on a log-log scale for several end-contacted (Fig. 2a) and bulk-contacted (Fig. 2b) ropes. In all cases, G_{av} decreases monotonically as T decreases, irrespective of the room temperature conductance G_{RT} , which varies greatly. That said, we can distinguish the following two categories of behavior. In the first, which contains most devices, $G_{RT} < e^2/h$, and the conductance decreases by up to an order of magnitude before it is Coulomb blocked at low T . For these devices we do not plot G at the lowest temperatures, where CB dominates, and at higher T we multiply G by a correction factor to compensate for the effect of classical CB [3]. Note that this factor is between one and two, and has no major qualitative effect on any of the data. In the second category, which contains only end-contacted devices, $G_{RT} > e^2/h$, the dependence on T is much weaker, and there is no Coulomb blockade at 4.2 K.

We begin by discussing the results (open symbols in Fig. 2) for devices in the first category, having $G_{RT} < e^2/h$. Note that the T dependence for all bulk-contacted ropes in Fig. 2b is very similar, and closely resembles a power law, $G \propto T^{\alpha_{bulk}}$, with $\alpha_{bulk} \approx 0.37$. For the end-contacted ropes in Fig. 2a the T dependences are steeper, and although not so clear cut they are roughly described by another power law, $G \propto T^{\alpha_{end}}$ with $\alpha_{end} \approx 0.7$. We have previously argued that these results are consistent with the existence of Luttinger liquids (LL) in nanotubes [3,8,9].

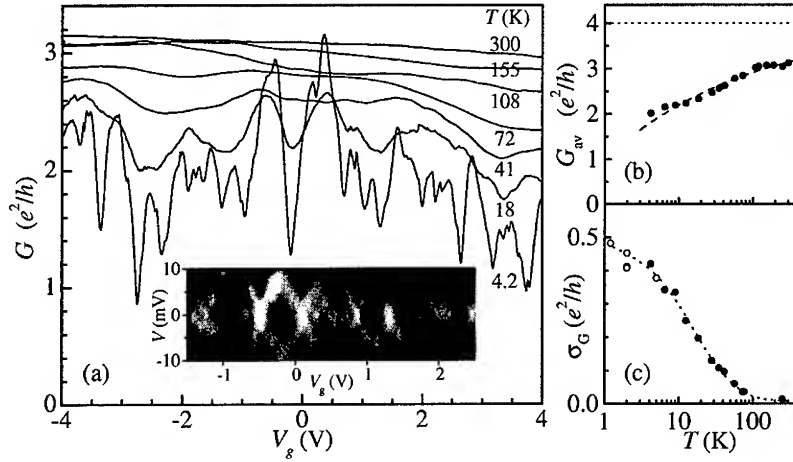


FIGURE 3. Gate-voltage characteristics at a series of T for a device with $G_{RT} \sim 3e^2/h$. Inset: grey scale plot of dI/dV vs V_g and V at 1.2 K (from a different cool-down). (b) Mean conductance (for $V_g < 0$) G_{av} vs T . The solid curve is a fit by eye to $G = 4 - aT^b$, yielding $a = 3$ and $b = -0.22$. (c) Standard deviation σ_G vs T . The solid and open circles are from different cool-downs. The dotted curve is a guide to the eye.

Tunneling from a metal contact into an LL is expected to be suppressed at low energies, resulting in power laws for the conductance, $G \sim T^\alpha$ (for $eV < k_B T$) and $dI/dV \sim V^\alpha$ (for $eV > k_B T$). Given a Luttinger parameter of $g \approx 0.28$ for a metallic nanotube [3], the exponent is predicted to be $\alpha = (g^{-1} - 1)/4 \approx 0.65$ for tunneling into the end of the tube, and $\alpha = (g^{-1} + g - 2)/8 \approx 0.24$ for tunneling into the bulk [3]. These numbers are in fair agreement with the measured quantities α_{end} and α_{bulk} above. Moreover, the prediction that the same exponent α should be seen in the bias as in the temperature dependence is also borne out well in the experiment. This is illustrated in the inset to Fig. 2b, where at high bias the dI/dV vs V traces for a bulk-contacted device can be seen to converge parallel to a line (on this log-log plot) of slope $\alpha_{bulk} = 0.37$.

We come now to the second category, having $G_{RT} > e^2/h$. Fig. 3 shows the characteristics of a device with $G_{RT} \sim 3e^2/h$, (diamonds in Fig. 2a), at a series of T . In strong contrast to Fig. 1, there is almost no T dependence above 100 K. At lower T , large, reproducible fluctuations start to develop in G vs V_g . In Figs. 3b and 3c we plot the mean conductance G_{av} and the standard deviation σ_G of these fluctuations. The bias spectroscopy plot inset to Fig. 3a exhibits a well behaved, symmetric cross structure. This implies quite generally that the conductance is dominated by transmission through a single object, symmetrically coupled to the

two contacts. The fluctuations are almost unaffected by a magnetic field of 7 T. This is consistent with their arising from a nanotube rope, whose thickness is much smaller than the magnetic length (24 nm) at this field.

Nevertheless, these fluctuations are quantitatively and qualitatively different from the CB oscillations in Fig. 1. We notice that G_{av} remains above $2e^2/h$, while G fluctuates by as much as $2e^2/h$, and even occasionally peaks above G_{RT} . These facts are completely at odds with standard Coulomb blockade. Rather, we suggest that high-transparency contacts exist between the gold and a metallic nanotube within the rope. Apart from the high conductance, further evidence for this comes from the very small value of $C_g/C \sim 0.01$ deduced from the spectroscopy plot, which means that the rope is much more weakly sensitive to V_g than are similar devices that behave as quantum dots. This is a natural result of very strong coupling to the electrodes. It is therefore possible that the fluctuations are related to transport through the LL in a tube. Any amount of disorder is expected to completely suppress the conductance of a LL at sufficiently low T . At high T a single impurity produces a power law suppression of G from its ideal value $G_0 = 4e^2/h$ [8]. In Fig. 3b the dashed line is a fit of G_{av} to the form $G_0 - aT^b$, yielding $b = -0.22$. Although the fit appears quite good, we make no claim to its validity, as the behavior of a disordered LL remains to be addressed theoretically.

In conclusion, when the conductance of a nanotube rope device is dominated by tunneling from the contacts, power law dependences on temperature and bias are observed which are consistent with the predicted existence of Luttinger liquids in nanotubes. Further, we find evidence that one can obtain highly transparent contacts between gold and nanotubes, which should soon enable experimental investigations of the intrinsic conducting properties of such a Luttinger liquid.

We would like to thank Poul-Erik Lindelof, Jia Lu, Reinhold Egger, Anders Kristensen and Leon Balents, for help and discussions.

REFERENCES

1. S. Tans *et al.*, Nature **386**, 474 (1997), S. Tans *et al.*, Nature **394**, 761 (1998), A. Bezryadin *et al.*, Phys. Rev. Lett. **80**, 4036 (1998).
2. M. Bockrath *et al.*, Science **275**, 1922 (1997), D.H. Cobden *et al.*, Phys. Rev. Lett. **81**, 681 (1998).
3. M. Bockrath *et al.*, Nature **397**, 598 (1999).
4. S. Tans *et al.*, Nature **393**, 4 (1998), R. Martel *et al.*, Appl. Phys. Lett. **73**, 2447 (1998).
5. J.E. Fischer *et al.*, Phys. Rev. B **55**, R4921 (1997).
6. A. Thess *et al.*, Science **273**, 483 (1996).
7. L. Kouwenhoven *et al.*, in *Mesoscopic Electron Transport*, edited by L. Kouwenhoven, G. Schon, and L.L. Sohn (Kluwer, Dordrecht, The Netherlands, 1997).
8. R. Egger, and A. Gogolin, Phys. Rev. Lett. **79**, 5082 (1997), Eur. Phys. J. B **3**, 281 (1998).
9. C. Kane, L. Balents, and M.P.A. Fisher, Phys. Rev. Lett. **79**, 5086 (1997).

Electrical transport in carbon nanotube rings: coherence and localization

Phaedon Avouris, Herbert R. Shea and Richard Martel

*IBM Research Division, T. J. Watson Research Center, Yorktown Heights,
New York 10598, USA*

Abstract. We present a study of the low temperature electrical properties of single-walled carbon nanotube rings. The ring topology allows the use of magneto-resistance to determine the coherence length of the electrons. A maximum coherence length of about 500 nm is determined at 4 K, and a dephasing mechanism involving electron-electron interactions is identified. Below ~ 1 K, a weak to strong localization transition is observed, as well as evidence for Kondo scattering.

Carbon nanotubes are ideal materials whose study can help evaluate theoretical models describing transport phenomena in low dimensional systems [1]. There are two types of carbon nanotubes: large diameter (typically 10-40 nm) multi-walled nanotubes (MWNTs) and small diameter (typically 1-2 nm) single walled tubes. MWNTs are essentially two-dimensional objects and magneto-resistance techniques have been used to investigate their transport properties [1]. SWNTs are attracting even more interest, as they are close to an ideal one-dimensional system. They are potentially ballistic conductors and have been predicted to undergo a number of different electronic transformations at low temperatures. However, attempts to evaluate the transport properties of SWNTs have been frustrated by two factors: first, their contact resistance with metal pads is high and this has led to Coulomb blockade effects at low temperatures. Second, as they are linear 1D systems, the electron path in the presence of an external magnetic field does not enclose flux and magneto-resistance studies cannot be used directly to evaluate transport properties.

Recently, we showed that straight SWNTs can be turned into nanotube rings [2]. These rings are composed of coiled SWNT ropes held together by van der Waals forces. Fig. 1 shows one such ring bridging two gold electrodes. The morphology of the rings makes possible the observation of electron interference phenomena. An electron wave injected from the metal pad can follow a clockwise or anti-clockwise path around the ring. As a result of time reversal invariance the two waves acquire the same phase shift and can interfere constructively leading to a quantum mechanical contribution (increase) to the resistance (R_{QM}) of the ring. By applying a magnetic field oriented perpendicular to the plane of the ring, time reversal invariance is destroyed and R_{QM} is reduced. From the dependence of the resistance on the strength

of the field, the coherence length of the electrons can be deduced. Here we focus on electrical transport in SWNT rings at low temperatures. We are able to determine the conduction mechanism, the coherence length of the electrons, the dominant dephasing mechanism, and observe a transition from a weak to a strong electron localization state. Experimental details are given elsewhere [3].

In Fig. 2 we show magneto-resistance (MR) curves for a 820 nm diameter ring at temperatures in the range of 2-6 K. A clear negative MR, i.e. a decrease in resistance with increasing magnetic field, is observed. This behavior is characteristic

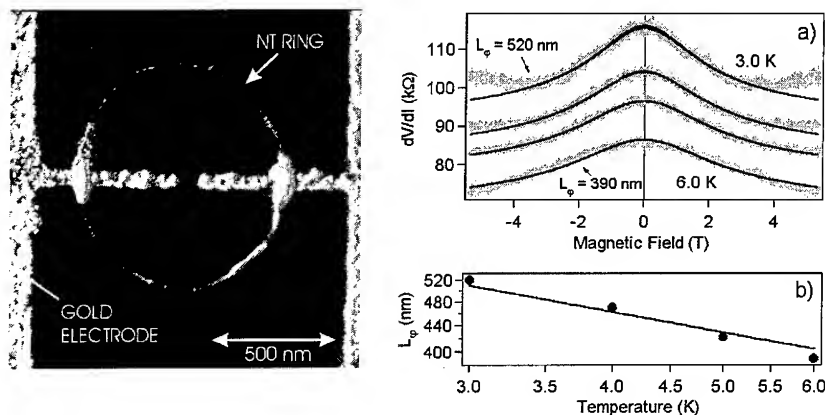


Figure 1: AFM image of a nanotube ring bridging two gold electrodes.

Figure 2: a) Magneto-resistance of a ring as a function of temperature. b) The dependence of the coherence length, L_ϕ , on temperature.

of disordered conductors in the weak localization regime [4]. The magnetic field lifts time reversal invariance and eliminates interference effects that are responsible for the quantum mechanical contribution to the resistance of the ring. The dark lines in Fig. 2a are fits to 1D weak localization theory (WLT) from which the coherence length L_ϕ of the conduction electrons is obtained. We find values of L_ϕ that range from 390 nm at 6 K to 520 nm at 3 K. The L_ϕ lengths are significantly smaller than the perimeter of the ring which is $\sim 2.6 \mu\text{m}$. By plotting the L_ϕ vs. temperature we can determine the dominant dephasing mechanism in this temperature range. The relation is best described as $L_\phi \propto T^{-1/3}$ (Fig. 2b). This temperature dependence of L_ϕ is characteristic of dephasing through electron-electron interactions (Nyquist mechanism) [5].

In Fig. 3a we show the temperature dependence of the zero-field resistance over a wider range. We observe a monotonic rise in resistance with decreasing

temperature. The data in the range 6-60 K (Fig. 3a) fit well a $dV/dI \propto T^{-1/3}$ relation which is characteristic of weak localization in a 1D system dephased through e-e scattering [5]. Thus, given also the good fit of the MR to 1D-WLT we conclude that coherence effects dominate the transport of the ring over a wide temperature range. Previous work [6] has shown that the temperature dependence of the resistance of SWNT ropes depends on their processing. In particular, acid treatment dopes the ropes. While sulfuric acid was used in the preparation of our rings, it was removed afterwards by careful annealing.

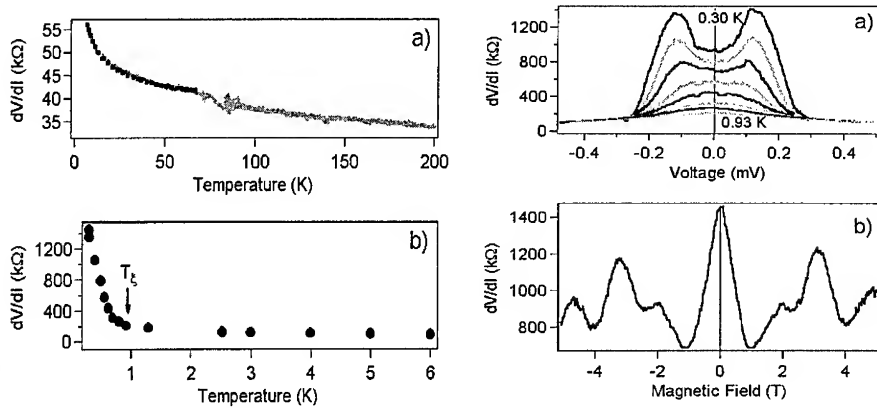


Figure 3: a) Temperature dependence of the zero-field resistance of the ring and fit to one-dimensional weak localization theory. b) Close up of the region near the weak to strong localization transition.

Figure 4: a) Behavior of the ring resistance below 1 K. b) Magneto-resistance of the ring at 0.3 K.

While the resistance of the nanotube rings evolves smoothly down to ~ 2 K (differences in the value of the contact resistance are, however, observed in different runs involving the same ring), as Fig. 3 shows, a drastic change is observed below ~ 1 K. The resistance within a range of only one degree increases from ~ 150 $k\Omega$ to ~ 1.5 $M\Omega$. The resistance can now be expressed as $R = R_0 \exp(T_0 / T)$, with $T_0 = 0.8$ K. Thus, $k_B T_0 \approx k_B T_\xi$, where T_ξ is the transition temperature. The scaling theory of localization [7] predicts that a transition will take place when the broadening of the electron levels as a result of phase breaking processes \hbar / τ_ϕ is reduced by the decreasing temperature, so that it becomes comparable to the spacing Δ_ξ between the levels in the domain of size ξ , the localization domain. At this point transport becomes an activated process as observed above.

Further evidence for a weak to strong localization transition comes from consideration of the I - V characteristics of the system. The development of the

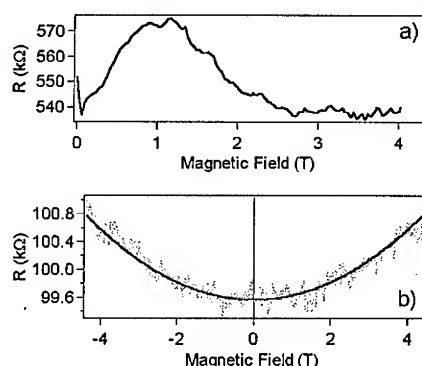
resistance peak below 1 K is shown in dV/dI vs. V curves (Fig. 4). When the temperature is decreased below ~ 0.7 K, a local resistance minimum is observed around zero bias resulting in a cusp-like shape. The corresponding dI/dV vs. V plot, which could be interpreted as representing the tunneling density of states, shows a gap and an associated weak peak, a zero-bias anomaly (ZBA).

A number of different interactions can lead to the opening of a gap in the nanotube ring spectrum. The lack of any gate effect argues against Coulomb blockade. Disorder-enhanced electron correlation-induced Fermi level singularities [8] which are expected to lead to a gap with a $\propto \sqrt{V}$ dependence do not match the observations. Recently, evidence has been presented that SWNT ropes behave as Luttinger liquids [9]. A characteristic of this state is the power law dependence of the tunneling conductance on T and V , i.e. $dI/dV \propto V^\alpha$, where α is independent of T , and for nanotubes $\alpha < 1$ [9]. For $T \geq 1$ K, we can fit the dI/dV plot for $V > 4$ mV to a power law with a nearly temperature-independent exponent $\alpha \approx 0.25$ suggestive of the presence of a Luttinger liquid. If, however, we fit the dI/dV plot in the gap region to a power law, we find a good fit, but now α is significantly larger than one, and depends strongly on temperature. A transition to a strongly localized state appears, therefore, to be the best explanation for the observed behavior. Additional evidence is provided by the examination of the MR at $T < T_g$. As Fig. 4b shows, the MR of the ring at 0.4 K is drastically different from that at $T > T_g$. The MR remains negative, but is a stronger function of the magnetic field strength, cannot be fitted by WLT, and new, aperiodic oscillations are seen. These observations are in accord with the expectations for the MR of strongly localized systems [10]. Weak annealing of the sample changes the aperiodic oscillations by changing the positions of the scattering centers. This behavior is characteristic of the phenomenon of universal conductance fluctuations [4].

We now consider the nature of the ZBA. Anomalies similar to the one observed here have been observed in tunneling and point contact spectra for a long time, and a number of possible interpretations have been proposed [11]. Experiments show that, in most cases, ZBA are the result of the existence of localized magnetic moments near the tunneling interface. Appelbaum and Anderson showed [11] that third-order scattering involving a Kondo term $H_{\text{Kondo}} = -2J\vec{S} \cdot \vec{\sigma}$ in the Hamiltonian can lead to a ZBA. This anomaly results when metal electrons are reflected by the exchange interaction with the magnetic moment and the reflected and transmitted electron waves interfere. In carbon nanotubes such as ours that are prepared using Ni and Co catalysts [12] it is to be expected that magnetic atoms are present despite the acid treatment purification procedure. The magnetic origin of the ZBA is demonstrated by the sensitivity of the ZBA to an applied magnetic field (Fig. 5).

While negative magneto-resistance is the normal behavior of the rings, in some samples and at low temperatures a weak positive magneto-resistance was observed at low fields (< 1 T) which then became negative at higher fields (Fig. 6a). This weak

“anti-localization” behavior may be the result of spin-orbit scattering [13] involving metal atoms from the metal pads or impurity atoms. Finally, a very weak, exclusively positive magneto-resistance up to ~ 5 T was observed (see Fig. 6b) in the case of a ring when the ring-gold contacts were irradiated with 25 keV (~ 30 C/cm²) electrons in a SEM in order to reduce the contact resistance [14]. Analysis of these results using the



model of ref. 15 indicates a dominant spin-flip scattering.

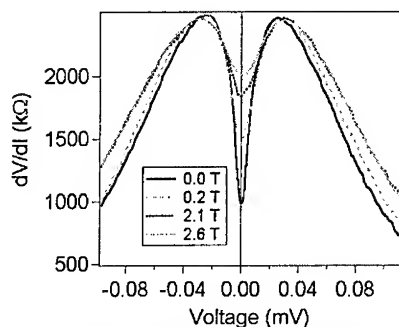


Figure 5: Magnetic field dependence of the zero bias anomaly.

Figure 6: a) Initially positive magneto-resistance of a ring at 0.4 K.

b) Positive ring magneto-resistance at 1.9 K observed after irradiation with 25 keV electrons.

References

- [1] R. Saito, G. Dresselhaus and M. S. Dresselhaus, Physical Properties of Carbon Nanotubes, Imperial College Press, London, 1998.
- [2] R. Martel, H. R. Shea, and Ph. Avouris, Nature **398**, 299 (1999).

- [3] H.R. Shea, R. Martel, and Ph. Avouris, to be published.
- [4] P. A. Lee and T. V. Ramakrishnan, *Rev. Mod. Phys.* **57**, 291 (1985).
- [5] B. L. Altshuler, A. G. Aronov, and D. M. Khmelnitskii, *J. Phys. C* **15**, 633 (1986).
- [6] A. G. Rinzler et al., *Appl. Phys. A.* **67**, 29 (1998).
- [7] D. J. Thouless, *Phys. Rev. Lett.* **39**, 1167 (1977).
- [8] B. L. Altshuler and A. G. Aronov, *Sov. Phys. JETP* **50**, 968 (1979).
- [9] M. Bockrath et al., *Nature* **397**, 598 (1999).
- [10] Yu. B. Khavin, M. E. Gershenson, A. Bogdanov, *Phys. Rev. B* **58**, 8009 (1998).
- [11] T. Walsh, *Internl. J. Mod. Phys. B* **6**, 125 (1992), and references cited therein.
- [12] A. Thess et al., *Science* **273**, 483 (1996).
- [13] G. Bergmann, *Physics Reports* **107**, 1 (1984).
- [14] I. Martin and P. Phillips, *Phys. Rev. B* **56**, 14883 (1997).
- [15] Ph. Avouris et al., *Appl. Surf. Sci.* **141**, 201 (1999).

Quantentransport in Multiwall Carbon Nanotubes

C. Schönenberger¹, A. Bachtold¹, C. Strunk¹, T. Nussbaumer¹, J.-P. Salvetat², L. Forró²

¹*Institut für Physik, Universität Basel, Klingelbergstrasse 82, CH-4056 Basel, Switzerland*

²*Institut de Génie Atomique, École Polytechnique Fédérale de Lausanne, CH-1015 Lausanne, Switzerland*

Abstract. Equilibrium electric resistance R and tunneling spectroscopy (dI/dV) measurements obtained on single multiwall nanotubes are reported. As a function of temperature T the resistance increases on decreasing T and saturates at $\approx 1 - 10$ K for all measured nanotubes. $R(T)$ cannot be related to the energy-dependent DOS of graphene but is mainly caused by interaction and interference effects. On a relatively small voltage scale of order ≈ 10 meV, a pseudogap is observed in dI/dV which agrees with Luttinger-Liquid theories for nanotubes.

INTRODUCTION

Carbon nanotubes are molecular wires whose electronic properties are largely determined by extended molecular orbitals. Depending on the specific realization, the nanotube may be a true one-dimensional metal or a semiconductor with a gap. On the fundamental side, a perfect metallic nanotube (NT) is supposed to be a ballistic conductor in which only two one-dimensional ($1d$) subbands carry the electric current.¹ Hence, the conductance should be given by $G = 4e^2/h = (6.4 \text{ k}\Omega)^{-1}$ independent of the NT diameter d . Because of the low carrier concentration and low-dimensionality, long-range Coulomb interaction is expected to strongly modify the Fermi liquid (FL) picture of quasi-particles. An appropriate effective description is believed to be given by the Luttinger liquid (LL) model.² Because there is striking evidence for LL-like behavior in SWNTs,³ one may wonder whether MWNTs are LLs too.

RESULTS AND DISCUSSION

We report electric transport measurements for single multiwall nanotubes (MWNTs) contacted by four metallic Au fingers from above. The four-terminal electrical resistances R always increases with decreasing temperature and saturates around $1 - 10$ K. A typical example is shown in Fig. 1. The increase from room temperature is moderate

amounting to a factor $\lesssim 2 - 3$. This together with the low-temperature saturation is taken as evidence for the metallic nature of the MWNTs. We emphasize that not only is the temperature dependence of $R(T)$ similar for all samples, but the absolute resistance values also fall into a relatively narrow range of $R_{4t} \approx 2 - 20 \text{ k}\Omega$ for a contact separation of $L \approx 0.5 \mu\text{m}$.

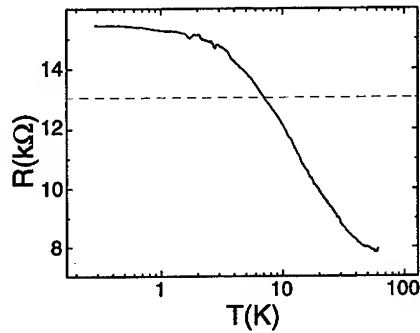


Figure 1: Typical temperature dependent electrical resistance $R(T)$ of a single MWNT measured in a four-probe configuration. The dashed line corresponds to the resistance quantum $h/2e^2$.

The resistance increase at low temperatures is markedly different to what is known from (HOPG) graphite. There, the resistivity decreases with decreasing temperature as commonly associated with metallic behavior. In trying to understand the temperature dependence of R , we consider the simplest possible model. We compare the absolute measured resistance values with an expression for the classical Drude resistance taking one graphene cylinder and assuming $2d$ -diffusive transport. We thereby completely disregard the quantization of the wavevector around the tube circumference leading to $1d$ subbands (for details, see Ref. 5). Due to the vanishing electron DOS of the graphene sheet for $E \rightarrow 0$, the resistance should increase with decreasing temperature following $R(T) \propto T^{-1}$. Although a resistance increase is observed, the increase is not compatible with a T^{-1} dependence. Moreover, $R(T)$ saturates below $\approx 4 \text{ K}$. This saturation could be explained by a finite overlap with additional graphene cylinders giving rise to a narrow band of width Δ at the Fermi energy as in graphite. In the limit $kT < \Delta$ a constant DOS develops. Taking reasonable values for the overlap one obtains an unphysically large mean-free path l_e , that is $l_e \gg L$. The only way to reconcile this model with the requirement $l_e \lesssim L$ is to assume that a large number of graphene cylinders carry the electric current equally. We know from the Aharonov-Bohm experiments that this is not the case.⁷ We therefore conclude that the specific temperature dependence of R cannot be related to the energy-dependent DOS of graphene.

Within this simple Drude picture, the discrepancy can be resolved if we take into account the band-structure modifications imposed by the periodic-boundary condition along the circumference of the cylinder leading to $1d$ -subbands. In contrast to graphene,

for which the DOS tends to zero for $E \rightarrow 0$, in $1d$ it is constant in an relatively large energy window centered around the Fermi energy. This energy window is given by the subband separation ΔE_{sb} . With $\Delta E_{sb} = 100$ meV, typically valid for the outermost cylinders of our MWNTs, one arrives at a mean-free path of $l_e \approx 50$ nm, which is of order of the circumference of the tube. This number is of reasonable magnitude and in agreement with magnetoresistance measurements.⁵ This argument suggests that electron transport in MWNTs is not $2d$ -diffusive, but rather one-dimensional. Most importantly, it demonstrates that the $1d$ -subbands need to be considered in MWNTs as well.

The classical $1d$ -Drude resistance due to static-disorder alone predicts a temperature-independent resistance. Temperature dependences can be caused by other scattering mechanism, like electron-phonon, electron-electron interaction, and interference corrections. Quantum interference corrections have been observed in the magnetoresistance (MR) of MWNTs before.⁶ A negative MR was observed at low temperatures indicative of weak localization (WL). However, the phase-coherence length l_ϕ was found to be small amounting to only $\lesssim 20$ nm at 0.3 K. Recently, we have observed a pronounced Aharonov-Bohm (AB) resistance oscillation with period $h/2e$ in MWNTs.⁷ The AB-MR agrees with theory only, if the current is assumed to flow through one or at most two metallic cylinders with a diameter corresponding to the measured outer diameter of the NT. Because the $h/2e$ period requires backscattering on the scale of the diameter of the NT it is clear that the NTs are *not ballistic*. From a detailed analysis of $l_\phi(T)$, we obtain $l_e = 90 \dots 180$ nm.⁵ Because $l_e \gtrsim \pi d$, transport in our MWNTs should be classified as *quasi-ballistic*. There are other observations in favour of this results. For example, van Hove-type singularities have been seen in a dI/dV tunneling spectrum.⁵ Because these features are associated with the formation of $1d$ -subbands, l_e should be of order or larger than the circumference of the NT. We have to emphasize, however, that the prevailing spectra display a pronounced zero-bias anomaly (ZBA) on a smaller energy scale of $1 - 10$ meV. For larger energies, a peak-structure develops in dI/dV on the scale of the subband separation (0.1 eV) which may be associated with (broadened) van-Hove singularities.

A typical ZBA is shown in Fig. 2 for six temperatures ranging from $2 - 20$ K. A suppression of the tunneling DOS is expected for a strongly correlated electron gas.⁸ Similar anomalies have recently been observed by Bockrath *et al.* for SWNTs.³ Their measurement and analysis provide the first convincing demonstration for Luttinger liquid (LL) behavior in carbon NTs due to long-range Coulomb interactions. LL theory predicts power laws both for the voltage and temperature dependence with the same exponent α . A power-law with $\alpha \approx 0.36$ is deduced from $dI/dV(T, V = 0)$, see the inset of Fig. 2. For comparison with the observed dI/dV -voltage dependence, the dashed-dotted curve $\propto V^{0.36}$ has been plotted.

The reported study of electric transport of single MWNTs gives rise to results which appear to be in contradiction. For example, the observation of an Aharonov-Bohm effect

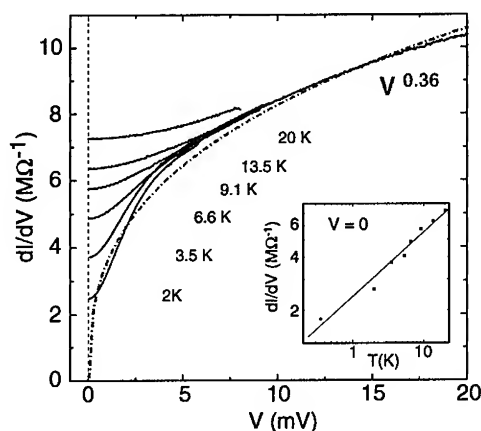


Figure 2: Differential tunneling conductance dI/dV measured on a single MWNT at different temperatures T displaying a pronounced zero-bias anomaly. Inset: log-log representation of dI/dV vs. T for $V = 0$. The dashed-dotted curve displays the power-law $dI/dV \propto V^\alpha$ with $\alpha = 0.36$ deduced from the inset.

with period $\hbar/2e$ suggests diffusive transport on the scale of the circumference of the nanotube, i.e. $l_e \lesssim \pi d$. On the other hand, we have observed a dI/dV spectrum which agrees with tight-binding models assuming the existence of 1d-subbands. This suggests the opposite, i.e. $l_e \gtrsim \pi d$. Our results are therefore consistent only if l_e is of the order of the circumference.

There is a second ‘contradiction’ inherent to our presentation. On the one hand, we have used weak-localization theory which is based on the Fermi liquid hypothesis. On the other hand, the observed suppression of the single-particle states suggests that NTs may develop a Luttinger liquid (LL) state. If LL is the correct description for NTs (including MWNTs) we need to know how the observed quantum interference corrections have to be described.

1. R. Saito *et al.*, Appl. Phys. Lett. **60**, 2204 (1992); J. W. Mintmire *et al.*, Phys. Rev. Lett. **68**, 631 (1992).
2. R. Egger and A. O. Gogolin, Phys. Rev. Lett. **79**, 5082 (1997); C. Kane, *et al.*, *ibid.* 5086.
3. M. Bockrath *et al.*, Nature **397**, 598 (1999).
4. A. Bachtold *et al.*, Appl. Phys. Lett. **73**, 274 (1998).
5. C. Schönenberger *et al.*, to appear in Appl. Phys. A.
6. S. N. Song *et al.*, Phys. Rev. Lett. **72**, 697 (1994); L. Langer *et al.*, Phys. Rev. Lett. **76**, 479 (1996).
7. A. Bachtold *et al.*, Nature **397**, 673 (1999).
8. M. P. A. Fisher and L. Glazman, in *Mesoscopic Electron Transport*, L. L. Sohn, L. P. Kouwenhoven, and G. Schön, eds., NATO ASI Series E: Applied Sciences **345** (Kluwer Academic, Dordrecht 1997).

Electron Interference Effect in Multi-wall Carbon Nanotubes

Akihiko Fujiwara*, Kozue Tomiyama*, Hiroyoshi Suematsu*, Motoo Yumura†, Kunio Uchida†

*Department of Physics, School of Science, University of Tokyo, Tokyo 113-0033, Japan

†Department of Chemical Systems, NIMC, 1-1 Higashi, Ibaraki 305-0046, Japan

Abstract. We have measured the resistance of individual multi-wall carbon nanotubes under magnetic fields with various directions. Resistance oscillates periodically depending on the magnetic field below about 30 K. The amplitude of oscillation increases with decreasing temperature. The period of this oscillation depends on $1/\cos\theta$, θ being the angle between the magnetic field and the nanotube axis; namely, the period reflects the flux penetrating the cross section of the nanotube. These results are well explained by a quantum interference of electrons along the circumference of the nanotube. We interpret these results in terms of the Aharonov-Bohm effect.

INTRODUCTION

Since its discovery [1], the carbon nanotube has attracted great attention as a very interesting electronic material because of the one-dimensional tubular network structure in the nanometer scale. Theoretical studies of the carbon nanotubes predict some novel electronic properties such as the band-structure characteristic of the tubular-honeycomb network, one-dimensional nature and the magnetic quantum effect [2,3].

In this paper we present the observation of quantum interference of electrons along the circumference of the nanotube in the magnetoresistance measurement of individual multi-wall carbon nanotubes. The resistivity shows an oscillatory dependence on the magnetic field and the period depends on $1/\cos\theta$, θ being the angle between field and the nanotube axis. The latter fact means that the period reflects the magnetic flux penetrating the cross section of the nanotube. This effect is discussed in terms of Aharonov-Bohm (AB) effect.

EXPERIMENTAL

The carbon nanotubes were obtained from carbon raw soot (Type I, Vacuum Metallurgical Co. Ltd., Japan) by physical purification processes, that is, repetition

of the centrifugation at 5000 r.p.m. for 20 min. and the filtration. Electric contacts to one nanotube were made with use of the electron-beam-lithography method [4,5]. Figure 1 shows a SEM image of one nanotube and gold contacts. The d.c. magnetoresistance measurements were carried out by using Quantum Design PPMS system with a rotating sample-mount. The measurements were performed in the ohmic region with the current 30 nA. The sample dimensions are estimated to be 190 Å in outer diameter and 1.0 μm in voltage contact distance by means of the SEM observation. The inner diameter is estimated as around 30 Å from the TEM observation of nanotubes in the same lot.

RESULTS AND DISCUSSION

Figure 2(a) shows the magnetoresistance for the magnetic field parallel to the nanotube axis at some temperatures. We have observed a periodic oscillation whose amplitude increases significantly at low temperatures. A most interesting feature of this oscillation is θ dependence of the peak field, H_n . Dependence of H_n on θ as shown in Fig. 2(b) can be represented by the relation,

$$H_n(\theta) = H_{n,0} / \cos \theta, \quad (1)$$

where n is the index of the peak and $H_{n,0}$ is the peak field at $\theta = 0^\circ$. The solid lines in Fig. 2(b) are fits by Eq. (1) with parameters $H_{1,0} = 2.4$ T and $H_{2,0} = 7.1$ T. The observed angle dependence tells us that peaks appear when the magnetic flux penetrating the cross section of the nanotube, ϕ , is the same, namely, the component of the magnetic field in the direction of the nanotube axis is effective to the oscillation. This result suggests that the oscillation comes from some interference effect relating to the sectional area of the nanotube.

We will show that the oscillation of magnetoresistance can be nicely explained by the AB effect predicted by Ajiki and Ando [3]. It is well known that the carbon

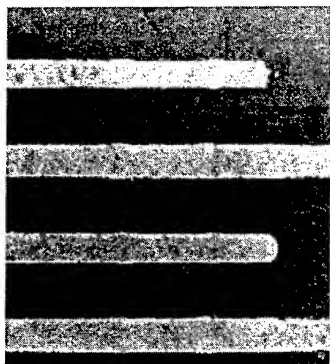


FIGURE 1. SEM image of a multi-wall nanotube and gold contacts for transport measurements. The stripe shaped gray areas are gold leads and a fine line presents a nanotube.

nanotubes are predicted to have three types of electronic structure depending on the periodic boundary condition, namely, the chirality and the diameter, which can be parameterized by a chiral vector (n,m) (n,m : positive integer) [2]. The electronic structure of (n,m) -nanotube can be determined by a parameter ν , when we define

$$n - m = 3N + \nu, \quad (2)$$

with integer N and $\nu (= 0, \pm 1)$ [3,2]. The nanotubes with $\nu = 0$ and ± 1 are metallic and semiconductive, respectively. In addition, Ajiki and Ando [3] predicted the effect of magnetic field parallel to the nanotube axis on their electronic structure. In this theory, in metallic nanotube ($\nu = 0$) the energy gap at the Fermi energy is vanished at $\phi = 0$ and linearly increases with increasing the magnetic field and then has a maximum value of $3E_g/2$ at $\phi = h/2e$. It linearly decreases to zero again at $\phi = \phi_0 \equiv h/e$. For two types of semiconductors ($\nu = \pm 1$), the magnetic field dependence of the electronic structure can be described by shifting the origin from zero to $h/3e$ and $2h/3e$ for $\nu = -1$ and 1 , respectively [3]. Therefore we can describe the magnetic field dependence of the energy gap as

$$E_{g\nu}(H) \equiv \frac{3}{2}E_g \times F_{tw} \left(\frac{H}{(\phi_0/\pi r^2)} + \frac{\nu}{3} \right), \quad (3)$$

where E_g is the energy gap of semiconductor phase at zero magnetic field, $F_{tw}(x)$ is triangular-chopped-wave function with the period of 1 and the amplitude of 1 and r is the radius of the nanotube. Our samples are multi-wall nanotubes and they are expected to have all three types of nanotubes. For simple, we consider a parallel connection of three-wall nanotubes, in which each wall has different ν each other, then, magnetoresistance can be described by

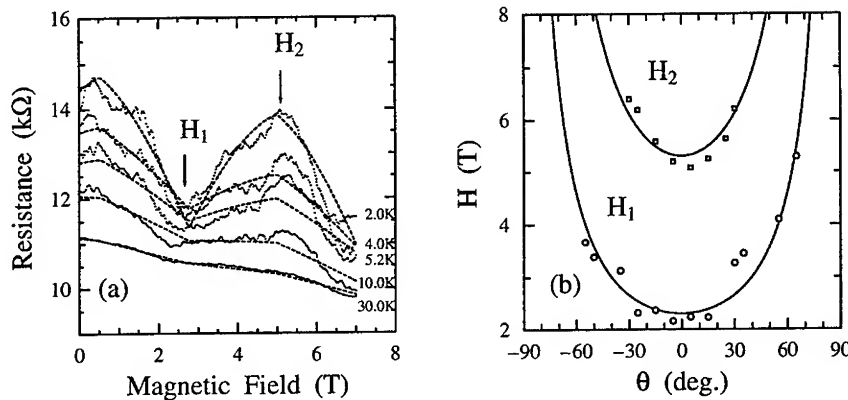


FIGURE 2. (a) Magnetoresistance for various temperatures with a magnetic field parallel to the nanotube axis. The dots and dashed lines are experimental data and fitting results by Eq.(4), respectively. (b) θ dependence of peak positions for H_1 and H_2 in Fig.2(a). The solid lines are fitting results by Eq.(1).

$$R(T, H) = \left[\sum_{\nu=-1}^1 \frac{1}{R_{\nu}(T)} \exp\left(\frac{-E_{g\nu}(H)}{k_B T}\right) \right]^{-1} + R'(T)H, \quad (4)$$

where R_{ν} is resistance at $E_{g\nu} = 0$, k_B is Boltzmann constant and R' is the coefficient of the non-oscillation term of magnetoresistance. In spite of this simple model, Eq. (4) can represent experimental data: dashed lines in Fig. 2(a) are fitting results with parameters $E_g = 2.9 \times 10^{-4}$ eV and $r = 100$ Å. What has to be noticed is that estimated diameter, $2r = 200$ Å, is very close to the outer diameter of nanotube, 190 Å. This result suggests that conduction electrons should mainly flow on a few layers around the outer wall. In addition, an occurrence of the AB effect caused by the periodic boundary condition requires the seamless cylindrical structure of graphen sheet. Therefore, the structure of multi-wall carbon nanotubes in this work is not the scroll type but the concentric type.

SUMMARY AND CONCLUSIONS

We have systematically measured the temperature and the angular dependences of magnetoresistance of individual multi-wall carbon nanotubes. A periodic oscillation of the magnetoresistance has been observed as a function of the magnetic flux penetrating the cross section of the nanotubes, which can be understood as an appearance of the AB effect. This is the first observation of transport properties reflecting the tubular figure and the honeycomb network of the carbon nanotubes. The result shows the evidence of the concentric structure of multi-wall carbon nanotubes and of the existence of three types of concentric nanotubes: one third are metallic and two thirds are semiconducting.

ACKNOWLEDGEMENTS

This work was supported by the research project, "Materials Science and Microelectronics of Nanometer-Scale Materials" (RFTF96P00104) from the Japan Society for the Promotion of Science, Japan. One of authors (A.F.) was supported by a Grant-in Aid for Encouragement of Young Scientists (09740270) from The Ministry of Education, Science, Sports and Culture of Japan.

REFERENCES

1. Iijima, S., *Nature* (London) **354**, 56-58 (1991).
2. Saito, R. *et al.*, *Appl. Phys. Lett.* **60**, 2204-2206 (1992).
3. Ajiki, H. and Ando, T., *J. Phys. Soc. Jpn.* **62**, 1255-1266 (1993).
4. Fujiwara, A. *et al.*, in *Molecular Nanostructures*, edited by H. Kuzmany *et al.* (World Scientific, Singapore, 1997), pp. 439-442.
5. Tomiyama, K. *et al.*, submitted to *Phys. Rev. B*.

Charge transport in carbon nanotube transistors

Kun Liu¹, Marko Burghard¹, Siegmund Roth¹, Parthick Bernier²

¹*Max-Planck-Institut für Festkörperforschung, Heisenbergstr.1, D-70569 Stuttgart, Germany*

²*Groupe de Dynamique des Phases Condensees, Universite Montpellier, 34095 Montpellier, France*

ABSTRACT

Carbon nanotube (CNT) field-effect transistors have been fabricated, and investigated by measuring the channel conductance as a function of the gate voltage at room temperature and 4.2K. In addition to the field effect, spikes are measured in the transfer characteristics. Based on these experimental observations, charge transport in CNT transistors is discussed.

INTRODUCTION

Carbon nanotubes^[1] (CNTs) are good candidates for nanoscale electronic devices^[2-5] due to their unique electrical properties^[6] and nanoscale dimensions. Very recently, CNT field-effect transistors have been fabricated and studied by Tans et al. and Martel et al. at room temperature^[7,8]. In order to describe charge transport in the CNT transistor, Tans et al. have used the semi-classical band-bending model. However, Martel et al. point out that the band-bending length is unlikely to be very long because of the large onset gate voltage needed for turning off the channel. In this paper, we present further investigations on CNT transistors at room temperature as well as at 4.2K. In addition to the field effect, spikes are clearly observed in the channel conductance as a function of the gate voltage. Based on this additional experimental observation, the implications on the charge transport in CNT transistors are discussed.

DEVICE FABRICATION AND EXPERIMENTAL SETUP

Purified single-walled carbon nanotubes were uniformly dispersed in an aqueous medium with the aid of the surfactant sodium dodecyl sulfate^[9]. A few drops of such dispersion are then deposited onto the substrate with predefined Au electrodes, as shown in Fig.1a. The distance between neighboring electrodes is 100nm, the Si wafer is heavily doped and acts as back gate, the gate insulation layer SiO₂ is 300nm thick. After a few minutes, the substrate was blown dry, and 'a few' tubes or bundles of tubes remained over the electrodes, as shown by the AFM image in Fig.1b. Between electrodes 2 and 6, and electrodes 3 and 6, the current can flow at beginning but not

after a few measurements, indicating the tubes between electrodes 2 and 6 and 3 and 6 have been destroyed. However, the bundle marked by the arrow is still perfect, detailed experiments were thus carried out on this bundle at 300K and 4.2K, in a vacuum of $<10^{-5}$ mbar using an electrometer with a sensitivity of 0.5pA and 10 μ V. AFM studies indicate that this bundle has a height of 3.5nm, and thus contains ~ 5 individual tubes.

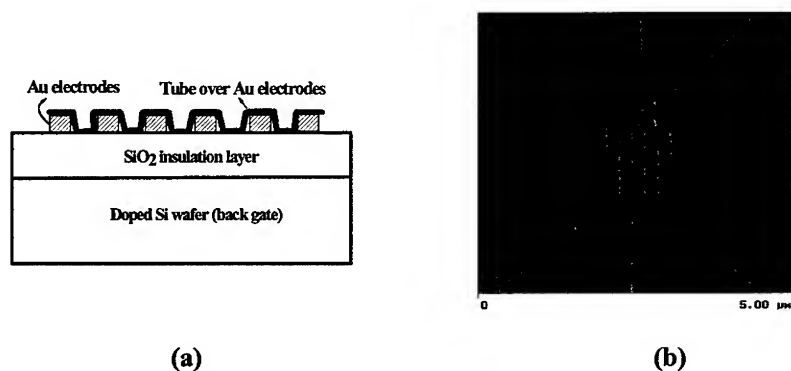


FIGURE 1, (a) Schematic of the tube transistor. (b) AFM image of the tubes in the transistor

EXPERIMENT RESULTS AND DISCUSSION

Fig.2a and 2b present the drain-source current I_{DS} as a function of the gate voltage V_G with applying different drain-source bias V_{DS} at 300K and 4.2K, respectively. The insets plot the channel conductance $G = I_{DS}/V_{DS}$. In the experimental range, the channel conductance has been modified 10^2 times at 300K and 10^5 times at 4.2K, showing a pronounced field effect. The majority carriers are holes, they can be accumulated or depleted with applying negative or positive gate voltage, leading to turning on and off of the channel, as indicated in the insets. In the transistor, the tube/Au contact resistance R_C is measured to be about 0.8 M Ω at 300K and 3.3M Ω at 4.2K, which is in agreement with the values reported in the CNT/Pt and CNT/Au contacts^[5-8]. In order to turn off the channel, a very large onset gate voltage V_G' [$V_G'(300K) \sim 38V$, $V_G'(4.2K) \sim 10V$,] is required, implying a large density of holes in the tubes. Using the method given by Martel et al.^[8] and the parameters of the transistor, the hole density N_h in the tubes is estimated to be about $6.4 \times 10^7/cm$ at 300K and $1.6 \times 10^7/cm$ at 4.2K, indicating that tubes are degenerate and the Fermi level lies below the valence band edge of the tubes.

In addition to the field effect as observed by Tans et al. and Martel et al., we have observed spikes in the channel conductance. These spike structures allow us to get a new insight into the charge transport in CNT transistors. First, these spikes are far above the noise level of the measuring system and very reproducible at low

temperatures. Secondly, these spikes are not caused by the Coulomb blockade oscillations (as observed previously by other authors at low temperatures^[3-5]), since the charging energy in the transistor, $E_c = e^2/2C_T$, is expected to be smaller than the thermal energy $k_B T$, the Coulomb blockade oscillations are smeared out. Here,

$C_T = 2\pi\epsilon_0 L / \ln(2L/d)$ ^[7] is the tube capacitance, $L=800\text{nm}$ is the tube length between electrodes 2 and 3. Using the semiclassical band-bending model^[7], it is also difficult to explain these conductance spikes. We attribute these spikes to van Hove singularities in the electronic density of states of the nanotubes.

Van-Hove singularities are related to the one-dimension nature of tubes^[10], they have been theoretically investigated by Dresselhaus et al.^[10] and experimentally observed in the STM measurements by Wildoer et al.^[11] and by Odom et al.^[12]. Van Hove singularities will lead to oscillation in the channel conductance of the tube transistor if, (1) the gate voltage can shift the DOS of the tubes with respect to the Fermi level of the electrodes and (2) the energy band-bending in the tubes is weak. Firstly, the tubes in the transistor are well decoupled from the Au electrodes since the contact resistance R_c is much more higher than the quantum resistance ($\sim 0.025\text{M}\Omega$). Therefore, the back gate can shift the energy band of the tubes. Secondly, Schottky barriers are formed at the tube/Au contacts, and the barrier width can be estimated by $d_b = \sqrt{\frac{2\epsilon\epsilon_0(\phi_b - k_B T/e)}{eN_A}}$ ^[13], where $\phi_b = W_{Au} - W_{CNT}$ is the work-function difference of Au and carbon nanotube, N_A is the acceptor concentration and which can be obtained from the hole density at 300K by $N_A = 4N_h / \pi d^2$. Using $W_{Au}=5.2\text{eV}$, $W_{CNT}=2.5\text{eV}$ and $N_h(300\text{K})=6.4\times 10^7/\text{cm}$, we obtain at 300K and 4.2K an almost unchanged d_b of about 3Å. Thus the Schottky barriers at the contacts are very thin, indicating that at zero gate voltage the band-bending in the tubes near the contacts has very small length compared with the tube length, and the energy band of the tubes keeps flat along the length.

Therefore, the energy band of the tubes along the whole length is expected to move up and down upon changing V_G , and conductance peaks should occur when different van Hove singularities pass the Fermi level one by one. Since the DOS

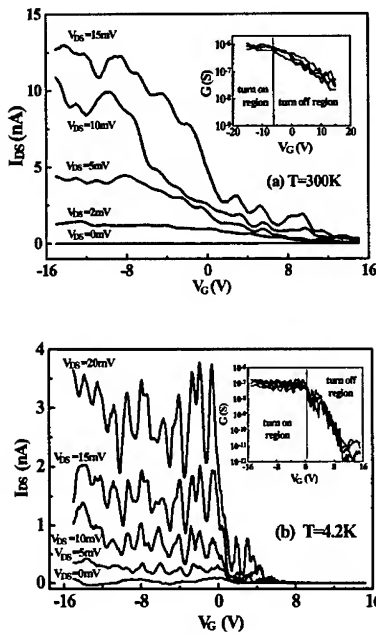


FIGURE 2. Drain-source current I_{DS} as a function of the gate voltage V_G at different bias V_{DS} at (a) 300K and (b) 4.2K. The insets plot the channel conductance G .

increases with energy from the band edge, the channel conductance increases with V_G in the negative direction. Detailed studies on van-Hove singularities using the tube field-effect transistor will be reported elsewhere^[14].

We note that no increase of the channel conductance is observed in the positive V_G region of the experimental range. This is due to the fact that there exists an energy gap E_g in the tubes and the Fermi level lies below the valence band edge due to degeneracy, and consequently, higher V_G is required to observe the conductance increase in the positive V_G region. We also note that considerably more spikes are observed here than in the STM measurements^[11,12]. This could arise from the difference of the tubes used. In our experiments, the tubes are purified by the soft centrifugation method, van Hove singularities could be well-defined in the tubes. In addition, high electric field in the STM experiments could modify the density of states and make it more difficult to observe van Hove singularities. In the room temperature experiments by Tans and Martel et al. no conductance spikes were observed^[7,8]. In our room temperature experiments, the conductance spikes are not well defined. These could be due to the hybridization effect of wave-functions^[11] at high temperatures.

CONCLUSIONS

In conclusion, carbon nanotube field-effect transistor have been fabricated and studied. The transistors operate at both room temperature and low temperature. In addition to the pronounced field-effect, conductance spikes have been observed. We attribute these spikes to van Hove singularities in the electronic density of states of the carbon nanotubes.

REFERENCES

1. S. Iijima Nature 354, 56(1991).
2. S. Saito, Science 278, 77(1997).
3. S. J. Tans, M. H. Devoret, H. Dai, et al., Nature 386, 474(1997).
4. M. Bockrath, D. H. Cobden, P. L. McEuen et al., Science 275, 1922(1997).
5. A. Bezryadin, A. R. M. Verschueren, S. J. Tans et al., Phys. Rev. Lett. 80, 4036(1998).
6. For a review, see T. W. Ebbesen, Carbon Nanotubes, CRC Press, Inc., 1997.
7. S. J. Tans, A. R. M. Verschueren and C. Dekker, Nature 393, 49(1998).
8. R. Martel, T. Schmidt, H. R. Shea, T. Hertel, Ph. Avouris, Appl. Phys. Lett. 73, 2447(1998).
9. G. S. Duesberg, M. Burghard, J. Muster et al., Chem. Commun. 435(1998).
10. M. S. Dresselhaus, Nature 391, 19(1998).
11. J. Wildoer, L. C. Venema, A. G. Rinzler, R. E. Smalley, & C. Dekker, Nature 391, 59(1998).
12. T. W. Odom, J. L. Huang, P. Kim, C. M. Lieber, Nature 391, 62(98).
13. S. M. Sze, Physics of Semiconductor Devices, John Wiley & Sons, Inc. P368.
14. Kun Liu, S. Roth, M. Burghard (Unpublished).

Luttinger liquid behavior in single-wall nanotubes

Andrei Komnik and Reinhold Egger

Fakultät für Physik, Albert-Ludwigs-Universität, D-79104 Freiburg

Abstract. Transport properties of metallic single-wall nanotubes are examined based on the Luttinger liquid theory. Focusing on a nanotube transistor setup, the linear conductance is computed from the Kubo formula using perturbation theory in the lead-tube tunnel conductances. For sufficiently long nanotubes and high temperature, phonon backscattering should lead to an anomalous temperature dependence of the resistivity.

Carbon nanotubes possess many fascinating properties and have recently attracted a lot of attention. Metallic nanotubes can behave as ballistic quantum wires over lengths of several μm [1] and hence constitute perfect experimental realizations of 1D conductors. It is now well-known that Fermi liquid theory must break down in such a 1D conductor because of the Coulomb interactions among the electrons. In fact, at temperatures above the milli-Kelvin range, an individual metallic single-wall nanotube (SWNT) can be accurately described in terms of Luttinger liquid (LL) theory [2]. The LL is a prototypical yet simple model for non-Fermi liquid behavior. The interaction strength is measured in terms of a single parameter $g \leq 1$, where $g = 1$ is the noninteracting limit. For a SWNT, the theoretical estimate is [2] $g \simeq \{1 + (8e^2/\pi\hbar\epsilon v_F) \ln(L/2\pi R)\}^{-1/2}$, where the only logarithmic dependence on the tube length $L \approx 1 \mu\text{m}$ and the radius $R \approx 1.4 \text{ nm}$ leads to a value around $g \approx 0.2$ to 0.3 . Here, ϵ is the background dielectric constant and $v_F \approx 8 \times 10^5 \text{ m/s}$ is the Fermi velocity. The LL should also show up in a variety of other systems, such as long chain molecules, the edge states in a fractional quantum Hall bar, or in single-channel quantum wires in semiconductor heterostructures. Unfortunately, despite of many efforts, a generally accepted experimental realization of the LL in these systems is still lacking. For a nanotube rope, however, transport experiments have recently been reported that provide clear evidence for a LL [3]. A rope should show LL behavior if three conditions are met: (a) only one metallic tube is contacted by the leads, (b) most tubes in the rope are not metallic, and (c) electron tunneling between different metallic tubes in the rope can be neglected.

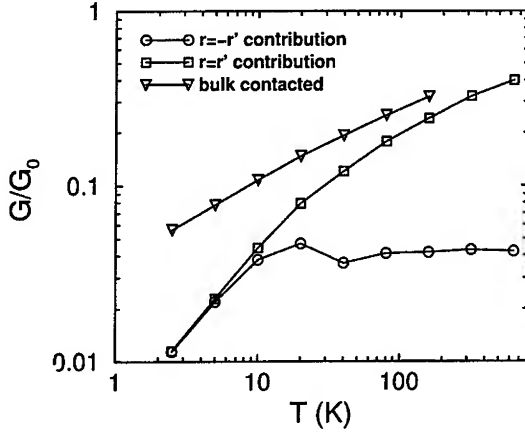


FIGURE 1. High-temperature conductance (3) for $g = 0.2$, $g_1=g_2=0.1$ and $L = 10^4 a = 2.46 \mu\text{m}$. Note the double-logarithmic scales. For the bulk- (end-) contacted case, $x_1 = L - x_2 = 3500a$ (5 a). For the end-contacted case, the $r = r'$ and $r = -r'$ contributions are plotted separately.

Let us consider a transistor consisting of a tube of length L , where contact to external leads is established at positions $0 < x_1 < x_2 < L$. The leads $i = 1, 2$ are modelled by free electrons, and we take the standard tunneling Hamiltonian for the lead-tube couplings. We assume pointlike contacts and focus on the linear dc conductance, which, according to the Kubo formula, takes the form

$$G = \lim_{\omega \rightarrow 0} \frac{1}{\hbar\omega} \text{Im} \left[\int_0^{\hbar\beta} d\tau \exp(i\Omega\tau) \langle I^{(1)}(\tau) I^{(2)}(0) \rangle \right]_{i\Omega \rightarrow \omega + i\delta}, \quad (1)$$

where $\beta = 1/k_B T$. Since the dc current through both contacts coincides, we may take an arbitrary linear combination $I^{(1)} = \epsilon_1 I_1 + \epsilon_2 I_2$ [where $\epsilon_1 + \epsilon_2 = 1$] of the currents I_1 and I_2 through the tunnel contacts at x_1 and x_2 , respectively. Since the transport voltage can also be split up arbitrarily [4], the second current operator can be written as $I^{(2)} = \kappa_1 I_1 + \kappa_2 I_2$ with $\kappa_1 + \kappa_2 = 1$. This gives

$$G = \sum_{ij=1,2} \epsilon_i \kappa_j G_{ij}, \quad (2)$$

where the matrix elements G_{ij} directly follow from Eq. (1). We compute these matrix elements by perturbation theory in the dimensionless bare tunnel conductances $g_i = R_K/R_{T,i}$ with the resistance quantum $R_K = h/e^2$ and the tunnel resistance $R_{T,i}$ through contact $i = 1, 2$. Under an exact calculation, one could use any choice for ϵ_1 and κ_1 in Eq. (2) [4]. Under a perturbative calculation for the G_{ij} , however, requiring independence of ϵ_1 and κ_1 is equivalent to maximizing Eq. (2) with respect to these parameters and gives $\epsilon_1 = (G_{21} + G_{22})/\sum_{ij} G_{ij}$ and $\kappa_1 = (G_{12} + G_{22})/\sum_{ij} G_{ij}$. The lowest-order result in g_i follows from the expansion $G_{ii} = G_i + \delta G_{ii}$, where δG_{ii} as well as G_{12} and G_{21} are of at least second order in (g_1, g_2) but G_i is of first order. Then Eq. (2) leads to

$$G = \frac{G_1 G_2}{G_1 + G_2}. \quad (3)$$

This formula describes sequential incoherent transport through the device and is appropriate for high temperatures, where $k_B T$ exceeds the charging energy $E_c \approx e^2 \ln(L/R)/\epsilon L$. In addition, the condition $\hbar v_F/k_B T \ll |x_2 - x_1|$ should hold. On the other hand, at lower temperatures coherent processes such as co-tunneling play a prominent role and lead to the breakdown of Eq. (3). From the general expression (2) we observe that $G \approx G_{12}/2$, since G_i vanishes as $T \rightarrow 0$ unless one has a resonance. This is consistent with the results of Ref. [5] for transport through a LL ring but at the same time indicates that the latter are only valid for thermal energies $k_B T$ well below the charging energy E_c . Therefore the “straightforward” application of the Kubo formula to such problems is not as simple as commonly thought.

Let us start with the high-temperature limit. Perturbation theory yields with $G_0 = 4e^2/h$ and the Fourier transformed LL Greens function $K(x_i, \xi)$ at equal sites,

$$G_i/G_0 = -\pi g_i \int d\xi (-dn_F(\xi)/d\xi) \text{Im} K(x_i, \xi). \quad (4)$$

The derivative of the Fermi function is $-dn_F(\xi)/d\xi = (4k_B T)^{-1} \cosh^{-2}[\xi/2k_B T]$. Technically speaking, $K(x_i, \xi)$ is obtained from a decomposition of the electron operator into 1D fermions $\psi_{r,\alpha,\sigma}$, where $r = \pm$ is the right- or left-moving part, $\alpha = \pm$ denotes the right or left Fermi point, and $\sigma = \pm$ is the spin index, and subsequent use of the bosonization method [2]. Eq. (4) shows that the conductance is related to the local tunneling density of states of the LL. The respective power laws are well-known [2], $G_i \propto T^\eta$, where the exponent η is given by $\eta_b = (g^{-1} + g - 2)/8$ for tunneling into the bulk, i.e., far away from the ends of the tube, and the end exponent is $\eta_e = (g^{-1} - 1)/4$, see Figure 1. These predictions have been verified in recent experiments [3]. For the bulk-contacted case, the slope coincides with the correct value $\eta_b = 0.4$ for $g = 0.2$. For the end-contacted case, the slope is close to the end value $\eta_e = 1.0$ for low temperatures, but exhibits a crossover to the smaller bulk exponent around $T \approx 50$ K. This can be rationalized by separately looking at the $r = r'$ and $r = -r'$ contributions to the conductance. Mixing of right- and left-movers ($r = -r'$) violates momentum conservation and is only allowed close to the end. Due to thermal decorrelation such processes are destroyed with increasing temperature.

For $k_B T \ll E_c$, we compute the conductance as $G_{12}/2$. Following Ref. [5], we employ the Wick theorem. Although strictly speaking this is not correct, at sufficiently low temperatures the corresponding errors in G are expected to become very small. The gate-voltage dependence of the conductance is shown in Fig. 2. Due to the Coulomb blockade, one finds characteristic peaks. Their lineshape accurately follows the standard $\cosh^{-2}(\Delta V_G/2k_B T)$ form, and also the temperature dependence of the peak heights is in agreement with conventional Coulomb blockade theory.

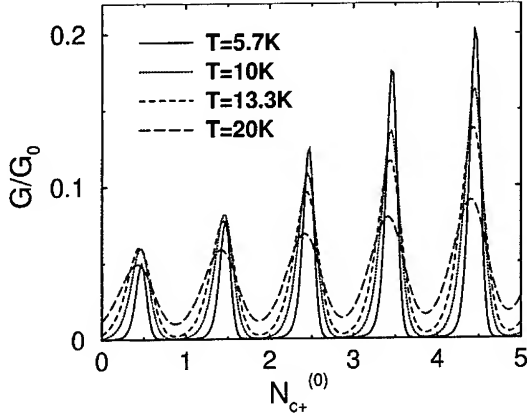


FIGURE 2. Low-temperature conductance $G = G_{12}/2$ as a function of the gate voltage $V_G \propto N_{c+}^{(0)}$ for $g = 0.2, g_1 = g_2 = 0.1, L = 10^4 a$ and $x_1 = L - x_2 = 0.1L$.

In the remainder, we investigate the effect of *phonon backscattering* on the SWNT conductance. In most other systems where LL behavior is thought to be present phonon backscattering does not play an important role for transport properties because of the large momentum transfer $2k_F$. However, in a SWNT the relevant momentum transfer is $2q_F$, where $q_F \ll k_F$ is tuned by the gate voltage. Thermal population of phonon modes is then much more significant. The only low-energy phonons that couple right- and left-movers are the acoustic torsional modes with dispersion $\Omega(q) = v_t|q|$, where $v_t \approx 1.4 \times 10^4$ m/s. Following Ref. [6], the electron-phonon coupling is

$$H_{e-p} = \lambda \int dx \vartheta(x) \sum_{\alpha\sigma} (\psi_{+, \alpha, \sigma}^\dagger \psi_{-, \alpha, \sigma} + \text{H.c.}) , \quad (5)$$

with $\lambda \simeq n \times 2.92$ eVÅ for a (n, n) tube. Using the bosonization method to describe the electronic degrees of freedom $\psi_{r, \alpha, \sigma}$, we focus on the lowest-order ($\propto \lambda^2$) contribution $\delta G_p(T)$ to $G(T)$. The phonon field $\vartheta(x)$ can be expressed in terms of free boson operators a_q . Since $v_t \ll v_F$, we can safely neglect the time-dependence of a_q , and hence the phonon averaging simply produces a boson mode occupation factor $\coth[\hbar\beta\Omega(q)/2]$. Furthermore, for exactly the same reason, this factor can be approximated by $2/\hbar\beta v_t|q|$, and we obtain

$$\delta G_p(T)/G_0 = -L \frac{\gamma_g \lambda^2}{a C_t v_F} (\pi a k_B T / v_F)^{(1+g)/2} , \quad (6)$$

with the twist modulus $C_t \simeq n^3 \times 18$ eVÅ [6] and the numerical prefactor $\gamma_g = 4\pi^{-2} g^{1+g/2} \sin[\pi(3+g)/4] \int_0^\infty dz z / \sinh^{(3+g)/2}(z)$. For example, $\gamma_1 = 2/\pi$ and $\gamma_{0.2} \simeq 0.112$. The tube length L appearing in Eq. (6) should be replaced by $|x_2 - x_1|$ if the phonon modes can be pinned at the locations of the tube-lead contacts. Further modifications might be necessary if strong interactions with the substrate influence the phonon dynamics.

To convert Eq. (6) into a resistivity, we note that $G \equiv G_0\tilde{g} = G_0 + \delta G_p$ is the two-terminal conductance of a nanotube in adiabatic contact to voltage sources. The resistivity is obtained from the four-terminal conductance $\tilde{G} = G_0\tilde{g}/(1-\tilde{g})$, so that the 1D relation $\tilde{G} = \sigma/L$ with $\rho = 1/\sigma$ yields the 1D resistivity due to phonon backscattering

$$\rho = \frac{h}{4e^2} \frac{\gamma_g \lambda^2}{a C_t v_F} (\pi a k_B T / v_F)^{(1+g)/2}. \quad (7)$$

For $g = 1$, Eq. (7) agrees with the theory for uncorrelated electrons and the corresponding experimental results found in many-rope systems and mats [6]. For an individual SWNT, the long-ranged Coulomb interactions among the electrons change this into an anomalous $\rho \sim T^{(1+g)/2}$ power law. It is apparent from Eq. (6) that the conductance will be dominated by phonon backscattering at sufficiently high temperatures, $T > T_g^*(L)$. Let us therefore estimate T^* employing the *ad hoc* criterion $|\delta G_p|/G_0 = \nu$ with, say, $\nu = 0.1$. This gives

$$T_g^*(L) \approx 8000 \left(\frac{3560 \gamma_g}{n} L \right)^{-2/(1+g)}, \quad (8)$$

where T^* is measured in Kelvin and L in μm . Putting $n = 10$ and $g = 1$, this gives $T^* = 180$ K for a $L = 200$ nm tube, and $T^* = 35$ K for a $L = 1\mu\text{m}$ tube. For strongly correlated electrons, the length dependence is even more dramatic. Putting $g = 0.2$ and again $n = 10$, for a $L = 200$ nm tube we get $T^* = 250$ K, while for a $L = 1\mu\text{m}$ tube, phonons already begin to dominate above $T^* = 17$ K.

We thank G. Göppert, A. Gogolin and H. Grabert for discussions, and acknowledge support from the DFG.

REFERENCES

1. S.J. Tans *et al.*, Nature **386**, 474 (1997); **394**, 761 (1998).
2. R. Egger and A.O. Gogolin, Phys. Rev. Lett. **79**, 5082 (1997); Eur. Phys. J. B **3**, 281 (1998); C.L. Kane *et al.*, Phys. Rev. Lett. **79**, 5086 (1997).
3. M. Bockrath *et al.*, Nature **397**, 598 (1999).
4. G. Göppert and H. Grabert, Phys. Rev. B **58**, R10155 (1998).
5. J.M. Kinaret *et al.*, Phys. Rev. B **57**, 3777 (1998).
6. C.L. Kane *et al.*, Europhys. Lett. **41**, 683 (1998).

Electric resistivity and magnetoresistance of some superhard and ultrahard fullerites in the range 300-2K

Vladimir D. Blank*, Sergei G. Buga*, Gennadii A. Dubitsky*,
Xiao-Mei Zhu†, Emmanuel Nyeanchi† and Bertil Sundqvist†.

** Technological Institute for Superhard and Novel Carbon Materials,
7a Centralnaya St., Troitsk, Moscow Region, 142092, Russia*

†Department of Experimental Physics, Umea University, S-90187 Umea, Sweden.

Abstract. Electric resistivity and magnetoresistance were measured on samples with disordered structure synthesized from pure C_{60} and C_{70} at pressure in the range 8-12.5 GPa and temperature 900-1500 K. Different types of behaviour were observed: semimetallic and semiconducting, depending on the particular short-range order of the structure.

INTRODUCTION

Superhard and ultrahard fullerites are new carbon materials created recently from C_{60} and C_{70} fullerites by high-pressure-high-temperature treatment [1,2]. Besides the very high hardness, competitive with that of diamond, the transport properties of these materials are also of great interest. It was found earlier, that room-temperature resistivity of these materials varies in the wide range $10^{-2} - 10^5 \Omega \text{ cm}$ depending on their structure and the ratio of the number of sp^2 to sp^3 sites. Both semimetallic and semiconductor temperature behaviour of resistivity were observed. In the present study we investigated electric resistivity and magnetoresistance of some samples synthesized from C_{60} and C_{70} fullerites by high-pressure-high-temperature treatment and correlated these data with the structures of the samples.

SAMPLES

Samples were synthesized at the Technological Institute for Superhard and Novel Carbon Materials in Troitsk, Russia. Their structure was investigated by X-ray powder diffraction using filtered Cu K_α radiation (Figures 1 and 2). Raman spectra, electron and neutron diffraction patterns for similar materials were described earlier [1-3]. As seen from Fig. 1, 2, the structures of the samples were very disordered, but the diffraction pattern of each sample shows particular features that reflect a particular short-range order.

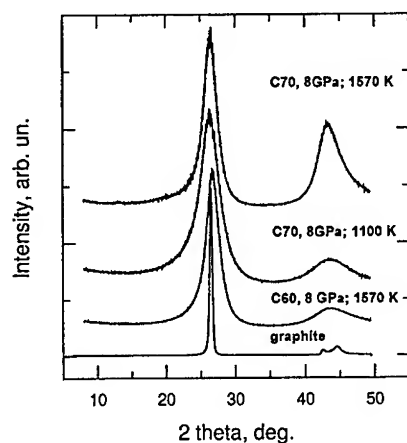


FIGURE 1. X-ray diffractograms of samples synthesized from C_{60} and C_{70} at a pressure of 8 GPa and different values of temperature. XRD of graphite is presented for comparison

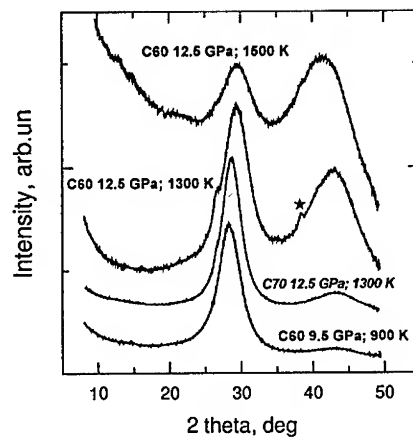


FIGURE 2. X-ray diffractograms of samples synthesized from C_{60} and C_{70} at $P= 9.5$ and 12.5 GPa and different values of temperature. Asterisk indicates instrumental peak.

Electric and magnetic measurements were carried out by a 4-probe method using an Oxford Instruments MagLab 2000 cryostat system at the Department of Experimental Physics, Umea University, Sweden. Silver paste contacts were used.

RESULTS

Samples treated at 8 GPa pressure exhibit a semimetallic type of temperature dependence of the conductivity $\sigma(T)$ (Fig. 3, 4). At low temperatures (2.5-10K) they have negative magnetoresistance (Fig. 5). The conductivity of the samples synthesized from C_{70} decreases approximately as \sqrt{T} at cooling. This is in agreement with the data obtained earlier in [4] on a sample of hard carbon synthesized from C_{60} at $P=3$ GPa; 1000 K. In the case of the sample synthesized from C_{60} at $P= 8$ GPa; $T= 1600$ K we observed a linear decrease of conductivity along with temperature. According to the neutron diffraction data and ^{13}C MAS NMR-spectroscopy, the structure of this sample contains disordered rhombohedral type graphite (ABC-stacking order) with cross-linking of the graphene sheets provided by residual 5-member carbon rings after coalescence of C_{60} -molecules during P,T-treatment [3]. The existence of 5-member carbon rings was observed recently by STM in hard carbon [5]. The degree of disorder in this sample is less than in the samples, synthesized from C_{70} at the same pressure, and the mean interplanar distance d_{002} is less than that in ordinary graphite (Fig. 1).

The negative magnetoresistance for the sample synthesized from C_{60} is smaller, than that of the samples synthesized from C_{70} , and is also smaller than for the different pyrocarbon samples studied in [6].

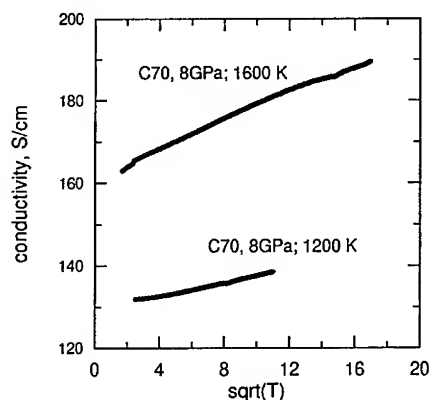


FIGURE 3. Conductivity σ as a function of \sqrt{T} for the samples synthesized from C_{70} at $P = 8$ GPa and different temperatures.

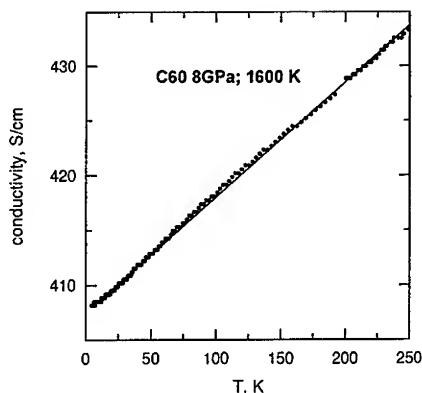


FIGURE 4. Conductivity σ as a function of T for the sample synthesized from C_{60} at $P = 8$ GPa, $T = 1600$ K.

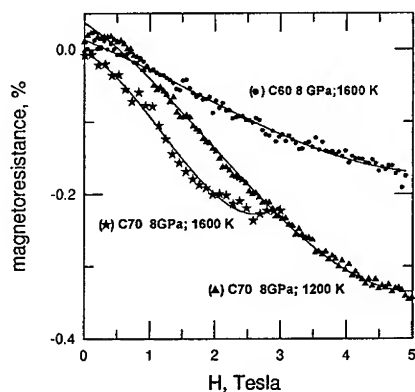


FIGURE 5. Magnetoresistance as a function of magnetic field at $T = 2.5$ K for the samples synthesized from C_{60} and C_{70} at $P = 8$ GPa.

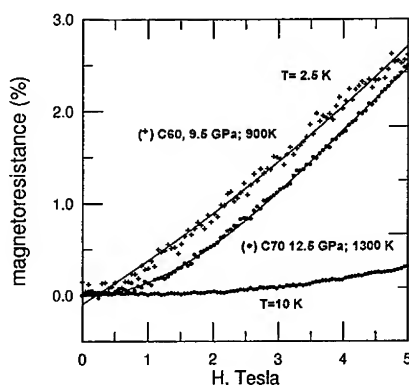


FIGURE 6. Magnetoresistance as a function of magnetic field at $T = 2.5$ K and 10 K for the samples synthesized from C_{60} at $P = 9.5$ GPa and from C_{70} at $P = 12.5$ GPa.

The room-temperature resistivity of our samples is higher by a factor of 2-10 than that of pyrocarbon with different degrees of disorder. Therefore, although samples synthesized from C_{60} and C_{70} at 8 GPa; 1200 -1600 K exhibit semimetallic electric properties, they are different from those of pyrocarbons. The square-root-of-temperature behaviour of the conductivity in samples obtained from C_{70} , Fig. 3 can be attributed to weak localization of charge carriers in disordered 3D electronic system

[7], while the linear dependence in the sample obtained from C₆₀, Fig. 4, indicates 2D weak localization in this system. Total measured resistivity in this case is affected by weak-localization effect and Boltzman thermal excitation of charge carriers [6]. The 2D character of the disorder may be due to 5-member carbon rings in the layers.

For the sample of C₆₀ treated at 9.5 GPa; 900K the data for $\rho(T)$ fit to Mott's VRH law $\rho = 0.07(\exp(1/T)^{1/4} - 1) \Omega\text{cm}$ (Fig. 7) much better than \sqrt{T} fit for $\sigma(T)$. Although the XRD pattern for this sample is very similar to that of the C₇₀ sample treated at 12.5 GPa; 1300K and their densities are actually the same, about 2.55 g/cm³, their electronic structures differ because in the case of the sample synthesized from C₇₀ $\sigma(T)$ fits to $(6.7+1.9\sqrt{T})$ S/cm up to about 200 K. The magnetoresistance in both samples is positive (Fig. 6).

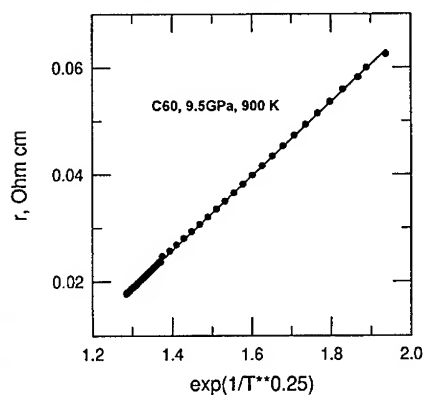


FIGURE 7. $r(T)$ dependence for the sample synthesized from C₆₀ at 9.5 GPa; 900K in Mott's coordinates.

samples of ultrahard and superhard fullerites thus provide helpful information for the understanding of the properties and short-range order of these materials.

For the samples synthesized from C₆₀ at P=12.5 GPa and T=1300; 1500 K we have observed the following temperature dependencies of conductivity :

$$\sigma = (8.5 + 1.8T^{3/2}) 10^{-4} \text{ S/cm}$$

in the range 2.5-220 K in the first case,

$$\sigma = (8.8 + 1.5 \cdot 10^{-7} T^4) 10^{-7} \text{ S/cm}$$

in the range 7-240 K in the second.

Densities of these samples are 2.8 and 3.05 g/cm³ respectively. Their XRD and Raman spectra reflect high contents of sp^3 sites and conjugated bonds. In this case the sp^2 sites introduce a positive doping effect on the electronic properties of the amorphous sp^3 -matrix. In conclusion, our data for the temperature dependence of conductivity in

ACKNOWLEDGMENTS

This work was financially supported by the Royal Swedish Academy of Sciences, the Swedish Research Councils NFR and TFR, and by the Russian Foundation for Intellectual Collaboration (Grant No. 98088). We thank N. Serebryanaya and S. Sulyanov for X-ray study of the samples.

REFERENCES

1. Blank, V., Buga, S., Sundqvist, B., et al, *Carbon* **36** 319-343(1998).
2. Blank V.D., Serebryanaya N.R., Dubitsky G.A., et al. *Phys.Lett. A* **248**, 415-422 (1998).

3. Blank V.D., Buga S.G., Trevino S. F., Sundqvist B., et al., Abstracts of XXXVI European High Pressure Research Group Meeting, Catania, Italy, 1998, pp. 96-98.
4. Smontara A., Biljankovic K., Kozlov M.E., et al., *Physica B* **219&220** 160-166 (1996).
5. Hassanien A, Kozlov M.E., Tokumoto M., see this volume.
6. Bayot V., Piraux L., Michenaud J.-P., et al, *Phys. Rev. B* **41**, 11770-11779 (1990).
7. Lee P.A., Ramakrishnan T.V., *Rev. of Mod. Phys.* **57**, 287-337 (1985).

Electron transport through a gold-bisthiolterthiophene-gold junction

C. Kergueris^a, J.-P. Bourgoin^{a1}, S. Palacin^a, D. Esteve^b, C. Urbina^b,
M. Magoga^c, C. Joachim^c

*a. Service de Chimie Moléculaire, b. Service de Physique de l'État Condensé,
CEA-Saclay, 91191 Gif-sur-Yvette Cedex, France
c. CEMES-CNRS BP 4347, 31055 Toulouse Cedex, France*

Abstract. Molecules of bisthiolterthiophene have been adsorbed on the two facing gold electrodes of a mechanically controllable break junction in order to form metal-molecule(s)-metal junctions. Current-voltage (I-V) characteristics have been recorded at room temperature. Zero bias conductances were measured in the 10-100 nS range and different kinds of non-linear I-V curves with step-like features were reproducibly obtained. A scattering model is used to interpret the experimental conductances as a function of the metal-molecule coupling strength.

I INTRODUCTION

The experimental investigation of the transport properties of a single or a very few molecules contacted with two metallic electrodes has seen significant advances in the last few years. Three different strategies have been used, so far, to solve the problem of connecting a molecule to two facing metallic electrodes. This includes: i) using a Scanning Tunneling Microscope (STM) to contact a molecule adsorbed on a planar substrate [1-5], ii) using planar electron-beam lithographed electrodes separated by a small gap bridged by the molecule [6,7], iii) placing the molecule in the gap of a mechanical break junction (MCB) [8-11].

In the present paper, we describe the use of gold MCB junctions to investigate the electronic transport properties of 2,5''-bis(acetylthio)-5,2'5'.2''-terthienyl (**T3**) molecules. We present different types of I-V characteristics and compare the experimental zero bias conductance with the value calculated by means of a scattering model based on an extended Hückel description of the system. In particular, we study the influence of the metal-molecule coupling strength on the results of the calculation.

¹⁾ Corresponding author. E-mail: jbourgoin@cea.fr

II EXPERIMENTAL RESULTS

The experimental details concerning the synthesis of the **T3** (Fig. 1) molecule, the fabrication of the suspended gold microbridges by e-beam lithography and the electrical measurement setup have been described in ref [11]. The elastic substrate supporting the microbridge was mounted in a three point bending configuration. It was bent by pushing in its center with a driving rod actuated by a coarse adjustment screw until the resistance becomes infinite, which indicated that the bridge was broken. The molecules were immediately self-assembled onto the freshly broken electrodes by immersion of the broken junction in a droplet of a solvent containing the molecules (a 5.10^{-4} mol l^{-1} solution of **T3** in trichloro-1,1,1-ethane was used; 0.1 % of dimethylaminoethanol were added to the solution 1 min before the experiment for deprotection). Then the solvent was evaporated and Argon was continuously flushed through the sealed box during the experiment. The experimental conditions (short time equilibration with the solution and Ar flow) were chosen to hinder as much as possible the formation of di- or polydi-sulfides. In a final step, the bridge gap was reduced using a piezoelectric fine adjustment of the driving rod until current detection.

Various control experiments have been performed including measurements on Au-air-Au junctions, for which the exponential variation of conductance with distance was checked, on Au-air-Au junctions after 1 min immersion in the pure solvent and on Au-dodecanethiol(s)-Au junctions: the corresponding I-V curves were featureless with a linear behaviour at low bias. [10] The results were markedly different when **T3** molecules were introduced in the gap of the junction. During a typical experiment on Au-**T3**-Au junctions, stability periods with a duration 1-20 min alternated with instability periods generally lasting a few minutes. This behavior was always observed on the four samples that have been measured. Although different I-V characteristics could be observed, the reproducible ones were of one

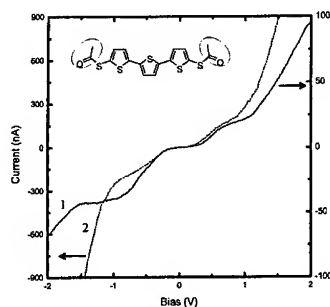


FIGURE 1. The **T3** molecule investigated (the circled protective groups are removed prior to assembly) and typical (1) asymmetric (solid line) and (2) symmetric (dashed line) I-V curves recorded at room temperature for gold-**T3**-gold junctions. Both curves were obtained by averaging over 5 voltage sweeps.

of the two types of I-Vs shown in Fig.1. Asymmetric I-Vs resembling type (1) were more often observed and more stable than symmetric ones of type (2). The measured zero bias conductance of type (1) junctions is of the order of 10 nS. The asymmetric I-V characteristic is non-linear with step-like features, and the current increases linearly at large voltage. The measured zero bias conductance of type (2) junctions is larger, about 80 nS. The symmetric I-V characteristic is also non-linear with smaller step-like features. At $V \geq 1$ V, the current rises faster than linearly with V .

III DISCUSSION

Several models have been proposed to explain the transport mechanism in this kind of metal-molecule-metal. They can be classified into sequential and coherent models. In the former, each electron (hole) transported from one metallic electrode to the other one temporarily charges negatively (positively) the molecule which is considered to be weakly coupled to the electrodes through tunnel barriers. In the latter the tunneling electrons never localize on the molecule which is considered to be strongly coupled to the electrodes. It should be noted that a more realistic model should consider at the same time coherent and sequential transport. In what follows, we use a coherent model, the Electron Scattering Quantum Chemistry (ESQC) technique, [12,13] that proved successful in interpreting metal- C_{60} -metal junction measurements, [14] to calculate the zero bias conductance of gold-T3-gold junctions and compare them with the experimental results. This technique treats the molecule as a defect which breaks the translational invariance of the metal, and therefore scatters incident electrons. In its present implementation, the ESQC technique ignores both the electron-electron and electron-phonon interactions and neglects charging effects. It assumes that the scattering is elastic because

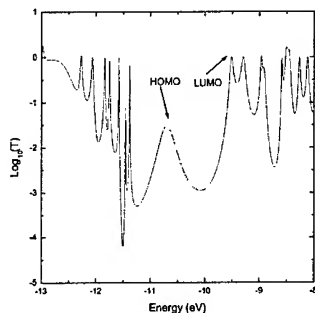


FIGURE 2. The transmission function of the gold-T3-gold junction calculated by the ESQC technique assuming a Au-S distance of 1.95 Å at both end of the molecule. HOMO and LUMO refer to the gap of T3 adsorbed on the two electrodes. The energy scale reference is arbitrary. The calculated position of the Fermi level of the electrodes falls in the hatched area.

for molecule of small length, the tunneling time is shorter than the intramolecular relaxation times. An extended Hückel model is used to build up the matrix representation of the multichannel scattering Hamiltonian taking into account the complete chemical description of the electrodes and of the molecule. The calculated multichannel transmission coefficient $T(E)$ of an electron at a given energy E is shown in Fig. 2. For this calculation, we made the assumption that a single molecule is involved, its geometry being optimized at the AM1 level in a forced planar conformation. [15] The linear conductance G of the metal-molecule-metal junction is then determined using the Landauer formula [16],

$$G = \frac{2e^2}{h} T(E_F)$$

where E_f is the Fermi level of the electrodes.

The prediction for G thus depends on the estimated position of the electronic spectrum relatively to the Fermi energy E_F , on the exact conformation of the molecule in the junction and of the coupling of the molecule to the electrodes. As shown in Ref [11], the position of the Fermi level depends on the exact amount of charge transferred upon formation of the Au-S bond. It can be reasonably estimated in the $[E_{HOMO}, E_{HOMO} + 0.7\text{eV}]$ range. The strength of coupling is determined by the length of the Au-S bonds. The S atoms were assumed to be adsorbed in a hollow site of the gold surface. A bond length of 1.905 Å was used in the present calculation [17]. This is the shortest distance we found in the literature. It thus provides an upper bound for the coupling strength. Assuming a symmetric coupling at both ends of the molecule, the calculated conductances for $E_F - E_{HOMO} = 0.6(\text{midgap}), 0.2$ and 0 eV are 87, 585, 2306 nS, respectively. Although the order of magnitude of these values is comparable with the measured one $G \simeq 10-80$ nS, the discrepancy indicates that the coupling of the molecule to the electrodes is smaller than estimated. In order to study the influence of the strength of coupling on the calculated spectrum, we performed systematic calculations, where we varied the distance between the gold electrodes and the molecules, first keeping a symmetric coupling at both ends of the molecule, and second keeping a fixed 1.905 Å at one end and varying the second distance. The results are shown in Fig.3. These results can be explained as follows. First, the smaller the coupling (symmetric or not) the thinner the resonance peaks. Second, as expected from a simple analogy with double barrier resonant tunneling devices, the height of the peaks decreases for an asymmetric coupling not for a symmetric one. Third, the transmission is dominated by the weakest coupling. Fourth, the resonance corresponding to the HOMO is strongly affected by the modification of coupling. This is due to the fact that it corresponds to the superposition of four peaks: two very small ones corresponding to two highly localized orbitals that are not efficient for the transport and two dominant ones, close in energy, that give rise to a destructive interference. When the coupling is modified, the width of the two dominant peaks decreases and the interference as well. Consequently, if the Fermi Level is located at the HOMO, a reduction of coupling should correspond to an increase of conductance. The curves

are relatively insensitive to the variation of coupling for Au-S distances up to 3\AA , but strongly modified for longer Au-S distances. As a consequence of the reduction of the coupling strength, the value of the conductance calculated assuming the Fermi level at midgap decreases. For example, for a symmetric (resp. asymmetric) coupling, the zero bias conductance reduces to 20 nS (48 nS) for $d(\text{Au},\text{S})=3\text{\AA}$ and 1.5 nS (12 nS) for $d(\text{Au},\text{S})=4\text{\AA}$. These results show i) that a reduction of coupling allows to get a more quantitative agreement between experiment and theory, except if the Fermi Level of the electrodes is very close to the HOMO and ii) that rather large values of Au-S bond lengths (i.e. small couplings) have to be used to obtain a good agreement between experiment and theory. This remark agrees with the interpretation of the results of ref [8] by Emberly and Kirckzenow [18].

IV CONCLUSION

In this paper, we have investigated the transport properties of molecules of 2,5'-bis(acetylthio)-5,2',5',2''-terthienyl self-assembled in the adjustable gap of a metallic break junction. We have observed that the I-V characteristics recorded at room temperature are not always symmetric with respect to the polarity of the applied bias and show two different regimes: a linear regime at low bias $V < 0.1\text{ V}$ and

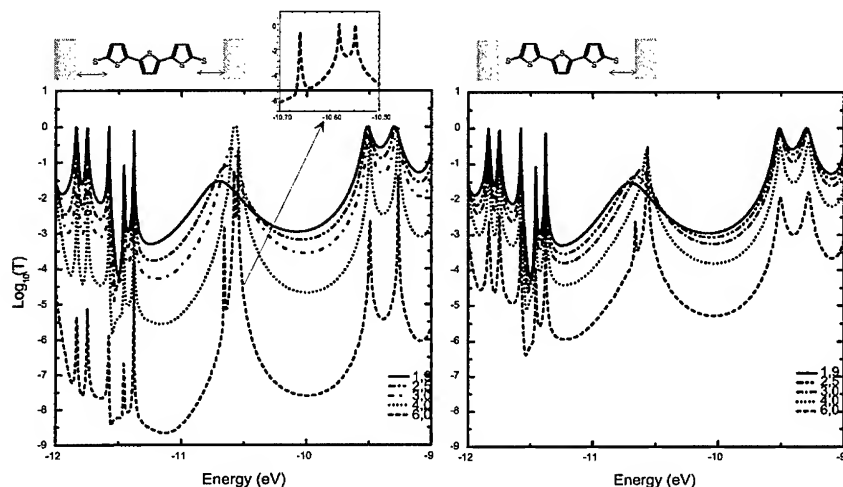


FIGURE 3. Transmission functions of the gold-T3-gold junction calculated by the ESQC technique as a function of coupling strength (symmetric: left; asymmetric: right). The strength of coupling is fixed by the Au-S distance (number in \AA at the bottom right of each plot). The inset of the left figure is a close-up view of the peaks of the curve corresponding to $d(\text{Au},\text{S})=6\text{\AA}$ calculated with a higher number of points. It shows that the reason why the peaks do not reach unity in the main graph is due to a lack of numerical accuracy.

a highly non-linear regime with step-like features at higher voltage. The order of magnitude of the measured zero bias conductance is comparable to the theoretical calculation made with the **ESQC** technique assuming a single molecule in the gap of the break junction. This indicates that these experiments likely involve a very few molecules.

REFERENCES

1. Joachim C. and Gimzewski J. K. *Chem. Phys. Lett.* **265**, 353 (1997).
2. Datta S, Tian W, Hong S, Reifenberger R, Henderson J I, Kubiak C P *Phys. Rev. Lett.* **79** 2530 (1997)
3. Bumm L.A., Arnold J.J., Cygan M.T., Dunbar T.D., Burgin T.P., Jones L., Allara D.L., Tour J.M., Weiss P.S. *Science* **271**, 1705 (1996).
4. Dhirani A., Lin P.-H., Guyot-Sionnest P., Zehner R.W. and Sita L.R. *J. Chem. Phys.* **106**, 5249 (1997).
5. Rosink J.J.W.M., Blauw M.A., Geerligs L.J., Van der Drift E. Rousseeuw B.A.C., Radelaar S., *Optical Mat.* **9** 416 (1998)
6. Tans S.J., Devoret M.H., Dai H., Thess A., Smalley R.E., Geerligs L.J. and Dekker C. *Nature*. **386**, 474 (1997).
7. Ebbesen T.W., Lezec H.J., Hiura H., Bennett J.W., Ghaemi H.F. and Thio T. *Nature*. **382**, 54 (1996).
8. M. A. Reed et al, *Science* **278**, 252 (1997).
9. Muller C.J, Vleeming B.J., Reed M.A., Lambda J.J.S., Hara R., Jones II L, and Tour J.M. *Nanotechnology* **7**, 409 (1996).
10. Kergueris C., Bourgoin J.P., Palacin S., *Nanotechnology* **10**, 8 (1999)
11. Kergueris C., Bourgoin J.P., Palacin S., Estève D., Urbina C., Magoga M., Joachim C., *Phys. Rev. B* **59** (1999)
12. Sautet P. and Joachim C., *Chem. Phys. Lett.* **185**, 23 (1989).
13. Joachim C. and Vinuesa J.F., *Europhys. Lett.* **33**, 635 (1996).
14. Joachim C., Gimzewski J.K., Schlitter R.R. and Chavy C., *Phys. Rev. Lett.* **74**, 2102 (1995).
15. For this calculation we used the following 3s, 3p and 3d parameters for the S atoms (S. Alvarez, *Extended Hückel parameters*, Barcelona University (1989)): $H_{ii} = -20$ eV, $\xi_{ii} = 2.122$, $H_{ij} = -11.1$ eV, $\xi_{ij} = 1.827$, $H_{ii} = -8$ eV, $\xi_{ii} = 1.5$. Standard Hoffmann parameters were used for the C and H atoms.
16. Büttiker M., Imry Y., R. Landauer R. and Pinhas S., *Phys. Rev. B* **31**, 6207 (1985).
17. Sellers H., Ulman A., Shnidman Y. and Eilers J.E., *J. Am. Chem. Soc.*, **115**, 9389 (1993).
18. Emberly E.G. and Kirczenow G. *Phys. Rev. B* **58**, 10911 (1998)

VII. APPLICATIONS

Capacitance Properties of Carbon Nanotubes

*E. Frackowiak, K. Méténier, R. Pellenq, S. Bonnamy and F. Béguin

**Poznan University of Technology, ul. Piotrowo 3, 60-965 Poznan, Poland
CRMD, CNRS - Université, 1B rue de la Férollerie, 45071 Orléans, France*

Abstract. Electrochemical cumulation of charges has been investigated in capacitor electrodes made from carbon multiwall nanotubes (MWNT) produced either by catalytic decomposition of acetylene on supported cobalt or by template carbonization of propylene. A good correlation has been found between the values of capacitance and the microtextural characteristics of the nanotubes. The highest specific capacitance, of the order of 70 F/g in 6M KOH electrolyte, could be reached for catalytic MWNT presenting mesopores due to the canal and to entanglement.

INTRODUCTION

Some attempts to use carbon nanotubes for the electrochemical storage of energy have already been proposed (1-4). Due to their entangled network and a developed surface functionality, they especially represent attractive electrode materials for supercapacitors. Our objective here is to correlate the electrochemical response of various multiwall carbon nanotubes (MWNT) with their microtexture in order to estimate their potential use in electrical double layer capacitors.

EXPERIMENTAL

The carbon MWNT used in this study were prepared by different methods:

1) Catalytic decomposition of acetylene:

- at 700°C (A700Co/Si) and 900°C (A900Co/Si) using a catalyst composed of metallic cobalt supported on silica (in the proportion of 10 wt%) (5). The raw sample was treated in 73 wt% aqueous HF solution and then refluxed in 3 mol.l⁻¹ nitric acid, to get rid of silica and free cobalt particles, respectively.

- at 600°C over Co/ NaY zeolite catalyst (A600Co/NaY) containing 2.5 wt% of metal (6). The zeolitic support was fully removed by hydrofluoric acid (40%) treatment. Thanks are due to J. B.Nagy's group, in Namur, Belgium, for providing this sample.

2) Chemical vapor deposition (CVD) of propylene at 800°C within the pores of an alumina membrane (P800AlTempl). The oxide template was dissolved in 46% HF solution (7). Thanks are due to T. Kyotani, in Sendai, Japan, for providing this sample.

The structural and microtextural characteristics of each sample described above were determined by means of Transmission Electron Microscopy (Philips CM20) and N₂ adsorption at 77K (ASAP 2010, Micromeritics). Prior to adsorption experiments, samples were outgassed (10⁻⁶ mbar) at 350°C during 12 hours. The surface area (BET) was measured from nitrogen adsorption isotherms at 77K, which were also used to determine the pore size distribution by applying the B.J.H. method.

The cumulation of charges in the electrical double layer was investigated by the voltammetry technique (Mac Pile, Biologic) in electrochemical capacitors with two composite electrodes. The carbon electrodes were pressed from a mixture of carbon MWNT as active material (85%), acetylene black (10%) and polyvinylidene fluoride (5%) as an organic binder. The electrolyte was 6M potassium hydroxide or a 1/1 mixture of ethylene carbonate (EC)/diethylcarbonate (DEC) containing 1M LiPF₆. Charge-discharge potentiodynamic cycling was performed from 0 to 1.0 V in KOH and from 0 to 2.0 V in EC:DEC/1M LiPF₆ at scan rates of potential from 1.0 to 10 mV s⁻¹. Taking into account the following dependence between the capacitance and the scan rate:

$$C = \frac{dQ}{dE} = I \frac{dt}{dE}$$

and estimating the current connected with charging of electrical double layer, the specific capacitance of the carbon material was calculated.

RESULTS AND DISCUSSION

Transmission Electron Microscopy (TEM) characterization showed that the nanotubes prepared by catalytic decomposition of acetylene have an entangled network (Fig. 1a); for P800AlTempl sample the tubes are straight and aligned due to the template method of preparation (Fig. 1b). The internal diameter of catalytic MWNT varies from 4 to 6 nm and the external diameter from 15 to 45 nm (Fig. 1c, 1d). P800AlTempl sample differs significantly from others due to its dimensions (70 nm internal and 110 nm external diameters) and the canal is accessible. Nanotubes A700Co/Si have straight aromatic layers partly coated with pyrolytic carbon, and the central canal is open. The sample obtained from the same method but at 900°C (A900Co/Si) is characterized by fishbone morphology with a lack of canal. Closed tips, straight aromatic layers and tubes externally covered by pyrolytic carbon are typical for A600Co/NaY sample.

The adsorption/desorption of nitrogen at 77K directly probes the texture of carbon MWNT and matches well with TEM observations. Particularly, all the investigated carbon MWNT present a mesoporous character (characterized by hysteresis between adsorption and desorption) (Table 1) connected to the entanglement

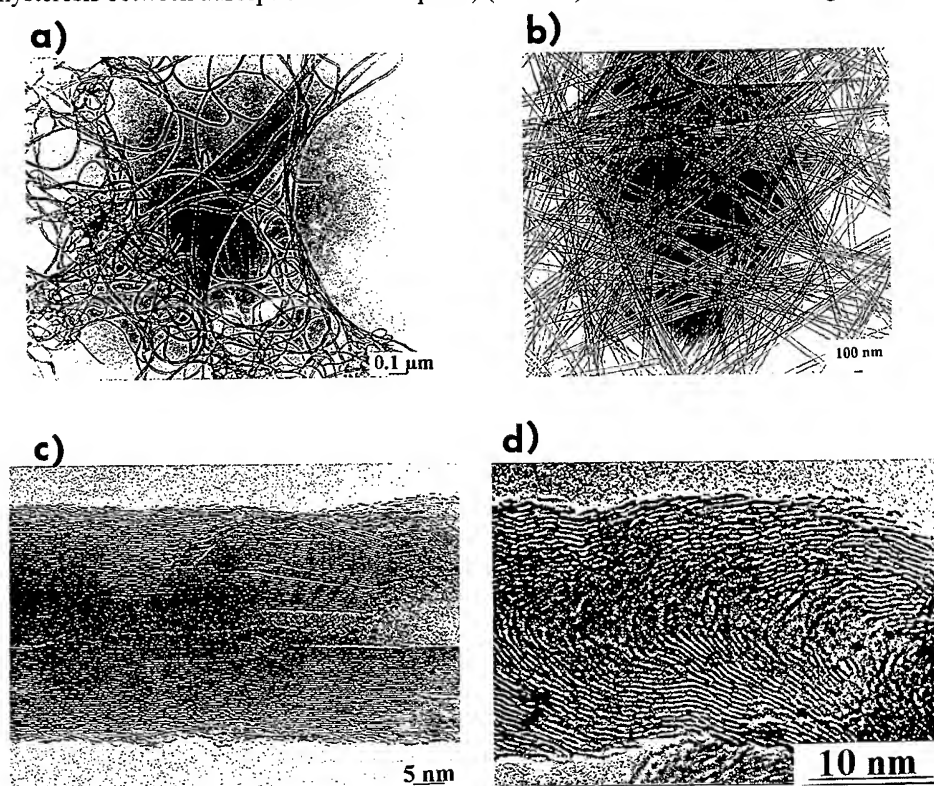


FIGURE 1. TEM 002 lattice fringes of carbon MWNT: (a) A600Co/NaY; (b) P800AlTempl; (c) A700Co/Si; (d) A900Co/Si.

and/or the presence of an accessible central canal. The BET surface area of carbon MWNT varies from about 100 to 400 m²/g.

TABLE 1. Data given by nitrogen adsorption on nanotubes

Sample	S_{BET} (m ² /g)	V_{mono} (cm ³ /g) ^a	Hysteresis
A700Co/Si	410	94	large
A900Co/Si	396	90	large
A600Co/NaY	128	29	small
P800AlTempl	311	71	large

^a V_{mono} is the volume corresponding to the formation of a nitrogen monolayer on carbon

A very important feature is the presence of a saturation plateau at P approaching P_0 for sample P800AlTempl, that is the signature of a rigid mesoporous network by contrast to other samples which mesoporous network is flexible.

TABLE 2. Specific capacitances of carbon MWNT (F/g)

Sample	A700Co/Si	A900Co/Si	A600Co/NaY	P800AlTempl
6M KOH	68	45	3	31
LiPF ₆ in EC:DEC	-	36	-	17

The electrical double layer is mainly formed in the micropores (< 2 nm) of carbon MWNT, however, mesopores play an important role for the transportation of ions. As compared to P800AlTempl, significant values of capacitance were obtained for the A700Co/Si and A900Co/Si samples (Table 2) which are characterized by a high surface area and an easily accessible network of mesopores created by entangling of the nanotubes, in good agreement with TEM and BET results. On the other hand, a non-accessible canal limits the cumulation of charges, as demonstrated by the poor value of capacitance exhibited by A600Co/NaY nanotubes which have closed tips. However, surface functional groups can determine pseudocapacitance properties, and the specific capacitance of sample A600Co/NaY could be multiplied by a factor of about 5 after being treated in concentrated HNO₃.

Entangled multiwall carbon nanotubes with an accessible canal appear to be promising electrode materials for electrochemical capacitors. Additionally, the investigation of the capacitive behavior allows to probe the microtextural and surface properties of carbon MWNT.

ACKNOWLEDGMENTS

This work has been supported by E. C. TMR program: NAMITECH, ERBFMRX-CT96-0067 (DG 12-MIHT) and by the Polish grant KBN 8T10A 011 13.

REFERENCES

1. G. Che, B.B. Lakshmi, E.R. Fisher and C.R. Martin, *Nature* **393**, 346-349 (1998).
2. E. Frackowiak, S. Gautier, H. Gaucher, S. Bonnamy and F. Béguin, *Carbon* **37**, 61-69 (1999).
3. C. Nutzenadel, A. Zuttel, D. Chartouni and Louis Schlapbach, *Electrochemical and Solid-State Letters* **2**, 30-32 (1999).
4. C. Niu, E.K. Sichel, R. Hoch, D. Moy and H. Tennent, *Appl. Phys. Lett.* **70**, 1480-1482 (1997).
5. A. Hamwi, H. Alvergnat, S. Bonnamy and F. Béguin, *Carbon* **35**, 723-728 (1997).
6. J-F. Colomer, P. Piedigrosso, I. Willems, C. Journet, P. Bernier, G. Van Tendeloo, A. Fonseca and J. B. Nagy, *J. Chem. Soc., Faraday Trans.* **94**, 3753-3758 (1998).
7. T. Kyotani, L. Tsai and A. Tomita, *Chem. Mater.* **7**, 1427 (1995); *ibid* **8**, 2109 (1996).

Electron Field Emission from Carbon

J. Robertson

Engineering Dept, Cambridge University, Cambridge CB2 1PZ, UK

Electron field emission from carbon nanotubes, nano-structured carbon, diamond and diamond-like carbon is reviewed, including experiments, models and applications.

Many forms of carbon, such as nanotubes, diamond and diamond-like carbon (DLC) are good electron field emitters, but for different reasons. Diamond is a semiconductor with a band gap of 5.5 eV. When its surface is terminated by hydrogen it has a negative electron affinity (NEA), that is its conduction band edge lies above the vacuum level [1]. Thus, any electrons in its conduction band could pass into the vacuum with no energy barrier. However, field emission requires electrons to travel round a complete circuit. This is a problem, as there is a large potential barrier at the back contact, and diamond has a high resistivity. Thus, to date, the best electron emission occurs in microcrystalline and nano-crystalline diamond, with emission varying inversely with grain size [2,3] (Fig 1(a)). Emission should be possible from n-type diamond. However, the most soluble donor is nitrogen, but this only has a deep donor level at 1.7 eV below the conduction band. It was recently found that phosphorus incorporates into diamond, and gives a shallower donor level ~0.5 eV below the conduction band [4]. This system could finally test the ideas of NEA field emission [5]. However, so far, doping has only been carried out on homo-epitaxial

films on gem diamonds, so making electrical contact to the back of the doped film is difficult.

Diamond-like carbon (DLC) is amorphous carbon or hydrogenated

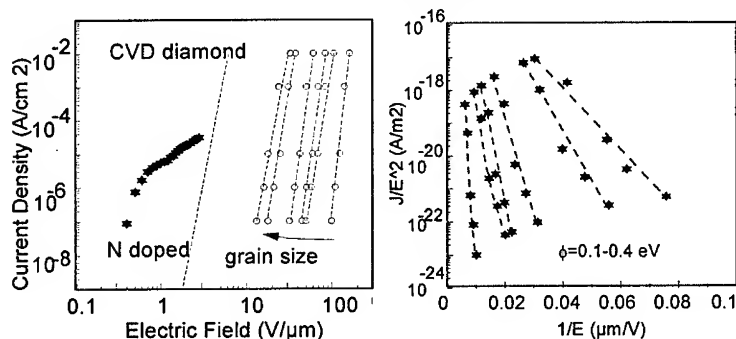


Figure 1. Field emission of CVD diamond and its Fowler-Nordheim plot, showing an apparent barrier $\phi=0.1-0.4$ V.

amorphous carbon (a-C:H) containing a substantial sp^3 bonding. It consists of very smooth films, usually grown by plasma deposition at room temperature. DLC is a reasonable electron emitter, particularly if doped with nitrogen [6,7]. Typical results are for a highly sp^3 form of carbon denoted tetrahedral amorphous carbon (ta-C)[7]. Here, the easiest emission appears to occur for films with the highest sp^3 content deposited by 100 eV ions.

The field emission current density J ($A.m^{-2}$) obeys the Fowler-Nordheim equation

$$J = a(\beta E)^2 \exp\left(-\frac{b\phi^{3/2}}{\beta E}\right)$$

where ϕ (eV) is the barrier height, E is the applied field (V/m) and a and b are constants, with $b = 6.8 \cdot 10^9$. β is a field enhancement factor due to sharp geometries. The emission currents of CVD diamond give a barrier height ϕ of 0.01 - 0.4 eV for $\beta=1$ (Fig 1(b)). Emission from ta-C gives barrier heights of 0.01 - 0.04 eV for $\beta=1$. These values are unphysically small. The real barrier must be over 1.5 eV, or we would get temperature-dependent Schottky emission rather than temperature independent Fowler-Nordheim emission. Thus, $\beta \gg 1$ [8].

Carbon nanotubes are good field emitters because of their sharp tips [9-11]. Saito [12] compared field emission from single walled nanotube (SWNT) bundles, open multiwalled nanotubes (MWNTs) and capped MWNTs. Open MWNTs gave the highest emission. Taking the NT work function as 5 eV, the Fowler-Nordheim plots give field enhancement $\beta \sim 1200$. Geometrically, $\beta = h/r$, the ratio of tip length to tip curvature, which is ~ 200 for a NT $1\mu m$ long and 5 nm radius, so the experimental value is much greater. Nanotubes have the narrowest electron energy distribution (EED) any emitter (0.17-0.21 eV)[13,14], so they have great potential as bright electron sources in FE guns.

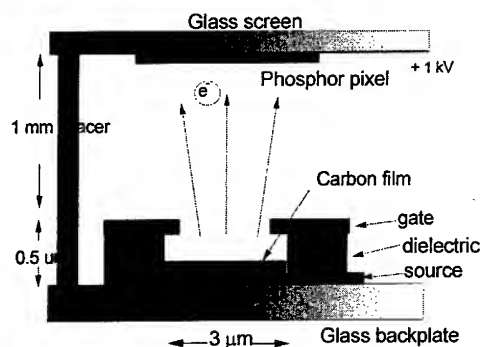


Figure 2. Schematic of a Field Emission Display with carbon film cathode.

The main application for carbon field emitters is the field emission display (FED). In this, electrons are emitted from gate-controlled microcathodes, accelerated by 1-3 kV across a vacuum gap, and form an image on a phosphorus pixel screen, about 1 mm away. Existing FEDs use sharp Spindt tips of Mo or Si. Such FEDs are just entering commercial production. The Spindt tip FEDs have gate holes about $0.3 \mu m$, and so need costly, large area lithography. Tips are needed to give the field enhancement for work functions of

5 eV. The facile emission from carbon allows us to replace tips by flat carbon cathodes (Fig 2). We can now use gate holes of 3-5 μm , considerably reducing the cost of lithography, while also benefitting from the chemical and physical inertness of carbon.

	T_{dep}	Emission Field	Site density	Stability
diamond				*
nano-diamond		*	*	*
a-C:H	*	*		
ta-C	*	*		*
nanotubes		*	*	(*)
ns-DLC	*	*	*	*

Carbon cathodes for FEDs must satisfy stringent requirements. First, they should be deposited at low temperatures (ideally $<300^\circ\text{C}$) to use glass substrates. Second, the emission field should be low; FEDs require a current density of about 1 mA/cm^2 at a field of under $\sim 20 \text{ V}/\mu\text{m}$.

Third, emission even from nominally smooth films occurs from local spots. Each microcathode needs one emission site, so the emission site density (ESD) should exceed 10^6 cm^{-2} . Fourth, cathodes should have stable emission currents. Table 1 rates various carbons accordingly. The temperature limit is a problem for CVD nanocrystalline diamond or CVD nanotubes. The ESD is a problem for DLCs. Stability tends to eliminate hydrogenated DLCs and could be a problem for open-end NTs. The most appropriate carbon so far is a nano-structured DLC deposited at room temperature [15]. It has short tip structure which appears to give some local field enhancement. Recently, Ren [16] and Fan [17] have described CVD growth of long nanotubes, but note that FED gate arrays are only 1-2 μm high, so they only require 100 nm long nanotubes!

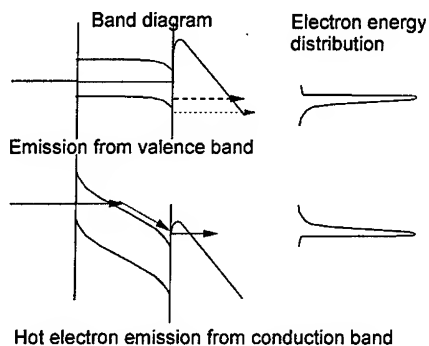


Figure 3. Electron Energy Distributions for emission from valence band or conduction band.

We finally discuss the emission mechanism. Considerable information on the emission mechanism can be derived from the electron energy distribution (EED) of the emitted electrons. The EED is the product of the distribution of the electron's initial energy and their escape probability. The escape probability at any energy is given by the Fowler-Nordheim equation, so that electrons from strongly bound states have less chance to escape. For a metal, electrons are emitted around the Fermi level, and the EED is the convolution of the Fermi occupation and the escape probability, with a broader slope to deeper energies and a sharper cut-off at the Fermi energy (Fig 3a). Experimentally, the centre of the EED referenced to the Fermi level of the back contact gives the mean energy of emission, while the EED width gives the local field, βE . For semiconductors, emission can occur from the valence band, from gap states or from the conduction band. Each type of emission has a signature. Emission from the valence band resembles that from a metal, with a deeper EED, a tail to lower emission energies and sharper cut-off at the top. Emission from the conduction band is centred at higher emission energies and tends to have a sharp low energy cut-off due to the conduction band edge and a broader tail on the high energy side due to hot electrons.

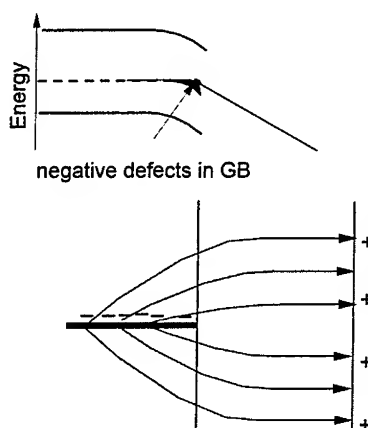
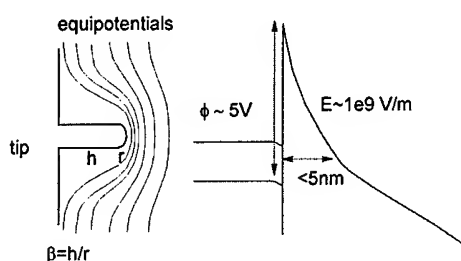


Figure 4. Field enhancement due to charge trapping at grain boundaries in nano-crystalline diamond.

Experimentally, the EED of diamond shows that emission comes from the valence band, with a very large field enhancement [18]. In DLC, EED also shows that the emission barrier is about 5 eV, which is of order the work function [19], as found by Kelvin probe measurements, and also the value deduced from photoemission spectra [8]. Thus, so far, the facile emission in diamond or DLC is not due to NEA, but to some unusual source of field enhancement, which is possible because they withstand very high breakdown fields [8].

Microcrystalline diamond has a rough surface due to the grains. Scanning probe measurements find that emission comes from the concave parts of the surface [20]. Thus emission comes from

grain boundaries in the dips between grains, not the grain tops where field might be enhanced. The grain boundaries are sp^2 bonded [3] and give amphoteric localised states in the band gap. Under the external field, these states acquire a negative charge, creating a depletion region and a downwards band-bending. The external field lines are focused to the charged states. Thus the grain boundary acts like an 'internal tip', giving field enhancement (Fig. 4).



Emission from DLC films is more difficult to explain. These films are very smooth, with a RMS roughness under 1 nm. Photoemission data and Kelvin probe measurements suggest that they have a positive electron affinity and a work function of 3-4 eV.

Figure 5. Equipotentials, field enhancement and barrier lowering at tips.

Many field emission models fail a voltage test. Consider emission from a solid with a 5 eV work function (Fig 5). The external field must lower the potential in the vacuum, so electrons can tunnel out at -5V. The potential falls rapidly where there is field enhancement and slowly where there is only the applied field. Tunnelling can only occur if the tunnel distance is less than ~ 2 nm, so the vacuum potential must be lowered down to -5 V by 2 nm for tunnelling to occur. If the high field only operates for 1 V, this is no use as there is still a long tunnel distance at -5V. The field enhancement at tips can be considered as an expulsion of equipotentials from inside the tip to just in front of the tip. The local field at the tip is $E_{\text{local}} = hE/r$, so voltage along the tip length $V = Eh$, in the absence of the tip, is dropped over a distance r in front of the tip, $E_{\text{local}} r = Eh = V$. Tunnelling requires $V > 5V$, which is non-trivial.

Finally, although the sharpness of nanotubes provides strong field enhancement, close packed nanotubes as provided by recent CVD methods could actually be counter-productive. This is because nearby tips screen the field enhancement if tip spacing is less than their length.

References

1. F J Himpsel, J S Knapp, J A VanVechten, D E Eastman, Phys Rev B **20** 624 (1979)
2. W Zhu, et al, J Appl Phys **78** 2707 (1995); Science **282** 1471 (1998)
3. D M Gruen, MRS Bulletin **23** p32 (Sept, 1998)
4. S Koizumi, H Ozaki, M Kamo, Y Sato, T Inuzuka, App Phys Lett **71** 1065 (1997)
5. T Sugino et al, Diamond Related Mater, to be published (1999)
6. G A J Amaratunga, S R P Silva, App Phys Lett **68** 2529 (1996)

7. B S Satyanarayana, A Hart, W I Milne, J Robertson, App Phys Lett **71** 1430 (1997)
8. J Robertson, Mat Res Soc Sym Proc **498** 197 (1998); J Vac Sci Techn B **17** xx (1999)
9. W A deHeer, et al, Science **270** 1179 (1995)
10. Q H Wang, et al, App Phys Lett **70** 3308 (1997)
11. JM Bonard et al, App Phys Lett **73** 918 (1998)
12. Y Saito et al, Jpn J App Phys **36** L1340 (1997); App Surf Sci **653** xxx (1999)
13. W A DeHeer, et al, Advanced Mater **9** 87 (1997)
14. M J Fransen, PhD thesis (TU Delft, 1998)
15. B F Coll, et al, Mat Res Soc Symp Proc **498** 185 (1998)
16. Z F Ren, et al, Science **282** 1105 (1998)
17. S Fan, et al, Science **283** 512 (1999)
18. C Bandis, B B Pate, App Phys Lett **69** 366 (1996)
19. O Groning, O Kuttel, P Groning, L Schlapbach, App Phys Lett **71** 2253 (1997)
20. A V Karabutov, V D Frolov, S M Pimenov, V I Konov, Diamond Related Mat (1999)

Field Emission from Carbon Nanotubes and Its Application to Electron Sources

Yahachi Saito* and Sashiro Uemura[#]

* *Department of Electrical and Electronic Engineering, Mie University, Tsu 514-8507, Japan*

[#] *Ise Electronics Corp., 728-23 Tsumura, Ise 516-1103, Japan*

Abstract. Field emission from (i) as-grown multiwall nanotubes (MWNTs), (ii) purified MWNTs and (iii) purified single-wall nanotubes (SWNTs) was investigated by field emission microscopy (FEM). As an application of nanotube field emitters, we manufactured cathode ray tube (CRT) lighting-elements by replacing conventional thermionic cathodes with nanotube field emitters. Stable electron emission, high emission current with low electric field ($\sim 10 \text{ mA/cm}^2$ at $1.5 \text{ V}/\mu\text{m}$), and long life of the emitters were demonstrated.

INTRODUCTION

Carbon nanotubes possess advantageous properties as electron field emitters. Due to their high aspect ratio and sharp tips, an electric field ($\sim 1 \text{ V/nm}$) strong enough to emit electrons through tunneling effects are realized at their tips under low applied voltages. Their chemical stability and high mechanical strength enable nanotubes to emit stably electrons under moderate vacuum environments. So far, field emission from MWNTs (1-6) and from SWNTs (7,8) was studied using various cathode structures. In 1998, we first succeeded in applying nanotube cathodes to display elements, cathode ray tube (CRT) lighting elements (9). Subsequently, Wang et al. (10) fabricated a nanotube-based flat panel display. In the present paper, emission characteristics of nanotubes studied by FEM are first described, and then performance of improved nanotube-based CRT lighting elements is reported.

FEM OF CARBON NANOTUBES

MWNTs and SWNTs were produced by carbon arc discharge in helium. Details of the production and purification procedures are described in Refs. 11 and 12 for MWNTs and in Refs. 13 and 14 for SWNTs. Purified MWNTs and SWNTs have a form of black, thin "mat" (a flake with thickness about a few hundredths of mm). For purified MWNTs, their tips were open after this purification process.

Three kinds of carbon nanotubes were employed as field emitters; (i) as-grown MWNTs with capped ends (hereafter, called "capped MWNTs"), (ii) purified

MWNTs with open ends ("open MWNTs"), and (iii) purified SWNTs. A bulk bundle of respective nanotubes for FEM study was fixed on the apex of a hair-pin wire of tungsten (0.2 mm in diameter) using conductive paste. Details of the tip preparation were described in our previous publications (6,7).

The emitter tip of the nanotubes was positioned 60 mm in front of an anode screen with a 1 mm probe hole. Field emission patterns could be observed on the anode screen on which phosphor was spread. Behind the probe hole was a Faraday cup, and electron current emitted from a restricted region of an emitter could be measured. The acceptance half angle of the probe hole was 17 mrad. The working pressure of the vacuum chamber was 10^{-6} - 10^{-7} Pa. The emitter tips were at room temperature.

Not only capped MWNTs but also SWNTs gave emission patterns consisting of a number of bright spots that originated respectively from individual MWNTs and from bundles of SWNTs. Since the brightness of each spot flickered, emission patterns apparently changed with time. No inner fine structure was observed within these spots. Emission patterns from MWNTs with open tips showed "doughnut-like" annular bright rings, the central black regions corresponding to the exposed cavities of nanotubes. The magnification of observed emission patterns in our FEM was estimated to be nearly one million from the size of "doughnut-like" rings on the screen.

Emission current (I_p) accepted by the probe hole was measured as a function of voltage applied to the tip (V). The I_p - V characteristics for the three kinds of nanotubes are shown in Fig. 1 (a), and the corresponding Fowler-Nordheim (F-N) plots (15) in Fig. 1 (b). The F-N plots give straight lines in a region of low emission, while the plots level off from the straight line in a higher current region for all nanotubes investigated.

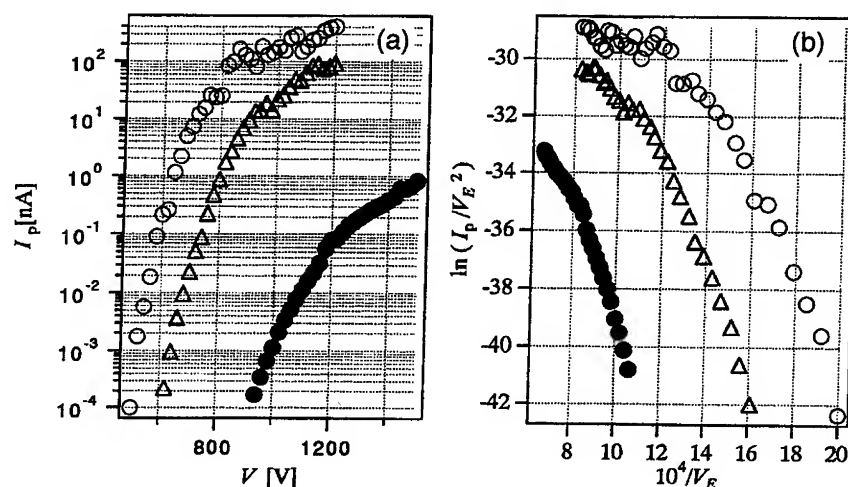


FIGURE 1. (a) Current vs. voltage characteristics and (b) F-N plots for a capped (●), an open MWNT (○), and a bundle of SWNTs (Δ). Current (I_p) was measured with the 1 mm probe hole.

TABLE 1. Field emission properties of the three kinds of carbon nanotubes. Since emission current was measured by the 1 mm probe hole, the properties come from a single tube for MWNTs and from one bundle for SWNTs.

Carbon nanotubes	Threshold voltage ^a (V)	Saturation current (nA)	Maximum current density ($\times 10^6$ A/cm ²)	β -factor ₁ ($\times 10^{-1}$)
Capped MWNT	900-1000	0.5-3	~ 1	2.6-3.9
Open MWNT	500-600	400-900	~ 100	5.7-27
SWNTs	600-700	50-300	~ 10	4.4-8.8

^a Threshold voltages represent tip voltages at which currents measured by the probe hole exceed 0.1 pA.

Field emission properties, e.g., threshold voltage, saturation current, maximum current density, and β -factor ($\beta = F/V$, where F is an electric field) in F-N equation, are summarized in Table 1 for the three kinds of nanotubes. The open MWNTs began to emit electrons at the lowest tip voltage and sustained highest current density.

NANOTUBE CATHODE IN FED DISPLAY ELEMENTS

The field emission display devices we employed for examining the performance of our nanotube field emitters are CRT lighting elements, which are used practically as outdoor giant displays. All parts other than cathodes are the same as those used for manufacturing the lighting elements in a plant (16,17). Figure 2 shows a longitudinal cross section of a CRT lighting bulb with a nanotube cold cathode.

Nanotubes we used were MWNTs produced by arc discharge. In our first trial fabrication, fibrous materials containing abundant MWNTs were directly glued onto a

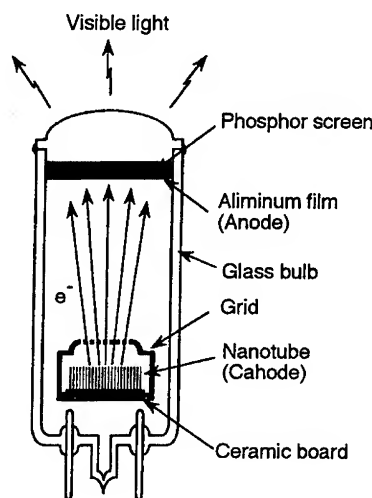


FIGURE 2. Longitudinal cross section of a CRT fluorescent display with a nanotube cold cathode.

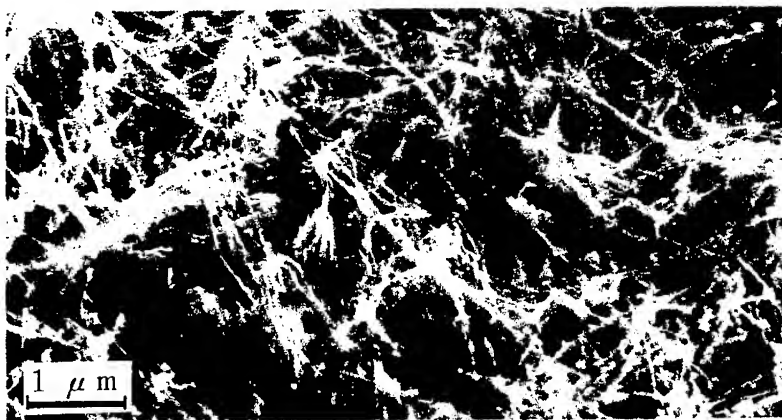


FIGURE 3. Scanning electron micrograph of the surface of the screen-printed nanotube cathode.

stainless steel plate by using conductive paste. Subsequently, several methods were examined to fix nanotubes on the cathode surface, and the screen printing technique was found to be the most effective for industrial application. Figure 3 shows a scanning electron microscope picture of a surface of the screen-printed cathode.

The nanotube cathode is covered with a grid electrode; the spacing between the cathode and the grid (d_{T-G}) is 0.2 - 1.0 mm. The phosphor screen is printed on the inner surface of a front glass and backed by a thin aluminum film. After sealing the vacuum tube, getter material was flashed to attain high vacuum on the order of 10^{-6} Pa.

The cathode was grounded (0 V), and the control grid was biased to a positive voltage. Figure 4 shows the total current emitted from the cathode as a function of voltage applied to the control grid. For $d_{T-G} = 0.2$ mm, total emission current of ca. 10 mA was obtained when the grid voltage was 300 V. Namely, current density on the cathode surface (effective area being about 2 mm²) was ca. 10 mA/cm² at an average field strength of 1.5 V/μm.

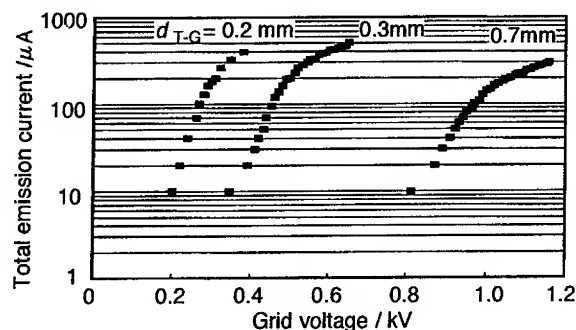


FIGURE 4. Total emission current as a function of the grid voltage for three different cathode-grid spacings $d_{T-G} = 0.2$ mm, 0.3 mm, and 0.7 mm.

A high voltage (typically 10 kV) was applied to the anode to accelerate electrons, which excite the phosphor screen. Luminance of the phosphor screens was intense enough for practical use; e.g., 6.3×10^4 cd/m² for green light (ZnS:Cu, Al for green phosphor) at an anode current of 200 μ A, which is two times more intense than that of commercially available conventional thermionic CRT lighting elements which are operated at 100 μ A. The light emission efficiency was ca. 70 lm/W for green light. A lifetime test showed that the nanotube cathode had a life of over 10,000 hours.

ACKNOWLEDGMENT

We thanks Dr. M. Yumura and Prof. K. Tohji for supplying us with purified MWNTs and SWNTs, respectively. This work was supported by the MESSC of Japan (Grants-in-Aid for Scientific Research B, No. 09555003, and on the Priority Area "Fullerenes and Nanotubes"), the Yazaki Foundation, and the Naito Foundation.

REFERENCES

1. Rinzler, A. G., Hafner, J. H., Nikolaev, P., Lou, L., Kim, S. G., Tománek, D., Nordlander, P., Colbert, D. T., and Smalley, R. E., *Science* **269**, 1550-1153 (1995).
2. De Heer, W. A., Châtelain, A., and Ugarte, D., *Science* **270**, 1179-1180 (1995).
3. Collins, P. G., and Zettl, A., *Appl. Phys. Lett.* **69**, 1969-1971 (1996).
4. Wang, Q. H., Corrigan, T. D., Dai, J. Y., Chang, R. P. H., and Krauss, A. R., *Appl. Phys. Lett.* **70**, 3308-3310 (1997).
5. Sinitsyn, N. I., Gulyaev, Yu. V., Torgashov, G. V., Chernozatonskii, L. A., Kosakovskaya, Z. Ya., Zakharchenko, Yu. F., Kiselev, N. A., Musatov, A. L., Zhdanov, A. I., Mevlyut, Sh. T., and Glukhova, O. E., *Appl. Surf. Sci.* **111**, 145-150 (1997).
6. Saito, Y., Hamaguchi, K., Hata, K., Uchida, K., Tasaka, Y., Ikazaki, F., Yumura, M., Kasuya, K., and Nishina, Y., *Nature* **389**, 554-555 (1997).
7. Saito, Y., Hamaguchi, K., Nishino, T., Hata, K., Tohji, K., Kasuya, A., and Nishina, Y., *Jpn. J. Appl. Phys.* **36**, L1340-L1342 (1997).
8. Bonard, J. -M., Salvetat, J. -P., Stöckli, T., De Heer, W. A., Foró, L., and Châtelain, A., *Appl. Phys. Lett.* **73**, 918-920 (1998).
9. Saito, Y., Uemura, S., and Hamaguchi, K., *Jpn. J. Appl. Phys.* **37**, L346-L348 (1998).
10. Wang, Q. H., Setler, A. A., Lauerhaas, J. M., Dai, J. Y., Seeling, E. W., and Chang, R. P. H., *Appl. Phys. Lett.* **72**, 2912-2913 (1998).
11. Saito, Y., Yoshikawa, T., Inagaki, M., Tomita, M., and Hayashi, T., *Chem. Phys. Lett.*, **204**, 277-282 (1993).
12. Ikazaki, F., Ohshima, S., Uchida, K., Kuriki, Y., Hayakawa, H., Yumura, M., Takahashi, K., and Tojima, K., *Carbon* **32**, 1539-1542 (1994).
13. Saito, Y., Koyama, T., and Kawabata, K., *Z. Phys. D* **40**, 421-424 (1997).
14. Tohji, K., Goto, T., Takahashi, H., Shinoda, Y., Shimizu, N., Jeyadevan, B., Matsuoka, I., Saito, Y., Kasuya, A., Ohsuna, T., Hiraga, K., and Nishina, Y., *Nature* **383**, 679 (1996).
15. See for example: Gomer, R., *Field Emission and Field Ionization*, Cambridge: Harvard University Press, 1961, ch. 1, pp. 6-14.
16. Morikawa, M., Seko, Y., Kamogawa, H., Uemura, S. and Shimojo, T., *Japan Display '92*, 385-388 (1992).
17. Uemura, S., Seko, Y., Kamogawa, H., Morikawa, M. and Shimojo, T., *ITE Tech. Rep.* **17**, 31-36 (1993).

Thin Film Cold Cathode from Nanostructured Carbon

A.N. Obraztsov[#], I.Yu. Pavlovsky[#], A.P. Volkov[#],
V.L. Kuznetsov⁺ and A.L.Chuvilin⁺

[#] *Physics Department of Moscow State University, Moscow 119899, Russia*
⁺ *Institute of Catalysis, Novosibirsk 630090, Russia*

Abstract. Thin films of nanostructured carbon material were grown on silicon substrates by a d.c. discharge plasma CVD technique. HREM investigation have shown that the films contain carbon nanotubes and flaked graphite nanocrystallites with predominant orientation of nanotube axes and basal graphene planes of crystallites along a normal to substrate surface. Electron field emission was observed at average fields above 1 V/ μm with emission site density higher than 10^6 1/ cm^2 and emission current density up to 10 mA/ cm^2 at 4 V/ μm . The prototypes of cathodoluminescent light emitting devices were manufactured with use of the nanostructured carbon films as cold cathodes. A brightness of 1000 cd/ m^2 was achieved at operational voltage of about 250 V.

INTRODUCTION

Usual thermionic cathodes for applications from televisions to power transmitters employ heating to produce electrons which escape from a metal into vacuum. However, these cathodes have rather poor power efficiency and other parameters to be used with micrometer-size structures which are required for flat-panel displays and some other applications. The discovery of carbon nanotubes has lead to much speculation about their properties and potential applications including field emission (FE) cathodes which could be used instead of heated emitters. Carbon nanotube material can now be produced in macroscopic quantities by either arc discharge or thermal decomposition of hydrocarbons. But, the raw material has a disordered structure, which restricts FE applications of nanotubes.

Here we report a synthesis of thin film material of nanostructured carbon nanotubes and nanosized graphite crystallites aligned by their graphene sheets along a normal to the film surface. The nanostructured carbon thin film cold cathodes were used for fabrication of prototypes of light emitting devices.

EXPERIMENTAL

The carbon films were produced on silicon substrates by a plasma-assisted chemical vapor deposition (CVD) method using a deposition system described in [1]. The plasma was activated by a direct current discharge in a methane-hydrogen gas mixture. The total gas pressure during the deposition was 8.5-9 kPa, and the deposition

duration was 45 min. By varying the substrate temperature in a range from 850 to 1100°C, methane concentration from 0.5 to 10%, we synthesized films with different ratios of diamond and non-diamond carbon.

Electron field emission current was measured in vacuum of 10^{-4} Pa with a 20 mm diameter tungsten plate anode positioned by a precision screw translator [2]. The accuracy of anode-to-cathode distance translation was 5 μm . The I - V measurements were PC controlled and performed in an automatic mode, the voltage being varied from 0 to 1500 V. The maximum current was limited during these measurements by a protective circuit to 1.5 mA. To characterize a spatial distribution of emission sites over the film surface, we used a 30 mm diameter glass plate covered with ITO and a layer of a phosphor with a thickness of several microns deposited over ITO. At relatively small anode-to-cathode distances (of 50 to 500 μm), the regions of phosphor luminosity caused by the electron impinging, in fact, coincided with the emission sites. To prevent the excessive sputtering of the phosphor by the electrons, in these measurements we used a pulsed voltage supply (pulse duration about 1 μs , repetition rate about 500 Hz, peak voltage set in a range from 200 to 2000 V). Images of emission sites distributions were captured by a video or photo camera.

RESULTS

Comparative study of the field emission and Raman scattering (RS) of the CVD films have definitely shown that the FE efficiency was essentially improved (emission threshold decreased, emission sites density and the emission current density increased) with an increase of non-diamond carbon contaminations in polycrystalline diamond films. The best emission was obtained for those films in Raman spectra of which no "diamond" RS peaks, but only peaks similar to "graphite" type of carbon materials were detected. Fig.1 shows I - V dependence obtained from such films in flat electrode diode type device with a distance between anode and cathode of 200 μm . Typical Raman spectrum corresponding to such "graphite" CVD film is shown in Fig.2.

I - V dependence in Fig.2 is plotted in Fowler-Nordheim coordinates and its linear behaviour, which is clearly seen, is an evidence of field emission origin of the detected current. The field emission is started at an average electric field of about 1.5 V/ μm and a slope of I - V dependence allows estimation of an effective energy barrier for electrons escaping from the cathode to vacuum for known local field. This field depends on cathode surface morphology as $E=E^*\beta$, where $E^*=V/d$ is an average electric field between flat electrodes at the applied voltage V and distance between them d , whereas β is field enhancement factor being equal to h/r for tip-like structures of height h and curvature radii of the tip end r .

To make the estimation of β we have performed HRTEM investigations of the CVD films by using a JEM-4000EX transmission electron microscope. Figures 3 and 4 present typical images which show that the surface of the CVD films consists of tip-

like structures (Fig.3) which exhibit typical for carbon nanotubes atomic structure (Fig.4).

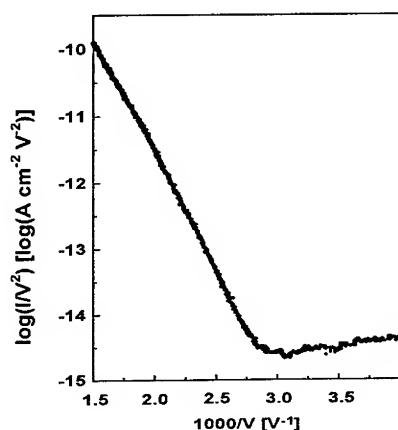


Fig. 1 FE I - V plot in F-N coordinates obtained at a distance between anode and cathode of 200 μm .

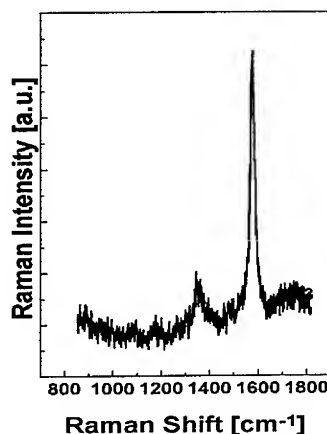


Fig. 2 Typical Raman spectrum for thin film carbon cathode with FE characteristics presented in Fig.1.

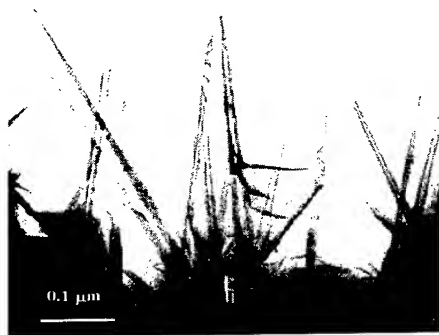


Fig. 3 Typical HRTEM image of the graphite-like thin film material.

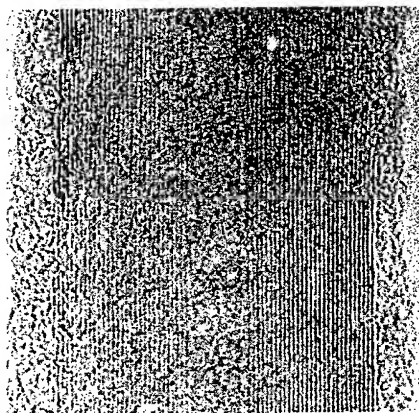


Fig. 4 HRTEM image of individual carbon nanotube from the CVD film.

We found from these HRTEM observations that the geometrical field enhancement factor β can be in a range of 100 to 1000. It means that the effective

energy barrier for electrons escaping into vacuum lies in a range of 0.5 to 2 eV [3] and is much smaller than 5 eV work function of graphite. Such decrease of the barrier can be explained by modification of electronic properties of the CVD graphite-like nanostructured material due to partial rehybridization of sp^2 bonds into sp^3 [4,5].

PROTOTYPE OF LIGHT EMITTING DEVICE

The described carbon nanostructured film cathodes were used to fabricate sealed cathodoluminescent (CL) lamps (see Fig.5). The glass envelope of the lamp cells in diode configurations was assembled using two overlapping glass slides 40×50 mm in size, coated with an Indium-Tin-Oxide (ITO) transparent conductive layer. The FE cathode was bonded to the bottom slide using conductive epoxy. Standard TV phosphor or special low-voltage phosphor was deposited over the conductive ITO layer of the top glass slide forming the phosphor screen. Two glass slides were bonded together using a vacuum cement allowing a separation distance between phosphor layer and field emission array within 0.1-1 mm range. The cell thickness was about 3 mm. Residual pressure in the flat glass cell was about 10^{-4} Pa.

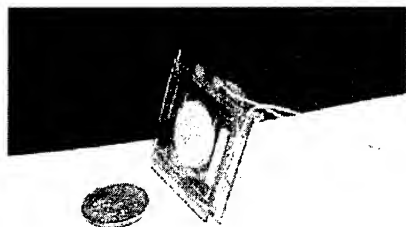


Fig. 5 Sealed diode type light emitting device of with carbon cold cathode.

Operational voltages for the CL lamps depended on the phosphor type and varied from 200 V for low-voltage phosphor to 1 kV for TV quality phosphors. Measured brightness of the lamps reached 500 cd/m² for low-voltage phosphors and was much higher for the TV phosphors. CL site distribution on the phosphor screen was homogeneous over the 25×25 mm area of FE cathode and was estimated as greater than 10⁶ cm⁻². Life-time tests of lamps were run for a period of up to 48 hours without significant decrease of brightness and emission sites density distribution.

REFERENCES

1. I.Yu. Pavlovsky and A.N. Obraztsov; Instr. and Exp. Tech., (1998), 41, 152.
2. A.N. Obraztsov, I.Yu. Pavlovsky, A.P. Volkov, et al., Diamond Films and Tech., (1999), (in press).
3. A.N. Obraztsov, I.Yu. Pavlovsky, and A.P. Volkov, J. Vac. Sci. Technol. B (1999), 17(2) (in press).
4. A.N. Obraztsov, A.P. Volkov, and I.Yu. Pavlovsky, JETP Lett., (1998), 68, 59.
5. A.N. Obraztsov, A.P. Volkov, I.Yu. Pavlovsky, et al., JETP Lett., (1999), 69, 381.

Field emission properties of carbon nanowires from *ab initio* calculations

M. Bianchetti*, P. Buonsante*, F. Ginelli*, A. Lorenzoni†,
H. E. Roman* and R. A. Broglia*,⁺

*Dipartimento di Fisica and INFN, Università di Milano, Via Celoria 16, 20133 Milano, Italy,

†Dipartimento di Fisica, Università di Pavia, Via A. Bassi 6, 27100 Pavia, Italy,

⁺The Niels Bohr Institute, University of Copenhagen, 2100 Copenhagen, Denmark.

Abstract. The field emission (FE) characteristics of linear carbon chains, relevant for understanding FE properties of complex carbon-based nanostructures, are studied by means of self-consistent density functional calculations in the presence of a constant electric field, making use of pseudopotentials and the local density approximation (LDA). The transmission coefficient for electron tunneling through the LDA potential barrier to the vacuum is obtained within the WKB approximation. It is found that chain polarization has remarkable effects on the emission properties, yielding currents of the order of 1 μA for a chain of 9 atoms under standard bias conditions. Such carbon chains may thus be seen as the atomic scale realization of metallic nanowires.

INTRODUCTION

Carbon based films consisting of nanotubes and related allotropic structures are currently attracting much attention because of their potential use as highly efficient field emitters (see e.g. [1–3]). Despite the strong interest in their practical applications, much less is known about these systems from a theoretical point of view. The main reason for this lack is due to the complexity of the intrinsically random structure of the emitting surface. In order to approach the problem theoretically, it is useful to identify simple carbon structures which can be studied accurately and may play a prominent role in the emission process. An interesting example is that of a linear carbon chain, argued to be formed at the open end of a (multiwall) nanotube in the presence of an applied electric field, yielding emission currents as high as few μA [4].

In this work, we study field emission (FE) properties of single carbon chains by solving the Kohn-Sham equations self-consistently in the presence of a constant electric field. It will be concluded that such linear carbon chains behave as metallic nanowires of atomic scale [5,6], yielding emission currents as high as few μA already for chains consisting of 9 atoms and for local electric fields of the order of 1 V/Å.

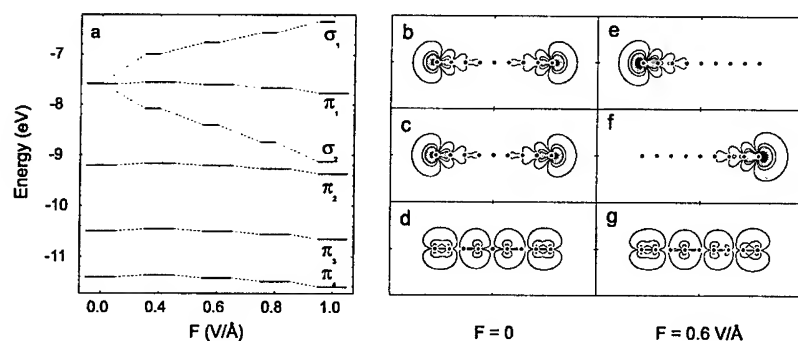


FIGURE 1. *Ab initio* electronic structure of C₉ in the presence of a constant electric field. The eigenvalues for the six highest occupied states are shown in (a) for five values of the field strength, F . The symbols σ (short thick lines) and π (long thick lines) indicate states with quantum numbers $m = 0$ and $m = \pm 1$ (two-fold degenerate), respectively. In the right panel, contour diagrams of the electronic densities, $|\psi(\rho, z)|^2$, are displayed for σ_1 , σ_2 and π_1 in: (b)-(c)-(d) for $F = 0$ and (e)-(f)-(g) for $F = 0.6$ V/Å, respectively. The dots represent the carbon ions located along the z axis. The electric field is directed from right to left, $\vec{F} = -F\hat{z}$.

CARBON CHAINS IN AN ELECTRIC FIELD

The electronic structure of linear carbon chains in the presence of a constant electric field parallel to the chain has been obtained self-consistently within the LDA, making use of pseudopotentials for the carbon ions and a standard parametrized form for the exchange and correlation potentials. The Kohn-Sham orbitals $\psi(\rho, z, \phi)$ have been expanded on a suitable basis in cylindrical coordinates (see [7] for details).

As an example, we study a closed shell carbon chain consisting of 9 atoms, C₉. The results, obtained assuming a constant (cumulenic) carbon-carbon spacing of 1.3 Å (see also [8–10]), are shown in Fig. 1. The detailed electronic structure of the occupied energy levels around the HOMO (Highest Occupied Molecular Orbital) is displayed in Fig. (1a), as a function of field strength, F . For $F=0$, the HOMO, located at -7.58 eV, consists of two σ -states (of quantum number $m=0^\pm$, being either symmetric (+) or antisymmetric (−) under the transformation $z \rightarrow -z$). The corresponding electronic charge distributions are concentrated at the tips of the chain as shown in Fig. (1b,1c) and may be regarded as “unsaturated” dangling bonds. The state just below the HOMO (the HOMO-1), located at -7.60 eV, is a π doubly-degenerate state having $m = \pm 1$, and is denoted as π_1 . Its charge distribution is shown in Fig. (1d). For $F > 0$, the two σ -states get strongly polarized (Fig. (1e,1f)), undergoing a linear Stark splitting as indicated in Fig. (1a) (see also [9]). In contrast, the π_1 state remains almost unchanged (Fig. (1a)), reflecting its rigidity against polarization by the electric field (cf. Figs. (1d) and (1g)). The

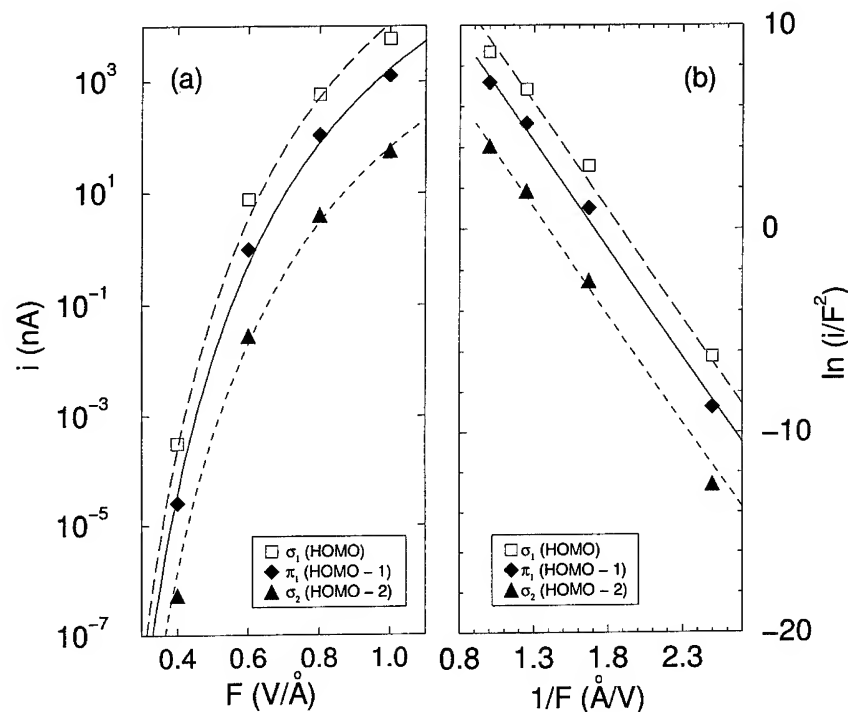


FIGURE 2. Field emission from the carbon chain C_9 : (a) Single level emission currents i [nA] versus electric field intensity F [V/Å], for the states σ_1 , σ_2 and π_1 displayed in Fig. (1). Non-vanishing currents are only due to π_1 and σ_2 , and are directed along $z \rightarrow +\infty$. The points for σ_1 indicate the values of i that one would obtain if emission were possible (see text). (b) Fowler-Nordheim (FN) plots corresponding to (a). The lines are fits using the form $i(E) = A(E) F^2 \exp(-\gamma W^{3/2}/F)$, where $\gamma = 4\sqrt{2m}/3e\hbar$ [11], with $W = 6.2$ eV and prefactors $A(E) = (2.5 \cdot 10^6, 6.5 \cdot 10^7, 4.3 \cdot 10^8)$ nA (Å/V) 2 .

lower lying π -states behave similarly as π_1 (cf. Fig. (1a)).

FIELD EMISSION FROM CARBON CHAINS

In a recent work, we have studied FE properties of carbon chains where the electric field is treated separately from the LDA calculation [5,6]. In what follows, we discuss the effect of the electric field on FE when it is included in the self-consistent Kohn-Sham equations as described above. Although the emission currents we obtain here essentially confirm the results found in [5,6], a different qualitative picture for FE emerges when polarization effects are taken into account.

The FE current from a single energy level E of the polarized chain, $i(E)$, is

described as a tunneling process through the confining potential barrier V_{LDA} to the vacuum and the corresponding transition probability $D(E)$ can be estimated within the WKB approximation [11]. The current can then be written as $i(E) \approx n_E \nu(E) P(E) D(E)$, where n_E is the level occupation number, $\nu(E) = |E|/h$ is the semi-classical knocking rate of the electron against the potential barrier and $P(E)$ (either 0 or 1) represents the probability to find the electron in the neighborhood of the emitting tip. In the case of C_9 , P vanishes for σ_1 , since its density distribution $|\psi|^2$ is localized at the opposite side of the emitting tip (see Fig. (1e)), while $P = 1$ for both π_1 and σ_2 . The total emitted current is then given by the sum of the single contributions $i(E)$ (see [7] for further details).

Results for C_9 are shown in Fig. (2). FE currents of the order of $1\mu\text{A}$ are obtained for fields of about 1 V/\AA (Fig. (2a)). In addition, the currents are well fitted by a Fowler-Nordheim type of equation with an effective work function $W \cong 6.2\text{ eV}$ (Fig. (2b)), suggesting a metallic behavior for the carbon chain [5,6]. A systematic study of FE behavior of carbon chains within the present scheme and its relevance to other carbon nanostructures will be discussed elsewhere [7].

ACKNOWLEDGMENTS

We gratefully acknowledge F. Biscarini, J.P. Bourgoin, G. Onida, A.G. Rinzler, and Y. Saito for illuminating discussions. Financial support by NATO under grant CRG 940231 is gratefully acknowledged. We are also indebted for financial support to INFM Advanced Research Project Class.

REFERENCES

1. de Heer, W. A., Chatelain, A., and Ugarte, D., *Science*. **270**, 1179-1180 (1995).
2. Collins, P. G., and Zettl, A., *Phys. Rev. B* **55**, 9391-9399 (1997).
3. Saito, Y., et al., *Nature* **389**, 554-555 (1997).
4. Rinzler, A. G., et al., *Science*. **269**, 1550-1552 (1995).
5. Lorenzoni, A., et al., *Chem. Phys. Lett.* **276**, 237-241 (1997).
6. Roman, H. E., et al., *Il Nuovo Cimento* **110**, 1165-1172 (1997).
7. Bianchetti, et al., to be published.
8. Raghavachari, K., and Binkley, J. S., *J. Chem. Phys.* **87**, 2191-2197 (1987).
9. Lou, L., and Nordlander, O., *Phys. Rev. B* **54**, 16659-16662 (1996).
10. Kim, S. G., et al., *Chem. Phys. Lett.* **264**, 345-350 (1997).
11. Gomer, R., *Field Emission and Field Ionization*, Cambridge, Massachusetts: Harvard University Press, 1961.

Electrocatalytic Properties of the C₆₀, C₇₀, C₇₆, C₇₈ and C₈₄ Fullerene Anions

F. D'Souza,^a J-P. Choi,^a and W. Kutner^{a, b}

^a Department of Chemistry, Wichita State University, Wichita, KS 6720-0051, USA

^b Institute of Physical Chemistry, Polish Academy of Sciences, Kasprzaka 44, 01-224 Warsaw, Poland

Abstract. Di- and trianions of the title fullerenes reduce electrocatalytically 1,2-dihaloethanes. The fullerene anions were generated electrochemically in 0.1 M tetra-*n*-butylammonium hexafluorophosphate benzonitrile solutions of the 1,2-dihaloethanes. Cyclic voltammetry experiments indicate that the electrocatalytic reduction results in dehalogenation of the 1,2-dihaloethanes in case of dianions of C₆₀, C₇₀, C₇₆ and C₇₈ as well as trianions of C₇₆, C₇₈ and C₈₄. Values of the second-order rate constant, *k*, for the electrocatalytic processes were determined by using a rotating-disk electrode voltammetry under pseudo-first-order conditions against the 1,2-dihaloethanes. The *k* values increase in the order: Cl < Br < I for each fullerene anion and in the order: C₆₀ < C₇₀ < C₇₆ < C₇₈ < C₈₄ for each 1,2-dihaloethane. In contrast to the C₆₀ⁿ⁻ electrocatalysis, no alkyl adducts were formed in case of the larger fullerene anions. Due to higher stability with respect to the adduct formation and more positive potentials of the electrocatalytic processes, the larger fullerene anions may serve as more useful catalysts than the C₆₀ anions despite that the respective electrocatalytic rate constants are smaller.

INTRODUCTION

Recently, we reported on electrocatalytic reduction and dehalogenation of α,ω -dihaloalkanes by anions of C₆₀ and C₇₀ (1, 2). This dehalogenation results mainly in different alkanes, alkenes, and mono haloalkanes. In a competing reaction, alkyl adducts of C₆₀ were also formed in presence of certain α,ω -diiodoalkanes (1). Advantageously, no alkyl adducts were formed, on a voltammetry time scale, in case of the C₇₀ electrocatalysis (2). It seemed that the larger fullerenes, being relatively more stable than C₆₀ with respect to derivatization, may serve as better electrocatalysts than C₆₀. Here and in (3), we address this issue by examining electrocatalytic reduction of 1,2-dihaloethanes by anions of larger fullerenes, i.e., C₇₆, C₇₈, and C₈₄.

EXPERIMENTAL

Chemicals. C₇₆ (+98 % purity), isomeric mixture of C₇₈ (98 % purity), and isomeric mixture of C₈₄ (99 % purity) were procured from BuckyUSA (Bellaire, TX). All the 1,2-dihaloethanes, tetra-*n*-butylammonium hexafluorophosphate, (TBA)PF₆, (98 % purity), and anhydrous benzonitrile (+99 % purity, water content < 0.005 %) were from Aldrich (Milwaukee, WI). All chemicals were used as received.

Electrochemical Measurements. Experiments of the rotating disk electrode (RDE) voltammetry and cyclic voltammetry (CV) were performed by using a Model 263A potentiostat/galvanostat of EG & G (Princeton, NJ). The RDE voltammetry was carried out at a 0.17 cm² platinum disk electrode by using a MSRX Speed Control Unit

and AFMSRX Modulated Speed Rotator of Pine Instrument Co. (Grove City, PA). A Pt wire was used as the counter electrode and an NaCl saturated Ag/AgCl electrode as the reference one.

GC-MS Measurements. The GC-MS analysis of gaseous products of the bulk electrolyses was performed by using a Model Q-Mass 910 of Perkin Elmer Co. (Norwalk, CT) on a DB-1 non-polar phase fused silica capillary column (30 m \times 0.253 mm) operating in an electron ionization mode.

HPLC Measurements. The HPLC analysis of solution products of the bulk electrolyses was carried out by using a Perkin Elmer chromatograph (Model 250 binary pump and a LC-290 UV-visible spectrophotometric detector set at 340 nm). Analytical Cosmosil Buckyprep column (250 \times 4.6 mm) of Nacalai Tesque (Kyoto, Japan) was used with toluene as a mobile phase at a flow rate of 1 mL min⁻¹.

RESULTS AND DISCUSSION

Fullerene anions were generated electrochemically under conditions of CV, RDE voltammetry or controlled-potential bulk electrolysis for qualitative and quantitative characterization of the electrocatalysis processes as well as for product characterization, respectively.

Qualitative CV investigations indicated that di- and trianions of C₇₆ and C₇₈ as well as trianions of C₈₄ electrocatalytically reduce and dehalogenate the 1,2-dihaloethanes.

Quantitative electrocatalytic experiments of the RDE voltammetry, performed in ca. tenfold excess of 1,2-dihaloethanes with respect to the fullerenes (i.e., under pseudo-first-order conditions against the 1,2-dihaloethanes), indicated that limiting currents, i_{lim} , were virtually independent of the rotation rate, for small rotation rates. Therefore, the second-order electrocatalytic rate constant, k , could be calculated (4):

$$k = i_{cat}^2 / (n F A C_{Ox})_2 D C_S \quad (1)$$

(Table 1) where i_{cat} is the catalytic current, D and C_{Ox} are the diffusion coefficient and concentration of the fullerene, respectively, C_S is the concentration of the substrate, i.e., 1,2-dihaloalkane, F is the Faraday constant, n is the number of electrons transferred and A is the electrode surface area. The D values of all fullerenes were determined from the i_{lim} values, in the absence of the dihaloethanes, and the Levich analysis. The values of i_{cat} were calculated by extrapolating the curves of i_{lim} vs. square root of rotation rate to the zero abscissa (4). These curves deviated positively from the linear Levich plots that were observed in the absence of the 1,2-dihaloethanes. For all 1,2-dihaloethanes, i_{cat} linearly depends on $C_S^{1/2}$ both for the fullerene di- and trianions.

Our earlier (1, 2) and present results show that all the di- and trianions of C₆₀, C₇₀, C₇₆, and C₇₈ as well as trianions of C₈₄ electrocatalytically reduce 1,2-dihaloethanes. Potential of the dehalogenation is governed by the formal redox potential, $E_{1/2}$, of the fullerene. Importantly, the larger the fullerene, the more positive are the $E_{1/2}$ values of the consecutive C_m^{n/(n+1)-} electroreductions (Table 1) and, hence, the more positive are the $E_{1/2}$ values of electrocatalytic reduction of 1,2-dihaloethanes. However, the k

value is smaller the larger the fullerene, as the Brønsted type dependence shows (Fig. 1). For each fullerene anion, k increases in the order: $\text{Cl} < \text{Br} < \text{I}$ for the 1,2-dihaloethanes, as the Savéant theory of dissociative reduction predicts (5).

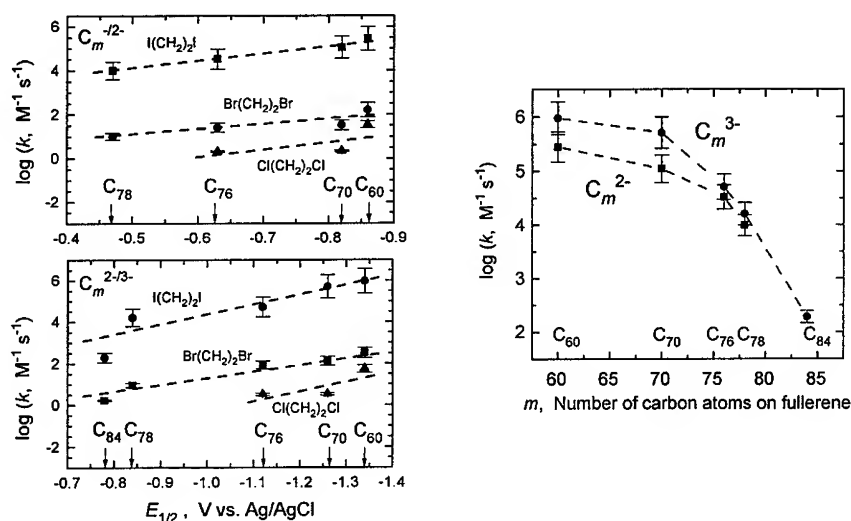


FIGURE 1. Dependence of $\log k$ on $E_{1/2}$ for the second, C_m^{2-} , and third, $C_m^{2-/3-}$, electroreduction of the fullerenes ($m = 60, 70, 76, 78$ and 84) in presence of different 1,2-dihaloethanes in 0.1 M (TBA)PF₆, in benzonitrile.

FIGURE 2. Dependence of $\log k$ on number of the fullerene carbon atoms for the fullerene dianions, C_m^{2-} , and trianions, C_m^{3-} , for 1,2-diiodoethane in 0.1 M (TBA)PF₆, in benzonitrile.

Moreover, the k value is smaller the larger the fullerene (Fig. 2). Presumably, the free energy difference, corresponding to the difference of formal redox potentials of the fullerene and the 1,2-dihaloethane, largely contributes to the activation energy of reduction of 1,2-dihaloethanes by the fullerene anions.

Our constant-potential bulk electrolysis experiments, followed by the HPLC and GC-MS analyses of products, indicated no reaction between the anions of larger fullerenes and the 1,2-dihaloethanes.

CONCLUSIONS

The dianions of C_{76} , and C_{78} as well as trianions of C_{76} , C_{78} and C_{84} electrocatalytically reduce and dehalogenate 1,2-dihaloethanes. The second-order rate constant for the electrocatalysis increase in the order: $\text{Cl} < \text{Br} < \text{I}$ for the investigated 1,2-dihaloethanes and in the order: $C_{84} < C_{78} < C_{76} < C_{70} < C_{60}$ for each

1,2-dihaloethane. The larger fullerenes are more stable than C₆₀ with respect to the alkyl adduct formation. Because of high stability with respect to the adduct formation and more positive $E_{1/2}$ values of the electrocatalytic processes, the larger fullerenes may be more useful than C₆₀ as catalysts, even though their corresponding catalytic rate constants are smaller.

TABLE 1. Values of the second-order rate constant, k , for electrocatalytic reduction of 1,2-dihaloethanes by C_mⁿ⁻ ($m = 60, 70, 76, 78, 84$, and $n = 2$ or 3) in 0.1 M (TBA)PF₆ in benzonitrile.

Fullerene Redox Couple	$E_{1/2}^a$ V vs. Ag/AgCl	$k,^b \text{ M}^{-1} \text{ s}^{-1}$			Ref.
		Cl(CH ₂) ₂ Cl	Br(CH ₂) ₂ Br	I(CH ₂) ₂ I	
C ₆₀ ⁻²⁻	-0.86	3.5×10	1.6×10^2	2.8×10^5	^c
C ₇₀ ⁻²⁻	-0.82	2.2	3.3×10	1.1×10^5	^d
C ₇₆ ⁻²⁻	-0.63	2.1	2.5×10	3.3×10^4	^e
C ₇₈ ⁻²⁻	-0.47	0	10	9.8×10^3	^e
C ₈₄ ⁻²⁻	-0.42	0	0	0	^e
C ₆₀ ^{2-/3-}	-1.34	5.5×10	3.2×10^2	9.4×10^5	^c
C ₇₀ ^{2-/3-}	-1.26	3.3	1.3×10^2	5.1×10^5	^d
C ₇₆ ^{2-/3-}	-1.12	3.2	8.3×10	5.1×10^4	^e
C ₇₈ ^{2-/3-}	-0.84	0	8.9	1.6×10^4	^e
C ₈₄ ^{2-/3-}	-0.78	0	1.7	1.9×10^2	^e

^a The $E_{1/2}$ values determined in the present work agree with the literature values (Refs. 6, 7). For the Fc^{+/0} couple, $E_{1/2} = 0.45$ V vs. Ag/AgCl under the present solution conditions. ^b The estimated error of the k values is $\pm 15\%$ (std). ^c From Ref. 1. ^d From Ref. 2. ^e Present work.

ACKNOWLEDGES

We thank BG Products, Wichita KS, for making accessible its GC-MS facility. Financial support of the US-Polish M. Skłodowska-Curie Fund II to FD and WK (PAN/NSF-96-275), the Petroleum Research Fund (administered by the American Chemical Society) to FD, as well as the Institute of Physical Chemistry of the Polish Academy of Sciences to WK is gratefully acknowledged.

REFERENCES

1. D'Souza, F., Choi, J.-P., Hsieh, Y.-Y., Shriver, K., Kutner, W. *J. Phys. Chem. B*, **102**, 212 (1998).
2. D'Souza, F., Choi, J.-P., Kutner, W. *J. Phys. Chem. B*, **102**, 4247 (1998).
3. D'Souza, F., Choi, J.-P., Kutner, W. *J. Phys. Chem. B*, **103**, (1999), in press.
4. Bard, A. J., Faulkner, L. R., *Electrochemical Methods: Fundamentals and Applications*, New York: John Wiley, 1980, ch. 11.4.4, pp4. 68-469.
5. Savéant, J.-M. in *Advances in Physical Organic Chemistry*; Bethell, D., Ed.; London: Academic Press, 1990, Vol. 26, pp. 1-130.
6. Yang, Y., Arias, F., Echegoyen, L., Chibante, L. P. F., Flanagan, S., Robertson, A., Wilson, L., *J. Am. Chem. Soc.*, **117**, 7801 (1995).
7. Ruoff, R. S., Kadish, K. M., Boulas, P., Chen, E. C. M., *J. Phys. Chem.*, **99**, 8843 (1995).

Carbon Nanotubes and Gas Adsorption

I Stepanek^{†‡}, LC de Menorval^{*}, R Edwards[†], P Bernier[†]

[†]GDPC, USTL Montpellier II, CC026, Place E. Bataillon, 34095 Montpellier Cedex 05-France

[‡]EI/IHCP, JRC, TP202, via Fermi, 21010 Ispra (VA)-Italia

^{*}ENSCM, Rue de La Gallera, 34000 Montpellier-France

Abstract. We report results on the physisorption of N₂ and H₂ at low temperatures by single-walled carbon nanotubes (SWNTs) produced by the arc discharge method. We characterized (SEM, TEM, and HRTEM characterizations) two batches of sample, raw collaret and chemically treated SWNTs, in order to determine the best nanotube-containing sample for gas storage. Treatments and the effectiveness of the chemical acid treatments are discussed. Adsorption measurements of N₂ on SWNTs allow us to obtain the specific surface area and pore size distribution. Acid treatments used to purify and open (by cutting) nanotubes decreased the surface area as a result of material compaction. Measurements of H₂ adsorption were performed in order to evaluate the adsorption capacity of the nanotubes at 133K and below 2 bar. We found up to H:C atomic ratio=0.35, ie.2.4wt% of adsorbed hydrogen by gram of sample for our raw material.

INTRODUCTION

Because of their cylindrical structure and hollow shape, single-walled carbon nanotubes could be thought of as containers for hydrogen storage system. Their empty space could be filled with different gas.

Typically, SWNTs are closed-packed in bundles on ropes of 10-100 well-aligned nanotubes in a two-dimensional periodic triangular lattice bonded by Van der Waals forces. In our material, the average tube diameter is 1,3nm, with a 3,4Å intertube distance and a 5,7Å interstitial spacing diameter in the triangular lattice. Generally, when they are synthesised, SWNTs are a few microns long and capped-ended. Rope entanglements form a porous material. Consequently, adsorption process could take place in different pore size ranges and the adsorption capacity of such material could be very high.

In this paper, we present results on N₂ and H₂ adsorption studies of raw and chemically treated nanotube materials (purified and opened by cutting nanotubes). Firstly, analysing N₂ adsorption isotherms at 77K of raw and chemically treated nanotube materials showed the effect on surface area and

pore size distribution. Secondly, evaluation of H₂ adsorption capacity is determined for the raw material from a thermogravimetric isotherm.

EXPERIMENTAL SECTION

We analysed 2 different batches of nanotube materials: raw and chemically treated materials. Our raw material is a collaret, synthesized by electric arc discharge technique in a reactor under static helium atmosphere. The arc is produced between two graphite rods in presence of a mixture of metallic catalysts Ni:Y:C (4,2:1:94,8 at%) (1). There is a high density of SWNTs : around 70% volume (Fig. 1). The remainder consists of different forms of carbon (amorphous, fullerenes...) and few % of metallic nanoparticles.

We investigated 2 types of chemically treated tubes. The first type is a purified nanotube sample obtained by refluxing raw collaret in HNO₃ for 48h followed by a cross flow filtration (2). After this acid treatment, the sample was annealed under N₂ atmosphere at 600°C or 1600°C. After annealing, 95% of material is SWNT bundles (Fig. 2). The second type of chemically treated tubes is obtained from the purified material by adding a nanotube-cutting step. The opening process has been inspired by a study done by *Liu et al* (4) from produced nanotubes by LASER ablation. Purified material (90 mg) was first dispersed in of 360 ml concentrated H₂SO₄/HNO₃ (3:1 vol.) mixture and then sonicated for 24h at 40°C. After being diluted in distilled water, the suspension was filtered through a 100nm-pore membrane and washed with 10mM NaOH solution to neutralise all the chemical species. Finally, we dispersed the resultant deposit in H₂SO₄ / 30% aqueous H₂O₂ (4:1 vol.) and stirred it 40 min at 70°C. The final material is much more compact (Fig. 3). TEM microscopy (Fig. 4a) shows that many bundles were cut during the chemical oxidation. The surface of the tubes is damaged. HRTEM permits to see clearly interference fringes corresponding to each nanotube in a bundle but it is very difficult to see if the individual SWNTs are open or not with this technique. However, sometimes we are able to find open nanotubes at some sites along bundles (Fig. 4b). Maybe, nanotubes do not stay open but tend to evolve in time by linking to another bundle (Fig. 4c).

All adsorption-desorption experiments were done on 50-100mg samples. N₂ measurements were performed at 77K on a computer-controlled Micrometrics ASAP

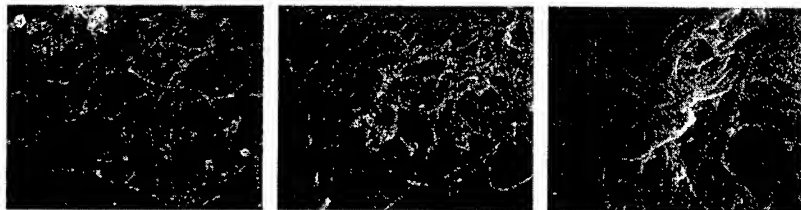


FIGURE 1. SEM picture of raw collaret.

FIGURE 2. SEM picture of purified material and annealed at 1600°C.

FIGURE 3. SEM picture of SWNTs opened by cutting.

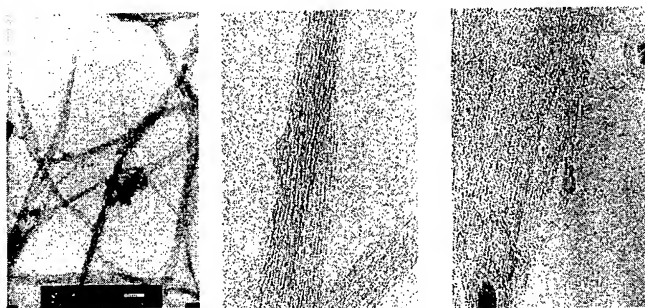


FIGURE 4. a) TEM picture of SWNT bundles, open by cutting just after experiment. b) HRTEM of open SWNT fragment on a outer bundle surface. c) Bonding of 2 bundles after opening.

apparatus. Materials were outgassed 12 hours at 250°C before each experiment. A gravimetric technique is used for H₂ experiments at constant temperature, which involves the measurement of the uptake of the gas, by the adsorbent with the aid of a HIDEN “IGA” thermobalance with a cryo.furnace. First, species were outgassed 10 hours at 150°C then temperature was lowered to 133K and pressure was raised in steps allowing about 30 min for the weight change to reach a steady value between steps.

RESULTS AND DISCUSSION

Specific surface areas

Nitrogen adsorption is used to estimate how much solid area is available for adsorption in a given sample. Knowing from adsorption isotherm data the gas volume needed to cover a monolayer on the solid surface, surface areas can be calculated using the BET equation (4). Specific surface areas (S_{BET}) of the different groups of SWNTs are reported in Table 1. For raw material, we note a big surface area (around 280 m²/g) but it is difficult to determine the real nanotube contribution. One expects purification treatments to increase the specific surface area by eliminating the coarser non-SWNT material. This effect is indeed observed especially in the 600°C-annealed material. The surface area observed corresponds to only about around 1/8 of the calculated external surface area of the nanotubes. Therefore, we think that adsorption takes place only on the outer surface of nanotube bundles. After annealing at 1600°C the specific area is less than the 600°C annealed material. This is most likely due to the agglomeration of nanotube bundles to form larger and less perfect bundles at 1600°C. A large specific surface area decrease is observed after the subsequent stage of “opening” by cutting. This suggests that nitrogen molecules cannot penetrate even the “cut” SWNTs; the surface reduction is probably connected to our observation (Fig. 3) that bundles after cutting treatments are even thicker than before because of further bundle agglomeration. We believe that the damaged external tubes favouring bonding

TABLE 1. Specific surface area calculated using BET equation (S_{BET}) for different samples and Volume of the adsorbed monolayer V_M .

Samples	S_{BET} (m^2/g)	V_M (cm^3/g)
Raw collaret	274	60,86
Purified and annealing at 600°C	324	74,46
Purified and annealing at 1600°C	239	54,945
"Cut"nanotubes	95	21,74

between existing bundles cause this effect. Then, acid intercalation might be possible inside bundles (5), so adsorption could be blocked. All treated samples showed larger hysteresis loops (Fig. 5-6) than the raw material. This suggests a diffusion barrier: comparing figures 1-3 we can suppose that the much more dense packing of bundles in the treated materials tends to occlude adsorption in the inner part of the specimen.

H₂ adsorption capacity of raw nanotube sample

Figure 7 shows H₂ adsorption up to 2 bar. Saturation of adsorption is reached at low pressure: 100mBar. For higher pressures, till 2Bar, there is a plateau: no increase of the adsorption capacity. The curious weight decrease at hydrogen pressures above 1 Bar may be due to hydrogen displacing a heavier adsorbed gas which was not completely removed by the preceding vacuum treatment. The material can adsorb 2.4wt.% of hydrogen per gram of sample at 133K (H:C atomic ratio=0.35); corresponding to 3.43 wt.% if all adsorption is ascribed to the 70% nanotubes in the material. This is less than Dillon et al. reported (6) for partially oxidized material from LASER ablation at near room temperature; which they ascribe to adsorption inside the SWNTs. Their values (5-10wt%) are approximate because a large correction is needed to account for proportion of SWNTs (0.1-0.2%) in their samples. The adsorption plateau corresponds to 2700cm³ hydrogen/gram. The nitrogen monolayer covering the

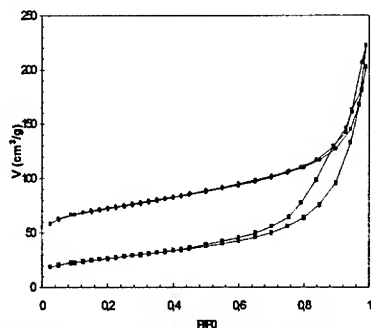


FIGURE 5. N₂ adsorption-desorption isotherms at 77K: (■) cut-nanotubes-containing material; (●) raw material. P_0

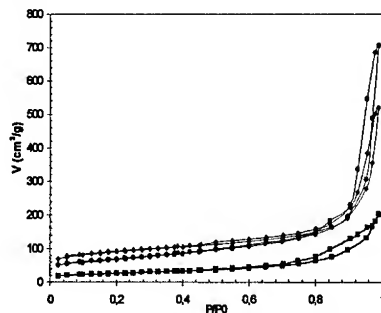


FIGURE 6. N₂ adsorption-desorption isotherms at 77K: (●) Purified +annealed at 1600°C sample; (♦) Purified +annealed at 600°C sample; (■) cut-nanotube-containing material. Adsorbed volume is expressed in function of relative pressure (P_0 is the vapour saturation pressure of N₂ at 77K)

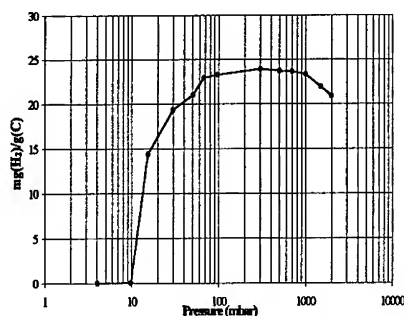


FIGURE 7. Hydrogen adsorption isotherm at 133K of raw collaret. Semi-log scale for the pressure range. The change in weight is measured in mg of H₂ per gram of

raw collaret corresponds to an atomic N/C ratio of only 0.065. Therefore, the hydrogen is accessing a greater surface of material than the nitrogen; indicating some penetration inside the bundles or even inside the nanotubes themselves.

conclusion

Nitrogen adsorption on SWNTs at 77K occurs only on the outer surfaces of the bundles. This area decreases as a result of thermal and acid treatments intended to open the SWNTs. However, there are indications that hydrogen penetrates the bundles, reaching a plateau coverage of $H/C \approx 0.35$ by $P=100\text{mBar}$ at 133K on raw collaret material (70% SWNTs). Measurements on purified and chemically open SWNTs are currently in progress. Furthermore, improvement on nanotube cutting by a mechanically way is under way.

acknowledgments

Thanks to L. Vaccarini for her help during the purification step and also to V Micholet, R. Aznar (GDPC, Montpellier, France). Thanks to J. Gavillet and A. Loiseau from ONERA (Paris-France) for HRTEM pictures and M. della Rossa from CCR Ispra (Italy) for experimental part of H₂ adsorption.

REFERENCES

- (1) Journet, C., Maser, W.K., Bernier, P., Loiseau, A., Lamy de la Chapelle, M., Lefrant, S., Deniard, P., Lee, R. and Fischer, J.E., *Nature* **388**, 756-758 (1997)
- (2) Rinzler, A.G., Liu, J., Dai, H., Nikolaev, P., Huffman, C.B., Rodriguez-Macias, F.J., Boul, P.J., Lu, A.H., Heymann, Colbert, D.T., Lee, R.S., Fisher, J.E., Rao, A.M., Eklund, P.C., Smalley, R.E., *Applied Physics A* **67**, 29-37 (1998)

- (3) Liu, J., Rinzler, A.G., Dai, H., Hafner, H., Bradley, R.K., Boul, P.J., Iverson, T., Shelimov, K., Huffman, C.B., Rodriguez-Macias, F.J., Shon, Y-S., Lee, T.R., Colbert, D.T., Smalley, R.E., *Science* **280**, 1253-1256 (1988)
- (4) Gress, S. J., Sing, K. S., *Adsorption, Surface Area and Porosity*, London : Academic Press, 1982, ch. 2, pp.42-55.
- (5) Bower, C., Kleinhammes, A., Wu, Y., Zhou, O., *Chemical Physics Letters*, 481-486 (1998)
- (6) Dillon, A.C., Jones, K.M, Bekkedahl, T.A., Kiang C.H., Bethune, D.S, Heben, M.J., *Nature* **386**, 377-379 (1997)

Electrochemical Storage of Hydrogen in Carbon Single Wall Nanotubes

Christoph Nützenadel, Andreas Züttel, and Louis Schlapbach

*Université de Fribourg, Institute de Physique, Pérolles, CH-1700 Fribourg
e-mail: christoph.nuetzenadel@unifr.ch*

One still unsolved problem for the use of hydrogen as clean fuel is the safe and efficient storage of hydrogen. Currently cryo tanks, gas cylinders or metal hydrides are used. Important parameters for a hydrogen storage system are weight and volume density, cost and safety. Recent publications [1-3] claimed that large amounts of hydrogen can be stored reversibly in carbon nanotubes from the gas phase. Similar to a gas phase experiment where the storage material absorbs hydrogen as a function of pressure the hydrogen absorption in a electrochemical system is controlled by the potential. We report results of experiments with carbon nanotubes charged reversibly with hydrogen. The density of hydrogen per weight exceeds the storage density of metal hydrides. Samples with different degrees of purity are compared.

EXPERIMENTAL

The experiments were performed in a half cell in 6 M KOH electrolyte. A nickel counter electrode was used. The voltages were referred to a Hg/HgO/OH⁻ reference electrode.

As received samples were grinded and mixed with gold powder (purity 99.95%, diameter <53 micron, Goodfellow UK) as compacting additive. Gold was used because it is noble and does not participate in any electrochemical reaction. A pellet (electrode) was pressed (500 MPa) of 20 mg carbon material and 80 mg gold powder. All weight densities given in this paper are normalised to the sample weight which is the weight of the entire carbon material, i.e. no correction due to the purity of the samples was made.

Different kind of SWNT samples have been investigated. All of them were produced with the arc discharge method. Samples were obtained from Patrick Bernier, Université de Montpellier (FR), MER Corporation (USA) [4], CarboLex (USA), and Dynamic Enterprise Limited (UK). For comparison C₆₀ [5] and high surface active graphite [6] were also measured. Some of their properties are listed in Table 1.

TABLE 1. Properties and max. discharge capacity of the samples

Producer	SWNT	Remainder	Catalyst	Process	Max discharge Capacity [mAh/g]
Patrick Bernier	70%	amorphous Carbon	N, Y	arc, non purified	85
MER	a few %	traces of C-60, C70, amorphous Carbon	Ni, Fe	arc, as-produced	170
CarboLex	50-70%	amorphous Carbon	pro-prietary	arc, AP-Grade 1	170
DEL	50%	traces of C-60, C70, amorphous Carbon	Ni, Fe	arc, purified	552
C60 Hoechst	0%	-	-	-	16
HSAG 300	0%	-	-	-	0

The maximal discharge capacity has been measured in a special cycle where the discharge current was repeatedly reduced while cycle life measurements were performed with a constant current of 25 mA/g. The discharge ends after reaching the cut-off potential which was set to 0.0 V vs. Hg/HgO/OH^- . The charge/discharge curves were measured with 100 current pulses of 10 mA/g. Three minutes after the end of each pulse the potential was measured at open circuit. The reaction resistance of the electrodes was tested by measuring the discharge capacity as a function of the discharge current. Starting from 5000 mA/g the current was repeatedly reduced each time after reaching the cut-off potential. The lowest current used was 0.5 mA/g. For the voltage step measurements the potential was set from 0.0 V to 0.9 V vs. Hg/HgO/OH^- for charging and vice versa for discharging.

The hydrogen weight density was calculated from the amount of discharged current: 1 Ah/g corresponds to 3.54 wt% hydrogen in carbon.

RESULTS AND DISCUSSION

Due to the reaction resistance the discharge capacity decreases with increasing discharge current because the cell voltage drops and the cutoff potential is reached earlier. Fig. 1 shows that for an electrode made of the DEL sample the capacity exceeds the capacity of typical metal hydrides for a discharge current lower than 1 mA/g.

A large number of subsequent charge/discharge cycles has been performed. After 50 charge/discharge cycles the electrode delivers more than 70% of the initial

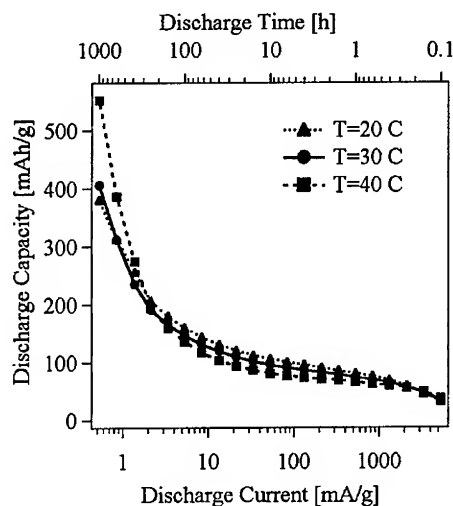


FIGURE 1. Discharge Capacity as a function of the discharge current

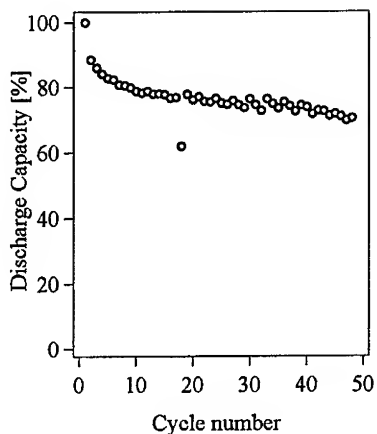


FIGURE 2. Discharge Capacity as a function of the number of cycles

capacity (Fig. 2). The decrease in capacity is mainly due to the mechanic instability of the electrodes. Black powder was found on the bottom of the cell. An improved electrode design might show a better stability.

Figure 3 shows the current after applying a voltage step. One can distinguish two processes. The first with a time constant of $t_{1/2} = 38.1$ s is due to the double layer capacity while the second with $t_{1/2} = 870$ s represents the ab- and desorption of the hydrogen into the sample.

The potential of the electrode is a function of the hydrogen concentration. The shape of the curves shown in Fig. 4. is typical for a rate limited ab-/desorption. In order to measure in equilibrium conditions it is necessary to wait at each data point at least several times 870 seconds.

Samples not containing carbon nanotubes do not show a measurable hydrogen storage capacity while 14 mAh/g was measured for C_{60} .

CONCLUSIONS

The hydrogen capacity per weight of at least one SWNT containing sample exceeds the capacity of typical metal hydrides. For most applications the kinetic properties need to be improved. Possible ways may be catalysts, cutting the tubes,

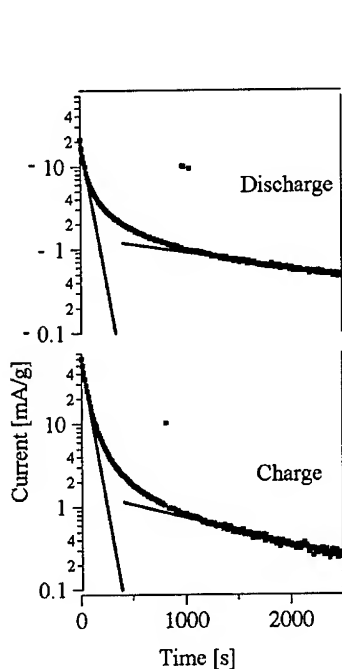


FIGURE 3. Current behavior after a voltage step

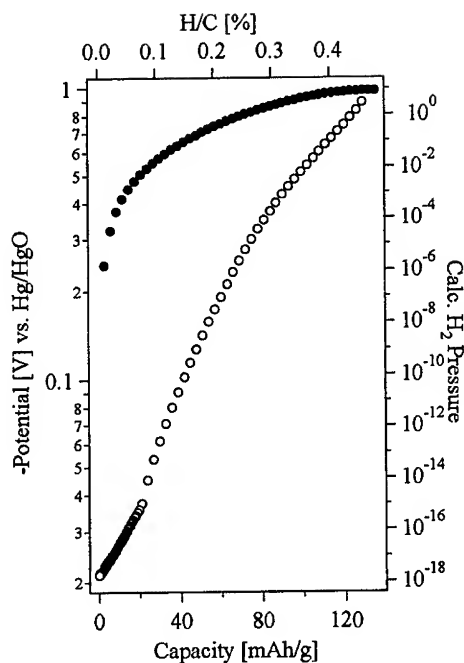


FIGURE 4. Charge/Discharge Curve
The closed circles show the potential as a function of hydrogen concentration during charge. The open circles show the discharge.

inducing defects or mixture with metal hydrides. In order to determine the thermodynamic parameters of the system equilibrium measurements at different temperatures should be performed

REFERENCES

- [1] Hill, 'Green Cars go farther with graphite', New Scientist, 12/28 December 1996
- [2] Dillon, 'Storage of hydrogen in single-walled carbon nanotubes', Nature Vol 386, 27 March 1997, pp 377
- [3] Chambers, J. Phys. Chem. B 102 (1998) 4253
- [4] Nützenadel, Electrochem. and Sol. State Lett., 2 (1) 30 (1999)
- [5] C₆₀ lag grade, purchased from Hoechst, Germany
- [6] HSAG, 300 m²/g surface area, TIMCAL, Switzerland

Characterization of multiwalled carbon nanotubes-PMMA composites

C. Stéphan^{1,*}, T. P. Nguyen¹, S. Curran^{1,2}, B. Lahr², S. Lefrant¹.

¹*Laboratoire de Physique Cristalline, IMN, Université de Nantes, France.*

²*Physics Department, Trinity College Dublin, Ireland.*

* Corresponding author: E-mail: christophe.stephan@cns-imm.fr.

Abstract. We report, for the first time, preliminary results obtained from analysis of poly(methyl methacrylate)–multiwalled carbon nanotubes composites thin films. These films were prepared by mixing the polymer with different nanotube concentrations and were deposited by spin coating on glass substrates. The composites were characterized by Raman spectroscopy and scanning electron microscopy. The evolution of the conductivity versus the nanotube concentration was carried out in the order to determine the transport process in these materials. Such a composite is promising for use as transporting layer in multilayer diodes.

INTRODUCTION

Electrical properties of nanotubes make them good candidates for new materials. Recently, composites in which nanotubes were dispersed in a polymer matrix have been studied (1, 2). In this work, we have investigated composites made of multiwalled nanotubes (MWNT's) and Poly(methyl methacrylate). Such a material appears interesting for use as a transporting layer in electronic devices because it possesses the advantages of both components. To investigate their structural properties, we have used scanning electron microscopy (SEM) to observe the dispersion of the nanotubes in the polymer and the homogeneity of the films. Vibrational properties of the composites with several nanotube concentrations have been studied by Raman spectroscopy in order to examine the organization of the nanotubes in the PMMA matrix and the possible interactions between the two materials. Finally, the conductivity was measured as a function of the nanotube concentration in the polymer in order to determine the percolation threshold.

EXPERIMENTS

Multiwalled nanotubes are produced by the arc discharge method (1). The

resulting powder contains high quantity of MWNT's (around 90%), amorphous carbon, and graphitic sheets or particles. The nanotube powder and PMMA are mixed together in toluene with several concentrations of nanotubes specified by the weight percentage in the polymer. The solution is mixed in an ultrasonic bath during 8 hours. Composite thin films are obtained by spin coating the solutions on KBr substrates for optical measurements and glass substrates for SEM observations. The samples used for the current-voltage measurements are obtained by depositing the solution onto glass substrates covered by a metallic bottom electrode. The top electrode is then deposited. Chromium is used for the electrodes.

RESULTS AND DISCUSSION

Scanning electron microscopy

Figure 1 shows the SEM images of the composites films for 1 and 16% concentrations. In the 16% concentration sample, aggregates emerge from PMMA while in the 1% sample, no aggregate was observed because the amorphous carbon is diluted in the matrix. In general, low concentration samples are uniform and homogeneous because of the low quantity of amorphous carbon in the MWNT's samples.

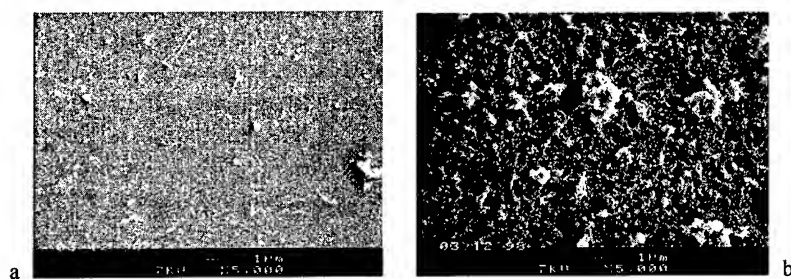


Figure 1. Scanning electron microscopy (SEM) of the composites films for 1% (a) and 16% (b) concentrations.

Raman spectroscopy

Raman measurements of PMMA-MWNT's composite films were performed with several nanotube concentrations obtained using an excitation wavelength of 1064 nm (figure 2). All the data are normalized to the 1581 cm^{-1} Raman peak of the nanotubes. Raman bands of MWNT's are clearly observed in the PMMA-MWNT's spectra but the PMMA features do not appear because of their low intensity. In addition to the nanotube features, an asymmetric hump attributed to a thermal effect (2) appears between 2250 and 3750 cm^{-1} . It increases in intensity with the nanotube concentrations but it is very weak in comparison to the MWNT's Raman spectrum. The peak at 1270 cm^{-1} and the corresponding second order one at 2540 cm^{-1} increase in

intensity with the nanotube concentrations suggesting a high dispersion of the amorphous carbon in the polymer matrix. This corroborates the results obtained by SEM. The peak at 1581 cm^{-1} is not changed by introduction of nanotubes in PMMA.

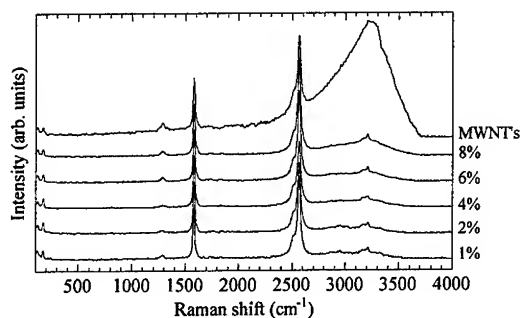


Figure 2. Raman spectra of PMMA-MWNT's for different concentrations using the infra-red excitation line.

Beside the characteristic bands of MWNT's, several peaks appear between 100 and 200 cm^{-1} . These bands do not change upon adding of MWNT's, contrarily to the behavior of the SWNT's-PMMA composites in similar range (2). Thus, these bands would correspond to breathing modes of the inner diameter of MWNT's or in an alternative way, to E_g modes (4).

Conductivity measurements

The conductivity of the composites was measured for several nanotube concentrations from 0.25 to 16% (fig. 3). The conductivity of PMMA is $7 \times 10^{-12}\text{ S/m}$.

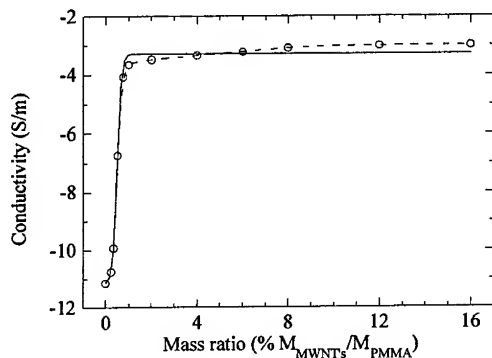


Figure 3. A semilogarithmic plot of the composite conductivity for different nanotube concentrations in PMMA. The dotted line is the experimental curve and the solid one is a fit from equation (1). Between 0.25 to 1% , the conductivity increases drastically by eight orders of

magnitude to 2.3×10^{-4} S/m. For a concentration of 16%, it is around 10^{-3} S/m. This behavior is characteristic of a percolation in a composite system and can be described by an analytical model proposed by Fourier et al (4):

$$\log(s_c) = \log(s_n) + [\log(s_p) - \log(s_n)]/[1 + \exp\{b(c - c_p)\}], \quad (1)$$

where s_c , s_n , s_p are the composite, nanotube and polymer conductivities respectively, c is the mass ratio, and b is an empirical parameter that leads to the change in conductivity at the percolation threshold c_p . The value of the threshold determined from the fitted curve is $c_p = 0.5\%$ indicating that a very low concentration of MWNT's is needed to obtain the percolation.

CONCLUSION

We have investigated composite thin films obtained by mixing multiwalled nanotubes and a non-conjugated polymer. Uniform and homogeneous films are obtained by spin coating, especially when the nanotube concentration is low as shown by scanning electron microscopy observation. Compared to pristine MWNT's, Raman spectra show changes in the intensity of the peak at 1270 cm^{-1} and that of the hump between 2250 and 3750 cm^{-1} which decrease by introduction of nanotubes in the polymer. The percolation threshold is 0.5% and an increase by nine orders of magnitude of the conductivity is observed with high concentrations. These properties make the composites good candidates for electrical devices and they are expected to be used as transporting layer in multilayer light emitting diodes.

ACKNOWLEDGMENTS

This work has been fully supported by the European Community through its Training and Mobility of Researcher program under network contract: NAMITECH, ERBFMRX-CT96-0067(DG12-MIHT) and by the French CNRS program: ULTIMATECH.

REFERENCES

1. Coleman J. N., Curran S., Dalton A. B., Davey A. P., McCarthy B., Blau W., and Barklie R. C., *Phys. Rev. B* **58**, 7492 (1998).
2. Stéphan C., Nguyen T. P., Lamy de la Chapelle M., Journet C. and Bernier P., submitted to *Synt. Met.*
3. Jantoljak H., Salvétat J. P., Forro L., Thomsen C., *Appl. Phys. A* **67**, 113 (1998).
4. Fourier J., Boiteaux G., Seytre G. and Marichy G., *Synt. Met.* **84**, 839 (1997).

Functionalisation of carbon nanotubes for composites

S. Delpeux, K. Méténier, R. Benoit, *F. Vivet, *L. Boufendi, S. Bonnamy and F. Béguin

CRMD, CNRS-Université, 1B, rue de la Férollerie, 45071 Orléans Cedex 2, France

**GREMI, CNRS-Université, 14, rue d'Issoudun, 45067 Orléans Cedex 2, France*

Abstract. Catalytic multiwall carbon nanotubes (MWNT) were functionalized by low-pressure ammonia plasma and chemical oxidation, and their surface groups were identified by X-ray Photoelectron Spectroscopy (XPS) and acid-base titration. The reactivity of MWNT with ammonia plasma largely depends on their microtexture and on residual oxygen pressure in the reactor. Using catalytic MWNT presenting numerous dangling bonds on their outer part, the N/C atomic ratio could reach 0.18. Oxidation by sodium chlorate was very efficient (O/C atomic ratio = 0.2) for the creation of surface carboxylic groups.

INTRODUCTION

Due to their shape and size, carbon nanotubes are believed to have mechanical strength unmatched by any material. These extraordinary properties derive from the special arrangement of the carbon bonds in a quasi-one-dimensional structure. Our specific focus is the potential use of carbon nanotubes as a filler element in the development of a novel generation of composite materials with enhanced structural, mechanical and electrical properties. However, due to their hydrophobic character, grafting polar functions on their surface should be considered in order to increase interfacial adhesion with the matrix, as it has already been done on carbon fibres (1, 2). In the present work, two ways of surface treatment were considered: low pressure ammonia plasma and controlled chemical oxidation. In order to better identify grafting, catalytic MWNT which present a large number of reactive edge planes were first tested.

EXPERIMENTAL

Catalytic multiwall carbon nanotubes (MWNT) were obtained by decomposition of acetylene at 900°C over silica supported cobalt (3) and then, silica and cobalt were eliminated by dissolution in hydrofluoric (73 wt%) and nitric (3 mol.l⁻¹) acids. The samples coming from these treatments will be referenced as pristine MWNT for the following study. For comparison, catalytic MWNT annealed at 1600°C under argon atmosphere for 3 hours were also studied (4).

Low-pressure plasma was generated by a radio-frequency (RF) discharge (13.56 MHz) in Argon/NH₃ flow. Argon was used as a buffer gas for its low ionization

potential and also for the efficient role of its cations and metastable species, both in the NH_3 dissociation mechanisms and in the generation of dangling bonds on the nanotubes surface. MWNT were deposited on the grounded electrode in a stainless steel crucible. The reactor chamber was evacuated under primary (10^{-3} mbar) or secondary vacuum (10^{-5} mbar) prior to gas admission. Plasma parameters were optimized using Tibbett's Vapor Grown Carbon Fibers (5), leading to the following experimental conditions : gas flows of 36 and 10 cm^3/min respectively for Ar and NH_3 , a RF power of 50 W and 3 hours treatment.

The samples (200 mg) were oxidized with a solution of NaClO_3 (200 mg) in H_2SO_4 (95 %) during 24 hours, at room temperature under Argon flow.

Surface groups were titrated accordingly to the method described by H. P. Boehm (6). Basic functions were neutralized by HCl, while bases of increasing strength, i.e. NaHCO_3 , Na_2CO_3 , NaOH and NaOC_2H_5 were used successively for the determination of carboxylic, lactonic, phenolic and carbonyl groups.

XPS analyses (VG Escalab MKII multidetection) were performed before and after treatment using Mg K_α radiation (1253.6 eV). The C1s spectra were fitted using a Doniach Sunjic peak shape (α and γ parameters) in order to account for the asymmetry due to conduction electrons (7).

RESULTS-DISCUSSION

Catalytic MWNT prepared at 900°C have wrinkled aromatic layers non-parallel to the tube axis (fishbone morphology), therefore their outer part presents numerous edge plans allowing more easy functionalisation. After nitric acid treatment of as-received MWNT, a O1s contribution was observed in the XPS spectra with an atomic ratio O/C of 0.038, that proves oxidation of MWNT surface. The C1s core level includes four components: an asymmetric peak at 284.6 eV (C-C, C-H) and three other peaks centered respectively at 286.2 eV (C-O), 288 eV (C=O) and 290 eV (COO) (figure 1). Contributions due to carbon-oxygen bonds were observed in the O1s core level. Acid-base titration gave carboxylic (0.35 meq/g), lactonic (0.1 meq/g), phenolic (0.99 meq/g) and basic (0.29 meq/g, pyrone and chromene type) groups in good agreement with the relative areas observed for the C1s peak (figure 1).

After ammonia/argon plasma treatment of pristine MWNT, XPS analyses clearly showed the incorporation of nitrogen with appearance of a N1s signal at 399.1-399.8 eV and broadening of the C1s peak due to a C-N contribution at 285.7 eV (figure 2). However, the amount of nitrogen grafted strongly depends on the purity of atmosphere in the plasma chamber. When primary vacuum was applied before admission of Ar/ NH_3 mixture, the N/C atomic ratio was 0.07, and surprisingly the amount of oxygen at the surface (O/C = 0.06) was larger than in pristine nanotubes, proving that residual oxygen present in the reactor is very reactive with nanotubes in the plasma conditions. If the reactor was evacuated under secondary vacuum, grafting of nitrogen onto the surface reached a high ratio (N/C = 0.18), but still an important

amount of oxygen was grafted ($O/C = 0.08$). A competition between nitrogen and oxygen reactive species is therefore suspected, showing that more drastic conditions have to be used in the future for limiting the presence of oxygen in the chamber.

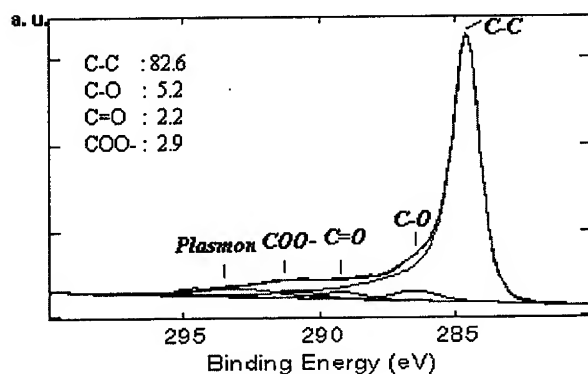


FIGURE 1. C1s XPS spectrum of pristine MWNT ($\alpha = 0.12$, $\gamma = 0.25$).
The values given for each contribution are atomic ratios.

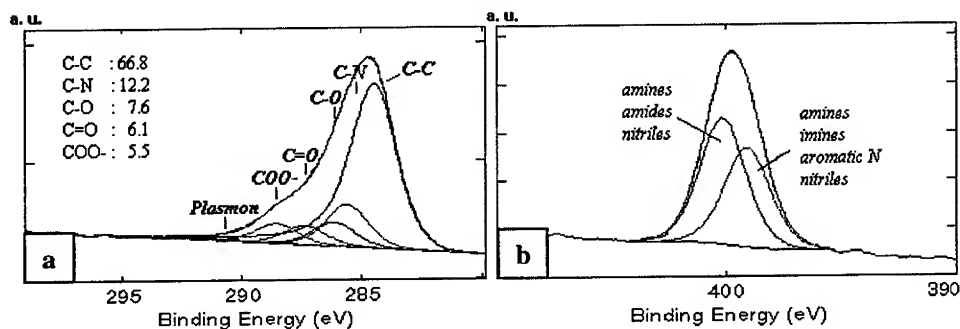


FIGURE 2. C1s (a) ($\alpha = 0.06$, $\gamma = 0.26$) and N1s (b) XPS spectra of pristine MWNT treated by Ar/ NH_3 plasma. The values given for each contribution are atomic ratios.

MWNT annealed at $1600^\circ C$ under argon flow did not present any O1s contribution detectable by XPS, indicating that surface is cleaned by thermal treatment. This has to be related with TEM observations showing important microtextural modifications, in particular curing of edge defects by the formation of more continuous aromatic layers. Ammonia plasma treatment on these nanotubes was obviously less efficient than for pristine MWNT and the N/C atomic ratio was only 0.033. A O1s peak ($O/C = 0.064$) and a C-O contribution at 286.2 eV in the C1s peak were detected, showing that in the plasma, reactivity of these tubes is higher with polluting oxygen than with nitrogen species.

Sodium chlorate treatment of pristine MWNT was found to increase efficiently the density of oxygenated functional groups. The O/C atomic ratio, measured by XPS,

reached a very high value ($\cong 0.2$), and the C1s peak showed an important contribution at 290 eV attributed to carboxylic groups (figure 3). Besides, acid-base titration confirmed that surface carboxylic acid has been increased from 0.35 meq/g, for pristine nanotubes, to 1.2 meq/g for the oxidized ones.

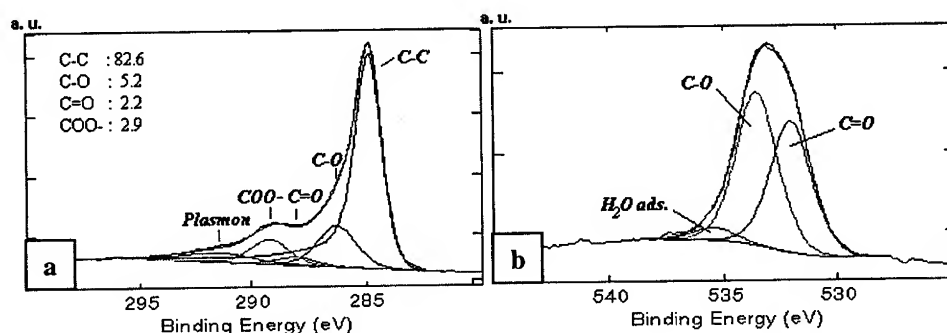


FIGURE 3. C1s (a) and O1s (b) XPS spectra of pristine MWNT oxidized by sodium chlorate. The values given for each contribution are atomic ratios.

Finally, we have to point out that the tubular morphology of MWNT, observed by TEM after plasma or oxidation treatments, is preserved. It means that it can be expected that the mechanical properties of nanotubes are not altered.

For future perspectives, the amine and carboxylic functions present at the surface of MWNT could be used to graft oligomers having anhydride end-groups. This should improve the wetting properties of nanotubes by suitable matrices. Perspectives of novel nanotube-based composites with interesting mechanical performance appear quite realistic.

ACKNOWLEDGEMENTS

This work has been supported by E.C. TMR program: NAMITECH, ERBFMRX-CT996-0067 (DG 12-MIHT).

REFERENCES

1. V.B. Wiertz and P. Bertrand, *Proc. Int. Conf. Polymer-Solid Interfaces ICPSI II*, Namur (1996).
2. C. Jones and E. Samman, *Carbon* **28**, 515-519 (1990).
3. A. Hamwi, H. Alvergnat, S. Bonnamy and F. Béguin, *Carbon* **35**, 723-728 (1997).
4. H. Gaucher, R. Pellenq, S. Bonnamy, F. Béguin, "Characteristics of catalytic carbon nanotubes : their evolution after thermal and chemical modifications", in *Proceedings of XI International Winterschool on Electronic Properties of Novel Materials, Molecular Nanostructures*, Kirchberg, ed. H. Kuzmany et al., 395-398 (1998).
5. G.G. Tibbetts, *Appl. Phys. Lett.* **42**, 666 (1983).
6. H.P. Boehm, *Carbon* **32**, 759-769 (1994).
7. M. Th. M. van Attekum and G. K. Wertheim, *Physical Review Letters* **43**, 1896-1898 (1979).

Chemical Functionalization of Carbon Nanotubes

S. Pekker¹, J.-P. Salvetat², E. Jakab³, J.-M. Bonnard⁴, L. Forró²

¹*Research Institute for Solid State Physics, H-1525 Budapest, P. O. Box 49, Hungary*

²*Institute de Génie Atomique, EPFL, 1015-Lausanne, Switzerland*

³*Chemical Research Center, H-1525 Budapest, P. O. Box 17, Hungary*

⁴*Institute de Physique Experimentale, EPFL, 1015-Lausanne, Switzerland*

Abstract. We present the functionalization of SWNT, MWNT and graphite with hydrogen. The covalently bonded hydrogen derivatives decompose at around 500°C resulting in the evolution of hydrogen. The maximum hydrogen content of nanotubes estimated from thermogravimetry-mass spectrometry corresponds to about a HC₈ composition. The addition reaction of hydrogen introduces longer, σ type C-C bonds giving rise to a significant disorder at the surface layers of the hydrogenated nanotubes as shown by electron microscopy.

I INTRODUCTION

Since the discovery of carbon nanotubes¹ great efforts were made to understand their structure and physical properties². On the other hand, chemistry was restricted to the production and purification without much interest in the chemical properties. The recent attempts on the intercalation^{3,4} and the oxidation⁵ attracted the attention on the chemical modification of nanotubes. Here we present our preliminary results on the formation and structure of hydrogenated nanotubes and other carbonaceous materials. Hydrogenated nanotubes can be considered as the prototypes of covalent nanotube derivatives. The formation of covalent CH bonds is accompanied by the development of equivalent amount of sp³ C without destroying the framework of hexagons of the tubes. Thus, hydrogenated nanotubes represent a new family of carbon derivatives with various physical and chemical properties.

II EXPERIMENTAL

Hydrogenation of the nanotubes was performed via a modified Birch reduction method with Li and methanol in liquid ammonia. The detailed process is described elsewhere⁶. Shortly, methanol was added slowly to the suspension of nanotubes in

Li/NH₃ solution. After evaporation of NH₃, the product was washed subsequently with methanol, water, hydrochloric acid, water and methanol, and dried in vacuum. In order to determine the reactivity of various carbonaceous materials with respect to hydrogenation we performed the reduction of single wall nanotubes (SWNT), multi-wall nanotubes (MWNT), extracted fullerene soot and two types of graphite.

The composition and the thermal stability of the samples were studied by thermogravimetry-mass spectrometry (TG-MS). The TG-MS instrument consists of a Perkin-Elmer TGS-2 thermobalance and a HIDEN HAL 2/301 PIC quadrupole mass spectrometer. Approximately 5 mg samples were heated at a 20°C/min heating rate from 30°C to 900°C in argon atmosphere. The volatile products were detected by the mass spectrometer operating at 70 eV in electron impact ionization mode.

High resolution transmission electron microscopy (HRTEM) was performed by a Philips CM300 electron microscope operating at 300 kV electron energy with a resolution of 0.19 nm.

III RESULTS AND DISCUSSION

The above hydrogenation method applies for the partial reduction of conjugated systems. The expected products are covalently bonded CH derivatives and are essentially different from the adsorbed H₂ derivatives⁷. Since no similar nanotube and graphite compounds were reported previously, it is of great importance to reveal the nature of these CH bonds. The thermal decomposition provides evidences on the H content of the samples and on the strengths of the CH bonds. Fig. 1. shows the TG-MS

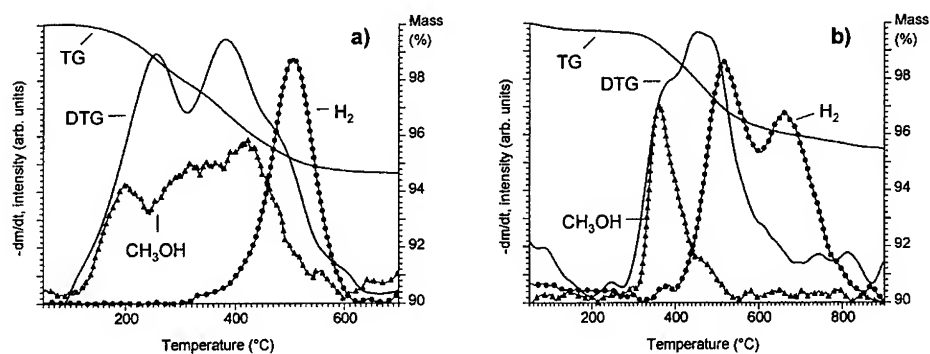


Fig. 1. Thermogravimetric curves and the evolution of hydrogen and methanol during the decomposition of MWNT (a) and SWNT (b).

curves of hydrogenated MWNT and SWNT samples. Similar curves were obtained for hydrogenated graphite samples. Two significant decomposition products were formed: hydrogen and methanol. The molar amount of hydrogen is about an order of magnitude

higher than that of methanol indicating that mainly hydrogen is built into the framework. In the lower temperature range ($T < 450^{\circ}\text{C}$) the mass loss of the samples is attributed to the evolution of methanol. Hydrogen evolves independently of methanol at higher temperatures with a characteristic decomposition peak at about 500°C . In SWNT a further decomposition peak of hydrogen is observed at about 650°C . The high evolution temperature of H_2 excludes the possibility of weak adsorption of hydrogen to carbon⁷ and strongly indicates the presence of covalent CH bonds. On the other hand hydrogen intercalation is also possible with the existence of partial ionic bonds. This may be the structure of graphite derivatives. Further structural studies are necessary to reveal the nature of bonding.

The hydrogen content was estimated from the mass loss corresponding to the temperature range of H_2 evolution. Table 1. summarizes the amounts of the evolved hydrogen and the estimated stoichiometries. For both graphite samples the maximum

Table 1. Hydrogen contents of various hydrogenated carbonaceous materials.

Sample	H_2 evolved (% m/m)	Estimated C : H molar ratio
Graphite	1.9	4 : 1
Graphitic soot	2.0	4 : 1
SWNT	0.7 - 1.1	(12 - 7) : 1
MWNT	0.5 - 0.9	(16 - 9) : 1
Fullerene soot	< 0.2	> 40 : 1

hydrogen contents correspond to a C_4H stoichiometry. The maximum hydrogen content of nanotubes is about half of the value of graphite and scatters from sample to sample. The variable H content indicates that the heterogeneous hydrogenation was incomplete and further H uptake would be possible. In contrast to graphite and nanotubes, no significant hydrogenation takes place on the fullerene soot.

The influence of hydrogenation on the walls of nanotubes was studied by electron microscopy. Fig. 2. shows the HRTEM images of hydrogenated and pristine MWNT.

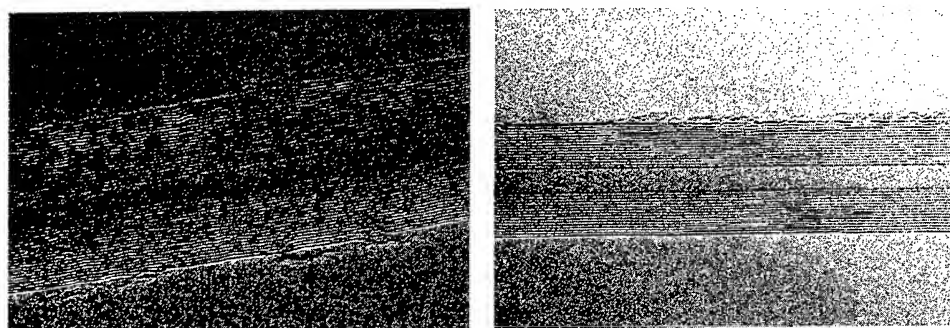


Figure 2. High resolution electron micrographs of hydrogenated (left) and pristine (right) MWNT samples.

Due to hydrogenation the walls became corrugated and partly disordered. Similar corrugation and more significant disorder can be observed on the SWNT walls. Corrugation can be attributed to the differences in bond lengths and angles of the unreacted sp^2 and the formed sp^3 carbons. In most cases, the inside shells of MWNT are also affected by the hydrogenation and show a corrugated structure (Fig. 2. a.). This unexpected observation is supported by the high H content of MWNT (Table 1.).

IV CONCLUSION

We have shown for the first time that MWNT, SWNT and similarly graphite can be chemically hydrogenated via a heterogeneous Birch reduction. The obtained maximum H:C ratio is 1:4 for graphite and about 1:8 for the nanotubes. The high decomposition temperature (500°C) gives evidence for a strong chemical bond between H and C. Unexpectedly, the inside shells of MWNT were also affected by hydrogenation. The corrugated structure of hydrogenated nanotube walls indicates the presence of sp^3 C formed due to the addition of hydrogen. Further structural studies on the nature of CH bonding and the arrangement of H in the hexagonal C frameworks are in progress.

V ACKNOWLEDGMENTS

This work was supported by the Hungarian National Research Fund OTKA T 019139 and T 025341, and the Swiss National Science Foundation program NFP 36.

REFERENCES

1. S. Iijima, *Nature*, **354**, 56 (1991).
2. For a review see M.S. Dresselhaus, G. Dresselhaus, P.C. Eklund, *Science of Fullerenes and Carbon Nanotubes*, Academic Press, San Diego, 1995.
3. R.S. Lee, H.J. Kim, J.E. Fischer, A. Thess, R.E. Smally, *Nature*, **388**, 255 (1997).
4. A.M. Rao, P.C. Eklund, S. Bandow, A. Thess, R.E. Smally, *Nature*, **388**, 255 (1997).
5. K. Méténier, S. Delpeux, R. Benoit, F. Vivet, L. Boufendi, S. Bonnamy, F. Béguin, this Volume.
6. S. Pekker, J.-P. Salvetat, E. Jakab, J.-M. Bonnard, L. Forró, submitted.
7. A.C. Dillon, K.M. Jones, T.A. Bekkedahl, C.H. Kiang, D.S. Bethune, M.J. Heben, *Nature*, **386**, 377 (1997).

Electronic Structures and Applications of Carbon Nanotubes

Philip Kim, Teri W. Odom, Jinlin Huang, and Charles M. Lieber

Harvard University, Cambridge, MA 02138, USA

Abstract. The electronic density of states (DOS) of atomically resolved single-walled carbon nanotubes have been investigated using scanning tunneling microscopy. Peaks in the DOS due to the one-dimensional (1D) nanotube band structure have been characterized and compared with the results of tight-binding calculations. In addition, a novel electromechanical device has been designed and fabricated using nanotubes.

INTRODUCTION

There has been intense effort focused on carbon nanotubes since their discovery by Iijima [1]. This attention on carbon nanotubes is not surprising in light of their promise to exhibit unique physical properties that could impact broad areas of science and technology, ranging from super strong composites to nanoelectronics [2]. According to theory [3], SWNTs can exhibit either metallic or semiconducting behavior depending on diameter and helicity. Recent scanning tunneling microscopy (STM) experiments [4,5] have resolved the atomic structure and electronic density of states of SWNTs, and have confirmed this predicted electronic behavior of SWNTs. In addition, the tunneling spectra reported in these studies exhibited peaks in the density of states (DOS), Van Hove singularities (VHS), that are believed to reflect the 1D band structure of the SWNT [6].

In this paper, we first review STM investigations of the electronic structure of atomically resolved SWNTs and compare these results with tight-binding calculations. Significantly, we find that the VHS in the DOS calculated using a straightforward zone-folding approach agree with the major features observed in the spectroscopic measurements. In addition, we will also discuss the design and fabrication of an electromechanical device that exploit these unique electrical and mechanical properties of nanotubes.

VAN HOVE SINGULARITIES IN SINGLE-WALLED NANOTUBES

SWNT samples were prepared by laser vaporization, purified and then deposited onto a Au (111)/mica substrate. Immediately after deposition, the sample was loaded into a UHV STM that was stabilized at 77 K; all of the experimental data reported in this paper were recorded at 77 K. Imaging and spectroscopy studies were carried out using etched tungsten tips with the bias (V) applied to the tip. STM spectroscopy measurements were made by recording and averaging 5 to 10 tunneling current (I) versus V (I - V) curves at specific locations on atomically resolved SWNTs. The tunneling conductance, dI/dV , was obtained by numerical differentiation.

An atomically resolved STM image of several SWNTs is shown in Fig. 1(a). The diameter and chiral angle measured for this tube were 1.35 ± 0.1 nm and $-20 \pm 1^\circ$, respectively after deconvolution of tip effects [7]. The measured diameter and chiral angle can be used to assign the (n, m) indices of the SWNT [4,7]. We find that (13, 7) and (14, 7) are consistent with the uncertainty in these values, where (13, 7) and (14, 7) are expected to be metallic and semiconducting respectively. The I - V exhibits metallic behavior with relatively sharp, stepwise increases at larger $|V|$ (Fig. 1(b)). The I - V curves have a finite slope, and thus the normalized conductance $(V/I)(dI/dV)$, which is proportional to the LDOS, has appreciable non-zero value at $V = 0$ as expected for a metal (Fig. 1(b) inset). This suggests that the (13, 7) indices are the best description of the tube (we address this point further below). At larger $|V|$, several sharp peaks are clearly seen in both the dI/dV and the normalized conductance. We attribute these peaks to the VHS

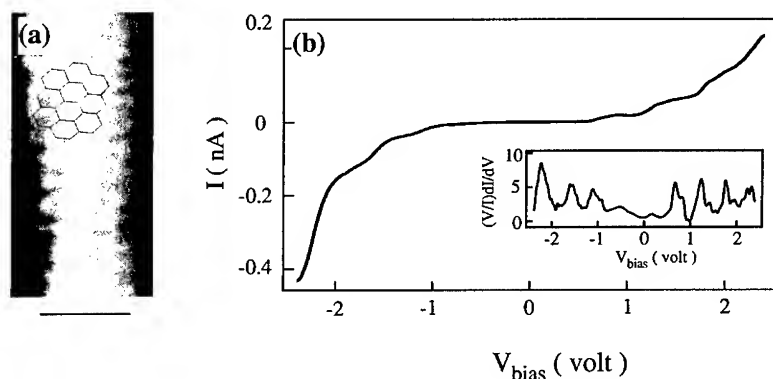


FIGURE 1. (a) STM image of SWNTs recorded at $I = 0.12$ nA and $V = 550$ mV. The black scale bar is 1 nm. A portion of a hexagonal lattice is overlaid to guide the eye. (b) I - V data recorded on the SWNT in (a). The inset shows the normalized conductance, $(V/I)(dI/dV)$. (adapted from [6]).

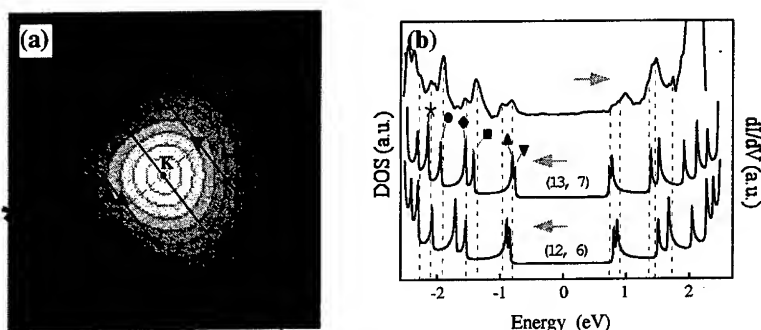


FIGURE 2. (a) Energy dispersion of the π -band of graphene sheet near **K**. The solid lines correspond to (13, 7) 1D bands obtained by the zone-folding. Symbols are located at the positions where VHS occur in these 1D bands. (b) Comparison of DOS obtained from our experiment (upper curve) and π -only tight binding calculation for (13, 7) and (12, 6) SWNT (the second curve from top). The broken vertical lines indicate the positions of VHS in the tunneling spectra after considering convolutions of thermal broadening. The symbols correspond to the VHS shown in (a) (adapted from [6]).

resulting from the extremal points in the 1D energy bands.

The availability of experimentally determined density of states for atomically-resolved nanotubes represent a unique opportunity for comparison with theory. In this regard, we have calculated the band structure of a (13, 7) SWNT using the tight-binding method. If only π and π^* orbitals are considered, the SWNT band structure can be constructed by zone-folding the 2D graphene band structure into the 1D Brillouin zone specified by the (n, m) indices [2]. Fig. 2(a) shows the graphene π band structure around the corner point (**K**) of the hexagonal Brillouin zone. For the metallic (13, 7) tube, the degenerate 1D bands which cross **K** result in a finite DOS at the Fermi level. Note that the energy dispersion is isotropic (circular contours) near **K**, and becomes anisotropic (rounded triangular contours) away from **K**. Therefore, the first two VHS in the 1D bands closest to **K** have a smaller splitting in the energy due to the small anisotropy around **K**, while the next two VHS have a larger splitting due to increasing anisotropy. If the energy dispersion were completely isotropic, both sets of peaks would be degenerate. We used the same value of the hopping integral $V_{pp\pi}$, 2.5 eV, determined from previous studies [4,7].

Our STS data shows relatively good agreement with the DOS for a (13, 7) tube calculated using the zone-folding approach (Fig. 2(b)). The agreement between the VHS positions determined from our dI/dV data and calculations are especially good below the Fermi energy (E_F) where the first seven peaks correspond well. Above the Fermi energy larger deviations between experiment data and calculations exist. The observed larger differences may be due to the band repulsion, which arises from the curvature-induced hybridization, or surface-tube interaction that

were not accounted for in our calculations. Detailed *ab initio* calculation [8] have shown that the effect of curvature induced by hybridization is greater in π^*/σ^* than π/σ orbitals. This could explain the greater deviations between experiment and calculation that we observe for the empty states. In the future, we believe that comparison between experiment and more detailed calculations will help to resolve such subtle but important points, and also help to understand how inter-tube and tube-substrate interactions affect the nanotube band structure. We have also investigated the sensitivity of the DOS to (n, m) indices. Specifically, we calculated the DOS of the next closest metallic SWNT to our experimental diameter and angle, a (12, 6) tube. Significantly, we find that the calculated VHS for this (12, 6) tube deviate much more from the experimental DOS peaks than in the case of the (13, 7) tube (Fig. 2(b)). We believe that this analysis not only substantiates our assignment of the indices in Fig. 1(a), but more importantly, demonstrates the sensitivity of detailed DOS to subtle variations in diameter and chirality.

ELECTROMECHANICAL DEVICES USING NANOTUBE: NANOTWEEZER

Carbon nanotubes are both electrically conducting and mechanically flexible, and thus offer many unique opportunities for creating nanoscale devices. In this section, we will discuss the design and fabrication of an electromechanical nanotube device, a nanotweezer.

A nanotweezer was fabricated in two basic steps. First, two independent, electrically isolated gold electrodes were deposited on the surface of a micro-pipette by shadow masking during thermal deposition. Second, multi-walled nanotubes were attached to each electrode, and firmly fixed by conducting carbon polymer tape [9,10].

The operation of the nanotweezer was investigated by applying a bias voltage to the electrodes. The mechanical deflection of tweezer arms was observed in an inverted optical microscope, and recorded using a CCD camera and frame grabber attached to the microscope. Figure 3 shows the voltage response of a typical nanotweezer. As the bias voltage increases from 0 V to 20 V, the end of tweezer arms gradually close, and then touch. It was found that the tweezer arms relaxed to the original position when the applied bias voltage was removed, and this process can be done several times producing the same deflection. This verifies that the deflection of tweezer arms is mainly attributed to elastic deformation of the nanotubes rather than plastic deformation between nanotubes and metal electrodes. Therefore, the device demonstrates repeatable tweezer operation, and moreover the bias voltage required for actuation is considerably lower than that was required for the previous microtweezer [11].

Once the tweezer arms are closed tightly (~ 20 V in Figure 3), they remain stuck together even after removing the applied bias voltage. The strong adhesion force between bundles of multi-walled nanotubes are presumably responsible for

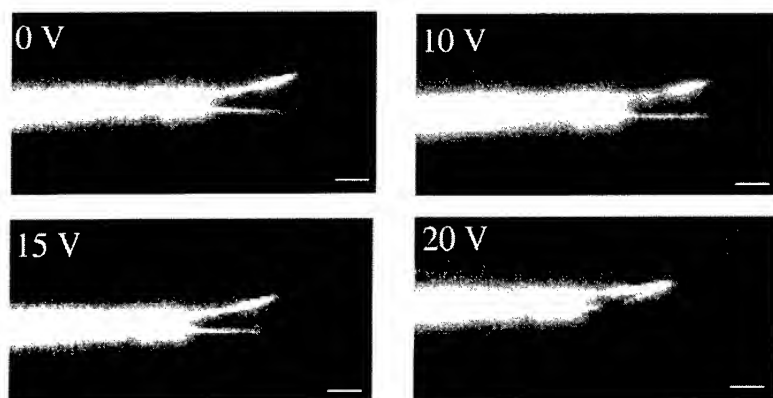


FIGURE 3. Mechanical deflection of nanotweezer in the response to bias voltages.

this observed behavior. The closed end of the tweezers, however, could reopen by applying the same polarity of voltage to both sides of the tweezer arms to charge the ends.

SUMMARY

We have discussed STM investigations of the electronic structure of atomically resolved SWNTs and compared these results with tight-binding calculations. Significantly, we find good agreement between the major features observed in the spectroscopic measurements and the VHS predicted by tight binding calculations. In addition, the unique properties of nanotubes were exploited to fabricate an electromechanical nanotweezer.

REFERENCES

1. S. Iijima, *Nature* **354**, 56 (1991).
2. M. S. Dresselhaus *et al.*, *Science of Fullerenes and Carbon Nanotubes* (Academic, San Diego, 1996).
3. J. W. Mintmire *et al.*, *Phys. Rev. Lett.* **68**, 631 (1992); N. Hamada, *et al.*, *Phys. Rev. Lett.* **68**, 1579 (1992); R. Saito *et al.*, *Appl. Phys. Lett.* **60**, 2204 (1992).
4. T. W. Odom *et al.*, *Nature* **391**, 62 (1998).
5. J. W. G. Wildoer *et al.*, *Nature* **391**, 59 (1998).
6. P. Kim *et al.*, *Phys. Rev. Lett.* **82**, 1225 (1999).
7. T. W. Odom *et al.*, *J. Mater. Res.* **13**, 2380 (1998).
8. X. Blase *et al.*, *Phys. Rev. Lett.* **72**, 1878 (1994).
9. H. Dai *et al.*, *Nature (London)* **384**, 147 (1996).
10. S. S. Wong *et al.*, *Nature (London)* **394**, 52 (1998).
11. N. C. Macdonald *et al.*, *Sensors and Actuators* **20**, 123 (1989).

Combinatorial Chemistry Approach to Development of Molecular Plastic Solar Cells

Dmitri Godovsky, Olle Inganäs,

IFM, Linköping University, S-581 83 Linköping, Sweden, dmigo@ifm.liu.se,

Christoph J. Brabec, N. Serdar Sariciftci,
CD Laboratory J. Kepler University, Linz, Austria,

Jan C. Hummelen, Rene A.J. Janssen,
University of Groningen and TU Eindhoven, Holland,

M.Prato, M.Maggini,

University of Trieste,

Jose Segura and Nazario Martin,
Facultad de Química, Universidad Complutense, Spain

Abstract. We used a combinatorial chemistry approach to develop the molecular plastic solar cells based on soluble fullerene derivatives or solubilized TCNQ molecules in combination with conjugated polymers. Profiles, formed by the diffusion of low molecular weight component in the spin-cast polymer host were used. The ratio between low molecular weight acceptor and polymer changed along the diffusion gradient direction from 100% to 0% at the distances 10-20 mm. Optical and electrophysical properties such as absorption, luminescence, short circuit current and open circuit voltage were measured using a specially designed installation with the resolution of 25 points per millimetre.

EXPERIMENTAL

As a first step on a way to develop molecular plastic solar cells using both advanced organic synthesis and supramolecular engineering approach on the device scale level we developed the combinatorial chemistry technique to investigate the behaviour of soluble fullerenes and TCNQ derivatives when mixed with the substituted BW-poly(paraphenylenevinylene) matrix. The method is based on the diffusion profiles, produced by low-molecular weight component and spreading from the phase boundary into the polymer layer as far as 20-30 mm. This is realised by means of putting the small drop of fullerene or TCNQ derivative, dissolved in mixture of toluene and chloroform in the centre of spin-cast BW-PPV layer. Since toluene swells the polymer, almost not dissolving it, and chloroform dissolves the polymer, varying the ratio between these two components, one can control the ratio between the diffusion through the swollen matrix and mutual intersolubility. This way we obtain the concentrations of fullerene within a polymer ranging from 100% to 0% at distances of 20-30 mm.

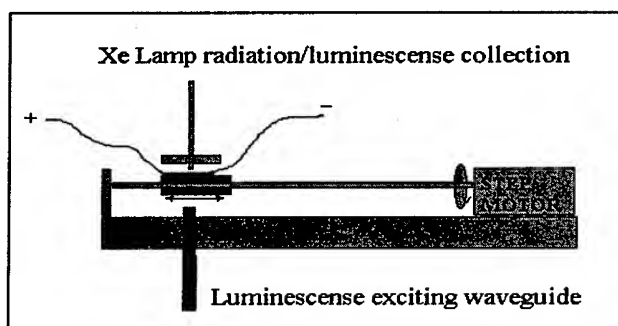


FIGURE 1. Installation Scheme.

In order to study the optical and photovoltaic properties of obtained mixtures the scanning measurement technique was developed (Fig.1), which allows to measure absorbance, photoluminescence, short circuit current and open circuit voltage with the spatial resolution as high as 25 points per millimetre. The scanning photoluminescence, short circuit current and open circuit voltage measurements are realised by means of focusing the light from Xe-lamp or luminescence exiting monochromatic light (WL ca.400 nm) onto the surface of the sample, which is then moved stepwise using the mechanical drive. The focused spot size is around 100 microns and each step moves the sample by 30 microns, thus allowing the measurements with the resolution of ca. 50 microns. The scanning absorbance measurements are realised by means of projecting of collimated beam from the Xenon lamp through the sample onto CCD array. The method permits us to make 500-1000 points measurements of all mentioned parameters depending on the ratio between soluble C_{60} or TCNQ derivatives and polymer which is changed from 0/1 to almost 1/0 along the diffusion gradient profile. The scanning absorbance and luminescence spectra of one of the fullerene derivatives blended with BW-PPV can be seen from Fig. 2. The ratio between peaks on the absorbance spectra of the blends compared with the absorbance of the ethalon blend structures, made for reference allowed us to estimate the ratio between the polymer and fullerene derivative along the diffusion profile.

RESULTS AND DISCUSSION

All the results are combined in concentration as estimated from the absorbance spectra. It can be seen, that luminescence is quenched completely within the fullerene concentration range of around 3 vol.%. This points out the fact that there is basically no problem with the photoinduced charge transfer in the molecular plastic solar cells. The more important problem is to separate charges on the device level to avoid recombination.

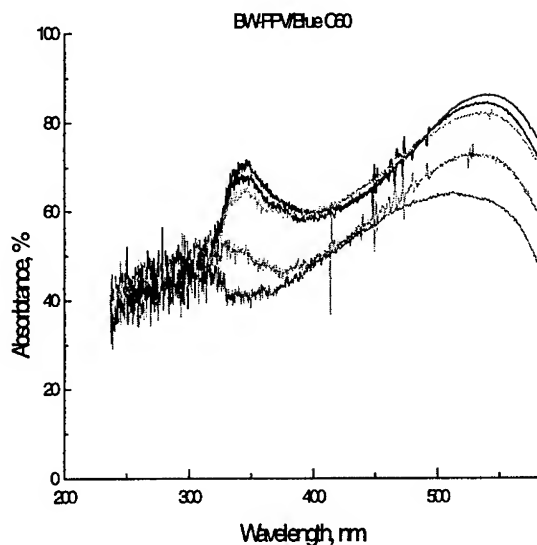


Figure 2. Scanning absorbance (distance between measurement points 300 microns) (a) and luminescence (distance between measurement points 100 microns) (b) spectra of BW-PPV+C60 blends along the diffusion profile.

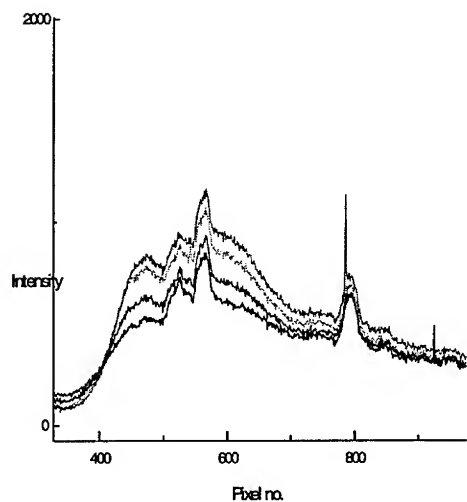


Figure 3. This figure shows the change of luminescence intensity, short circuit current and approximate fullerene derivative volume

The dependence of short circuit current on the fullerene concentration looks quite surprising, since it manifests the fact that the more fullerene we add to the blend up to the concentrations as high as ca.90 vol. % the higher short circuit current is. This fact contradicts the existing paradigm, stating that photoinduced charge transfer from polymer to fullerene is the main source of photocurrent. A probable explanation follows from the analysis of IPCE spectra of the blends (to be communicated elsewhere) which shows significant peak at 320-350 nm associated with $C_{60} h_u - t_{1g}$ which provides up to 60 % of the photocurrent once illuminated by AM01 Sun Spectral Ethalon.

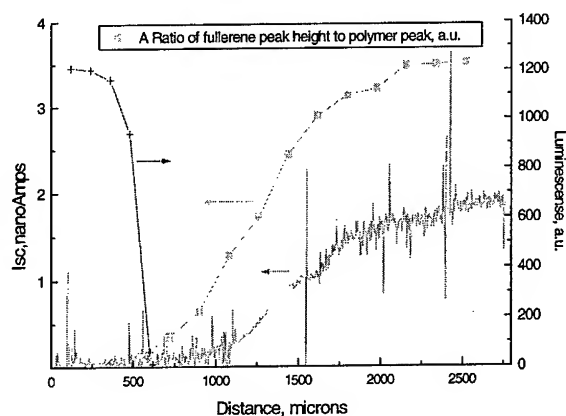


Figure 4. The dependencies of luminescence, I_{sc} and concentration on distance along diffusion gradient.

The difference between the sharp interface structures and blends is provided by the nanocrystalline character of fullerene phase in blends. If in the bulk fullerene layer the electron excited to the t_{1g} level can easily drop down to the long living h_{1g} , in the nanocrystal this process can be suppressed due to discrete character of phonon spectrum, and difficulty to dissipate the energy of the order of 1 eV. This fact probably gives rise to the enhanced quantum efficiency of $h_u - t_{1g}$ transition in polymer-fullerene blends with the phase separation on the nanometer scale.

CONCLUSIONS

The first conclusion that we would like to outline consists of the fact that the combinatorial technique along with the scanning optical and photovoltaic parameters measurements is a convenient tool for the investigation of polymer photovoltaic solar cells, since it allows to avoid the routine blend-and measure way of studying the concentration dependencies.

The second result is that the photovoltaic properties of fullerene based photovoltaic cells vary significantly, depending on the morphology of fullerene phase: whether it is bulk phase (as in the case of bi-layer structures) or nanocrystals (as in the case of the polymer-fullerene blends).

ACKNOWLEDGMENTS

We would like to thank Prof. Anvar Zakhidov for fruitful discussions.

The Authors would like to acknowledge the support in the frame of EC Joule 3 Project "Development of Molecular Plastic Solar Cells".

Charge Transfer and Relaxation Dynamics of excited electronic states in organic photoreceptor materials with and without C₆₀

C.Schlebusch, J.Morenzin, B.Kessler, and W.Eberhardt

Forschungszentrum Jülich, IFF, D-52425 Jülich, Germany

Abstract. Photoelectron spectroscopy from different photoreceptor materials which are in contact with C₆₀ demonstrates that a possible improvement in terms of charge-generation efficiency strongly depends on the specific materials: whereas for different metal-phthalocyanines (M-Pc) and polyvinylcarbazol (PVK) C₆₀ has a strong potential for improvement, no such improvement is expected from energetic reasons for 1,4-Dithioketo-3,6-diphenyl-pyrrolo-[3,4-c]-pyrrol (DTPP). Time-resolved 2-photon photoemission experiments using femto-second laser pulses give insight into the dynamics of the photoexcited electronic states.

INTRODUCTION

Organic photoreceptor materials are of strong commercial interest due to their wide application in xerographic devices and fax machines (1). Our aim is to study whether an admixture of C₆₀ improves some typical organic photoreceptor materials due to its unique electron accepting properties (2). The basic idea of the improvement is that directly after the photoexcitation a fast electron transfer onto the C₆₀ takes place which reduces the recombination probability of the photoexcited state and thereby enhances the charge generation efficiency. We study the energetics of this process by photoelectron spectroscopy. The life time of the excited states is measured using 2-photon photoelectron spectroscopy with fs-laser pulses.

EXPERIMENTAL

Layers of the organic materials are produced by vacuum sublimation from Ta boats onto sputter-cleaned metal substrates. The thickness of the layers is sufficient to exclude any contribution from the substrate to the signal. Thin overlayers (between 0.5

monolayers (ML) and 2 ML) of C_{60} are sublimed under ultra-high vacuum conditions. The layer thickness is estimated via the evaporation rate using a quartz microbalance.

A He-resonance lamp ($h\nu=21.2\text{eV}$) is used for the photoelectron spectroscopy (UPS). The kinetic energy of the photoelectrons is measured by a hemispherical electron analyzer. The overall energy resolution amounts to about 0.15eV . All photoemission spectra are displayed on a binding energy scale referenced to the Fermi energy.

Experiments studying the dynamics of the excited states are performed using 2 frequency multiplied Ti-sapphire fs-laser pulses with a variable delay: the first pulse (pump, $h\nu=3\text{eV}$) creates an excited state. The lifetime of this states is probed by the second pulse (probe, $h\nu=4.5\text{eV}$) which delivers sufficient energy to photoemit an electron from the decaying excited state. The time resolution of the experiment is around 200fs as determined by an auto correlation experiment (3).

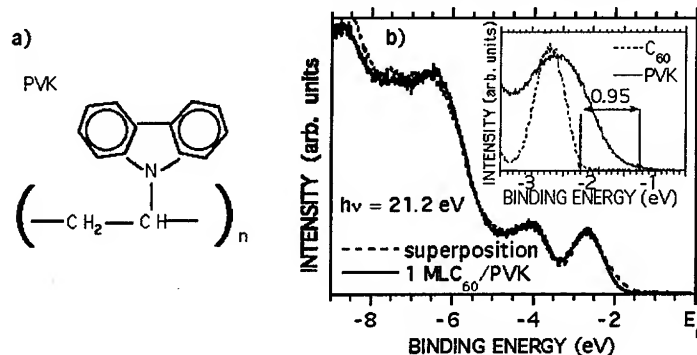


FIGURE 1. a. Model of polyvinylcarbazole (PVK). b. Photoelectron spectra of 1ML C_{60} /PVK (solid line), superposition (dashed line) of spectra from pure PVK and pure C_{60} . The inset shows the spectra of the pure components (position on energy axis as in superposition in main frame), the energy separation of the HOMO-onset of both components is marked by bars.

RESULTS AND DISCUSSION

Figure 1 displays the valence-band region of polyvinylcarbazole (PVK) with a coverage of 1 ML of C_{60} as measured by UPS (solid line). The spectral features can be reproduced by a superposition between the spectra of pure PVK and pure C_{60} using appropriate weighting factors. From these spectra it is possible to obtain the energy of the highest occupied molecular orbitals (HOMO) of both materials when they are in contact to each other. Their splitting amounts to 0.95eV with the PVK states at the lower binding energy. From photoemission and inverse photoemission experiments it is known that the corresponding lowest unoccupied molecular orbital (LUMO) of C_{60} is separated by 2.3eV from the HOMO (4). Therefore an electron needs $2.3\text{eV}-0.95\text{eV}=1.35\text{eV}$ in order to be transferred from the HOMO of PVK into the LUMO of C_{60} . This is the final-state energy of the charge separated state. The primarily excited

state has an energy of 2.3 eV as can be concluded from optical absorption spectra (5,6). Since this energy is higher than what is needed in order to separate the electron and the hole on different molecules, we can conclude that an electron transfer from the PVK towards the C₆₀ via an excited state of the PVK is energetically possible. Therefore it is to be expected that an admixture of C₆₀ improves the charge generation efficiency of PVK. Such an effect has already been observed in thin films (7).

A different situation is observed for DTPP in contact to C₆₀. From the UPS spectra we conclude that the separation between the HOMO of both materials is about 0.7 eV. Therefore the electron needs 2.3 eV - 0.7 eV = 1.6 eV when it is to be transferred towards the C₆₀. Since the optical excitation spectra reveal that the excited state has only an energy of 1.4 eV (8,9) it is unlikely that such an electron transfer will occur. In contrast to PVK we therefore do not expect an improvement of the charge generation probability when DTPP is mixed with C₆₀.

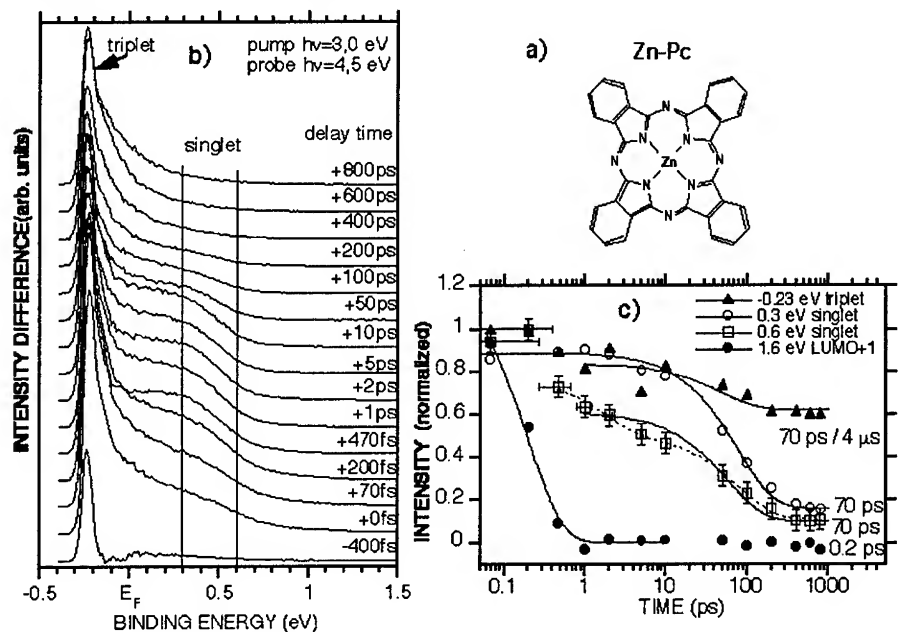


FIGURE 2. a. Model of Zn-phthalocyanine (Zn-Pc). b. 2-photon photoemission spectra from Zn-Pc for different delay times between pump and probe pulse. c. Lifetime of different excited states as determined from the intensity of specific energy regions in Fig.2b as a function of the delay time.

An electron transfer via an excited state may occur if the energy of the final state is lower than that of the excited state, but some other decay mechanism still could dominate if it happens faster than the electron transfer. A pump-probe 2-photon photoemission experiment with fs-laser pulses not only delivers the time scales of the decaying excited state, but also reveals which states are populated subsequently. Fig.2b displays the spectra for pure Zn-Pc at different delay times between pump and probe

pulse. The background intensity corresponding to the signal from each single laser has been subtracted. The normalized intensity for specific energies which correspond to different states as a function of the delay time is shown in Fig.2c. Lifetimes can be obtained by fits assuming exponential decay. A very fast decay which corresponds to the time resolution of the experiment can be observed for the directly excited state, the LUMO+1. Moderate lifetimes of about 70ps (\pm 50ps) are observed for 2 states at intermediate energies which are identified as singlet excitonic states. The spectral features at lower energies may partly be assigned as belonging to a long living triplet excitonic state which is not completely depopulated within the repetition rate of the pulsed laser excitation.

SUMMARY

Using the technique of photoelectron spectroscopy with ultraviolet radiation (UPS) we are able to predict that in contrast to polyvinylcarbazol (PVK), 1,4-Dithioketo-3,6-diphenyl-pyrrolo-[3,4-c]-pyrrol (DTPP) is not likely to be improved in terms of charge generation efficiency when C₆₀ is admixed. For pure Zn-Pc the lifetimes of excited states has been determined with 2-photon photoemission with fs-laser pulses. We find a very fast decay of the primarily excited LUMO+1 which is at the limit of our experimental time resolution and a very slow decay of the triplet excitonic state. Two states which are assigned to singlet excitons reveal a lifetime of about 70ps. In the near future we would like to measure the expected changes upon admixtures of C₆₀.

ACKNOWLEDGEMENTS

The financial support by the BMBF-VDI under contract number 13N6906 is acknowledged. B.K. is grateful for the financial support by the Ministerium für Wissenschaft und Forschung des Landes Nordrhein-Westfalen.

REFERENCES

1. K.-Y.Law, *Chem.Rev.* **93** (1993) 449.
2. B.Kessler, *Appl.Phys. A* **67** (1998) 125.
3. R.Jacquemin, S.Kraus, W.Eberhardt, *Solid State Commun.* **105** (1998) 449.
4. R.W.Lof, M.A. van Veenendaal, B.Koopmans, H.T.Jonkman, G.A.Sawatzky, *Phys.Rev.Lett.* **68** (1992) 3924.
5. Napo, *J.Mat.Sci.* **27** (1992) 6219.
6. M.Pope, C.E.Swenberg, "Electronic Processes in Organic Crystals", Oxford University Press (1982).
7. Y.Wang, *Nature* **356** (1992) 585; Y.Wang, R.West, C.H.Yuan, *J.Am.Chem.Soc.* **115** (1993) 3844.

-
8. J.Mizuguchi, G.Giller, and E.Baeriswyl, *J.Appl.Phys.* **75** (1994) 514 .
 9. M.Arita, K.Fukushima, S.Homma, H.Kuras, H.Yamamoto, and M. Okamura, *J.Appl.Phys.* **70** (1991) 4065.

Optical Limiting Materials Based on Fullerene Derivatives

Maurizio Prato,^a Michele Maggini,^b Gianfranco Scorrano,^b Giovanna Brusatin,^c Massimo Guglielmi,^c Moreno Meneghetti,^d Raffaella Signorini,^d Renato Bozio^d and Dirk M. Guldie^e

^a*Dipartimento di Scienze Farmaceutiche, Università di Trieste, Piazzale Europa, 1, 34127 Trieste, Italy*

^b*Centro Meccanismi di Reazioni Organiche del CNR, Dipartimento di Chimica Organica, Università di Padova, Italy*

^c*Dipartimento di Ingegneria Meccanica, Università di Padova, Italy*

^d*Dipartimento di Chimica Fisica, Università di Padova, Italy*

^e*Radiation Laboratory, University of Notre Dame, Notre Dame, IN 46656, U.S.A.*

Abstract. A functionalized fulleropyrrolidine has been synthesized and investigated for optical limiting applications. Solid materials have been prepared for optical limiting devices by incorporation in sol-gel glasses. Their nonlinear transmission properties have been measured and found comparable with those of solution samples. We show that clustering of the fullerene spheres, which might affect the optical limiting properties, is not relevant. Multilayer structures following a bottleneck design are prepared and their NL transmission properties are characterized.

INTRODUCTION

Ever since the fullerenes were discovered (1) and produced in bulk quantities (2), much effort has been devoted to the development of practical applications of these new forms of carbon (3,4). During the course of these investigations, it was soon clear that the new spheroidal molecules were particularly promising in the fields of materials science and medicinal chemistry. And, in fact, [60]fullerene and its relatives have been proposed for use as lubricants, catalysts, superconductors, organic magnets, in the production of batteries, electro- and photoluminescent materials, electronic and optical devices.

One of the most actively investigated fields in the fullerene area relates to the development of photo-optical and electro-optical devices. [60]Fullerene, in fact, is an excellent electron-acceptor and in many instances, photoinduced electron-transfer from

donor units to the fullerene occurs fast and efficiently, for the generation of long-lived charge-separated species (5-9).

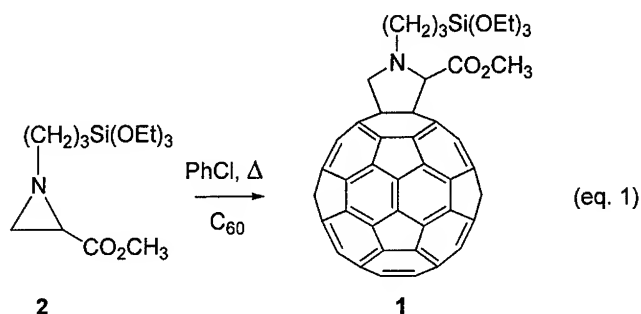
RESULTS AND DISCUSSION

A very promising applicative perspective of the fullerenes is in the field of optical limiting (OL). A few years ago, it was found that, in solution, [60]fullerene is an excellent reverse saturable absorption (RSA) material, with OL properties comparable to those of other materials currently under consideration for practical use (10). In the RSA mechanism, an important requisite is the efficient pumping to a strongly absorbing excited state. As a matter of fact, the ground state absorption spectrum of [60]fullerene is characterized by intense absorptions in the UV region with weaker bands extending throughout the visible region up to 700 nm. Upon irradiation, [60]fullerene is excited to a short-lived singlet state (lifetime = 1.3 ns), which converts almost quantitatively into a longer-lived triplet state (lifetime = 50-100 μ s) (11). More importantly, the triplet excited state is a strongly absorbing species with a maximum centered at about 750 nm. A major drawback for practical use is represented by the poor solubility of [60]fullerene in most solvents and solid matrices. The same considerations do not apply to fullerene derivatives. Solubilizing appendages can be covalently attached to the fullerene, thus making it soluble in virtually any solvent. On the other hand, for practical applications, it is very important to incorporate [60]fullerene, or the solubilized derivatives, into a solid, transparent matrix.

An excellent and versatile way for the construction of thin solid films is represented by the sol-gel technique (12-17). The sol-gel process consists in the polymerization of metal alkoxides. A solution (sol) is formed, which becomes then a xerogel, and eventually, upon heating, densifies to a glass or a ceramic material. The sol-gel process can be performed preferentially in ethanol or tetrahydrofuran (THF). The latter solvent is much better for dissolving fullerene derivatives. For the purpose of the present work, derivative **1** was prepared according to eq. (1). Thermolysis of aziridine **2** in the presence of [60]fullerene led to very good yields of fulleropyrrolidine **1** as the only monoadduct (18,19).

The solubility of derivative **1** in THF was found to be 43 mg/ml, a value that allows the preparation of relatively concentrated solutions. In the same solvent, the solubility of unmodified [60]fullerene is virtually zero (20). The presence of the alkoxysilane

moiety in **1** guarantees the chemical grafting of the fullerene derivative to the solid matrix, affording homogeneous dispersions of **1** in the glass.



Thin multilayer films were prepared according to the "bottleneck" model (21). They were characterized of 2.15 mm total thickness, and composed of ten fullerene-doped sol-gel layers, each 50 μm thick, interleaved with soda lime glass layers of thickness 150 μm each. The total transmittance of the multilayer structure was 77%.

A very common problem in fullerene materials is represented by the tendency of the carbon spheres to form clusters. And even when a solubilizing appendage is covalently attached to [60]fullerene, which ensures solubilisation in polar media, clustering cannot be avoided (22,23). According to several reports, formation of clusters decreases the lifetime of the excited triplet state by 2-3 orders of magnitude (24,25), strongly limiting the use of fullerenes as RSA materials. The degree of aggregation is usually detected by UV-Vis spectrophotometry, pulse radiolysis or light-scattering. In UV-Vis spectrophotometry aggregation causes a broadening of the absorption bands with loss of structural features (22,24,26,27). However, in the case of our sol-gel glasses, no clustering was observed by means of UV-Vis spectrophotometry: the absorption spectrum of most of the thin glassy film prepared in our labs showed the characteristic features of [60]fullerene monoadducts, with a small, sharp peak at 430 nm and a broader, smooth absorption at 700 nm. Also, the detection in the solid films of triplet lifetimes typical of [60]fullerene derivatives, obtained by transient absorption spectroscopy, points to a very small degree of aggregation.

As a matter of fact, OL measurements performed in solution and in sol-gel multilayer films gave results in excellent agreement. Optical limiting measurements were performed using an excimer pumped pulsed dye laser, operating with different dyes (LDS 690 at 690 nm) and emitting 10 ns pulses, with 1 Hz repetition rate. The

laser beam was focused onto the sample using a 200 mm lens. The incident and transmitted laser pulse energies were measured by using photodiodes calibrated against the signal from a surface absorbing calorimeter (28).

Figure 1A shows the nonlinear transmission for a toluene solution of derivative **1** with linear transmission of 74 % measured at 690 nm and plotted against the logarithm of the incident energy. Figure 1B shows the same measurement for the multilayer structure described above performed at 690 nm with f/66 optics (the same used for solution samples).

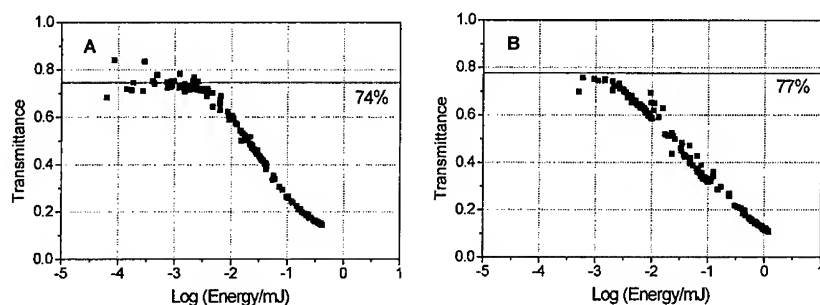


Figure 1

The results of these investigations demonstrate that fullerene derivatives can be considered suitable materials for OL in the red region. The incorporation and homogeneous dispersion of functionalized fullerene derivatives in sol-gel glassy matrices is achieved by covalent attachment of the silicon alkoxide end groups. The materials produced show nonlinear properties in agreement with those observed in solution.

ACKNOWLEDGEMENTS

This work was supported in part by the Office of Basic Energy Sciences of the U.S. Dept. of Energy, by MURST (Italy), by C.N.R. through the program "Materiali Innovativi (legge 95/95)" and the European Commission (DG XII) through Brite-Euram III Contract BRPR-CT97-0564. This is contribution No. NDRL-4124 from the Notre Dame Radiation Laboratory.

REFERENCES

1. Kroto, H. W., Heath, J. R., O'Brien, S. C., Curl, R. F. and Smalley, R. E. *Nature* **318**, 162-163 (1985).
2. Krätschmer, W., Lamb, L. D., Fostiropoulos, K. and Huffman, D. R. *Nature* **347**, 354-358 (1990).
3. Prato, M. *J. Mater. Chem.* **7**, 1097-1109 (1997).
4. Prato, M. in *Fullerenes and Related Structures* (ed. Hirsch, A.) 173-188 (Springer, Berlin, 1999).
5. Sariciftci, N. S., Smilowitz, L., Heeger, A. J. and Wudl, F. *Science* **258**, 1474-1476 (1992).
6. Imahori, H. and Sakata, Y. *Adv. Mater.* **9**, 537-546 (1997).
7. Martin, N., Segura, J. and Seoane, C. *J. Mater. Chem.* **7**, 1661-1676 (1997).
8. Martin, N. and Seoane, C. in *Handbook of Organic Molecules and Polymers* (ed. Nalwa, H. S.) 1-86 (John Wiley, New York, 1997).
9. Martin, N., Sánchez, L., Lescas, B. and Pérez, I. *Chem. Rev.* **98**, 2527 (1998).
10. Tutt, L. W. and Kost, A. *Nature* **356**, 225-226 (1992).
11. Foote, C. S. *Top. Curr. Chem.* **169**, 347-363 (1994).
12. Schubert, U., Hüsing, N. and Lorenz, A. *Chem. Mater.* **7**, 2010-2027 (1995).
13. Judeinstein, P. and Sanchez, C. *J. Mater. Chem.* **6**, 511-525 (1996).
14. Avnir, D. *Acc. Chem. Res.* **28**, 328-334 (1995).
15. Levy, D. and Esquivias, L. *Adv. Mater.* **7**, 120-129 (1995).
16. Corriu, R. J. P. and Leclercq, D. *Angew. Chem., Int. Ed. Engl.* **35**, 1420-1436 (1996).
17. Hench, L. L. and West, J. *Chem. Rev.* **90**, 33-72 (1990).
18. Maggini, M., Scorrano, G. and Prato, M. *J. Am. Chem. Soc.* **115**, 9798-9799 (1993).
19. Bianco, A., et al. *J. Am. Chem. Soc.* **119**, 7550-7554 (1997).
20. Ruoff, R. S., Tse, D. S., Malhotra, R. and Lorents, D. C. *J. Phys. Chem.* **97**, 3379-3383 (1993).
21. Miles, P. A. *Appl. Opt.* **33**, 6965-6979 (1994).
22. Guldi, D. M., Hungerbühler, H. and Asmus, K.-D. *J. Phys. Chem.* **99**, 13487-13493 (1995).
23. Guldi, D. M. *Res. Chem. Intermed.* **23**, 653-673 (1997).
24. Eastoe, J., Crooks, E., Beeby, A. and Heenan, R. *Chem. Phys. Lett.* **245**, 571-577 (1995).
25. Guldi, D. M. *J. Phys. Chem. A* **101**, 3895-3900 (1997).
26. Bensasson, R. V., Bienvenue, E., Dellinger, M., Leach, S. and Seta, P. *J. Phys. Chem.* **98**, 3492-3500 (1994).
27. Lamparth, I. and Hirsch, A. *J. Chem. Soc., Chem. Commun.* 1727-1728 (1994).
28. Signorini, R., et al. in *Fullerenes and Photonics III* (ed. Kafafi, Z. H.) 130-139 (SPIE, Bellingham, 1996).

SPM Investigation of Superhard Carbon prepared from C₆₀ Fullerene

A. Hassanien*, M. E. Kozlov† and M. Tokumoto*

*Electrotechnical Laboratory, 1-1-4 Umezono, Tsukuba, Ibaraki, 305-8568 Japan

†AlliedSignal Inc., Morristown, New Jersey 07952-1021, USA

Abstract. A very hard and conducting form of carbon was obtained from C₆₀ fullerene at moderately high pressure (2.6-3 GPa) and temperature (700°C). The hardness of the material is more than 4000 kg/mm². Its electrical conductivity is about 100 S/cm and is weakly dependent on temperature. A comparative ¹³C NMR study shows no explicit evidence for the presence of diamond like sp³-character. So far, it has been of great difficulties to correlate between the atomic structure and these remarkable physical properties, as X-ray diffraction and Raman measurements show lack of long-range crystalline order. In this report we shall present structure and property analysis measured by STM and STS techniques. High-resolution topographic images reveal the mesoscopic structure in which spherical metallic nano-clusters of size up to 6 nm, are covalently interlinked. The atomic structure of the nano-clusters contains pentagon rings, which in turn introduces a curvature in the graphene lattice. The presence of pentagon rings suggests that the bonding carry non-planer sp²-character which might be correlated with the observed significant hardness.

INTRODUCTION

The study of hard carbon has been motivated by the technological utility of infrared window coatings with properties approaching the physical characteristics of diamond. Among hard carbon materials a special attention is paid to hydrogen free amorphous hard carbon particularly due to its enormous technological applications. The production of such material requires a chemically pure source of carbon in the vapor state, which upon condensation form sp³ bonded carbon. As a pure source of carbon, fullerenes materials have shown remarkable properties, among them, its high vapor pressure at modest temperature. Maiken et al. (1) have used sparked fullerene vapor, as source of carbon, and prepared hydrogen free amorphous carbon thin films by condensing the ionized molecular carbon onto a substrate. Kozlov et al. (2) have demonstrated the use of fullerenes to produce bulk hard carbon at moderate conditions of pressure and temperature. Briefly, C₆₀ was nonhydrostatically pressurized at 2.6-3 GPa and heated at 700°C. The material enjoy variety of

remarkable physical properties, namely; the hardness is more than 4000 kg/mm², the electrical conductivity is about 100 S/cm. X-ray diffraction and Raman measurements show lack of long-range crystalline order and loss of C₆₀ molecular symmetry. (2) In addition, the macrodensity is about 1.9 g/cm³, only 12% bigger than the initial fullerenes, which might indicate partial destruction of the initial fullerenes and formation of covalent bonds between C₆₀ cages might occurred. On the other hand, a comparative ¹³C NMR study (3) shows no explicit evidence for the presence of diamond like *sp*³-character, in contrast to C₆₀ polymers.

In order to correlate between the structure and these remarkable physical properties, we have used scanning tunneling microscope to explore the atomic structure and the electronic properties of this material. High-resolution images show the mesoscopic structure in which spherical clusters of size 4-6 nm are separated by flat area. On top of the nano-clusters we resolve a pentagonal arrangement of carbon atoms which might suggest that bonding in this material carry partial *sp*³ character or non-planar *sp*² character.

EXPERIMENTAL PROCEDURE

We have carried out STM measurements on a bulk sample of hard carbon (2) using a Digital Instruments Nanoscope IIIa operated at room temperature in ambient conditions. High quality images of the atomic structure were obtained by recording the tip (Pt-Ir) height at constant current. Typical bias parameters are 400 pA tunnel current and 100 mV bias voltage. The images presented here have not been processed in any way. Scanning tunneling spectroscopy (STS) measurements were performed by interrupting the lateral scanning as well as the feed back loop and measuring the current (*I*) as a function of tip-sample voltage at a fixed tip-sample distance. A combination of STM and STS measurements have allowed us to investigate the microscopic structure and electronic properties respectively.

RESULTS AND DISCUSSION

We present here high resolution STM topographic images showing the atomic structure of this unique form of fullerene based material. Fig. 1 shows an STM image of size 3.5×3.5 nm², the dark spots represent the centers of hexagons and/or pentagons rings and show a cluster of spherical shape. The curvature of such a cluster might be due to a direct consequence of pentagonal rings which originate from the transformed fullerene. The highlighted pentagon in Fig.1 shows the location of fivefold rings. As pentagons tend to introduce curvature in the graphene lattice, bonding will carry partial *sp*³ character. The less corrugated region, A, mark an area between two spherical nano-clusters which indicates no sign of curvature.

This might suggest that the bonding between the nano-clusters is most likely due to sp^2 .

Moreover, we have observed also triangular pattern, which indicate asymmetry between the so called A and B sites. The asymmetry between A and B sites (as in the case of hexagonal graphite, e.g. HOPG), result from the fact that the tip sense preferentially surface atoms with no neighbors in the adjacent layer below (4) and therefore the STM image will show triangular rather than hexagonal pattern. This conclude that these clusters are not hollow but indeed host other structure of carbon.

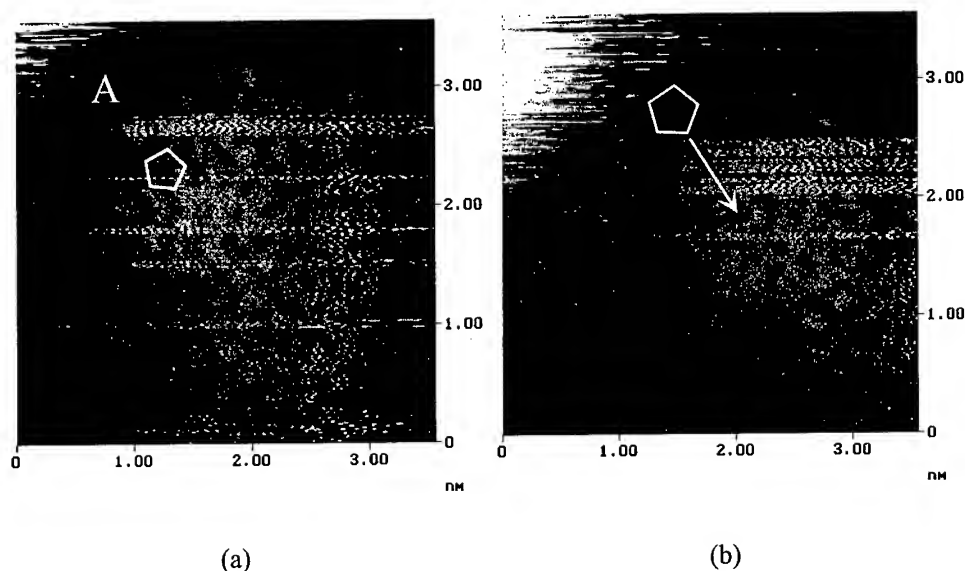


Figure 1. High resolution STM images of an area on top two different clusters. The dark spots are centers of hexagons and/or pentagons rings. Typical distances between centers are 0.25 ± 0.02 nm as expected for graphene lattice. The arrow in b) points at a pentagon center.

Fig.2 shows I-V STS measurement on top of one cluster. Different curves correspond to different location on the cluster surface. The linear I-V relations indicate metallic behavior for this material. From the topographic images and the STS curves we conclude that a significant transformation occurs in the fullerenes structure in which nano-sized metallic clusters are formed. Two types of bonding might exist here; sp^2 bonding between the clusters and partial sp^3 or non-planer sp^2 within the clusters due to the existence of pentagons.

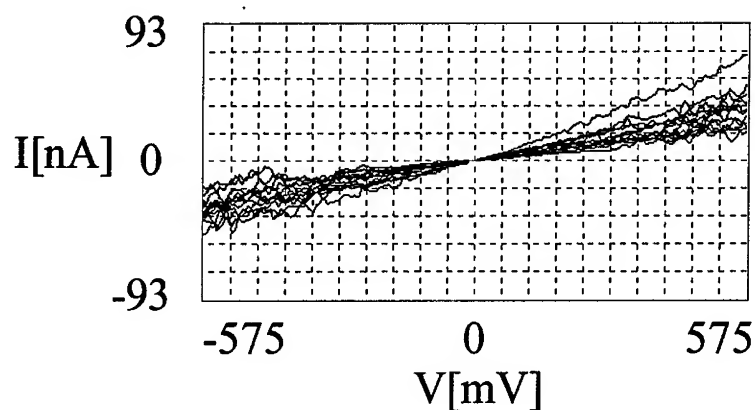


Figure 2. I-V STS curves on different location of one nano-grain. The linear I-V relations suggest a metallic behavior.

CONCLUSION

High-resolution images and STS curves show the structures of fullerene-based hard carbon in which metallic nano-clusters of size 4-6 nm are formed. The observed triangular pattern in the atomic resolution images on top of the clusters might indicate that these clusters are not hollow. The clusters incorporate pentagonal arrangement. This introduces a curvature in the cluster surface structure, which result in partial sp^3 or non-planer sp^2 type of bonding within the clusters.

REFERENCES

1. Maiken E. B. and Taborek P., *J. Appl. Phys.* **78**, 541 (1995).
2. Kozlov M. E., Hirabayashi M., Nozaki K, Tokumoto M. and Ihara H., *Appl. Phys. Lett.* **66**, 1199 (1995).
3. Maniwa Y., Sato M., Kume K., Kozlov M.E. and Tokumoto M., *Carbon* **34**, 1287 (1995)
4. Tomanek D. and Louie S. G., *Phys. Rev. B.* **37**, 8327 (1988).

Raman Spectrum and Stability of $(C_{59}N)_2$

C. Jögl¹, H. Kuzmany¹, M. Krause¹, W. Plank¹,
O. Dubay², N. Tagmatarchis³, K. Prassides³

¹ Universität Wien, Institut für Materialphysik, Strudelhofgasse 4,
A-1090 Wien, AT

² Comenius University, Faculty of Mathematics and Physics,
80 000 Bratislava, SK

³ University of Sussex, School of Chemistry, Physics and Environmental Science,
BN1 9QJ Brighton, GB

Abstract. Raman spectra of $(C_{59}N)_2$ are presented for various laser lines and for temperatures between 300 K and 620 K. The material exhibits a reliable stability versus laser illumination for the full temperature range and a remarkable resonance enhancement of the cross section for red light excitation. The Raman intensity versus the used laserpower shows a linear dependence in the entire region observed.

The spectra show a strong relation to those of C_{60} , particularly in the spectral range of the tangential modes. Calculations of the mode frequencies with the semiempirical AM1 technique reveal good agreement with the observed Raman lines, in particular for the intermolecular modes observed at 82, 103 and 111 cm^{-1} .

INTRODUCTION

The biazafullerene $(C_{59}N)_2$ is an interesting modification of C_{60} since the substituted nitrogen provides an additional electron to the cage which was supposed to partly fill the t_{1u} derived conduction band [1]. Since this extra electron turned out to be strongly localized [2] it does not contribute to the conductivity. Other works showed that the C_{60} dimers as well as the photopolymer and the pressure polymers are very unstable versus temperature [4]. Theoretical work predicted an even lower stability of $(C_{59}N)_2$ as in this dimer the two cages are only bound by one C—C bond in contrast to the two C—C bonds in the other dimeric compounds.

We measured the Raman-spectra of $(C_{59}N)_2$ for different temperatures, different excitation energies and different laser powers to clarify the thermal and photostability of the material. The signatures of the dimeric state were analyzed by the variation of the laser wavelength and by AM1 calculations.

EXPERIMENTAL

The $(C_{59}N)_2$ samples used were prepared by dissolving a cluster-opened MEM-substituted ketolactam of C_{60} (MEM = methoxyethoxymethyl) in 1,2-dichlorobenzene as described previously [5]. A solution of this material in toluene was dropped on a gold coated silicon substrate, dried to a polycrystalline film under ambient conditions and treated in high vacuum at 473 K to remove residual solvents.

For the excitation we used an Ar^+ and a Kr^+ gas laser. The Raman measurements were performed in backscattering geometry. The scattered light was analyzed by a triple DILOR (XY) spectrometer equipped with a multichannel detector. During all measurements the samples were kept in a cryostat with a vacuum better than 3×10^{-7} mbar. For the temperaturedependent measurements it could be cooled with liquid nitrogen and heated up to temperatures of 620 K. In the whole temperature region a temperature stability of $\Delta T \approx \pm 1K$ could be achieved.

RESULTS AND DISCUSSION

Comparison C_{60} / $(C_{59}N)_2$ and resonance excitation

Figure 1 shows Raman spectra of $(C_{59}N)_2$ and C_{60} . A strong splitting of the lines in the former in comparison to C_{60} can be observed. In the spectral range close to 100 cm^{-1} three additional modes occur in $(C_{59}N)_2$, which do not have a counterpart in C_{60} .

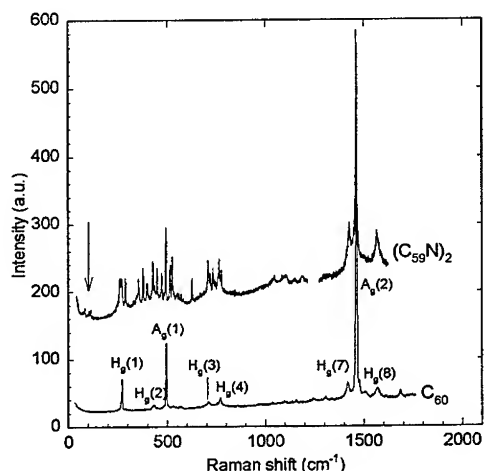


FIGURE 1. Raman spectrum of $(C_{59}N)_2$ excited with 647 nm and C_{60} excited with 514 nm. The arrow indicates the modes in $(C_{59}N)_2$ which correspond to the intermolecular vibrations.

Replacing two C-atoms in the two C_{60} cages by two nitrogens yields a symmetry-reduction $I_h \rightarrow C_{2h}$ which causes the strong linesplitting. The 3 additional low frequency modes arise from intermolecular vibrations activated by the transformation

of 3 translational and 3 rotational into 6 vibrational degrees of freedom; 3 of the 6 are Raman active, 3 are IR active.

For the lower frequency range of the spectra we studied their dependence on the exciting laser wavelength (Fig. 2).

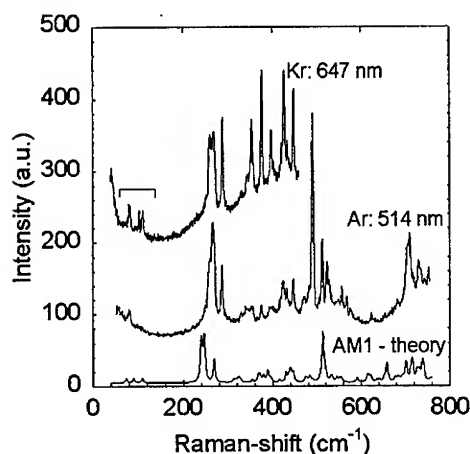


FIGURE 2. Raman spectra of $(C_{59}N)_2$ for various laserlines compared to the results of semiempirical AM1-calculations.

Obviously the modes are resonant for the excitation with the krypton laser at 647 nm, which is particularly important for the rather weak intermolecular modes. For the theoretical description of the Raman frequencies the semiempirical AM1-theory was used [5]. For each frequency calculated a Lorentzian peak was assumed; the intensity for the various lines was estimated from the symmetry of the mode and from its relation to C_{60} . The resulting calculated spectrum is in good agreement with the measurements.

Spectra as a function of temperature

For the study of the temperature dependence we measured in two different spectral ranges: close to the laserline, where the intermolecular modes and the $H_g(1)$ mode are found and in the region of the $A_g(2)$ -pinch-mode. In Fig. 3 the corresponding spectra are shown.

All observed modes remained unchanged over the entire temperature range except for a small broadening and a downshift of some modes. This downshift is steady without any sudden changes.

The continuous change in the frequency of the modes indicates, that no structural or chemical transitions take place throughout the entire temperature range.

Spectra as a function of the laser power

As long as no changes in the molecular structure occur, the intensity of all Raman lines must be proportional to the power of the exciting laser. Figure 4 shows spectra excited with laser powers covering a range from 100 μ W to 5 mW. Figure 5 shows the Raman intensity of two selected modes.

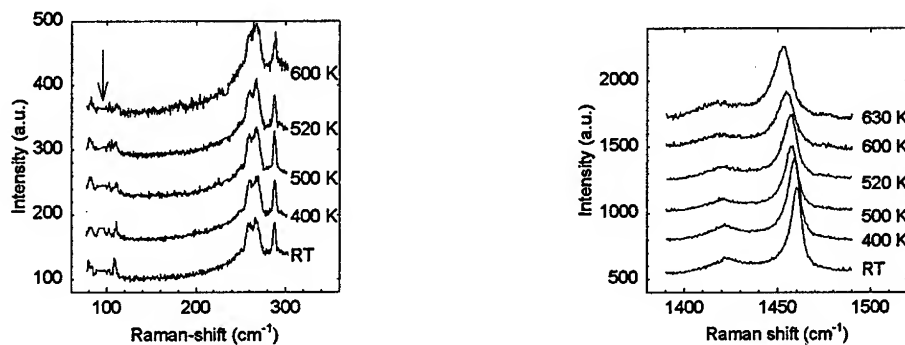


FIGURE 3. Temperature dependence of the $(C_{59}N)_2$ spectra in different spectral ranges. The arrow indicates the spectral range of the plasmalines, which have been removed.

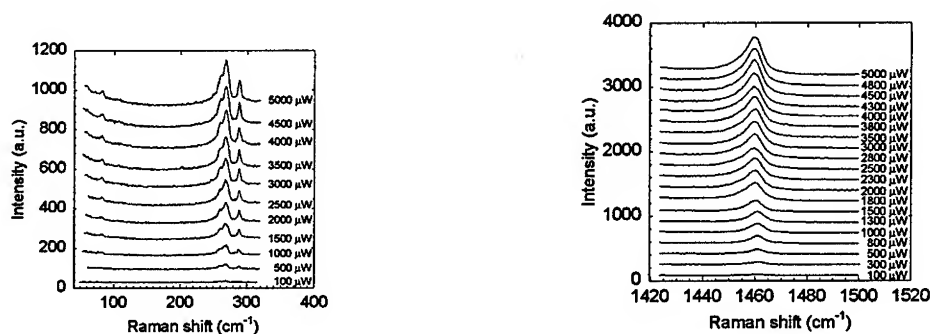


FIGURE 4. Spectra of $(C_{59}N)_2$ as a function of the used laser power in two different spectral ranges. The maximum power used corresponds to an intensity of about 3×10^3 W/cm²

The position of the modes is not dependent on the laser power and the intensities are in good agreement to the expected linear behavior.

From the linear behavior we learn, that the material is not degraded by the laser illumination and no photoinduced transition takes place.

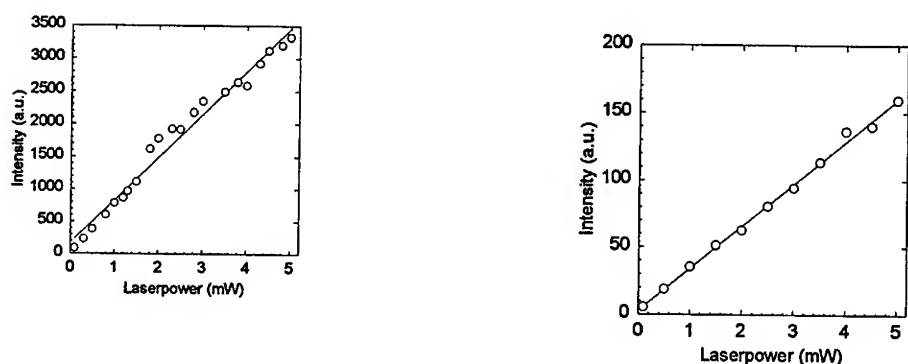


FIGURE 5. Intensity of the $A_g(2)$ mode at 1460 cm^{-1} (left) and of the 268 cm^{-1} component of the $H_g(1)$ derived mode (right) as a function of the laser power used. The data were obtained by fitting the curves in Fig. 4 to Vogt-lines.

CONCLUSIONS

Diazafullerene turned out to be stable at last up to 630 K and for light intensities up to 5 mW. This means, that $(C_{59}N)_2$ is much more stable than the C_{60} dimer $(C_{60})_2$. This unexpected behavior can be explained by the absence of a stable fission product for $(C_{59}N)_2$.

The intermolecular modes are a direct spectroscopic probe for the formation of a dimeric structure. Also the position of the $H_g(1)$ mode at 296 cm^{-1} gives strong evidence for the dimeric structure. In polymeric structures, such as $[C_{60}]_n$ this line is found at 340 cm^{-1} .

A tentative assignment for the origin of the vibrational modes as compared to C_{60} is possible. [5] This assignment works particularly well for the modes with a strong Raman activity. The lines in the spectral range of the radial cage modes should be a valuable signature for a further treatment of the material such as doping or exposure to strong light.

ACKNOWLEDGMENTS

Work supported by the European Community, TMR project ERBFMRXCT97-0155 and by a Marie Curie Fellowship at the University of Sussex.

REFERENCES

1. J. C. Hummelen et.al., Science **269**, 1554 (1995).
2. W. Andreoni, Ann. Rev. Phys. Chem. **49**, (1998).
3. B. Burger et. al., Z. Physik B **101**, 227 (1996).
4. P. C. Eklund et. al., Thin Sol. Films **257** (1995).
5. H. Kuzmany et. al., Phys. Rev. B, in press.

AUTHOR INDEX

A

Achiba, Y., 120, 124, 313, 328
Akimoto, I., 7
Alloul, H., 42
Alvarez, L., 254
Ambe, F., 120
Ando, Y., 328
Andrievsky, G., 200
Anglaret, E., 245, 254, 299
Antich, A. V., 217
Antonov, R., 379
Arčon, D., 37
Arzt, E., 371
Asai, K., 120
Aslanis, E., 52
Astashkin, Y., 200
Avouris, P., 393

B

Bachtold, A., 399
Bao, J., 3
Bauer, H.-D., 288
Baumgartner, G., 42, 56, 64
Bayerl, S., 231
Bayerl, T., 231
Béguin, F., 273, 429, 470
Belz, T., 205
Benilov, A., 200
Benito, A., 245, 254
Benoit, J. M., 292
Benoit, R., 470
Bergeron, D. J., 308
Bernier, P., 254, 292, 407, 456
Beton, P. H., 165
Bianchetti, M., 448
Bietsch, W., 3
Bíró, L. P., 323
Blank, V. D., 416
Blinç, R., 37
Bockrath, M., 379, 388
Bonard, L.-M., 226
Bonnamy, S., 273, 429, 470
Bonnard, J.-M., 474
Boufendi, L., 470

Bourgoin, J.-P., 421
Bozio, R., 492
Brabec, C. J., 483
Broglia, R. A., 448
Brouet, V., 42
Brusatin, G., 492
Buga, S. G., 416
Bukalo, V., 200
Bulusheva, L. G., 217
Buonsante, P., 448
Burghard, M., 221, 338, 407
Butcher, M. J., 165
Buzaneva, E., 200
Byrne, H. J., 338
Byszewski, P., 258

C

Cabioch, T., 346
Camps, X., 231
Čegar, N., 64
Céolin, R., 28
Cevc, P., 37
Chernozatonskii, L. A., 284
Chi, D. H., 115
Choi, J.-P., 452
Chuvilin, A. L., 444
Clausen-Schaumann, H., 231
Clauss, W., 308
Cobden, D. H., 388
Cochon, J.-L., 237
Cohen, M. L., 183
Colliex, C., 268
Colomer, J.-F., 241
Conard, J., 273
Crespi, V. H., 364
Curran, S., 466

D

Danno, T., 213
Degiorgi, L., 64
de la Fuente, G. F., 245
Delpeux, S., 470
de Menorval, L. C., 456

Demoncey, N., 268
 Dennis, J., 90
 Dennis, T. J. S., 136, 148, 187
 Ding, A., 205
 Dinse, K.-P., 101, 144
 Drichko, N. V., 191
 D'Souza, F., 452
 Dubay, O., 501
 Dubitsky, G. A., 416
 Duclaux, L., 273
 Duesberg, G. S., 338
 Dunsch, L., 95, 106, 128, 132, 140, 288
 Durov, G. S., 200

E

Eberhardt, W., 304, 487
 Edwards, R., 456
 Effenberger, F., 161
 Egger, R., 411
 Eisebitt, S., 304
 Elliman, R. G., 196
 Erwin, S. C., 47
 Esteve, D., 421

F

Faigel, G., 20, 78
 Fink, J., 132, 288, 346, 351
 Fischer, J. E., 56
 Fitch, A. N., 52
 Flamant, G., 254
 Fonseca, A., 241, 249
 Forró, L., 42, 56, 64, 78, 226, 399, 474
 Fowler, P. W., 170
 Frackowiak, E., 273, 429
 Freitag, M., 308
 Friedlein, R., 288, 346, 351
 Fujii, Y., 124
 Fujiki, S., 69
 Fujiwara, A., 60, 69, 124, 403

G

Gal'pern, E. G., 284
 Gamaly, E. G., 196
 Gavillet, J., 237

Georgi, P., 95, 106
 Ginelli, F., 448
 Godovsky, D., 483
 Goedde, B., 144
 Golden, M. S., 132, 288, 346, 351
 Gorbunov, A. A., 288
 Gorchinskyi, A., 200
 Gránásy, L., 20
 Grell, A.-S., 28
 Gromow, A., 95
 Grossman, J. C., 183
 Grube, G., 161
 Grupp, A., 32, 161
 Guglielmi, M., 492
 Guillard, T., 254
 Guldi, D. M., 492
 Gyulai, J., 323

H

Haluška, M., 24
 Hanfland, M., 52
 Harigaya, K., 342
 Hassanien, A., 313, 497
 Heine, T., 170
 Hertel, T., 384
 Hetzer, M., 231
 Hirsch, A., 231
 Hone, J., 32, 47, 375, 379
 Huang, J., 478
 Huang, Z. P., 263
 Huczko, A., 258
 Hulman, M., 90, 136, 187, 278
 Hummelen, J. C., 155, 483
 Hunt, M. R. C., 132

I

Inada, Y., 115
 Inakuma, M., 90, 132, 136
 Inganäs, O., 483
 Ishii, K., 60, 69, 124
 Ishikawa, R., 213
 Iwasa, Y., 60, 115

J

Jakab, E., 474
 Janicskó-Csáthy, J., 226
 Jánossy, A., 56

Janssen, R. A. J., 155, 483

Joachim, C., 421

Jogl, C., 16, 501

Johnson, A. T., 308, 375, 379

Jones, F. H., 165

Jost, O., 288

Journet, C., 292

K

Kamarás, K., 20

Kann, G., 304

Kan'no, K.-i., 7

Kanzow, H., 205

KäB, H., 101

Kashino, S., 69

Kataura, H., 313, 328

Kavan, L., 209

Kazama, S., 328

Kergueris, C., 421

Kessler, B., 487

Kheifets, A. S., 196

Kikuchi, K., 115, 120, 124

Kim, P., 478

Kirghisov, Y., 200

Knapp, C., 101

Knol, J., 155

Knorr, S., 32, 161

Knupfer, M., 132, 288, 346, 351

Kodama, T., 124

Kohler-Redlich, P., 371

Kojima, N., 328

Komnik, A., 411

Konarev, D. V., 191

Kónya, Z., 241, 249

Kooi, M. E., 333

Koshio, A., 258

Kozlov, M. E., 497

Krause, M., 90, 128, 136, 140, 501

Krstic, V., 221

Kubozono, Y., 69

Kumazawa, Y., 313, 328

Kuran, P., 95, 106, 132, 140

Kürti, J., 278

Kutner, W., 452

Kuzmany, H., 16, 24, 90, 136, 187, 278, 501

Kuznetsov, V. L., 333, 444

Kvarnström, C., 16

L

Lahr, B., 466

Lambin, P., 319, 323

Lammert, P. E., 364

Lamy de la Chapelle, M., 237, 292

Lange, H., 258

Langeveld-Voss, B. M. W., 155

Laplaze, D., 254

Lappas, A., 52

László, I., 355

Lauginie, P., 273

Launois, P., 47

Lebedkin, S., 12

Lefebvre, J., 375

Lefrant, S., 292, 466

Lieber, C. M., 478

Lips, K., 85, 148

Liu, K., 407

Loiseau, A., 237, 268

Lorenzoni, A., 448

Lotz, H. T., 333

Louie, S. G., 183

Luther-Davies, B., 196

Luzzi, D. E., 360

Lyubovskaya, R. N., 191

M

Maggini, M., 483, 492

Magoga, M., 421

Maniwa, Y., 313, 328

Margadonna, S., 73, 187

Márk, G. I., 323

Martel, R., 393

Martin, N., 483

Martínez, M. T., 245, 254

Maser, W. K., 245, 254

Masin, F., 28

Masubuchi, S., 328

Matsuoka, Y., 124

McEuen, P. L., 379, 388

Mehring, M., 32, 161

Meingast, C., 12

Meneghetti, M., 492

Messari, I., 28

Méténier, K., 273, 429, 470

Meunier, V., 319

Mihailovič, D., 37

Mihály, L., 64
 Milnera, M., 278
 Mitani, T., 60
 Moos, G., 384
 Morenzin, J., 487
 Moret, R., 47
 Moriarty, P., 165
 Mukhopadhyay, K., 346, 351
 Mukhopadhyay, K. M., 249
 Muñoz, E., 245
 Murakami, K., 213
 Muro, T., 115
 Muster, J., 221, 338

N

Nagai, K., 115
 Nagaraju, N., 249
 Nagel, P., 12
 Nagy, J. B., 241, 249
 Nakahara, H., 120
 Nakao, H., 124
 Nemes, N. M., 56
 Neugebauer, H., 16
 Nguyen, T. P., 466
 Nussbaumer, T., 399
 Nuttall, C. J., 115
 Nützenadel, C., 462
 Nyeanchi, E., 416
 Nygård, J., 388

O

Obraztsov, A. N., 444
 Obraztsova, E. D., 333
 Odom, T. W., 478
 Ohkubo, Y., 120
 Ohtsuka, Y., 328
 Ohwada, K., 124
 Okotrub, A. V., 217
 Olalde, G., 254
 Omerzu, A., 37
 Ory, M., 237
 Osadchy, A. V., 333
 Ōsawa, E., 179
 Oszlányi, G., 20, 78

P

Paasonen, V. M., 217
 Päch, M., 148
 Palacin, S., 421
 Pascard, H., 268
 Pasler, V., 12
 Pavlovsky, I. Y., 444
 Peeters, E., 155
 Pekker, S., 20, 78, 474
 Pellenq, R., 429
 Pichler, T., 132, 288, 346, 351
 Piedigrosso, P., 241
 Pietzak, B., 85, 148
 Pigache, D., 237
 Pirotte, P., 28
 Piskoti, C., 183
 Plank, W., 501
 Pogorelov, F. V., 200
 Pompe, W., 288
 Prassides, K., 52, 73, 165, 175, 187, 501
 Prato, M., 483, 492
 Prilutski, Y., 200
 Pusztai, T., 20

Q

Quéré, F., 42

R

Radosavljevic, M., 375
 Rahmer, J., 32
 Reibold, M., 288
 Ren, Z. F., 263
 Richter, M., 128
 Robertson, J., 433
 Rode, A. V., 196
 Rogers, K. M., 170
 Rols, S., 299
 Roman, H. E., 448
 Roth, G., 12
 Roth, S., 221, 338, 407
 Rudolf, P., 132

Rühle, M., 371
Ruzicka, B., 64

S

Saito, Y., 439
Salvetat, J.-P., 273, 399, 474
Sariciftci, N. S., 16, 483
Sato, W., 120
Sauer, H., 205
Sauvajol, J. L., 245, 254, 299
Scharff, P., 200
Schilder, A., 3
Schlapbach, L., 462
Schlebusch, C., 487
Schlögl, R., 205
Schönenberger, C., 399
Schouten, J. A., 333
Schwoerer, M., 3
Scorrano, G., 492
Segura, J., 483
Seifert, G., 128, 170
Serebryanaya, N. R., 284
Shea, H. R., 393
Shimoda, H., 60
Shinohara, H., 90, 132, 136, 187, 258,
346, 351
Shul'ga, Y. M., 191
Sienkiewicz, A., 64
Signorini, R., 492
Simon, F., 64
Sitter, H., 16
Slanina, Z., 179
Smith, B. W., 360
Soldatov, A., 12
Spolenak, R., 371
Stankevich, I. V., 284
Stepanek, I., 456
Stéphan, C., 466
Stéphan, O., 268
Stösser, R., 148
Strunk, C., 399
Suecki, K., 120
Suematsu, H., 60, 69, 124, 403
Sugai, T., 346, 351
Sundqvist, B., 12, 416
Suzuki, S., 120, 313, 328
Szwarc, H., 28

T

Tagmatarchis, N., 165, 175, 501
Takabayashi, Y., 69
Takenobu, T., 60, 115
Tamási, A., 249
Tekely, P., 28
Thiën-Nga, L., 226
Thiry, P. A., 323
Tokumoto, M., 313, 497
Tomiyama, K., 403

U

Uchida, K., 403
Udvardi, L., 111
Uemura, S., 439
Uhlík, F., 179
Urmez, I., 328
Urbina, C., 421

V

Vajtai, R., 226
van Hal, P. A., 155
Vietze, K., 128
Vivet, F., 470
Volkov, A. P., 444
Vostrowsky, O., 231

W

Waiblinger, M., 85, 148
Wang, D. Z., 263
Wang, J. H., 263
Watanabe, Y., 115
Watanuki, T., 60, 124
Wei, B., 371
Weiden, N., 101, 144
Weidinger, A., 85, 148
Willems, I., 241
Wirth, I., 304

X

Xu, J. W., 263

Y

Yoshida, Y., 69

Yudanova, E. I., 191

Yumura, M., 403

Z

Zaikovskii, V. I., 333

Zettl, A., 32, 47, 183, 379

Zhang, P., 364

Zhao, X., 179, 328

Zhou, O., 278

Zhu, X.-M., 416

Zubavichus, Y. V., 191

Züttel, A., 462